frontiers | Research Topics

10 Years of frontiers in energy research

Edited by
Uwe Schröder, Zhongyang Luo, David Howe Wood, Covadonga Pevida, Hailong Li, Haiping Yang, Yogendra Kumar Mishra, Ah-Hyung Alissa Park, Ellen B. Stechel, Fanglin Chen, Andreas Borgschulte, Felice Arena, Michael Carbajales-Dale, Sheng S. Zhang, Michael Folsom Toney, Shripad T. Revankar, Kui Jiao, Francois M. A. Marechal, ZhaoYang Dong, S. M. Muyeen and Anil Pahwa

Published in
Frontiers in Energy Research

ISSN 1664-8714
ISBN 978-2-8325-6470-7
DOI 10.3389/978-2-8325-6470-7

About Frontiers

Frontiers is more than just an open access publisher of scholarly articles: it is a pioneering approach to the world of academia, radically improving the way scholarly research is managed. The grand vision of Frontiers is a world where all people have an equal opportunity to seek, share and generate knowledge. Frontiers provides immediate and permanent online open access to all its publications, but this alone is not enough to realize our grand goals.

Frontiers journal series

The Frontiers journal series is a multi-tier and interdisciplinary set of open-access, online journals, promising a paradigm shift from the current review, selection and dissemination processes in academic publishing. All Frontiers journals are driven by researchers for researchers; therefore, they constitute a service to the scholarly community. At the same time, the *Frontiers journal series* operates on a revolutionary invention, the tiered publishing system, initially addressing specific communities of scholars, and gradually climbing up to broader public understanding, thus serving the interests of the lay society, too.

Dedication to quality

Each Frontiers article is a landmark of the highest quality, thanks to genuinely collaborative interactions between authors and review editors, who include some of the world's best academicians. Research must be certified by peers before entering a stream of knowledge that may eventually reach the public - and shape society; therefore, Frontiers only applies the most rigorous and unbiased reviews. Frontiers revolutionizes research publishing by freely delivering the most outstanding research, evaluated with no bias from both the academic and social point of view. By applying the most advanced information technologies, Frontiers is catapulting scholarly publishing into a new generation.

What are Frontiers Research Topics?

Frontiers Research Topics are very popular trademarks of the *Frontiers journals series*: they are collections of at least ten articles, all centered on a particular subject. With their unique mix of varied contributions from Original Research to Review Articles, Frontiers Research Topics unify the most influential researchers, the latest key findings and historical advances in a hot research area.

Find out more on how to host your own Frontiers Research Topic or contribute to one as an author by contacting the Frontiers editorial office: frontiersin.org/about/contact

10 Years of frontiers in energy research

Topic editors
Uwe Schröder — University of Greifswald, Germany
Zhongyang Luo — Zhejiang University, China
David Howe Wood — University of Calgary, Canada
Covadonga Pevida — Institute of Carbon Science and Technology (INCAR), Spain
Hailong Li — Central South University, China
Haiping Yang — Huazhong University of Science and Technology, China
Yogendra Kumar Mishra — University of Southern Denmark, Denmark
Ah-Hyung Alissa Park — University of California, Los Angeles, United States
Ellen B. Stechel — Arizona State University, United States
Fanglin Chen — University of South Carolina, United States
Andreas Borgschulte — Swiss Federal Laboratories for Materials Science and Technology, Switzerland
Felice Arena — Mediterranea University of Reggio Calabria, Italy
Michael Carbajales-Dale — Clemson University, United States
Sheng S. Zhang — United States Army Research Laboratory, United States
Michael Folsom Toney — University of Colorado Boulder, United States
Shripad T. Revankar — Purdue University, United States
Kui Jiao — Tianjin University, China
Francois M. A. Marechal — Swiss Federal Institute of Technology Lausanne, Switzerland
ZhaoYang Dong — City University of Hong Kong, Hong Kong, SAR China
S. M. Muyeen — Qatar University, Qatar
Anil Pahwa — Kansas State University, United States

Citation
Schröder, U., Luo, Z., Wood, D. H., Pevida, C., Li, H., Yang, H., Mishra, Y. K., Park, A.-H. A., Stechel, E. B., Chen, F., Borgschulte, A., Arena, F., Carbajales-Dale, M., Zhang, S. S., Toney, M. F., Revankar, S. T., Jiao, K., Marechal, F. M. A., Dong, Z., Muyeen, S. M., Pahwa, A., eds. (2025). *10 Years of frontiers in energy research*. Lausanne: Frontiers Media SA. doi: 10.3389/978-2-8325-6470-7

Table of contents

frontiers | Frontiers in Energy Research

TYPE Editorial
PUBLISHED 04 June 2025
DOI 10.3389/fenrg.2025.1633889

OPEN ACCESS

EDITED AND REVIEWED BY
Haiping Yang,
Huazhong University of Science and Technology, China

*CORRESPONDENCE
Hailong Li,
hailong_li@126.com

RECEIVED 23 May 2025
ACCEPTED 29 May 2025
PUBLISHED 04 June 2025

CITATION
Li H (2025) Editorial: 10 Years of frontiers in energy research.
Front. Energy Res. 13:1633889.
doi: 10.3389/fenrg.2025.1633889

Editorial: 10 Years of frontiers in energy research

Hailong Li*

School of Energy Science and Engineering, Central South University, Changsha, Hunan, China

KEYWORDS

energy research, sustaianability, renewable energy, energy management, carbon nuetrality

Editorial on the Research Topic
10 Years of frontiers in energy research

As Frontiers in Energy Research marks its 10th anniversary, we reflect on a transformative decade defined by groundbreaking discoveries, interdisciplinary collaboration, and global efforts to address humanity's most pressing energy challenges. Since its inception, this journal has served as a beacon for cutting-edge research, bridging the gaps challenging the sustainable developments and technological advances of energy. This commemorative issue not only celebrates our shared achievements but also underscores the urgency of accelerating the energy transition in an era of climate imperatives and technological revolutions. In the following pages, we invite readers to explore visionary contributions that redefine possibilities for a sustainable future.

From theoretical frameworks to practical applications, this issue exemplifies the multi-scale approach required for energy innovation. Campbell et al. comprehensively examined the concept of emergy as a thermodynamic metric for evaluating ecological and social systems, emphasizing its role in quantifying evolutionary competitiveness through the principle of 'maximum empower'. Their white-box Geobiosphere model refines emergy accounting through spatiotemporal boundary expansion, proposing blockchain-enhanced platforms to improve global ecosystem management via standardized thermodynamic benchmarking. Complementing this systems-level perspective, Kowalski et al. addressed electronic correlation challenges in energy materials through advanced computational methods. Their work demonstrates how DFT + U approaches with Hubbard U parameters enable accurate predictions of metal oxide properties, bridging theoretical simulations with electrochemical energy storage design.

The transition from theoretical foundations to material innovation finds expression in Sankarasubramanian et al. analysis of titanium-based redox flow batteries. With 50-fold greater crustal abundance and 90% lower cost than vanadium, titanium systems emerge as high-potential alternatives for grid-scale storage (Sankarasubramanian et al.), contingent upon advancements in catalyst development. Expanding the electrocatalyst frontier, Santos et al. reviewed transition metal-based alternatives to precious metal catalysts. Their analysis highlights how polyoxometalates and metal-organic frameworks enhance catalytic activity while reducing reliance on scarce materials, accelerating sustainable energy conversion.

Bioenergy innovations demonstrate nature-inspired solutions across multiple scales. Igathinathane et al. quantified break-even transportation distances for 14 biomass

feedstocks, revealing ship transport's superiority through large cargo capacities and steady operations. Building on biomass logistics, Chundawat et al. engineered supercharged enzymes to overcome lignin inhibition in bioethanol production. Their work on ammonia-pretreated corn stover reveals strategic protein modification as key to high-temperature biorefining. Ieropoulos et al. further extended biomass applications through microbial fuel cells that convert organic matter to electricity, showcasing microalgae's potential for carbon-neutral energy cycles despite persistent cultivation challenges.

Dynamic energy management emerges as critical in evolving consumption landscapes. Ali et al.'s ANFIS2 model demonstrated 45% error reduction in pandemic-era residential energy use forecasting, providing adaptive frameworks for uncertain environments. Zhang et al. further addressed pandemic impacts through EV charging load models responsive to public health crises, capturing load shifts between outbreak/non-outbreak periods via dynamic feature integration. For grid-scale optimization, Lai et al. developed storage dispatch strategies for China's deregulated power markets, balancing renewable integration with multi-market revenue streams. Pahwa et al. reinforced the economic imperative for PV-battery hybrids, showing how integrated systems offset efficiency losses through peak demand reduction.

Converging technological and policy dimensions, Naqvi et al. synthesized the evolution of net-zero emissions and circular economy paradigms. Their analysis of carbon capture innovations and policy frameworks like the EU Green Deal underscores the need for context-specific solutions to bridge technical potential with socio-economic realities.

In summary, the Research Topic of 10 Years of Frontiers in Energy Research highlights scientific and technological advancements of energy conversion, use, and management. We sincerely thank authors, reviewers, and readers. Together, we will continue pioneering sustainable solutions to global energy challenges.

Author contributions

HL: Writing – original draft, Writing – review and editing.

Funding

The author(s) declare that no financial support was received for the research and/or publication of this article.

Conflict of interest

The author declares that the research was conducted in the absence of any commercial or financial relationships that could be construed as a potential conflict of interest.

The author(s) declared that they were an editorial board member of Frontiers, at the time of submission. This had no impact on the peer review process and the final decision.

Generative AI statement

The author(s) declare that no Generative AI was used in the creation of this manuscript.

Publisher's note

frontiers | Frontiers in Energy Research

TYPE Mini Review
PUBLISHED 10 October 2022
DOI 10.3389/fenrg.2022.1021201

OPEN ACCESS

EDITED BY
Sheng S. Zhang,
United States Army Research Laboratory, United States

REVIEWED BY
Yuxun Ren,
University of Maryland, United States

*CORRESPONDENCE
Shrihari Sankarasubramanian,
Shrihari.sankarasubramanian@utsa.edu

†These authors have contributed equally to this work

SPECIALTY SECTION
This article was submitted to Electrochemical Energy Conversion and Storage, a section of the journal Frontiers in Energy Research

RECEIVED 17 August 2022
ACCEPTED 21 September 2022
PUBLISHED 10 October 2022

CITATION
Ahmed SIU, Shahid M and Sankarasubramanian S (2022), Aqueous titanium redox flow batteries—State-of-the-art and future potential. *Front. Energy Res.* 10:1021201. doi: 10.3389/fenrg.2022.1021201

Aqueous titanium redox flow batteries—State-of-the-art and future potential

Sheikh Imran Uddin Ahmed[1†], Mohamed Shahid[1,2†] and Shrihari Sankarasubramanian[1,3,4*]

[1]Department of Biomedical Engineering and Chemical Engineering, University of Texas at San Antonio, San Antonio, TX, United States, [2]Department of Chemical Engineering, University of Petroleum and Energy Studies, Dehradun, India, [3]NASA MIRO Center for Advanced Measurements in Extreme Environments (CAMEE), University of Texas at San Antonio, San Antonio, TX, United States, [4]Texas Sustainability Research Institute (TSERI), University of Texas at San Antonio, San Antonio, TX, United States

Market-driven deployment of inexpensive (but intermittent) renewable energy sources, such as wind and solar, in the electric power grid necessitates grid-stabilization through energy storage systems Redox flow batteries (RFBs), with their rated power and energy decoupled (resulting in a sub-linear scaling of cost), are an inexpensive solution for the efficient electrochemical storage of large amounts of electrical energy. Titanium-based RFBs, first developed by NASA in the 1970s, are an interesting albeit less examined chemistry and are the focus of the present review. Ti, constituting 0.6% of the Earth's crust and an ingredient in inexpensive white paints, is amongst the few elements (V and Mn being some others) which exhibit multiple soluble oxidation states in aqueous electrolytes. Further, the very high (approaching 10 M) solubility of Ti in low pH solutions suggests the possibility of developing exceptionally high energy density aqueous Redox Flow Batteries systems. With these advantages in mind, we present the state-of the-art in Ti-RFBs with a focus on Ti/Mn, Ti/Fe and Ti/Ce couples and systems that use Ti as an additive (such as Ti/V/Mn). The inherent advantages of inexpensive Ti actives and relatively high energy density is contrasted with potential side-reactions resulting in reduced energy efficiency. Technological pathways are presented with a view to overcoming critical bottlenecks and a vision is presented for the future development of Ti-RFBs.

KEYWORDS

energy storage, redox flow batteries, titanium, kinetics, solvation, energy storage (batteries)

1 Introduction

The rapid, market-driven deployment of economical but intermittent renewable energy sources such as solar and wind necessitates the integration of reliable energy storage solutions with the electric grid to ensure grid stability and reliability. Amongst various energy storage technologies redox flow batteries (RFBs) are an economical solution at scale due to their characteristic decoupling of energy and power that

ensures sublinear scaling of cost (Chen et al., 2009; Zhao et al., 2015). A plethora of possible RFBs have been investigated and proposed in the literature, such as, Fe-X (X = Cr, Mn, Fe, Zn) (Fedkiw and Watts, 1984; Skyllas-Kazacos et al., 2011; Gong et al., 2016; Selverston et al., 2017; Archana et al., 2020; Zhen et al., 2020), V-X (X = Mn, Ce, Br, V) (Chen et al., 2009; Prifti et al., 2012; Cunha et al., 2015; Zhao et al., 2015; Sankarasubramanian et al., 2019; Reynard et al., 2020; Raja et al., 2021; Wang et al., 2021) and Zn-X (X = Ce, Br, Mn, V) (Chen et al., 2009; Leung et al., 2011; Dewage et al., 2015; Zhao et al., 2015; Jiang et al., 2018; Ulaganathan et al., 2019; Naresh et al., 2021) RFBs. Critically, the translation of these RFBs to the market hinges on numerous factors, namely - 1) cell potential, 2) energy density (a function of salt solubility in the electrolyte), 3) chemical and electrochemical stability of the cell components, and finally (and possibly most importantly) 4) availability of the redox active species at low marginal cost and at scale. The energy storage cost of RFBs hinges on the cost of the electrolyte actives and their degradation and loss during operation. The loss of electrolyte due to crossover results in poor coulombic efficiency at the system level and hinders economical operation. The crossover of electrolyte species is largely determined by the nature of the separator employed. Three classes of separators are typically encountered in RFBs i.e., cation exchange membrane (CEM), anion exchange membrane (AEM), and porous membrane (PM) (Varcoe et al., 2014; Barry et al., 2021). The two classes of ion exchange membranes operate on the principle of charge-based repulsion and hence exclusion of redox active species. Selectivity is conferred by the nature of the charged species attached to the separator backbone and density of these species. Porous separators, on the other hand, rely on size-based exclusion of redox active species. Here, ionic species and chemical species in solution (irrespective of charge) are prevented from crossing over on the basis of their size relative to the pores across the separator. CEMs (typically Nafion®) are relatively expensive and exhibit high ionic conductivity. Given that most RFBs utilize cationic redox species, the use of CEMs in these systems results in cation cross-over and hence a drastic reduction in capacity over time (Gubler, 2019). This makes CEMs suitable only for systems employing catholytes and anolytes consisting of different oxidation states of the same chemical species (e.g., V^{2+}/V^{3+} and V^{4+}/V^{5+} in all-V RFBs). AEMs, on the other hand, mitigate cation crossover but typically exhibit lower ionic conductivity and chemical stability compared to CEMs (Barry et al., 2021). PMs allow the cross-over of the ions that have smaller diameter than the pore size of the separator irrespective of the nature of the charge they carry and hence show poor ion selectivity (Lu et al., 2017). All separators may require mechanical rebalancing to adjust the osmotic pressure (Bhattarai et al., 2019) and chemical rebalancing to maintain electrolyte purity (Wu et al., 1983; Fedkiw and Watts, 1984).

All-V RFBs are the farthest along the commercialization route and have been reported to operate at typical power densities of 100 mW cm^{-2} with cycle life of 10–15 years with 1000 cycle per year (Holland-Cunz et al., 2018). A recent study has reported small, lab-scale (4cm^2 electrode area, 20 ml catholyte and anolyte) all-V RFB operating for ~20,000 cycles at 600 mA cm^{-2} (>8 months) (Jiang et al., 2020). Despite concerns stemming from component degradation while operating at such current densities, the demonstration of similar cycle life (even at lower current density) at a practical, pilot scale would be a major advancement in commercializing all-V RFBs. Although the V-X family of RFBs are quite successful in terms of providing high power densities with stability, the availability of V in the earth's crust and its susceptibility to degradation during cycling is a limiting factor for successful industrialization. On the other hand, the Ti-X (X = Fe, Mn, Ce) family of RFBs offer several advantages over the V-X systems as -

1) Ti is *ca* 50x as abundant as V in the Earth's crust and is produced at *ca* 100x the rate of V (Figures 1A,B).
2) The market price of Ti is 1/10th that of V in the US (Figures 1A,B).
3) The half-cell potential of Ti^{4+}/Ti^{3+} redox couple is 0.1 V (vs SHE) as compared to -0.26 V (vs SHE) for V^{3+}/V^{2+} which makes Ti^{4+}/Ti^{3+} redox couple less prone to hydrogen evolution side reactions (Figure 1C).
4) The maximum possible storage capacity of Ti-Ce RFBs would be 9.9 TWh as compared to 6.95 TWh for all-V RFBs considering all exploitable worldwide reserves of V, Ti, and Ce.
5) The Ti-X (X = Fe, Mn, Ce) RFBs also meets the DOE cost target of <100 $/kWh (Dong et al., 2015; Kaku et al., 2016; Funding opportunity announcement advanced research projects agency, 2016; Kaku et al., 2019; Sankarasubramanian et al., 2021).

Given these advantages, in this work we critically review the developmental state of Ti-X RFBs and chart a course for their future development.

2 The Ti-X (X = Fe, Mn, Ce) family of RFBs

A schematic representation of Ti-X RFBs is shown in Figure 1D. The anolyte is the Ti salt dissolved in an acid and the catholytes are either Fe or Mn or Ce dissolved in their appropriate acidic counterparts. As discussed in literature, the oxidation states of Ti vary from +2 to +4 and the Ti ions exist stable in the salts as Ti^{3+} (+3 oxidation state), and TiO^{2+} (+4 oxidation state) but not as Ti^{2+}. Their stability is confined to a very narrow region i.e., ~1 pH and lesser, as seen in the Pourbaix diagram (Pourbaix, 1966). $TiOSO_4$ (titanium

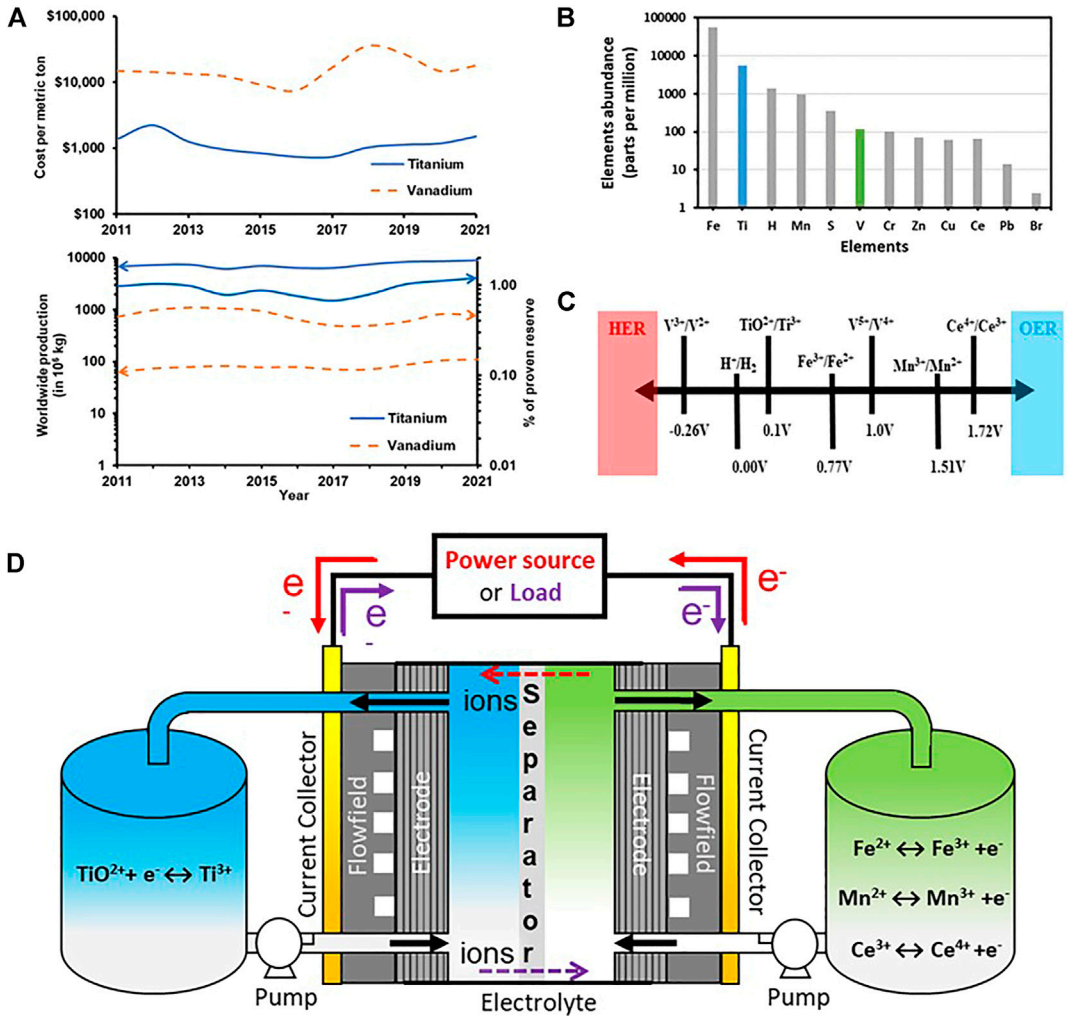

FIGURE 1
(A) Cost per metric ton, worldwide production, and proven reserves of Ti, and V; **(B)** Abundance of Ti in the Earth crust **(C)** Half-cell potentials (vs SHE); for some redox couple for possible use in RFBs; **(D)** Schematic diagram of Ti- X (X = Fe, Mn, Ce) RFBs.

oxysulfate) and $TiCl_3$ (titanium chloride) with Ti in +4 and +3 oxidation state are the most widely used salts for Ti-X RFBs with supporting electrolytes including H_2SO_4, HCl, HNO_3 and H_3PO_4. Thus, the solvation and coordination of Ti species in the strong acidic electrolytes influences the reversibility and stability of the Ti^{4+}/Ti^{3+}redox couple and impacts the energy density of the Ti-X RFBs. The following section summarizes Ti solution chemistry in the context of RFBs.

2.1 Ti^{4+}complexes in acids

Extensive literature report (Lingane and Kennedy, 1956; Miyanaga et al., 1990; Kavan et al., 1993; Cservenyák et al., 1996; Sole, 1999; Bahdad, 2020; Tsurumura et al., 2020; Choe et al., 2021) the solvation behavior of Ti^{4+}/Ti^{3+} redox couple with different ligands in various acids solutions like H_2SO_4, HCl, HNO_3 and H_3PO_4. The redox stability of Ti^{4+}/Ti^{3+} is influenced by the formation of different reaction/intermediate complexes that appear in various acids as discussed below. Critically, we are considering only strong mineral acids in our discussion given that the Ti^{4+}/Ti^{3+} redox couple is stable only in low pH (< *ca* pH 1.5) conditions.

2.1.1 The H_2SO_4 system

In case of H_2SO_4 solution comprising dissolved $TiOSO_4$ salt, hereafter called the Ti-O-SO_4 system, the half-cell reaction is represented by the following equation,

$$Ti^{3+} + H_2O \rightleftharpoons TiO^{2+} + 2H^+ + e^- \quad (1)$$

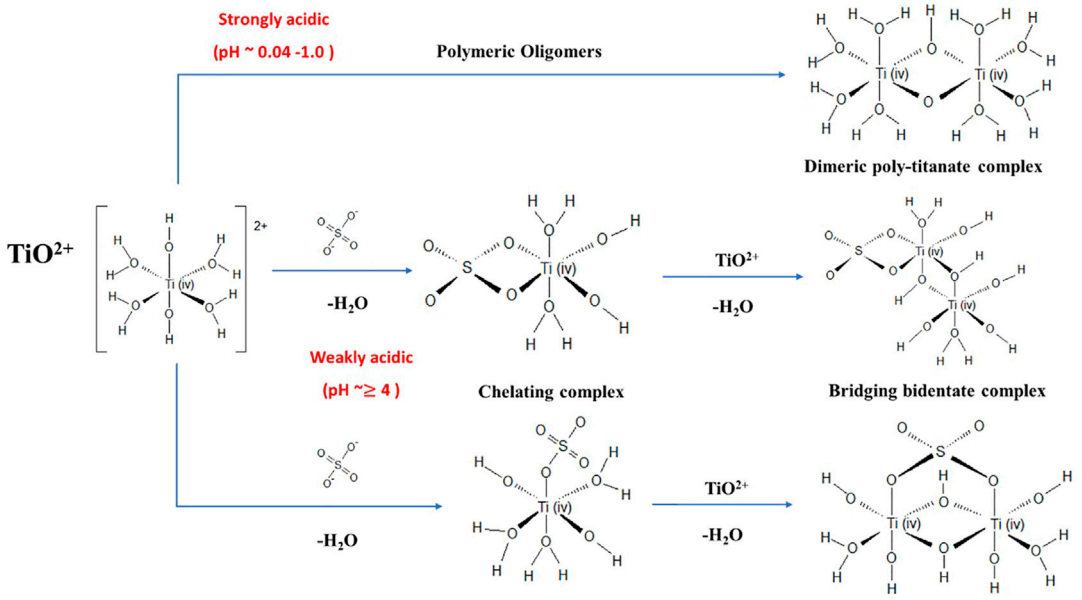

FIGURE 2
Schematic representation of various Ti^{4+} complexes under weakly and strongly acidic conditions.

The Ti^{3+} and Ti^{4+} (i.e., as TiO^{2+}) species of the redox couple co-exist in the concentrated Ti-SO_4 system. Ti^{4+} is the most stable oxidation state of Ti. The high charge density (ratio of charge to ionic radius) of Ti^{4+} prevents it from forming simply hydrated $[Ti(H_2O)_6]^{4+}$ (Miyanaga et al., 1990). Ti^{4+} appears as $[Ti(OH)_2(H_2O)_4]^{2+}$ in 1 M H_2SO_4 aqueous solutions (Bahdad, 2020) and in solutions where 0.04 < pH < 1 (Beukenkamp and Herrington, 1960; Kotsyubynsky et al., 2017), represented in short as TiO^{2+}. These TiO^{2+} complexes tend to form oligomers (Figure 2A) when the oxo-oxygen of the titanyl ion is readily protonatable through hydrolysis reactions (Shepherd, 2013). The formation of oligomers is predominant when the concentration of TiO^{2+} is between 0.1–0.5 M, the H^+ concentration between 1.0–2.5 M, and the temperature between 236–323 K (Comba and Merbach, 1987). In the presence of H^+, SO_4^{2-} and HSO_4^-–ions (H_2SO_4 dissociation products in an aqueous solution (Choe et al., 2021)), Ti^{4+} forms complexes containing SO_4^{2-} or HSO_4^- ligands exhibiting the possible structures shown in Figure 2B. The competing coordination of Ti^{4+} to SO_4^{2-} or HSO_4^- depends on the strength of SO_4^{2-} concentration in the electrolyte [for e.g., 3 M H_2SO_4 concentration results in the dominance of Ti^{4+} to SO_4^{2-} coordination (Bahdad, 2020)]. The coordination of HSO_4^- with Ti^{4+} proceeds through a deprotonation pathway wherein H^+ is accepted by a proton acceptor such as H_2O to form H_3O^+ or Ti=O^+ to form Ti-OH SO_4^{2-} and a Ti^{4+}-SO_4^{2-} complex results. At higher SO_4^{2-} concentrations (and higher pH values), Ti^{4+} is predicted to exist as either mononuclear complexes (chelating complexes) or multinuclear complexes (bridging bidentate complexes) (Kotsyubynsky et al., 2017). Mononuclear complexes are formed by the coordination of Ti^{4+} ion with SO_4^{2-} leading to formation of $[Ti(OH)_2SO_4(H_2O)_3]^0$, $[Ti(OH)_2(SO_4)_2(H_2O)_2]^{2-}$ and $[Ti{=}O(OH)_2(H_2O)_3]^0$. The multinuclear complexes are formed either due to polymerized Ti^{4+} complexes formed *via* oxygen atoms leading to -Ti-O-Ti-O- zigzag structures (Tsurumura et al., 2018) or *via* formation of $[Ti_2O_2(H_2O)_5(OH)_2SO_4]$ (Choe et al., 2021). These Ti^{4+} complexes are either electrically neutral or anionic in the Ti-O-SO_4 system under high pH conditions. Ti^{4+} tends to form multinuclear complexes (nanoscale aggregates) in solutions of high SO_4^{2-} and Ti^{4+} concentrations which eventually results in the nucleation and precipitation to TiO_2. Thus, high pH conditions (typically with high SO_4^{2-} concentrations and low H^+ concentration) are to be avoided when designing electrolytes for Ti RFBs.

Upon electrochemical reduction of Ti^{4+} to Ti^{3+}, there occurs substantial change in the structures of Ti-ion complexes and nanoscale Ti^{4+} aggregates are gradually disrupted to yield mononuclear Ti^{3+} complexes (Tsurumura et al., 2020). The Ti^{3+} ion is stable at very low pH (< *ca* 1.5) as seen through Pourbaix diagram. In dilute (higher pH) aqueous solutions, Ti^{3+} usually exists in the form of $[Ti(H_2O)_6]^{3+}$. Literature also report using EXAFS (Extended X-ray Absorption Fine Structure) analysis, that Ti-Ti bond does not exist in Ti^{3+} solution, and the possibility for Ti-O bond exists in Ti^{3+} solution (Miyanaga et al., 1990) with Ti^{3+} ions existing in various other forms in aqueous solutions as $Ti(OH)^{2+}$, TiO^+, $Ti(OH)_2^+$, and other complexes (Sole, 1999). However, with

H_2SO_4 solution, Ti^{3+} react with SO_4^{2-} ion to form Ti^{3+}-SO_4^{2-} complexes (Cservenyák et al., 1996).

2.1.2 The HCl system

In case of HCl solutions containing $TiCl_3$ salt, both the H^+, and Cl^- ions play a significant role in the reversibility of Ti^{4+}/Ti^{3+} redox couple. Ti^{3+} exist as a $TiOH^{3+}$ complex in acidified solutions (pH 2–2.5) and, due to hydrolysis of Ti^{3+}, $Ti(OH)_2^{2+}$ is formed with proton liberation as shown below (Kavan et al., 1993; Lokhande et al., 2004),

$$TiOH^{3+} + H_2O = Ti(OH)_2^{2+} + H^+ \ (Fast\ Reaction) \quad (2)$$

$$Ti(OH)_2^{2+} \rightarrow Ti(IV)oxo\ species + e^- \rightarrow TiO_2(Undesired\ side\ reaction) \quad (3)$$

Unfortunately, $Ti(OH)_2^{2+}$ leads to the formation of TiO_2 by precipitation as shown above, through an intermediate Ti(iv)oxo species which limits the reversibility of the redox couple. The Ti(iv)oxo species consist of partly dehydrated polymeric Ti(IV) hydroxide (Kavan et al., 1993), which get converted to TiO_2 (Lokhande et al., 2005). The Ti^{4+} ions in HCl exist in the form of $TiOCl^+$, an oxy-chloro ion which reduces to a Ti^{3+} chloro complex, $TiCl_4^-$ as shown below,

$$TiOCl^+ + e^- + 2H^+ + 3Cl^- = TiCl^{4-} + H_2O \quad (4)$$

The Ti^{3+}/Ti^{4+} redox couple was found to be reversible only in >1 M HCl solution. The irreversibility observed in <1 M HCl solutions indicates the necessity of Cl^- ion for the reversibility of Ti^{4+} and Ti^{3+} as shown in Eq. 4 (Lingane and Kennedy, 1956). In the presence of HCl and H_2O, Ti^{4+} ions form unstable $[Ti(OH)_2(H_2O)_4]Cl_2$ which eventually results in the formation of TiO_2. In the context of RFBs requiring high reversibility of the Ti^{4+}/Ti^{3+} redox couple, addition of (unfortunately unstable) organic compounds with oxygen-containing functional groups, such as acetylacetone, can partially suppress the hydrolysis reaction owing to the affinity between TiO^{2+} and oxygen-containing functional groups (Wang et al., 1984). HCl concentrations up to 6 M have been found to mitigate the precipitation of TiO_2 (Qiao et al., 2022). However, it enhances H^+ concentration in the electrolyte and accelerates another undesired side reaction, namely the hydrogen evolution reaction (HER), thereby decreasing the RFB efficiency. The choice of the catholyte to be paired with the Ti anolyte can also preclude the use of HCl supporting electrolytes due to the occurrence of the chlorine evolution reaction (+1.36V vs. SHE).

2.1.3 The HNO_3 system

In case of HNO_3 solutions containing $TiOSO_4$, the salt dissolves as small clusters as observed through Small-angle X-ray scattering (SAXS) experiments (Molina et al., 2017). The analysis of $TiOSO_4$ dissolved in 1 M HNO_3 solution, suggests that the clusters contain a dense 1.2 nm diameter core (dominated by Ti–oxo) with a dynamic shell of water, sulfate, and nitrate which also results in precipitation for any dilution below 0.25 M $TiOSO_4$ (Molina et al., 2017). No complexation of Ti^{4+} was observed in dilute HNO_3 solutions (0.73–2.2 $mM.L^{-1}$) with 0.05 $mM.L^{-1}$ ortho-titanic acid (TiH_4O_4) due to their weak tendency to form nitrato complexes with most metal ions (Morris et al., 1978). This is markedly different from the formation of divalent mononuclear species like $[Ti(OH)_2]^{2+}$ in H_2SO_4 solutions (Mangold et al., 2021). But, however HNO_3 is not actively used as supporting electrolyte due to the reduction of NO^{3-} leading to degraded performance during cycling in RFBs (Xie et al., 2011a).

2.1.4 The H_3PO_4 system

Studies with H_3PO_4 solutions containing Ti salts are very scarce in the literature (Lingane and Kennedy, 1956; Oldenburg et al., 2018; Mangold et al., 2021) as the solubility and stability of Ti^{4+} ions in these systems is a practical limitation (Lingane and Kennedy, 1956). The reversibility of Ti^{4+}/Ti^{3+} redox couple and their stability was studied under different concentrations (1–10 M) of H_3PO_4 with 10 mM and lower concentrations of Ti^{4+} [as the $Ti(OH)_4$ salt]. It was found that a 10 mM solution of Ti^{4+} ions in 1M H_3PO_4 was unstable and precipitated after 24 h but stabilized in 4M H_3PO_4 without any phase separation. But upon increasing the Ti^{4+} ion concentrations to >10 mM, the electrolyte was again unstable in 4M H_3PO_4 leading to precipitation. Interestingly, the reversibility of Ti^{4+}/Ti^{3+} redox couple is more pronounced at 1M H_3PO_4 as compared to 4M H_3PO_4 (Shepherd, 2013). In this electrolyte system, Ti^{4+} is present as mononuclear ($\mu = 1$) or polynuclear ($\mu > 1$) free cation(s), $[(TiO)_\mu]^{2\mu+}$ in diluted H_3PO_4 solutions (<0.1 $mol.L^{-1}$). Ti^{4+} ions progressively form $[(TiO)_\mu(H_{3-m}PO_4)_\delta]^{2\mu-\delta m}$ complexes as the concentration of H_3PO_4 is increased to >1 $mol.L^{-1}$ and $[(TiO)_\mu(H_{3-m}PO_4)_\delta(H_{3-n}PO_4)_\beta]^{2\mu-\delta m-\beta n}$ complexes at >6 $mol.L^{-1}$ H_3PO_4 (Mangold et al., 2021). The poor solubility and reversibility of Ti solutions in H_3PO_4 precludes their use in RFBs.

2.2 Performance of Ti RFBs

Given the discussion above, reports on the Ti-X family of RFBs consist predominantly of systems using H_2SO_4 as the supporting electrolyte due to the stability and reversibility of the Ti^{4+}/Ti^{3+} redox couple at relatively high Ti concentrations (~0.5–1.5 M). This configuration also avoids any side reactions (H_2-, Cl_2-, and NO_2- evolution) thereby increasing the overall energy efficiency of the RFBs.

Ti - Fe RFB: Fe based RFBs (coupled with Ti or Cr) have been widely investigated by NASA in the early 1970s due to the low cost and abundant supply of Fe. These RFBs can achieve a theoretical energy density of nine Wh. L^{-1} (at 0.67V open circuit potential (OCP)). Cr-Fe RFBs was initially assessed for space applications and scale-up studies were conducted, but the system was not commercially developed due to several drawbacks

like, low energy density of the mixed electrolyte (containing both Fe and Cr in the anolyte and catholyte), membrane fouling, the slow Cr redox kinetics requiring expensive noble metal catalysts and parasitic HER on the Cr side (Skyllas-Kazacos et al., 2011). The Ti-Fe RFBs was studied by Thaller in aqueous HCl solution (Thaller and inventor, 1976). In this system, during the charge cycle, Ti^{4+} (i.e., TiO^{2+}) reduced to Ti^{3+} on the negative side and Fe^{2+} is oxidized to Fe^{3+} in positive side. The half-cell charge reactions of the Ti-Fe RFB are,

$$Negative\ Electrode:\ TiO^{2+} + 2H^{+} + e^{-} \rightleftharpoons Ti^{3+} + H_2O\,(+0.1V\ vs\ SHE) \quad (5)$$

$$Positive\ Electrode:\ Fe^{2+} \rightleftharpoons Fe^{3+} + e^{-}\,(-0.771V\ vs\ SHE) \quad (6)$$

Initially, $TiCl_3$ and $FeCl_3$ were the salts used at the anolyte and catholyte respectively in the HCl supported electrolytes. This system suffered from the formation of TiO_2 particles as an undesired side reaction, decreasing the overall coulombic efficiency. The maximum current density of these initial Ti-Fe RFBs with HCl supporting electrolyte was 8.16–14 $mAcm^{-2}$ with a nominal cell voltage around 0.67V (Savinell et al., 1979). Recent improvements in Ti-Fe RFBs have consisted of using H_2SO_4 as supporting electrolyte instead of HCl and using $TiOSO_4$ and $FeSO_4$ salts in the anolyte and catholyte respectively. In the presence of H_2SO_4, the interaction between H_2O and Ti^{4+} ions are diminished, thereby inhibiting the formation of $Ti(OH)_2{}^{2+}$ and improving the stability of the electrolyte. Such as second generation Ti-Fe RFB with bismuth (Bi) catalyst at the positive electrode and a carbon felt at the negative electrode exhibited a diffusion coefficient of $19.18\times10^{-8}cm^2\ s^{-1}$ for Fe^{3+}/Fe^{2+} and $0.36\times10^{-8}cm^2\ s^{-1}$ for Ti^{4+}/Ti^{3+} (Qiao et al., 2022) with a rate constant of $3.828\times10^{-4}cm\ s^{-1}$ for Fe^{3+}/Fe^{2+} and $0.203\times10^{-4}cms^{-1}$ for Ti^{4+}/Ti^{3+} respectively (Qiao et al., 2022). It suggests that both the diffusion coefficient and rate constant for Fe^{3+}/Fe^{2+} is higher than Ti^{4+}/Ti^{3+} with the reactions of Ti redox couple being rate limited. The Ti-Fe RFBs in 3M H_2SO_4 were cycled at current densities as high as 120 $mAcm^{-2}$ with the highest energy efficiency of 85.6% (at 40 $mAcm^{-2}$). This system showed 80% discharge capacity after 1000 cycles (30 min per cycle) with a low-capacity decay of 0.193 Ah. $cycle^{-1}$ (Qiao et al., 2022). CEMs like Nafion® 212, sulfonated poly (ether ketone) (SPEEK) have been used in Ti-Fe RFB. Non-fluorinated SPEEK is predominantly used as it reduces the cost for energy production from $165.79/kWh (Nafion® 212) to $88.22/kWh (SPEEK) (Qiao et al., 2022).

Ti-Mn RFB: Ti-Mn RFBs was first developed by Dong et al, (2012) where a relatively high OCP of 1.41 V was obtained (as compared to 0.67 V for Ti-Fe RFBs) resulting in superior power density (Dong et al., 2015; Kaku et al., 2016). These RFBs can achieve a theoretical energy density of 18.9 Wh. L^{-1}. The half-cell charge redox reactions of Ti-Mn RFB are represented by the following equations.

$$Negative\ Electrode:\ TiO^{2+} + 2H^{+} + e^{-} \rightleftharpoons Ti^{3+} + H_2O\,(+0.1V\ vs\ SHE) \quad (7)$$

$$Positive\ Electrode:\ Mn^{2+} \rightleftharpoons Mn^{3+} + e^{-}\,(-1.51V\ vs\ SHE) \quad (8)$$

Unfortunately, Mn^{3+} is highly unstable and inclined to form manganese dioxide (MnO_2) *via* the following reaction-

$$2Mn^{3^{+}} + 2H_2O \rightarrow Mn^{2^{+}} + MnO_2 + 4H^{+}\,(Disproportionation\ Reaction) \quad (9)$$

The precipitated MnO_2 particles start to aggregate and hinder the flow of electrolyte by blocking the pores of the membrane thereby reducing the columbic efficiency. So, it is required to reduce the formation of MnO_2 particles as well as to ensure that the MnO_2 particle are small enough to avoid aggregation and prevent membrane fouling (Kaku et al., 2016). Several approaches have been proposed for stabilization of Mn^{3+} such as by increasing the acidity, by increasing the Mn^{2+} concentration, or *via* complex formation (Davies, 1969). However, increasing Mn^{2+} concentration necessitates limiting the cycling of the cell to only 50% state of charge (SOC) to prevent Mn^{3+} disproportionation, thereby negating any advantages due to increased reactant concentration. On the other hand, the formation of Mn complexes (i.e., MnOOH) results in loss of electro-activity (Dong et al., 2015; Bahdad et al., 2021).

$$MnO_2 + H^{+} + e^{-} \rightarrow MnOOH \quad (10)$$

The disproportionation reaction and the morphology of MnO_2 were significantly influenced by addition of H_2SO_4 solution containing TiO^{2+} ions (Kaku et al., 2016). $TiOSO_4$ solutions of varying molarities was added to 1M $MnSO_4$ and the characteristic of the composite electrolyte was studied in the context of suppressing the disproportionation of Mn^{3+} ions. The MnO_2 aggregates were found to be > 1000 nm without adding $TiOSO_4$ or with the addition of 0.25M $TiOSO_4$ in $MnSO_4$. The particles size reduced to less than 100 nm with addition of 0.5M–1M of $TiOSO_4$ in $MnSO_4$ (Kaku et al., 2016). The optimal composition of 1.5 M $TiOSO_4$ in the 1 M $MnSO_4$ electrolyte improved the performance of the Ti-Mn RFB in terms of energy density to achieve ~11.75 Wh. L^{-1} (accounting for the electrolyte in both tanks) with coulombic efficiency of 99.8% and energy efficiency of 88.7%, both of which were stable over 40 cycles (Dong et al., 2015; Dong et al., 2017; Kaku et al., 2019). Unfortunately, the addition of $TiOSO_4$ with $MnSO_4$ also reduces the cell voltage by more than 100 mV and increases the cost of energy components (Kaku et al., 2016). An alternate approach using V^{5+} ions to stabilize the Mn electrolyte has also been proposed (Reynard et al., 2020). These V/Ti/Mn RFB systems will exhibit higher voltages compared to the Ti/Mn system given the lower standard electrode potential of the V^{3+}/V^{2+} couple (-0.26V vs SHE). But this system is economically unattractive given the increased cost associated with the use of vanadium and thus we do not believe this is a viable future direction. Various thicknesses of Nafion® i.e., Nafion® 115, Nafion® 212, Nafion® 211 have been

evaluated to investigate their impact on the performance of Ti-Mn RFBs. The energy efficiency was found to be function of separator thickness with the energy efficiency being 84%, 83%, and 81% for Nafion® 211 (25 μm), Nafion® 212 (51 μm), and Nafion® 115 (127 μm) respectively (Kaku et al., 2017).

Ti-Ce RFB: An alternative Ti based RFB which provides a higher OCP compared to, Ti-Fe and Ti-Mn RFBs, are Ti-Ce RFB. The OCP of Ti-Ce RFB is 1.61V, which results in higher operating power density at the same operating current density and higher energy density for the same electrolyte concentration compared to Ti-Fe and Ti-Mn systems (Sankarasubramanian et al., 2021). These RFBs can achieve a theoretical energy density of 19.4 Wh/L. The half-cell redox reactions of Ti-Ce RFB are represented by the following equations.

$$Negative\ Electrode:\ TiO^{2+} + 2H^{+} + e^{-} \rightleftharpoons Ti^{3+} + H_2O\ (+0.1V\ vs\ SHE) \quad (11)$$

$$Positive\ Electrode:\ Ce^{3+} \rightleftharpoons Ce^{4+} + e^{-}\ (-1.72V\ vs\ SHE) \quad (12)$$

The Ce Pourbaix diagram shows that cerium ions are soluble in strong acids but forms stable, insoluble hydroxyl complexes above pH ~7. Given the exceptionally high standard reduction potential for Ce (the highest amongst all the catholyte candidates considered here), the stability of the supporting electrolyte is a particular concern - HCl and HNO_3 cannot be used due to their side reactions that produce Cl_2 and NO_2 respectively (Sankarasubramanian et al., 2021). The Ce^{4+}/Ce^{3+} redox couple exhibits unusual solubility behavior as a function of the supporting electrolyte (acid) concentration. The solubility of both species in this redox couple decreases in inverse proportion to H_2SO_4 concentration and the highest concentration achieved was 0.5M Ce in 1M H_2SO_4 (Xie et al., 2011b). But interestingly, in CH_3SO_3H, the solubility of Ce^{3+} decreases and the solubility of the Ce^{4+} increases with increasing acid concentration and this results in a solubility maximum of 0.9M Ce in 4M CH_3SO_3H (Kreh et al., 1989; Shi et al., 1989; Sankarasubramanian et al., 2021). Thus, the energy density of this system is circumscribed by the solubility of the Ce catholyte as $TiOSO_4$ is highly soluble in both H_2SO_4 and CH_3SO_3H (Sankarasubramanian et al., 2021). On the other hand, the Ti electrode is the rate-limit electrode (relevant for achieving higher operating current densities) as the rate constants of the Ce^{4+}/Ce^{3+} couple is 3x that of the Ti^{4+}/Ti^{3+} redox couple (Klingler and Kochi, 1981; Sankarasubramanian et al., 2021). Cyclic voltammetry shows the anodic to cathodic peak separation for Ti^{3+}/Ti^{4+} to be 1V and 0.67V for the Ce^{4+}/Ce^{3+} couple (Sankarasubramanian et al., 2021), indicating these reactions are not electrochemically reversible and suggesting high charge and discharge overpotentials (Bard and Faulkner, 2000). Nevertheless, in both H_2SO_4 and CH_3SO_3H supporting electrolytes, the Ti-Ce RFB exhibited nearly 100% coulombic efficiency with over 70% energy efficiency (charging and discharging at 100 mA/cm^2) during 1300 and 700 h of diurnal cycling, respectively (Sankarasubramanian et al., 2021). These cells employed highly permselective quaternary cardo-poly ether ketone (QPEK-C) AEM separators (Yun et al., 2014; Yun et al., 2015; Yun et al., 2016) which demonstrated negligible crossover (<0.4%) over 1000 h of operation with 24 h cycle as compared to commercial CEM which suffers from drastic cation crossover and loss in capacity early in the cycling of the RFB (Sankarasubramanian et al., 2021).

3 Future Directions and Prospects

The Ti-X family of RFBs represent an interesting new direction in the development of aqueous RFB systems given their high theoretical energy density and economic competitiveness enabled by the high solubility and low cost of Ti. We anticipate the following future directions –

1) Unlocking the high energy density of the Ti electrolyte by pairing it with a stable and high solubility counter electrolyte. The long-term stability of the low pH Ti electrolytes needs to be demonstrated.
2) Catalyzing Ti^{4+}/Ti^{3+} redox kinetics to overcome its nature as the rate-limiting electrode. The catalysts should be low cost to preserve the cost advantage enjoyed by the Ti electrolyte.
3) Increasing the thermal stability of the Ti electrolyte to prevent TiO_2 formation by hydrolysis.
4) Using AEM and pore tailored PM instead of CEM to reduce crossover of the predominantly cationic redox active species, thereby enabling electrode decoupled RFBs. (Wang et al., 2018).

The continued development of these systems is anticipated to result in a commercially viable, high-energy density aqueous RFB that can economically be integrated into the electric grid.

Author contributions

SIUA and MS contributed equally to this manuscript. SIUA and MS prepared the first draft of the manuscript. All authors reviewed and revised the manuscript. SS conceived and supervised the project.

Funding

The authors acknowledge funding from the US Department of Energy through grant # DE-FE0032011. SS gratefully acknowledges funding through a start-up grant from the University of Texas at San Antonio.

Conflict of interest

The authors declare that the research was conducted in the absence of any commercial or financial relationships that could be construed as a potential conflict of interest.

Publisher's note

References

Archana, K. S., Suresh, S., Ragupathy, P., and Ulaganathan, M. (2020). Investigations on new Fe–Mn redox couple based aqueous redox flow battery. *Electrochimica Acta* 345, 136245. doi:10.1016/j.electacta.2020.136245

Bahdad, A. O. O. (2020). *Characterization of the electron transfer reaction mechanism of TiOSO4 and MnSO4 in sulfuric acid solution*. Kansas, US: University of Kansas.

Bahdad, A. O. O., Li, Y., and Van Nguyen, T. (2021). Characterization of the electrochemical behavior of $MnSO_4$ with and without $TiOSO_4$ in H_2SO_4 solution. *J. Electrochem. Soc.* 168 (7), 070524. doi:10.1149/1945-7111/ac0e4e

Bard, A. J. B., and Faulkner, L. R. (2000). *Electrochemical methods: Fundamentals and applications*. 2 ed. New York: Wiley.

Barry, E., Burns, R., Chen, W., De Hoe, G. X., De Oca, J. M. M., de Pablo, J. J., et al. (2021). Advanced materials for energy-water systems: The central role of water/solid interfaces in adsorption, reactivity, and transport. *Chem. Rev.* 121 (15), 9450–9501. doi:10.1021/acs.chemrev.1c00069

Beukenkamp, J., and Herrington, K. D. (1960). Ion-exchange investigation of the nature of titanium(IV) in sulfuric acid and perchloric acid. *J. Am. Chem. Soc.* 82 (12), 3025–3031. doi:10.1021/ja01497a014

Bhattarai, A., Whitehead, A. H., Schweiss, R., Scherer, G. G., Skyllas-Kazacos, M., Wai, N., et al. (2019). Anomalous behavior of anion exchange membrane during operation of a vanadium redox flow battery. *ACS Appl. Energy Mat.* 2 (3), 1712–1719. doi:10.1021/acsaem.8b01816

Chen, H., Cong, T. N., Yang, W., Tan, C., Li, Y., and Ding, Y. (2009). Progress in electrical energy storage system: A critical review. *Prog. Nat. Sci.* 19 (3), 291–312. doi:10.1016/j.pnsc.2008.07.014

Choe, Y-K., Tsuchida, E., Tokuda, K., Otsuka, J., Saito, Y., Masuno, A., et al. (2021). First-principles molecular dynamics simulation study on Ti4+ ion in aqueous sulfuric acid. *AIP Adv.* 11 (3), 035224. doi:10.1063/5.0038061

Comba, P., and Merbach, A. (1987). The titanyl question revisited. *Inorg. Chem.* 26 (8), 1315–1323. doi:10.1021/ic00255a024

Cservenyák, I., Kelsall, G. H., and Wang, W. (1996). Reduction of TiIV species in aqueous hydrochloric and sulfuric acids II. ECE model of the behaviour in sulfate media. *Electrochimica Acta* 41 (4), 573–582. doi:10.1016/0013-4686(95)00344-4

Cunha, Á., Martins, J., Rodrigues, N., and Brito, F. P. (2015). Vanadium redox flow batteries: A technology review. *Int. J. Energy Res.* 39 (7), 889–918. doi:10.1002/er.3260

Davies, G. (1969). Some aspects of the chemistry of manganese (III) in aqueous solution. *Coord. Chem. Rev.* 4 (2), 199–224. doi:10.1016/s0010-8545(00)80086-7

Dewage, H. H., Wu, B., Tsoi, A., Yufit, V., Offer, G., and Brandon, N. (2015). A novel regenerative hydrogen cerium fuel cell for energy storage applications. *J. Mat. Chem. A Mat.* 3 (18), 9446–9450. doi:10.1039/c5ta00571j

Dong, Y., Kaku, H., Miyawaki, H., Tatsumi, R., Moriuchi, K., and Shigematsu, T. (2017). Titanium-manganese electrolyte for redox flow battery. *SEI Tech. Rev.* 84, 35

Dong, Y-R., Shigematsu, T., Kumamoto, T., Kubata, M., and inventors (2012). *Sumitomo electric industries, ltd., assignee. Redox flow battery*. Alexandria, VA: United States Patent and Trademark Office.

Dong, Y. R., Kaku, H., Hanafusa, K., Moriuchi, K., and Shigematsu, T. (2015). A novel titanium/manganese redox flow battery. *ECS Trans.* 69 (18), 59–67. doi:10.1149/06918.0059ecst

Kaku, H., Yamaguchi, H., Dong, Y- R., Tatsumi, R., Miyatake, K., Moriuchi, K., et al. (2019). "A 10kW class Ti/Mn redox flow battery," in *ECS meeting abstracts* (IOP Publishing).

Fedkiw, P. S., and Watts, R. W. (1984). A mathematical model for the iron/chromium redox battery. *J. Electrochem. Soc.* 131 (4), 701–709. doi:10.1149/1.2115676

Funding opportunity announcement advanced research projects agency (2016). *Energy (arpa-E) duration addition to electricity storage (DAYS)*. Dep. Energy. Governmental Announcement.

Gong, K., Xu, F., Grunewald, J. B., Ma, X., Zhao, Y., Gu, S., et al. (2016). All-soluble all-iron aqueous redox-flow battery. *ACS Energy Lett.* 1 (1), 89–93. doi:10.1021/acsenergylett.6b00049

Gubler, L. (2019). Membranes and separators for redox flow batteries. *Curr. Opin. Electrochem.* 18, 31–36. doi:10.1016/j.coelec.2019.08.007

Holland-Cunz, M. V., Cording, F., Friedl, J., and Stimming, U. (2018). Redox flow batteries—concepts and chemistries for cost-effective energy storage. *Front. Energy* 12 (2), 198–224. doi:10.1007/s11708-018-0552-4

Jiang, H. R., Sun, J., Wei, L., Wu, M. C., Shyy, W., and Zhao, T. S. (2020). A high power density and long cycle life vanadium redox flow battery. *Energy Storage Mater.* 24, 529–540. doi:10.1016/j.ensm.2019.07.005

Jiang, T., Lin, H., Sun, Q., Zhao, G., and Shi, J. (2018). Recent progress of electrode materials for zinc bromide flow battery. *Int. J. Electrochem. Sci.* 13, 5603–5611. doi:10.20964/2018.06.34

Kaku, H., Dong, Y. R., Hanafusa, K., Moriuchi, K., and Shigematsu, T. (2016). Effect of Ti(IV) ion on Mn(III) stability in Ti/Mn electrolyte for redox flow battery. *ECS Trans.* 72 (10), 1–9. doi:10.1149/07210.0001ecst

Kaku, H., Kawagoe, Y., Dong, Y-R., Tatsumi, R., Moriuchi, K., and Shigematsu, T. (2017). Enhanced performance of Ti/Mn redox flow battery. *ECS Trans.* 77 (11), 173–183. doi:10.1149/07711.0173ecst

Kavan, L., O'Regan, B., Kay, A., and Grätzel, M. (1993). Preparation of TiO_2 (anatase) films on electrodes by anodic oxidative hydrolysis of $TiCl_3$. *J. Electroanal. Chem.* 346 (1), 291–307. doi:10.1016/0022-0728(93)85020-h

Klingler, R. J., and Kochi, J. K. (1981). Electron-transfer kinetics from cyclic voltammetry. Quantitative description of electrochemical reversibility. *J. Phys. Chem.* 85 (12), 1731–1741. doi:10.1021/j150612a028

Kotsyubynsky, V. O., Myronyuk, I. F., Chelyadyn, V. L., Hrubiak, A. B., Moklyak, V. V., and Fedorchenko, S. V. (2017). The effect of sulphate anions on the ultrafine titania nucleation. *Nanoscale Res. Lett.* 12 (1), 369. doi:10.1186/s11671-017-2144-3

Kreh, R. P., Spotnitz, R. M., and Lundquist, J. T. (1989). Mediated electrochemical synthesis of aromatic aldehydes, ketones, and quinones using ceric methanesulfonate. *J. Org. Chem.* 54 (7), 1526–1531. doi:10.1021/jo00268a010

Leung, P. K., Ponce-de-León, C., Low, C. T. J., Shah, A. A., and Walsh, F. C. (2011). Characterization of a zinc–cerium flow battery. *J. Power Sources* 196 (11), 5174–5185. doi:10.1016/j.jpowsour.2011.01.095

Lingane, J. J., and Kennedy, J. H. (1956). Polarography of titanium in strong mineral acid media. *Anal. Chim. Acta* 15, 294–300. doi:10.1016/0003-2670(56)80053-6

Lokhande, C., Sun-Ki, M., Jung, K-D., and Joo, O-S. (2004). Cathodic electrodeposition of amorphous titanium oxide films from an alkaline solution bath. *J. Mater. Sci.* 39 (21), 6607–6610. doi:10.1023/b:jmsc.0000044903.93296.a4

Lokhande, C. D., Min, S-K., Jung, K-D., and Joo, O-S. (2005). Cathodic electrodeposition of amorphous titanium oxide films from an alkaline solution bath. *J. Mat. Sci.* 40 (2), 491–494. doi:10.1007/s10853-005-6111-5

Lu, W., Yuan, Z., Zhao, Y., Zhang, H., Zhang, H., and Li, X. (2017). Porous membranes in secondary battery technologies. *Chem. Soc. Rev.* 46 (8), 2199–2236. doi:10.1039/c6cs00823b

Mangold, L., Halleux, H., Leclerc, S., Moncomble, A., Cote, G., and Chagnes, A. (2021). New insights for titanium(iv) speciation in acidic media based on UV-visible and 31P NMR spectroscopies and molecular modeling. *RSC Adv.* 11 (43), 27059–27073. doi:10.1039/d1ra04284j

Miyanaga, T., Watanabe, I., and Ikeda, S. (1990). Structures of hydrated titanium and vanadium ions in aqueous solutions studied by X-ray absorption spectroscopy. *Bull. Chem. Soc. Jpn.* 63 (11), 3282–3287. doi:10.1246/bcsj.63.3282

Molina, P. I., Kozma, K., Santala, M., Falaise, C., and Nyman, M. (2017). Aqueous bismuth titanium–oxo sulfate cluster speciation and crystallization. *Angew. Chem. Int. Ed.* 56 (51), 16277–16281. doi:10.1002/anie.201709539

Morris, D. F., MacCarthy, J. D., and Newton, R. J. (1978). Outer-sphere and inner-sphere interactions in the formation of metal-ion nitrate complexes. *Electrochimica Acta* 23 (12), 1383–1386. doi:10.1016/0013-4686(78)80021-8

Naresh, Rp, Mariyappan, K., Dixon, D., Ulaganathan, M., and Ragupathy, P. (2021). Investigations on new electrolyte composition and modified membrane for high voltage Zinc–Manganese hybrid redox flow batteries. *Batter. Supercaps* 4 (9), 1464–1472. doi:10.1002/batt.202100071

Oldenburg, F. J., Bon, M., Perego, D., Polino, D., Laino, T., Gubler, L., et al. (2018). Revealing the role of phosphoric acid in all-vanadium redox flow batteries with DFT calculations and *in situ* analysis. *Phys. Chem. Chem. Phys.* 20 (36), 23664–23673. doi:10.1039/c8cp04517h

Pourbaix, M. (1966). *Atlas of electrochemical equilibria in aqueous solutions*. Oxford; New York: Pergamon Press.

Prifti, H., Parasuraman, A., Winardi, S., Lim, T. M., and Skyllas-Kazacos, M. J. M. (2012). Membranes for redox flow battery applications. *Membranes* 2 (2), 275–306. doi:10.3390/membranes2020275

Qiao, L., Fang, M., Liu, S., Zhang, H., and Ma, X. (2022). New-generation iron–titanium flow batteries with low cost and ultrahigh stability for stationary energy storage. *Chem. Eng. J.* 434, 134588. doi:10.1016/j.cej.2022.134588

Raja, M., Khan, H., Sankarasubramanian, S., Sonawat, D., Ramani, V., and Ramanujam, K. (2021). Binder-free thin graphite fiber mat sandwich electrode architectures for energy-efficient vanadium redox flow batteries. *Catal. Today* 370, 181–188. doi:10.1016/j.cattod.2021.02.012

Reynard, D., Maye, S., Peljo, P., Chanda, V., Girault, H. H., and Gentil, S. (2020). Vanadium–manganese redox flow battery: Study of MnIII disproportionation in the presence of other metallic ions. *Chem. Eur. J.* 26 (32), 7250–7257. doi:10.1002/chem.202000340

Sankarasubramanian, S., Zhang, Y., He, C., Gregory, T., and Ramani, V. (2021). *An aqueous, electrode-decoupled redox-flow battery for long duration energy storage*. Research. Square. Pre-print.

Sankarasubramanian, S., Zhang, Y., and Ramani, V. (2019). Methanesulfonic acid-based electrode-decoupled vanadium–cerium redox flow battery exhibits significantly improved capacity and cycle life. *Sustain. Energy Fuels* 3 (9), 2417–2425. doi:10.1039/c9se00286c

Savinell, R. F., Liu, C. C., Galasco, R. T., Chiang, S. H., and Coetzee, J. F. (1979). Discharge characteristics of a soluble iron-titanium battery system. *J. Electrochem. Soc.* 126 (3), 357–360. doi:10.1149/1.2129043

Selverston, S., Savinell, R. F., and Wainright, J. S. (2017). Zinc-iron flow batteries with common electrolyte. *J. Electrochem. Soc.* 164 (6), A1069–A1075. doi:10.1149/2.0591706jes

Shepherd, S. (2013). *An investigation into aqueous titanium speciation utilising electrochemical methods for the purpose of implementation into the sulfate process for titanium dioxide manufacture*. Callaghan, NSW: University of Newcastle. Degree Thesis.

Shi, L., Wang, W., Wang, Y., and Huang, Y. (1989). The first example of a catalytic Wittig-type reaction. Tri-n-butylarsine-catalyzed olefination in the presence of triphenyl phosphite. *J. Org. Chem.* 54 (9), 2027–2028. doi:10.1021/jo00270a001

Skyllas-Kazacos, M., Chakrabarti, M. H., Hajimolana, S. A., Mjalli, F. S., and Saleem, M. (2011). Progress in flow battery research and development. *J. Electrochem. Soc.* 158 (8), R55. doi:10.1149/1.3599565

Sole, K. C. (1999). Recovery of titanium from the leach liquors of titaniferous magnetites by solvent extraction: Part 1. Review of the literature and aqueous thermodynamics. *Hydrometallurgy* 51 (2), 239–253. doi:10.1016/s0304-386x(98)00081-4

Thaller, L. H., and inventor (1976). The United States of America as represented by the Administrator of the National Aeronautics and Space Administration, assignee." in *Electrically rechargeable redox flow cell*. The United States of America patent US3996064A.

Tsurumura, T., Ohkubo, K., Tanaka, T., and Fujii, K. (2020). Structural study on Ti-ion complexes in concentrated aqueous electrolytes: Raman spectroscopy and high-energy X-ray total scattering. *J. Mol. Liq.* 305, 112867. doi:10.1016/j.molliq.2020.112867

Tsurumura, T., Tanaka, T., Yagi, K., Morita, M., Kameda, Y., and Fujii, K. (2018). Local structures of titanium-ion complexes in redox flow battery electrolytes as revealed by X-ray scattering with difference analysis. *J. Mol. Liq.* 261, 468–472. doi:10.1016/j.molliq.2018.04.074

Ulaganathan, M., Suresh, S., Mariyappan, K., Periasamy, P., and Pitchai, R. (2019). New zinc–vanadium (Zn–V) hybrid redox flow battery: High-voltage and energy-efficient advanced energy storage system. *ACS Sustain. Chem. Eng.* 7 (6), 6053–6060. doi:10.1021/acssuschemeng.8b06194

Varcoe, J. R., Atanassov, P., Dekel, D. R., Herring, A. M., Hickner, M. A., Kohl, P. A., et al. (2014). Anion-exchange membranes in electrochemical energy systems. *Energy Environ. Sci.* 7 (10), 3135–3191. doi:10.1039/c4ee01303d

Wang, Y., Lin, M., and Wan, C. (1984). A study of the discharge performance of the Ti/Fe redox flow system. *J. power sources* 13 (1), 65–74. doi:10.1016/0378-7753(84)80054-3

Wang, Z., Sankarasubramanian, S., and Ramani, V. (2018). Advances in anion exchange membranes for electrochemical energy conversion. *Curr. Opin. Electrochem.* 12, 240–245. doi:10.1016/j.coelec.2018.11.011

Wang, Z., Sankarasubramanian, S., Willey, J., Feng, H., Xu, H., and Ramani, V. (2021). Engineering block co-polymer anion exchange membrane domains for highly efficient electrode-decoupled redox flow batteries. *Sustain. Energy Fuels* 5 (14), 3606–3616. doi:10.1039/d1se00543j

Wu, C. D., Calvo, E. J., and Yeager, E. (1983). *Electrochemical studies of redox systems for energy storage*. Cleveland, OH: Center for Electrochemical Sciences. NASA.

Xie, Z., Xiong, F., and Zhou, D. (2011). Study of the Ce3+/Ce4+ redox couple in mixed-acid media (CH3SO3H and H2SO4) for redox flow battery application. *Energy fuels.* 25 (5), 2399–2404. doi:10.1021/ef200354b

Xie, Z., Zhou, D., Xiong, F., Zhang, S., and Huang, K. (2011). Cerium-zinc redox flow battery: Positive half-cell electrolyte studies. *J. Rare Earths* 29 (6), 567–573. doi:10.1016/s1002-0721(10)60499-1

Yun, S., Parrondo, J., and Ramani, V. (2015). A vanadium-cerium redox flow battery with an anion-exchange membrane separator. *ChemPlusChem* 80 (2), 412–421. doi:10.1002/cplu.201402096

Yun, S., Parrondo, J., and Ramani, V. (2016). Composite anion exchange membranes based on quaternized cardo-poly(etherketone) and quaternized inorganic fillers for vanadium redox flow battery applications. *Int. J. Hydrogen Energy* 41 (25), 10766–10775. doi:10.1016/j.ijhydene.2016.04.060

Yun, S., Parrondo, J., and Ramani, V. (2014). Derivatized cardo-polyetherketone anion exchange membranes for all-vanadium redox flow batteries. *J. Mat. Chem. A* 2 (18), 6605–6615. doi:10.1039/c4ta00166d

Zhao, H., Wu, Q., Hu, S., Xu, H., and Rasmussen, C. N. (2015). Review of energy storage system for wind power integration support. *Appl. Energy* 137, 545–553. doi:10.1016/j.apenergy.2014.04.103

Zhen, Y., Zhang, C., Yuan, J., Zhao, Y., and Li, Y. (2020). A high-performance all-iron non-aqueous redox flow battery. *J. Power Sources* 445, 227331. doi:10.1016/j.jpowsour.2019.227331

frontiers | Frontiers in Energy Research

TYPE Original Research
PUBLISHED 12 January 2023
DOI 10.3389/fenrg.2022.1096190

OPEN ACCESS

EDITED BY
Sheng S. Zhang,
United States Army Research Laboratory, United States

REVIEWED BY
Sicong Zhu,
Wuhan University of Science and Technology, China
Yujin Tong,
University of Duisburg-Essen, Germany

*CORRESPONDENCE
Piotr M. Kowalski,
p.kowalski@fz-juelich.de

SPECIALTY SECTION
This article was submitted to Electrochemical Energy Conversion and Storage, a section of the journal Frontiers in Energy Research

RECEIVED 11 November 2022
ACCEPTED 19 December 2022
PUBLISHED 12 January 2023

CITATION
Kowalski PM, Bornhake T, Cheong O, Dohrmann N, Koch Liston AL, Potts SK, Shad A, Tesch R and Ting YY (2023), Fundamentals of energy storage from first principles simulations: Challenges and opportunities.
Front. Energy Res. 10:1096190.
doi: 10.3389/fenrg.2022.1096190

Fundamentals of energy storage from first principles simulations: Challenges and opportunities

Piotr M. Kowalski[1,2]*, Thomas Bornhake[1,2,3], Oskar Cheong[1,2,3], Noah Dohrmann[4], Andre Luiz Koch Liston[5], Shannon Kimberly Potts[6], Alison Shad[7], Rebekka Tesch[1,2,3] and Yin-Ying Ting[1,2,3]

[1]Forschungszentrum Jülich GmbH, Institute of Energy and Climate Research—IEK-13: Theory and Computation of Energy Materials, Jülich, Germany, [2]Jülich Aachen Research Alliance JARA Energy & Center for Simulation and Data Science (CSD), Jülich, Germany, [3]Chair of Theory and Computation of Energy Materials, Faculty of Georesources and Materials Engineering, RWTH Aachen University, Aachen, Germany, [4]Department of Chemistry, University of Chicago, Chicago, IL, United States, [5]Department of Chemistry, Princeton University, Princeton, NJ, United States, [6]Forschungszentrum Jülich GmbH, Institute of Energy and Climate Research—IEK-6: Nuclear Waste Management, Jülich, Germany, [7]Walter Scott Jr. College of Engineering, Colorado State University, Fort Collins, CO, United States

Efficient electrochemical energy storage and conversion require high performance electrodes, electrolyte or catalyst materials. In this contribution we discuss the simulation-based effort made by Institute of Energy and Climate Research at Forschungszentrum Jülich (IEK-13) and partner institutions aimed at improvement of computational methodologies and providing molecular level understanding of energy materials. We focus on discussing correct computation of electronic structure, oxidation states and related redox reactions, phase transformation in doped oxides and challenges in computation of surface chemical reactions on oxides and metal surfaces in presence of electrolyte. Particularly, in the scope of this contribution we present new simulated data on Ni/Co and Am/U-bearing oxides, and Pb, Au and Ag metal surface materials. The computed results are combined with the available experimental data for thoughtful analysis of the computational methods performance.

KEYWORDS

atomistic simulations, energy materials, electronic structure, electrodes for batteries, thermodynamics, electrolyte, electrochemical conditions

1 Introduction

Energy transition requires cost efficient, compact and durable materials for energy production, conversion and storage (Grey and Tarascon, 2017; Stamenkovic et al., 2017). There is a race in finding materials with increased energy and/or power density for energy storage devices (Grey and Tarascon, 2017). Energy fuels of the future such as hydrogen require efficient electrocatalysts that are economically viable and

available for mass production of the fuels. Fuel cells used in conversion of hydrogen to electricity, besides electrocatalyst material, require durable and efficient electrolytes that can offer enhanced ionic conduction and withstand different operational conditions (Wang et al., 2020). Last, but not least, nuclear energy is still foreseen as clean energy resource. Deep understanding of behavior of nuclear fuel during and post reactor operation requires enhanced knowledge of the phase formations, redox reactions and oxidation states that prevail in uranium oxide materials. Understanding the phase transitions in uranium oxides is essential for assuring safety and security of nuclear technology, including efficient, post operational management of nuclear waste (Neumeier et al., 2017a; Bosbach et al., 2020).

In the last two decades, atomistic modeling became a popular research tool in various research fields, including energy materials (Chroneos et al., 2013; Jahn and Kowalski, 2014; Wu et al., 2019). Steady advancements in high performance computing and computational software enable investigation of complex systems containing hundreds of atoms from first principles (Jahn and Kowalski, 2014). Over the past decade, *ab initio* methods have been intensively applied, including our own studies, for computational investigation of various classes of energy materials, including these of importance in electrochemistry, energy storage and nuclear energy production, delivering information on: the structural (Rustad, 2012; Feng et al., 2013; Blanca-Romero et al., 2014; Beridze et al., 2016; Connor et al., 2021), the electronic structure (Blanca-Romero et al., 2014; Kowalski et al., 2017a; Lee et al., 2017; Kowalski et al., 2021; Murphy et al., 2021; Cui et al., 2022; Tesch and Kowalski, 2022), the elastic (Wang et al., 2005; Feng et al., 2013; Ali et al., 2016; Kowalski and Li, 2016; Ji et al., 2017a; Kowalski et al., 2017b), the thermodynamic (Mogilevsky, 2007; Feng et al., 2013; Li et al., 2014; Kowalski et al., 2015; Kowalski et al., 2016; Ji et al., 2017b; Neumeier et al., 2017b; Eremin et al., 2019; Kowalski et al., 2021), the thermochemical (Rustad, 2012; Beridze et al., 2016; Kowalski, 2020) parameters, properties of electrochemical interfaces (Krishnamurthy et al., 2004; Lee et al., 2017; Tesch et al., 2021) and the radiation damage resistance (Kowalski et al., 2016; Li et al., 2016; Ji et al., 2017c; Jolley et al., 2017; Cui et al., 2022), to name but a few. Energy materials often contain *d* and *f* elements (e.g., transition metals (TM), lanthanides (*Ln*), actinides (*An*)), which play an active part in determining the materials properties. These contain strongly correlated electrons, which represent a challenge to the computational quantum chemistry (Vogiatzis et al., 2019). In a series of papers we have demonstrated that only with proper accounting for the electronic correlation effects, beyond standard methods such as the DFT + *U* approach, one can deliver correct information on the molecular scale properties of energy materials (Beridze and Kowalski, 2014; Blanca-Romero et al., 2014; Kowalski et al., 2015; Li and Kowalski, 2018; Murphy et al., 2021; Tesch and Kowalski, 2022). Among other aspects, we found the importance of derivation of the Hubbard *U* parameter for the cations in different oxidation states and structural arrangements, and careful choice of projectors for the estimation of occupancy of *d* and *f* orbitals within the DFT + *U* scheme (Maxisch and Ceder, 2006; Kvashnina et al., 2018; Kick et al., 2019; Kowalski et al., 2021; Murphy et al., 2021). In particular, we apply the linear response method for computation of the Hubbard *U* parameter (Cococcioni and de Gironcoli, 2005) and Wannier-type functions as representation of *d* or *f* orbitals (Kvashnina et al., 2018; Kowalski et al., 2021). Here we will demonstrate the impact of these procedures on the correct computation of the TM oxides materials that are considered as electrodes in energy storage devices. In addition, we will discuss certain aspects of computation of electrochemical interfaces, including simulations under realistic conditions such as presence of aqueous electrolyte and the applied potential (Tesch et al., 2021).

In this contribution we provide an overview of our recent atomistic modeling activities on various aspects of energy materials, focusing on the studies that allowed for better characterization of these materials, including electronic structure, interface charging relations and thermodynamics aspects of surface chemistry in the presence of electrolyte. Besides such an overview, we present new results on computation of common TM and actinide oxides, and different aspects of Au, Ag, Pb and Pt metal surfaces under realistic electrochemical conditions.

2 Computational approach

Most of the *ab initio* calculations discussed and performed here were performed with the density functional theory (DFT)-based plane wave Quantum-ESPRESSO simulation package (Giannozzi et al., 2009)[1]. To represent the core electrons of atoms we applied the ultrasoft pseudopotentials (Vanderbilt, 1990). The plane-wave energy cutoff of 50 Ryd was sufficient to obtain converged results. Because we are specifically interested in correct computation of structural data, we applied the PBEsol exchange-correlation functional (Perdew et al., 2008). The DFT + *U* calculations were performed with the Hubbard *U* parameter values computed from first principles using the linear response method of Cococcioni and de Gironcoli (2005), as in our previous studies (Blanca-Romero et al., 2014; Li et al., 2015; Beridze et al., 2016; Murphy et al., 2021). We applied the poormanwannier. x tool implemented in Quantum-ESPRESSO

1 In this contribution we call DFT methods an *ab initio* approach as the exchange-correlation functionals utilized in our studies were designed based on pure-theoretical considerations.

to construct realistic projectors for occupations of *d* orbitals. This computational setup was successfully applied in our previous studies [e.g., Blanca-Romero et al. (2014); Beridze et al. (2016); Finkeldei et al. (2017); Murphy et al. (2021); Kowalski et al. (2021)].

For the structural models used in calculations of Li_xNiO_2 in **Section 3.2.1** we selected the most favorable arrangement of Li atoms and vacancies, which give the most negative (most stable) Coulomb energies among all possible configurations. The Coulomb energies were calculated using the package designed by Okhotnikov et al. (2016).

The DFT-based calculations of the 3 × 3 Pb(100) surface discussed in **Section 3.3.2** were performed with the PBE exchange correlational functional using the VASP package (Perdew et al., 1996; Kresse and Hafner, 1993; Kresse and Furthmüller, 1996b; a). We used the projector augmented wave (PAW) method to describe the core electrons and the plane-wave cutoff energy was set to 500 eV. The 3 × 3 Pb(100) surface was represented by a five-layers slab and the model was created using the atomic simulation environment (ASE) (Hjorth Larsen et al., 2017). In order to mimic the bulk-like environment at the bottom of the slab, the two bottom Pb layers were kept fixed during the geometry optimization, while the other three layers were allowed to relax. In order to avoid any undesired interaction between the periodically repeated surface, in the direction perpendicular to the surface, a 20 Å vacuum layer has been applied. A Monkhorst–Pack 4 × 4 × 1 *k*-point grid was used for the structure relaxations (Monkhorst and Pack, 1976). The calculated equilibrium bulk Pb lattice constant of 5.03 Å is comparable to the measured value of 4.95 Å (Fan et al., 2020). The adsorption energy of HCOO* and COOH* species on the Pb(100) metal surface was defined as follows:

$$E_{ads} = E_{\mathrm{HCOO/COOH}+surface} - E_{surface} - E_{\mathrm{CO_2}} - 0.5E_{\mathrm{H_2}}, \quad (1)$$

where $E_{\mathrm{HCOO/COOH}+surface}$, $E_{surface}$, $E_{\mathrm{CO_2}}$, $E_{\mathrm{H_2}}$ correspond to the energy of Pb(100) surface with adsorbed HCOO* and COOH* species, the energy of bare Pb(100) surface and the energies of gas phase CO_2 and H_2 species, respectively. The water solvent was simulated using the VASPsol continuum solvation scheme (Mathew et al., 2014; 2019).

The effective screening medium reference interaction site method (ESM-RISM) implementation applied in **Section 3.3.3** is that implemented in Quantum-ESPRESSO code. Within the ESM framework (Otani and Sugino, 2006), a potentiostat is implemented (Bonnet et al., 2012) that allows to grand-canonically vary the charge of the electrode, and thus to simulate it at an applied electrode potential. The RISM setup was identical to the one applied by Tesch et al. (2021). The DFT calculations of Au(111) surface were performed with the PBE exchange-correlation functional (Perdew et al., 1996), with the optimized lattice constant of 4.17 Å. The surface was modeled with the single atom 1 × 1 surface unit cell and six layers thick slab with the positions of two bottom layers fixed to the bulk configuration. The 12 × 12 × 1 *k*-point mesh has been applied. The Lennard-Jonnes parameters for Au atoms required for the RISM calculations were $\sigma = 2.629$, Å and $\epsilon = 5.29$ kcal/mol (Heinz et al., 2008). These values were selected in a way that the resulting water density profile matches well the *ab initio* molecular dynamics data of Goldsmith et al. (2021).

For the calculation of molar entropies of molecules presented in **Section 3.3.4** we applied the two-phase thermodynamic (2PT) method (Lin et al., 2010; 2003; Pascal et al., 2011). The molecular dynamics (MD) trajectories necessary for this approach were simulated with the LAMMPS software package (Plimpton, 1995). The OPLS AA/L (Jorgensen and Tirado-Rives, 1988) and the Interface Force Field (IFF) (Heinz et al., 2013) were applied to describe interaction between the solutes and metal surfaces atoms, respectively. The SPC water model (Berendsen et al., 1987) was used to represent water molecules. The random initial configuration of solvent molecules was created using the PACKMOL package (Martínez et al., 2009). MD simulations of the solute molecule (HCOOH) in a solvent were 200 ps long. For the 2PT analysis, we performed a NPT ensemble equilibration run followed by a 20 ps NVT ensemble production run. This setup follows from previous studies of Lin et al. (2003), who have shown that 20 ps long trajectory is sufficient for obtaining accurate thermodynamic properties. The longer applied equilibration runs are essential to assure equilibrated water structure at metal surfaces (Cheong et al., 2022).

3 Results and discussion

3.1 Computation of electronic structure

Correct computation of the electronic structure of TM elements bearing materials is a challenge for computational electrochemistry. This is because the underlying chemistry is driven by the strongly correlated *d* electrons (Vogiatzis et al., 2019). DFT often fails to predict the electronic structure of these materials, also on the qualitative level. Wide-band gap materials considered as electrodes in energy storage, conversion or catalysts devices are often predicted by DFT or DFT + *U* methods to be metals. These include, for instance, NiOOH electrocatalyst (Zaffran and Caspary Toroker, 2016). Below we discuss specific aspects of computation of the electronic structure of TM elements-bearing compounds.

3.1.1 NiO and CoO

As a test case we computed here the simple oxides: NiO and CoO, both containing TM-cation in + 2 oxidation state. The Hubbard *U* parameters derived for TMs and the resulting band gaps in these two compounds are provided in **Table 1**.

CoO and NiO are wide band gap charge transfer Mott insulators (Zhang et al., 2021). For such materials, the band gap should be equivalent to half of the Hubbard U parameter (expected shift of the unoccupied d states). The Hubbard U parameters computed here for these compounds are large and indicate wide band gaps (**Table 1**). The band gaps computed with the DFT + U method are consistent with the measurements. This is, however, somewhat misleading, as it results from incorrect occupations of d states. Because the atomic orbitals are applied as projectors, these result in significant, fractional occupations of empty orbitals (**Table 2**) and overestimated total occupancy of the d states. This shortcoming is corrected with the Wannier-functions as projectors. The resulting occupation matrix and number of d electrons are also reported in **Table 2**. These reflect the expected values, which has also significant impact on the computed band gaps. In set of previous studies we obtained similar improvement for occupations of d and f orbitals of various other elements [e.g., Murphy et al. (2021); Kowalski et al. (2021)]. The band gaps computed with the DFT + U(WF) method are larger than the ones predicted with the standard DFT + U approach. We note that for this case, the hybrid functionals such as HSE06 also predict correct band gaps of the considered oxide materials (Seo et al., 2015). This is opposite to the case of lithiated transition metal oxides, which show significant level of d elements delocalization and overestimation of the band gaps of these materials by the hybrid functionals approaches (Seo et al., 2015).

3.1.2 Metals with DFT + U

Metal phases consisting of transition metal elements play a key role in the electrochemical devices. The strong correlation character of d electrons these systems contain has been illustrated by the computation of large Hubbard U parameters in a series of computational studies (Schnell et al., 2002; Nakamura et al., 2006; Şaşıoğlu et al., 2011; Tesch and Kowalski, 2022). This would imply the importance of Hubbard model corrections also for these systems. On the other hand, it has been demonstrated that the standard DFT method results in very good prediction of metal properties, including good description of the x-ray photoelectron spectroscopy (XPS) spectra by the resulting density of states (DOSes) (Hofmann et al., 2012). This apparent contradiction could be explained by the delocalized character of d electrons in metals and inapplicability of the fully localized limit (FLL) of standard DFT to metals. An "around mean field" (AMF) version of DFT has been proposed instead for computation of metals (Czyżyk and Sawatzky, 1994; Petukhov et al., 2003; Himmetoglu et al., 2014; Ryee and Han, 2018). In this approach, the occupations are forced to reproduce the mean values, instead of the preference of fully occupied or unoccupied orbitals, as in the standard DFT + U approach. This causes no overall change in the DOSes when the AMF version of the DFT + U method is applied. Nevertheless, it has been also proposed that the correct computation of metals should be done with a combination of the FLL and AMF methods (Petukhov et al., 2003). Having wide popularity of the FLL version of the DFT + U approach, it is thus of importance to understand the performance of this method when applied to metallic systems.

Tesch and Kowalski (2022) derived the Hubbard U parameters for all the 3d, 4d and 5d transition metals applying the linear response method (Cococcioni and de Gironcoli, 2005). The values (up to 11 eV) and trends of increasing the U parameter values with increasing number of valence electrons, observed in previous studies (Şaşıoğlu et al., 2011), have been reproduced. These show that the 3d metals exhibit the largest Hubbard U parameter values, followed by 4d and 5d metals. Having these results, Tesch and Kowalski (2022) performed a thoughtful analysis of the performance of the DFT + U method for metals. When computing transition metals with the DFT +U approach, they observed a shift of the d-band to lower energies, comparing to the experimental XPS spectra. Interestingly, they found a very similar behavior when hybrid functionals (like PBE0) were applied. As mentioned, this behavior could be prevented when the AMF approach is applied. However, Tesch and Kowalski (2022) also demonstrated the importance of the projectors of d orbitals for the overall results. When the Wannier functions-based projectors of the occupancy of d states were applied, the spurious shift of the d-band was prevented. A correct description of metal d-bands is extremely important, since they are often used as descriptors for catalytic activity, like in the famous d-band model (Hammer and Norskov, 1995; Ruban et al., 1997).

3.2 Voltage of electrode materials

3.2.1 $LiNiO_2$

Layered oxides are the most widely used electrode materials in rechargeable lithium-ion batteries. Among them, $LiCoO_2$ (LCO) is one of the successfully commercialized cathodes (Blomgren, 2016). However, the increased demand of cobalt resulted in a high cost of such materials, triggering a widespread research effort to find alternative cobalt-free cathode materials, applicable especially for automotive applications (Olivetti et al., 2017). In the past decades, $LiNiO_2$ (LNO) has been considered as an alternative cathode material for rechargeable lithium batteries. This is because of its high availability and associated low cost, as well as safety and energy-density when compared to the commercial cobalt counterpart (Kalyani and Kalaiselvi, 2005; Mukai et al., 2010). If accurately described by first principles methods, a valuable, molecular-level insight into the properties that determine the cycle stability and charge capacity, when these materials are used in electrochemical compounds, could be obtained

TABLE 1 The Hubbard *U* parameter and the band gap values (direct band gap) of CoO and NiO compounds computed with different methods, and measured. We note that for the two compounds we obtained the same Hubbard *U* parameter values with both considered *d* orbitals projector types.

Compound	Value of Hubbard *U* (eV)	DFT + *U*	DFT + *U*(WF)	exp
CoO	7.6	2.9	4.7	2.7–5.4[a]
NiO	6.7	3.2	3.5	3.6–4.3[b]

[a](Anisimov et al., 1990; Gillen and Robertson, 2013), [b](Gillen and Robertson, 2013; Malik et al., 2020).

TABLE 2 The occupancies of 3*d* orbitals obtained with the atomic orbital- and Wannier functions (WF)-based projectors. The resulting number of *d* electrons is reported in the last column.

element	spin	d_1	d_2	d_3	d_4	d_5	*d* electrons
Co	↑	0.991	0.991	0.999	1.000	1.000	7.4
	↓	0.151	0.151	0.578	0.578	0.992	
Co (WF)	↑	0.992	0.992	0.997	0.998	0.998	7.0
	↓	0.005	0.005	0.005	0.996	0.996	
Ni	↑	0.998	0.998	1.001	1.001	1.001	8.4
	↓	0.203	0.203	0.999	0.999	0.999	
Ni (WF)	↑	0.992	0.992	0.999	0.999	0.999	8.0
	↓	0.009	0.009	0.999	0.999	0.999	

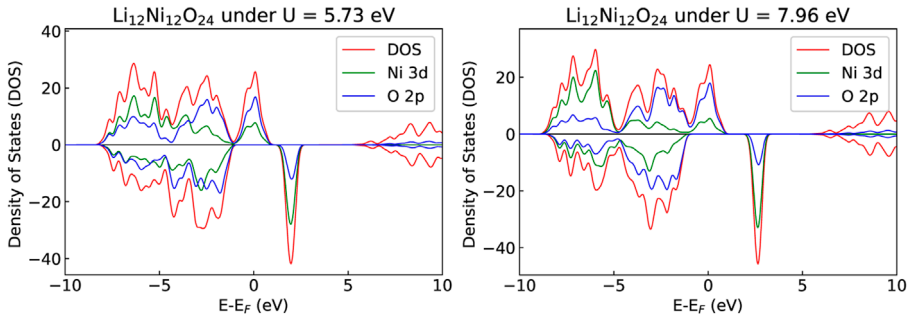

FIGURE 1
The partial and total DOSes computed for LNO with the derived (right) and rescaled (left) Hubbard *U* parameters.

(Chakraborty et al., 2018). There exist several first-principle studies on LNO [e.g., Yoshida et al. (2019); Zhu et al. (2011); Chen et al. (2011); Mock et al. (2021)]. However, DFT fails to correctly predict the electronic structure of these systems: the band gap is severely underestimated and oxidation states of cations are incorrectly described (Pavarini et al., 2012).

The DFT + *U* method improves the materials description in the outlined aspects (Seo et al., 2015; Kowalski et al., 2021). However, even this correction can fail for the TM elements with more than five *d*-electrons, such as iron or nickel (Kowalski et al., 2021). The description of *d*-electrons in nickel can be further improved by representing the orbitals with strongly correlated electrons with Wannier-type functions (Marzari et al., 2012; Gu et al., 2020; Kowalski et al., 2021; Murphy et al., 2021).

Here, we computed the Hubbard *U* parameter for Ni in the layered rhombohedral ($R\bar{3}m$) structure and obtained the value of 7.96 eV. It is well known that LCO has a stronger covalency compared to CoO, which induces less charge localization on the TM (van Elp et al., 1991; Galakhov et al., 1996). Seo et al. (2015) studied the LCO and LNO compounds with first-principle calculation using the HSE06 hybrid functional and showed that the optimal exact exchange admixing parameter α for LCO and LNO is substantially lower than the default one ($\alpha = 0.25$), namely 0.17 for LCO and 0.18 for LNO. We assume here that the strong covalency in LCO and LNO will also affect the derived Hubbard *U* parameter and that the more realistic value should

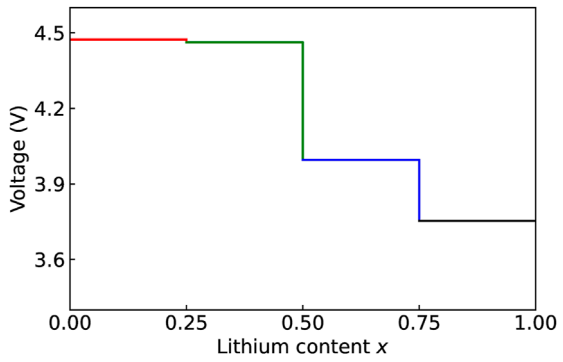

FIGURE 2
Computed specific voltage of Li_xNiO_2 as a function of Li content *x*.

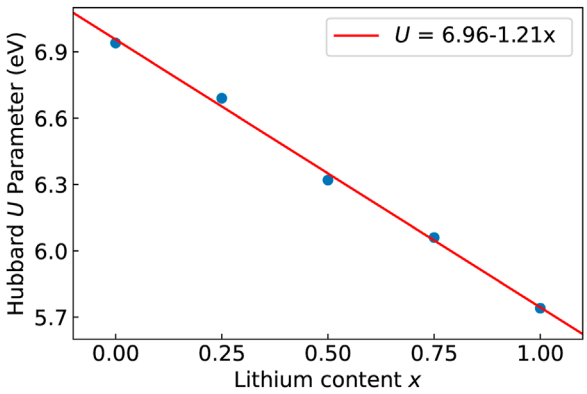

FIGURE 3
The Hubbard *U* parameter obtained with the linear response approach as a function of Li content. The linear fit to the data is presented in upper right corner.

be these rescaled to $U = 0.18/0.25 \cdot 7.96$ eV = 5.73 eV. As shown in **Figure 1**, comparing to the derived *U* parameter, the rescaled parameter describes more accurately the density of states of $LiNiO_2$ (Chakraborty et al., 2018).

In order to track the effect of delithiation, series of Li_xNiO_2 compounds was computed with different Li concentration, namely with x = 1.00, 0.75, 0.50, 0.25 and 0.00. The geometries were relaxed and the Hubbard *U* parameter was computed and rescaled for all the considered structures. Beyond the expected oxidation of Ni^{3+} into Ni^{4+} (three atoms at a time with increasing Li content), no disproportionation of Ni^{3+} into Ni^{2+} and Ni^{4+} species was observed during delithiation process, after wannierization scheme was applied. This suggests that the instability of Ni^{4+} reported in literature is due to other chemical forces during the synthesis of the material rather than to an inherent instability of the final structure itself (Li et al., 2022). The DFT + *U*(WF) method resulted in overall more stable structures, lower in energy by at least 10 kJ/mol, and the correct occupations of *d* orbitals, as in the case of NiO and CoO.

The intercalation voltage was estimated using standard approach (Aydinol et al., 1997; Dixit et al., 2016):

$$V = -\frac{[E(Li_{x+dx}NiO_2)] - [E(Li_xNiO_2) + dx \cdot E(Li_{bcc})]}{dx}, \quad (2)$$

with $dx = 0.25$ as a step change of Li content, $E(Li_xNiO_2)$ the total energy per formula unit at Li content *x*, and $E(Li_{bcc})$ the total energy per formula unit of Li in the bulk material. As shown in **Figure 2**, the average calculated value of 4.17 eV is in good agreement with the measured value (Ohzuku et al., 1993).

In order to test the performance of the applied method for predicting the formation enthalpy of LNO, we also computed the Li_2O and NiO compounds, and the molecular O_2. Assuming the following LNO formation reaction:

$$0.5\,Li_2O + NiO + 0.25\,O_2 \rightarrow LiNiO_2, \quad (3)$$

we estimate the formation energy of LNO from oxide to be 65.12, kJ/mol. When the entropy of gas phase (oxygen) is considered ($S = 205$ J/mol/K at 293 K), the resulting free energy of formation is 50.31, kJ/mol, is in good agreement with the measured value of 53.35, kJ/mol (Wang and Navrotsky, 2004).

During the delithiation process, as a result of oxidation of Ni atoms, removal of Li causes a linear increase of the Hubbard parameter *U* (**Figure 3**). Such a dependence of the Hubbard *U* parameter on the oxidation state is consistent with our previous studies [e.g., Beridze et al. (2016); Beridze and Kowalski (2014); Kowalski et al. (2021)]. The change in the oxidation state of Ni from + 3 to + 4 results in change in the DOS and the band gap (**Figure 4**), and in shortening of the Ni-Ni, Ni-O and O-O bond lengths, and increase of Ni-Li distances, as shown in **Table 3**. The cell parameters of the optimized supercell show excellent agreement with the crystallographic data.

It is worth noting that, while the applied Wannierization scheme contributes to the correct description of the oxidation states of Ni cations, it also replicates the small experimental band gap of 0.4 eV in $LiNiO_2$ (Laubach et al., 2009; Shishkin and Sato, 2016), as indicated in **Figure 4**. On the other hand, in most of the computational studies, perfect-layered LNO was computed as half-metal even with the computationally intensive hybrid functionals (Laubach et al., 2009; Shishkin and Sato, 2016; Chakraborty et al., 2018). In our studies, the accurate computation of occupation of *d* orbitals was prioritized, as the changes in the oxidation state of Ni are crucial to correctly describe the delithiation process.

3.2.2 $LiCoO_2$

Similar computations were performed for $LiCoO_2$ in the layered rhombohedral ($R\bar{3}m$) structure. We derived a Hubbard *U* parameter of 6.8 eV, which for the same reason as in the case of LNO, we assume to be overestimated. The computed Hubbard *U* parameter value was rescaled, taking the optimal

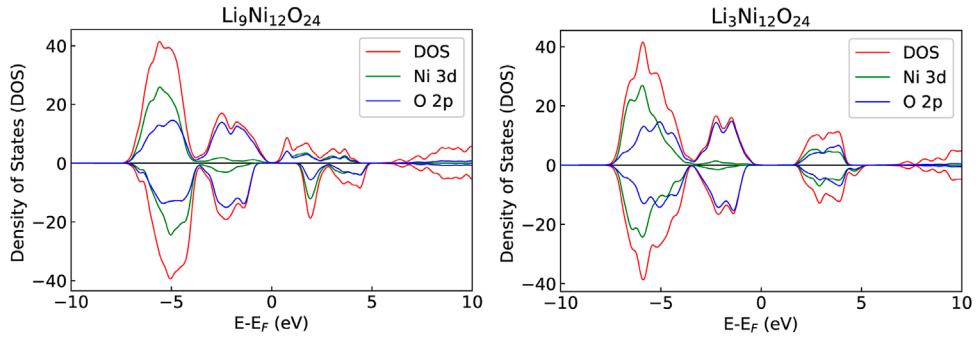

FIGURE 4
The partial and total DOSes of Li_xNiO_2 with x = 0.75 (left) and 0.25 (right). The overlap between Ni d-bands and O p-bands is more pronounced upon delithiation, as expected.

TABLE 3 Different bond lengths computed for LNO compound (Li_xNiO_2) at different delithiation level. The experimental data are those of Molenda et al. (2002).

Bond Type	Li content (x)	Distance (Å)
Ni-Ni	x = 1.00	2.8726
	0.75	2.8841
	0.50	2.8333
	0.25	2.8104
	0.00	2.7992
Ni-O	x = 1.00	1.9496
	0.75	1.9504
	0.50	1.9292
	0.25	1.8710
	0.00	1.8758
Ni-Li	x = 1.00	2.8917
	0.75	2.8920
	0.50	2.9181
	0.25	2.9677
	0.00	–
O-O	x = 1.00	2.9203
	0.75	2.8999
	0.50	2.8529
	0.25	2.8122
	0.00	2.7992
Cell Parameter	computed	exp
a (Å)	2.873	2.880
c (Å)	14.214	14.180
V (Å^3)	101.58	101.86

TABLE 4 The band Gap of LCO computed with different methods and U parameters (computed and rescaled). The values are provided in eV.

Value of Hubbard U	DFT + U	DFT + U(WF)
4.6 (rescaled)	2.4	3.4
6.8	2.8	4.4

mixing parameter α for the exact Hartree-Fock exchange as a reference (Seo et al., 2015). This procedure gave a value of 4.6 eV. The computed band gaps with different U parameter values and with the DFT + U and DFT + U(WF) methods are shown in Table 4. A good agreement with the experimental value of 2.7 eV (Galakhov et al., 1996) is obtained with the rescaled value of Hubbard U parameter.

Applying the same computational approach as for LNO, we also computed the formation energy of LCO from oxides, following the reaction:

$$0.5\,Li_2O + CoO + 0.25\,O_2 \rightarrow LiCoO_2. \quad (4)$$

We obtained the value of 128.50 kJ/mol. Though less accurate than the one obtained for LNO, the computed LCO formation enthalpy from oxides shows reasonable agreement with the experimental value of 140.18 kJ/mol (Wang and Navrotsky, 2004; Takahashi et al., 2007).

3.3 Thermodynamic aspects of energy materials

3.3.1 Am-doped U_3O_8

Spent nuclear fuel contains significant amount of fission products or minor actinides (Np, Am, Cm), elements which can alter the material structure and performance

TABLE 5 The Hubbard *U* parameters derived for Am doped U_3O_8 compounds. The values are given in eV.

Cation	C2mm	P62m
U(VI)	3.2	3.0
U(V)	2.7	2.8
Am(III)	5.0	5.1

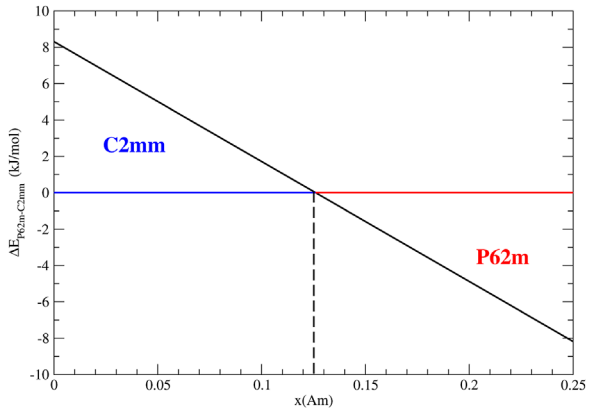

FIGURE 5
The computed difference in enthalpy between the *C2mm* and *P62m* phases of U_3O_8. The predicted phase transition is at the content of Am of 1.2%.

(Bosbach et al., 2020). Doping of a phase with an element of other oxidation state can trigger a phase transition and stabilization of the new phase. This is for instance the case of yttria-stabilized zirconia, where doping of zirconium dioxide phase with ~8% of tri-valent element like yttrium, stabilizes the cubic phase of that compound, which is one of the fastest known ionic conductors (Kowalski et al., 2021). Here we investigate the phase transition upon doping U_3O_8 phase (realized as a phase with the space group *C2mm*) with small amount of Am. This system has been investigated experimentally by Caisso et al. (2016). They found stabilization of a phase with the space group *P62m* phase upon doping with ~10% of Am. Here we confirm this finding with the aid of atomistic simulations.

First, we computed the Hubbard *U* parameters for U and Am in both structures. The resulting values are reported in **Table 5**. These are consistent with our previous studies (Beridze and Kowalski, 2014; Beridze et al., 2016). We notice, however, that the values derived for U species in U_3O_8 are larger than the ones obtained in Kvashnina et al. (2018). This is because in those studies another structure of U_3O_8 was investigated.

The computed formation enthalpy difference between the phases with space groups *P62m* and *C2mm* as a function of Am content are shown in **Figure 5**. Following studies of Caisso et al. (2016) we assumed that Am is incorporated as +3 species on U +5 site and the charge is compensated by the

TABLE 6 The computed and measured volumes of pure and Am doped U_3O_8 (at Am/U ratio of 1/9). The measured data are those of **Caisso et al. (2016)**. The values are in $Å^3$ per two formula units.

Phase	Computed	Measured
U_3O_8	335.6	333.0
Am:U_3O_8	341.7 (+6.1)	338.1 (+5.1)

conversion of the two U +5 species to the oxidation state of +6. We predict the phase transition at very low content of Am of ~1.2%. It is thus not surprising that Caisso et al. (2016) measured the *P62m* phase at higher Am content of ~10%. The obtained volumes of pure and Am doped U_3O_8 are also well consistent with the measurements of Caisso et al. (2016) (see **Table 6**). The computed values are within 1% of those measured, and the computed increase in volume upon doping with Am is also well consistent with the measured values.

3.3.2 Solvent effects on surface chemistry

To show the importance of solvation for computation of surface electrochemical pathways, as a test case we investigated the effect of explicit and implicit solvation on the CO_2 reduction reaction towards CO and HCOOH on the Pb(100) surface. We considered the following reaction pathways for the formation of CO and HCOOH species:

$$CO_2\,(g) + H^+ + e^- \rightarrow HCOO^* \quad (5)$$

$$HCOO^* + H^+ + e^- \rightarrow HCOOH\,(g) \quad (6)$$

$$CO_2\,(g) + H^+ + e^- \rightarrow COOH^* \quad (7)$$

$$COOH^* + H^+ + e^- \rightarrow CO\,(g) + H_2O \quad (8)$$

We assumed that the CO_2 forms either a HCOO* intermediate, which reacts further to formic acid (HCOOH), or COOH* which further reacts to CO and water.

Figure 6 shows the energy diagram for both pathways computed in three ways: (M1) assuming no solvation, (M2) in the presence of explicit solvation and (M3) by applying the continuum solvation model. In the approach M2, the aqueous phase was modeled by explicitly adding 12 water molecules. The case M3 was computed using the implicit solvation model implemented in VASPsol method (Mathew et al., 2019). The adsorption energies for HCOO* and COOH* intermediates computed with M1 are -0.45 eV and 0.73 eV, respectively. In the presence of implicit solvation, the HCOO* and COOH* adsorption energy increases to −0.61 eV and 0.52 eV. These indicated bonded HCOO* and unbonded COOH*. Applying method M2, the adsorption energy of the two species increases by 0.27 eV and 1.00 eV,

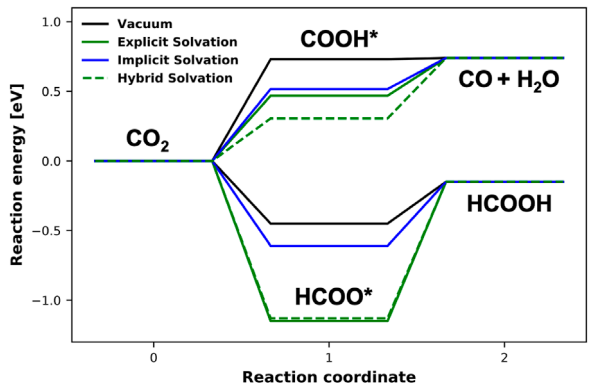

FIGURE 6
Reaction energy diagram for CO_2 reduction towards HCOOH and CO on the Pb(100) surface, computed in vacuum as well as with the implicit/explicit/hybrid solvation models.

respectively. These results show the importance of including solvent effects, when computing chemical pathways on metal surfaces.

The method M3 is a fast way to include solvent effects in the DFT calculations. In the considered cases, it results in increase in the adsorption energies, but significantly smaller than the explicit solvation schemes. The adsorption energies are changing by 0.1 eV only.

In **Figure 6**, we also show the results of hybrid solvation approach, where on top of the 12 explicit water molecules we have applied the implicit solvation, to preserve continuity of the solvent medium. While for the HCOO* intermediate, the effect of implicit solvation leads to an insignificant change, COOH* is stabilized by more than 0.2 eV. This shows that for the adsorbed species, the effect of first hydration shell dominates the solvent effect on the bonding energy between the adsorbate and the metal surface. In case of the weak bonding, the long-range interaction between the species and the solvent plays an important role.

3.3.3 Metal interfaces with the ESM-RISM approach

Simulation of electrochemical solid/liquid interfaces at an applied electrode potential is a challenge in computational electrochemistry (Schwarz and Sundararaman, 2020). It requires an approach that can consistently describe charging of the electrode as well as effects of an electrolyte solution. Both conditions are realized by the DFT-based effective screening medium reference interaction site method (ESM-RISM) (Nishihara and Otani, 2017). The RISM (Chandler and Andersen, 1972; Hansen and McDonald, 2013) is an implicit solvent model that relies on the classical theory of liquids. It computes in a statistical way correlations between electrolyte species and thus takes into account the electrolyte structure. Electrolyte–electrolyte as well as electrode–electrolyte interactions are described by the parameterized interparticle interaction potentials. The method requires a choice of classical water model for description of the aqueous electrolyte solution, a set of Lennard–Jones parameters for the electrode–electrolyte interaction and the partitioning of the system into quantum-mechanically and classically treated parts (i.e., treatment of near-surface water layers at the level of DFT) (Nishihara and Otani, 2017; Tesch et al., 2021).

We applied this method in our previous study for computation of the partially oxidized Pt(111)/electrolyte interface (Tesch et al., 2021). Taking into account the potential-dependent oxygen coverage of Pt(111) surface, we were able to accurately describe the chemisorption and charging state of the interface, correctly reproducing the chemisorption-induced non-monotonic charging relation of this specific interface [see **Figure 8** of Tesch et al. (2021)]. Here, we applied the ESM-RISM approach to model the interface between the Au(111) electrode and an 0.1 M aqueous HCl solution. **Figure 7** shows the obtained interface structure of the electrolyte solution as represented by the density distribution functions of water and electrolyte ions species. The near-surface structure of water solvent shows alternating shells of water, with the main peaks positions that agree well with the AIMD simulations (Goldsmith et al., 2021). The effects of the applied potential and the resulting surface charge on excess or depletion of ions near the interface, as expected from the electrostatic arguments, are clearly seen. This indicates that the electrode charge is correctly balanced by the arrangement of electrolyte ions. The relation between the surface charge and the applied potential is linear (see **Figure 8**). This is expected because the Au(111) surface under these conditions (the considered potential range) is characterized by the formation of double layer and is not covered by adsorbed species, as indicated by the cyclic voltammetry (Hamelin, 1996). Other computational studies have derived very similar charging relation (Letchworth-Weaver and Arias (2012); Goldsmith et al. (2021), see in **Figure 8**). The trends are consistent with the experimental findings of linearly decreasing (i.e. opposite) charge at the outer Helmholtz plane (Saha and Zenyuk, 2021). The double layer capacitance, as derived from the slope of linear fit, is 23.4 μF/cm^2 and compares well to the experimental (Vasiljevic et al., 2004; Garlyyev et al., 2018) and other computational (Kastlunger et al., 2018; Hörmann et al., 2019; Goldsmith et al., 2021) results.

3.3.4 Entropy of solvation

The reliable computation of surface chemical reactions at electrochemical conditions requires correct estimates of thermodynamic parameters. In particular, entropy effects are usually omitted in atomistic modeling studies [e.g.,

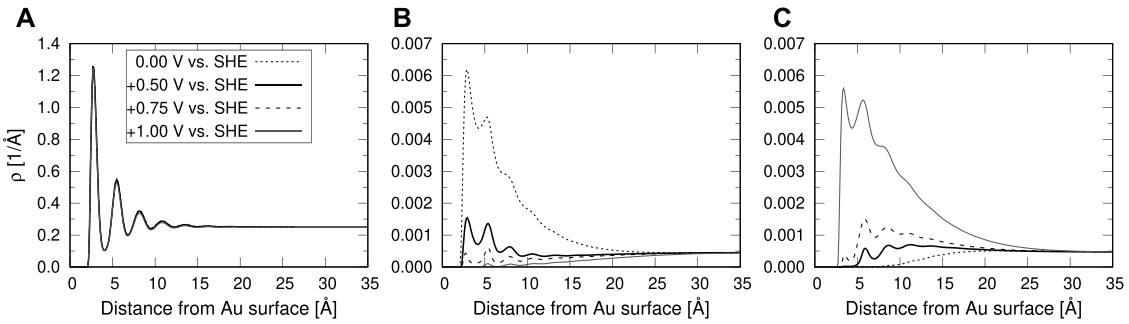

FIGURE 7
Density profiles as a function of distance from the Au(111) surface. Different panels show results for: **(A)** water molecules, **(B)** H_3O^+ electrolyte ions and **(C)** Cl^- electrolyte ions. Different lines represent the results computed with the ESM–RISM approach at different electrode potentials. The potential of zero charge (pzc) is located at 0.5 V vs. SHE.

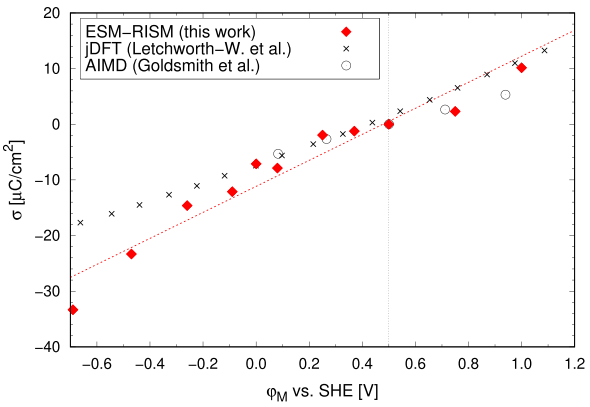

FIGURE 8
The computed surface charge vs. the applied electrode potential for the Au(111)/electrolyte interface in 0.1 M aq. HCl solution (our data), in pure water by Goldsmith et al. (2021) and in an electrolyte of 1 M ionic strength by Letchworth-Weaver and Arias (2012). The dashed red line represents a linear fit to our data. The vertical dashed line shows the pzc assumed here [0.5 V vs. SHE (Le et al., 2017)].

Klinkova et al. (2016))]. However, most of the electrocatalytic reactions on a solid catalyst surface happen in the presence of a dense electrolyte. The entropic contributions from the solvation effects can have a non-negligible effect on the reactions free energy. There are ways to compute the entropy of species in a solvent phase. These are based either on the theoretical consideration [e.g., Garza (2019)] or simulation based approaches, such as thermodynamic integration (Baranyai, 2018) or analysis of the velocity autocorrelation function (Pascal et al., 2011). Garza (2019) proposed a simplified approach to the computation of entropy of liquid phases and obtained agreements with the measured values within 12 J/mol/K. Regarding entropy at the interfaces,

TABLE 7 Standard molar entropies of HCOOH in bulk solution and at the Pb(100) and Ag (100) surfaces. All entropy values except the experimental value are calculated using the 2PT method.

Location of HCOOH	Standard molar entropy [J/mol K]
Gas phase (exp)	248.7[a]
Bulk (exp)	131.8[b]
Bulk	124.1
Pb(100)	100.7
Ag (100)	91.6

Ref: [a]Millikan and Pitzer. (1957), [b]Stout and Fisher. (1941).

Jung et al. (2021) applied the two-phase thermodynamics (2PT) approach (Lin et al., 2010; 2003; Pascal et al., 2011) and computed entropy of aqueous phase as a function of distance from the Pt(111) interface. Here we applied the 2PT approach to evaluate different entropy contributions for HCOOH molecules submerged in aqueous phase, in the bulk and at the Pb(100) and Ag (100) surfaces. The so estimated total entropy is given in **Table 7**.

The computed molar entropy of HCOOH in bulk water is in good agreement with the experimental values. For HCOOH on Pb(100) surface and Ag (100) surface, we observe a reduction in entropy by ~30 J/mol/K. However, we observe a slightly different magnitude in entropy reduction at the Ag (100) and Pb(100) surfaces, with the Ag (100) surface causing larger reduction in entropy. This can be explained by more hydrophilic character of Ag (100) surface than that of Pb(100), and thus easier movement of HCOOH when adsorbed in the latter case. The reduction of ~30 J/mol/K, moving a species from the bulk water to the metal surface, contributes to the reaction free energy by ~0.1 eV, which is a non-negligible effect. This indicates necessity of accounting for the solvation entropy effects when computing the electrochemical reactions under realistic reaction conditions.

4 Conclusion

In this contribution we presented an overview of the atomistic modeling research on energy materials we have performed in the last decade. We focused on discussing various challenges associated with the computation of molecular-level materials properties. In particular, we discussed the computation of electronic structure, phase transitions, surface chemistry and electrochemical interfaces, focusing on accounting for the presence of electrolyte phase. For the class of electrode materials we show the performance of the parameter-free DFT + *U* approach as well as the importance of application of realistic projectors for counting the occupancy of orbitals containing strongly correlated *d* and *f* electrons for obtaining correct description of electronic structure, and the related parameters, such as formation energies, specific voltage or phase stability. Materials important for electrochemistry and energy sector, such as LCO, LNO, U_3O_8 or metal surfaces have been considered, with some parameters essential for understanding of their performance computed. Last but not least, we discussed the importance of entropic effects on the computational surface (electro) chemistry.

Besides discussing various successful applications of atomistic modeling to computation of atomic-scale properties of energy materials, we outlined challenges encountered by computational electrochemistry. We highlight the importance of thoughtful analysis of the computed results vs. the available experimental data. Overcoming the challenges faced by the atomistic simulations of energy materials will lead to accurate, simulation-based materials design, that will facilitate development of more efficient materials for fulfilling future energy demands.

Data availability statement

The original contributions presented in the study are included in the article/Supplementary Material, further inquiries can be directed to the corresponding author.

Author contributions

Y-YT, AKL, ND, and PK performed calculations of the transition metal and actinide oxides. RT performed analysis of the electronic structure and calculations of metal surfaces with the ESM-RISM method. TB, OC, and AS performed calculation of the chemistry at metal surfaces. OC performed analysis of the entropies at metal surfaces. SP contributed expertise on doped uranium oxide materials. PK led the project and performed collective analysis of the data and editing of the manuscript. All parties contributed to writing the manuscript. The authors list after PK is arranged according to alphabetical order and name positioning does not reflect individual contributions.

Acknowledgments

The authors gratefully acknowledge the computing time granted by the JARA Vergabegremium and provided on the JARA Partition part of the supercomputers JURECA at Forschungszentrum Jülich and CLAIX at RWTH Aachen University (Project cjiek61).

Conflict of interest

The authors declare that the research was conducted in the absence of any commercial or financial relationships that could be construed as a potential conflict of interest.

Publisher's note

References

Aydinol, M. K., Kohan, A. F., Ceder, G., Cho, K., and Joannopoulos, J. (1997). *Ab initio* study of lithium intercalation in metal oxides and metal dichalcogenides. *Phys. Rev. B* 56, 1354–1365. doi:10.1103/PhysRevB.56.1354

Ali, K., Arya, A., Ghosh, P. S., and Dey, G. K. (2016). A first principle study of the pressure dependent elastic properties of monazite $LaPO_4$. *AIP Conf. Proc.* 1728, 020090. doi:10.1063/1.4946141

Anisimov, V. I., Korotin, M. A., and Kurmaev, E. Z. (1990). Band-structure description of Mott insulators (NiO, MnO, FeO, CoO). *J. Phys. Condens. Matter* 2, 3973–3987. doi:10.1088/0953-8984/2/17/008

Baranyai, A. (2018). Thermodynamic integration for the determination of nonequilibrium entropy. *J. Mol. Liq.* 266, 472–477. doi:10.1016/j.molliq.2018.05.113

Berendsen, H. J. C., Grigera, J. R., and Straatsma, T. P. (1987). The missing term in effective pair potentials. *J. Phys. Chem.* 91, 6269–6271. doi:10.1021/j100308a038

Beridze, G., Birnie, A., Koniski, S., Ji, Y., and Kowalski, P. M. (2016). DFT+*U* as a reliable method for efficient *ab initio* calculations of nuclear materials. *Prog. Nucl. Energy* 92, 142–146. doi:10.1016/j.pnucene.2016.07.012

Beridze, G., and Kowalski, P. M. (2014). Benchmarking the DFT+*U* method for thermochemical calculations of uranium molecular compounds and solids. *J. Phys. Chem. A* 118, 11797–11810. doi:10.1021/jp5101126

Blanca-Romero, A., Kowalski, P. M., Beridze, G., Schlenz, H., and Bosbach, D. (2014). Performance of DFT+*U* method for prediction of structural and thermodynamic parameters of monazite-type ceramics. *J. Comput. Chem.* 35, 1339–1346. doi:10.1002/jcc.23618

Blomgren, G. E. (2016). The development and future of lithium ion batteries. *J. Electrochem. Soc.* 164, A5019–A5025. doi:10.1149/2.0251701jes

Bonnet, N., Morishita, T., Sugino, O., and Otani, M. (2012). First-principles molecular dynamics at a constant electrode potential. *Phys. Rev. Lett.* 109, 266101. doi:10.1103/PhysRevLett.109.266101

Bosbach, D., Brandt, F., Bukaemskiy, A., Deissmann, G., Kegler, P., Klinkenberg, M., et al. (2020). Research for the safe management of nuclear waste at Forschungszentrum Jülich: Materials chemistry and solid solution aspects. *Adv. Energy Mat.* 22, 1901417. doi:10.1002/adem.201901417

Caisso, M., Roussel, P., Den Auwer, C., Picart, S., Hennig, C., Scheinost, A. C., et al. (2016). Evidence of trivalent Am substitution into U_3O_8. *Inorg. Chem.* 55, 10438–10444. doi:10.1021/acs.inorgchem.6b01672

Chakraborty, A., Dixit, M., and Major, D. T. (2018). Accurate cathode properties of $LiNiO_2$, $LiCoO_2$, and $LiMnO_2$ using the SCAN meta-GGA density functional. *Npj Comput. Mat.* 4, 60. doi:10.1038/s41524-018-0117-4

Chandler, D., and Andersen, H. C. (1972). Optimized cluster expansions for classical fluids. II. Theory of molecular liquids. *J. Chem. Phys.* 57, 1930–1937. doi:10.1063/1.1678513

Chen, Z., Zou, H., Zhu, X., Zou, J., and Cao, J. (2011). First-principle investigation of Jahn–Teller distortion and topological analysis of chemical bonds in $LiNiO_2$. *J. Solid State Chem.* 184, 1784–1790. doi:10.1016/j.jssc.2011.05.024

Cheong, O., Eikerling, M. H., and Kowalski, P. M. (2022). Water structures on Pb(100) and (111) surface studied with the Interface force field. *Appl. Surf. Sci.* 589, 152838. doi:10.1016/j.apsusc.2022.152838

Chroneos, A., Rushton, M., Jiang, C., and Tsoukalas, L. (2013). Nuclear wasteform materials: Atomistic simulation case studies. *J. Nucl. Mat.* 441, 29–39. doi:10.1016/j.jnucmat.2013.05.012

Cococcioni, M., and de Gironcoli, S. (2005). Linear response approach to the calculation of the effective interaction parameters in the LDA + *U* method. *Phys. Rev. B* 71, 035105. doi:10.1103/PhysRevB.71.035105

Connor, T., Cheong, O., Bornhake, T., Shad, A. C., Tesch, R., Sun, M., et al. (2021). Pyrochlore compounds from atomistic simulations. *Front. Chem.* 9, 733321. doi:10.3389/fchem.2021.733321

Cui, Y., Sukkurji, P. A., Wang, K., Azmi, R., Nunn, A. M., Hahn, H., et al. (2022). High entropy fluorides as conversion cathodes with tailorable electrochemical performance. *J. Energy Chem.* 72, 342–351. doi:10.1016/j.jechem.2022.05.032

Czyżyk, M. T., and Sawatzky, G. A. (1994). Local-density functional and on-site correlations: The electronic structure of La_2CuO_4 and $LaCuO_3$. *Phys. Rev. B* 49, 14211–14228. doi:10.1103/PhysRevB.49.14211

Dixit, M., Kosa, M., Lavi, O. S., Markovsky, B., Aurbach, D., and Major, D. T. (2016). Thermodynamic and kinetic studies of $LiNi_{0.5}Co_{0.2}Mn_{0.3}O_2$ as a positive electrode material for Li-ion batteries using first principles. *Phys. Chem.* 18, 6799–6812. doi:10.1039/C5CP07128C

Eremin, N. N., Marchenko, E. I., Petrov, V. G., Mitrofanov, A. A., and Ulanova, A. S. (2019). Solid solutions of monazites and xenotimes of lanthanides and plutonium: Atomistic model of crystal structures, point defects and mixing properties. *Comput. Mat. Sci.* 157, 43–50. doi:10.1016/j.commatsci.2018.10.025

Fan, M., Eslamibidgoli, M. J., Garbarino, S., Tavares, A. C., Eikerling, M. H., and Guay, D. (2020). A computational-experimental investigation of the mechanisms responsible for the enhanced CO_2 electrochemical reduction of dendritic Sn_1Pb_3 alloy. *J. Electrochem. Soc.* MA2020-01, 2630–17979. doi:10.1149/ma2020-01462630mtgabs

Feng, J., Xiao, B., Zhou, R., and Pan, W. (2013). Anisotropy in elasticity and thermal conductivity of monazite-type $REPO_4$ (RE=La, Ce, Nd, Sm, Eu and Gd) from first-principles calculations. *Acta Mater* 61, 7364–7383. doi:10.1016/j.actamat.2013.08.043

Finkeldei, S., Kegler, P., Kowalski, P., Schreinemachers, C., Brandt, F., Bukaemskiy, A., et al. (2017). Composition dependent order-disorder transition in $Nd_xZr_{1-x}O_{2-0.5x}$ pyrochlores: A combined structural, calorimetric and *ab initio* modeling study. *Acta Mater* 125, 166–176. doi:10.1016/j.actamat.2016.11.059

Galakhov, V., Kurmaev, E., Uhlenbrock, S., Neumann, M., Kellerman, D., and Gorshkov, V. (1996). Degree of covalency of $LiCoO_2$: X-Ray emission and photoelectron study. *Solid State Commun.* 99, 221–224. doi:10.1016/0038-1098(96)00251-7

Garlyyev, B., Xue, S., Watzele, S., Scieszka, D., and Bandarenka, A. S. (2018). Influence of the nature of the alkali metal cations on the electrical double-layer capacitance of model Pt(111) and Au(111) electrodes. *J. Phys. Chem. Lett.* 9, 1927–1930. doi:10.1021/acs.jpclett.8b00610

Garza, A. J. (2019). Solvation entropy made simple. *J. Chem. Theory Comput.* 15, 3204–3214. doi:10.1021/acs.jctc.9b00214

Giannozzi, P., Baroni, S., Bonini, N., Calandra, M., Car, R., Cavazzoni, C., et al. (2009). Quantum espresso: A modular and open-source software project for quantum simulations of materials. *J. Phys. Condens. Matter* 21, 395502. doi:10.1088/0953-8984/21/39/395502

Gillen, R., and Robertson, J. (2013). Accurate screened exchange band structures for the transition metal monoxides MnO, FeO, CoO and NiO. *J. Phys. Condens. Matter* 25, 165502. doi:10.1088/0953-8984/25/16/165502

Goldsmith, Z. K., Calegari Andrade, M. F., and Selloni, A. (2021). Effects of applied voltage on water at a gold electrode interface from *ab initio* molecular dynamics. *Chem. Sci.* 12, 5865–5873. doi:10.1039/D1SC00354B

Grey, C. P., and Tarascon, J. M. (2017). Sustainability and *in situ* monitoring in battery development. *Nat. Mat.* 16, 45–56. doi:10.1038/NMAT4777

Gu, Y., Zhu, S., Wang, X., Hu, J., and Chen, H. (2020). A substantial hybridization between correlated Ni-d orbital and itinerant electrons in infinite-layer nickelates. *Commun. Phys.* 3, 84–89. doi:10.1038/s42005-020-0347-x

Hamelin, A. (1996). Cyclic voltammetry at gold single-crystal surfaces. Part 1. Behaviour at low-index faces. *J. Electroanal. Chem.* 407, 1–11. doi:10.1016/0022-0728(95)04499-X

Hammer, B., and Norskov, J. K. (1995). Why gold is the noblest of all the metals. *Nature* 376, 238–240. doi:10.1038/376238a0

Hansen, J., and McDonald, I. (2013). *Theory of simple liquids: With applications to soft matter*. Elsevier Science. doi:10.1016/C2010-0-66723-X

Heinz, H., Lin, T.-J., Kishore Mishra, R., and Emami, F. S. (2013). Thermodynamically consistent force fields for the assembly of inorganic, organic, and biological nanostructures: The INTERFACE force field. *Langmuir* 29, 1754–1765. doi:10.1021/la3038846

Heinz, H., Vaia, R. A., Farmer, B. L., and Naik, R. R. (2008). Accurate simulation of surfaces and interfaces of face-centered cubic metals using 126 and 96 Lennard-Jones potentials. *J. Phys. Chem. C* 112, 17281–17290. doi:10.1021/jp801931d

Himmetoglu, B., Floris, A., de Gironcoli, S., and Cococcioni, M. (2014). Hubbard-corrected DFT energy functionals: The LDA+*U* description of correlated systems. *Int. J. Quantum Chem.* 114, 14–49. doi:10.1002/qua.24521

Hjorth Larsen, A., Jørgen Mortensen, J., Blomqvist, J., Castelli, I. E., Christensen, R., Dułak, M., et al. (2017). The atomic simulation environment—A python library for working with atoms. *J. Phys. Condens. Matter* 29, 273002. doi:10.1088/1361-648X/aa680e

Hofmann, T., Yu, T. H., Folse, M., Weinhardt, L., Bär, M., Zhang, Y., et al. (2012). Using photoelectron spectroscopy and quantum mechanics to determine *d*-band energies of metals for catalytic applications. *J. Phys. Chem. C* 116, 24016–24026. doi:10.1021/jp303276z

Hörmann, N. G., Andreussi, O., and Marzari, N. (2019). Grand canonical simulations of electrochemical interfaces in implicit solvation models. *J. Chem. Phys.* 150, 041730. doi:10.1063/1.5054580

Jahn, S., and Kowalski, P. M. (2014). Theoretical approaches to structure and spectroscopy of Earth materials. *Rev. Mineral. Geochem.* 78, 691–743. doi:10.2138/rmg.2014.78.17

Ji, Y., Beridze, G., Bosbach, D., and Kowalski, P. M. (2017a). Heat capacities of xenotime-type ceramics: An accurate *ab initio* prediction. *J. Nucl. Mat.* 494, 172–181. doi:10.1016/j.jnucmat.2017.07.026

Ji, Y., Beridze, G., Li, Y., and Kowalski, P. M. (2017b). Large scale simulation of nuclear waste materials. *Energy Procedia* 127, 416–424. doi:10.1016/j.egypro.2017.08.108

Ji, Y., Kowalski, P. M., Neumeier, S., Deissmann, G., Kulriya, P. K., and Gale, J. D. (2017c). Atomistic modeling and experimental studies of radiation damage in monazite-type $LaPO_4$ ceramics. *Nucl. Instrum. Methods Phys. Res. Sect. B* 393, 54–58. doi:10.1016/j.nimb.2016.09.031

Jolley, K., Asuvathraman, R., and Smith, R. (2017). Inter-atomic potentials for radiation damage studies in $CePO_4$ monazite. *Nucl. Instrum. Methods Phys. Res. B* 393, 93–96. doi:10.1016/j.nimb.2016.10.016

Jorgensen, W. L., and Tirado-Rives, J. (1988). The OPLS [optimized potentials for liquid simulations] potential functions for proteins, energy minimizations for crystals of cyclic peptides and crambin. *J. Am. Chem. Soc.* 110, 1657–1666. doi:10.1021/ja00214a001

Jung, C. K., Braunwarth, L., Sinyavskiy, A., and Jacob, T. (2021). Thermodynamic description of interfaces applying the 2PT method on ReaxFF molecular dynamics simulations. *J. Phys. Chem. C* 125, 24663–24670. doi:10.1021/acs.jpcc.1c07327

Kalyani, P., and Kalaiselvi, N. (2005). Various aspects of $LiNiO_2$ chemistry: A review. *Sci. Technol. Adv. Mater.* 6, 689–703. doi:10.1016/j.stam.2005.06.001

Kastlunger, G., Lindgren, P., and Peterson, A. A. (2018). Controlled-potential simulation of elementary electrochemical reactions: Proton discharge on metal surfaces. *J. Phys. Chem. C* 122, 12771–12781. doi:10.1021/acs.jpcc.8b02465

Kick, M., Reuter, K., and Oberhofer, H. (2019). Intricacies of DFT+*U*, not only in a numeric atom centered orbital framework. *J. Chem. Theory Comput.* 15, 1705–1718. doi:10.1021/acs.jctc.8b01211

Klinkova, A., De Luna, P., Dinh, C.-T., Voznyy, O., Larin, E. M., Kumacheva, E., et al. (2016). Rational design of efficient palladium catalysts for electroreduction of carbon dioxide to formate. *ACS Catal.* 6, 8115–8120. doi:10.1021/acscatal.6b01719

Kowalski, P. M. (2020). Formation enthalpy of $Ln_2B_2O_7$-type (B=Ti, Sn, Hf, Zr) compounds. *Scr. Mater* 189, 7–10. doi:10.1016/j.scriptamat.2020.07.048

Kowalski, P. M., Beridze, G., Ji, Y., and Li, Y. (2017a). Towards reliable modeling of challenging f electrons bearing materials: Experience from modeling of nuclear materials. *MRS Adv.* 2017, 491–497. doi:10.1557/adv.2017.46

Kowalski, P. M., Beridze, G., Li, Y., Ji, Y., Friedrich, C., Sasioglu, E., et al. (2016). Feasible and reliable *ab initio* approach to computation of materials relevant for nuclear waste management. *Ceram. Trans.* 258, 205–217. doi:10.1002/9781119236016.ch21

Kowalski, P. M., Beridze, G., Vinograd, V. L., and Bosbach, D. (2015). Heat capacities of lanthanide and actinide monazite-type ceramics. *J. Nucl. Mat.* 464, 147–154. doi:10.1016/j.jnucmat.2015.04.032

Kowalski, P. M., He, Z., and Cheong, O. (2021). Electrode and electrolyte materials from atomistic simulations: Properties of Li_xFePO_4 electrode and zircon-based ionic conductors. *Front. Energy Res.* 9. doi:10.3389/fenrg.2021.653542

Kowalski, P. M., Ji, Y., Li, Y., Arinicheva, Y., Beridze, G., Neumeier, S., et al. (2017b). Simulation of ceramic materials relevant for nuclear waste management: Case of $La_{1-x}Eu_xPO_4$ solid solution. *Nucl. Instrum. Methods Phys. Res. Sect. B* 393, 68–72. doi:10.1016/j.nimb.2016.09.029

Kowalski, P. M., and Li, Y. (2016). Relationship between the thermodynamic excess properties of mixing and the elastic moduli in the monazite-type ceramics. *J. Eur. Ceram. Soc.* 36, 2093–2096. doi:10.1016/j.jeurceramsoc.2016.01.051

Kresse, G., and Furthmüller, J. (1996a). Efficiency of *ab-initio* total energy calculations for metals and semiconductors using a plane-wave basis set. *Comput. Mat. Sci.* 6, 15–50. doi:10.1016/0927-0256(96)00008-0

Kresse, G., and Furthmüller, J. (1996b). Efficient iterative schemes for *ab initio* total-energy calculations using a plane-wave basis set. *Phys. Rev. B* 54, 11169–11186. doi:10.1103/PhysRevB.54.11169

Kresse, G., and Hafner, J. (1993). *Ab initio* molecular dynamics for liquid metals. *Phys. Rev. B* 47, 558–561. doi:10.1103/PhysRevB.47.558

Krishnamurthy, R., Yoon, Y.-G., Srolovitz, D. J., and Car, R. (2004). Oxygen diffusion in yttria-stabilized zirconia: A new simulation model. *J. Am. Ceram.* 87, 1821–1830. doi:10.1111/j.1151-2916.2004.tb06325.x

Kvashnina, K. O., Kowalski, P. M., Butorin, S. M., Leinders, G., Pakarinen, J., Bès, R., et al. (2018). Trends in the valence band electronic structures of mixed uranium oxides. *Chem. Commun.* 54, 9757–9760. doi:10.1039/C8CC05464A

Laubach, S., Laubach, S., Schmidt, C. P., Ensling, D., Schmid, S., Jaegermann, W., et al. (2009). Changes in the crystal and electronic structure of $LiCoO_2$ and $LiNiO_2$ upon Li intercalation and de-intercalation. *Phys. Chem. Chem. Phys.* 11, 3278–3289. doi:10.1039/B901200A

Le, J., Iannuzzi, M., Cuesta, A., and Cheng, J. (2017). Determining potentials of zero charge of metal electrodes versus the standard hydrogen electrode from density-functional-theory-based molecular dynamics. *Phys. Rev. Lett.* 119, 016801. doi:10.1103/PhysRevLett.119.016801

Lee, K., Youn, Y., and Han, S. (2017). Identification of ground-state spin ordering in antiferromagnetic transition metal oxides using the Ising model and a genetic algorithm. *Sci. Technol. Adv. Mater* 18, 246–252. doi:10.1080/14686996.2017.1300046

Letchworth-Weaver, K., and Arias, T. A. (2012). Joint density functional theory of the electrode-electrolyte interface: Application to fixed electrode potentials, interfacial capacitances, and potentials of zero charge. *Phys. Rev. B* 86, 075140. doi:10.1103/PhysRevB.86.075140

Li, X., Wang, Q., Guo, H., Artrith, N., and Urban, A. (2022). Understanding the onset of surface degradation in linio$_2$ cathodes. *ACS Appl. Energy Mat.* 5, 5730–5741. doi:10.1021/acsaem.2c00012

Li, Y., Kowalski, P. M., Beridze, G., Birnie, A. R., Finkeldei, S., and Bosbach, D. (2015). Defect formation energies in $A_2B_2O_7$ pyrochlores. *Scr. Mat.* 107, 18–21. doi:10.1016/j.scriptamat.2015.05.010

Li, Y., Kowalski, P. M., Beridze, G., Blanca-Romero, A., Ji, Y., Vinograd, V. L., et al. (2016). Atomistic simulations of ceramic materials relevant for nuclear waste management: Cases of monazlte and pyrochlore. *Ceram. Trans.* 255, 165–175. doi:10.1002/9781119234531.ch15

Li, Y., Kowalski, P. M., Blanca-Romero, A., Vinograd, V., and Bosbach, D. (2014). *Ab initio* calculation of excess properties of solid solutions. *J. Solid State Chem.* 220, 137–141. doi:10.1016/j.jssc.2014.08.005

Li, Y., and Kowalski, P. M. (2018). Energetics of defects formation and oxygen migration in pyrochlore compounds from first principles calculations. *J. Nucl. Mat.* 505, 255–261. doi:10.1016/j.jnucmat.2017.11.005

Lin, S.-T., Blanco, M., and Goddard, W. A. (2003). The two-phase model for calculating thermodynamic properties of liquids from molecular dynamics: Validation for the phase diagram of Lennard-Jones fluids. *J. Chem. Phys.* 119, 11792–11805. doi:10.1063/1.1624057

Lin, S.-T., Maiti, P. K., and Goddard, W. A. (2010). Two-phase thermodynamic model for efficient and accurate absolute entropy of water from molecular dynamics simulations. *J. Phys. Chem. B* 114, 8191–8198. doi:10.1021/jp103120q

Malik, R., Tomer, V. K., Mishra, Y. K., and Lin, L. (2020). Functional gas sensing nanomaterials: A panoramic view. *Appl. Phys. Rev.* 7, 021301. doi:10.1063/1.5123479

Martínez, L., Andrade, R., Birgin, E. G., and Martínez, J. M. (2009). Packmol: A package for building initial configurations for molecular dynamics simulations. *J. Comput. Chem.* 30, 2157–2164. doi:10.1002/jcc.21224

Marzari, N., Mostofi, A. A., Yates, J. R., Souza, I., and Vanderbilt, D. (2012). Maximally localized Wannier functions: Theory and applications. *RMP* 84, 1419–1475. doi:10.1103/RevModPhys.84.1419

Mathew, K., Kolluru, V. S. C., Mula, S., Steinmann, S. N., and Hennig, R. G. (2019). Implicit self-consistent electrolyte model in plane-wave density-functional theory. *J. Chem. Phys.* 151, 234101. doi:10.1063/1.5132354

Mathew, K., Sundararaman, R., Letchworth-Weaver, K., Arias, T. A., and Hennig, R. G. (2014). Implicit solvation model for density-functional study of nanocrystal surfaces and reaction pathways. *J. Chem. Phys.* 140, 084106. doi:10.1063/1.4865107

Maxisch, T., and Ceder, G. (2006). Elastic properties of olivine Li_xFePO_4 from first principles. *Phys. Rev. B* 73, 174112. doi:10.1103/PhysRevB.73.174112

Millikan, R. C., and Pitzer, K. S. (1957). Infrared spectra and vibrational assignment of monomeric formic acid. *J. Chem. Phys.* 27, 1305–1308. doi:10.1063/1.1743996

Mock, M., Bianchini, M., Fauth, F., Albe, K., and Sicolo, S. (2021). Atomistic understanding of the $LiNiO_2$–NiO_2 phase diagram from experimentally guided lattice models. *J. Mat. Chem. A* 9, 14928–14940. doi:10.1039/D1TA00563D

Mogilevsky, P. (2007). On the miscibility gap in monazite–xenotime systems. *Phys. Chem. Min.* 34, 201–214. doi:10.1007/s00269-006-0139-1

Molenda, J., Wilk, P., and Marzec, J. (2002). Structural, electrical and electrochemical properties of $LiNiO_2$. *Solid State Ion.* 146, 73–79. doi:10.1016/S0167-2738(01)00992-4

Monkhorst, H. J., and Pack, J. D. (1976). Special points for brillouin-zone integrations. *Phys. Rev. B* 13, 5188–5192. doi:10.1103/PhysRevB.13.5188

Mukai, K., Sugiyama, J., and Aoki, Y. (2010). Structural, magnetic, and electrochemical studies on lithium insertion materials $LiNi_{1-x}Co_xO_2$ with $0 < x < 0.25$. *J. Solid State Chem.* 183, 1726–1732. doi:10.1016/j.jssc.2010.05.019

Murphy, G. L., Zhang, Z., Tesch, R., Kowalski, P. M., Avdeev, M., Kuo, E. Y., et al. (2021). Tilting and distortion in rutile-related mixed metal ternary uranium oxides: A structural, spectroscopic, and theoretical investigation. *Inorg. Chem.* 60, 2246–2260. doi:10.1021/acs.inorgchem.0c03077

Nakamura, K., Arita, R., Yoshimoto, Y., and Tsuneyuki, S. (2006). First-principles calculation of effective onsite coulomb interactions of 3*d* transition metals: Constrained local density functional approach with maximally localized wannier functions. *Phys. Rev. B* 74, 235113. doi:10.1103/PhysRevB.74.235113

Neumeier, S., Arinicheva, Y., Ji, Y., Heuser, J. M., Kowalski, P. M., Kegler, P., et al. (2017a). New insights into phosphate based materials for the immobilisation of actinides. *Radiochim. Acta* 105, 961–984. doi:10.1515/ract-2017-2819

Neumeier, S., Kegler, P., Arinicheva, Y., Shelyug, A., Kowalski, P. M., Schreinemachers, C., et al. (2017b). Thermochemistry of $La_{1-x}Ln_xPO_4$ monazites (Ln=Gd, Eu). *J. Chem. Thermodyn.* 105, 396–403. doi:10.1016/j.jct.2016.11.003

Nishihara, S., and Otani, M. (2017). Hybrid solvation models for bulk, interface, and membrane: Reference interaction site methods coupled with density functional theory. *Phys. Rev. B* 96, 115429. doi:10.1103/physrevb.96.115429

Ohzuku, T., Ueda, A., and Nagayama, M. (1993). Electrochemistry and structural chemistry of LiNiO2 (R3m) for 4 volt secondary lithium cells. *J. Electrochem. Soc.* 140, 1862–1870. doi:10.1149/1.2220730

Okhotnikov, K., Charpentier, T., and Cadars, S. (2016). Supercell program: A combinatorial structure-generation approach for the local-level modeling of atomic substitutions and partial occupancies in crystals. *J. Cheminformatics.* 8, 17. doi:10.1186/s13321-016-0129-3

Olivetti, E. A., Ceder, G., Gaustad, G. G., and Fu, X. (2017). Lithium-ion battery supply chain considerations: Analysis of potential bottlenecks in critical metals. *Joule* 1, 229–243. doi:10.1016/j.joule.2017.08.019

Otani, M., and Sugino, O. (2006). First-principles calculations of charged surfaces and interfaces: A plane-wave nonrepeated slab approach. *Phys. Rev. B* 73, 115407. doi:10.1103/PhysRevB.73.115407

Pascal, T. A., Lin, S.-T., and Goddard, W. A. (2011). Thermodynamics of liquids: Standard molar entropies and heat capacities of common solvents from 2PT molecular dynamics. *Phys. Chem. Chem. Phys.* 13, 169–181. doi:10.1039/C0CP01549K

Pavarini, E., Koch, E., Anders, F., and Jarrell, M. (Editors) (2012). Correlated electrons: from models to materials. lecture notes of the Autumn School Correlated Electrons 2012: at Forschungszentrum Jülich, 3-7 September 2012. No. Band 2 in Schriften des Forschungszentrums Jülich. Reihe Modeling and Simulation (Jülich: Forschungszentrum Jülich, Zentralbibliothek, Verl)for Advanced Simulation, I., and for Simulation Sciences, G. R. S.

Perdew, J. P., Burke, K., and Ernzerhof, M. (1996). Generalized gradient approximation made simple. *Phys. Rev. Lett.* 77, 3865–3868. doi:10.1103/PhysRevLett.77.3865

Perdew, J. P., Ruzsinszky, A., Csonka, G. I., Vydrov, O. A., Scuseria, G. E., Constantin, L. A., et al. (2008). Erratum: Restoring the density-gradient expansion for exchange in solids and surfaces [phys. Rev. Lett.**100**, 136406 (2008)]. *Phys. Rev. Lett.* 100, 039902. doi:10.1103/physrevlett.102.039902

Petukhov, A. G., Mazin, I. I., Chioncel, L., and Lichtenstein, A. I. (2003). Correlated metals and the LDA + *U* method. *Phys. Rev. B* 67, 153106. doi:10.1103/PhysRevB.67.153106

Plimpton, S. (1995). Fast parallel algorithms for short-range molecular dynamics. *J. Comput. Phys.* 117, 1–19. doi:10.1006/jcph.1995.1039

Ruban, A., Hammer, B., Stoltze, P., Skriver, H., and Nørskov, J. (1997). Surface electronic structure and reactivity of transition and noble metals1Communication presented at the First Francqui Colloquium, Brussels, 19–20 February 1996.1. *J. Mol. Catal. A Chem.* 115, 421–429. doi:10.1016/S1381-1169(96)00348-2

Rustad, J. R. (2012). Density functional calculations of the enthalpies of formation of rare-Earth orthophosphates. *Am. Mineral.* 97, 791–799. doi:10.2138/am.2012.3948

Ryee, S., and Han, M. J. (2018). The effect of double counting, spin density, and Hund interaction in the different DFT+*U* functionals. *Sci. Rep.* 8, 9559. doi:10.1038/s41598-018-27731-4

Saha, P., and Zenyuk, I. V. (2021). Electrokinetic streaming current method to probe polycrystalline gold electrode-electrolyte interface under applied potentials. *J. Electrochem. Soc.* 168, 046511. doi:10.1149/1945-7111/abf4aa

Şaşıoğlu, E., Friedrich, C., and Blügel, S. (2011). Effective coulomb interaction in transition metals from constrained random-phase approximation. *Phys. Rev. B* 83, 121101. doi:10.1103/PhysRevB.83.121101

Schnell, I., Czycholl, G., and Albers, R. C. (2002). Hubbard-*U* calculations for Cu from first-principle Wannier functions. *Phys. Rev. B* 65, 075103. doi:10.1103/PhysRevB.65.075103

Schwarz, K., and Sundararaman, R. (2020). The electrochemical interface in first-principles calculations. *Surf. Sci. Rep.* 75, 100492. doi:10.1016/j.surfrep.2020.100492

Seo, D.-H., Urban, A., and Ceder, G. (2015). Calibrating transition metal energy levels and oxygen bands in first principles calculations: Accurate prediction of redox potentials and charge transfer in lithium transition metal oxides. *Phys. Rev. B* 92, 115118. doi:10.1103/PhysRevB.92.115118

Shishkin, M., and Sato, H. (2016). Self-consistent parametrization of DFT + *U* framework using linear response approach: Application to evaluation of redox potentials of battery cathodes. *Phys. Rev. B* 93, 085135. doi:10.1103/PhysRevB.93.085135

Stamenkovic, V. R., Strmcnik, D., Lopes, P. P., and Markovic, N. M. (2017). Energy and fuels from electrochemical interfaces. *Nat. Mat.* 16, 57–69. doi:10.1038/NMAT4738

Stout, J. W., and Fisher, L. H. (1941). The entropy of formic acid. The heat capacity from 15 to 300°K. Heats of fusion and vaporization. *J. Chem. Phys.* 9, 163–168. doi:10.1063/1.1750869

Takahashi, Y., Kijima, N., Dokko, K., Nishizawa, M., Uchida, I., and Akimoto, J. (2007). Structure and electron density analysis of electrochemically and chemically delithiated $LiCoO_2$ single crystals. *J. Solid State Chem.* 180, 313–321. doi:10.1016/j.jssc.2006.10.018

Tesch, R., Kowalski, P. M., and Eikerling, M. H. (2021). Properties of the Pt(111)/electrolyte electrochemical interface studied with a hybrid DFT-solvation approach. *J. Phys. Condens. Matter* 33, 444004. doi:10.1088/1361-648X/ac1aa2

Tesch, R., and Kowalski, P. M. (2022). Hubbard *U* parameters for transition metals from first principles. *Phys. Rev. B* 105, 195153. doi:10.1103/PhysRevB.105.195153

van Elp, J., Wieland, J. L., Eskes, H., Kuiper, P., Sawatzky, G. A., de Groot, F. M. F., et al. (1991). Electronic structure of CoO, Li-doped CoO, and $LiCoO_2$. *Phys. Rev. B* 44, 6090–6103. doi:10.1103/PhysRevB.44.6090

Vanderbilt, D. (1990). Soft self-consistent pseudopotentials in a generalized eigenvalue formalism. *Phys. Rev. B* 41, 7892–7895. doi:10.1103/PhysRevB.41.7892

Vasiljevic, N., Trimble, T., Dimitrov, N., and Sieradzki, K. (2004). Electrocapillarity behavior of Au(111) in $SO_4^{2-}$and F^-. *Langmuir* 20, 6639–6643. doi:10.1021/la049632f

Vogiatzis, K. D., Polynski, M. V., Kirkland, J. K., Townsend, J., Hashemi, A., Liu, C., et al. (2019). Computational approach to molecular catalysis by 3d transition metals: Challenges and opportunities. *Chem. Rev.* 119, 2453–2523. doi:10.1021/acs.chemrev.8b00361

Wang, J., Zhou, Y., and Lin, Z. (2005). First-principles elastic stiffness of $LaPO_4$ monazite. *Appl. Phys. Lett.* 87, 051902. doi:10.1063/1.2005392

Wang, L., Li, J., Lu, G., Li, W., Tao, Q., Shi, C., et al. (2020). Fundamentals of electrolytes for solid-state batteries: Challenges and perspectives. *Front. Mat. Sci.* 7. doi:10.3389/fmats.2020.00111

Wang, M., and Navrotsky, A. (2004). Enthalpy of formation of $LiNiO_2$, $LiCoO_2$ and their solid solution. LiNi1xCoxO2. *Solid State Ionics* 166, 167–173. doi:10.1016/j.ssi.2003.11.004

Wu, X., Kang, F., Duan, W., and Li, J. (2019). Density functional theory calculations: A powerful tool to simulate and design high-performance energy storage and conversion materials. *Prog. Nat. Sci.* 29, 247–255. doi:10.1016/j.pnsc.2019.04.003

Yoshida, T., Hongo, K., and Maezono, R. (2019). First-principles study of structural transitions in $LiNiO_2$ and high-throughput screening for long life battery. *J. Phys. Chem. C* 123, 14126–14131. doi:10.1021/acs.jpcc.8b12556

Zaffran, J., and Caspary Toroker, M. (2016). Benchmarking density functional theory based methods to model NiOOH material properties: Hubbard and van der waals corrections vs hybrid functionals. *J. Chem. Theory Comput.* 12, 3807–3812. doi:10.1021/acs.jctc.6b00657

Zhang, Z., Mondal, S., Mandal, S., Allred, J. M., Aghamiri, N. A., Fali, A., et al. (2021). Neuromorphic learning with Mott insulator NiO. *Proc. Natl. Acad. Sci.* 118, e2017239118. doi:10.1073/pnas.2017239118

Zhu, X., Chen, N., Lian, F., Song, Y., and Li, Y. (2011). First principle calculation of lithiation/delithiation voltage in Li-ion battery materials. *Chin. Sci. Bull.* 56, 3229–3232. doi:10.1007/s11434-011-4705-7

frontiers | Frontiers in Energy Research

TYPE Review
PUBLISHED 22 March 2023
DOI 10.3389/fenrg.2023.1108389

OPEN ACCESS

EDITED BY
Uwe Schröder,
University of Greifswald, Germany

REVIEWED BY
Sunil A. Patil,
Indian Institute of Science Education and Research Mohali, India
Feng Zhao,
Institute of Urban Environment (CAS), China

*CORRESPONDENCE
Ioannis Ieropoulos,
i.ieropoulos@soton.ac.uk

SPECIALTY SECTION
This article was submitted to Bioenergy and Biofuels, a section of the journal Frontiers in Energy Research

RECEIVED 26 November 2022
ACCEPTED 06 March 2023
PUBLISHED 22 March 2023

CITATION
Ieropoulos I and Greenman J (2023), The future role of MFCs in biomass energy. *Front. Energy Res.* 11:1108389. doi: 10.3389/fenrg.2023.1108389

The future role of MFCs in biomass energy

Ioannis Ieropoulos[1]* and John Greenman[2]

[1]Civil, Maritime and Environmental Engineering, University of Southampton, Southampton, United Kingdom, [2]Department of Applied Sciences, University of the West of England, Bristol, United Kingdom

Microbial fuel cells (MFC) are an emerging green technology which offers several comparative advantages over other technologies for utilizing biomass. It is a technology that treats (cleans) wet organic waste, converting chemical energy to electricity that is used for connected peripherals and target applications. The main advantage is the technology's ability to utilise wet biomass in suspension or in solution (i.e., too wet to burn) and change the biomass directly into bioenergy in the form of electricity. All other technologies either combust the biomass directly (e.g., wood fuel) or change the biomass into refined fuels which are then combusted or fed to chemical fuel cells to generate heat or electricity. Excluding methane production from biomass, and fermentation leading to hydrogen production, all other biomass/biofuel technologies utilize dry plant matter, which mainly consists of cellulose or lignocellulose and they cannot directly utilize sludge or slurries of organic detritus material. The substrates used for MFCs are not traditionally made into organic fuels, as with other biomass technologies, but are used directly as fuel, recasting the "waste" suspensions and solutions, and promoting them into fuels themselves. To a stack of MFCs, a polluted river, landfill leachate or farmland run-off, can all be reassigned as fuel. This wet fuel is widespread around the planet, the amounts found and the energy contained within are significant, and the cost as a fuel is close to zero. This review gives a general overview of biomass energy along with extraction techniques and compares advantages and disadvantages of MFCs with other biomass technologies for producing electrical energy.

KEYWORDS

microbial fuel cells, biomass, bioenergy, clean water, environmentally friendly

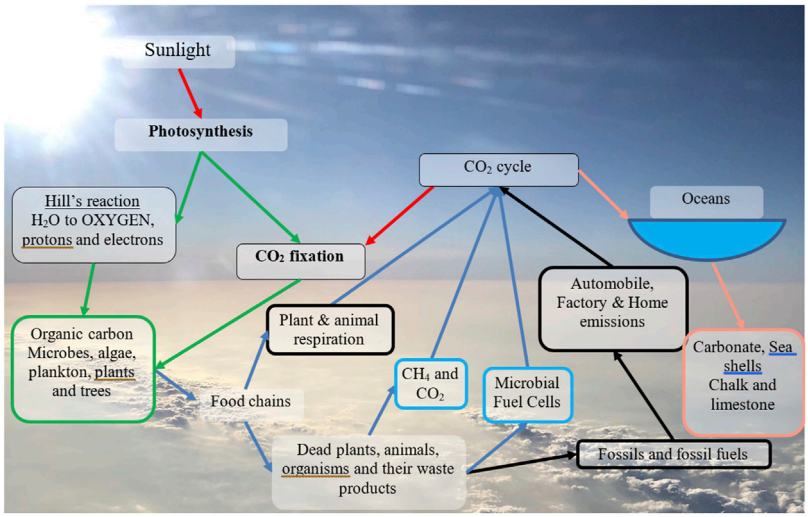

GRAPHICAL ABSTRACT

Introduction

Plants and photosynthetic microorganisms are examples of autotrophs that use sunlight to make their own organic molecules by fixing carbon dioxide. Because they make their own food by photosynthesis, they are the main form of primary producers of biomass, acting as the conduit for energy and bio-matter to enter food chains or webs (Mestre et al., 2022). A food chain describes which species feed off which other species whilst a food web describes the food chains that contribute to making a whole ecosystem. The position of a species within an ecosystem is referred to as a trophic level in the web or food chain. The base of the trophic pyramid is made from primary producers, these being autotrophic species that are nearly always photosynthetic (plants, bacteria or algae). The next level above the primary producers are the primary consumers, typically herbivores. Further levels include secondary and then tertiary consumers typically omnivores and/or carnivores, with the top level being termed the apex predators. Each food chain is typically composed of five or six trophic levels. Trophic level zero refers to species that do not fit into the existing trophic levels. These species are the detritivores or scavengers. They play a vital role in the flow of carbon and energy through an ecosystem by decomposing dead organisms into their constituent organic or inorganic materials, which become available as nutrients to the primary producers. The detritivores or scavengers include earthworms, termites, and millipedes although most decomposers are fungi, protozoa and bacteria. Bacteria are the energy conversion drivers inside microbial fuel cells (MFCs), which when employed as integrated *living* power sources in robots (Ieropoulos, Greenman and Melhuish, 2010), introduce a new hybrid system, i.e., bio-robots or "Symbots," on trophic level zero.

Allometric scaling

All lifeforms are subject to allometric scaling, which also determines their position in an ecosystem. With respect to primary and secondary biomass, smaller organisms (whether multicellular or unicellular) grow faster than larger lifeforms. The study of the laws of growth rate *versus* size originate from the allometric formula by Otto Snell (Snell, 1892) although the term "allometric scaling" was introduced by Huxley and Teissier (1936) following the work of Kleiber (1932). The concept of allometry extends to all forms of life, although the relationship between growth rate and size does not apply uniformly, in that the relationship for prokaryotes is superlinear, for protists is linear and for metazoa is sublinear (Delong et al., 2010). As recently reported, allometric scaling can also be applied to hybrid systems, i.e., non-living vessels containing living microorganisms; here we make specific reference to Microbial Fuel Cells (Greenman and Ieropoulos, 2017). Allometric scaling is the metric by which ecosystems operate and its significance will also be discussed in the Conclusion section.

With regard to biomass transformation, a wide range of processes can be applied to plants, wood and waste including direct combustion, co-firing, gasification, pyrolysis, fermentation and anaerobic decomposition. However, all processes involving heat or combustion are inefficient if the biomass is too wet, and has been the motivation for developing efficient biotransformation techniques, which are listed and discussed below.

Biomass and biofuels

Biomass generation removes an equivalent amount of CO_2 from the atmosphere to that emitted from combustion, which means that in theory, this is truly a net-zero process (World Bioenergy Association, 2019). Fossil fuel combustion for heat, electricity, and transportation fuels, contributed ca. 80% of global GHG emissions in 2017 (World Bioenergy Association, 2019). Bioenergy production worldwide reached nearly 584 TWh in 2020 (Black et al., 2021). Globally in 2019, bioenergy accounted for about 11.6% of total energy consumption. With regard to the bioenergy-biomass sector, the largest source is from burning wood

(or wood related products, wood chips, sawdust, coppiced branches, recycled cardboard and paper) allowing energy to be extracted by combustion with oxygen, from small fires to large incinerators. The energy is released in the form of heat, which is converted to electricity through inefficient generators. Nevertheless, all biomass reserves are potentially renewable, remove CO_2 and produce O_2, although slow growing tree species are not efficient for biomass growth, as their primary purpose is fruit production for human and animal consumption. Micro-algae, microbial sludge and microbial cultures have much higher productivity per unit of biomass than types of grass or plant and are totally renewable. Plants, wood, and waste are the most common forms of biomass material for producing energy. These types of biomass feedstock can be combusted to create heat (direct energy) which *via* steam production (as the driving force for turbines) can be used to produce electricity. These biomass substrates can also be processed into biofuels (indirect energy).

Biomass mainly in the form of plants and algae rather than dead animal matter, is perhaps the only renewable source that can be converted into ethanol and/or biodiesel. These two biofuels—currently produced by gasification in the US, Austria and Sweden-are currently used for transportation. Based mainly on the biomass, biofuels are classified broadly into three major generations (Lee and Lavoie, 2013). Biofuels of the first-generation come from the fermentation of carbohydrates (sugar beet, sugarcane, corn starch or wheat) to give bioethanol, an alcoholic fuel that when refined can be used directly in a conventional chemical fuel cell to produce electricity or serve as an additive to gasoline. The problem with first-generation fuels is that they are made from biomass that is generally edible by humans or animals. Ethanol requires significant land use; an acre of corn, for example, produces ~400 gallons of ethanol but limits the use of this land to only corn, which in turn implies intensive use of pesticides. Biodiesel is produced from oily plants and seeds, including soy, palm and canola. Alternatively, used edible oils, such as vegetable oil or recycled cooking fat, can also be used following esterification and transesterification using methanol.

Second-generation biofuels, can be produced from non-food-based biomass such as lignocellulosic agricultural waste and municipal waste. This is an advantage shadowed by economic uncertainty and technical complexity of the hydrolysis process required to overcome the chemical barriers and structural rigidity of lignocellulosic biomass. Lignin and cellulose have been reported as co-substrates in Microbial Fuel Cells for energy and biofuel generation, which gives the technology a competitive advantage and provides a possible alternative to the aforementioned challenges. When using the right bacteria, the otherwise recalcitrant lignocellulose is efficiently broken down.

The costs associated with bioethanol production depend mainly on the costs of feedstock substrates which give different yields depending on (a) the species of microbes chosen for the fermentation reactions (b) the addition of cellulase for enzymatic hydrolysis of cellulose into sugars, and (c) the nature of the pre-treatment (e.g., yield of sugars available for fermentation). Most current ethanol production is based on corn, starch and sugars but their use may not be desirable due to their edible value. In contrast, the straw of rice, wheat and corn as well as bagasse are now more commonplace because they contain cellulose, hemicellulose and lignin rather than edible sugars. In theory, there is sufficient rice straw in the world to produce 205 billion litres of bioethanol per year. Physicochemical treatment may include milling, grinding, cutting, thermal heating, microwaving, steam explosion, pyrolysing, chemical pre-treatment, wet oxidation, acid or alkali pre-treatment and the current cost of ethanol is $3.93/gallon, compared to $4.70/gallon for petrol (Sondhi et al., 2020).

Algae

The third generation of biofuels is based on photosynthetic organisms that do not require land but live in water, hydroponically, producing new or "primary" biomass. Microalgae can thrive in non-fresh i.e., salty, brackish water, contaminated with municipal, agricultural, industrial or even nuclear run-off. Microalgae are multiple times more efficient than terrestrial crops used for producing fuel. Third generation biofuels are also favoured because of the high growth rate of microalgae (*vis* allometric scaling) compared to any larger terrestrial plant; only microalgae can double their biomass every 1–2 days. The productivity is high compared to even the fastest of grass species. Moreover, they can grow in lagoons in marginal areas, which does not impose on the use of arable land for the production of food. The problem with microalgae lies when one needs a particular strain or species, especially strains that have been genetically modified (GM). Examples include strains capable of producing a high lipid content to make bio-diesel, and strains capable of synthesizing sugars, lactate and food supplements such as astaxanthin *via* photosynthesis (Shah et al., 2016). In these cases, they must be grown as a strict monoculture (i.e., be free of contamination) and (in GM strains) following lipid extraction, their DNA must be rendered before safe disposal or further utilization of cell debris. These steps can be very energy intensive, adding to the costs of production however, not entirely impossible. Sun et al. (2020) reported high growth rates for *Synechococcus elongatus* UTEX 2973, in photobioreactor volumes ranging from 50 mL to 100 L under non-sterile conditions, without contamination.

Algae (macro- and micro-algae) carry enormous potential for bio (mass)-energy. Seaweed or *Chlorella*, photosynthesise up to 30x faster than crops used for food or fuel, and do not impose on either land or freshwater. Although algae release carbon dioxide when burned, the amount is never more than what they fixed from carbon dioxide in the first place and the biomass can be replenished as a living organism through cultivation, releasing oxygen and absorbing pollutants and this would require less land than that needed for harvesting corn. Algae's high-value lipids can be converted to biofuel, which has been the main objective in the race for alternative fuels, necessitating genetic modification of certain species for ever higher lipid content. Algal growth requires carbon dioxide, making the process an excellent CO_2 scrubber. When algae are put under certain stress conditions to produce the desired by-product (for example, *Haematococcus pluvialis* producing astaxanthin; Shah et al., 2016), this comes at a high cost and still quite far from the current price of biodiesel (not from algae) of $5.34/gallon (US DoE, 2022).

Algal biodiesel (third-generation) is derived from microalgae or photosynthetic bacteria and has been considered as a viable option

TABLE 1 Advantages and challenges (*at present*) for microalgae-based fuel.

Advantages	Challenges
Sustainable, renewable and environmentally friendly resources	Still use fossil fuel-based techniques for manufacturing bioreactors, equipment
Non-toxic chemicals; and no competition with edible food	Other competing technologies
High photosynthetic energy conversion efficiency	Pre-treatment is required to process the biomass
High productivity, rapid growth rate high biomass yield	Low lipid extraction efficiency
Ability to adapt in a wide range of climatic conditions	High initial capital investment
Abundant and relatively cheap nutrient resources	High biofuel production cost
Can grow in arable or marginal land	Nutrient-rich water or fertilisers are needed for algal cultivation
Biodegradable products with moderately fast bioremediation	Commercialisation

to the problem of energy insecurity and climate change and removing the need for fossil fuels. This is particularly important when taking into account that for every tonne of algal biomass produced, approximately 1.83 tonnes of carbon dioxide are fixed, whereas petroleum diesel carries a massive negative balance; this is a significant competitive advantage in the context of GHG externalities (Um and Kim, 2009).

The commercialisation of algal biomass production *via* aquafarming faces significant economic challenges. The current annual production is around 38 million litres (Karthikeyan et al., 2020). Co-production of microalgae is possible, whilst treating wastewater, or for biogas upgrading, and whilst producing value-added products (VAPs) including exopolysaccharides, protein or the pharmaceutical, astaxanthin. This can drastically reduce biodiesel production costs. For example, the co-production of astaxanthin and biolipids for diesel can reduce the cost of biodiesel production from $3.90 to $0.54/L (Rafa et al., 2021). The economic analysis reveals that although there are technical challenges, the strategy is cost-effective; both feasible and profitable. The cost of producing microalgal biodiesel can be lowered to $0.73/kg dry weight when cultivated in wastewater and $0.54/L when co-produced with astaxanthin (Rafa et al., 2021). Microalgae-based value-added products are estimated to rise to $53.43 billion in 2026 (Rahman, 2020). The recent (2022–2023) increase in global fossil fuel prices is helping to reduce the gap in production costs that persist between biodiesel and petroleum diesel.

Biomass alongside other combustible renewable sources are promising alternatives, being the fourth largest energy source behind fossil fuels (Lam et al., 2019; Hoang et al., 2022), with a good capacity to address global energy needs (Azevedo et al., 2019). On the other hand, various types of biodiesel (Mofijur et al., 2021), mostly produced from biomass sources *via* transesterification (Hazrat et al., 2022), make up >80% of total biofuel production (Yin et al., 2020), but the real advantages can be gained from microalgal produced biodiesel. This is due to the microorganisms' ability to double biomass, through efficient sunlight, CO_2 and water utilisation that results in rapid rates of lipid accumulation for harvesting all year-round (Mubarak et al., 2019; Yin et al., 2020). Table 1 shows the advantages and challenges of microalgae-based fuel.

Cost reduction in microalgal biodiesel production are constantly developing whether these are improvements in bioreactor design, optimisation of the physicochemical conditions for cultivation, choice in the strains and species that are supplied as inoculum and insights into the processes and factors that affect yield, efficient harvesting and extraction methods (Peng et al., 2020; Ananthi et al., 2021; Rafa et al., 2021). Although many cost reduction strategies have been applied to algal cultivation which can make up a significant proportion of the cost, other areas, particularly pre-treatment, harvesting and dewatering have also been considered (Kang et al., 2019). Scientists worldwide have been elaborating the case for fuels derived from microalgae to close knowledge gaps; in particular Um and Kim (Um and Kim, 2009) and Rafa et al. (Rafa et al., 2021).

Biomethane from biomass

When biomass decays anaerobically it has the tendency to produce (bio)-methane, following a chain of reactions involving initially hydrolysis, then acidogenesis and acetogenesis and finally methanogenesis; this biomethane can replace methane obtained from fossil fuels. However, methane is a very potent greenhouse gas and any leakage to the atmosphere is a problem. The first description of an anaerobic methane digester was in 1859, more than 160 years ago, in India (Marsh, 2008). Despite it being one of the earliest methods for producing a biofuel, it is not classed as a first-generation biofuel because it does not utilise edible plants. It can however be classed as a second-generation biofuel because it uses biomass sources such as lignocellulosic agricultural and municipal waste which are non-food-based. Anaerobic digesters were originally designed for sewage sludge and manure, but units nowadays operate with two or more types of feedstocks, e.g., dairy manure mixed with grass and corn (found on the land) which can significantly increase gas production (Ma et al., 2017) as can the addition of kitchen grease (fats and oils) collected from restaurants or household waste. Animal fat and abattoir waste can also be used.

Microbial anaerobic digestion produces methane and carbon dioxide that can be purified into biosynthetic natural gas. This can then be pressurised into compressed natural gas (CNG) or liquefied natural gas (LNG) for use in vehicles or injected into the pipeline network. In general terms, methanogenesis is a slow process, requiring a retention time of 14–20 days in an anaerobic digester.

The process is sensitive to both high and low pH levels, with the optimum being between pH 6.5 and pH 8.0, as well as to many other inhibitors, especially oxygen. Substrates must have a high carbon to nitrogen (C:N) ratio, which usually results in N-rich feedstock having to be mixed with substrates high in C. Conversion yields can be up to 75% (usually stays between 60% and 70%) of which 50%–75% is CH_4, 25%–45% CO_2, 2%–8% water vapour and traces of H_2S, H_2, N_2, NH_3, and O_2. This biogas mixture will require reforming to remove particularly H_2S and siloxanes, unless it is being used for heat, following combustion. Reformed gas can then be converted to electricity using steam generation (40%) or methane fuel cells (45%). The effluent from anaerobic digestion still contains high COD and therefore requires further treatment and the process requires energy input for pumping water and gas compression. According to Bhatt et al. (2020), producing biomethane from carboxylate utilisation can be equal to or greater than biogas yield, whilst this is comparable with that of chemical plants, making this economically viable and environmentally friendly as it is a waste treatment process.

At present (2023) the price of biomethane can actually be 30% lower than the current natural gas pricing. Biomethane can be produced starting from €55/MWh, whereas natural gas costs are around €80/MWh, without considering CO_2 prices (European Biogas Association, 2023). As a renewable gas this will likely remain cheaper than natural gas in the short- and long-term. Methane is a very potent greenhouse gas, more than 80 times the warming power of carbon dioxide over the first 20 years after it reaches the atmosphere, so methane emissions (*via* fossil fuel oil and gas companies) are problematic in a world trying to be carbon neutral. The problem of methane emissions is not restricted to the fossil fuel industries and some research has looked into the characterisation and assessment of GHG emissions from typical operational biomethane facilities (Adams and McManus, 2019). This has revealed that there is a wide degree of variability in potential emission sources throughout the supply chain and there are several reasons for this. These include anything from weather, geological conditions, all the way to farming practice and experimental/measurement error. Biomethane emissions occur from crops, fertiliser production and application, the latter resulting in N_2O emission, crop yield, methane leakage, electricity use, and diesel use. It is therefore important for biomethane to be utilised locally, where it is produced (just like hydrogen) to avoid high complex systems of high maintenance thereby rendering biomethane a viable, low carbon fuel.

Hydrogen

The majority of hydrogen production-as much as 95% - is still predominantly produced from sources derived from fossil-based fuels, although there is a wider range of green sources that it could be produced from [Ferraren-De Cagalitan and Abundo, 2021). A large part of the industrial hydrogen is obtained from steam-methane reforming (SMR), while oil and coal gasification (CG) follow closely behind. The production costs are between 2 and 3 $/kg. These methods of producing hydrogen also generate greenhouse gases, which are the main drivers of climate change. Alternative methods of producing hydrogen arise from biological processes—hence the name "biohydrogen"—but as with any new technology, this is currently a more expensive process, costing between 3.7 and 7.02 $/kg for photofermentation and MEC respectfully (Ferraren-De Cagalitan and Abundo, 2021).

Biohydrogen production

Sustainable, carbon-neutral hydrogen fuel cells are only possible if they are supplied with renewable hydrogen (Taibi et al., 2018). As with algal biofuel, hydrogen production rates should be economically comparable with other sources of hydrogen. There is a number of different ways of producing biohydrogen, including dark- and photo-fermentation, direct and indirect biophotolysis and *via* microbial electrolysis cells (MECs) and microbial electrosynthesis cells (MES) (Vasiliadou et al., 2018). The majority of the relevant literature is on bio-hydrogen from MECs. This is a good way of recovering nutrients from waste streams in the cathode chamber, by applying an external potential (using a power source) to recombine electrons and protons, coming from the anode, to H_2 with the help of a catalyst. In some cases, phototrophic bacteria are used, which generate true bio-hydrogen when switching from the Krebs cycle to the Calvin cycle; this is also a neat way of nitrogen removal (Vasiliadou et al., 2018). An electrode potential still needs to be applied in order to help accelerate the otherwise sluggish reactions (by comparison).

In photo-fermentation, strains of photosynthetic purple non-sulphur bacteria are employed to convert added organic acids (carboxylate anaerobic fermentation) to CO_2 and H_2 under N-limited nutrient conditions (Sinha and Pandey, 2011; Sağır and Hallenbeck, 2019; Weber and Lipman, 2019). The naturally occurring organisms used include *Rhodobacter*, *Rhodobium*, *Rhodopseudomonas*, and *Rhodospirillum* strains, which are capable of transforming a whole list of substrates into H_2 across a wide range of light conditions (Das et al., 2014). Photofermentation (unlike biophotolysis) does not generate oxygen which inhibits the H_2 production. The yield of hydrogen is comparable to that of biophotolysis although this depends on the design of the photo-fermenter, light intensity, types of medium substrates and species of microorganism (Sağır and Hallenbeck, 2019).

Dark fermentation produces hydrogen in the absence of light. It has been known for many years that *Escherichia coli* and other facultative anaerobes (*Alcaligenes*, *Enterobacter* and *Citrobacter*) and some strictly anaerobic *Clostridium* species can ferment sugar substrates into short chain fatty acids including formic acid, which in turn is split by the formate hydrogen lyase (FHL) complex to produce hydrogen (Yoshida et al., 2005). It is well established that the highest theoretical yield for hydrogen is 4 mol of H_2 per mole of glucose, as shown below.

$$C_6H_{12}O_6 + 2H_2O \rightarrow 2CH_3COOH + 2HCOOH + 2H_2$$

$$2HCOOH \rightarrow CO_2 + 2H_2$$

Green algae and cyanobacteria can utilise light to break up water into its constituent components O_2 and H_2, *via* direct or indirect biophotolysis. Direct biophotolysis occurs when green algae such as *Chlamydomonas reinhardtii* or subspecies of the *Synechocystis*

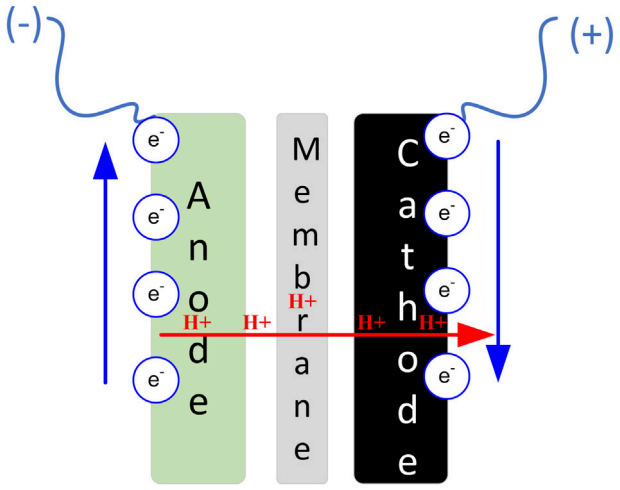

FIGURE 1
Basic diagram of a standard microbial fuel cell.

cyanobacterium, photosynthesise, i.e., when oxygen is also produced (Azwar et al., 2014), which can be explosive. Indirect biophotolysis is possible whereby certain strains of cyanobacteria can be grown through two distinct stages (Huesemann et al., 2010) a first stage of photosynthesis where carbon dioxide and water are converted into organic molecules some of which are used to make new cell material and oxygen which is evolved. A second phase (which is light independent) is then capable of breaking down the organic molecules into hydrogen, carbon dioxide and other soluble metabolites (Weber and Lipman, 2019). The advantage of the indirect method is that the hydrogen is free of oxygen, whereas the disadvantages are, firstly, the low amounts of H_2 produced by this method and secondly, the need for more complex (and more expensive) two phase cultivation systems (Ferraren-De Cagalitan and Abundo, 2021).

Microbial carboxylates

Carboxylates is the collective term for short chain fatty acids including acetate, propionate, lactate and butyrate. These are the intended "products" of the system and can be separated and used as feedstocks for other chemical conversions into a wide range of useful products (e.g., plastics and liquid fuels). The advantages of the carboxylate system are that they can cope with a wide range of organic wastes (Agler et al., 2011) as the inputs and the fermentation steps are far more rapid per gram of mixture than methane production. The challenge is in finding a way to select against methanogens and other "slow" pathways in order to maximise hydrolysis and primary fermentation steps. In conventional fermentation this is achieved by: 1) controlling hydrogen gas concentrations in the liquid phase (dissolved hydrogen); by keeping them low there is no methanogenesis. 2) by removing acetate or higher acid products as soon as they are formed (by continuous flow electro-osmosis or other membrane techniques); this removes the primary substrates (acetate) for methane production. Another method for controlling methanogenesis is to introduce oxygen at low partial pressures which inhibits methanogenesis but has little effect on fermentation to acids by facultative anaerobes. The pH control may also be critical since hydrolysis of polymers is less efficient at low pH levels. All the above factors influence the acetate flux of the system.

The polymeric carbohydrates, lipids, proteins and nucleic acids, of animal tissues, plant or microbial cells are broken down into smaller cell-permeable organic molecules by hydrolytic enzymes that are (a) found widespread in microbes and (b) most often secreted as extracellular enzymes into the external environment by the bacteria that are involved. The metabolites from the breakdown of polymeric substrates are used by heterotrophic species in the synthesis of structural polymers (minor usage) and for synthesising NADH and ATP (major usage), obtained either by fermentation (in an anaerobic environment), anaerobic or aerobic respiration, depending on the microbial species and the presence of oxygen or other end-terminal electron acceptors (such as NO_3^- or SO_4^{2-}).

All organic feedstocks or wastes can be best described with regard to their principal carbon-energy polymeric components which can be generally classified as polysaccharides, proteins, glycoproteins, lipids, phospholipids and nucleic acids. This implies the presence of a plethora of corresponding hydrolytic depolymerising enzymes, including amylases, pectinases, chitinases, cellulases, proteases (endopeptidases, aminopeptidases and carboxypeptidases), sialidases, glycosidases, pentosidases, lipases, phospholipases, esterases, DNAses and RNAses.

Microbial fuel cells technology

The MFC is a platform technology capable for converting wet biomass directly into electricity. With appropriate redox control, the technology can simultaneously facilitate green chemistry, whilst also treating (cleaning) the waste that is used fuel. In a way, the technology bridges the gap with the aforementioned industrial processes, thereby offering significant value-add. In their simplest form, MFCs contain two electrodes, with an electrochemical bridge/membrane between them. This facilitates the movement of ions that are dragged during charge (e^-) transfer from the anode (e^- source) to the cathode (e^- sink). The standard half equations that characterise the reactions in the two half-cells are:

$$\text{Anode: } C_2H_4O_2 + 2H_2O \rightarrow 2CO_2 + 8e^- + 8H^+ \text{ (for sodium acetate)}$$

$$\text{Anode: } C_{12}H_{22}O_{11} + 13H_2O \rightarrow 12CO_2 + 48H^+ + 48e^- \text{ (for sucrose)}$$

$$\text{Cathode: } O_2 + 4H^+ + 4e^- \rightarrow 2H_2O \text{ (using } O_2 \text{ as the oxidising agent)}$$

Based on electron transfer by microorganisms, MFCs can be mediator-based and mediator-less. Based on transfer of protons, or other ions from the anode to the cathode and *vice versa*, MFCs can be membrane-based and membrane-less. Some MFCs are truly membrane-less and rely on sedimentation and the formation of redox gradients whilst others (termed 'single chamber MFC') are not really membrane-less, but they have very thin membrane open-to-

air cathodes without a cathodic chamber; the membrane in this case forms part of the cathode. Figure 1 illustrates the MFC principle of operation in a general, non-container-confined manner diagram.

MFC containers can be of cuboid, cylindrical (tubular), "H"-shaped, flat, large, small or micro-scale embodiment and depending on the bacterial species used, oxidising agents (in the form of O_2, SO_4^{2-}, NO^{3-}) can also be used as end-terminal electron acceptors, thereby widening the types of reaction that can take place and therefore the types of by-product that can be generated. MFC technology has a number of major advantages over conventional remediation treatments of pollutants including 1) adaptation to a wide range of pollutants, organic and inorganic 2i) reduced sludging 3) requires zero energy input, unless special conditions require this 4) has not gas treatment requirements 5) can be operated at ambient temperatures, 6) residence time (HRT) is in hours rather than days. It is a fast-growing field, as evidenced by the increasing number of publications globally, especially those focussing on different types of polluted wastewater. A recent review by Mandal and Das (2018) covers 25 different types of wastewater ranging from municipal/domestic wastewater, recalcitrant pharmaceutical industrial effluent, steroidal drug production wastewater and petrochemical industry wastewater, which implies the removal of antibiotics, synthetic dyes, toluene, polycyclic aromatic hydrocarbons and emerging contaminants, amongst many others.

Depending on the type of cathode used, water can be abstracted from wastewater following treatment and can also be synthesised as a result of the oxygen reduction reaction (ORR) at the cathode, which can be a source of clean, not-potable water. When configured as stacks, MFCs can function as domestic electrical generators for powering small devices, for example, small portable electronic devices like mobile phones, small lamps, computers, electronic toys, batteries and supercapacitor charging machines, fridges and self-feeding robots. The higher the steady state power output, the wider the potential applications.

Aqueous suspensions (sludge) or solutions (sugar) cannot be combusted. However, these ubiquitous solvents are still suitable fuels for microbial fuel cells.

Other types of microbial electrochemical technologies: Microbial electrolysis cell

As already mentioned, protons (or other cations) and electrons recombine at the cathode along with an oxidising agent to close the circuit but under the right conditions, protons and electrons associate to form H_2 at the cathode half-cell (Hua et al., 2019). The performance of the MEC depends upon the types of microorganisms in the anodic and cathodic chambers, the type of feedstock substrate, the applied voltage and the nature of the electrode materials. The presence of methanogens must be discouraged since they compete for substrate in the anode and consume hydrogen at the cathode. Methanogenesis can be chemically inhibited, although this will increase operational cost and complexity, so more work needs to be done to improve methane suppression whilst increasing the H_2 yield. The MEC architecture and the cost of materials also determine the economic success and operation of the MECs.

MECs require energy input to generate hydrogen from organic matter. Ideally the electrical power can be supplied by a renewable source such as an MFC or solar panels. Electroactive microorganisms in the anode consume an organic energy source and release electrons and protons. This creates a potential of up to 0.3 V which is used to generate electricity in a conventional MFC. In contrast with an MFC, an additional voltage from an outside source is supplied to a working MEC. The combined voltage (providing the cathodic catalysts are suitable), is sufficient to reduce protons (H^+) and therefore create H_2. The total electrical power that has to be supplied to a MEC is less than for electrolysis of water because a high fraction of the energy required for this reduction is derived from organic fuel *via* microbial activity at the anode. For hydrogen production, values between 1 and 4 m^3H_2/m^3d have been achieved when 0.8 V was externally supplied (Kadier et al., 2016). The amount of hydrogen production depends on the type of organic substrates employed. Acetic and lactic acid achieve the highest efficiency (82%), whilst the values for glucose or non-pretreated cellulose are significantly lower (63%). It should be noted that the efficiency of hydrogen production by conventional electrolysis of water is only 60%–70%. Therefore, the MEC can produce 144% more energy than they consume in the form of external electrical inputs.

The high costs of the conventional catalytic cathode material (platinum) is between 47% and 85% of the total costs, so this must be overcome (Rozendal et al., 2008). A much cheaper option is to use biocathodes which are made from less expensive materials colonised by microbial species that can use the electrons to produce H_2 (Croese et al., 2011). The grouping of species which are naturally photofermentative and can produce H_2 (yet do not produce O_2) might be an interesting combination. An MEC design that can incorporate both high H_2 yields and low costs is very much needed for upscale purposes.

Microbial desalination cells

A microbial desalination cell (MDC) has similarities to MFCs, but the main operation is *in situ* desalination of salt-water in a third chamber sandwiched between the anode and the cathode. The central chamber interfaces the anode and cathode with a cationic and anionic exchange membrane (or bipolar membranes), respectively. This allows mineral ions in the central chamber (e.g., Na^+ and Cl^-) to migrate into the cathode or anode respectively, depending on their charge.

Photo-microbial fuel cells

The type of bioelectrochemical system that combines photosynthesis and electricity generation is known as a photo-microbial fuel cell (PMFC) (an alternative term used is bio-photovoltaics). Such devices utilise the microalgae in the cathodic chamber where they grow and utilise the carbon dioxide produced by the microorganisms in the anodic chamber. They also produce oxygen which improves the cathode electrical output. Such PMFC may be useful in the future to provide a significant resolution of both environmental and energy crises at the same time. Both the MDC

TABLE 2 Energy content of biofuels.

Biofuel (or fuel)[3]	Energy content (MJ/kg)
Hydrogen (H_2)[2]	120–142
Methane (CH_4)[2]	50–55
Natural gas[b]	52.2
Methanol (CH_3OH)[2]	22.7
Ethanol[b]	29.8
Dimethyl ether - DME (CH_3OCH_3)[2]	29.0
Petrol/gasoline[b]tbl2fnb	44–46
Diesel fuel[b]	42–46
Crude oil[b]	42–47
Liquefied petroleum gas (LPG)[b]	46–51
Natural gas[b]	42–55
Hard black coal (IEA definition)[b]	>23.9
Hard black coal[b] (Australia & Canada)	c. 25
Sub-bituminous coal (IEA definition)[b]	17.4–23.9
Sub-bituminous coal (Australia & Canada)[b]	18.0
Lignite/brown coal (IEA definition)[b]	<17.4
Lignite/brown coal (Australia, electricity)[b]	c. 10
Firewood (dry)[b]	16.5
Sugar cane bagasse[b]	16.4
Newsprint[b]	18.6
Cellulose[b]	17.3
Biodiesel[b]	46.3
Animal Dung/Manure[b]	10–15
Alfalfa straw[a]	18.5
Charcoal[a]	30
Coal[a]	28
Coconut husks[a]	10
Coconut shells[a]	18
Coffee husks[a]	16
Commercial wastes[a]	16
Cotton hulls[a]	19.5
Cotton stalks[a]	17.5
Domestic refuse[a]	9
Dung, dried[a]	16
Grass, fresh[a]	4
Groundnut shells[a]	20
Maize cobs[a]	19
Maize stalks[a]	18

(Continued on following page)

TABLE 2 (*Continued*) Energy content of biofuels.

Biofuel (or fuel)[3]	Energy content (MJ/kg)
Methane from biogas[a]	55
Paper, newspaper[a]	17
Peat[a]	14.5
Petroleum Oil[a]	42
Rice hulls[a]	15.5
Rice straw[a]	15
Soybean stalks[a]	19
Straw, harvested, baled	15
Sorghum bagasse[a]	19
Sugar cane residues[a]	17
Wheat straw[a]	19
Wood, green with 60% moisture[a]	6
Wood, air-dried to 20% moisture[a]	15
Wood, oven-dried to 0% moisture[a]	18

[a]Engineering ToolBox, (2001). [online] Available at: https://www.engineeringtoolbox.com [Accessed 25th October 2022].
[b]Fuel Properties Comparison; Alternative Fuels Data Center. US, department of energy, Energy Efficiency and Renewable Energy, Energy's Vehicle Technologies Office.
[c]National Renewable Energy Laboratory at www.nrel.gov/publications.

and the PMFC continue to produce usable amounts of electricity whilst functioning in desalination or recycling of oxygen and carbon dioxide. Neither of these technologies require an external source of electricity.

Hydrogen fuel cells

Hydrogen fuel cells carry a high potential for the future energy needs of our civilisation. As already mentioned, if hydrogen comes from renewables, of which there are abundant resources, then it can be a truly clean source of energy. However, the main challenge of the technology is the flammability of H_2 when mixed in either air (4%–74%) or pure O_2 (4%–94%), under atmospheric pressure; hydrogen will also escape from most containment vessels resulting in leaks (Rhodes, 2016). The above make storage, containment, and transportation of hydrogen, challenging which can be overcome if H_2 is used as it is being produced. High cost of materials and production, as it is common with other technologies, are still to be addressed. Hydrogen is an important topic for national governments and the European Commission in particular, giving emphasis to bio-hydrogen and novel/sustainable ways of production. Under the current climate and war in Ukraine there needs to be a real shift from current practices/systems and this shift needs to be more decentralised to eliminate dependency on mainstream pipelines that can easily be turned off; biohydrogen is one way of achieving this. There are fundamental challenges in storage and containment which in turn implies local and immediate consumption to avoid having to store it. Hydrogen fuel cells are now becoming more commonplace for powering transportation (trains, boats, buses and cars) and they are also being tested on aircraft.

TABLE 3 The relationship of water content and calorific value (Li et al., 2012).

Water content (%)	Calorific value (kcal/kg)
0	1781
10	1,543
20	1,305
30	1,067
40	828
50	591
60	352
70	114
80	−124
90	−362

Biomass and the environment

The carbon cycle describes how carbon is distributed around our planet, on land, in water and in the atmosphere and explains the processes that involve carbon exchange between the atmosphere, hydrosphere, biosphere, and lithosphere. As carbon dioxide (and to a lesser extent carbon monoxide, methane and volatile carbon compounds), the carbon helps to regulate the amount of sunlight that enters the planet's atmosphere. The process by which carbon dioxide is exchanged from atmosphere to the hydrosphere and biosphere is by photosynthesis *via* plants, macro- and micro-algae or photosynthetic bacteria including cyanobacteria. It is

exchanged between the land or water biosphere back to the atmosphere or lithosphere through food chains *via* decomposition, plant, animal or bacterial respiration, and human activity. Carbon (in the form of organic compounds) can be absorbed by soil from plants *via* root deposits (rhizodeposition) or by waste products from animals (urine or excrement) or when organisms die and are decomposed. Under the right conditions, carbon can reach the lithosphere *via* fossilisation, which turns decomposing biomass into peat or coal or petroleum, before re-entering the atmosphere *via* natural or anthropogenic combustion. Between periods of exchange, carbon is sequestered, or stored either as fossil fuels or as chalk or limestone. The fossil fuel carbon cycle is distinct from the exchange events between biosphere and atmosphere which are caused through respiration, fermentation or natural oxidation. The former has a half-life of many millions of years whilst the latter cycling is more immediate and is sometimes referred to as the immediate carbon cycle. When fossil fuels are exploited, their carbon content (which may have taken millions of years to produce) is released into the atmosphere over a relatively short period of time, mainly just a few hundred years. This overburdens the planets atmosphere. In comparison with fossil fuels, biomass carbon exchange can continue *via* the immediate carbon cycle. In order for humans to effectively allow Earth to continue the carbon cycle process they must rely more on the immediate carbon cycle and leave fossil fuels alone. Moreover, biomass use and soil conditioning have to be sustainably balanced to take into account the rate of carbon sequestration in—for example, - trees and plants.

Humans and biomass

Plants absorb carbon dioxide by photosynthesis and the amount they absorb is greater than or at least equal to that produced *via* conventional fuel processing and usage.

The energy content of biofuels is of some interest. With the exception of biohydrogen (which has the highest energy content per kg), all the biofuels are carbon-based. Table 2 presents a list of all the main biofuels. The fossil fuels (petrol, diesel fuel, crude oil, natural gas and coal) are also included for comparison. Because of the significant water content of wet fuels their energy content per kg will be less than that of wet grass, and significantly less, possibly by as much as 90% than the combustible biofuels. The relationship between the water content of sewage sludge and calorific value is shown in Table 3. The higher the water content, the lower the calorific value, per unit of mass.

The world's top ten biofuel crops in order of extent per annum are: switchgrass, wheat, sunflower, cottonseed oil, soy, jatropha, palm oil, sugar cane, canola and corn. The planet as a whole, produces billions of tonnes of wet waste detritus each year from natural estuarine flow, from run off from rotting processes (leaf litter, humus, compost, etc.). Organic biomass is an interesting proposition since globally, it is the most abundant type of fuel. There is more produced "naturally" each year across the planet than the total amounts of fossil fuel abstracted and combusted by humans. The planet produces more than enough biomass to replace fossil fuels entirely. There is no shortage of potential fuel or feedstock that a technology such as MFCs can utilise, including sewage, sludge, farm manure, landfill leachate, black- brown- and white-water run-off, mine water run-off, algal and seaweed waste and river sludge.

The overall biomass composition of the planet (all forms of life) is thought to be ≈ 550 gigatons of carbon (Gt C) (Bar et al., 2018). Plants, the dominant kingdom, are ≈450 Gt C and are mainly terrestrial, whilst animals, at around 2 Gt C, are mainly marine. With regard to microorganisms, these are predominantly located in deep subsurface environments with bacteria (at ≈70 Gt C) outnumbering the archaea (≈7 Gt C) (Bar et al., 2018), and fungi thought to be around 12 Gt C. In terms of annual productivity of biomass (i.e., new biomass per year) then the total annual primary production is thought to be just over 100 billion tonnes C/yr, (Field et al., 1998).

It is expected that by 2050, approximately half of the world's energy demand/consumption (about 400 EJ/yr) could be met by biomass and that 60% of the world's electricity market could be supplied by renewables. In energy terms, the production of cereals (−40 EJ), crop residues (−60 EJ), pasture (−75 EJ) and industrial roundwood (−20 EJ) was substantially less than the extraction/production of fossil fuels: gas, (−70 EJ), coal (−40 EJ) and oil (−170 EJ), (IEA, 2021). If wet organic matter (sludges) were regarded as a biofuel it would even be possible to meet all the world's demand for energy.

The microbes in the MFC (the anodic biofilms) have high affinity metabolic systems for the transport and uptake of nutrient substrates. For example, *Escherichia coli* (considered to be a typical heterotrophic fermentative species) has a reported k_s value of 5.4 μM for acetate (Gimenez et al., 2003) and 20 μM for the transport of glucose (Hunter and Kornberg, 1979). For the anodophilic *Geobacter sulferreducens*, the Km value for acetate has been reported to range from 2.6 to 0.42 mM acetate (Korth et al., 2020). The k_s value gives the concentration of substrate that can produce half the maximum rate of substrate uptake. It should be noted that microbial cells (and therefore microbial fuel cells) continue to take up substrates at even lower concentrations than indicated by the k_s value, albeit at low transport rates. The high affinity transport systems for microbes ensure that MFC and related technology (MDC and PMFC) can efficiently clean up waste streams in addition to producing electricity and can manage to produce electricity from very diluted feedstocks (e.g., estuarine river water). Table 4 below summarises the advantages and disadvantages, as well as the key biological mechanisms at play for the different types of biofuel and biotechnology included in this review. The purpose of this summary is to enable readers to more easily see how biology-based solutions compare and how well (or not) they can serve a particular purpose or address a specific problem. As can be seen, BESs show important advantages over existing, much more mature technologies but are still lagging in terms of commercialisation. Although generally, this is not unusual for nascent technologies, human factors i.e., politics, personal preferences/agenda, lobbying, seem to be affecting progress more than other technologies by comparison; this is currently an unexplored research area.

The International Renewable Energy Agency (Irena, 2022) have described the need for a growth in production and use of modern bioenergy in order for humanity to make the critical changes required for ensuring global energy transition from the current situation (82% use of fossil fuels; 18% renewables) with low, to net zero carbon emission scenarios. Bioenergy currently contributes the

TABLE 4 Comparison between different types of biofuel and biotechnology.

Biofuel or technology	Raw substrates	Microbe/plant species	Advantages	Disadvantages	References
Biomethane	Abattoir, cheese and food waste, pig slurry and wastewater treatment sludge. (± grass & corn, i.e., starch, cellulose, lignocellulose)	Over 50 species of methanogens have been described, e.g.,*Methanobacterium spp. Methanococcus spp. Methanosarcina spp. Methanobrevibacter spp. Methanopyrus spp.*	Product (CH_4) easy to separate (insoluble gas). Some degree of bio-remediation performed. Pure methane is a good fuel	Requires high substrate loading. Gas must be purified for many purposes. Production rate is slow and easily disrupted. CH4 is emitted [potent greenhouse gas. Waste BOD residues	Allen et al. (2013) Ma et al. (2017)
Biohydrogen	Dark fermentation: Fermentable substrates inc. Sugars, carbohydrates and some amino acids	Dark fermentation: *Enterobacter, Citrobacter, Klebsiella, Escherichia coli*	Dark fermentation: Light independent. Can process a wide variety of substrates	Dark fermentation: Low levels of H2 produced compared with other methods. O_2 inhibits	Mishra et al. (2019)
	Photofermentation: Butyrate, succinate, malate and acetate	*Clostridium beijerinckii, Rhodobacter sphaeroides*	Photo fermentation: Photosynthetic bacteria exploit wide spectral energy. Can process a variety of substrates	Photo fermentation: Metabolic shift from H_2 to PHB. Efficiency of light conversion is lower than photolysis systems	Dutta et al. (2005)
	Direct & indirect photolysis:Water and solar radiation	Photolysis and photofermentation	Inc. Dark fermentation effluent Biomediation is performed	Direct photolysis: High light intensity and O_2 work as inhibitors of H_2 production. H_2 and O_2 make explosive mix	Sharma & Arya, (2017)
		Cyanobacteria: *[Anabaena, Calothrix Synechococcus, Nostoc, Microcystis, Mycrocystis]* Green algae: [Chlorella spp. Dunaliella spp. Chlamydomonas]	Direct photolysis: Simple cultivation, H2O is substrate &: CO_2 consumed	Indirect photolysis: Hydrogenase enzyme generates CO2 and is low yielding	
			Indirect photolysis: Uses blue-green algae. Nitrogen-fixation from air (initially). Separate stages, O_2, then H_2		
Carboxylates (Volatile Fatty Acids, VFA,s)	Complex wastewaters with sugars, starch, cellulose, hemicellulose or lignocellulose)	*Acetobacter*, *Clostridium*, *Kluyveromyces Moorela Propionobacterium* and mixed communities	Relatively fast hydrolysis and fermentation. VFAs used as precursors in methane production and to produce hydrogen in photofermentation	Lignocellulose biomass must be pre-treated	Bhatia & Yang, (2017) Levin et al. (2004)
ethanol	Sugar beet, sugarcane, molasses, whey, starches (corn, wheat, root crops) Lignocellulose (following pre-treatment)	*Saccharomyces* spp. *Saccharomyces* (genetic engineered strains) Zymobacter mobilis Zymobacter palmae	Ethanol Fuel is cost-effective compared to other biofuels and is fully renewable, easily accessible and has a variety of sources of raw material	Requires vast acres of land	Bušić et al. (2018)
				Distillation process uses significant energy. Pure ethanol is hygroscopic. Water in ethanol is corrosive to engines	Alternative Fuels Data Center Fuel Properties Comparison (2022) bib_afdcfpc_2022
Biodiesel	Biodiesel is produced from a wide variety of oilseed crops, (soybeans, mustard, rapeseed, canola, rice bran oil, sunflower, jatropha), animal fats, macroalgae (e.g., seaweed) and microalgae	Microalgae: *Chlorella, Dunaliella, Scenedesmus, Botryococcus Spirulina* Cyanobacteria: *Anabaena Synechocystis Synechococcus*	Easy to use: No vehicle modification required	More expensive than petroleum diesel	Firoz, (2017)
			Power, performance and economy as good as fossil fuels. Part of the immediate CO_2 cycle so does not add to global warming	Can damage rubber housings in some engines	Nozzi et al. (2013)
			Biodiesel is less toxic than petroleum	Biodiesel fuel distribution infrastructure needs development	
				Processing required (transesterification)	

(Continued on following page)

TABLE 4 (*Continued*) Comparison between different types of biofuel and biotechnology.

Biofuel or technology	Raw substrates	Microbe/plant species	Advantages	Disadvantages	References
MEC [Microbial Electrolysis Cell]	Wide range of carbon-energy substrates (carbohydrates, proteins, Lipids, complex mixtures or single chemicals)	Exoelectrogens and heterotrophic fermentative species at the anode. Can use hydrogenase containing species at the cathode	Bioremediation at the anode Pollution free hydrogen. Can process effluent from dark fermentation. High recovery of H2. No requirement for expensive solar light photobioreactor	Need for power source Capital costs can be high and system suffers from scalability problems Technology not yet mature enough for large scale commercialisation	Katuri et al. (2019) Wang et al. (2021) Call & Logan (2008)
MFC/MDC [Microbial Fuel Cell/Microbial Desalination Cell]	Wide range of carbon-energy substrates (carbohydrates, proteins, Lipids, complex mixtures or single chemicals)	Exoelectrogens and heterotrophic fermentative species at the anode	Generate electricity MDC can be used to desalinate salty solutions including sea water and urine	Technology not yet mature enough for large scale commercialisation	Obileke et al. (2021) Al-Mamun et al. (2018)
PMFC [Photo-Microbial Fuel Cell]	Wide range of carbon-energy substrates [including dead algal biomass] at the anode	Exoelectrogens and heterotrophic fermentative species at the anode. Cyanobacteria or microalgae at the cathode	Can be used to recycle CO_2, O_2, and mineral elements as well as clean waste streams and produce electricity	Technology not yet mature enough for large scale commercialisation	Ieropoulos, Greenman and Melhuish (2010)

largest share (two-thirds) of renewables utilisation worldwide, when including the traditional use of biomass. To meet the "1.5°C climate goal scenario," bioenergy production would need to increase significantly by 2050. Achieving this goal may be challenging without the deployment of sustainable biomass for different purposes since the current deployment of bioenergy remains well below what is needed to achieve the energy transition. This is where collective and interconnected approaches that may include the use of MFCs, can really make a difference, since if appropriately engineered, the outcome will always be greater than the sum of the individual components—a principle well proven in our natural ecosystems.

The vast majority of people on the planet still rely on the traditional (yet inefficient) use of biomass for cooking and heating, affecting health and gender inequality, while leading to deforestation in many areas of the world and adding to climate change. Bioenergy is a multidisciplinary complex area, involving a wide range of stakeholders and issues; more than most other forms of renewable energy. Bioenergy interacts with many sectors, including agriculture, forestry, water industry, waste management and environmental protection. It can have positive impacts if the supply chain is managed well, or potentially negative impacts if the supply chain is poorly managed or indeed bioenergy is abused. The potential sustainability risks of the bioenergy supply chain and its deployment are linked to land use, air pollution, water and soil quality, biodiversity, competition with food supply, and effects on indigenous communities and smallholders.

This is by no means a solved problem, and there is still a lot of work to be done. Typically, over 50% of biomass is likely to be water which has to be extracted to make biofuels. Some estimates suggest that transporting biomass over distances of 100 miles or so from the processing plant is not economically efficient. In addition to carbon dioxide, burning biomass releases nitrogen oxides, carbon monoxide, particulates, and other pollutants. Unless there is use of special technology to capture and recycle the pollutants, burning biomass can create smog and atmospheric pollution as bad as, or even exceeding that of fossil fuels. Biotransformation of biomass however does not produce the same harmful by-products; this is where smart solutions exploiting microbial transforming power can be extremely valuable.

Conclusion

Despite the high water content of sewage sludge, its energy content is comparable with many types of fuel (ranges from 8 to 21 MJ/kg, depending on water content and origin) (Singh et al., 2020). With appropriate treatment using MFCs, municipal sewage sludge can be utilised efficiently and the sludge can be considered as a source of energy even if highly diluted. For high-demand systems the greater the dilution of the sludge the higher the number of MFC stacks required for full utilisation. The finding that small MFCs are more power dense than large volume systems is important and in line with natural ecosystems (for example, electric eel or mammalian blood circulation). A large stack can be built from a few large volume MFCs, or it can be built from a much larger number of small-scale MFCs. Empirical research suggests that the latter strategy will be more successful, especially when considering essential voltage increases and energy density at the small scale, which is in line with allometric scaling in natural systems but also with the approaches adopted for other technologies such as photovoltaics. MFCs work with live microorganisms, which have their own circadian rhythm. This is an important trait of the technology, yet it is often wrongly compared with other forms of electricity sources, such as chemical fuel cells or batteries that are governed by fast-rate chemical reactions, which in turn implies high instantaneous power output for a finite/short period of time. This is one important reason why microbial electrochemical technologies cannot be directly compared to chemical or other abiotic electrochemical systems, as they operate on different levels: high energy for microbial electrochemical technologies vs. high power for chemical or electrochemical systems. When technologies such as MFC stacks are employed, then this allows for vertical stacking, much like vertical

farming, thereby getting around the problem of using a large footprint. Because MFCs can "treat" organic sludge and lower the BOD as well as generate electricity this serves a justifiable purpose to start developing large scale stacks. To fully extract the energy content of the waste-stock fuel the MFC or PMFC have to be stacked using cascades of 7–9 individual units (empirical finding) in order to fully reduce the BOD to an acceptable level. In a cascade, the fuel is sequentially treated and the treatment time to allow for full hydrolysis and digestion of microbial biomass can be competitively short, with enrichment of the most efficient microflora. The hydraulic retention time within the cascades can be appropriately tuned to suit the composition of the incoming feedstock, rendering the MFC/BES technology suitable for both highly concentrated and dilute waste streams. For very dilute feedstocks the uptake and utilisation of substrates depends upon the affinity values (k_s) of the microbial species the macromolecular structure, the size of molecules and the concentration of the substrate being digested. The supply rate of substrate is also important, and this can be actively controlled by changing the speed of the feedstock pump, or passively by introducing flow-restrictors or even dynamically by changing the volume of the anodic chambers *in situ*, using soft or compliant materials. With the exception of hydrogen, nearly all fuels used on the planet are carbon-based. In the near future fossil fuels will be phased out leaving only the biofuels made from primary plants and microbes. Because these are part of the immediate carbon cycle, if used responsibly they will not contribute to planetary overload of methane or carbon dioxide, allowing the climate to rebalance in time, hopefully before all lifeforms become extinct.

Author contributions

All authors listed have made a substantial, direct, and intellectual contribution to the work and approved it for publication.

Acknowledgments

II is a Bill & Melinda Gates Foundation grantee (INV-042655). Some of the reported findings have been produced as part of the EU COST Action PHOENIX, CA-19123.

Conflict of interest

The authors declare that the research was conducted in the absence of any commercial or financial relationships that could be construed as a potential conflict of interest.

Publisher's note

References

Adams, P. W. R., and McManus, M. C. (2019). Characterisation and variability of greenhouse gas emissions from biomethane production via anaerobic digestion of maize. *J. Clean. Prod.* 218, 529–542. doi:10.1016/j.jclepro.2018.12.232

Agler, M. T., Wrenn, B. A., Zinder, S. H., and Angenent, L. T. (2011). Waste to bioproduct conversion with undefined mixed cultures: The carboxylate platform. *Trends Biotechnol.* 29, 70–78. doi:10.1016/j.tibtech.2010.11.006

Alternative Fuels Data Center Fuel Properties Comparison (2022). US department of energy, energy efficiency and renewable energy, Energy's vehicle technologies Office.

Ananthi, V., Raja, R., Carvalho, I. S., Brindhadevi, K., Pugazhendhi, A., and Arun, A. (2021). A realistic scenario on microalgae based biodiesel production: Third generation biofuel. *Fuel* 284, 118965. doi:10.1016/j.fuel.2020.118965

Azevedo, S. G., Sequeira, T., Santos, M., and Mendes, L. (2019). Biomass-related sustainability: A review of the literature and interpretive structural modeling. *Energy* 171, 1107–1125. doi:10.1016/j.energy.2019.01.068

Azwar, M. Y., Hussain, M. A., and Abdul-Wahab, A. K. (2014). Development of biohydrogen production by photobiological, fermentation and electrochemical processes: A review. *Renew. Sustain. Energy Rev.* 31, 158–173. doi:10.1016/j.rser.2013.11.022

Bar, Y. M., Phillips, R., and Milo, R. (2018). The biomass distribution on. *Earth. Proc. Natl. Acad. Sci.* 115, 6506–6511.

Bhatt, A. H., Ren, Z., and Tao, L. (2020). Value proposition of untapped wet wastes: Carboxylic acid production through anaerobic digestion. *iScience* 23, 101221. doi:10.1016/j.isci.2020.101221

Black, R., Cullen, K., Fay, B., Hale, T., Lang, J., Mahmood, S., et al. (2021). "Taking stock: A global assessment of net zero targets," in *Energy & climate intelligence unit and oxford net zero*.

Croese, E., Pereira, M. A., Euverink, G. J. W., Stams, A. J. M., and Geelhoed, J. S. (2011). Analysis of the microbial community of the biocathode of a hydrogen-producing microbial electrolysis cell. *Appl. Microbiol. Biotechnol.* 92, 1083–1093. doi:10.1007/s00253-011-3583-x

Das, D., Khanna, N., and Dasgupta, C. N. (2014). "Biohydrogen production," in *CRC press taylor & francis group (2014)*. First Edition, 55–79.

Delong, J. P., Okie, J. G., Moses, M. E., Sibly, R. M., and Brown, J. H. (2010). Shifts in metabolic scaling, production, and efficiency across major evolutionary transitions of life. *Proc. Natl. Acad. Sci.* 107, 12941–12945. doi:10.1073/pnas.1007783107

Engineering ToolBox (2001). Engineering ToolBox. [online] Available at: https://www.engineeringtoolbox.com (Accessed October 25, 2022).

European Biogas Association (2023). A way out of the EU gas price crisis with biomethane. Available at: https://www.europeanbiogas.eu/(Accessed January 23, 2023).

Ferraren-De Cagalitan, D. D. T., and Abundo, M. L. S. (2021). A review of biohydrogen production technology for application towards hydrogen fuel cells. *Renew. Sustain. Energy Rev.* 151, 111413. doi:10.1016/j.rser.2021.111413

Field, C. B., Behrenfeld, M. J., Randerson, J. T., and Falkowski, P. (1998). Primary production of the biosphere: Integrating terrestrial and oceanic components. *Science* 281, 237–240. doi:10.1126/science.281.5374.237

Gimenez, R., Nunez, M. F., Badia, J., Aguilar, J., and Baldoma, L. (2003). The Gene yjcG, co-transcribed with the gene acs, encodes an acetate permease in *Escherichia coli*. *J. Bacteriol.* 185, 6448–6455. doi:10.1128/jb.185.21.6448-6455.2003

Greenman, J., and Ieropoulos, I. A. (2017). Allometric scaling of microbial fuel cells and stacks: The lifeform case for scale-up. *J. Power Sources* 356, 365–370. doi:10.1016/j.jpowsour.2017.04.033

Hazrat, M. A., Rasul, M. G., Khan, M. M. K., Ashwath, N., Fattah, I. M. R., Ong, H. C., et al. (2022). Biodiesel production from transesterification of Australian Brassica napus L. Oil: Optimisation and reaction kinetic model development. *Environ. Dev. Sustain.* doi:10.1007/s10668-022-02506-0

Hoang, A. T., Huang, Z. H., Nižetić, S., Pandey, A., Nguyen, X. P., Luque, R., et al. (2022). Characteristics of hydrogen production from steam gasification of plant-originated lignocellulosic biomass and its prospects in Vietnam. *Int. J. Hydrogen Energy* 47, 4394–4425. doi:10.1016/j.ijhydene.2021.11.091

Hua, T., Li, S., Li, F., Zhou, Q., and Ondon, B. S. (2019). Microbial electrolysis cell as an emerging versatile technology: A review on its potential application, advance and challenge. *J. Chem. Technol. Biotechnol.* 94, 1697–1711. doi:10.1002/jctb.5898

Huesemann, M. H., Hausmann, T. S., Carter, B. M., Gerschler, J. J., and Benemann, J. R. (2010). Hydrogen generation through indirect biophotolysis in batch cultures of the nonheterocystous nitrogen-fixing cyanobacterium *Plectonema boryanum*. *Appl. Biochem. Biotechnol.* 162, 208–220. doi:10.1007/s12010-009-8741-6

Hunter, I. S., and Kornberg, H. L. (1979). Glucose transport of *Escherichia coli* growing in glucose-limited continuous culture. *Biochem. J.* 178, 97–101. doi:10.1042/bj1780097

Huxley, J. S., and Teissier, G. (1936). Terminology of relative growth. *Nature* 137, 780–781. doi:10.1038/137780b0

IEA (2021). *Key world energy statistics 2021*. Paris: IEA. License: CC BY 4.0 Available at: https://www.iea.org/reports/key-world-energy-statistics-2021.

IRENA (2022). *Bioenergy for the energy transition: Ensuring sustainability and overcoming barriers*. Abu Dhabi: International Renewable Energy Agency. ISBN: 978-92-9260-451-6. Available at: https://www.irena.org//media/Files/IRENA/Agency/Publication/2022/Aug/IRENA_Bioenergy_for_the_transition_2022.pdf?rev=875a997481f04168b17499f1e5dc1473 (Accessed January 19, 2023).

Kadier, A., Kalil, M. S., Abdeshahian, P., Chandrasekhar, K., Mohamed A,Azman, N. F., et al. (2016). Recent advances and emerging challenges in microbial electrolysis cells (MECs) for microbial production of hydrogen and value-added chemicals. *Renew. Sustain. Energy Rev.* 61, 501–525. doi:10.1016/j.rser.2016.04.017

Kang, S., Heo, S., and Lee, J. H. (2019). Techno-economic analysis of microalgae-based lipid production: Considering influences of microalgal species. *Ind. Eng. Chem. Res.* 58, 944–955. doi:10.1021/acs.iecr.8b03999

Karthikeyan, S., Periyasamy, M., and Prathima, A. (2020). Biodiesel from microalgae: Environmental Aspects. *Mater. Today Proc.* 33, 3664–3667. doi:10.1016/j.matpr.2020.05.779

Kleiber, M. (1932). Body size and metabolism. *Hilgardia* 6, 315–353. doi:10.3733/hilg.v06n11p315

Korth, B., Kretzschmar, J., Bartz, M., Kuchenbuch, A., and Harnisch, F. (2020). Determining incremental coulombic efficiency and physiological parameters of early stage Geobacter spp. *Enrich. Biofilms. PLoS ONE* 15 (6), e0234077.

Lam, S. S., Tsang, Y. F., Yek, P. N. Y., Liew, R. K., Osman, M. S., Peng, W., et al. (2019). Co-Processing of oil palm waste and waste oil via microwave Co-torrefaction: A waste reduction approach for producing solid fuel product with improved properties. *Process. Saf. Environ. Prot.* 128, 30–35. doi:10.1016/j.psep.2019.05.034

Lee, R. A., and Lavoie, J-M. (2013). From first-to third-generation biofuels: Challenges of producing a commodity from a biomass of increasing complexity. *Anim. Front.* 3, 6–11. doi:10.2527/af.2013-0010

Li, Y., Wang, H., Zhang, J., Wang, J., and Ouyang, L. (2012). The industrial practice of Co-processing sewage sludge in cement kiln. *Sci.* 16, 628–632. doi:10.1016/j.proenv.2012.10.086

Ma, G., Neibergs, J. S., Harrison, J. H., and Whitefield, E. M. (2017). Nutrient contributions and biogas potential of co-digestion of feedstocks and dairy manure. *J. Waste Manag.* 64, 88–95. doi:10.1016/j.wasman.2017.03.035

Mandal, S. K., and Das, N. (2018). Application of microbial fuel cells for bioremediation of environmental pollutants: An overview. *J. Microbiol. Biotechnol. Food Sci.* 7, 437–444. doi:10.15414/jmbfs.2018.7.4.437-444

Marsh, G. (2008). Rise of the anaerobic digestor. Renew. *Energy Focus* 9, 28–30.

Mestre, F., Gravel, D., García-Callejas, D., Pinto-Cruz, C., Matias, M. G., and Araújo, M. B. (2022). Disentangling food-web environment relationships: A review with guidelines. *Basic Appl. Ecol.* 61, 102–115.

Mofijur, M., Siddiki Sk, Y. A., Shuvho Md, B. A., Djavanroodi, F., Fattah I-M, R., Ong, H. C., et al. (2021). Effect of nanocatalysts on the transesterification reaction of first, second and third generation biodiesel sources- A mini-review. *Chemosphere* 270: 128642, doi:10.1016/j.chemosphere.2020.128642

Mubarak, M., Shaija, A., and Suchithra, T. V. (2019). Flocculation: An effective way to harvest microalgae for biodiesel production. *J. Environ. Chem. Eng.* 7, 103221. doi:10.1016/j.jece.2019.103221

National Renewable Energy Laboratory National renewable energy laboratory. Available at: www.nrel.gov/publications.

Peng, L., Fu, D., Chu, H., Wang, Z., and Qi, H. (2020). Biofuel production from microalgae: A review. *Environ. Chem. Lett.* 18, 285–297. doi:10.1007/s10311-019-00939-0

Rafa, N., Ahmed, S. F., Badruddin, I. A., Mofijur, M., and Kamangar, S. (2021). Strategies to produce cost-effective third-generation biofuel from microalgae. *Front. Energy Res.* 9 (749968), 10. doi:10.3389/fenrg.2021.749968

Rahman, K. M. (2020). "Food and high value products from microalgae: Market opportunities and challenges," in *Microalgae biotechnology for food, health and high value products*. Editors M. A. Alam, J. L. Xu, and Z. Wang (Singapore: Springer Nature), 3–28.

Rhodes, R. (2016). "NASA ask magazine," in *Explosive lessons in hydrogen safety*. 46–50.

Rozendal, R. A., Hamelers, H. V. M., Rabaey, K., Keller, J., and Buisman, C. J. N. (2008). Towards practical implementation of bioelectrochemical wastewater treatment. *Trends Biotechnol.* 26, 450–459. doi:10.1016/j.tibtech.2008.04.008

Sağır, E., and Hallenbeck, P. C. (2019). "Photofermentative hydrogen production," in *Biomass, biofuels, biochemicals: Biohydrogen*. Second Edition (Elsevier), 141–157.

Shah, M. M. R., Liang, Y., Cheng, J. J., and Daroch, M. (2016). Astaxanthin-producing green microalga Haematococcus pluvialis: From single cell to high value commercial products. *Front. Plant Sci.* 7, 531. doi:10.3389/fpls.2016.00531

Singh, V., Phuleria, H. C., and Chandel, M. K. (2020). Estimation of energy recovery potential of sewage sludge in India: Waste to watt approach. *J. Clean. Prod.* 276, 122538. doi:10.1016/j.jclepro.2020.122538

Sinha, P., and Pandey, A. (2011). An evaluative report and challenges for fermentative biohydrogen production. *Int. J. Hydrogen Energy* 36, 7460–7478. doi:10.1016/j.ijhydene.2011.03.077

Snell, O. (1892). Die Abhängigkeit des Hirngewichts von dem Körpergewicht und den geistigen Fähigkeiten. *Arch. Psychiatr.* 23, 436–446. doi:10.1007/bf01843462

Sondhi, S., Kaur, P. S., and Kaur, M. (2020). Techno-economic analysis of bioethanol production from microwave pretreated kitchen waste. *SN Appl. Sci.* 2, 1558. doi:10.1007/s42452-020-03362-1

Sun, T., Zhang, Y., Zhang, C., Wang, H., Pan, H., Liu, J., et al. (2020). Cyanobacteria-based bio-oxygen pump promoting hypoxia-resistant photodynamic therapy. *Front. Bioeng. Biotechnol.* 8, 237–311. doi:10.3389/fbioe.2020.00237

Taibi, E., Miranda, R., Vanhoudt, W., Winkel, T., Barth, F., and Lanoix, J. C. (2018). Hydrogen from renewable power: Technology outlook for the energy transition. IRENA, Policy Paper. September. Available at: https://www.h2knowledgecentre.com/content/policypaper1306 (Accessed January 19, 2023).

Um, B-H., and Kim, Y-S. (2009). Review: A chance for korea to advance algal-biodiesel technology, *J. Industrial Eng. Chem.* 15, 1–7. doi:10.1016/j.jiec.2008.08.002

US DoE (2022). Energy efficiency & renewable energy, alternative fuel price report. Available at: https://afdc.energy.gov/fuels/prices.html (Accessed November 5, 2022).

Vasiliadou, I. A., Berná, A., Manchon, C., Melero, J. A., Martinez, F., Esteve-Nuñez, A., et al. (2018). Biological and bioelectrochemical systems for hydrogen production and carbon fixation using purple phototrophic bacteria. *Front. Energy Res.* 6, 107. doi:10.3389/fenrg.2018.00107

Weber, A. Z., and Lipman, T. E. (2019). *Fuel cells and hydrogen production*. New York, NY: Springer, 1–8.Fuel cells and hydrogen production: Introduction

World Bioenergy Association (2019). Global bioenergy statistics. Available at: http://www.worldbioenergy.org/uploads/191129%20WBA%20GBS%202019_HQ.pdf (Accessed November 04, 2022).

Yin, Z., Zhu, L., Li, S., Hu, T., Chu, R., Mo, F., et al. (2020). A comprehensive review on cultivation and harvesting of microalgae for biodiesel production: Environmental pollution control and future directions. *Technol* 301, 122804. doi:10.1016/j.biortech.2020.122804

Yoshida, A., Nishimura, T., Kawaguchi, H., Inui, M., and Yukawa, H. (2005). Enhanced hydrogen production from formic acid by formate hydrogen lyase-overexpressing *Escherichia coli* strains. *Appl. Environ. Microbiol.* 71, 6762–6768. doi:10.1128/aem.71.11.6762-6768.2005

frontiers | Frontiers in Energy Research

TYPE Original Research
PUBLISHED 22 November 2023
DOI 10.3389/fenrg.2023.1285270

OPEN ACCESS

EDITED BY
Hailong Li,
Central South University, China

REVIEWED BY
Zequn Yang,
Central South University, China
Junwei Yang,
City University of Hong Kong, Hong Kong SAR, China

*CORRESPONDENCE
Chun Sing Lai,
chunsing.lai@brunel.ac.uk

RECEIVED 29 August 2023
ACCEPTED 02 November 2023
PUBLISHED 22 November 2023

CITATION
Yan M, Li Z, Lai CS, Zhao Z, Zobaa AF, Lai LL and Shi Z (2023), Energy management considering multiple power markets and microgrid storage.
Front. Energy Res. 11:1285270.
doi: 10.3389/fenrg.2023.1285270

Energy management considering multiple power markets and microgrid storage

Mengxuan Yan[1,2], Zhanlian Li[1], Chun Sing Lai[1,3]*, Zhuoli Zhao[1], Ahmed F. Zobaa[3], Loi Lei Lai[1] and Zebing Shi[4]

[1]School of Automation, Guangdong University of Technology, Guangzhou, China, [2]Jiangmen Power Supply Bureau of Guangdong Power Grid Co Ltd., Jiangmen, China, [3]Department of Electronic and Electrical Engineering, Brunel University London, Uxbridge, United Kingdom, [4]China Southern Power Grid Co. Ltd., Guangzhou, China

The operational cost of a microgrid is significantly influenced by the response of storage systems and the complexities of the power market's tariff structures. This paper addresses the challenges arising from the coexistence of new market entries and traditional tariffs, which contribute to a complex market environment. To tackle this issue, the paper establishes a microgrid market environment encompassing four types of tariffs. By modeling the response of electric storage and cold storage in a microgrid, the study formulates a non-linear mixed-integer optimization problem. Numerical studies are then conducted to verify the model and analyze market performance. The results reveal a trade-off in behavior among different market entries when optimizing the total cost of microgrid operation. These findings shed light on the complexities and trade-offs involved in microgrid operational cost optimization within a diverse market environment, offering valuable insights for market participants.

KEYWORDS

coordinated operation, natural gas network, electrical network, credit rank indicator, microgrid

1 Introduction

Power market deregulation brings competitive trading to generation and consumer areas. Multiple market participants from both sides are allowed to submit their bids and are matched by market operators (Tabar et al., 2019; Tian et al., 2023). Unlike a regulated power market, deregulated trading may contain more uncertainties, which leads to a higher risk. Thus, a deregulated power market may contain multiple sub-markets to hedge the risk of uncertainties, such as a wholesale market, spot market, capacity market, and several ancillary markets in PJM (Rabiee et al., 2016; Fan et al., 2022; MansourLakouraj et al., 2022). In general, power market deregulation will improve the entire efficiency of power system operation and management. It can also promote the latest technologies by constructing specified market structures (He et al., 2016; Chen et al., 2021; Zhang et al., 2023).

Energy management in a microgrid has become an important issue in recent studies. Nowadays, energy management strategies are growing rapidly (Zhao et al., 2023). In this paper, a new energy management strategy has been proposed for a hybrid microgrid, including demand response and the internal power market (Al-Awami et al., 2017). In this regard, a configuration of multiple markets is considered in the proposed method, and interactions between the consumers, microgrid, and incentive strategies are included in the

presented planning (Garcia-Torres et al., 2020; Huang et al., 2020). Due to the presence of various types of consumers, such as critical and normal loads, different power tariffs and contracts are utilized in energy management. Energy storage is an attractive area for academic and industrial researchers. It presents significant capabilities in power system efficiency enhancement, renewable energy integration, and demand response (Zhao et al., 2012; Zhao and Ding, 2017; Lin et al., 2019; Wang et al., 2021). It also improves the stability and reliability of the power grid (Zhao et al., 2017). Energy storage is also popular in microgrid operations. In a microgrid, energy storage helps in reducing risks due to the intermittence of renewable energy (Kwon et al., 2016; Olabi, 2017; Khaloie et al., 2021; Li et al., 2021). A coalitional game model for the trading of a biomass power plant (BPP) integrated with PV and wind farms was proposed (Khalilpour and Vassallo, 2016; Zhang et al., 2017a; Lai and McCulloch, 2017). It reported the need to have a different method to calculate the energy generation cost due to the installation of energy storage in solar energy production (Lai and McCulloch, 2016). The sizing requirements of solar PV and storage systems need to be considered in relation to biogas power plants. Solar irradiance could be affected by fluctuations introduced by passing clouds. The analysis of these fluctuations with regard to solar energy production could be focused by studying the instantaneous clearness index.

Demand response is another application of energy storage in minimizing the difference between peak and valley loads (Hakimi and Moghaddas-Tafreshi, 2014a; Zhang et al., 2017b; Lai et al., 2017c). Lai et al. (2017a) and Lai et al. (2017b) reported the future of energy storage applications with a focus on large-scale solar energy penetration. Chen et al. (2013), Amrollahi and Bathaee (2017) and Liu et al. (2018) reported the impact of energy storage degradation costs. Vehicle to Grid (V2G) technology is also a popular area for energy storage utilization. As an energy storage unit, batteries of electric vehicles (EVs) participate in microgrid peak shaving and frequency modulation (Lai and McCulloch, 2016; Lai et al., 2017a; Lai et al., 2017b). Gough et al. (2017) proposed an energy storage system (ESS) to minimize the total operation cost of the microgrid. The proposed model constructs an ESS with both electrical and cooling storage to simulate performance in the energy market (Hakimi and Moghaddas-Tafreshi, 2014b; Zidan et al., 2015; Valinejad et al., 2020; Rostamnezh et al., 2022).

By reviewing the aforementioned materials, at least three areas for improvement have been identified:

1. Decision makers in the microgrid and energy storage sectors face the challenge of choosing from multiple markets while aiming to minimize operating costs. In order to navigate these complex market entries, it is crucial to consider both market opportunities and tariff capability distribution. By assessing the available market opportunities and understanding the distribution of tariffs, decision makers can optimize their strategies for achieving minimum operating costs.
2. Microgrids in China have multiple market entries, including markets created by recent evolution and existing traditional tariffs. New regulations may lead to different storage responses in microgrids.
3. In many research works (Jiang et al., 2022), the cold generation in a cooling system is linearly modeled with boundary constraints and a steady coefficient of performance (COP). Chillers of cold generations operate non-linearly with non-steady-state COP.

The main contributions of this work are as follows:

- This paper presents a complex market environment for the microgrid with up to four different parallel tariffs. This environment represents a transition period in the initial stage of change.
- Both electricity and thermal network operations for storage response analysis have been considered. A dynamic COP from historical operational data was developed. Furthermore, this paper considers the pumping power switching mechanism in a cooling system with logical variables. These logical variables create the optimization of a cooling network and formulate a non-linear mixed-integer programming problem.
- Practically, different tariffs may not prevent the same economic values from generating multiple minimum points for optimization. In this case, not all local optimal solutions have a high industrial potential for change in behavior. This paper introduces a new regulation term in the objective function for less behavioral variation to increase the industrial implementation potential of the model.
- Numerical investigation is implemented for model verification and further analysis. Three different studies are selected for impact analysis from different market tariffs. The results show that trading-off occurs in response to storage toward different market entries.

This paper is organized as follows: multiple microgrid market entries are introduced in Section 2. Relevant storage response modeling and simulation construction are shown in Section 3. Section 4 gives a numerical study for storage response analysis. The conclusion is provided in Section 5.

2 Multiple market entries for a microgrid

2.1 Dynamic daily electricity price

In the retail section of catalog price, time-of-use (TOU) is implemented.

In the latest power market evolution, trading of contracts for differences (CFDs) is introduced. For price difference (PD) trading, bilateral negotiation (BN) and monthly bidding (MB) are constructed. A BN market is a yearly market that allows consumers and power plants to deploy transactions. Their trading willingness will be submitted to the power dispatch center for feasibility verification. The submission of BN takes place once a year. In an MB market, power consumption bids and generation bids are received. The market operators match bids with the consideration of dispatch feasibility. The submission of MB takes place once a month. For a dynamic daily price scheme, such as TOU, PD is compensated to give prices for each hour so that the shape of TOU remains the same to fulfill the requirements in catalog price (CP). Eq. 1 gives the power consumption cost with CP based on PD.

$$\begin{cases} C_{TOU} = \sum_{t=1}^{T} S \cdot P_{netload}(t) \cdot TL \cdot A_{TOU}^{E}(t), \\ P_{netload}(t) = P_{load} - P_{ES}^{dis} - P_{PV}, \\ A_{TOU,i}^{E}(t) = A_{TOU,i}^{E}(t) - A_{i}^{E}, i = 1, 2, ..., 5, \end{cases} \quad (1)$$

$$S = \begin{cases} 1, P_{load} > P_{PV}, \\ 0, P_{load} \le P_{PV}, \end{cases} \quad (2)$$

where C_{TOU} represents the cost of power consumption from the daily dynamic electricity price. P_{load} represents the total power time series vector. P_{PV} represents the total power generation vector. TL is a time step, with a step length of 15 min. $A_{TOU,i}^{E}(t)$ represents the dynamic daily electricity price vector. A_{i}^{E} is the bid-matched price difference. The dynamic daily electricity price in China does not cover the bi-directional power flow. When electricity storage wins the bids in MRGPAS, the charging of electricity storage is covered and will not be charged again in dynamic daily electricity price calculation.

2.2 Capacity-based charging (CBC)

Two-part tariff is a pricing scheme for electricity in China. The first part is the daily electricity price mentioned previously. The second part is the basic price or capacity price, which is charged on CNY/kVA or CNY/kW. In Hong Kong, basic price is also called demand charge. The basic price is charged on the monthly maximum consumer injecting power or the maximum capacity of a consumer-based local transformer. In recent years, there has been an evolution in the power market, with the advancement of new technologies and the implementation of new policies aimed at promoting sustainable energy practices. Eq. 3 gives the cost generated from the basic price.

$$C_{capacity} = \max\left(S \cdot P_{netload} \cdot A_{chr}^{E}\right), \quad (3)$$

where $C_{capacity}$ represents the cost generated from the basic price. A_{chr}^{E} represents the price of capacity-based charging. The function max( ) receives a vector and returns the maximum value from the inputted vector.

2.3 Macro-renewable generation promoting ancillary services (MRGPAS)

The market construction of ancillary services is one of the main tasks of power market deregulation in China. Unlike traditional ancillary services, this ancillary service market is specially designed for power peak shaving in supporting renewable generation. Energy storage inside consumers can trade mainly with wind power plants or solar power plants on the ancillary service trading platform to reduce the amount of abandoned wind/solar generation (Xu et al., 2012).

Wind/solar generation abandonment is an obvious phenomenon that occurs in the preliminary stage of renewable power development. For example, in wind generation, when the load decreases, the generation capability of thermal power plants is reduced with higher priority under power dispatch regulation in China. The reason for this is that the marginal cost of generation in wind farms is zero, and the government promotes the development of renewable energy. However, thermal units have lower operational bounds. The generation of thermal plants cannot be reduced over this bound for the start and stop of large cost of units. When a lower bound of thermal units is reached, wind generation abandonment occurs. As load reduction usually occurs at nighttime, wind generation abandonment and the trading chances of MRGPAS for electricity storage usually occur at night. In some MRGPAS markets, electricity storages of consumers' microgrids can only trade with wind/solar power plants (Kumar and Palanisamy, 2020).

In a MRGPAS market, owners of electricity storages and power plants should submit their bids to the trading platform. The information includes the compensation price, trading time and time length, charging power, and 15-min time step load curves. The market operator matches bids from electricity storages and wind power plants with the consideration of grid operational constraints. When bids are matched, the storage should be charged with a certain compensation price. MRGPAS markets in some provinces have upper and lower limits for the compensation price. The upper and lower limits of the compensation price in a typical market in China are 0.2 CNY/kWh and 0.1 CNY/kWh, respectively. Eq. 4 gives the cost generated from MRGPAS.

$$C_{anci} = (-1) \cdot \sum_{t=1}^{96} \left[H(t) \cdot P_{anci}(t) \cdot TL \cdot A_{anci}^{E}(t)\right], \quad (4)$$

$$H(t) = \begin{cases} 0, \text{fail to bid} \\ 1, \text{successful to bid} \end{cases}, \quad (5)$$

where C_{anci} represents the cost generated from MRGPAS. A_{anci}^{E} represents the matched compensation price in MRGPAS. H represents the microgrid chances of MRGPAS participation in a day. P_{anci} represents the charging range of electricity storage in bids of macro-renewable-generation promoting ancillary services (MRGPAS), which will be described later. The element H(t) in Eq. 5 is a logical variable, with 0 and 1 representing the microgrid's failed and successful bids at the time step, respectively.

2.4 Distributed solar generation feedback tariff

To enhance clean power generation and support relevant local industries, the Chinese government provides its first bi-directional tariff for microgrids on distributed PV generation. Consumers with distributed PV have two sub-tariff selections. The first sub-tariff is named full feed-in tariff (FFI). The PV operator is required to feed-in all its capacity to the power grid with specified installed protection and meters. The connection point of PV is not inside consumers in FFI, and consumer behavior is fully decoupled with PV generation variation. Therefore, FFI does not influence operation of the microgrid. The second sub-tariff is named surplus feed-in tariff (SFI). In SFI, consumers will consume PV generation as a priority. If surplus PV generation exists, this surplus capacity can be fed into the grid. In SFI, consumer behavior and PV time series generation will influence each other. Consumers with distributed PV can select either FFI or SFI. This paper mainly focuses on SFI modeling for its high integration capability with storage response. Eq. 5 gives the cost generated from SFI.

$$PV\_\text{cha} = \text{Comp} + \text{Ben}. \tag{6}$$

In Eq. 6, *PV_cha* represents the cost generated from the PV tariff. The cost generated from SFI is constructed in two parts. The first part, *Comp*, is from the compensation of governmental policy (Chen et al., 2013). The Chinese government offers compensation for all power generated under the full feed-in tariff (FFI) and surplus feed-in tariff (SFI). The second part, *Ben*, is the benefit from the surplus capacity feeding into the grid at the consumer side for SFI only. Eq. 7 calculates *Comp* and *Ben*, where negative 1 represents customer benefit.

$$\begin{cases} \text{Comp} = (-1) \cdot \sum_{t=1}^{T} (\text{Ggen}_t \cdot \text{PRsub}_t \cdot TL), \\ \text{Ben} = (-1) \cdot \sum_{t=1}^{T} \{TL \cdot \text{PRcoal} \cdot Gb_t\}. \end{cases} \tag{7}$$

In Eq. 7, *PRsub* represents the price of government compensation. *PRcoal* represents the local price of electricity generated from desulfurized fire coal. Gb_t represents the PV generation power (kW) at the *t*th time step. Details of Gb_t are given in Equations 8 and (9).

$$Gb_t = \text{Min} - \text{sele}[(\text{Ggen}_t - \text{Puse}_t)| \cdot R_t, \text{Ggen}_t], \tag{8}$$

$$R_t = \frac{|\ \text{Ggen}_t - \text{Puse}_t\ | + (\text{Ggen}_t - \text{Puse}_t)}{2 \cdot (\text{Ggen}_t - \text{Puse}_t)}, \tag{9}$$

where the function *Min_sele( )* receives two scalar inputs and outputs the lower value. The reason for choosing the function *Min_sele* is that SFI only admits the power generated from the SFI PV panel to feed into the grid. If the feed-in power load is larger than $Ggen_t$, the extra section is not admitted. The ratio R_t gives the benefit from the consumer to the grid.

Turning to microgrid cost with high industrial implementation potential, the aim of the microgrid is to satisfy the operational requirements with a minimum cost for industrial and commercial consumers. The objective function of microgrid operation is given in Eq. 10.

$$\text{F} = \text{C}_{\text{TOU}} + \text{C}_{\text{capicity}} + \text{C}_{\text{anci}} + \text{C}_{\text{PV}}, \tag{10}$$

$$\text{Min}: \text{Obj} = F + \mu \cdot \sum_{j=1}^{J} \sigma_j. \tag{11}$$

It is assumed that there are J periods within 1 day. The dynamic daily electricity price in each period is the same. Then, σ_j in (11) represents the standard deviation of P_{load} in the *j*th period. Eq. 11 adds a regulation of fluctuation in the objective function to control the fluctuation degree.

Tariffs may not prevent all economic equivalence of all daily time periods. For example, the price value is the same under TOU for the same period. Even real-time prices may contain periods with similar price levels. In this period with similar economic equivalence, different response schemes with the same total consumption may have the same cost, leading to multiple optimal points of optimization. Some of these optimal points may contain high response fluctuation between different time periods that consumers find difficult to follow. A fluctuation regulation term is added to the objective function Eq. 11 to reject the solution with high fluctuation so that the potential for consumer implementation is increased.

3 Response of electric/thermal storage

3.1 Microgrid electrical network

Figure 1 introduces a typical electrical network of a large group of consumers.

Figure 1 shows a typical microgrid of a large group of consumers with the following devices: devices for manufacturing or other vocational devices, electricity storage, and distributed generation, including PV and electric-supported equipment in a cooling network. Eq. 12 gives the total power load from the electrical network.

$$\begin{cases} \text{P}_{\text{load}} = \text{P}_{\text{other}} + \text{P}_{\text{cool}} + \text{P}_{\text{ES}}^{\text{chr}}, \\ \text{P}_{\text{cool}} = \sum_{\text{n}=1}^{2} \left[\text{P}_{\text{ch,n}}(\text{t}) + \text{P}_{\text{pump,n}}\right] \cdot \text{S}_{\text{w,n}}(\text{t}), \end{cases} \tag{12}$$

$$\text{S}_{\text{w,n}}(\text{t}) = \begin{cases} 0, \text{switched off}, \\ 1, \text{switched on}, \end{cases} \tag{13}$$

where P_{other} represents the time series load vector of all devices except electricity storage and devices in the cooling system. The element $\text{P}_{\text{ch,n}}(\text{t})$ represents the value of the *n*th chiller power at the *t*th time step. $\text{P}_{\text{pump,n}}$ represents the power of the *n*th pump. Due to the scheme of chiller control, the pumping power is usually kept at the same value. As this work studies storage response, P_{other} is set to be an unchangeable boundary condition during optimization. The pumping power is usually kept at a large constant value, which ensures a sufficient flow rate for the security of chiller operations. It will be changed when the pump and chiller are switched off together. Thus, $\text{S}_{\text{w,n}}(\text{t})$ in Eq. 13 represents the on–off status of chiller n and is between 0 and 1.

3.1.1 Electricity storage response

Naturally, the operation of the electricity storage must be within its physical limit. The first limit is that the rate of charging or discharging should satisfy the storage's security. Eq. 14 introduces the limit as constraints. In Eq. 15, $\text{P}_{\text{ES}}^{\text{max}}$ represents the maximum charging rate, and $\text{P}_{\text{ES}}^{\text{min}}$ represents the maximum discharging rate (negative). Eq. 15 reflects the continuously adjusting capability of electricity storage performance.

$$\text{P}_{\text{ES}}^{\text{min}} \le \text{P}_{\text{ES}}(\text{t}) \le \text{P}_{\text{ES}}^{\text{max}}, \tag{14}$$

where $\text{P}_{\text{ES}}(\text{t})$ represents the value of charging power at the t^{th} time step.

The second limit is that the energy stored in electricity storage must be within its maximum and minimum limits. Eq. 15 shows this limit.

$$\begin{gathered} \text{E}_{\text{ES}}^{\text{min}} \le \text{E}_{\text{ES}}(\text{t}) \le \text{E}_{\text{ES}}^{\text{max}}, \\ \text{E}_{\text{ES}}(\text{t}) = \text{E}_{\text{ES}}(\text{t}-1) + \text{TL} \cdot \text{P}_{\text{ES}}(\text{t}), \end{gathered} \tag{15}$$

where $\text{E}_{\text{ES}}(\text{t})$ represents the value of stored energy at the t^{th} time step.

If the consumer joins MRGPAS and has contracted with power plants at the specified time, the power of charging is fixed by the constraints detailed in the bid and contracts. Eq. 16 introduces this constraint.

$$\text{P}_{\text{ES}}(\text{t}) = \text{P}_{\text{anci}}(\text{t}), \text{if H}(\text{t}) = 1. \tag{16}$$

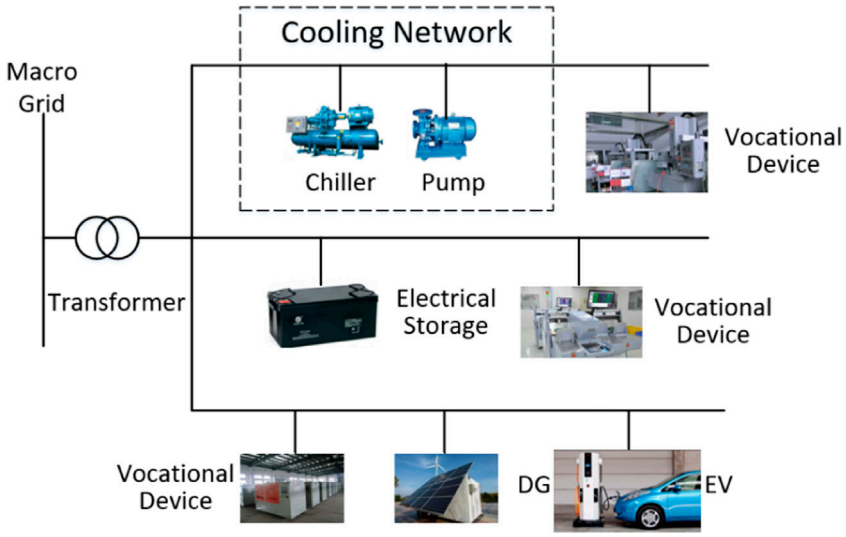

FIGURE 1
Electrical network in a typical large group of consumers.

TABLE 1 Relevant boundary conditions of the numerical study.

TOU in CP		Parameter	Value
0:00–8:00	0.3461 CNY/kWh	Pump power	30 kW
8:00–14:00	0.6473 CNY/kWh	P_{ES}^{min}	−10,000 kW
14:00–17:00	1.039 CNY/kWh	P_{ES}^{max}	10,000 kW
17:00–19:00	0.6473 CNY/kWh	E_{ES}^{min}	10,000 kWh
19:00–22:00	1.039 CNY/kWh	E_{ES}^{max}	50,000 kWh
22:00–24:00	0.6473 CNY/kWh	P_{ch}^{max}	40 kW
-	-	Q_{in}^{min}	−8,000 kW
-	-	Q_{in}^{max}	8,000 kW
-	-	$COhs^{min}$	3,200 kWh
-	-	$COhs^{max}$	25,500 kWh

3.2 Microgrid cooling network

A typical cooling network for a large group of consumers is shown in Figure 2.

The cooling network is for the generation and transmission of cold from chillers to consumers' space. From Figure 2, chiller units are the only cold generation system in the network. The cold generated will be passed to the user network to satisfy the cooling requirement or be stored in cold storage.

3.3 Dynamic transformation rate from electrical power to cooling power

Cold is initially generated by chillers in a cooling network. COP is widely preferred to evaluate a chiller's cold generation efficiency. Eq. 17 gives this relationship.

$$E_{CS,n}(t) = P_{ch,n}(t) \cdot COP_n(t), n = 1, 2 \quad (17)$$

COP is not a constant. It will change while P_{ch} changes. Figure 3 shows the operational statistics among COP, P_{ch}, and E_{CS}.

As shown in Figure 3, COP decreases nonlinearly while P_{ch} increases. Thus, there is a peak point of E_{CS} in the range of P_{ch}. With curve fitting, the approximation of COP and E_{CS} in Figure 3 is given by Eq. 20, which is the red line in the figure. The result of Eq. 18 is based on polynomial approximation.

$$E_{CS,i}(t) = \sum_{m=0}^{6} \alpha_m \cdot P_{ch,i,j}(t). \quad (18)$$

Moreover, the power of each chiller should not exceed its rated working range given in Eq. 19.

$$P_{ch}^{min} \le P_{ch}(t) \le P_{ch}^{max}. \quad (19)$$

On a certain day, the requirement of time series indoor temperature depends on the requirements of vocational work, so the time series cold requirement is constant. To balance the cold generation and consumption, the cooling network should satisfy the requirement given in Eq. 20.

$$\sum_{n=1}^{2} E_{CS,n}(t) \cdot S_{w,n}(t) = Q_{tot}(t) + Q_{in}(t), \quad (20)$$

where $Q_{tot}(t)$ represents the cold consuming rate of the microgrid at the *t*th time step. $Q_{in}(t)$ represents the cold charging rate of cold storage at the *t*th time step. Eq. 17 shows that the generated cold will be either consumed by the microgrid's cooling requirements or by charging the cold storage.

In Figure 2, the power exchanging speed of cold storage can be controlled by thermal energy exchanging areas through switching the corresponding valves, so the control of charging/discharging rate in cold storage can be given by Eq. 21. Q_{in}^{max} and Q_{in}^{min} represent the maximum and minimum charging rates of cold storage, respectively.

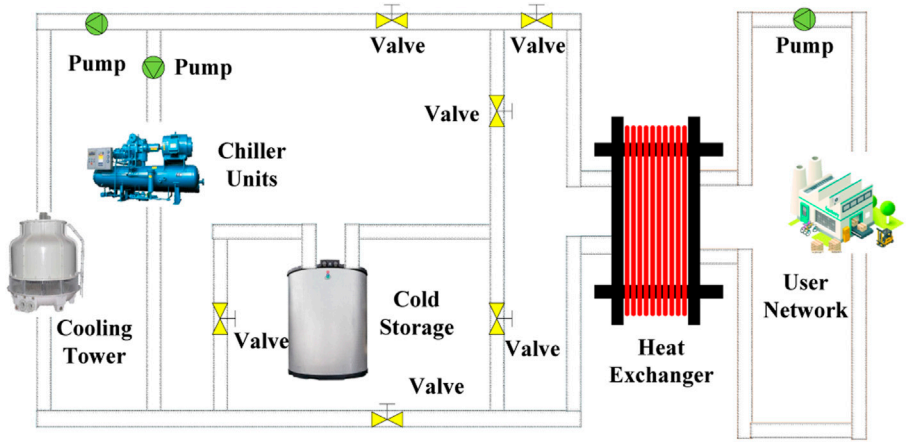

FIGURE 2
Cooling network in a typical large group of consumers.

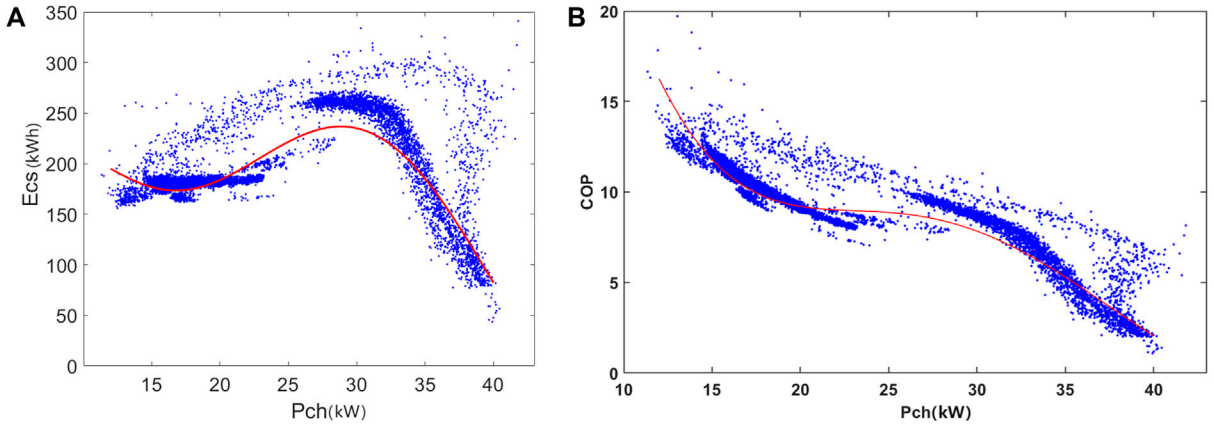

FIGURE 3
Operational statistics of cold generation in chillers. **(A)** Operational statistics among Ecs and Pch. **(B)** Operational statistics among COP and Pch.

$$Q_{in}^{\min} \le Q_{in}(t) \le Q_{in}^{\max}. \tag{21}$$

Eq. 22 gives the limits for cold storages, where $COhs_t$ represents the value of stored cold at the tth time step.

$$\begin{cases} \mathrm{COhs}^{\min} \leqslant \mathrm{COhs}_t \leqslant \mathrm{COhs}^{\max} \\ \mathrm{COhs}_t = \mathrm{Qin}(t)\cdot \mathrm{TL} + \mathrm{COhs}_{t-1}. \end{cases} \tag{22}$$

Eq. 22 shows that cold storage cannot exceed its maximum and minimum operational limits at any time of the day.

For an electric vehicle charging station, the probability density function (PDF) of the arrival time of EVs is described by Eq. 23:

$$f_{EV}^{ar}(t) = \begin{cases} \dfrac{1}{\sqrt{2\pi}\sigma_1} \exp\left[-\dfrac{(t+24-\mu_1)^2}{2\sigma_1^2}\right] & 0 < t \le \mu_1 - 12, \\ \dfrac{1}{\sqrt{2\pi}\sigma_1} \exp\left[-\dfrac{(t-\mu_1)^2}{2\sigma_1^2}\right] & \mu_1 - 12 < t \le 24, \end{cases} \tag{23}$$

where μ and μ_1 are the mean values of the time when EVs arrive and depart from EVCS, respectively, and σ_1 and σ_2 are the standard deviations of the time when EVs arrive and leave EVCS, respectively.

The daily load demand of EV charging is related to the daily driving mileage and charging duration. In general, the daily travel mile of an EV is considered to obey a normal distribution, and its PDF is described by Eq. 24:

$$f_M(M_d) = \frac{1}{\sqrt{2\pi}\sigma_M M_d} \exp\left[-\frac{(\ln M_d - \mu_M)^2}{2\sigma_M^2}\right], \tag{24}$$

where M_d represents the daily mileage of EVs and σ_M and μ_M are the standard deviation and the mean value of M_d, respectively.

4 Numerical study and analysis

4.1 Material and methods

To analyze the storage impact under multiple market accesses and verify model feasibility, a numerical study with practical data is implemented. The device's power load time series under general operation is selected from a typical factory. The TOU tariff data used

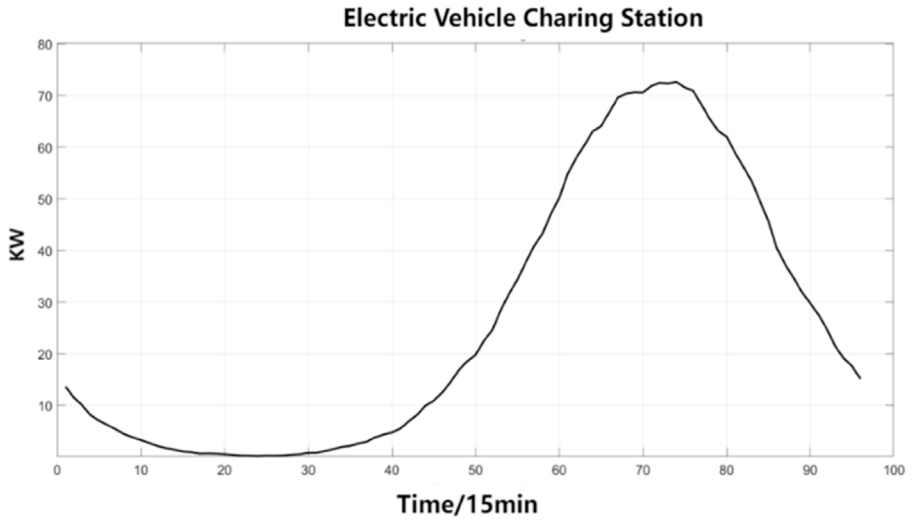

FIGURE 4
Electric vehicle power consumption.

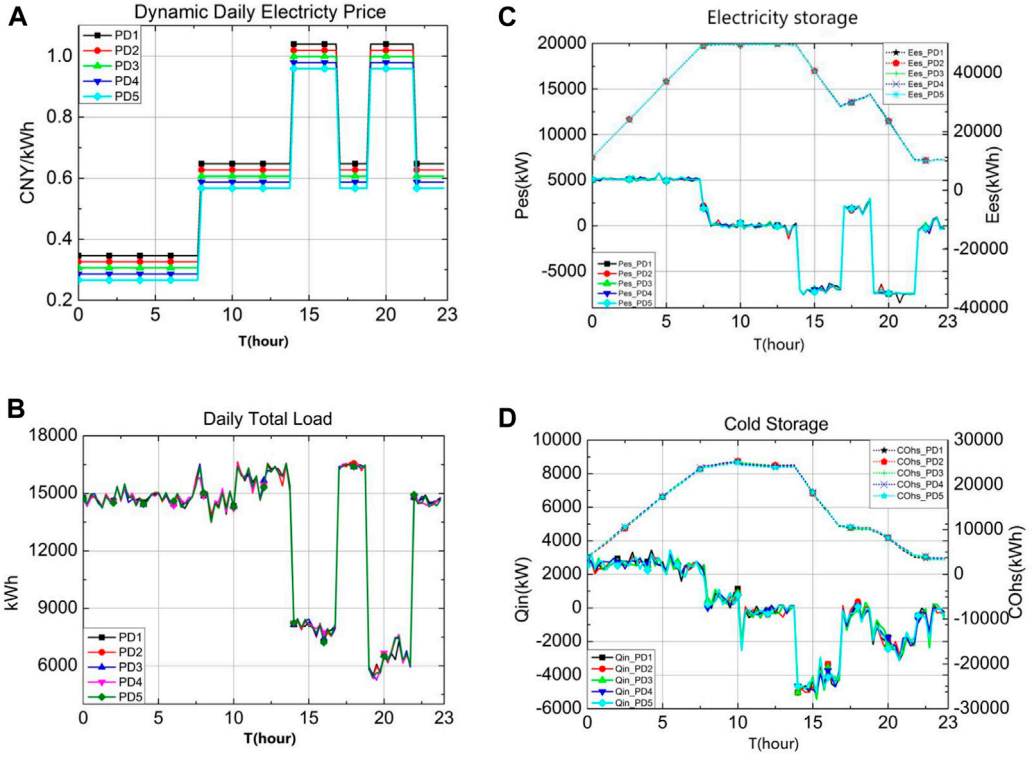

FIGURE 5
Optimization result of storage performance in case study 1. **(A)** Dynamic daily electricty Price **(B)** Daily total load **(C)** Electricity storage performance **(D)** Cold storage performance.

in this study were sourced from the official website of the Guangdong Provincial Development and Reform Commission in China. The compensation bid price of MRGPAS is assumed to be at its lowest limit, that is, 0.1 CNY/kWh. This assumption ensures the minimum benefit and the participation of the target factory in MRGPAS. MRGPAS also provides a bottom limit for participating electricity storage's maximum charging/discharging rate, which is 10 MW.

The cooling system in this target factory contains three sub-cooling units. Each unit includes eight chillers connecting together on the same flowing pipe. Each chiller is associated with an

TABLE 2 Cost analysis under different MRGPAS participation time periods.

Scenario	Participation time	Cost from TOU (CNY)	Cost from CBC (CNY)	Cost from MRGPAS (CNY)	Total cost (CNY)
0	None	185,363.2	17,989.4	0.0	203,352.6
1	2:00–3:00	183,828.9	17,535.6	1,501.1	202,865.6
2	2:00–4:00	181,374.7	17,453.0	3,002.2	201,830.0
3	2:00–5:00	172,327.2	21,254.3	7,382.9	200,964.4
4	2:00–6:00	168,903.8	21,259.7	9,843.9	200,007.4
5	2:00–7:00	169,888.6	19,037.4	9,843.9	198,770.0

independent pump. The total cooling requirement is collected from a typical day in summer in the factory's historical data.

The target factory has one flywheel electric power storage group and one phase-changing cold power storage. The relevant boundary conditions in the numerical study are given in Table 1. As stochastic optimization is one of the typical methods for microgrid planning, the genetic algorithm is selected to solve the optimization. MATLAB GA Global Optimization Toolbox was used to carry out the study. The crossover rate was set at 0.8, while the mutation rate was at 0.01. The numerical study was carried out in MATLAB (version R2019a) on a computer with an AMD Ryzen 71,700 Eight-Core Processor, 3.00 GHz, and 8.0 GB of RAM.

4.2 Case 1: storage performance on binary market accesses: TOU with price difference and capacity-based charging

Case study 1 aims to demonstrate the storage performance when the microgrid joins dynamic daily electricity price and CBC together. Figures 5A–D show the optimization results.

From Figures 5A–D, the following three main points are observed:

Dynamic daily electricity price promotes storages to charge when the price is low and discharge when the price is high. The energy stored in both storages increases when the price is low and decreases when the price is high. The reason for this is that the cost of the microgrid will be decreased by consuming cheaper energy.

Different PD values will not influence the storage performance. As shown in Figure 4, results under different PD values are nearly the same. The reason for this is that the optimal cost of the microgrid under TOU only depends on the shape of the price curve. Because the same PD is added to the price level at each hour, shifting the price curve entirely will not change the relationship of price between any two time points. Therefore, time with a lower price will always be lower in different PD values, and different PD values will not influence the cost from CBC. Thus, catalog price with PD will not influence the storage performance.

The discharging rate of energy storage systems does not reach its maximum in price-peak time. Figure 4 shows that the absolute value of the discharging rate is still smaller than the storage's maximum discharging rate. There is a remaining discharging capability in price-peak time. The reason for this is that the marginal cost from CBC will increase faster than cost reduction under TOU if the discharging rate increases in price-peak time.

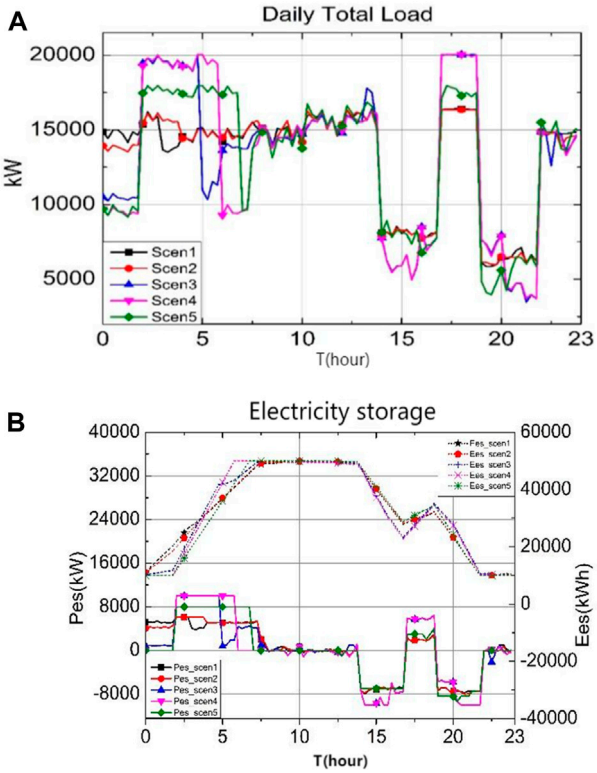

FIGURE 6
Result of storage performance optimization in case study 2. **(A)** Daily total load **(B)** Electricity storage performance.

4.3 Case 2: storage behavior in three-traffic market accesses: TOU with price difference, CBC, and MRGPAS

Case study 2 demonstrates the storage performance when the microgrid is under three-market accesses together. Considering that MRGPAS has a focus on renewable power generation, the bid of MRGPAS is assumed to happen at nighttime, for most wind

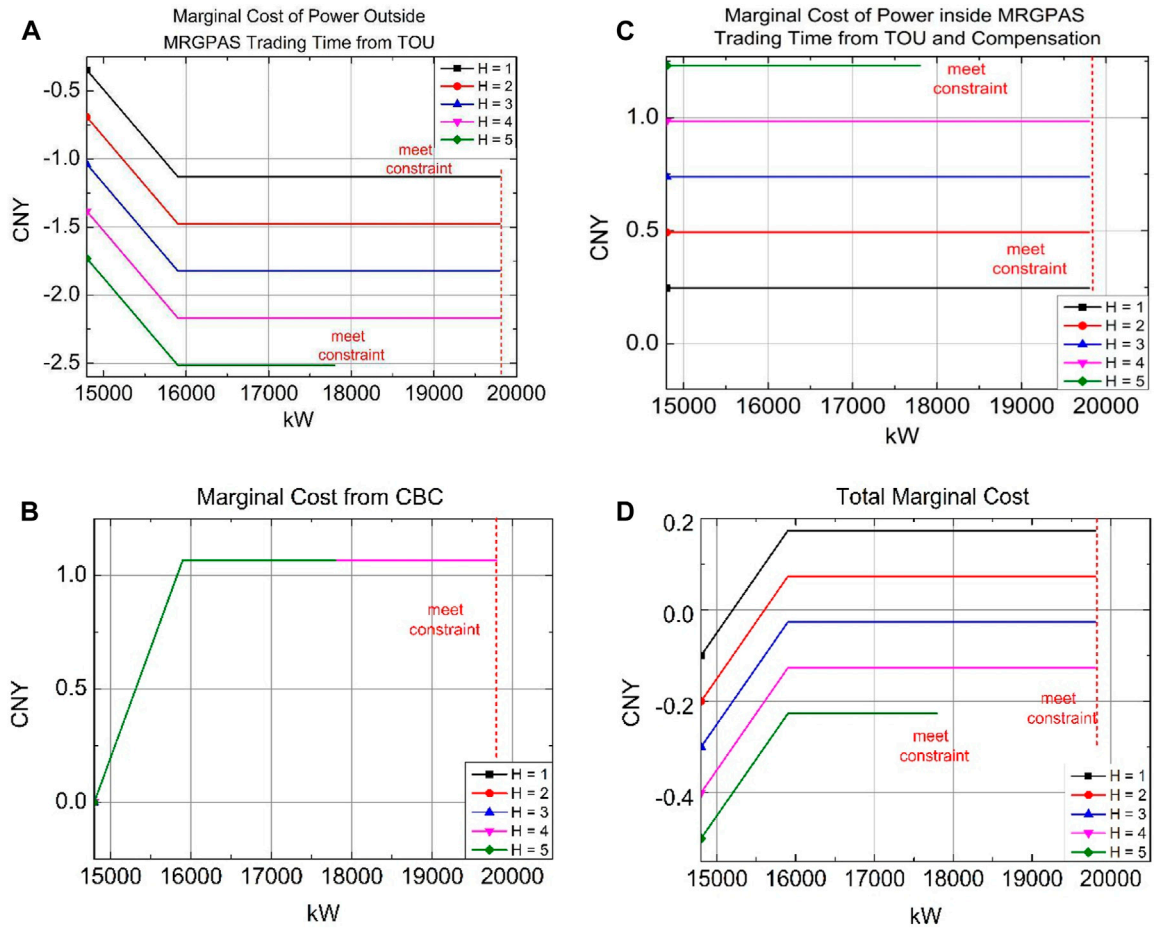

FIGURE 7
Marginal cost variation under three-market accesses. **(A)** Marginal cost of Powepr outside MRGPAS trading time from TOU. **(B)** Marginal cost from CBC. **(C)** Marginal cost of power inside MRGPAS trading time from TOU and compensation. **(D)** Total marginal cost.

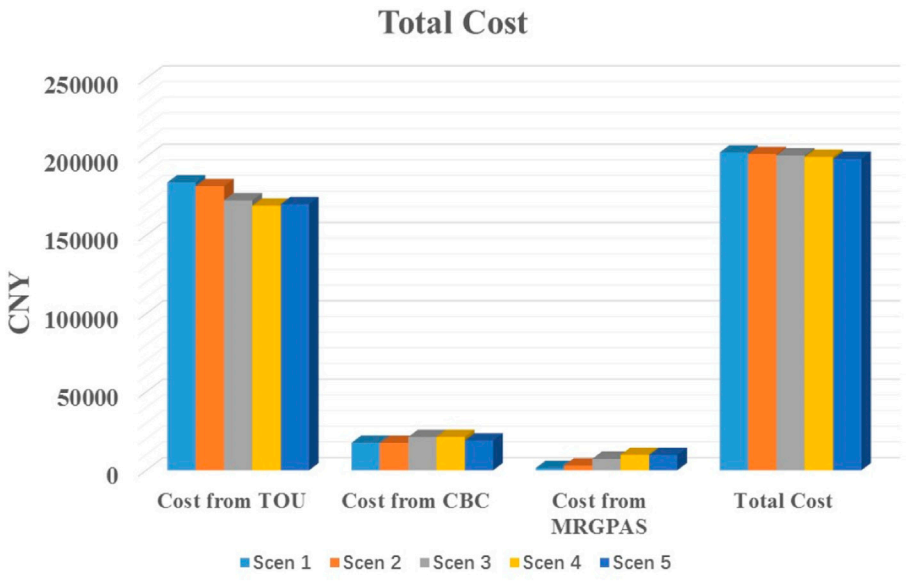

FIGURE 8
Cost variation details under three-market accesses.

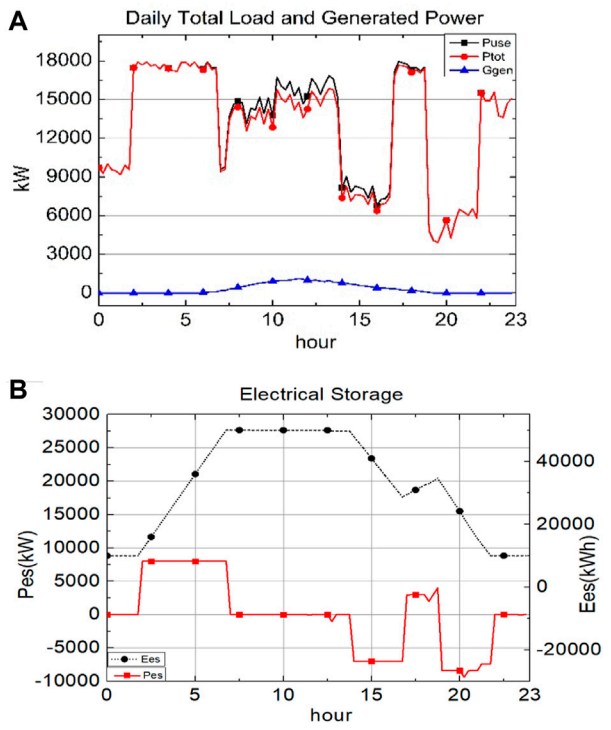

FIGURE 9
Microgrid operation under four-market accesses. **(A)** Daily total load and generated power. **(B)** Response behavior of electrical storage.

generation abandonment occurs at night. Figures 5A–D and Table 2 give the result of optimization on different time lengths of MRGPAS participation. From MRGPAS requirements, cold storage is not allowed to join MRGPAS.

From Figures 6A, B, the following two points can be seen.

At the time of MRGPAS trading, the charging rate of electrical storage is higher than the charging rate outside of MRGPAS trading time at night. The reason for this is that charging within the MRGPAS bid will generate extra revenue from the MRGPAS market other than charging under the daily dynamic price tariff. Therefore, a greater amount of charging rate is shifted into MRGPAS trading time in all scenarios. This means that choosing to release the control of electricity storage to charge in MRGPAS trading will lead to a lower cost than charging under the daily dynamic price.

The charging rate of electric storage will rise to a higher level than the charging rate outside the MRGPAS trading time at night when the length of trading time is not less than 3 h. When the length of trading time is larger than or equal to 3 h, the charging rate within trading time will have a significant increase. This phenomenon is due to the comparison between the marginal cost in CBC and that of MRGPAS trading. A detailed analysis is given in Figures 7A–D.

Due to the compensation from the MRGPAS market, power shifts from outside the MRGPAS trading time to the trading time, which can generate extra benefits from MRGPAS. This shifting will increase the reference power and cost of CBC.

TABLE 3 Microgrid cost analysis under four-market accesses.

Market accesses	Without PV	With PV
Cost from TOU (CNY/kWh)	169,888.60	164,405.05
Cost from CBC (CNY/kWh)	19,037.42	18,988.87
Cost from MRGPAS (CNY/kWh)	9,843.93	9,843.91
Cost from solar generation (CNY/kWh)	0	−3,955.92
Total cost (CNY/kWh)	198,769.95	189,281.91

In addition, the load in the target period is limited to a threshold in case study 1 when the marginal cost of CBC becomes positive. Therefore, when charging power inside the MRGPAS trading time increases at night, the threshold of load limitation in the target period could be increased. Thus, the remaining capability in price-peak time can be shifted to the time between 17:00 and 19:00, which can reduce the cost further. When MRGPAS trading is larger than or equal to 3 h, the sum of MRGPAS compensation and threshold releasing will be larger than the cost increase of CBC. Thus, more charging power can be added inside the MRGPAS trading time. Reflecting on Figure 7 d), the marginal cost of H≥3 is negative, and so the cost will be decreased.

Figure 8 show the comparison of optimal cost under different trading time lengths. It shows that increasing the time length of the MRGPAS trading time will decrease the microgrid's cost. Analysis of this case study shows that the time length of the MRGPAS bid will influence the cost in all three markets and thus influence the storage performance.

4.4 Case 3: storage performance in four-market accesses

When the microgrid is integrated with distributed solar generation, less power from the grid is needed. This case study integrates all four-market accesses together for microgrid analysis. A typical daily generation capacity variation is shown in Figures 9A, B. Figures 9A, B and Table 3 give the results of solar generation. Scenario 5 from case study 3 is selected for MRGPAS access in this case study.

From Figures 9A, B, solar generation integration in a large network of consumers will compensate for an obvious section of the power consumption between 8:00 and 19:00. Between 14:00 and 17:00, the price reaches the maximum level in TOU; therefore, storages and PV panels will output their electricity to decrease the total load. Finally, the cost from TOU will be reduced from 169,888 CNY/day to 164,405 CNY/day for solar generation, and the microgrid will receive approximately 4,000 CNY/day as governmental compensation. Generally, solar power generation mainly occurs in the daytime. Thus, it only duplicates with the discharging of storage. The CBC reference and MRGPAS do not occur within these areas, and thus, solar power generation will not influence the response behavior of storage.

5 Conclusion

This paper presents market models with four different types of tariffs for the microgrid market environment. The performance of both electricity storage and cold storage systems is modeled to formulate a non-linear mixed-integer programming problem. The numerical study shows that different market accesses will influence the storage system's response together. A trade-off of different market participation occurs on storage performance. However, generally, a microgrid with energy storage systems will achieve a reduced cost with more market participation. From the study and discussion, a better insight was provided into energy trading within a microgrid, including energy storage. A future work based on standard development could be considered.

Data availability statement

The raw data supporting the conclusions of this article will be made available by the authors, without undue reservation.

Author contributions

MY: conceptualization, data curation, investigation, methodology, writing–original draft, and writing–review and editing. ZL: conceptualization, formal analysis, investigation, methodology, and writing–original draft. CL: conceptualization, formal analysis, investigation, resources, and writing–review and editing. ZZ: conceptualization and writing–review and editing. AZ: writing–review and editing. LL: funding acquisition, methodology, resources, supervision, writing–original draft, and writing–review and editing. ZS: data curation, formal analysis, project administration, and writing–review and editing.

Funding

The author(s) declare that financial support was received for the research, authorship, and/or publication of this article. This research was supported by the National Natural Science Foundation of China (62206062) and the Guangdong Basic and Applied Basic Research Foundation (2021A1515010742).

Conflict of interest

Author MY was employed by Jiangmen Power Supply Bureau of Guangdong Power Grid Co Ltd. Author ZS was employed by China Southern Power Grid Co. Ltd.

The remaining authors declare that the research was conducted in the absence of any commercial or financial relationships that could be construed as a potential conflict of interest.

The author(s) declared that they were an editorial board member of Frontiers, at the time of submission. This had no impact on the peer review process and the final decision.

Publisher's note

References

Al-Awami, A. T., Amleh, N. A., and Muqbel, A. M. (2017). Optimal demand response bidding and pricing mechanism with fuzzy optimization: application for a virtual power plant. *IEEE Trans. Industry Appl.* 53 (5), 5051–5061. doi:10.1109/tia.2017.2723338

Amrollahi, M. H., and Bathaee, S. M. T. (2017). Techno-economic optimization of hybrid photovoltaic/wind generation together with energy storage system in a stand-alone micro-grid subjected to demand response. *Appl. energy* 202, 66–77. doi:10.1016/j.apenergy.2017.05.116

Chen, T. H., Hsieh, T. Y., Yang, N. C., Yang, J. S., and Liao, C. J. (2013). Evaluation of advantages of an energy storage system using recycled EV batteries. *Int. J. Electr. Power & Energy Syst.* 45 (1), 264–270. doi:10.1016/j.ijepes.2012.08.037

Chen, W., Qiu, J., Zhao, J., Chai, Q., and Dong, Z. Y. (2021). Bargaining game-based profit allocation of virtual power plant in frequency regulation market considering battery cycle life. *IEEE Trans. Smart Grid* 12 (4), 2913–2928. doi:10.1109/tsg.2021.3053000

Fan, W., Huang, L. L., Cong, B., Degejirifu, Tan, Z., and Xing, T. (2022). Research on an optimization model for wind power and thermal power participating in two-level power market transactions. *Int. J. Electr. power & energy Syst.* 134, 107423. doi:10.1016/j.ijepes.2021.107423

Garcia-Torres, F., Bordons, C., Tobajas, J., Marquez, J. J., Garrido-Zafra, J., and Moreno-Munoz, A. (2020). Optimal schedule for networked microgrids under deregulated power market environment using model predictive control. *IEEE Trans. Smart Grid* 12 (1), 182–191. doi:10.1109/tsg.2020.3018023

Gough, R., Dickerson, C., Rowley, P., and Walsh, C. (2017). Vehicle-to-grid feasibility: a techno-economic analysis of EV-based energy storage. *Appl. energy* 192, 12–23. doi:10.1016/j.apenergy.2017.01.102

Hakimi, S. M., and Moghaddas-Tafreshi, S. M. (2014a). Optimal planning of a smart microgrid including demand response and intermittent renewable energy resources. *IEEE Trans. Smart Grid* 5 (6), 2889–2900. doi:10.1109/tsg.2014.2320962

Hakimi, S. M., and Moghaddas-Tafreshi, S. M. (2014b). Optimal planning of a smart microgrid including demand response and intermittent renewable energy resources. *IEEE Trans. Smart Grid* 5 (6), 2889–2900. doi:10.1109/tsg.2014.2320962

He, G., Chen, Q., Kang, C., Xia, Q., and Poolla, K. (2016). Cooperation of wind power and battery storage to provide frequency regulation in power markets. *IEEE Trans. Power Syst.* 32 (5), 3559–3568. doi:10.1109/tpwrs.2016.2644642

Huang, H., Nie, S., Lin, J., Wang, Y., and Dong, J. (2020). Optimization of peer-to-peer power trading in a microgrid with distributed PV and battery energy storage systems. *Sustainability* 12 (3), 923. doi:10.3390/su12030923

Jiang, Z., Hlanze, P., and Cai, J. (2022). Optimal predictive control of phase change material-based energy storage in buildings via mixed-integer convex programming. *Appl. Therm. Eng.* 215, 118821. doi:10.1016/j.applthermaleng.2022.118821

Khalilpour, K. R., and Vassallo, A. (2016). A generic framework for distributed multi-generation and multi-storage energy systems. *Energy* 114, 798–813. doi:10.1016/j.energy.2016.08.029

Khaloie, H., Toubeau, J. F., Vallée, F., Lai, C. S., and Lai, L. L. (2021). An innovative coalitional trading model for a biomass power plant paired with green energy resources. *IEEE Trans. Sustain. Energy* 13 (2), 892–904. doi:10.1109/tste.2021.3138777

Kumar, G. V. B., and Palanisamy, K. (2020). A review of energy storage participation for ancillary services in a microgrid environment. *Inventions* 5 (4), 63. doi:10.3390/inventions5040063

Kwon, S., Ntaimo, L., and Gautam, N. (2016). Optimal day-ahead power procurement with renewable energy and demand response. *IEEE Trans. Power Syst.* 32 (5), 3924–3933. doi:10.1109/tpwrs.2016.2643624

Lai, C. S., Jia, Y., Lai, L. L., Xu, Z., McCulloch, M. D., and Wong, K. P. (2017b). A comprehensive review on large-scale photovoltaic system with applications of electrical energy storage. *Renew. Sustain. Energy Rev.* 78, 439–451. doi:10.1016/j.rser.2017.04.078

Lai, C. S., Jia, Y., McCulloch, M. D., and Xu, Z. (2017a). Daily clearness index profiles cluster analysis for photovoltaic system. *IEEE Trans. Industrial Inf.* 13 (5), 2322–2332. doi:10.1109/tii.2017.2683519

Lai, C. S., Jia, Y., Xu, Z., Lai, L. L., Li, X., Cao, J., et al. (2017c). Levelized cost of electricity for photovoltaic/biogas power plant hybrid system with electrical energy storage degradation costs. *Energy Convers. Manag.* 153, 34–47. doi:10.1016/j.enconman.2017.09.076

Lai, C. S., and McCulloch, M. D. (2016). Sizing of stand-alone solar PV and storage system with anaerobic digestion biogas power plants. *IEEE Trans. Industrial Electron.* 64 (3), 2112–2121. doi:10.1109/tie.2016.2625781

Lai, C. S., and McCulloch, M. D. (2017). Levelized cost of electricity for solar photovoltaic and electrical energy storage. *Appl. energy* 190, 191–203. doi:10.1016/j.apenergy.2016.12.153

Li, X., Wang, L., Yan, N., and Ma, R. (2021). Cooperative dispatch of distributed energy storage in distribution network with PV generation systems. *IEEE Trans. Appl. Supercond.* 31 (8), 1–4. doi:10.1109/tasc.2021.3117750

Lin, J., Kahrl, F., Yuan, J., Liu, X., and Zhang, W. (2019). Challenges and strategies for electricity market transition in China. *Energy Policy* 133, 110899. doi:10.1016/j.enpol.2019.110899

Liu, Z., Chen, Y., Zhuo, R., and Jia, H. (2018). Energy storage capacity optimization for autonomy microgrid considering CHP and EV scheduling. *Appl. Energy* 210, 1113–1125. doi:10.1016/j.apenergy.2017.07.002

MansourLakouraj, M., Shahabi, M., Shafie-khah, M., and Catalão, J. P. (2022). Optimal market-based operation of microgrid with the integration of wind turbines, energy storage system and demand response resources. *Energy* 239, 122156. doi:10.1016/j.energy.2021.122156

Olabi, A. G. (2017). Renewable energy and energy storage systems. *Energy* 136, 1–6. doi:10.1016/j.energy.2017.07.054

Rabiee, A., Farahani, H. F., Khalili, M., Aghaei, J., and Muttaqi, K. M. (2016). Integration of plug-in electric vehicles into microgrids as energy and reactive power providers in market environment. *IEEE Trans. Industrial Inf.* 12 (4), 1312–1320. doi:10.1109/tii.2016.2569438

Rostamnezhad, Z., Mary, N., Dessaint, L. A., and Monfet, D. (2022). Electricity consumption optimization using thermal and battery energy storage systems in buildings. *IEEE Trans. Smart Grid* 14 (1), 251–265. doi:10.1109/tsg.2022.3194815

Tabar, V. S., Ghassemzadeh, S., and Tohidi, S. (2019). Energy management in hybrid microgrid with considering multiple power market and real time demand response. *Energy* 174, 10–23. doi:10.1016/j.energy.2019.01.136

Tian, X., Chen, W., and Hu, J. (2023). Game-theoretic modeling of power supply chain coordination under demand variation in China: a case study of Guangdong Province. *Energy* 262, 125440. doi:10.1016/j.energy.2022.125440

Valinejad, J., Marzband, M., Korkali, M., Xu, Y., and Saad Al-Sumaiti, A. (2020). Coalition formation of microgrids with distributed energy resources and energy storage in energy market. *J. Mod. Power Syst. Clean Energy* 8 (5), 906–918. doi:10.35833/mpce.2019.000116

Wang, C., Zhang, Z., Abedinia, O., and Farkoush, S. G. (2021). Modeling and analysis of a microgrid considering the uncertainty in renewable energy resources, energy storage systems and demand management in electrical retail market. *J. Energy Storage* 33, 102111. doi:10.1016/j.est.2020.102111

Xu, Z., Guan, X., Jia, Q. S., Wu, J., Wang, D., and Chen, S. (2012). Performance analysis and comparison on energy storage devices for smart building energy management. *IEEE Trans. Smart Grid* 3 (4), 2136–2147. doi:10.1109/tsg.2012.2218836

Zhang, T., Qiu, W., Zhang, Z., Lin, Z., Ding, Y., Wang, Y., et al. (2023). Optimal bidding strategy and profit allocation method for shared energy storage-assisted VPP in joint energy and regulation markets. *Appl. Energy* 329, 120158. doi:10.1016/j.apenergy.2022.120158

Zhang, X., Chen, H., Xu, Y., Li, W., He, F., Guo, H., et al. (2017a). Distributed generation with energy storage systems: a case study. *Appl. Energy* 204, 1251–1263. doi:10.1016/j.apenergy.2017.05.063

Zhang, X., Hug, G., Kolter, J. Z., and Harjunkoski, I. (2017b). Demand response of ancillary service from industrial loads coordinated with energy storage. *IEEE Trans. Power Syst.* 33 (1), 951–961. doi:10.1109/tpwrs.2017.2704524

Zhao, H., Hong, M., Lin, W., and Loparo, K. A. (2017). Voltage and frequency regulation of microgrid with battery energy storage systems. *IEEE Trans. smart grid* 10 (1), 414–424. doi:10.1109/tsg.2017.2741668

Zhao, T., and Ding, Z. (2017). Cooperative optimal control of battery energy storage system under wind uncertainties in a microgrid. *IEEE Trans. Power Syst.* 33 (2), 2292–2300. doi:10.1109/tpwrs.2017.2741672

Zhao, X., Lyon, T. P., and Song, C. (2012). Lurching towards markets for power: China's electricity policy 1985–2007. *Appl. energy* 94, 148–155. doi:10.1016/j.apenergy.2012.01.035

Zhao, Z., Xu, J., Guo, J., Ni, Q., Chen, B., and Lai, L. L. (2023). Robust energy management for multi-microgrids based on distributed dynamic tube model predictive control. *IEEE Trans. Smart Grid*, 1. (Early Access). doi:10.1109/tsg.2023.3290191

Zidan, A., Gabbar, H. A., and Eldessouky, A. (2015). Optimal planning of combined heat and power systems within microgrids. *Energy* 93, 235–244. doi:10.1016/j.energy.2015.09.039

frontiers | Frontiers in Energy Research

TYPE Original Research
PUBLISHED 07 December 2023
DOI 10.3389/fenrg.2023.1297356

OPEN ACCESS

EDITED BY
Zijun Zhang,
City University of Hong Kong, China

REVIEWED BY
Zicheng Fei,
City University of Hong Kong, China
Zhongju Wang,
University of New South Wales, Australia

*CORRESPONDENCE
Anil Pahwa,
✉ pahwa@ksu.edu

RECEIVED 19 September 2023
ACCEPTED 27 November 2023
PUBLISHED 07 December 2023

CITATION
Nematirad R, Pahwa A, Natarajan B and Wu H (2023), Optimal sizing of photovoltaic-battery system for peak demand reduction using statistical models.
Front. Energy Res. 11:1297356.
doi: 10.3389/fenrg.2023.1297356

Optimal sizing of photovoltaic-battery system for peak demand reduction using statistical models

Reza Nematirad, Anil Pahwa*, Balasubramaniam Natarajan and Hongyu Wu

Electrical and Computer Engineering Department, Kansas State University, Manhattan, KS, United States

Due to increasing environmental concerns and demand for clean energy resources, photovoltaic (PV) systems are becoming more prevalent. Considering that in several instances, customers pay for both energy and power, PV installations not only must reduce the customers' energy purchases but also lower their peak demand for maximum financial benefits. However, in many cases, the peak demand does not coincide with the peak of photovoltaic generation. To address this issue, excess energy generated during low-demand periods can be stored in a battery, which can then be used to meet peak demand. Determining the optimal size of photovoltaic and battery components while ensuring system performance and financial benefits is significantly challenging. This study proposes a novel statistical methodology for optimizing PV-battery system size. In the proposed method, the PV-battery system must meet peak demand thresholds with a specific probability. Further, cost and benefit functions are used for financial evaluation. Finally, Monte Carlo simulations, developed using time series clustering and a Bayesian model are utilized to assess system performance and financial feasibility.

KEYWORDS

photovoltaic-battery system, peak demand reduction, time series clustering, statistical analysis, Monte Carlo simulation

1 Introduction

Photovoltaic (PV) systems have been widely used to generate electricity in recent years due to their advantages over traditional power resources (Mirzapour and Arpanahi, 2018). Based on the U.S. Department of Energy Solar Energy Technologies Office (SETO) and the National Renewable Energy Laboratory (NREL) PV vision, solar energy can supply 40 percent of the nation's electricity by 2035 (Solar Futures Study, 2023). PV systems play an important role in power systems because they are able to generate clean and environmentally friendly energy from solar irradiance (Thirunavukkarasu and Sawle, 2021). Stand-alone, grid-connected PV, hybrid PV systems, and building-integrated PV systems, are among the most functional types of PV systems (Verma et al., 2011). From an economic point of view, the utilization of PV systems must be beneficial both for utilities and customers. In several instances, customers pay for both energy and peak demand. Consequently, PV system installation not only must reduce electrical energy purchase but also must reduce peak demand. Electricity energy reduction can be done by PV systems at any time of PV operations, but peak demand reduction needs more analysis. Because the

PV generation in many cases does not coincide with peak demand hours. For example, during winter and partially in spring and fall the peak demand may occur in the early morning hours when PV generation is infinitesimal or zero. To tackle this problem, batteries can be used to store excess energy generated during low-demand periods, which can then be used to meet peak demand (Nkuriyingoma et al., 2022). Nevertheless, one of the main challenges is finding the appropriate size for PV systems and associated batteries that can meet a specific peak with high probability, resulting in peak demand reduction while considering the stochastic nature of both the system peak demand and solar irradiance. The literature review on PV-battery systems indicates a few studies focused on PV-battery systems sizing with consideration of risk analysis for peak demand reduction.

Several studies have been conducted to optimize PV-battery systems for residential load applications. These studies use various methodologies and objectives to achieve optimal PV-battery system performance and financial benefits. Among the most common optimization methodologies are deterministic optimization, stochastic optimization, robust optimization, and multi-objective optimization.

Deterministic optimization approaches involve using predetermined parameters and mathematical modeling to determine the optimal size of the PV and battery components (Okoye and Solyalı, 2017). proposes a deterministic optimization model to minimize the total cost of PV-battery systems while satisfying load demand and system constraints. The deterministic methodology described in (Belfkira et al., 2011) aims to optimize PV systems by utilizing long-term data. The goal of this methodology is to determine the optimal component numbers of the system while minimizing the total cost and ensuring the availability of energy.

Stochastic optimization approaches incorporate uncertainty in PV generation and other parameters to optimize the sizing of PV battery systems (Ensslen et al., 2018). presents a stochastic optimization model for determining the optimal size of a Solar System with battery storage. The sensitivity analysis shows that the PV size significantly relates to labor cost and demand, while the battery size is influenced by battery cost and demand. Further (Bagheri et al., 2022), presents a two-stage stochastic programming model that incorporates a conditional generative adversarial network to generate scenarios for generated PV power and demand. It aims to minimize costs and highlights the efficiency of PV-battery systems.

Robust optimization is a new technique in PV-battery sizing that considers the inherent uncertainty associated with parameters, such as solar irradiance, ambient temperature, demand, etc. By modeling the uncertain parameters by specific intervals, robust optimization seeks to find the optimal solution (Carli et al., 2022). Few studies in the literature incorporate the robust counterpart in their PV-battery optimal sizing problems. For example (Aghamohamadi et al., 2021), proposes an adaptive robust optimization to determine the optimal size of PV and battery while minimizing operating costs under the worst-case realization of uncertainties in a residential area. The 10 percent perturbation is considered for the uncertain parameters around their nominal values. A multi-objective robust optimization is proposed by (Rodríguez-Gallegos et al., 2018) to minimize the CO_2 emissions, cost of energy, and voltage deviations under the worst-case scenarios.

Finally, multi-objective optimization approaches in PV-battery optimization aim to simultaneously optimize multiple conflicting objectives such as cost, PV-battery size, environmental impact, etc. (Khezri et al., 2020) proposes a multi-objective optimization scheme for grid-connected households, where the cost of energy and grid dependency are considered as the objectives (Emrani et al., 2021). presents a multi-objective methodology to choose the optimal size of the PV-battery system using load and solar irradiance profiles. That study aims to minimize the total cost of the PV-battery system investment. A multi-objective function is developed in (Kelepouris et al., 2022) to find the optimal size of a PV-battery system and the impact of different energy costs and load profiles on the objective functions are discussed. Authors in (Celik et al., 2020) propose a multi-objective problem in a grid-connected PV-battery system where energy autonomy, power autonomy, payback period, and lifetime capital cost are considered as the objective functions. The goal of the study in (Alramlawi and Li, 2020) is to minimize energy costs by using lead-acid batteries and PV panels, maximize battery depth-of-discharge, and maximize solar panel tilt angle. That study aims to improve system reliability by accounting for annual power supply losses and providing accurate battery lifespan estimations for economic analysis.

Although valuable studies are conducted in terms of long-term optimal planning of PV-battery system sizing, the robustness to withstand unpredictable conditions and risks of not meeting their proposed schemes are not evaluated adequately in most of them. Since the design of a PV-battery system is based on historical data, it is necessary to evaluate the capability and robustness of the designed PV-battery system for the expected load and solar irradiance profiles in the future.

Once the optimal PV-battery sizing methodologies have been established, evaluating the performance of the model becomes crucial. The robustness and risk of the system are critical aspects to consider when evaluating the performance of the optimized PV-battery system. Assessing the system behavior under various scenarios and uncertainties helps determine its ability to withstand unpredictable conditions and ensure reliable operation. Monte Carlo simulation, forecasting, historical data analysis, and stochastic analysis are among the most popular tools for assessing PV-battery systems. Stochastic approaches, such as stochastic optimization, often rely on assumptions about probability distributions or use simplified models to approximate system behavior. In (Cheng et al., 2018), the authors use clustering techniques to group wind energy generation and load data into different sets. This clustering approach helps identify distinct patterns and characteristics within the data. Monte Carlo simulation is used to generate various scenarios for planning purposes. In (Fu, 2022) a statistical machine learning technique is utilized to generate multi-scenarios in a distribution network. Besides, forecasting techniques can be used to generate various demand scenarios (Gonzalez-Briones et al., 2019). For example, a new method using the clustering technique and the autoregressive integrated moving average is proposed in (Nepal et al., 2020) to forecast the load demand for planning. Further (Berriel et al., 2017), proposes a modified long-short-term memory to forecast the energy consumption at a residential site. In addition (Morteza et al., 2023), explores the use of deep neural networks for medium and long-term energy demand prediction.

While several studies have been conducted on the long-term optimal sizing of PV-battery systems, certain gaps still remain. Many existing studies focus on deterministic approaches, which do not consider uncertainties in PV generation, load demand, and other parameters. In addition, some studies utilize stochastic approaches, but they often rely on simplified models, which may not accurately capture the complex behavior of PV-battery systems. Similarly, a robust optimization could be over-conservative since in most cases it deals with the worst-case scenarios (Aghamohamadi et al., 2021). Further, several studies are based on synthetic data and they do not explicitly address the trade-off between peak demand and energy consumption reduction.

An important problem in power system planning is to reduce peak demand and flatten demand profiles (Mahmud et al., 2018). This study aims to introduce a novel methodology for installing PV-battery systems that explicitly considers peak demand reduction as a key factor in determining the optimal solution to maximize the benefits over the life cycle of the project. The methodology is suitable for those residential, commercial, and industrial customers who pay for peak demand charges for electricity. Since the problem formulation has both continuous and discrete variables along with a search of thresholds with 95% probability of not exceeding the peak load, it is difficult and complex to use a conventional optimization approach to solve this problem. To address these issues, we have proposed a search approach, which is simple and easy to implement with the capability to integrate various aspects of the proposed problem. It also has low computation burden. A case study of a small municipal utility in the United States is considered in this paper for illustration of the methodology. Real system data of 3 years is used for cost and benefit computations over the project lifetime.

The main contributions of this paper can be summarized as follows:

1) The study recognizes the importance of reducing peak demand in PV-battery systems and incorporates it as a key objective in the optimization process. By considering the technical and economic requirements, the study aims to find the optimal size of the PV-battery system that can effectively reduce peak demand.
2) The paper introduces a new statistical methodology specifically designed to address the optimization of PV-battery sizing. This methodology offers a systematic approach to assess and determine the optimal size of the PV-battery system while considering the peak demand reduction effectively. This is a novel contribution as it provides alternative approaches to be utilized in decision-making.
3) Build a risk-based robust model to determine the optimal PV-battery system by incorporating advanced techniques including time series clustering and Monte Carlo simulation based on a Bayesian model. These techniques are used to generate a large number of realistic demand and solar irradiance data scenarios, allowing for a comprehensive evaluation of the system performance under different conditions.

2 Methodology

This section outlines the techniques employed to achieve the optimal size of a PV-battery system.

2.1 PV-battery system component model

The system under this study consists of PV panels, battery storage, and inverters. PV panels directly convert solar irradiance into electrical DC power. If the size of the PV system is X kW, the overall output power of the PV system can be obtained as follows (Yan et al., 2019):

$$PV(h) = \frac{X}{G} \times I(h) \tag{1}$$

where, $PV(h)$ indicates DC output power of the PV system in kW at hour h, G is the solar constant equal to 1000 W/m^2, and $I(h)$ represents solar irradiance in W/m^2. DC to AC inverter model can be expressed as follows (Yan et al., 2019):

$$P_{inv}(h) = PV(h).\eta_{inv}.K \tag{2}$$

where, $P_{inv}(h)$ indicates the output power of the inverter, K is the oversize coefficient, and η_{inv} presents the efficiency of the inverter.

2.2 System costs

2.2.1 Investment costs

The investment costs refer to the initial capital cost required to install the PV-battery system, including PV modules cost (Ndwali et al., 2020):

$$C_{pv}^{ini} = X.C_{pv} \tag{3}$$

where, C_{pv}^{ini} is the total installation cost for the PV modules ($) and C_{pv} is the module cost (/W).

Inverter cost (Ndwali et al., 2020):

$$C_{inv}^{ini} = X.\eta_{inv}.K.C_{inv} \tag{4}$$

where, C_{inv}^{ini} is total installation cost for the inverters ($) and C_{inv} is the capital cost of the inverters ($/W).

Labor costs:

$$C_{labor}^{ini} = X.C_{labor} \tag{5}$$

where, C_{labor}^{ini} is the total initial human and labor cost ($) and C_{labor} is the cost of labor ($/W). The total equipment costs including wiring, racking, and switchgear for installing a photovoltaic system are as follows:

$$C_{eq}^{ini} = X.C_{eq} \tag{6}$$

where, C_{eq}^{ini} is the total initial equipment cost ($) and C_{eq} is the capital cost of equipment ($/W).

Additionally, PV system installation has overhead costs as follows:

$$C_{over}^{ini} = X.C_{over} \tag{7}$$

where, C_{over}^{ini} is the total initial overhead cost ($) and C_{over} is cost of overhead ($/W). Batteries are installed initially and they need to be replaced after a certain amount of time because they typically last less than the project lifetime. It should be noted that according to rapidly growing battery technologies, the cost of the replaced battery is expected to be less than the current value (Berckmans et al., 2017).

Accordingly, if the cost of the initial battery is C^1_{bat}, cost of the secondary battery would be C^2_{bat}. With M as the lifetime of the initial batteries, the present worth of battery investment cost is as follows (Disney et al., 2013):

$$C^{ini}_{bat} = C^2_{bat}\left[\frac{1}{(1+i)^M}\right] + C^1_{bat} \tag{8}$$

where i is the discount rate used to compute the present worth of replacement batteries. C^1_{bat} (similarly C^2_{bat}) can be expressed as follows:

$$C^1_{bat} = Y.C_{bat} \tag{9}$$

where, C_{bat} is capital cost of battery ($/kWh) and Y is size of the battery in kWh.

With C^{ini}_{trans} as the cost of the transformer needed to connect the system to the grid, the total installation cost of the PV-battery system C^{ini}_{total} can be expressed as follows:

$$C^{ini}_{total}=C^{ini}_{pv}+C^{ini}_{inv}+C^{ini}_{labor}+C^{ini}_{eq}+C^{ini}_{over}+C^{ini}_{trans}+C^{ini}_{bat} \tag{10}$$

2.2.2 Operation, maintenance, and insurance costs

The total annual operation and maintenance costs of a PV-battery system are an annuity and they need to be converted to the present worth as follows (Disney et al., 2013):

$$C^{present}_{O\&M} = X.C^{year}_{O\&M}\left[\frac{1-(1+i)^{-N}}{i}\right] \tag{11}$$

where, $C^{year}_{O\&M}$ is the yearly operation and maintenance costs, $C^{present}_{O\&M}$ present worth of the operation and maintenance costs over the project lifetime, and N is the project lifetime. It should be noted that the yearly insurance cost is included in the operation and maintenance costs.

2.2.3 Peak demand charge

The peak demand charge is calculated based on the highest level of power demand typically over a month. Here the peak demand charge is calculated before and after PV-battery installation. The present worth of peak demand charges for year n before PV-battery installation can be expressed as follows (Risbeck and Rawlings, 2020):

$$PDCH^{present}_{origianl}=\left(\sum P^{peak}_m.C_{peak}\right).\left[\frac{1}{(1+i)^n}\right] \tag{12}$$

Where, $PDCH^{present}_{origianl}$ represents the present worth of peak demand charge cost without PV-battery, P^{peak}_m indicates the peak demand in each month (kW), And C_{peak} states the peak demand rate ($/W). However, when the PV-battery system is installed, the present worth of the yearly peak demand charge for year n can be expressed as follows (Risbeck and Rawlings, 2020):

$$PDCH^{present}_{pv-Bat}=\sum \max\left\{P^{original}_d(h)-P^{PV-Bat}_d(h)\right\}.C_{peak}.\left[\frac{1}{(1+i)^n}\right] \tag{13}$$

Where $PDCH^{present}_{pv-Bat}$ is the present value of peak demand charge with PV-battery, $P^{original}_d(h)$ is the original demand, and $P^{PV-Bat}_d(h)$ is demand reduction by PV-battery system.

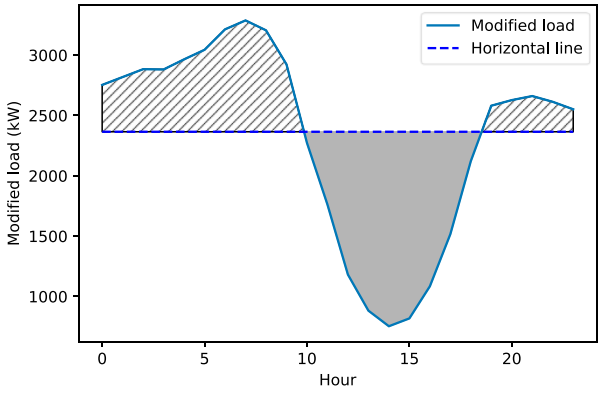

FIGURE 1
Modified load curve and equalization of areas for the needed battery.

2.2.4 Energy cost

The present worth of energy cost before PV-battery installation $COE^{present}_{original}$ and after them $COE^{present}_{PV-Bat}$ for year n can be expressed as Eqs. 14, 15, respectively (Ndwali et al., 2020).

$$COE^{present}_{original} = \left(\sum P^{original}_d(h).C_{grid}\right)\left[\frac{1}{(1+i)^n}\right] \tag{14}$$

$$COE^{present}_{PV-Bat} = \left(\sum\left(P^{original}_d(h)-P^{PV-Bat}_d(h)\right).C_{grid}\right).\left[\frac{1}{(1+i)^n}\right] \tag{15}$$

Where, C_{grid} is the energy cost ($/kWh). It is assumed that the electrical grid $P_{grid}(h)$ is used to meet the energy required beyond that provided by the PV-battery system. Therefore,

$$0 \le P_{grid}(h) \le +\infty \tag{16}$$

2.2.5 Benefit

The total benefit over the project lifetime can be expressed as the difference between the total cost of the system with and without the installation of the PV-battery system, which can be expressed as follows:

$$\begin{aligned}\text{Benefit} = &\left\{PDCH^{present}_{original}+COE^{present}_{original}\right\}\\ &-\left\{C^{ini}_{total}+C^{present}_{O\&M}+PDCH^{present}_{PV-Bat}+COE^{present}_{PV-Bat}\right\}\end{aligned} \tag{17}$$

2.3 Battery operation and updated peaks

In this section, a new simple but efficient algorithm is proposed to determine daily battery operation. For an X kW PV size, Eq. 1 gives the output power of the PV. Then, an updated daily load profile, named modified load is generated by subtracting the original load profiles from the PV generation for all days. The needed battery size for each day to flatten the load curve is determined by drawing a horizontal line such that the upper area between the modified load and the horizontal line is equal to the roundtrip efficiency multiplied by the lower area between the horizontal line and the modified load below this line as expressed by:

$$A_{upper} = A_{lower} \times \eta_R \tag{18}$$

where A_{upper} and A_{lower} represent the upper and lower areas between the modified load and the horizontal line, respectively, and η_R is the battery roundtrip efficiency. For example, in Figure 1, the modified load curve for a random day is shown, and a horizontal line has been placed to cut the curve in such a way that the dashed area above the line is equal to the roundtrip efficiency multiplied by the gray area below the line. Positioning the horizontal line in this way ensures that the battery can be charged when the modified load is below the horizontal line and it is discharged when the modified load is above the horizontal line while limiting the peak load for the day at the value corresponding to the horizontal line. These calculations can be modified to include battery efficiencies during charging and discharging. The calculated lower area, which corresponds to energy going to the battery from the grid, is multiplied by battery charging efficiency and divided by the battery utilization factor to give the needed battery sizes for the specific day as follows:

$$B_{needed} = \frac{A_{lower} \times \eta_B}{U_B} \tag{19}$$

Where B_{needed} represents the daily needed battery capacity to flatten the load curve, η_B represents the battery charging efficiency, and U_B represents the battery utilization factor. Utilization factor is defined as the range from the minimum recommended charge to the maximum recommended charge levels for the battery (typically 20%–90%, which gives a utilization factor of 0.7).

Since each day will need a different battery size to flatten the load curve, the largest needed battery size would be able to flatten the load curve for all the days. However, choosing the largest battery size is not prudent because the cost will be prohibitive. Hence, determining an optimal size for flattening the load curve on most of days while having the risk of not being able to flatten the load curve on a few days is important. For these days, a new horizontal line is drawn such that the upper area between the modified load and the new horizontal line corresponds to the battery capacity while considering the battery efficiency and utilization factor. In other words, this is the maximum peak load reduction that can be obtained by the selected battery size. It should be noted that considering roundtrip efficiency in the battery sizing algorithm simulates battery loss. That means although battery installation is expected to reduce peak demands, battery operational losses increase the energy purchase from the grid.

2.4 Statistical modeling

With prior knowledge of daily energy and peak load, a range of battery sizes from Y_1 to Y_n can be defined for a given X PV size. Further, the updated daily peak loads are calculated for battery sizes Y_1 to Y_n. Subsequently, for each battery size, a histogram can be drawn for the daily peak loads. Based on the scaled histogram, an appropriate probability distribution function (PDF) is fitted for each histogram. To accomplish this, Gamma and Lognormal distributions are considered. The general PDF of the Gamma distribution is as follows (Schellenberg et al., 2005):

$$f(x) = \frac{\left(\frac{x-\mu}{\beta}\right)^{\alpha-1} \exp\left(-\frac{x-\mu}{\beta}\right)}{\beta\,\Gamma(\alpha)} \tag{20}$$

$$\text{where, } x \geq \alpha;\ \beta, \alpha > 0$$

and μ, α, and β are location, shape, and scale parameters, respectively. The $\Gamma(\alpha)$ is the Gamma function as follows (Schellenberg et al., 2005):

$$\Gamma(\alpha) = \int_0^\infty t^{\alpha-1} \exp(-t) dt \tag{21}$$

And PDF of the Lognormal is as follows (Chen et al., 2019):

$$f(x) = \frac{1}{x\sigma\sqrt{2\pi}} \exp\left(-\frac{1}{2}\left(\frac{\ln(x)-\mu}{\sigma}\right)^2\right) \tag{22}$$

where μ is the mean, and σ indicates the standard deviation. Further, to evaluate the goodness-of-fit of the fitted PDFs, the Kolmogorov-Smirnov (KS) statistic test is used that compares the empirical cumulative distribution function (CDF) of daily peak data with the CDF of the fitted PDF. Lower KS statistic values indicate better fits, while higher p-values suggest better fits (Ghatak et al., 2022). After finding the most suitable PDFs for the daily peak histograms, the next step involves determining peak demand thresholds with 0.95 probability for all fitted PDFs. For example, for a given X and Y, the peak demand threshold T associated with the 95% probability for a fitted PDF can be calculated as follows:

$$F^{-1}(P = 0.95) = T \tag{23}$$

where F^{-1} is the inverse of the CDF of a fitted PDF. This threshold indicates the ability of the designed PV-battery system to meet peak demand from zero to T with a 95% probability. This procedure is used for all the fitted PDFs and the peak demand thresholds associated with the 95% probability for each battery size are calculated.

2.5 Optimal PV-battery sizing

In the proposed heuristic method, the unique demand thresholds associated with the 95% probability for each battery size for the given PV size are utilized. Determination of the optimal battery size for a given X PV size involves identifying a point where the 95% threshold exhibits a significant change compared to the other thresholds associated with different battery sizes. This approach is based on the fact that increasing battery size leads to reduction in the 95% threshold, but after a certain size the reduction becomes smaller. Hence, to determine the optimal battery size, an elbow point in the 95% peak load threshold *versus* battery size curve is sought. The elbow point represents a battery size where the reduction in the 95% threshold is significantly greater than neighboring points. This indicates a significant improvement in the ability of the system to meet peak demand. Besides, this enhances the system performance in meeting peak demand while maintaining a desired probability. By repeating this methodology for a range of PV sizes from X_1 to X_n, the optimal battery size for each PV size can be determined.

The proposed methodology determines multiple combinations of optimal PV-battery sizes. The optimal PV-battery system size is chosen based on financial benefit analysis. Besides, it is crucial to test the system under multiple scenarios to ensure its performance and effectiveness under various conditions. By subjecting the system to different scenarios, such as varying solar irradiance and demand its robustness and risk can be evaluated. For this purpose, time series clustering, and the Monte Carlo simulation technique is developed in the following sections.

2.6 Monte Carlo simulation

Monte Carlo simulation is a computational technique used to model and generate a large number of random scenarios. It relies on random sampling and repeated experiments to estimate and understand the range of possible outcomes for a given problem (Raychaudhuri, 2008). By clustering demand and solar irradiance data, more realistic scenarios can be created. Additionally, clustering allows Monte Carlo simulations to take into account the interdependencies between demand and irradiance, leading to more meaningful and effective scenarios.

2.6.1 Time series clustering

Time series clustering is a technique that groups similar time series data into distinct clusters based on their patterns, trends, or behaviors over time. Electricity demand and solar irradiance are time series data that include time intervals indicating the timesteps and corresponding demand and solar irradiance values. Time series clustering is a complex technique in data analysis and includes data preprocessing, similarity measures, cluster prototypes, clustering algorithms, and evaluation metrics (Ali et al., 2019). The preprocessing may include working with missing data or outliers, and normalization. This study uses Min-Max normalization to normalize the time series data (Petegrosso et al., 2020). A similarity measure quantifies the similarity between time series datasets. Dynamic time warping (DTW) is utilized in this study as a similarity measure and its efficiency is proven in several time series clustering (Aghabozorgi et al., 2015). A prototype is a time series that represents the characteristics of a cluster. This study utilized the medoid prototype that is proper for the DTW similarity measure (Ma and Angryk, 2017). Further, two types of most practical time series clustering methods including K-medoid and agglomerative hierarchical clustering algorithms are used. The K-medoid clustering method is a partitioning clustering algorithm suitable for building energy analysis. K-medoid clustering can handle non-Euclidean distance measures, resistance to outliers, and offers a superior level of computational efficiency over other partitioning-based clustering methods (Cui et al., 2023). The K-medoid algorithm utilizes medoids as prototypes of clusters. It selects medoids by minimizing the dissimilarity or distance between data points within each cluster. However, K-medoid requires that the number of clusters must be specified in advance (Gupta et al., 2021). Agglomerative hierarchical clustering is a specific type of hierarchical clustering, which offers a distinct advantage in building energy analysis. This method eliminates the need to predetermine the number of clusters. This approach generates a tree-like structure known as a dendrogram,

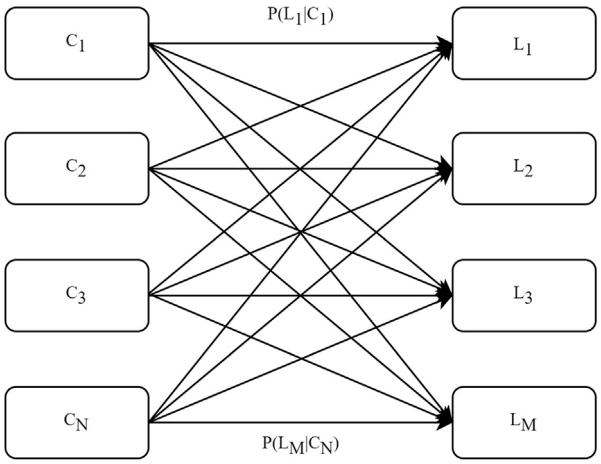

FIGURE 2
Process of determining the conditional probabilities.

which serves as a visual representation and helps in determining the optimal number of clusters (Li et al., 2018). Time series agglomerative hierarchical clustering organizes time series data into a hierarchy of clusters using a cumulative approach. It merges clusters based on similarity measures (Ali et al., 2019). Finally, the quality of time series clustering algorithms should be evaluated to figure out if the clustering algorithms are able to capture patterns and trends in the time series datasets. In this study, the Silhouette coefficient and gap statistic are used for the evaluation of K-medoid, and dendrogram plot for hierarchical clustering (Aghabozorgi et al., 2015). It should be noted that a combination of different time series clustering algorithms provides robust and reliable results and provides deeper insights into the underlying patterns.

2.6.2 Bayesian model

By considering the clustering results of the previous section, conditional probabilities are calculated to assess the relationship between demand and solar irradiance patterns for a computationally efficient implementation of Monte Carlo simulation. These conditional probabilities quantify the likelihood of a specific demand pattern occurring given a certain solar irradiance pattern. Figure 2 illustrates the process of determining these conditional probabilities for a month. $C = \{C_1, C_2, \ldots, C_N\}$ indicates the set of solar irradiance clusters and $L = \{L_1, L_2, \ldots, L_M\}$ is the set of demand clusters. The simulation starts by randomly selecting the solar irradiance cluster using the probabilities of each cluster and uniform distribution. In the next step, a load cluster is randomly selected based on conditional probabilities of load clusters conditioned on the selected irradiance cluster using a uniform distribution. Since the selected irradiance and load clusters may have multiple days, one irradiance profile and one load profile from these clusters are selected randomly with equal probability for each profile with the respective clusters. The selected irradiance profile and load profile represent a day in the selected month. This process is repeated for each day of all the months to generate profiles for solar irradiance and demand for a large number of instances to generate a wide range of scenarios. Besides, the organizational flowchart of the simulation procedure in this study is shown in Figure 3.

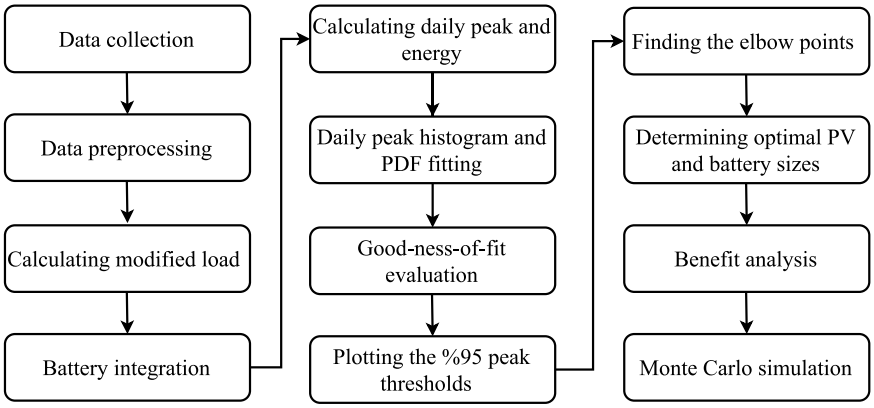

FIGURE 3
Organizational flowchart of the simulation procedure in this study.

TABLE 1 Quantity values used in this study.

PV module ($/W)	Inverter ($/W)	Equipment ($/W)
0.35	0.04	0.18
Overhead ($/W)	O&M ($/kW)	Transformer ($)
0.1	15	150,000
Energy cost ($/kWh)	Power cost ($/kW)	Tax credit (%)
0.025	22	30
Initial battery ($/kWh)	Replacement battery ($/kWh)	Project lifetime
150	100	20 years
Labor ($/W)	Discount rate	Battery roundtrip efficiency
0.1	0.08	0.9025
Inverter coefficient	Battery efficiency	Battery utilization
1.2	0.95	0.7
Inverter efficiency		
0.9		

3 Results and discussion

3.1 Data collection and assumption

In this study, the hourly demand and actual solar irradiance data of Greensburg, Kansas, United States of America, from 1 January 2019, to 31 December 2021, are collected. The values of different parameters used in this study are provided in Table 1. Further, the study is conducted with the assumption that the battery operates on a daily cycle, which means that the battery is charged and discharged fully within the same day. A tax credit of 30% for the initial cost of PV and batteries including the transformer, racking, switchgear, and wiring is considered. Tax credit is not considered for the replacement batteries that will be acquired 10 years later.

3.2 Statistical modeling

3.2.1 Proposed methodology

The load demand and PV generation profile of the peak demand day of January 2019 are shown in Figure 4. The peak demand occurs early in the day when there is no solar irradiance. Therefore, PV installation does not help in peak demand reduction, but batteries can be used as a complement to PV systems. For example, on this day, a battery can be discharged at the beginning of the day to reduce the peak and be charged during mid-day for possible use late in the day. Modified load profiles are calculated for the entire data of 3 years for PV sizes ranging from 200 kW to 10000 kW in steps of 100 kW. Subsequently, for each PV size, corresponding battery sizes are selected from 1000 kWh to 10000 kWh in steps of 100 kWh. Next, updated daily peak demand values for each combination of battery and PV sizes are calculated for the 3-year period. Then, the scaled histograms of peak demands are created, considering the frequencies of occurrence of different peak demands over the 3-year period. After fitting the PDFs (lognormal and Gamma) to the generated histograms, the goodness-of-fit is evaluated using the KS statistic test. KS statistic test results show the *p*-values for the Gamma PDFs are significantly greater than the typical significance level of 0.05, indicating a good fit for the data. However, for the Lognormal PDFs, some *p*-values are much less than 0.05, suggesting poor fits. For example, for PV size of 2000 kW and battery size of 2000 kWh and 3000 kWh, the *p*-values are 0.0053 and 0.027, respectively. Furthermore, both PDFs exhibit relatively small KS statistic test scores. Consequently, the KS statistic test indicates that the Gamma distribution fits the observed data better than the Lognormal PDF. These fitted Gamma PDFs for various combinations of PV and battery size are used in the proposed methodology to determine optimal PV and battery sizes.

Based on the calculated fitted PDFs, the 95% peak thresholds are determined for all fitted Gamma PDFs. For example, Figure 5 shows the 95% peak threshold for a battery size of 4000 kWh and a PV size of 2000 kW for the corresponding fitted Gamma PDF. The peak demand threshold with a 95% probability for the given case is

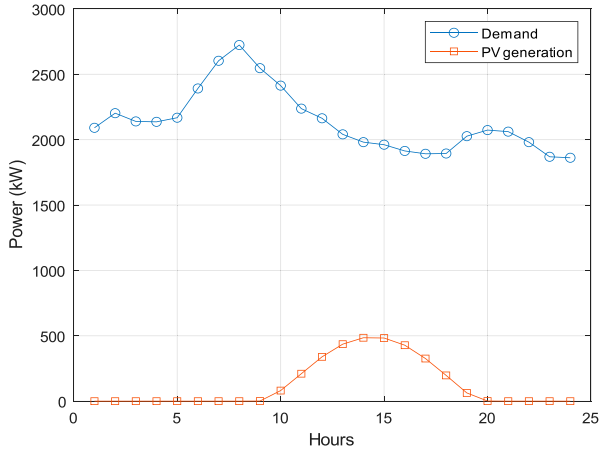

FIGURE 4
Original load and PV generation on the peak day of January 2019.

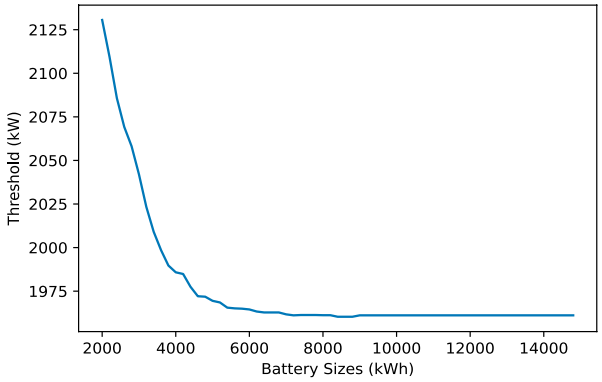

FIGURE 6
Thresholds with the 95% probability for the PV size of 2000 kW vs. various battery sizes.

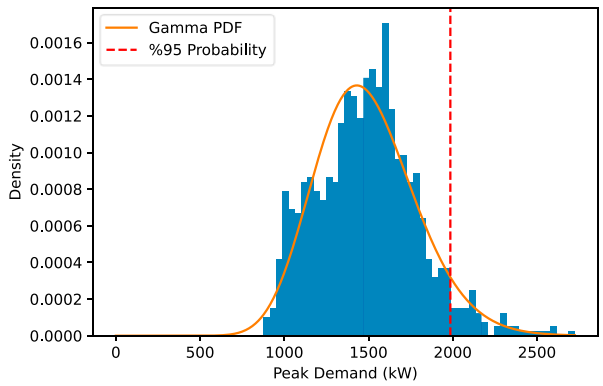

FIGURE 5
The 95% peak threshold for a fitted Gamma PDF with a battery size of 4000 kWh and a PV size of 2000 kW.

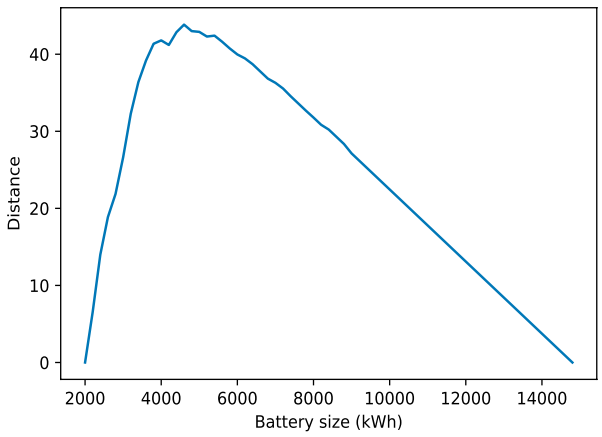

FIGURE 7
Elbow curve associated with thresholds with the 95% probability for the PV size of 2000 kW.

1985 kW. This means that with 95% probability, the PV-battery system is expected to meet peak demand ranging from 0 kW to 1985 kW. Figure 6 displays the peak load thresholds with a 95% probability for the PV size of 2000 kW and various battery sizes. It can be observed that the thresholds for meeting peak demand with a 95% probability decrease as the battery size increases. This trend is particularly significant up to a battery size of 4400–4800 kWh, indicating that increasing the battery size within this range leads to a substantial reduction in the thresholds. But further increasing the battery size does not provide significant additional benefits in terms of improving the system ability to meet peak demand with a 95% probability. Therefore, to determine the optimal battery size for a PV size of 2000 kW, an elbow point in the 95% peak threshold *versus* the battery size curve is sought. The elbow point represents the size of the battery at which the 95% threshold is reduced significantly more than its neighboring points. Figure 7 illustrates the elbow curve (Antunes et al., 2018) derived from the data presented in Figure 6. By examining the elbow curve, the point with the highest value represents the optimal battery size for the given PV size of 2000 kW. Based on the elbow curve depicted in Figure 7, the maximum value occurs at a battery size of 4600 kWh for the given PV size of 2000 kW with a peak load threshold of 1971 kW. If this analysis is repeated for different PV sizes, the optimal battery size corresponding to each PV size can be obtained. Table 2 provides selected optimal combinations of PV and battery size with consideration for the 95% probability. For example, a PV size of 3600 kW with a battery size of 4400 kWh can meet peak demand ranging from 0 kW to 1931 kW with 95% probability, indicating the best combination in terms of peak reduction. However, the PV size 400 kW can meet the 2167 kW peak with specified probability with battery size 6200 kWh, indicating a poor combination. However, to determine the best PV and battery size, a benefit analysis must be conducted over all the optimal combinations of PV and battery sizes. The final size of the PV-battery system is the combination of PV and battery sizes that yield the highest overall benefit for the system over 20 years.

TABLE 2 Selected optimal combinations of PV and battery sizes.

PV size (kW)	400	800	1200	1600	2000	2400	2800	3200	3600
Battery size (kWh)	6200	5000	3200	4400	4600	5400	4600	4200	4400
Threshold (kW)	2167	2090	2078	1995	1971	1952	1958	1955	1931

TABLE 3 Financial benefits for optimal combinations of PV and battery sizes.

PV size (kW)	400	600	800	1000	1200	1400
Battery size (kWh)	6200	5500	5000	4800	3200	4200
Benefit ($)	579,970	538,390	563,450	777,510	820,370	783,450
PV size (kW)	1600	1800	2000	2200	2400	2600
Battery size (kWh)	4400	4600	4600	5000	5400	5000
Benefit ($)	719,810	535,090	719,560	775,570	616,460	647,040
PV size (kW)	2800	3000	3200	3400	3600	3800
Battery size (kWh)	4600	4400	4200	4800	4400	4400
Benefit ($)	657,760	559,640	600,780	476,670	506,680	426,250

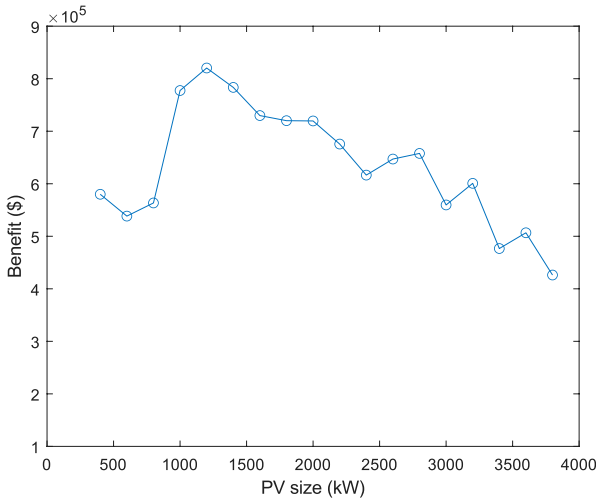

FIGURE 8
Benefit of the various combinations of optimal PV and battery size.

3.3 Benefit analysis

The benefit analysis is conducted to evaluate the financial profitability of PV and battery size combinations over 20 years. Data from 3 years, including both demand and solar irradiance, are grouped on a monthly basis. Energy and peak demand costs are calculated individually for each month over the 3-year period and subsequently averaged to obtain the monthly average costs. Table 3 presents the financial benefits associated with each combination of optimal PV and battery sizes. Figure 8 illustrates the financial benefit of each optimal PV and battery size combinations. It should be noted due to the limitation of the plotting, the optimal battery sizes associated with each PV size are not explicitly shown in the figure. The best PV and battery size combination among all the combinations is a PV size of 1200 kW, battery size of 3200 kWh, peak threshold of 2078 kW, and the financial benefit associated with this combination is $820,373 over 20 years. Table 4 provides a detailed financial analysis of the optimal PV-battery system considering the energy and peak demand costs before and after PV-battery installation over a 20-year period for this case. The original energy and peak demand costs (before PV and battery installation) are $3,788,907 and $6,913,926.51, respectively over the 20-year period. Peak demand charges are approximately twice the energy cost, indicating the importance of peak demand in reducing overall costs. The PV installation results in a reduction of 12.9% in energy costs and 5.58% in peak demand costs. These reductions indicate that PV installation is more successful at reducing energy costs than peak demand costs. However, the total cost of PV installation, in this case, amounts to $1,093,847. The calculated net benefit, which is -$190,366, indicates that PV installation does not yield a positive economic outcome. So, although PV reduces energy and peak demand charges, the high total installation cost outweighs the cost savings achieved. Therefore, from an economic perspective, PV installation alone is not profitable. Despite adding additional costs to the system, the installation of a battery results in a notable 25.28% reduction in peak demand costs compared to the original peak demand costs. Furthermore, the difference of $27,647 in energy costs between PV-only and PV-battery system is the cost of losses associated with charging and discharging of the battery. However, incorporating the battery system increases the overall benefit of the PV-battery system, which indicates that the combined effect of battery and PV is more advantageous than relying solely on PV installation. Finally, in order to assess the performance and effectiveness of the PV-battery system based on the proposed method, it is necessary to test the designed PV-battery system under different scenarios and conditions. To generate multiple scenarios with Monte Carlo simulation, the demand and solar irradiance profiles must be clustered.

3.4 Monte Carlo simulation

3.4.1 Time series clustering

The first step in the time series clustering is to prepare the datasets. To achieve this goal, the data is grouped monthly. For instance, the demand and solar irradiance data for all Januarys in the 3 years are combined, resulting in 93 time series datasets in which, each time series contains 24 hourly data points. Then, all datasets are normalized based on Min-Max normalization. Subsequently,

TABLE 4 Economic analysis of the optimal PV-battery system.

	Without PV-battery	With PV	With PV-battery
Energy cost ($)	3,788,907	3,337,719	3,365,366
Peak cost ($)	6,913,926	6,539,467	5,166,301
Equipment cost ($)	0	1,016,013	1,350,792
Benefit ($)	-	−190,366	820,373

K-medoid and agglomerative hierarchical time series clustering algorithms are utilized to group similar profiles in a cluster using the DTW similarity measure. Gap statistics and Silhouette scores are used as evaluation metrics to determine the proper number of clusters of the K-medoid algorithm. To obtain the gap statistic and Silhouette scores, the K-medoid algorithm performs clustering for a range of integer values representing the number of clusters. The clustering results demonstrate that each cluster represents a group of similar demand and solar irradiance profiles based on their patterns allowing for the discovery of distinct monthly variations in electricity demand and solar irradiance. For example, Figure 9 demonstrates the gap statistic and Silhouette coefficient scores for different numbers of clusters for July load demand profiles. Based on Figure 9, the maximum gap statistic score of 0.114 suggests that 3 clusters are meaningful for July load demand profiles. Similarly, the Silhouette coefficient peaks at 0.472 with 3 clusters. These results offer valuable insights into choosing the optimal number of clusters. These distinct clusters represent high electricity demand, moderate demand, and relatively low demand for the month of July. These variations can be attributed to factors like differences between weekdays, weekends, and weather conditions.

The agglomerative hierarchical clustering algorithm starts by treating each individual demand and solar irradiance time series as a separate cluster. It calculates pairwise distances between these clusters using the DTW similarity measure. Clusters are then merged iteratively based on their distances, creating a hierarchy of clusters. This hierarchy for July load demand profiles is visualized in Figure 10 as a dendrogram graph. In the dendrogram graph, the vertical lines indicate clusters at different levels of the hierarchy and a point where vertical lines merge together demonstrates a cluster formation. Besides, the height of the vertical lines represents the dissimilarity or distance between the clusters and longer lines show significant dissimilarity. Intuitively, if a horizontal line cuts through the highest vertical lines in a dendrogram, the intersections can indicate the desired number of clusters. Accordingly, in Figure 10, the red horizontal line intersects three vertical lines that represent the largest dissimilarities compared to other clusters. This suggests that dividing the data into three clusters could be a suitable choice based on the dendrogram structure. Given that both K-medoid and hierarchical clustering suggests a similar number of clusters for the July demand profiles, July load data can be confidently divided into three distinct clusters. By applying the same clustering methods to the remaining demand and solar irradiance data, the time series clustering process is completed for use in the Monte Carlo simulation.

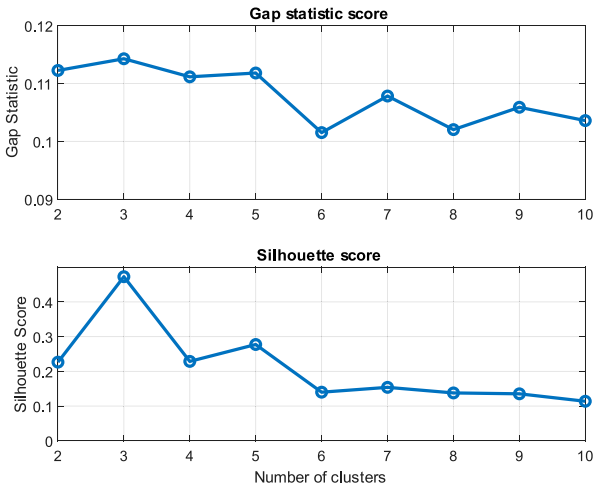

FIGURE 9
Gap statistic and Silhouette score for K-medoids algorithm.

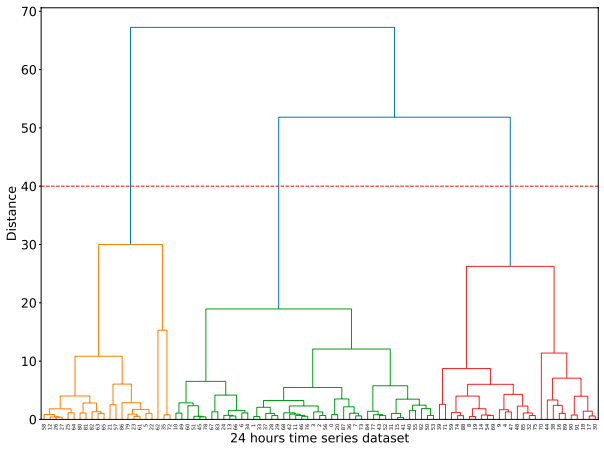

FIGURE 10
Dendrogram associated with the hierarchical clustering.

3.4.2 Bayesian simulation

Based on the mentioned methodology, a Monte Carlo simulation is performed to generate 10,000 scenarios in which each scenario contains yearly load and solar irradiance data. These scenarios are generated based on the conditional probability between demand and solar irradiance profiles. Previously selected best PV and battery sizes of 1200 kW and 3200 kWh, respectively, with a peak load threshold of 2078 kW are used to calculate the benefits for various scenarios. Among the 10,000 scenarios, 20 scenarios are randomly selected to calculate the benefits over a 20-year period to create one sample benefit in the Monte Carlo simulation. The process is repeated 500 times to determine 500 benefit samples without replacement. Figure 11 shows the histogram of these benefit samples. The mean benefit value is determined to be $822,440, indicating the average benefit that can be expected from implementing the proposed method with

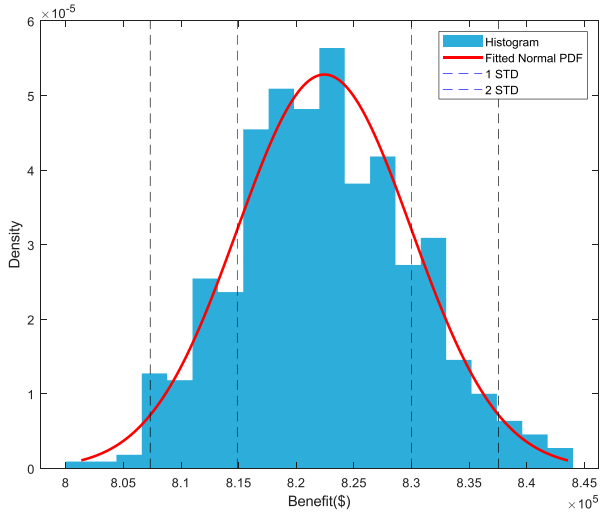

FIGURE 11
Histogram of benefit values based on the Monte Carlo results.

the determined PV and battery sizes over the 20-year period. Furthermore, the standard deviation is $7554 indicating the variability of the benefit around the mean. In this case, the coefficient of variation (CV), which is the ratio of the standard deviation to the mean is 0.0092 which is relatively small compared with the general CV (Chen and Mili, 2013). It suggests that the benefits obtained from the Monte Carlo simulation are relatively consistent and close to the mean value. This level of low variability can be seen as a positive characteristic, indicating a higher level of predictability and reliability in the benefits obtained from the simulation. Besides, a Normal PDF is fitted to the histogram. The KS statistic is calculated to be 0.0235, and the p-value is found to be 0.957. These values indicate a good fit between the Normal PDF and the benefits data. Moreover, a 95% confidence interval for the mean of the benefits is computed, resulting in the range [821,773, 823,100]. That means, it is estimated that the average benefit value is likely to be between $821,773 and $823100 with a 95% confidence. To perform a risk analysis, three predetermined benefits are considered as desired benefits to be achieved over the project lifetime. If the predetermined benefit is less than $821,773, it suggests that with 95% confidence, the estimated mean benefit is likely to be higher than the threshold. This indicates a favorable outcome, as the estimated mean benefit is expected to surpass the desired threshold. On the other hand, if a predetermined benefit is higher than $823,100, it indicates with 95% confidence, the estimated mean benefit may fall below the predetermined threshold, suggesting a potential failure to meet the desired benefit. Finally, if the predetermined benefit falls between the lower and upper bounds of the 95% confidence interval, this means there is an uncertainty about whether the estimated average benefit will be higher or lower than the predetermined threshold. Further, the first and second STDs represent the lower and upper bounds around the mean benefit value (see Figure 11), indicating the potential range within which benefits are likely to occur. Considering the first and second STDs, the benefits will be within the range of $814,880 to $829,990 and $807,330 to $837,550, respectively with approximately 68% and 95% confidence. The first and second standard deviations can provide insight into the range within which benefits are likely to fluctuate, helping decision-makers make thorough assessments.

4 Conclusion

This study addresses the significance of peak demand in solar PV system planning and management. While PV installations reduce energy flow from the grid, their impact on peak demand reduction is limited in some cases. Batteries for energy storage are used to overcome this limitation. An innovative methodology is proposed for determining the optimal sizes of PV and battery. The proposed method considers variable peak load thresholds with a 95% probability for all PV and battery sizes and identifies optimal sizes based on the elbow point. To evaluate various optimal combinations of PV and battery sizes economically, the total benefit for these combinations is calculated to identify the best sizes of the PV and battery for the given system. Finally, a novel Monte Carlo simulation is used to evaluate the effects of uncertainties and risk on the results comprehensively by generating multiple load and solar and irradiance scenarios. Since many small municipal utilities and rural electric cooperatives buy electricity from large suppliers for distribution to their customers, the methodology presented in this paper provides a valuable tool for them in planning solar PV-battery system installations. However, it should be noted that the proposed methodology is not suitable for general sizing of solar PV and batteries, but suitable for only those utilities with a goal to reduce the peak demand. In future research, an investigation can be conducted with a fixed peak load threshold for the PV-battery system. Additionally, various aspects such as demand response, power system topologies and associated reliability indices can be included in the analysis.

Data availability statement

The original contributions presented in the study are included in the article/Supplementary material, further inquiries can be directed to the corresponding author.

Author contributions

RN: Data curation, Formal Analysis, Investigation, Software, Writing–original draft. AP: Conceptualization, Funding acquisition, Investigation, Methodology, Project administration, Supervision, Writing–original draft. BN: Formal Analysis, Investigation, Supervision, Writing–review and editing. HW: Writing–review and editing.

Funding

The author(s) declare financial support was received for the research, authorship, and/or publication of this article. This research was conducted with funding from NSF through award No. 2125548.

Acknowledgments

The authors thank the City of Greensburg, Kansas, and Kansas Power Pool (KPP) for supporting this research by providing load and billing data. Also, thanks to Kansas State University Agricultural Extension for providing the solar irradiation data.

Conflict of interest

The authors declare that the research was conducted in the absence of any commercial or financial relationships that could be construed as a potential conflict of interest.

The author(s) declared that they were an editorial board member of Frontiers, at the time of submission. This had no impact on the peer review process and the final decision.

Publisher's note

References

Aghabozorgi, S., Seyed Shirkhorshidi, A., and Ying Wah, T. (2015). Time-series clustering – a decade review. *Inf. Syst.* 53, 16–38. doi:10.1016/j.is.2015.04.007

Aghamohamadi, M., Mahmoudi, A., and Haque, M. H. (2021). Two-stage robust sizing and operation Co-optimization for residential PV–battery systems considering the uncertainty of PV generation and load. *IEEE Trans. Ind. Inf.* 17, 1005–1017. doi:10.1109/TII.2020.2990682

Ali, M., Alqahtani, A., Jones, M. W., and Xie, X. (2019). Clustering and classification for time series data in visual analytics: a survey. *IEEE Access* 7, 181314–181338. doi:10.1109/ACCESS.2019.2958551

Alramlawi, M., and Li, P. (2020). Design optimization of a residential PV-battery microgrid with a detailed battery lifetime estimation model. *IEEE Trans. Ind. Appl.* 56, 2020–2030. doi:10.1109/TIA.2020.2965894

Antunes, M., Gomes, D., and Aguiar, R. L. (2018). "Knee/elbow estimation based on first derivative threshold," in 2018 IEEE Fourth International Conference on Big Data Computing Service and Applications (BigDataService), Bamberg, Germany, March, 2018, 237–240. doi:10.1109/BigDataService.2018.00042

Bagheri, F., Dagdougui, H., and Gendreau, M. (2022). Stochastic optimization and scenario generation for peak load shaving in Smart District microgrid: sizing and operation. *Energy Build.* 275, 112426. doi:10.1016/j.enbuild.2022.112426

Belfkira, R., Zhang, L., and Barakat, G. (2011). Optimal sizing study of hybrid wind/PV/diesel power generation unit. *Sol. Energy* 85, 100–110. doi:10.1016/j.solener.2010.10.018

Berckmans, G., Messagie, M., Smekens, J., Omar, N., Vanhaverbeke, L., and Van Mierlo, J. (2017). Cost projection of state of the art lithium-ion batteries for electric vehicles up to 2030. *Energies (Basel)* 10, 1314. doi:10.3390/en10091314

Berriel, R. F., Lopes, A. T., Rodrigues, A., Varejao, F. M., and Oliveira-Santos, T. (2017). "Monthly energy consumption forecast: a deep learning approach," in 2017 International Joint Conference on Neural Networks (IJCNN), Anchorage, AK, USA, May, 2017, 4283–4290. doi:10.1109/IJCNN.2017.7966398

Carli, R., Cavone, G., Pippia, T., De Schutter, B., and Dotoli, M. (2022). Robust optimal control for demand side management of multi-carrier microgrids. *IEEE Trans. Automation Sci. Eng.* 19, 1338–1351. doi:10.1109/TASE.2022.3148856

Celik, B., Suryanarayanan, S., Roche, R., and Hansen, T. M. (2020). Quantifying the impact of solar photovoltaic and energy storage assets on the performance of a residential energy aggregator. *IEEE Trans. Sustain Energy* 11, 405–414. doi:10.1109/TSTE.2019.2892603

Chen, J., Wang, Q., Wang, J., and Li, N. (2019). Change detection of water index in danjiangkou reservoir using mixed log-normal distribution based active contour model. *IEEE Access* 7, 95430–95442. doi:10.1109/ACCESS.2019.2929178

Chen, Q., and Mili, L. (2013). Composite power system vulnerability evaluation to cascading failures using importance sampling and antithetic variates. *IEEE Trans. Power Syst.* 28, 2321–2330. doi:10.1109/TPWRS.2013.2238258

Cheng, L., Zhao, E., Liu, M., Wang, Z., and Zhang, Y. (2018). "A planning scenario clustering method based on monte-carlo simulation," in 2018 International Conference on Power System Technology (POWERCON), Guangzhou, China, November, 2018, 212–217. doi:10.1109/POWERCON.2018.8601961

Cui, Y., Zhu, Z., Zhao, X., and Li, Z. (2023). Energy schedule setting based on clustering algorithm and pattern recognition for non-residential buildings electricity energy consumption. *Sustainability* 15, 8750. doi:10.3390/su15118750

Disney, S. M., Warburton, R. D. H., and Zhong, Q. C. (2013). Net present value analysis of the economic production quantity. *IMA J. Manag. Math.* 24, 423–435. doi:10.1093/imaman/dpt002

Emrani, A., Berrada, A., and Bakhouya, M. (2021). Optimal sizing and deployment of gravity energy storage system in hybrid pv-wind power plant. *SSRN Electron. J.* doi:10.2139/ssrn.3878686

Ensslen, A., Ringler, P., Dörr, L., Jochem, P., Zimmermann, F., and Fichtner, W. (2018). Incentivizing smart charging: modeling charging tariffs for electric vehicles in German and French electricity markets. *Energy Res. Soc. Sci.* 42, 112–126. doi:10.1016/j.erss.2018.02.013

Fu, X. (2022). Statistical machine learning model for capacitor planning considering uncertainties in photovoltaic power. *Prot. Control Mod. Power Syst.* 7, 5. doi:10.1186/s41601-022-00228-z

Ghatak, G., Mohanty, H., and Rahman, A. U. (2022). Kolmogorov–Smirnov test-based actively-adaptive thompson sampling for non-stationary bandits. *IEEE Trans. Artif. Intell.* 3, 11–19. doi:10.1109/TAI.2021.3121653

Gonzalez-Briones, A., Hernandez, G., Corchado, J. M., Omatu, S., and Mohamad, M. S. (2019). "Machine learning models for electricity consumption forecasting: a review," in 2019 2nd International Conference on Computer Applications and Information Security (ICCAIS), Riyadh, Saudi Arabia, May, 2019, 1–6. doi:10.1109/CAIS.2019.8769508

Gupta, D., Bhatia, M. P. S., and Kumar, A. (2021). Resolving data overload and latency issues in multivariate time-series IoMT data for mental health monitoring. *IEEE Sens. J.* 21, 25421–25428. doi:10.1109/JSEN.2021.3095853

Kelepouris, N. S., Nousdilis, A. I., Bouhouras, A. S., and Christoforidis, G. C. (2022). Cost-effective hybrid PV-battery systems in buildings under demand side management application. *IEEE Trans. Ind. Appl.* 58, 6519–6528. doi:10.1109/TIA.2022.3186295

Khezri, R., Mahmoudi, A., and Aki, H. (2020). "Multi-objective optimization of solar PV and battery storage system for A grid-connected household," in 2020 IEEE International Conference on Power Electronics, Drives and Energy Systems (PEDES), Jaipur, India, December, 2020, 1–6. doi:10.1109/PEDES49360.2020.9379481

Li, K., Ma, Z., Robinson, D., and Ma, J. (2018). Identification of typical building daily electricity usage profiles using Gaussian mixture model-based clustering and hierarchical clustering. *Appl. Energy* 231, 331–342. doi:10.1016/j.apenergy.2018.09.050

Ma, R., and Angryk, R. (2017). "Distance and density clustering for time series data," in 2017 IEEE International Conference on Data Mining Workshops (ICDMW), New Orleans, LA, USA, November, 2017, 25–32. doi:10.1109/ICDMW.2017.11

Mahmud, K., Hossain, M. J., and Town, G. E. (2018). Peak-load reduction by coordinated response of photovoltaics, battery storage, and electric vehicles. *IEEE Access* 6, 29353–29365. doi:10.1109/ACCESS.2018.2837144

Mirzapour, O., and Arpanahi, S. K. (2018). "Photovoltaic parameter estimation using heuristic optimization," in 2017 IEEE 4th International Conference on Knowledge-Based Engineering and Innovation, KBEI 2017, Tehran, Iran, December, 2017, 0792–0797. doi:10.1109/KBEI.2017.8324904

Morteza, A., Yahyaeian, A. A., Mirzaeibonehkhater, M., Sadeghi, S., Mohaimeni, A., and Taheri, S. (2023). Deep learning hyperparameter optimization: application to electricity and heat demand prediction for buildings. *Energy Build.* 289, 113036. doi:10.1016/j.enbuild.2023.113036

Ndwali, K., Njiri, J. G., and Wanjiru, E. M. (2020). Multi-objective optimal sizing of grid connected photovoltaic batteryless system minimizing the total life cycle cost and the grid energy. *Renew. Energy* 148, 1256–1265. doi:10.1016/j.renene.2019.10.065

Nepal, B., Yamaha, M., Yokoe, A., and Yamaji, T. (2020). Electricity load forecasting using clustering and ARIMA model for energy management in buildings. *Jpn. Archit. Rev.* 3, 62–76. doi:10.1002/2475-8876.12135

Nkuriyingoma, O., Özdemir, E., and Sezen, S. (2022). Techno-economic analysis of a PV system with a battery energy storage system for small households: a case study in Rwanda. *Front. Energy Res.* 10. doi:10.3389/fenrg.2022.957564

Okoye, C. O., and Solyalı, O. (2017). Optimal sizing of stand-alone photovoltaic systems in residential buildings. *Energy* 126, 573–584. doi:10.1016/j.energy.2017.03.032

Petegrosso, R., Li, Z., and Kuang, R. (2020). Machine learning and statistical methods for clustering single-cell RNA-sequencing data. *Brief. Bioinform* 21, 1209–1223. doi:10.1093/bib/bbz063

Raychaudhuri, S. (2008). "Introduction to Monte Carlo simulation," in 2008 Winter Simulation Conference, Miami, FL, USA, December, 2008, 91–100. doi:10.1109/WSC.2008.4736059

Risbeck, M. J., and Rawlings, J. B. (2020). Economic model predictive control for time-varying cost and peak demand charge optimization. *IEEE Trans. Autom. Contr* 65, 2957–2968. doi:10.1109/TAC.2019.2939633

Rodríguez-Gallegos, C. D., Yang, D., Gandhi, O., Bieri, M., Reindl, T., and Panda, S. K. (2018). A multi-objective and robust optimization approach for sizing and placement of PV and batteries in off-grid systems fully operated by diesel generators: an Indonesian case study. *Energy* 160, 410–429. doi:10.1016/j.energy.2018.06.185

Schellenberg, A., Rosehart, W., and Aguado, J. (2005). Cumulant-based probabilistic optimal power flow (P-opf) with Gaussian and Gamma distributions. *IEEE Trans. Power Syst.* 20, 773–781. doi:10.1109/TPWRS.2005.846184

Solar Futures Study, (2023). Solar futures study. https://www.energy.gov/eere/solar/solar-futures-study.

Thirunavukkarasu, M., and Sawle, Y. (2021). A comparative study of the optimal sizing and management of off-grid solar/wind/diesel and battery energy systems for remote areas. *Front. Energy Res.* 9. doi:10.3389/fenrg.2021.752043

Verma, D., Midtgard, O.-M., and Satre, T. O. (2011). "Review of photovoltaic status in a European (EU) perspective," in 2011 37th IEEE Photovoltaic Specialists Conference, Seattle, WA, USA, June, 2011, 003292–003297. doi:10.1109/PVSC.2011.6186641

Yan, K., Du, Y., and Ren, Z. (2019). MPPT perturbation optimization of photovoltaic power systems based on solar irradiance data classification. *IEEE Trans. Sustain Energy* 10, 514–521. doi:10.1109/TSTE.2018.2834415

frontiers | Frontiers in Energy Research

TYPE Correction
PUBLISHED 14 August 2024
DOI 10.3389/fenrg.2024.1399443

OPEN ACCESS

EDITED BY
Joao Soares,
Instituto Superior de Engenharia do Porto (ISEP), Portugal

REVIEWED BY
Wenlei Bai,
Baylor University, United States
José Almeida,
Polytechnic Institute of Porto, Portugal

*CORRESPONDENCE
Anil Pahwa,
pahwa@ksu.edu

RECEIVED 11 March 2024
ACCEPTED 08 April 2024
PUBLISHED 14 August 2024

CITATION
Nematirad R, Pahwa A, Natarajan B and Wu H (2024), Corrigendum: Optimal sizing of photovoltaic-battery system for peak demand reduction using statistical models.
Front. Energy Res. 12:1399443.
doi: 10.3389/fenrg.2024.1399443

Corrigendum: Optimal sizing of photovoltaic-battery system for peak demand reduction using statistical models

Reza Nematirad, Anil Pahwa*, Balasubramaniam Natarajan and Hongyu Wu

Electrical and Computer Engineering Department, Kansas State University, Manhattan, KS, United States

KEYWORDS

photovoltaic-battery system, peak demand reduction, time series clustering, statistical analysis, Monte Carlo simulation

A Corrigendum on
Optimal sizing of photovoltaic-battery system for peak demand reduction using statistical models

by Nematirad R, Pahwa A, Natarajan B and Wu H (2023). Front. Energy Res. 11:1297356.
doi: 10.3389/fenrg.2023.1297356

In the published article, there was an error in Table 1 as published. The top row is not header for the columns. It includes quantities whose values appear in the next row. Also, the value in the first column of second row should be 0.35 instead of 0.035. The corrected Table 1 and its caption appear below.

The authors apologize for this error and state that this does not change the scientific conclusions of the article in any way. The original article has been updated.

Publisher's note

All claims expressed in this article are solely those of the authors and do not necessarily represent those of their affiliated organizations, or those of the publisher, the editors and the reviewers. Any product that may be evaluated in this article, or claim that may be made by its manufacturer, is not guaranteed or endorsed by the publisher.

10.3389/fenrg.2024.1399443

TABLE 1 Quantity values used in this study.

PV module ($/W)	Inverter ($/W)	Equipment ($/W)
0.35	0.04	0.18
Overhead ($/W)	O&M ($/kW)	Transformer ($)
0.1	15	150,000
Energy cost ($/kWh)	Power cost ($/kW)	Tax credit (%)
0.025	22	30
Initial battery ($/kWh)	Replacement battery ($/kWh)	Project lifetime
150	100	20 years
Labor ($/W)	Discount rate	Battery roundtrip efficiency
0.1	0.08	0.9025
Inverter coefficient	Battery efficiency	Battery utilization
1.2	0.95	0.7
Inverter efficiency		
0.9		

frontiers | Frontiers in Energy Research

TYPE Original Research
PUBLISHED 08 January 2024
DOI 10.3389/fenrg.2023.1292183

OPEN ACCESS

EDITED BY
ZhaoYang Dong,
Nanyang Technological University,
Singapore

REVIEWED BY
Linfei Yin,
Guangxi University, China
Anna Diva Lotufo,
UNESP campus of Ilha Solteira, Brazil

*CORRESPONDENCE
Mohd. Hasan Ali,
mhali@memphis.edu

RECEIVED 11 September 2023
ACCEPTED 30 November 2023
PUBLISHED 08 January 2024

CITATION
Alam SMM and Ali MH (2024), Residential load forecasting by a PSO-tuned ANFIS2 method considering the COVID-19 influence.
Front. Energy Res. 11:1292183.
doi: 10.3389/fenrg.2023.1292183

Residential load forecasting by a PSO-tuned ANFIS2 method considering the COVID-19 influence

S. M. Mahfuz Alam[1] and Mohd. Hasan Ali[2]*

[1]Department of EEE, Dhaka University of Engineering and Technology, Gazipur, Bangladesh, [2]Department of ECE, The University of Memphis, Memphis, TN, United States

The most important feature of load forecasting is enabling the building management system to control and manage its loads with available resources ahead of time. The electricity usage in residential buildings has increased during the COVID-19 period, as compared to normal times. Therefore, the performance of forecasting methods is impacted, and further tuning of parameters is required to cope with energy consumption changes due to COVID-19. This paper proposes a new adaptive neuro-fuzzy 2 inference system (ANFIS2) for energy usage forecasting in residential buildings for both normal and COVID-19 periods. The particle swarm optimization (PSO) method has been implemented for parameter optimization, and subtractive clustering is used for data training for the proposed ANFIS2 system. Two modifications in terms of input and parameters of ANFIS2 are made to cope with the change in the consumption pattern and reduce the prediction errors during the COVID-19 period. Simulation results obtained by MATLAB software validate the efficacy of the proposed ANFIS2 in residential load forecasting during both normal and COVID-19 periods. Moreover, the performance of the proposed method is better than that of the existing adaptive neuro-fuzzy inference system (ANFIS), long short-term memory (LSTM), and random forest (RF) approaches.

KEYWORDS

Adaptive neuro-fuzzy 2 inference system, COVID-19, load forecasting, residential load, particle swarm optimization

1 Introduction

The amount of energy consumption in residential buildings creates a huge burden on the energy-providing utilities. This problem becomes severe during the peak hours of the day when the utility might have to look for alternative resources of energy. In addition, consumers have to pay a high electricity price during the peak hours. However, load forecasting can help overcome this problem from both the grid side and the consumer's perspective. From the grid perspective, based on the knowledge of energy demands, alternative resources of energy can be allocated ahead of time (Kapoor and Sharma, 2018; Almalaq and Edwards, 2019). Moreover, from the consumer's point of view, the loads can be scheduled based on the price of energy from the grid, available resources in the buildings, and energy storage. In addition, it creates an opportunity for the consumers to sell some of their residential energy to the grid, if possible, during peak hours. Therefore, researchers have been continuously searching for efficient load forecasting methods.

Among the various methods of load forecasting, time series or regression-based predictions are frequently found in the literature. The autoregressive integrated moving average (ARIMA) model has attracted scholars for predictions (Kim et al., 2019; Rana et al., 2022). ARIMA is the improved combination of the auto-regressive (AR) and moving average (MA) methods. However, without a large dataset and in changing load conditions, the performance of the ARIMA model deteriorates. Moreover, regression trees are also proposed as a forecasting method by many authors (Phyo and Jeenanunta, 2021; Sun and Bi, 2021). It is a machine learning tool that sub-divides the total data space into smaller clusters of data and divides the sub-division into small divisions whenever an interaction can be managed. Regression trees proceed with decisions in the form of a tree that starts from the root to the leaf node, where the leaf node gives the output. Random forest (RF) is the most popular homogeneous regression tree method found in the literature (Moon et al., 2018; Wang et al., 2018; Yiling and Shaofeng, 2020) that provides the decision without having any bias among the decision trees. The multiple linear regression method is also recommended by some researchers (Chowdhury et al., 2018; Oprea and Bâra, 2019). In this method, the dependent variable is expressed as a sum of non-dependent variables. Furthermore, Zheng et al. (2019) and Sharma et al. (2020) have investigated predictor systems that utilize state space models, such as the Kalman filter. However, the performance of the Kalman filter deteriorates as the non-linearity of the system increases.

The common problem associated with these above-mentioned methods is the degradation of performance with the increase in nonlinearity in the system. The nonlinear nature of residential load has enforced researchers (Wang and Srinivasan, 2017; Nair et al., 2018) to search for more robust prediction systems that can predict well when the system is highly nonlinear. The fuzzy logic system, which performs on the IF–THEN logic, has been reported in the literature (Alrizq and Doncker, 2018; Alam and Ali, 2020a) to have performed well in nonlinear conditions. Moreover, temperature and historical data are the most considered inputs for the fuzzy systems that are proposed in the literature (Anoop and Kanchana, 2017; Shao et al., 2018), although performance can still be improved further by increasing the input number. However, limited input numbers are considered because as the input number increases, the fuzzy rules also increase, which makes the system slower.

Moreover, Shabbir et al. (2019) and Moradzadeh et al. (2022) have preferred the support vector regression (SVR) method for load prediction. Although it can perform well for nonlinear systems, the performance of the SVR system heavily depends on tuning the parameters properly, and a large amount of data are required for training purposes. Long short-term memory (LSTM) is another recommended method (Kong et al., 2019; Wang et al., 2021; Zang et al., 2021) that can predict well the nonlinearity of the system. However, like SVR, for the best prediction, it requires a large number of input features and a huge amount of data for proper tuning of the parameters.

The artificial neural network (ANN) is another method that has been reported (Alonso and Chávez, 2017; Khan et al., 2018; Sulaiman et al., 2019; Banitalebi et al., 2020; Chandran et al., 2021) in the literature to show better performances under the nonlinear condition. In ANN, during training of data, hidden layer parameters such as gains and biases are to be tuned properly. Moreover, the performance of the ANN method highly depends on the conditions such as the availability of a huge amount of previous data or historical data, ensuring a good relationship between the inputs and output and appropriate tuning of the hidden and output layers. However, the adaptive neuro-fuzzy inference system (ANFIS) is reported to show better performance than the ANN system as it combines the beneficial features of both ANN and the fuzzy system (Alam and Ali, 2020b). However, like the fuzzy system, if the number of the input of ANFIS becomes more than three, a sluggish response due to high computational burden makes the system practically nonviable. Moreover, with an increase in the number of membership functions for each input, the computational burden increases further.

These above-mentioned problems can be alleviated by implementing subtractive clustering-based ANFIS. Subtractive clustering is a very efficient way to determine the number of clusters along with their centers when data characteristics are unpredictable. Therefore, a new subtractive clustering-based ANFIS is proposed (Alam and Ali, 2020a) for predicting residential loads. In that work, temperature is considered the first input. Moreover, occupancy and day type are used to formulate an equation to determine R, the second input for ANFIS.

However, the parameters of ANFIS in Alam and Ali (2020b) are tuned only by the hybrid algorithm that is a combination of backpropagation of input membership function parameters and the linear regression method for the output. It is found that converting the type-1 membership function into type-2 membership functions and tuning the parameters of ANFIS by particle swarm optimization (PSO) can improve the performance of ANFIS. Alam and Ali (2020a) proposed an equation-based system that predicts load consumption by dividing input data into different ranges and provides an equation to predict data whose parameters are tuned by the data that fall within that range. Because of this, the proposed equation-based system performs better than ANFIS.

However, this system is not robust for changing situations as the energy consumption pattern has changed dramatically during the COVID-19 situation, as reported in the recent literature. The COVID-19 impact on residential load consumption in Memphis City, United States, was investigated by Alam and Ali (2020b). In this work, the energy consumption in residential buildings during COVID-19 periods is reported to have increased during office hours for normal working days for different types of occupants. The overall per-day energy consumption on working days has also increased. Similar analyses for both short-time and long-time energy consumption were done for 87 regions of Zhejiang province, China (Zhang et al., 2021), where it is reported to have a time shift in electricity consumption in some regions and a permanent change in the energy consumption pattern in the rest of the regions. In Bompard et al. (2020), the impact of COVID-19 on the European electricity market was analyzed. Another work is found in the literature where the authors (Sławomir et al., 2020) investigated the impact of COVID-19 lockdown on energy consumption in Warsaw city in 2020 and found that the residential users who stayed at home during lockdown consumed more energy, with a change in consumption patterns as well. Moreover, pattern changes in load forecasting, demand, generations, and frequency deviations were also analyzed by Aviad et al. (2021). In this work, energy consumption is reported to have changed with load shifts from the

industrial and commercial sectors to the private sectors. As new variants of the virus have been emerging, it is difficult to predict how long this situation will continue. The energy consumption pattern will be continuously changing, as compared to that before the COVID-19 period.

Based on the above background, a new subtractive clustering-based ANFIS2 is implemented in this work for residential load forecasting. To the best of our knowledge, this method has never been proposed for load forecasting. The performance of the proposed ANFIS2 has been compared with that of the subtractive clustering-based ANFIS proposed by Alam and Ali (2020a), RF and LSTM methods. The predicted outputs of all systems are simulated in the MATLAB environment first for normal conditions (before COVID-19). The same inputs, as proposed by Alam and Ali (2020a, 2020b), are considered for both ANFIS and ANFIS2 methods. Different prediction errors are computed to analyze the performance of all the methods and tabulated as performance indices.

Moreover, the impact on the performance of the proposed ANFIS2 is investigated for predicting energy consumption during the COVID-19 period due to changes in energy consumption. Moreover, one input of ANFIS2, which is determined by the number of occupants and the day type, is modified to investigate the improvements in predictions. Finally, with inputs and COVID-19 data, the parameters of ANFIS2 are tuned to further improve efficacy in predictions.

To summarize the novelty and contribution, this work does the following:

- First, it proposes a new subtracting clustering-based ANFIS2 for energy consumption prediction during the normal period.
- It investigates the performance of the proposed ANFIS2 in predicting the energy conduction during the COVID-19 pandemic situation as the residential load consumptions drastically changed during this time.
- It proposes two modifications in ANFIS2 that can efficiently predict the energy consumption during the COVID-19 situation.
- It makes a performance comparison between the proposed ANFIS2 and the conventional ANFIS, LSTM, and RF systems during both normal and COVID-19 periods.

The rest of the paper is structured as follows: the problem statement, i.e., the motivation behind the current work, is represented in Section 2. In Section 3, all the methodologies are described. Simulation results are analyzed, and performances of all the methods are provided in Section 4. In Section 5, the paper ends with the conclusion and is followed by references in Section 6.

2 Problem statement

Electrical load forecasting is a crucial element that can be effectively used to provide power to consumers by proper management of energy and keeping the cost of power at a comfortable level for the consumers. Effective forecasting requires well-trained models where the model parameters are tuned based on the parameters (inputs) that contribute to energy consumption (outputs). However, the performance of the conventional models deteriorates if there are changes in the input pattern or the system is not trained with many datasets. Therefore, it is evident that a new model is required for load forecasting that will predict well under normal conditions with limited data for training. Moreover, it should be able to predict well under varying conditions.

As the energy consumption patterns are reported to have changed significantly during the COVID-19 period, a new forecasting method has been explored to solve the problem. The performance of the proposed and existing systems is investigated for the intermittent conditions with the models tuned with data available for normal conditions. Moreover, the modifications of the proposed system that are needed to predict well under varying consumption patterns are also investigated to utilize the proposed model for any future epidemic or emergency conditions.

3 Proposed ANFIS2 prediction method

Figure 1 shows the block diagram of the proposed ANFIS2, in which the type-1 fuzzy system is Sugeno-type, and the considered two inputs are the same as in Alam and Ali (2020a). In the neural part of the ANFIS2 section, both temperature and R data on 568 days are used. The value of R is determined from occupancy and the day type, as described by Alam and Ali (2020a). When training the data, the number of membership functions for both inputs is determined by subtractive clustering, which utilizes a hybrid algorithm.

The number of membership functions, along with tuning of the membership function, is facilitated by backpropagation methods, and the linear regression function is tuned for the output section for predicting data based on the fuzzy rules. Another benefit of subtractive clustering is that the fuzzy rules are always selected based on the clustering number by the algorithm during the training period and are always less than the conventional fuzzy systems. Therefore, ANFIS runs faster compared to the fuzzy systems.

In subtractive clustering, the input space (Yeom and Kwak, 2018) is divided into several clusters by considering the radius of the cluster (range of influence). The values of the range of influence can be from 0 to 1. If the radius (range of influence) is considered to be small, then the number of clusters increases and so do the fuzzy rules. The squash factor is a positive scalar that is utilized for grading the range of influence of the centers of clusters. The accept ratio is a positive number that indicates the fraction of potential of one cluster. Another data point can be considered as the center of the cluster if its fraction of potential value is above the acceptance ratio. Moreover, any point cannot be considered the center of the cluster if its fraction of potential value falls below the rejection ratio value.

In this work, when the above stages are completed, the conventional Sugeno-type fuzzy system is converted into the type-2 fuzzy system, where the input membership functions are different from the conventional input membership function as it has both the upper and lower membership functions with an area between them considered as the footprint of uncertainty (FOU), as shown in Figure 2. For the conventional fuzzy system, the membership function has only the upper membership function, as will be shown later. Moreover, the output membership functions of the type-2 fuzzy system remain the same as in the conventional

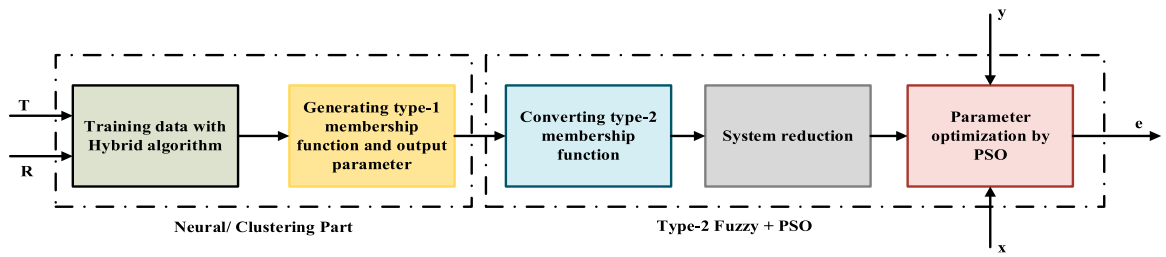

FIGURE 1
ANFIS System.

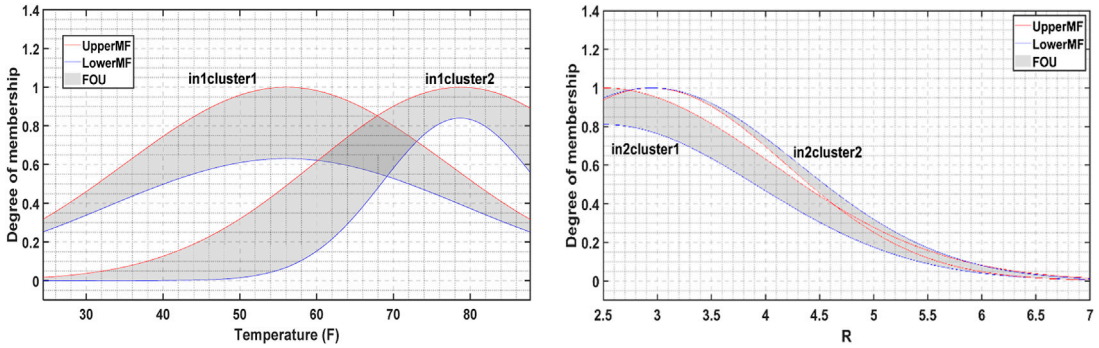

FIGURE 2
Input membership functions for ANFIS2 system.

fuzzy system, which are linear functions considered for this work [38]. The parameters of the upper membership functions of type-2 fuzzy systems remain the same as the corresponding membership functions of conventional fuzzy systems [39].

From Figure 2, it is evident that the type-2 membership function is defined by the upper and lower membership functions that are represented by red and blue lines, respectively. The fuzzification of input values is done by calculating the degree of membership from both the upper and lower membership functions based on the rule antecedent. Then, the range of strength firing rules is obtained by implementing the fuzzy operator to the fuzzified values of the membership functions. In this case, the maximum value of the upper membership function and the minimum value of the lower membership function are considered for the Sugeno-type system. In the aggregation step, the output level of each rule of the type-2 fuzzy system remains the same as in the conventional system; however, in the conventional system, they are done in consequent steps. In addition, in the aggregation step, the rule output levels are arranged in an ascending order, which defines the universe of discourse for the type-2 fuzzy set. The upper and lower membership values for each output level are chosen based on the maximum and minimum firing range values of the corresponding rule. Finally, the type-2 fuzzy set is reduced to type-1 interval fuzzy sets using the reduction method to obtain the clear output for the inference system. The type-1 interval fuzzy set considers a range of values with lower (C_L) and upper (C_R) limits that are considered centroids and can be approximated by the following equations (40):

$$C_L \approx \frac{\sum_{k=1}^{L} x_k \mu_{umf}(x_k) + \sum_{k=L+1}^{N} x_k \mu_{lmf}(x_k)}{\sum_{k=1}^{L} \mu_{umf}(x_k) + \sum_{k=L+1}^{N} \mu_{lmf}(x_k)}, \quad (1)$$

$$C_R \approx \frac{\sum_{k=1}^{R} x_k \mu_{umf}(x_k) + \sum_{k=R+1}^{N} x_k \mu_{lmf}(x_k)}{\sum_{k=1}^{R} \mu_{umf}(x_k) + \sum_{k=R+1}^{N} \mu_{lmf}(x_k)}, \quad (2)$$

where N, x_k, μ_{umf}, and μ_{lmf} correspond to the number of samples considered over the output variable range, kth output sample value, and upper and lower membership functions, respectively. The enhanced iterative algorithm with stop condition (EIASC) is used for this work as it is reported (Wu and Nie, 2011) to be the most promising method. Finally, after the reduction steps, the input and output membership function parameters are tuned and updated by the PSO optimizing algorithm, as recommended by Banitalebi et al. (2020), based on the input (x) and anticipated output that are obtained from smart meter data.

3.1 Conventional adaptive neuro-fuzzy inference system

As already mentioned, in this work, the efficacy of the proposed ANFIS2 has been verified with the system reported by Alam and Ali (2020a) in predicting energy consumption data. Subtractive clustering is also used for the system proposed by Alam and Ali (2020b), and the block diagram of the system is shown in Figure 3.

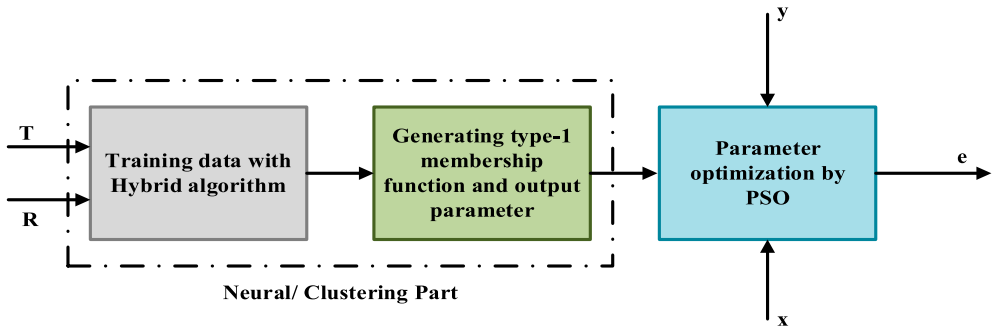

FIGURE 3
Block diagram of ANFIS System.

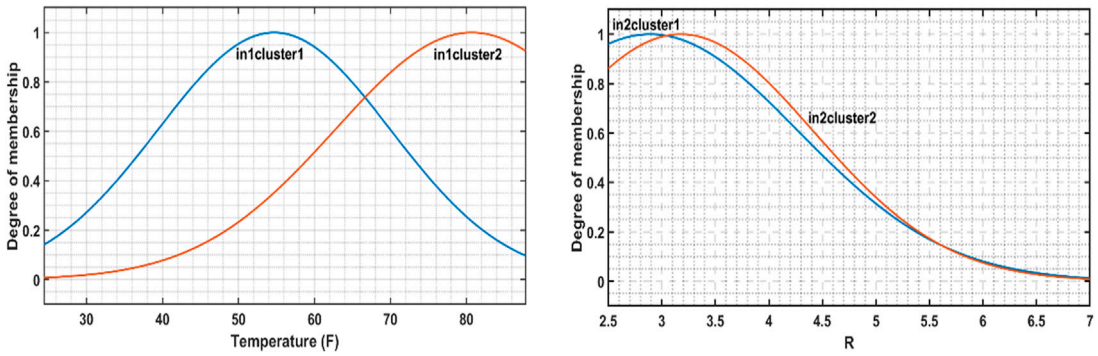

FIGURE 4
Input membership functions of ANFIS System.

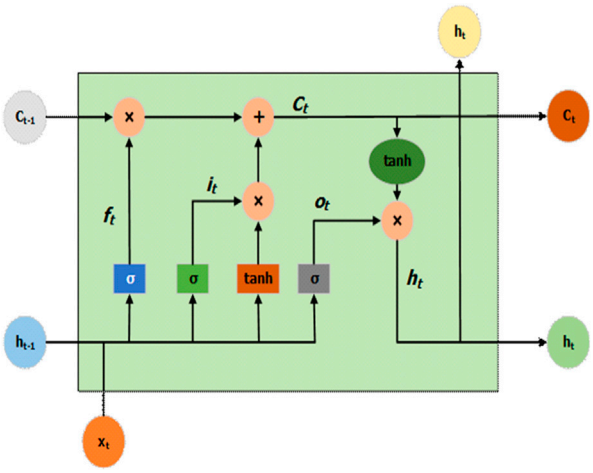

FIGURE 5
Block diagram of the LSTM system.

However, for predicting data, different parameters are determined by the PSO algorithm.

Figure 4 indicates that each input has two membership functions; therefore, only two fuzzy rules are needed for output predictions. The Gaussian fuzzy membership functions are tuned by a hybrid algorithm for both inputs. Then, the fuzzy system, based on the input membership functions, output parameters, and the input (x), as shown in Figure 3, provides the output, which comprise the energy predictions.

3.2 Long short-term memory (LSTM) method

To compare the performance of the proposed ANFIS2, the LSTM system is used as it is a very popular method for heating load for power plants (Liu et al., 2020; Rafi et al., 2021), household load forecasting (Ageng et al., 2021), and electrical load forecasting (Islam et al., 2020; Kim et al., 2020). The block diagram of the LSTM system is shown in Figure 5 and can be explained by the following sets of equations from (3)-(8):

$$f_t = \sigma(W_f \cdot [h_{t-1}, x_t] + b_f), \quad (3)$$

$$i_t = \sigma(W_f \cdot [h_{t-1}, x_t] + b_i), \quad (4)$$

$$o_t = \sigma(W_o \cdot [h_{t-1}, x_t] + b_o), \quad (5)$$

$$\tilde{C}_t = tanh(W_C \cdot [h_{t-1}, x_t] + b_C), \quad (6)$$

$$C_t = f_t \Theta C_{t-1} + i_t \Theta \tilde{C}_t, \quad (7)$$

$$h_t = o_t \times tanh(C_t), \quad (8)$$

TABLE 1 ANFIS2, ANFIS, LSTM, and RF parameters.

Method	Parameter	Value
Subtractive clustering parameter for ANFIS and ANFIS2	Range of influence	0.80
	Squash factor	0.95
	Accept ratio	0.50
	Reject ratio	0.05
ANFIS and ANFIS2	Number of nodes	17
	Number of linear parameters	6
	Number of nonlinear parameters	8
	Total number of parameters	14
	Number of training data pairs	568
	Number of checking data pairs	0
	Number of fuzzy rules	2
LSTM	Number of hidden units	250
	Fully connected layer	150
	Dropout layer	0.5
	Maximum number of epoch	550
	Mini batch size	3
	Initial learn rate	0.01
	Learn rate drop period	250
RF	Maximum number of split	1
	Minimum leaf size	1
	Number of learning cycles	324

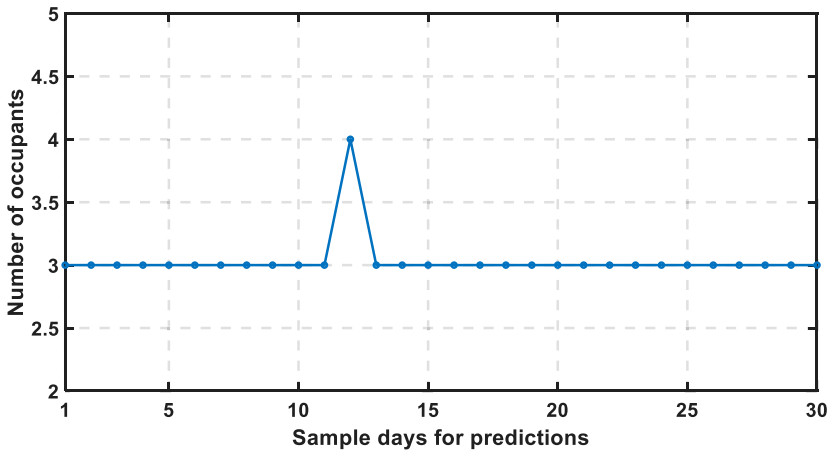

FIGURE 6
Input occupant data considered for prediction during normal time.

where f_t indicates the forget gates that regulate the influence of the previous states on the current states, whereas i_t and o_t correspond to the input and output gates, respectively. The input gates control how much of new information is to be updated in the cell state, and the output gates control the output based on the updated cell state. Σ controls the output values between 0 and 1. Based on current input x_t and previous output h_{t-1}, all the gates change their states. C_t and $\widetilde{C}_t$ correspond to the cell state and the estimated values of the cell state, respectively.

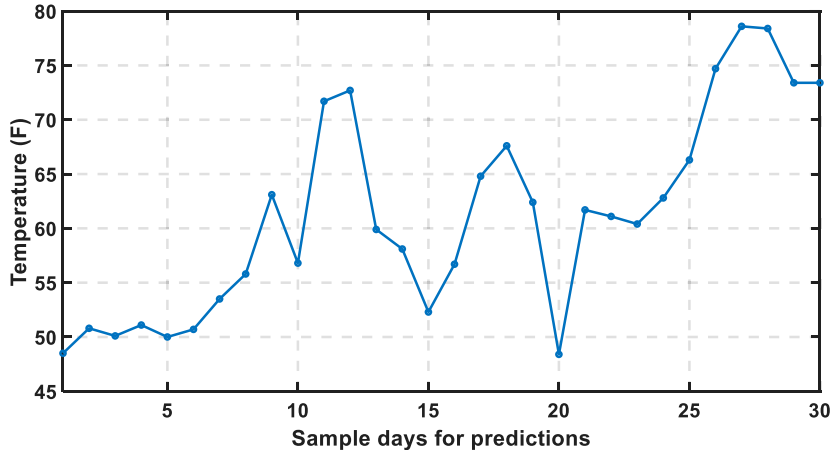

FIGURE 7
Input temperature data considered for prediction during normal time.

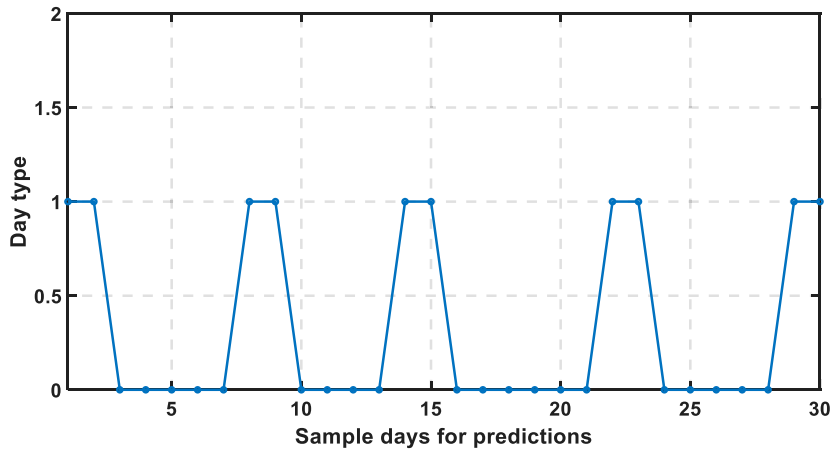

FIGURE 8
Input day-type data considered for prediction during normal time.

The ADAM optimization method is utilized for training parameter optimizations, as proposed by Wang et al. (2019).

3.3 Random forest (RF) method

The random forest method is also popular (Qi et al., 2017; Yin et al., 2020; Phyo and Jeenanunta, 2021; Sun and Bi, 2021) and widely used for load forecasting. Random forest is an ensemble approach that predicts based on the combination of decisions of all the independent trees. The randomly chosen samples are incorporated into the trees. The process of incorporation of the samples into the trees is known as bagging, whereas the chosen sample is termed a bootstrap, which is continuously changed in each step. All the decisions from each independent tree are considered with the same probability value. The classification is done by bagging algorithms, and the cart algorithm is used for determining the set of regression trees. The following equation is used to calculate the average of the output of all the trees:

$$\hat{\boldsymbol{Y}}' = \frac{\mathbf{1}}{\boldsymbol{r}}\sum_{i=1}^{r}\hat{\boldsymbol{h}}(\boldsymbol{X}', \boldsymbol{S}_{\boldsymbol{n}}^{\boldsymbol{\theta}_i}), \tag{9}$$

where $\hat{Y}'$ is the estimated output based on new input X' and $\hat{h}(X', S_n^{\theta_i})$ is the predicted output of the bootstrap sample of S_n. θ_i indicates a variable that has an identical distribution. The training parameters of the rf system are optimized by grid search optimization techniques.

4 Simulation results and discussion

4.1 Simulation data and conditions

The energy consumption data are obtained through the smart energy meter of an apartment in Memphis, TN, United States. The

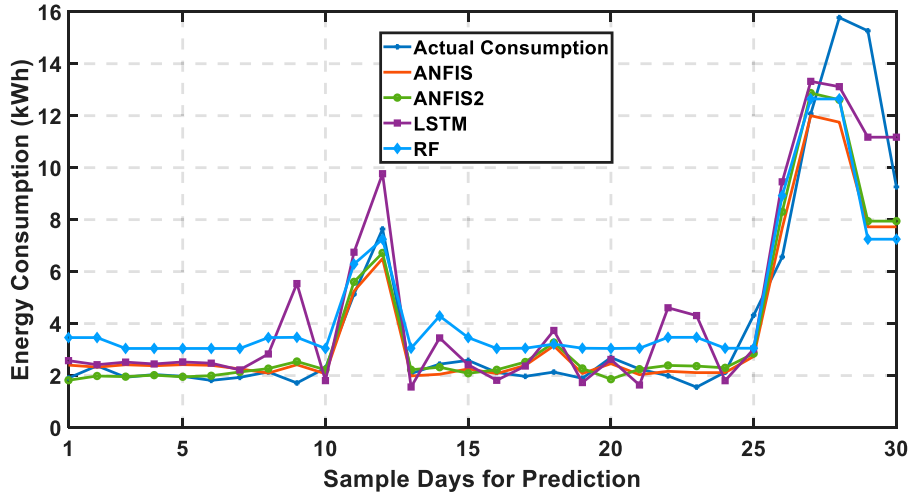

FIGURE 9
Performance of ANFIS, ANFIS2, LSTM, and RF systems for energy consumption prediction.

TABLE 2 Prediction errors of all predicted systems.

	Errors		
	AVG (kWh)	RMSE (kWh)	MAPE (%)
ANFIS	0.8163	1.6756	17.81
ANFIS2	0.8098	1.5995	17.36
LSTM	1.2199	1.6574	39.87
RF	1.4771	1.9949	48.62

temperature is collected for Memphis City. Occupancy and day-type data are obtained from the family members living in the apartment. A total of 598 days' data are considered in this work, and 568 days' data are used for ANFIS2 and ANFIS network training. The remaining 30 days' data are used for the performance evaluation of ANFIS, ANFIS2, LSTM, and RF systems for both normal and COVID-19 conditions. The parameters used for ANFIS2, ANFIS, LSTM, and RF systems are summarized in Table 1.

4.2 Efficacy of the proposed ANFIS2 prediction system over ANFIS and other methods under normal conditions

As previously discussed, in this work, for both prediction systems, arbitrarily selected 30 days' data were utilized for prediction and performance evaluation. For both systems, input occupancy data for 30 days are shown in Figure 6. Figure 7 shows input temperature data on the same days. In addition, input day-type data are shown in Figure 8.

The performance of the ANFIS2 method and the ANFIS-based prediction systems, and the LSTM and RF methods for energy consumption data prediction are shown in Figure 9, which validates the efficacy of the proposed ANFIS2-based prediction system over ANFIS reported by Alam and Ali (2020b), LSTM, and RF system during normal times.

4.3 Index calculations for the proposed ANFIS2 and other prediction methods

The absolute percentage of error, the absolute average error, root mean square error, and mean average percentage error in prediction, which can be represented as shown in equations (10)–(13), respectively, are used for ANFIS2, ANFIS, LSTM, and RF systems as the performance index.

$$\%Err = \left|\frac{Actual - Predicted}{Actual}\right| \times 100. \tag{10}$$

$$A.E = \frac{1}{N}\sum_{i=1}^{N}|Actual_i - Predicted_i|. \tag{11}$$

$$RMSE = \sqrt{\frac{1}{N}\sum_{i=1}^{N}(Actual_i - Predicted_i)^2}. \tag{12}$$

$$MAPE = \frac{1}{N}\sum_{i=1}^{N}\%Err_i. \tag{13}$$

Here, $N = 30$ was used for the equations (10) to (13). Moreover, from Table 2, it can be seen that the average errors of the ANFIS2 prediction system are smaller than those of ANFIS reported in [30], LSTM, and RF systems. In this case, the performances of the ANFIS2-based system are 0.80%, 33.62%, and 45.18% better than those of ANFIS, LSTM, and RF systems, respectively. Moreover, from RMSE values calculations for all systems, it can be concluded that ANFIS2 performs 4.54%, 3.49%, and 19.82% better than the ANFIS, LSTM, and RF systems, respectively. In addition, ANFIS2 performs 2.54% better than ANFIS in terms of MAPE. Therefore, based on the performance indices tabulated in Table 2, it is obvious that the

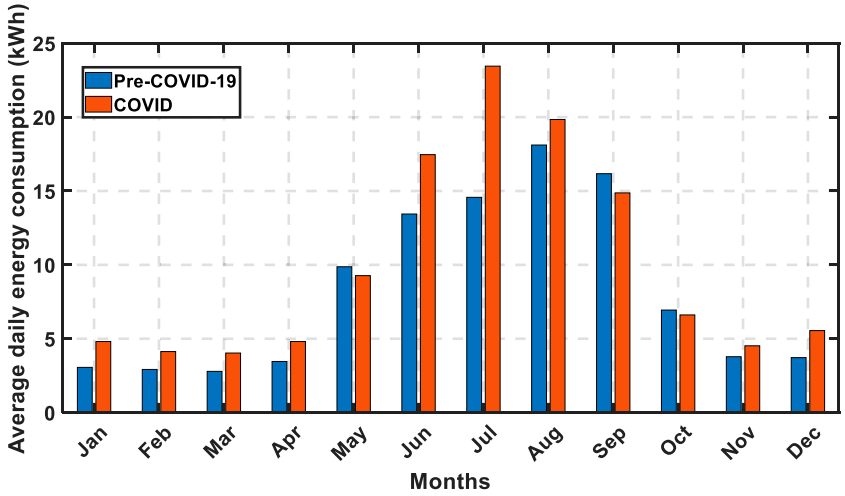

FIGURE 10
Daily average energy consumption of consumers in Memphis, United States.

TABLE 3 Analysis of energy consumption between pre-COVID-19 and COVID-19 conditions.

Month	Energy consumption (kWh)		% increase
	Pre-COVID-19	COVID-19	
January	3.06	4.81	57.37
February	2.92	4.13	41.54
March	2.79	4.03	44.21
April	3.46	4.81	38.87
May	9.87	9.27	−6.08
June	13.44	17.46	29.96
July	14.57	23.45	60.97
August	18.11	19.84	9.54
September	16.17	14.87	−8.03
October	6.94	6.61	−4.70
November	3.78	4.52	19.73
December	3.72	5.55	49.23

performance of the proposed ANFIS2-based prediction system is better than that of the ANFIS, LSTM, and RF systems in all cases during normal conditions.

4.4 Effect of COVID-19 on the load pattern change and load forecasting

As already mentioned, the energy consumption patterns of residential consumers changed significantly during the COVID-19 time. The energy consumption pattern for the residential load in Memphis city, United States, is shown in Figure 10, which considers data from August 2018 to June 2021, where the data from August 2018 to 24 March 2020 are considered pre-COVID-19 data, and data from 25 March 2020 to June 2021 are considered COVID-19 data [32]. Similarly, Table 3 provides an analysis of energy consumption between pre-COVID-19 and COVID-19 conditions. Moreover, Figure 10 shows that energy consumption increased significantly for all months except May, September, and October. The maximum energy consumption increased for the month of July. In addition, from Table 3, it is evident that energy consumption has increased from January to April, ranging from 38.87% to 57.37%. The maximum increase is 60.97%, which is also

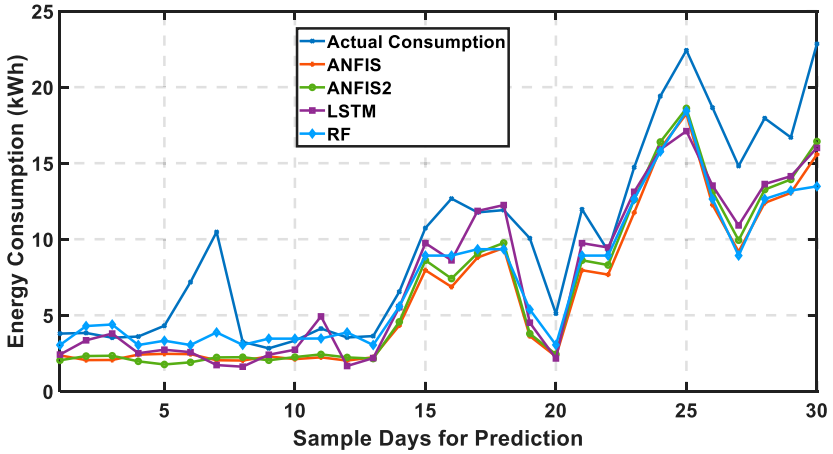

FIGURE 11
Comparison of performance of ANFIS2, ANFIS, LSTM, and RF systems for prediction during COVID-19 conditions.

TABLE 4 Prediction errors of predicted systems for COVID-19 data.

	Errors		
	AVG (kWh)	RMSE (kWh)	MAPE (%)
ANFIS	3.2955	3.8902	36.78
ANFIS2	3.0057	3.5645	35.06
LSTM	2.5190	3.3317	27.90
Rf	2.6102	3.4819	24.08

TABLE 5 Prediction error comparison of ANFIS2 system.

ANFIS2	Errors		
	AVG (kWh)	RMSE (kWh)	MAPE (%)
Pre-COVID-19	0.8098	1.5995	17.36
COVID	3.0057	3.5645	35.06

evident from Figure 10. On the other hand, the minimum increase in average daily energy consumption between the pre-COVID-19 condition and the COVID-19 condition was 9.54% in August. Due to the energy consumption pattern change during the COVID-19 period, the performance of ANFIS2, ANFIS, LSTM, and RF systems requires investigations. Therefore, all systems that were tuned with normal time data are tested for COVID-19 data prediction, and randomly chosen 30 days' data during COVID-19 conditions are used as input to all the systems.

Figure 11 shows the performances of the ANFIS2, ANFIS, LSTM, and RF systems in predicting daily average energy consumption during the COVID-19 period, which also validates the efficacy of ANFIS2 over ANFIS. However, the LSTM and RF systems perform better than ANFIS and ANFIS2 in predicting COVID-19 data, as shown in Table 4, as they predicted higher energy consumption for normal conditions. Therefore, predicted data by the LSTM and RF methods are closer to the actual data during COVID-19 periods. Table 4 shows that the absolute mean, RMSE, and MAPE are less (which indicates improvements of 16.19%, 6.53%, and 20.42%, respectively) for the LSTM system compared to the proposed ANFIS2.

However, the prediction errors increased for ANFIS2 for COVID-19 data, as compared to the normal condition data, which is evident from Table 5. Therefore, the absolute mean, RMSE, and MAPE of ANFIS2 have increased by 271.17%, 122.85%, and 101.96%, respectively. This means ANFIS2 should be modified so that it can also predict well for COVID-19 data.

4.5 Tuning of the ANFIS2 method parameters to adapt with the changed load due to COVID-19

To improve the performance of ANFIS2, two situations are considered. In the first situation, the input of ANFIS2 is changed to cope with the energy consumption pattern while keeping the same ANFIS2 that has been tuned with normal condition data. In the second situation, the changed parameter is considered while ANFIS2 is tuned with COVID-19 data.

4.5.1 Condition 1

As ANFIS2 has only two inputs, one of them can be changed to cope with the energy consumption pattern change. Moreover, the first input is the temperature that cannot be changed. Therefore, the second input, R, should be changed as compared to the normal conditions. R is determined from occupancy and the day type (Alam and Ali, 2020b). The value of day type (d) is considered to be 0, 1, and 2 for weekdays, weekends, and special days, respectively. The reason behind

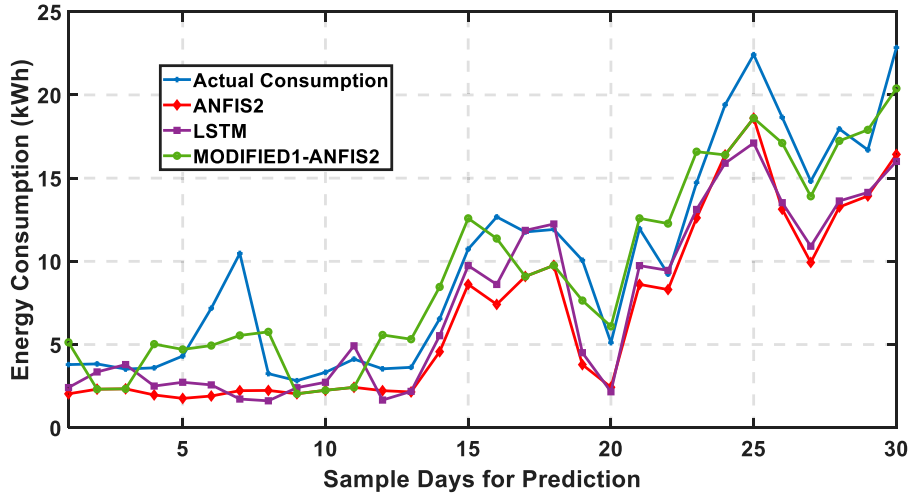

FIGURE 12
Comparison of performances of ANFIS2, modified1-ANFIS2, and LSTM systems for prediction during COVID-19 conditions.

TABLE 6 Prediction error comparison among ANFIS2 and LSTM system.

COVID	Errors		
	AVG (kWh)	RMSE (kWh)	MAPE (%)
Modified1-ANFIS2	1.8440	2.0846	25.96
ANFIS2	3.0057	3.5645	35.06
LSTM	2.5190	3.3317	27.90

choosing these values is that during weekdays, most of the family members will be out for work, and during the weekend, they will stay at home. Moreover, during special days, the energy consumption will be higher than the conventional days. However, during COVID-19 periods, most of the family members worked from home on weekdays. Therefore, the energy consumption changed tremendously for weekdays. As the number of occupants has not changed during COVID-19 time, the values of d for the weekdays, weekends, and special days can be considered 2, 1, and 2, respectively, for COVID-19 data.

Finally, based on the changed input R and ANFIS2 that was tuned with normal time data, the 30 days' daily average energy consumption, which are the same as shown in Figure 11, are shown in Figure 12. Figure 12 indicates that the performance of the modified1 ANFIS2 has improved by just adjusting R and without retuning ANFIS2. Moreover, the errors are reduced, as shown in Table 6. The absolute mean error, RMSE, and MAPE are reduced by 38.65%, 41.51%, and 25.95%, respectively.

Moreover, the absolute mean error, RMSE, and MAPE are less than that of the LSTM system that performs better than ANFIS2 without any modification for COVID-19 data.

4.5.2 Condition 2

Figure 13 shows the modified model for ANFIS2 that can predict well both normal data and COVID-19 data. All the data are incorporated into ANFIS2, which separates normal data and COVID-19 data, and these different data are sent to two different sections. Normal data are sent to ANFIS2 that was tuned with normal data. This section will have the same parameters as shown in Table 1 and Figure 2. Similarly, COVID-19 data are received by ANFIS2 that was tuned by COVID-19 data. This section, as tuned by the COVID-19 data, has different parameters, which are shown in Table 7 and Table 8.

Moreover, the membership function is different, as shown in Figure 14, which has eight membership functions for each input compared to two membership functions for each input for the ANFIS2 section that will process normal data. The eight membership functions are selected based on subtractive clustering that considers the type of data and correlation between input and output data during the COVID-19 situation. Similar to the fuzzy-2 system, the membership function has upper and lower membership functions. All the membership functions inside a particular figure are tuned based on the correlation between the input and output for various ranges of input. Moreover, the output membership functions of the type-2 fuzzy system remain the same as in the conventional fuzzy system, which are linear functions considered for this work. In both sections, the two inputs are kept the same, and the day type is considered the same for both normal and COVID-19 periods, which were considered for ANFIS2. The data separation unit provides COVID-19 data input (X_1) and normal data input (X_2) to two separate sections. The COVID-19 (e1) and normal predicted data (e2) are incorporated into the data accumulator, which will provide predicted data (e) from modified2-ANFIS2. Therefore, both normal and COVID-19 data can be predicted by modified2-ANFIS2, and it will be robust for all conditions.

The performance of modified2-ANFIS2 along with modified1-ANFIS2 and LSTM systems, for the same data prediction, as shown in Figure 11 and Figure 12, is shown in Figure 15. For the purpose of performance comparison, the predicted data by modified1-ANFIS2 are also shown in Figure 15. Figure 15 shows that modified2-ANFIS2 performs better than the modified1-ANFIS2 and LSTM systems for

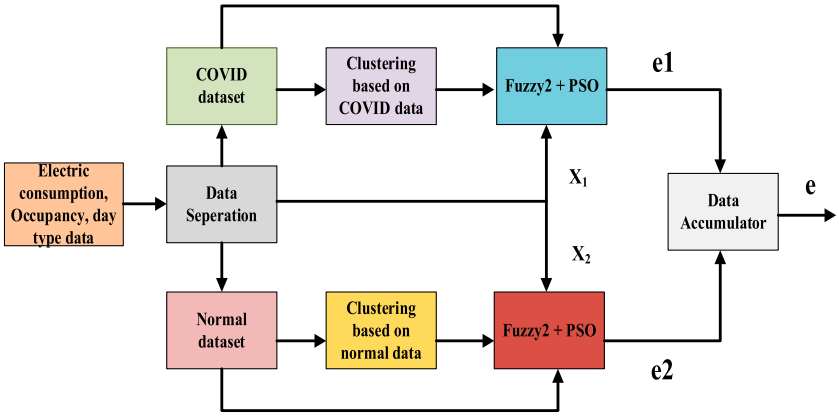

FIGURE 13
Modified2-ANFIS2 system for prediction during COVID-19.

TABLE 7 Subtractive clustering parameter for COVID-19 data tuning.

Parameter	Value
Range of influence	0.50
Squash factor	0.50
Accept ratio	0.50
Reject ratio	0.15

TABLE 8 ANFIS2 parameter for COVID-19 data tuning.

Parameter	
Number of nodes	53
Number of linear parameters	24
Number of nonlinear parameters	32
Total number of parameters	56
Number of training data pairs	276
Number of checking data pairs	0
Number of fuzzy rules	8

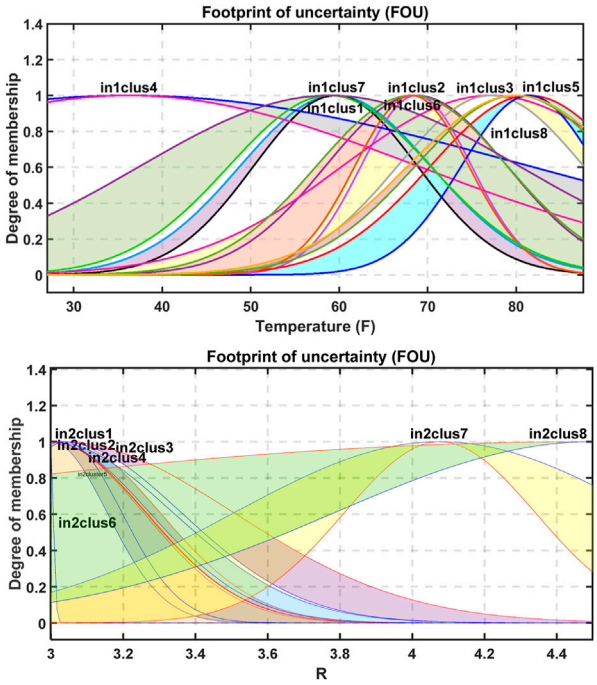

FIGURE 14
Input membership functions for modified2-ANFIS2 system that are tuned with COVID-19 data.

predicting the same data. Therefore, the error is further reduced, which is evident from Table 9. The absolute mean error, RMSE, and MAPE are reduced by 32.77%, 2.15%, and 45.42%, respectively. So the modified2-ANFIS2 system performs the best in predicting energy consumption during the COVID-19 situation.

5 Conclusion

In this work, a new ANFIS2 method is implemented for the prediction of residential energy consumption for both normal days and COVID-19 conditions. To validate the efficacy of the proposed ANFIS2, its performance has been compared with the proposed ANFIS reported in Alam and Ali (2020a), LSTM, and RF systems. For training purpose of the systems, 598 days' data are utilized, and data of 30 days are considered for the prediction of energy consumption. Moreover, the performances of all the systems are evaluated for COVID-19 situations as the change in energy consumption is reported in the literature. Two modifications in terms of the input and parameters of ANFIS2 are made to cope with the change in the consumption pattern and to reduce the prediction errors during COVID-19. Based on the obtained results, the following conclusions can be made:

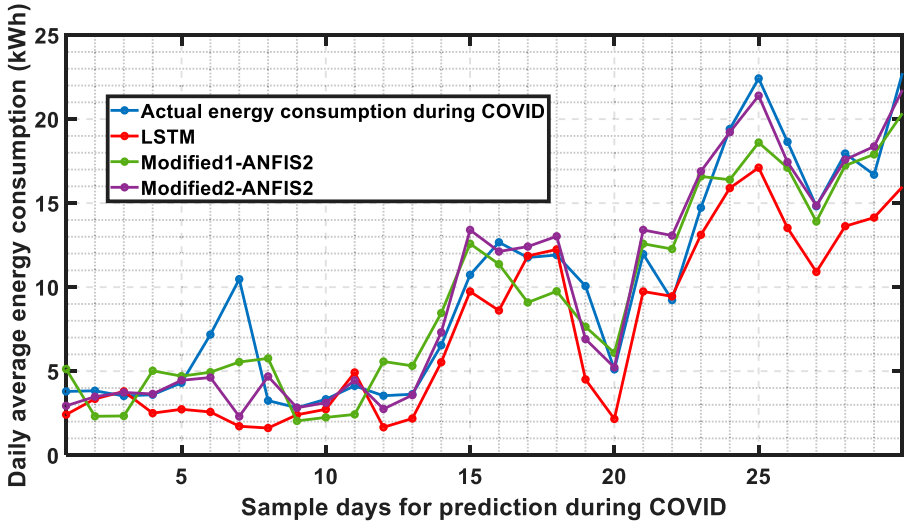

FIGURE 15
Comparison of performances of LSTM, modified1-ANFIS2, and modified2-ANFIS2 systems for prediction during COVID-19.

TABLE 9 Prediction error comparison among modified ANFIS2 and LSTM methods.

COVID-19	Errors		
	AVG (kWh)	RMSE (kWh)	MAPE (%)
Modified1-ANFIS2	1.8440	2.0846	25.96
Modified2-ANFIS2	1.2396	2.0398	14.12
LSTM	2.5190	3.3317	27.90

a) The proposed ANFIS2-based prediction system is effective in forecasting residential loads during both normal and COVID-19 periods.
b) The performance of the proposed ANFIS2 method is better than that of the existing ANFIS, LSTM, and RF approaches during both normal and COVID-19 situations.
c) The proposed ANFIS2 can be easily implemented in real practice for both normal and COVID-19 conditions.

In the near future, other new methods for load forecasting will be explored. In addition, the performance of those methods will be compared with that of the proposed ANFIS2. The limitation of the proposed modified2-ANFIS2 is that data are manually separated, which is done by the consumer. In the future, a more robust system that can automatically separate the pre-COVID-19 and COVID-19 data by analyzing the pattern will be explored.

Data availability statement

The original contributions presented in the study are included in the article/Supplementary Material; further inquiries can be directed to the corresponding author.

Author contributions

SMMA: conceptualization, data curation, formal analysis, investigation, methodology, validation, and writing–original draft. MHA: conceptualization, investigation, project administration, resources, supervision, and writing–review and editing.

Funding

The author(s) declare that no financial support was received for the research, authorship, and/or publication of this article.

Conflict of interest

The authors declare that the research was conducted in the absence of any commercial or financial relationships that could be construed as a potential conflict of interest.

The author(s) declared that they were an editorial board member of Frontiers at the time of submission. This had no impact on the peer review process and the final decision.

Publisher's note

References

Ageng, D., Huang, C.-Y., and Cheng, R.-G. (2021). "A short-term household load forecasting framework using LSTM and data preparation," in *IEEE access*, 9, 167911–167919.

Alam, S. M. M., and Ali, M. H. (2020a). "A new subtractive clustering based ANFIS system for residential load forecasting," in *IEEE PES innovative smart grid technologies (ISGT) conference* (Washington D.C., USA, 1–5.

Alam, S. M. M., and Ali, M. H. (2020b). Equation based new methods for residential load forecasting. *Energies* 13, 6378. doi:10.3390/en13236378

Alam, S. M. M., and Ali, M. H. (2020c). "A new fuzzy logic based method for residential loads forecasting," in *2020 IEEE/PES transmission and distribution conference and exposition (T&D)* (IEEE), 1–6.

Alam, S. M. M., and Ali, M. H. (2021). Analysis of COVID-19 effect on residential loads and distribution transformers. *Int. J. Electr. Power and Energy Syst.* 129, 106832. doi:10.1016/j.ijepes.2021.106832

Almalaq, A., and Edwards, G. (2019). "Comparison of recursive and non-recursive ANNs in energy consumption forecasting in buildings," in *2019 IEEE green technologies conference (GreenTech)*, 1–5.

Alonso, R., and Chávez, A. (2017). "Short term load forecast method using artificial neural network with artificial immune systems," in *2017 ieee urucon*, 1–4.

Alrizq, M., and de Doncker, E. (2018). "A novel fuzzy based human behavior model for residential electricity consumption forecasting," in *2018 IEEE power and energy conference at Illinois (PECI)*, 1–7.

Anoop, K. J., and Kanchana, K. (2017). "Short term load forecasting using fuzzy logic control," in *2017 IEEE international conference on power, control, signals and instrumentation engineering (ICPCSI)*, 2983–2986.

Aviad, N., Machlev, R., Carmon, D., Onile, A. E., Belikov, J., and Levron, Y. (2021). Effects of the COVID-19 pandemic on energy systems and electric power grids—a review of the challenges ahead. *Energies* 14 (4), 1056. doi:10.3390/en14041056

Banitalebi, B., Appadoo, S. S., Thavaneswaran, A., and Hoque, M. E. (2020). "Modeling of short-term electricity demand and comparison of machine learning approaches for load forecasting," in *2020 IEEE 44th annual computers, software, and applications conference (COMPSAC)*, 1302–1307.

Bompard, E., Mosca, C., Colella, P., Antonopoulos, G., Fulli, G., Masera, M., et al. (2020). The immediate impacts of COVID-19 on European electricity systems: AFirst assessment and lessons learned. *Energies* 14 (1), 96. doi:10.3390/en14010096

Chandran, L. R., Jayagopal, N., Lal, L. S., and Narayanan, C. (2021). "Residential load time series forecasting using ANN and classical methods," in *2021 6th international conference on communication and electronics systems (ICCES)*, 1508–1515.

Chowdhury, D., Sarkar, M., Haider, M. Z., and Alam, T. (2018). "Zone wise hourly load prediction using regression decision tree model," in *2018 international conference on innovation in engineering and technology (ICIET)*, 1–6.

Islam, M. R., Al Mamun, A., Sohel, M., Hossain, M. L., and Uddin, M. M. (2020). "LSTM-based electrical load forecasting for chattogram city of Bangladesh," in *2020 international conference on emerging smart computing and informatics (ESCI)*, 188–192.

Kapoor, A., and Sharma, A. (2018). "A comparison of short-term load forecasting techniques," in *2018 IEEE innovative smart grid technologies - asia* (ISGT Asia), 1189–1194.

Khan, A. R., Razzaq, S., Alquthami, T., Moghal, M. R., Amin, A., and Mahmood, A. (2018). "Day ahead load forecasting for IESCO using artificial neural network and bagged regression tree," in *2018, 1st international conference on power* (Energy and Smart Grid ICPESG), 1–6.

Kim, W., Han, Y., Kim, K. J., and Song, K. (2020). Electricity load forecasting using advanced feature selection and optimal deep learning model for the variable refrigerant flow systems. *Energy Rep.* 6, 2604–2618. doi:10.1016/j.egyr.2020.09.019

Kim, Y., Son, H., and Kim, S. (2019). Short term electricity load forecasting for institutional buildings. *Energy Rep.* 5, 1270–1280. doi:10.1016/j.egyr.2019.08.086

Kong, W., Dong, Z. Y., Jia, Y., Hill, D. J., Xu, Y., and Zhang, Y. (2019). Short-term residential load forecasting based on LSTM recurrent neural network. *IEEE Trans. Smart Grid* 10 (1), 841–851. doi:10.1109/TSG.2017.2753802

Liu, J., Wang, X., Zhao, Y., Dong, B., Lu, K., and Wang, R. (2020). "Heating load forecasting for combined heat and power plants via strand-based LSTM," in *IEEE access*, 8, 33360–33369.

MathWorks (2021a). *Type-2 fuzzy inference systems*. Available at: https://www.mathworks.com/help/fuzzy/type-2-fuzzy-inference-systems.html (Accessed December 9, 2021).

MathWorks (2021b). *Type-2 fuzzy inference systems*. Available at: https://www.mathworks.com/help/fuzzy/mamfistype2.converttotype2.html (Accessed December 9, 2021).

Mendel, J. M., Hagras, H., Tan, W.-W., Melek, W. W., and Ying, H. (2014). *Introduction to type-2 fuzzy logic control*. Hoboken, NJ.: Wiley and IEEE Press.

Moon, J., Kim, Y., Son, M., and Hwang, E. (2018). Hybrid short-term load forecasting scheme using random forest and multilayer perceptron. *Energies* 11 (12), 3283. doi:10.3390/en11123283

Moradzadeh, A., Mohammadi-Ivatloo, B., Abapour, M., Anvari-Moghaddam, A., and Roy, S. S. (2022). Heating and cooling loads forecasting for residential buildings based on hybrid machine learning applications: a comprehensive review and comparative analysis. *IEEE Access* 10, 2196–2215. doi:10.1109/access.2021.3136091

Nair, A. S., Hossen, T., Campion, M., and Ranganathan, P. (2018). "Optimal operation of residential EVs using DNN and clustering based energy forecast," in *2018 north American power symposium (NAPS)* (Fargo, ND, 1–6.

Oprea, S., and Bâra, A. (2019). Machine learning algorithms for short-term load forecast in residential buildings using smart meters, sensors and big data solutions. *IEEE Access* 7, 177874–177889. doi:10.1109/access.2019.2958383

Phyo, P. P., and Jeenanunta, C. (2021). Daily load forecasting based on a combination of classification and regression tree and deep belief network. *IEEE Access* 9, 152226–152242. doi:10.1109/access.2021.3127211

Qi, Y., Luo, B., Wang, X., and Wu, L. (2017). "Load pattern recognition method based on fuzzy clustering and decision tree," in *2017 IEEE conference on energy internet and energy system integration (EI2)*, 1–5.

Rafi, S. H., Nahid, A. M., Deeba, S. R., and Hossain, E. (2021). "A short-term load forecasting method using integrated CNN and LSTM network," in *IEEE access*, 9, 32436–32448.

Rana, M., Sethuvenkatraman, S., and Goldsworthy, M. (2022). A data-driven approach based on quantile regression forest to forecast cooling load for commercial buildings. *Sustain. Cities Soc.* 76, 103511. doi:10.1016/j.scs.2021.103511

Shabbir, N., Ahmadiahangar, R., Kütt, L., and Rosin, A. (2019). "Comparison of machine learning based methods for residential load forecasting," in *2019 electric power quality and supply reliability conference (PQ) and 2019 symposium on electrical engineering and mechatronics (SEEM)*, 1–4.

Shao, H., Sun, X., Zhao, L., and Wang, J. (2018). "Interval day-ahead load forecast of micro grid with fuzzy similar data selection and Gaussian process," in *2018 IEEE 8th annual international conference on CYBER technology in automation, control, and intelligent systems (CYBER)*, 1578–1583.

Sharma, S., Majumdar, A., Elvira, V., and Chouzenoux, E. (2020). Blind Kalman filtering for short-term load forecasting. *IEEE Trans. Power Syst.* 35 (6), 4916–4919. doi:10.1109/tpwrs.2020.3018623

Sławomir, B., Skoczkowski, T., Sobczak, L., Buchoski, J., Maciąg, Ł., and Dukat, P. (2020). Impact of the lockdown during the COVID-19 pandemic on electricity use by residential users. *Energies* 14 (4), 980. doi:10.3390/en14040980

Sulaiman, S. M., Aruna Jeyanthy, P., Devaraj, D., Mohammed, S. S., and Shihabudheen, K. V. (2019). "Smart meter data analytics for load prediction using extreme learning machines and artificial neural networks," in *2019 IEEE international conference on clean energy and energy efficient electronics circuit for sustainable development (INCCES)*, 1–4.

Sun, H., and Bi, Z. (2021). "Hybrid forecasting model of electric heating load based on CART decision tree regression," in *2021 IEEE international conference on artificial intelligence and computer applications (ICAICA)*, 204–208.

U Yeom, C.-, and Kwak, K.-C. (2018). Performance comparison of ANFIS models by input space partitioning methods. *Symmetry* 10, 700. doi:10.3390/sym10120700

Wang, Y., Zhang, N., and Chen, X. (2021). A short-term residential load forecasting model based on LSTM recurrent neural network considering weather features. *Energies* 14 (10), 2737. doi:10.3390/en14102737

Wang, Y., Zhu, S., and Li, C. (2019). "Research on multistep time series prediction based on LSTM," in *2019 3rd international conference on electronic information technology and computer engineering (EITCE)*, 1155–1159.

Wang, Z., and Srinivasan, R. S. (2017). A review of artificial intelligence-based building energy use prediction: contrasting the capabilities of single and ensemble prediction models. *Renew. Sustain. Energy Rev.* 75, 796–808. doi:10.1016/j.rser.2016.10.079

Wang, Z., Wang, Y., Zeng, R., Srinivasan, R. S., and Ahrentzen, S. (2018). Random Forest based hourly building energy prediction. *Energy Build.* 171, 11–25. doi:10.1016/j.enbuild.2018.04.008

Wu, D., and Nie, M. (2011). "Comparison and practical implementation of type-reduction algorithms for type-2 fuzzy sets and systems," in *2011 IEEE international conference on fuzzy systems (FUZZ-IEEE 2011)* (Taipei, 2131–2138.

Yiling, H., and Shaofeng, H. (2020). "A short-term load forecasting model based on improved random forest algorithm," in *2020 7th international forum on electrical engineering and automation (IFEEA)*, 928–931.

Yin, L., Sun, Z., Gao, F., and Liu, H. (2020). Deep forest regression for short-term load forecasting of power systems. *IEEE Access* 8, 49090–49099. doi:10.1109/access.2020.2979686

Zang, H., Xu, R., Cheng, L., Ding, T., Liu, L., Wei, Z., et al. (2021). Residential load forecasting based on LSTM fusing self-attention mechanism with pooling. *Energy* 229, 120682. doi:10.1016/j.energy.2021.120682

Zhang, Z., Cheshmehzangi, A., and Ardakani, S. P. (2021). A data-driven clustering analysis for the impact of COVID-19 on the electricity consumption pattern of Zhejiang province, China. *Energies* 14 (23), 8187. doi:10.3390/en14238187

Zheng, Z., Chen, H., and Luo, X. (2019). A Kalman filter-based bottom-up approach for household short-term load forecast. *Appl. Energy* 250, 882–894. doi:10.1016/j.apenergy.2019.05.102

frontiers | Frontiers in Energy Research

TYPE Original Research
PUBLISHED 13 February 2024
DOI 10.3389/fenrg.2024.1341246

OPEN ACCESS

EDITED BY
Hailong Li,
Central South University, China

REVIEWED BY
Yongxi Zhang,
Changsha University of Science and Technology, China
Sonali Goel,
Independent Researcher, India

*CORRESPONDENCE
Gang Zhang,
zhanggang3463003@163.com

RECEIVED 20 November 2023
ACCEPTED 31 January 2024
PUBLISHED 13 February 2024

CITATION
Xie T, Zhang Y, Zhang G, Zhang K, Li H and He X (2024), Research on electric vehicle load forecasting considering regional special event characteristics.
Front. Energy Res. 12:1341246.
doi: 10.3389/fenrg.2024.1341246

Research on electric vehicle load forecasting considering regional special event characteristics

Tuo Xie[1], Yu Zhang[2], Gang Zhang[1]*, Kaoshe Zhang[1], Hua Li[3] and Xin He[4]

[1]School of Electrical Engineering, Xi'an University of Technology, Xi'an, China, [2]State Grid Shaanxi Electric Power Co, LTD. Ultra High Voltage Company, Xi'an, China, [3]Electric Power Research Institute of State Grid Shaanxi Electric Power Company, Xi'an, China, [4]School of Water Resources and Hydropower, Xi'an University of Technology, Xi'an, China

With the rise of electric vehicles and fast charging technology, electric vehicle load forecasting has become a concern for electric vehicle charging station planners and operators. Due to the non-stationary nature of traffic flow and the instability of the charging process, it is difficult to accurately predict the charging load of electric vehicles, especially in sudden major events. In this article, We proposes a high-precision EV charging load forecasting model based on mRMR and IPSO-LSTM, which can quickly respond to the epidemic (or similar emergencies). Firstly, the missing data in the original EV charging load data are supplemented, and the abnormal data are corrected. Based on this, a factor set is established, which included five epidemic factors, including new confirmed cases, the number of moderate risk areas, the number of high risk areas, epidemic situation and epidemic prevention policies of the city, and other factors such as temperature. Secondly, the processed load data and other data in the influencing factor set are normalized, and the typical characteristic curve is established for personalized processing of the relevant data of epidemic factors, so as to improve the sensitivity of load response to epidemic changes and the ability to capture special data (peak and valley values and turning points of load). Then the maximum relevant minimum redundancy (mRMR) is used to select the optimal feature set from the set of influencing factors. Then, the processed load data and its corresponding optimal selection are input into the IPSO-LSTM model to obtain the final prediction result. Finally, taking the relevant data of EV charging load in a city in China from November 2021 to April 2022 (the city experienced two local epidemics in December 2021 and March 2022 respectively) as an example, the model is evaluated and compared with other models under the forecast period of 1 h. Meanwhile, the performance of the model under different foresight periods (2 h, 4 h, 6 h) is compared and analyzed. The results show that the model has good stability and representativeness, and can be used for EV charging load prediction under the COVID-19 pandemic.

KEYWORDS

electric vehicle charging load forecast, feature correlation, maximum relevant minimum redundancy, improved particle swarm optimization -long short term memory, special event characteristics

1 Introduction

Effective renewable friendly smart grid technologies contribute to the development of RWJ projects, indirectly facilitating friendly interactions between EVs and the grid (Zhong et al., 2014). The multi-time scale short-term prediction of EV charging load is an important reference for intraday demand-side response (Li and Pye, 2018), and can provide a reference for the optimal scheduling of the distribution network with electric vehicles (Zakernezhad et al., 2022), so accurate multi-time-scale electric vehicle charging load forecasting is of great significance. At the end of 2019, the spread of COVID-19 had an impact on the entire electricity industry and renewable energy in many countries (Liu, 2020), and renewable energy consumption affects economic growth (The State Council of the People's Republic of China). Under the general strategy of " foreign defense against imports, internal defense against rebound" and the general policy of "dynamic clearing" in China, people's willingness to travel will be reduced when the epidemic occurs, and travel will be restricted at certain times (Xi'an Municipal People's Government, 2022), which will lead to significant changes in the charging load of electric vehicles. Large-scale use of electric vehicles can significantly reduce carbon emissions, but the load of large-scale electric vehicles has strong randomness, which is a huge challenge for power system security and stability (Leou et al., 2014; SALAH et al., 2015).

At present, the main research methods of electric vehicle charging load forecasting can be divided into two categories: model-driven and data-driven forecasting methods. The former uses mathematical statistics to establish a probability model, and on this basis uses Monte Carlo simulation to predict (Iversen et al., 2017; Zhang et al., 2018; Iwafune et al., 2020). Compared with such methods, relying on data-driven methods for EV charging load forecasting is more transferable and can reduce forecasting costs. The development of IoT technology has driven the development of a large number of cloud-based electric vehicle services (Atif et al., 2016; Chen and Chang, 2016), and data integration platforms have been established in many provinces in China (Shaanxi Provincial Development and Reform Commission, 2022; State-owned Assets Supervision, 2022; State-owned Assets Supervision and Administration Commission of the State Council, 2022). In this context, data-driven forecasting methods have received more attention (Wang et al., 2022). Back Propagation Neural Network (BPNN) (Dabbaghjamanesh et al., 2021), Auto-Regressive and Moving Average (ARMA) (Wen et al., 2019), Convolutional Neural Network (CNN) (Zhang X. et al., 2021), Long Short-Term Memory (LSTM) (Zhu et al., 2019), and other methods are beginning to be applied to EV charging load prediction. Since the impact of COVID-19 on EV charging loads is not instantaneous, this requires predictive models to remember information delivered over longer periods of time. Therefore, this paper will continue to take advantage of the LSTM network's ability to learn long-range dependencies to build an effective EV charging load forecasting model (Bayrak et al., 2020).

Under normal circumstances, the electric vehicle charging load is similar to the power load in terms of data characteristics, and both show periodic changes. The influence of influencing factors is often considered in power load forecasting (Lin et al., 2021; Bian et al., 2022). Therefore, in order to further improve the forecasting accuracy, factors such as temperature, electricity price, and date type have also begun to be considered in electric vehicle charging load forecasting (Abbas et al., 2019; Feng et al., 2021; Zhang et al., 2022). Among them (Abbas et al., 2019) used meteorological data and historical load as influencing factors to accurately predict the load; Literature (Feng et al., 2021) considered two related factors of electricity price and temperature, using EMGM to predict the charging load of electric vehicles, and using LSTM for error correction; Literature (Zhang et al., 2022) using The multi-channel 1DCNN extracts the load characteristics of different time scales under the influence factors such as meteorological characteristics and date characteristics (seasonal type, week type), and inputs them into the TCN to establish a time-dependent relationship for each characteristic and improve the forecast accuracy. But the COVID-19 outbreak is a non-periodic emergency, and its impact on EV load is contingent and persistent. As of August 2022, the COVID-19 outbreak is ongoing, with concentrated outbreaks continuing across China. The establishment of a forecasting model capable of rapid response to the epidemic (or similar emergencies) and with high accuracy is conducive to the development of demand-side response plans and scheduling plans (National Health Commission of the People's Republic of China, 2022). Therefore, during the epidemic period, electric vehicle load not only needs to consider the impact of temperature, electricity price and other factors, but also the impact of epidemic-related factors.

In the process of load forecasting using machine learning methods, it is necessary to perform feature selection on relevant factors. Commonly used feature analysis methods include the covariance method, the Pearson coefficient method, the maximal information coefficient (MIC) (Reshef et al., 2011) and the MIC-based mRMR (Peng et al., 2005). Among them, literature (Xie et al., 2022) used Pearson coefficients to determine the key influencing factors of loads, which were regarded as multivariate information, and then input them into LSTM to obtain a load prediction model with multi-information fusion. However, the Pearson coefficient can only reflect the linear correlation, but there may be a nonlinear relationship between the EV charging load and the related factors, and it is difficult to describe the change of EV charging load linearly, so it is more suitable for the MIC and mRMR. Literature (Sun et al., 2022) for the existing in different moments of each influential factors to load the same degree of contribution to the problem, the use of mutual information (MI) to portray different moments under the degree of contribution of each factor, and then use the Bidirectional Long Short-Term Memory (Bi-LSTM) to get the final prediction results. MIC was applied to short-term electricity load forecasting, effectively improving the screening effect of the feature sequence (Ge et al., 2021), and literature (Zhang et al., 2023) utilized MIC and Akaike information criterion to select input variables, obtain key information, and reduce the difficulty of model training. However, the redundancy of epidemic-related feature sequences in EV charging load in the context of COVID-19 is high, which is not considered in the MIC, while the mRMR incorporates the redundancy in the sequences into the screening metrics (Dai et al., 2014), which is more suitable for electric vehicle charging load forecasting under the COVID-19 outbreak.

This paper aims to implement a predictive model that can quickly respond to an outbreak (or similar emergencies) with high accuracy. This method fully considers the impact of the epidemic, establishes five epidemic-related influencing factors, uses mRMR to select the optimal feature set from the set of influencing factors including epidemic factors and meteorological

factors, and uses IPSO-LSTM to predict the short-term load of EV charging load with multiple foresight periods. The main novelties of this paper are as follows:

(1) A charging load forecasting model for electric vehicles that can quickly respond to the epidemic (or similar emergencies) and has high accuracy is established.
(2) The epidemic-related data are processed to make the data more suitable for the forecasting of electric vehicle charging load during the COVID-19 pandemic, and mRMR is used to select the best input features according to the characteristics of the epidemic feature sequence.
(3) For the determination of model parameters, IPSO is used to optimize the training parameters, which improves the forecast accuracy, and the effectiveness of the proposed model is verified by an example.

The organization of this paper is as follows: Section 2 introduces the above methods, including mRMR, IPSO-LSTM prediction model, and predictive performance evaluation indicators; Section 3 introduces data trends and related characteristics; Section 4 carries out case studies; Section 5 discusses the results; and Section 6 gives research conclusions.

2 Methods

2.1 Maximum relevant minimum redundancy

In order to consider the correlation between the single feature variable and the target variable, and consider the linear relationship and nonlinear relationship at the same time, the MIC method can be selected to judge the correlation between the two sequences.

The MIC method was proposed by Reshef in 2011, which can effectively detect linear or other functional relationships between two variables (Li et al., 2015). The concept of using mutual information in the MIC method can be expressed as:

$$I\left(d_x, d_y\right) = \int p\left(d_x, d_y\right) \log_2 \frac{p\left(d_x, d_y\right)}{p\left(d_x\right) p\left(d_y\right)} \tag{1}$$

Where: d_x and d_y are the values of the sequence x and y respectively; $I(\cdot)$ is the mutual information function; $p(\cdot)$ is the probability density distribution function. It is relatively difficult to calculate the joint probability density distribution function. Therefore, on the basis of mutual information, the MIC method discretizes the relationship of the two variables into a two-dimensional space to estimate the probability density function.

MIC can be calculated by formula (2) and (3):

$$I\left(d_x, d_y\right) \approx I\left(d_X, d_Y\right) = \int p\left(d_X, d_Y\right) \log_2 \frac{p\left(d_X, d_Y\right)}{p\left(d_X\right) p\left(d_Y\right)} \tag{2}$$

$$I_{MIC}(x, y) = \max_{ab<0.6} \frac{I\left(d_X, d_Y\right)}{\log_2 \left(\min\left(a, b\right)\right)} \tag{3}$$

In the formula: a and b are the discretized numbers in the d_X and d_Y directions; $I_{MIC}(x, y)$ is the MIC of the sequence x and y.

The mRMR method can penalize redundant features with high correlation among the selected features (Zhang et al., 2019). Among all feature sequences, new feature sequences are incrementally selected, each time the locally optimal feature is selected.

Defined $D(S, y)$ as the correlation between all features and the target variable y, $R(S)$ is the redundancy of all features, where is the feature set composed of all features, that is:

$$D(S, y) = \frac{1}{m} \sum_{d_i \in S} I_{MIC}\left(d_i, y\right) \tag{4}$$

$$R(S) = \frac{1}{m^2} \sum_{d_i, d_j \in S} I_{MIC}\left(d_i, d_j\right) \tag{5}$$

$$I_{mRMR} = \max_{S} \left(D(S, y) - R(S)\right) \tag{6}$$

Where: d_i is the ith feature sequence; m is the number of feature sequences in the finally selected feature set; I_{mRMR} is the mRMR value of the feature sequence. The final feature subset can be obtained by solving the optimization problem shown in Eq. 6.

2.2 Improved particle swarm optimization–long short term memory (IPSO-LSTM)

2.2.1 Long short term memory

LSTM is a neural network obtained by improving RNN (Hochreiter and Schmidhuber, 1997). Compared with RNN, LSTM can better deal with the problem of gradient disappearance and gradient explosion. The difference between LSTM and RNN is that LSTM adds a memory unit Cell and three gates (input gate, forget gate and output gate) to the neurons in the hidden layer. The internal structure of LSTM is shown in Figure 1.

The propagation formula of the LSTM computing node at time t can be expressed as Eqs 7–11.

$$i_t = g\left(W_{hi} h_{t-1} + W_{xi} x_t + b_i\right) \tag{7}$$

$$c_t = f_t \cdot c_{t-1} + i_t \cdot \tanh\left(W_{hc} h_{t-1} + W_{xc} x_t + b_c\right) \tag{8}$$

$$f_t = g\left(W_{hf} h_{t-1} + W_{hf} x_t + b_f\right) \tag{9}$$

$$o_t = g\left(W_{ho} h_{t-1} + W_{ox} x_t + W_{co} c_t + b_o\right) \tag{10}$$

$$h_t = o_t \cdot \tanh\left(c_t\right) \tag{11}$$

In Figure 1, the input gate controls the information entering the node, the forget gate controls the retention of the historical state in the Cell, and the output gate controls the information of the computing node output.

2.2.2 Improved particle swarm optimization algorithm (IPSO)

The particle swarm optimization algorithm can be described as: Assuming that there is a population of particles in the dimension space, the velocity and position of the ith particle are respectively, and the optimal position of the individual particle and the optimal position of the group at time are evaluated by the objective function. Then iteratively update the velocity and position of each particle by the following formula (Zhang Y. G. et al., 2021).

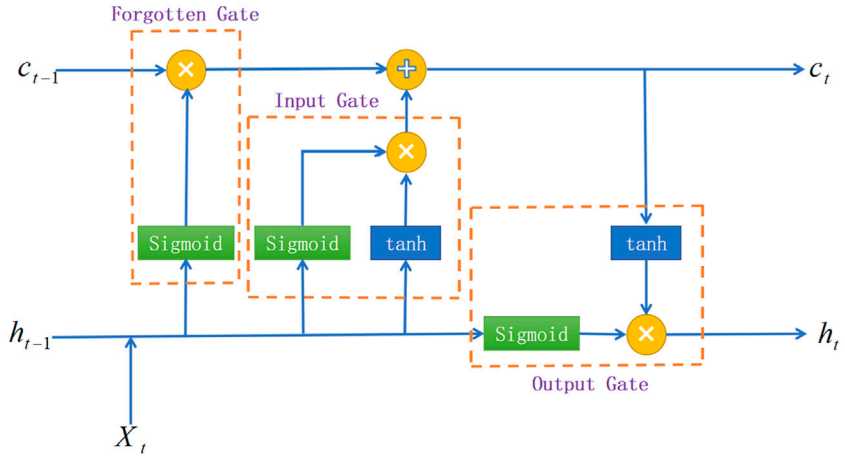

FIGURE 1
The basic LSTM cell.

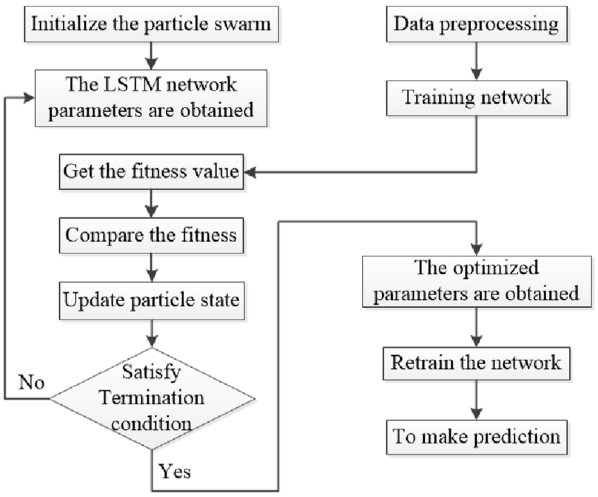

FIGURE 2
IPSO-LSTM flow chart.

$$V_{id}^{k+1} = wV_{id}^{k} + c_1 r_1\left(P_{id}^{k} - X_{id}^{k}\right) + c_2 r_2\left(P_{gd}^{k} - X_{gd}^{k}\right) \quad (12)$$

$$X_{id}^{k+1} = X_{id}^{k} + V_{id}^{k+1} \quad (13)$$

The inertia weight w directly affects the convergence efficiency of the PSO algorithm. Increasing w can improve the global convergence ability of the algorithm, and decreasing can increase the local convergence ability of the algorithm. The constant of the original w algorithm will not change with the increase of the number of iterations, which will weaken the global optimization ability of the algorithm and reduce the convergence speed of the algorithm. A new nonlinear inertia weight w is proposed, which makes the algorithm have better global convergence ability in the initial stage of iteration, and decreases w in the later stage of iteration, thereby improving the local convergence ability of the algorithm. The form w is as follows.

$$w = a \cdot \sin\left(\frac{\pi}{2} \cdot \left(1 - \frac{k}{K_{\max}}\right)\eta\right) + b \quad (14)$$

In the formula: w is the inertia weight; $d = 1, 2, \cdots, n$; $i = 1, 2, \cdots, m$; k is the number of iterations; V_{id} is the velocity of the ith particle in the dth dimension; c_1 and c_2 is a non-negative constant; r_1 and r_2 is the maximum number of iterations; k is the curvature adjustment parameter.

2.2.3 IPSO-LSTM model

The LSTM neural network optimized by the IPSO algorithm is called the IPSO-LSTM model. Taking the two-layer LSTM network as an example, the particles in the IPSO algorithm are, which represents the number of neurons in the first hidden layer of the LSTM network, and represents the second LSTM network. The number of neurons in the hidden layer represents the learning rate of the LSTM network.

The flowchart of the IPSO-LSTM network model is shown in Figure 2.

The specific steps in Figure 2 are as follows:

Step 1: Preprocess the sample data, remove abnormal data, fill in the incomplete data, convert the input data into matrix form, and initialize the IPSO algorithm parameters

Step 2: Define fitness. The mean square error of the predicted value of the LSTM network is used as the particle fitness value fit;

$$fit = \frac{1}{n}\sum(\hat{y} - y)^2 \quad (15)$$

Step 3: Using the position information of the particles as the parameters of the LSTM network, construct multiple LSTM networks

Step 4: Train all networks to get the fitness value of each particle. Update individual extrema and group extremum

Step 5: Iteratively update particle velocity and position information with nonlinear inertia weights according to individual extremum and group extremum

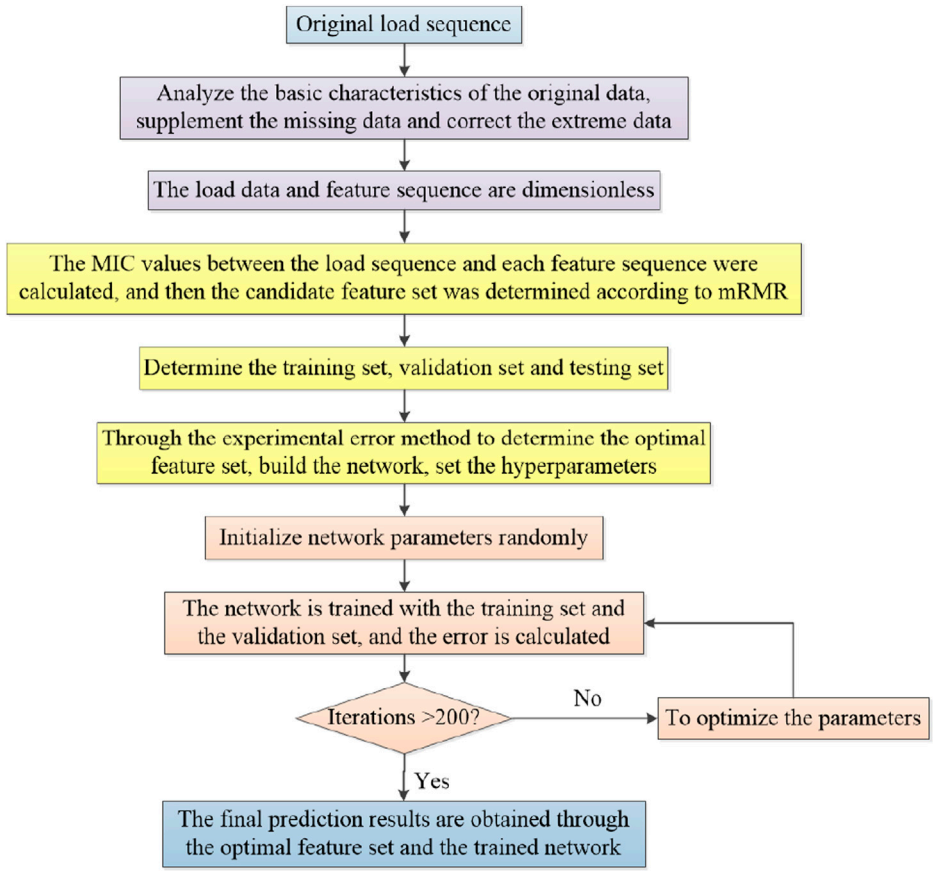

FIGURE 3
Overall framework.

Step 6: Stop iterating after meeting the conditions or reaching the maximum number of iterations, otherwise go back to Step 3

Step 7: Get the optimized parameters, increase the number of iterations to 100, and retrain the LSTM network

Step 8: Predict through the trained IPSO-LSTM network.

2.3 A novel hybrid model based on mRMR and IPSO-LSTM

Based on the above analysis, this section proposes a forecasting model based on mRMR and IPSO-LSTM for the short-term forecasting of EV charging loads during the COVID-19 pandemic, and the overall framework is shown in Figure 3.

The framework shown in Figure 3 can be summarized into three parts, which are as follows.

Part 1: Data processing. Analyze the basic characteristics of original data, supplement missing data, and correct extreme data and abnormal data.

Part 2: Feature extraction. Considering the hysteresis of epidemic factors, a factor set containing five groups of 20 epidemic factors was established, and the feature sequence is dimensionless processed, and the mRMR method is used to obtain the optimal feature set.

Part 3: Final forecast. The optimized LSTM model is obtained by IPSO, and the elements in the optimal feature set are added to predict the electric vehicle charging load to obtain the final forecast result.

2.4 Evaluation indicators

In this study, the mean absolute error (MAE), root mean square error (RMSE) and symmetric mean absolute percentage error (SMAPE) were selected as the evaluation criteria for evaluating the forecast accuracy of each model, and the calculation formula is shown in Eqs 16–18.

$$MAE = \frac{1}{N}\sum_{i=1}^{N}\left|\hat{y}_i - y_i\right| \tag{16}$$

$$RMSE = \sqrt{\frac{1}{N}\sum_{i=1}^{N}\left(\hat{y}_i - y_i\right)^2} \tag{17}$$

$$SMAPE = \frac{100}{N}\sum_{i-1}^{N}\frac{\left|\hat{y}_i - y_i\right|}{0.5\left(\left|\hat{y}_i\right| + \left|y_i\right|\right)} \tag{18}$$

Where: N is the number of samples, y_i is the measured value, $\hat{y}_i$ is the predicted value.

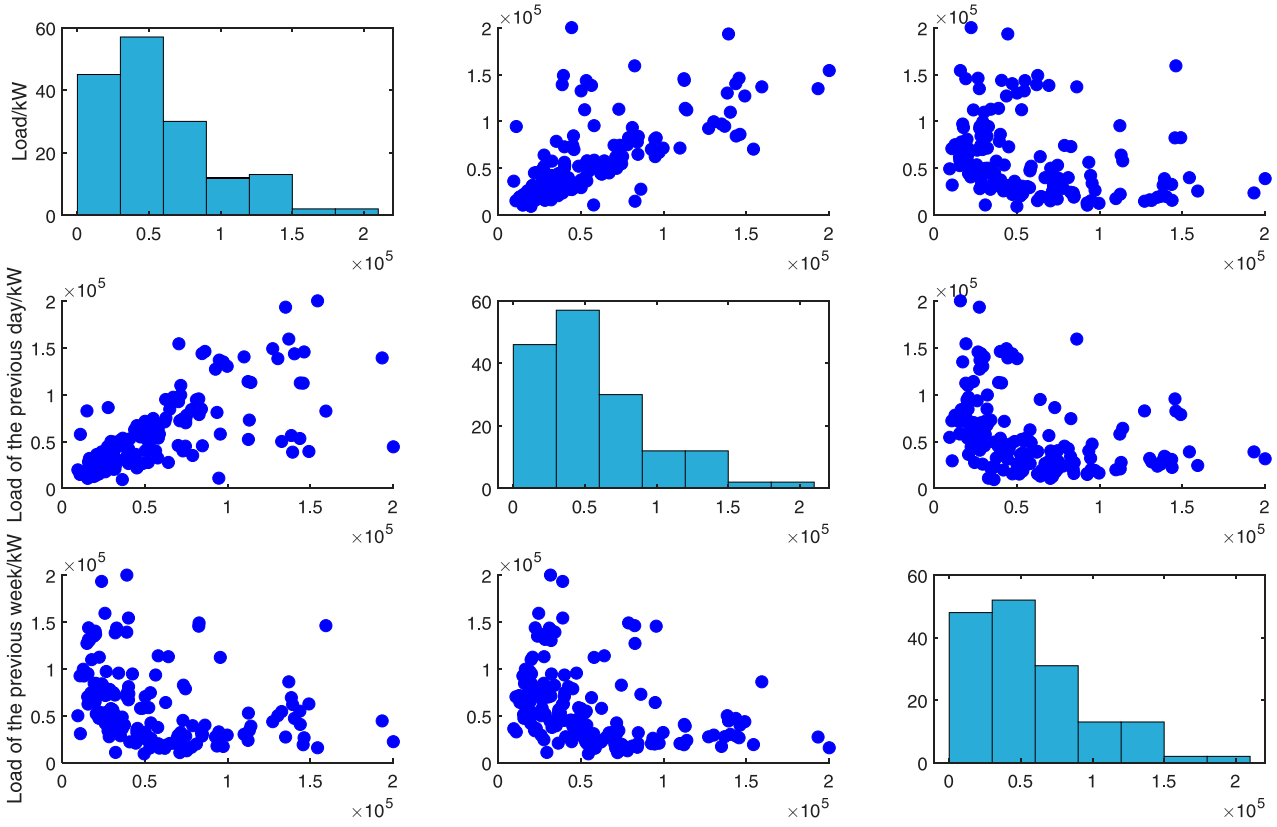

FIGURE 4
Correlation between time factor and charging load.

3 Analysis of influencing factors of electric vehicle charging load

The charging load of electric vehicles is mainly affected by travel willingness, and its daily variation is mainly affected by charging habits and charging prices. Under normal circumstances, the production and life in an area have regularity, so the charging load changes have periodicity, and the fluctuation of adjacent days will not be very large. However, in some regional special events, some traffic control measures may be taken, or some policies and guidelines may be implemented to restrict people's travel, which may directly or indirectly affect the user's travel psychology, thereby changing the travel route or reducing the travel, and then affecting the charging load of some regions or the whole region's charging station.

3.1 The influence of conventional factors on charging load

Conventional factors mainly consider the impact of time, date type, weather and so on.

3.1.1 Influence of time factor on charging load

Time factors mainly include seasonal, holiday and cyclical factors. Cyclical factors can be divided into daily cyclical factors, weekly cyclical factors, monthly cyclical factors and annual cyclical factors. The data selected in this paper is from November 2021 to April 2022, a total of 6 months, so only the influence of daily cyclical factors and weekly cyclical factors are considered. The correlation between time factor and charging load is shown in Figure 4.

Figure 4 shows the degree of correlation between the load of the previous day and the load of the previous week and the current load at the current time, in which the load of the previous day and the current load show an obvious positive correlation, while the correlation between the previous week and the current load is not obvious, and the three factors also have mutual influence.

3.1.2 The impact of date type on charging load

The user's travel habits may be affected by the date type, and there is a difference between non-working days such as weekends or holidays and working days, which will cause changes in the charging load. Load statistics are collected from Monday to Sunday, as shown in Table 1.

As can be seen from Table 1, the load varies from Monday to Sunday. The maximum load from Monday to Friday is 218000 kW (Tuesday), which is larger than the load on Sunday, while the minimum load is 159000 kW (Monday), which is smaller than the load on Saturday, with no obvious difference. Therefore, the effect of date type on charging load needs further study.

TABLE 1 Date type and charging load statistics.

Date type	Maximum load/	Average load/
Monday	1.59	5.59
Tuesday	2.18	6.22
Wednesday	1.49	5.14
Thursday	1.48	5.24
Friday	1.93	5.98
Saturday	1.62	4.97
Sunday	2.00	5.56

3.1.3 The influence of meteorological factors on the charging load

The charging load of electric vehicles will be affected by users' willingness to travel. For example, when encountering extreme weather, users will reduce unnecessary travel, leading to a decrease in charging load, while weather types will affect temperature, relative humidity and air quality index. For example, when there is heavy rain, it may cause a decrease in temperature, an increase in relative humidity, a decrease in air quality index and a decrease in wind. The temperature will affect the driving range of electric vehicles, the longest driving range when the temperature is moderate, the shortest driving range when the temperature is too high or too low, and the temperature will also affect the use of air conditioning in the car, the use of air conditioning will increase power consumption. Figure 5 shows the correlation between temperature, relative humidity, wind, air quality index, and charging load.

As shown in Figure 5, there is a strong positive correlation between temperature and load. As the temperature rises, the use of air conditioning in the car increases the load. However, it can also be seen that when the temperature is low, the load is also at a higher level due to the increase in vehicle power consumption. There is a strong negative correlation between relative humidity and load, because the change of humidity is related to precipitation in many cases, when the weather is not good, it will affect the desire to travel, avoid unnecessary travel and lead to load reduction. When the weather is particularly good, travel enthusiasm is strong, and the increase of vehicle frequency leads to the increase of load. There was no significant correlation between wind and air quality index and charging load.

3.1.4 Influence of time-of-use price on charging load

Most of the public charging stations in the city adopt time-of-use (TOU), and the implementation of TOU is of great significance to guide the orderly charging of electric vehicles and reduce the pressure on the grid. The charging price of charging stations using TOU is mostly divided into 6 periods (the price may be different), each period and the corresponding price are shown in Table 2. The price in the table is electricity, excluding service fee.

As can be seen from Figure 6, the peak daily load of electric vehicle charging load appears at 0, and the trough price is just from 23 to 6. During this period of time, the load is high in most cases, and the charging price during the time of 11:00–18:00 is medium, but after a morning of power consumption, some vehicles that need to supplement the power during the day will choose to charge at this time, and after 18:00 is the rush hour, some commuter cars will

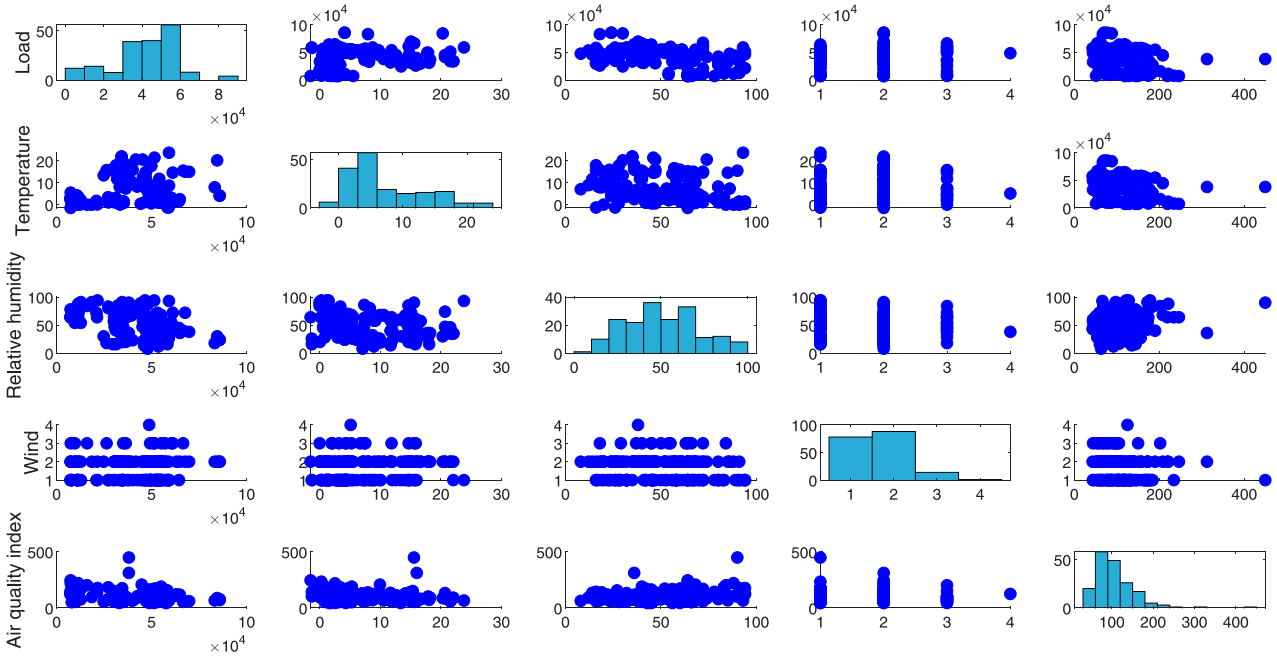

FIGURE 5
Correlation between temperature, relative humidity, wind, air quality index and charging load.

TABLE 2 Electric vehicle charging station price information.

Time	Price (Yuan/degree)
0:00–6:00	0.25
6:00–8:00	0.60
8:00–11:00	0.95
11:00–18:00	0.60
18:00–22:00	0.95
22:00–24:00	0.25

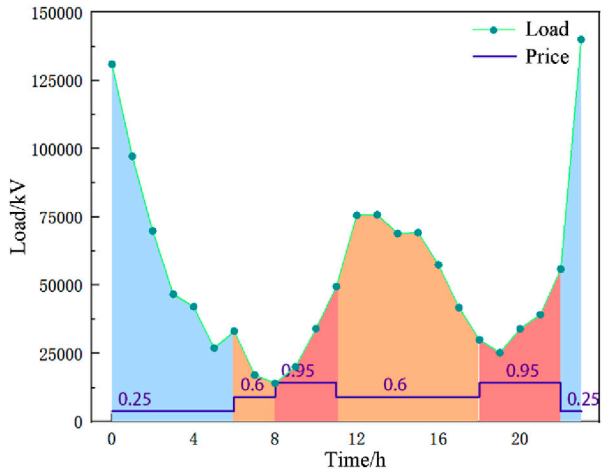

FIGURE 6
Time division tariff and its corresponding load change.

charge at this time, so the load is larger. However, on the whole, it basically conforms to the characteristics of large load when the price is high and small load when the price is low.

3.2 The influence of unconventional factors on charging load

In addition to the routine factors mentioned in 3.2, taking into account the key events in recent years in China, the novel coronavirus epidemic, which has had a huge impact on people's production and life in the past 3 years, is selected as the main unconventional factors to study from four aspects: the number of new confirmed cases, the number of high-risk areas, the number of medium-risk areas, and epidemic prevention policies. The correlation between epidemic factors and charging load is shown in Figure 7.

As can be seen from Figure 7, the number of newly confirmed cases, the number of high-risk areas, the number of medium-risk areas, and epidemic prevention policies are negatively correlated with the charging load. The more new confirmed cases, the more serious the outbreak. The greater the number of high risk areas indicates the greater the number of areas seriously affected by the epidemic, which indicates the depth of the development of the epidemic to a certain extent. The more at-risk areas, the more areas affected by the epidemic, to a certain extent indicates the breadth of the epidemic development, and the more stringent epidemic prevention policies, indicating that the more areas are sealed and controlled, the more restrictions on people's travel, all of which will reduce the load. The new confirmed cases were negatively correlated with the epidemic prevention policy, indicating that the epidemic prevention policy has been dynamically adjusted in strict accordance with the development of the epidemic situation, and the epidemic prevention policy has indeed prevented the further spread of the epidemic, which is in line with the development law of the epidemic, and is suitable for epidemic prevention and control. The number of high-risk areas and the number of medium-risk areas is positively correlated with epidemic prevention policy. According to China's epidemic prevention policy, according to the number of newly confirmed cases, regions can be divided into high-risk areas and medium-risk areas, and at some times, they are also divided into prevention areas, while high-risk areas will be banned or restricted to go out (by time or by number of people), indicating that the more the number of medium-risk areas, the more the number of high-risk areas, the more the number of high-risk areas. The more stringent the epidemic prevention policy. Therefore, when making predictions, it is very necessary to consider such unconventional factors as the epidemic.

4 Case analysis

4.1 Data sources

In this paper, the load of electric vehicles under the influence of COVID-19 in a city in China is taken as the research object. In recent years, the city's new energy vehicle industry has developed rapidly. The province's electric power company built a new energy vehicle intelligent monitoring platform in July 2019, which can monitor the operation of charging piles in real time. This article obtained the electric vehicle load data for a total of 181 days in the capital city of the province from 1 November 2021 to 30 April 2022 through this platform, and obtained meteorological data such as temperature on the website of the city's meteorological bureau. The data sampling interval for 1 h, a total of 4,344 samples were collected. The epidemic-related data was obtained on the website of the Provincial Health and Health Commission. The data sampling interval was 1 day, and a total of 181 samples were collected. In this process, there may be data missing and data mutation. In this paper, the interpolation method is used to ensure the smoothness of the data. When it is judged that the original data is 0 or abrupt, the data average of the previous time and the next time is used to replace the missing data. If the continuous data is 0, the data of the previous moment will be uniformly used instead.

$$d_t^{'} = \begin{cases} 0.5\left(d_{t-1} + d_{t+1}\right) & d_t = 0, d_{t+1} \neq 0 \\ d_{t+1} & d_t = 0, d_{t+1} = 0 \\ d_t & d_{t+1} \neq 0 \end{cases} \tag{19}$$

Where: d_{t-1} is the data at the previous moment; d_{t+1} is the data at the next moment; d_t and $d_t^{'}$ are the data before and after the correction at the current moment, respectively.

During this period, the city experienced two local outbreaks in December 2021 and March 2022 respectively, among which the

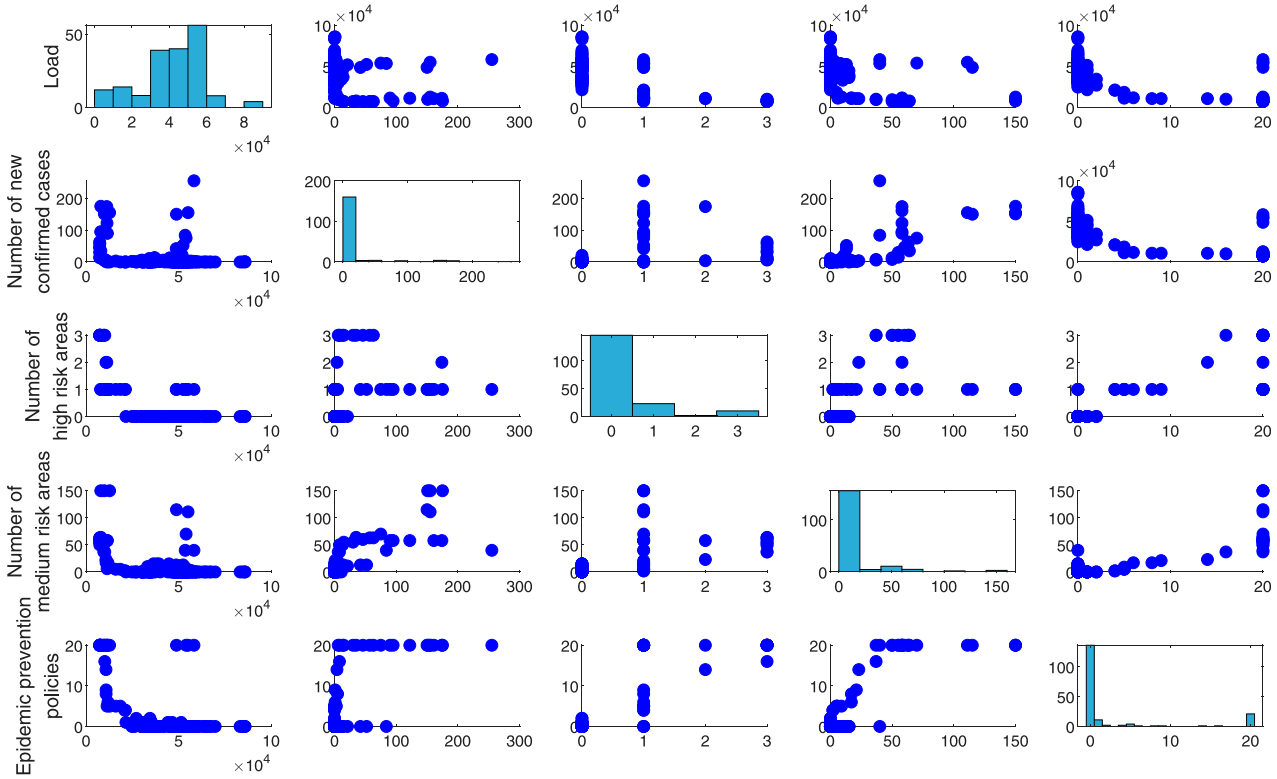

FIGURE 7
Correlation between epidemic factors and charging load.

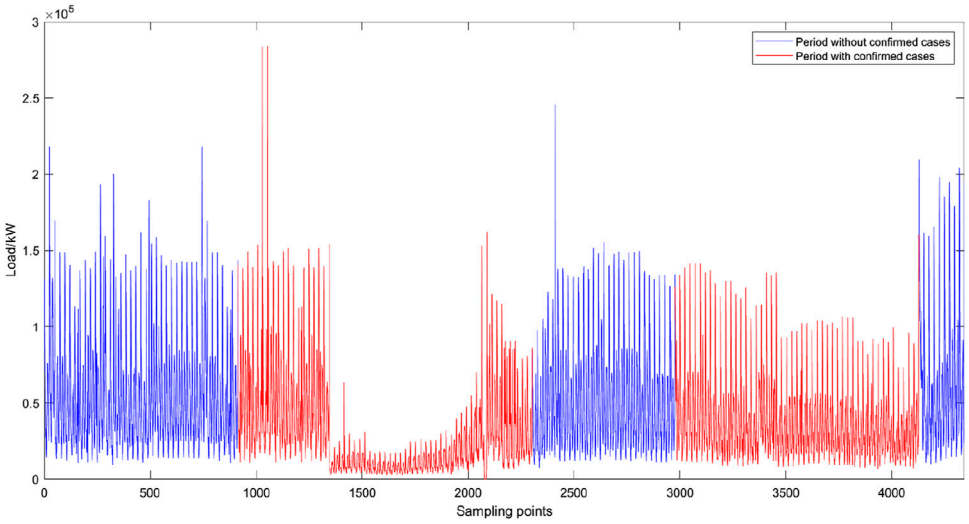

FIGURE 8
The load in the period with and without confirmed cases.

outbreak on 9 December 2021 was the most severe outbreak in the city since the COVID-19 outbreak in 2019. The load in the period with and without confirmed cases is shown in Figure 8.

It can be seen from Figure 8 that COVID-19 has a significant impact on EV load, and the two impacts have different degrees, with the impact of the December epidemic being greater than that of the March epidemic. COVID-19 indirectly affects EV load by affecting people's travel conditions to a certain extent. Compared with other factors, this impact is more complex, irregular, non-cyclical and has a lag. Table 3 shows the electric vehicle load and epidemic statistics in the city.

TABLE 3 Statistics of electric vehicle load and epidemic situation.

The data type	Data length	Maximum value	Minimum value	Average value	Standard deviation
Electric vehicle load	4,344	283871.68	51.04	41961.76	34491.67
New confirmed cases	181	255	0	13.34	39.15
Number of moderate risk areas	181	150	0	11.03	26.85
Number of high risk areas	181	3	0	0.31	0.76

The data presented in Table 1 can be seen as follows: (1) For the charging load of electric vehicles, its maximum value is large, indicating that the city has a high ownership of electric vehicles. There is a huge difference between the maximum value and the minimum value, and the standard deviation is large, and the ratio to the average value is also large but less than 1, indicating that the load is volatile. (2) For the new confirmed cases and the number of medium-risk areas, the two types of data had a large maximum value, indicating that there was a large-scale epidemic in the city in some periods. There is a big difference between the maximum value and the minimum value, and it has a large standard deviation. The ratio of the standard deviation and the average value is between two to three, indicating that these two types of data are highly volatile, which can reflect the impact scope of the epidemic to a certain extent, and their changes may cause some epidemic prevention policy changes. (3) For the number of high-risk areas, the maximum value is not large, and there is little difference between the minimum value and the maximum value. The standard deviation is also small, but the ratio to the average is large, which indicates that the data is highly volatile and reflects the severity of the epidemic to a certain extent. The change of the data may also cause some epidemic prevention policy changes.

4.2 Feature selection based on mRMR

There are many kinds of feature sequences in EV load forecasting, and it is necessary to calculate the correlation between these feature sequences and the load series to be predicted, and select an appropriate set of feature sequences as the input of the forecasting model. The influence of meteorological factors such as temperature and date types are usually considered in the prediction of power load. It is assumed that these factors will also have a certain impact on the charging load of electric vehicles. Therefore, these influencing factors and the impact of COVID-19 are taken into account in this paper. Considering the hysteresis of epidemic factors, it is assumed that EV charging load will be affected by epidemic factors 1–3 days before the current day, and the influencing factor set is established as shown in Table 4.

Take P_t、 DL_t and CC_t in the table as examples, P_0 represents the current electricity price, P_1 represents the electricity price 1 h ago; DL_1 represents the load value at the same time 1 day ago, DL_2 represents the load value at the same time 2 days ago, CC_0 represents the new confirmed cases of the day, CC_1 represents the new confirmed cases of the day before.

Before feature selection, data should be processed dimensionless to make the data have the same specification and accelerate the convergence of neural network. Electric vehicle load, meteorological series and electricity price data can be normalized to the interval [−0.5, 0.5] to achieve dimensionless. Different from the common [0, 1] interval, neural networks tend to input data centered on 0. Therefore, setting the center of the normalized interval as 0 is conducive to the convergence of neural networks, and normalization is shown in Eq. 20.

$$d = \frac{d - \frac{d_{\max}+d_{\min}}{2}}{d_{\max} - d_{\min}} \tag{20}$$

Where: d_{max} and d_{min} are the maximum and minimum values of d respectively.

The date type sequence defines working days as 0, weekends as 1, and holidays as 2 to identify the load characteristics of different date types.

Since the time granularity of epidemic data was inconsistent with EV charging load data, MIC was first used to analyze the correlation between epidemic data and daily average load. The results showed that MIC values of 20 epidemic related information were all above 0.8, showing strong correlation. In order to improve the sensitivity of intra-day load to epidemic information, the charging load of electric vehicles was divided according to whether there was an epidemic (the first confirmed case was regarded as the beginning of an epidemic, and the 7-day absence of new cases was regarded as the end of an epidemic). The average value of the two groups of data was respectively taken as the typical characteristic curve of epidemic period and non-epidemic period. Thus, the proportion of load at each moment in the total load of a day can be obtained, that is, the proportion of epidemic period and non-epidemic period. Then, multiply the epidemic information to get the epidemic data with unified time granularity. For such data, if the interval −[−0.5, 0.5] is used, the discrimination degree is low. Therefore, the interval of epidemic data is mapped to [0,10] to improve the sensitivity to epidemic information with a larger interval range.

In order to consider the correlation between the single characteristic variable and the target variable, as well as the linear and nonlinear relationships, MIC method can be chosen to judge the correlation between two sequences. The correlation between each sequence is shown in Figure 9.

The MIC value of some sequences in Figure 9 and itself is not 1, because it is necessary to grid d_X and d_Y when calculating the MIC. When the series is discrete data and the distribution is very uneven, the MIC value of the same series is likely to be different from 1, which is a normal situation and does not affect the conclusion. The feature set with MIC values greater than 0.6 were selected from high to low according to the MIC, as shown in Table 5.

As can be seen from Figure 9, the feature subset selected according to the MIC method in Table 3 have a lot of redundant

TABLE 4 Influencing factor set.

Factors type	Influencing factors	Display method
Meteorological factors	Temperature	T
	Relative humidity	H
	Wind	W
	Air quality index	A
Electricity prices	Current time and previous 1 h electricity price	P_t
The date type	Date type	D
Historical load value	Load value 1–3 h before the current time	HL_t
	Load value 1–3 days before the current time	DL_t
	Load value 1–3 weeks before the current time	WL_t
Epidemic factors	New confirmed cases in the city on that day and the previous 1–3 days	CC_t
	Number of medium risk areas in the city for the day and the previous 1–3 days	NM_t
	Number of high risk areas in the city for the day and the previous 1–3 days	NH_t
	Whether the city was infected on that day and 1–3 days before	YN_t
	Epidemic prevention policy of the City for the day and the previous 1–3 days (Lockdown/No-lockdown)	EP_t

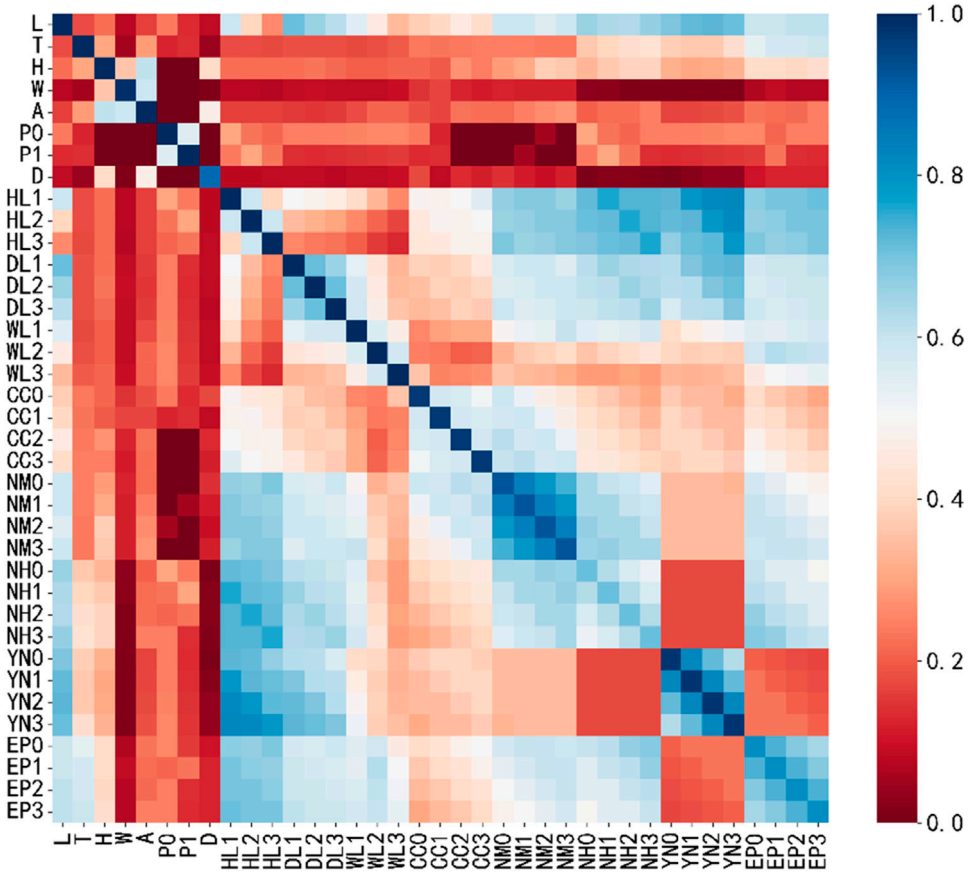

FIGURE 9
MIC between each sequences.

TABLE 5 Feature sets obtained by feature selection (MIC and mRMR).

The sorting	Feature selection method	
	MIC	mRMR
1	YN_2	DL_1
2	YN_1	DL_2
3	DL_1	YN_2
4	YN_3	HL_1
5	YN_0	EP_3
6	NH_0	NH_3
7	NH_2	NM_3
8	DL_2	CC_3
9	NH_3	T
10	NH_1	DL_3
11	DL_3	EP_0
12	EP_3	A
13	EP_2	H
14	EP_1	WL_1
15	HL_1	WL_2
16	EP_0	HL_2

information. For example, the correlation of: YN_1 and YN_0、YN_2, YN_3 and YN_2 are very high (0.83), and the information is almost completely repeated. They should not exist in the feature subset at the same time. Therefore, in order to reduce the redundancy of feature sequences, mRMR method is selected on the basis of MIC to achieve feature selection (Xie et al., 2017). The feature subset selected by mRMR is shown in Table 5.

4.3 Electric vehicle charging load forecast based on IPSO-LSTM

Set the data according to 6: 2: 2 is divided into training set, validation set and testing set, where the data of training set is the first 109 days (data volume is 2,616, accounting for 60.22%), validation set is the middle 36 days (data volume is 864, accounting for 19.89%), and testing set is the last 36 days (data volume is 864, accounting for 19.89%), as shown in Figure 10.

In Figure 10, blue is the training set, green is the validation set, and red is the testing set. Both the training set and the testing set included epidemic period and non-epidemic period, which ensured the accuracy of the model establishment and the reliability of the test. The validation set is used to determine the number of input features and the input parameters in the IPSO-LSTM model.

The initial parameters in the IPSO-LSTM model were set as: the number of individuals in the population was 10; The iteration number $K_{\max}$ is 20; The value range of neuron number l_{1i} and l_{2i} in hidden layer of particle X_i $(l_{1i}, l_{2i}, \varepsilon_i)$ is (The State Council of the People's Republic of China; Peng et al., 2005); The value range of learning rate ε is [0.005,0.05]; The value range of velocity of each dimension is [−1,1], [−1,1], [−0.002,0.002]; a = 0.6; b = 0.3; η = 1.7; The optimizer is Adam; The number of input neurons is three load values and their corresponding characteristics; The number of output neurons is 1 (Zhang Y. G. et al., 2021). IPSO was used to optimize the three parameters in LSTM, and the

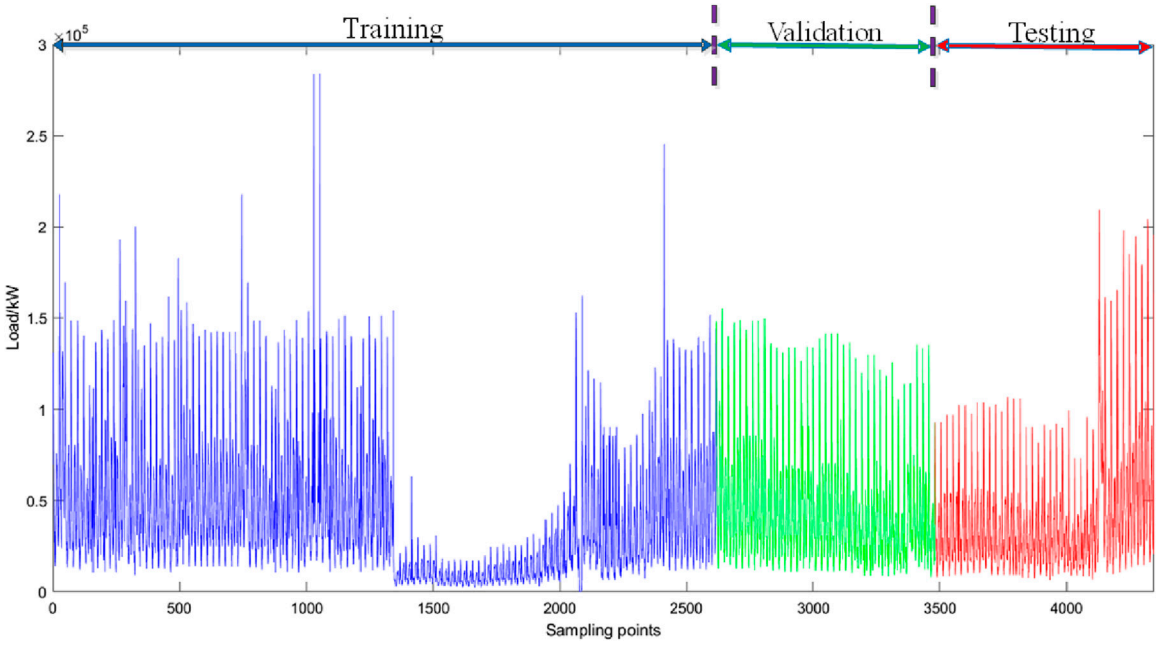

FIGURE 10
The load value of training and testing data set ranged from 1/11/2021 to 30/4/2022.

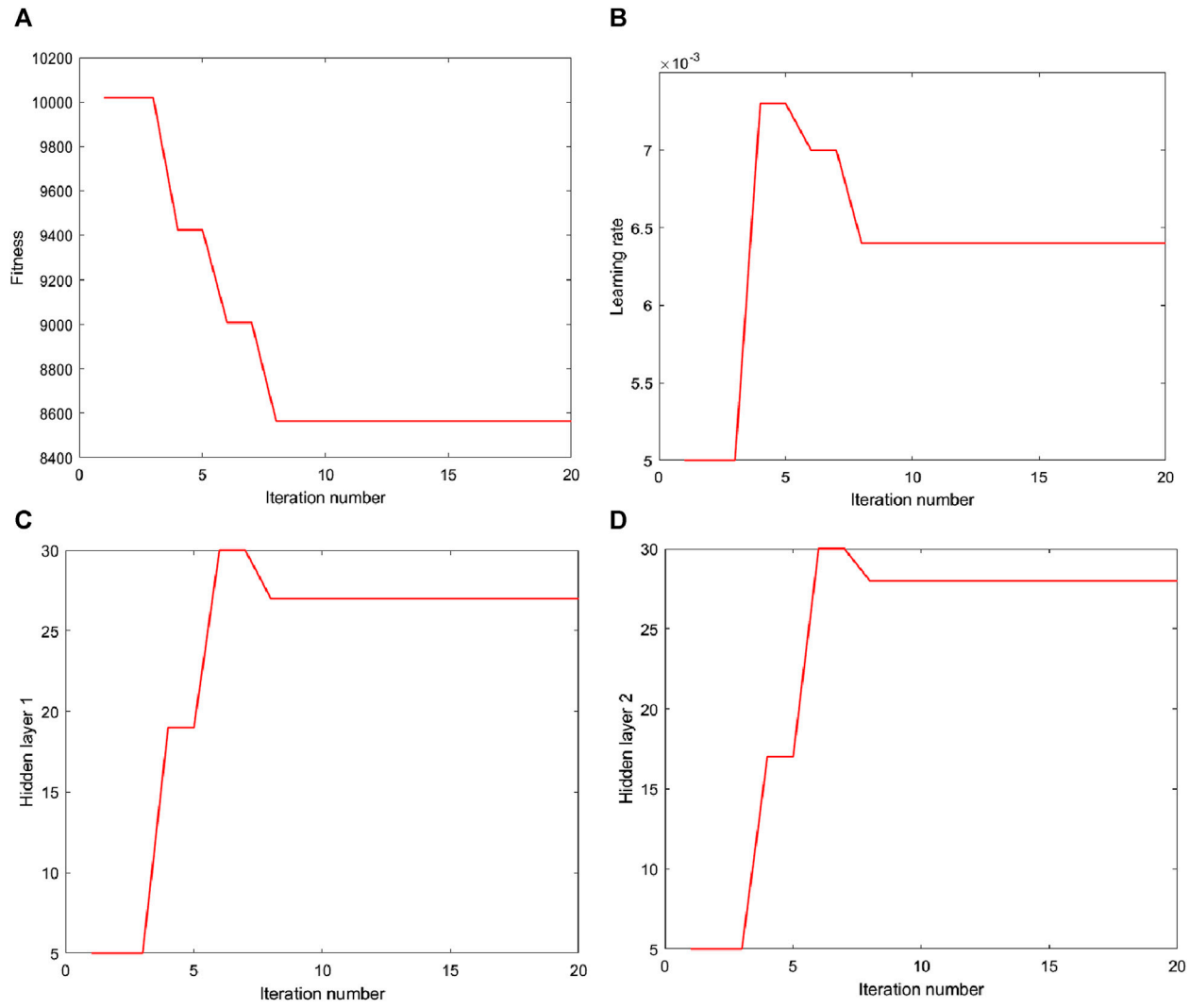

FIGURE 11
Adaptation and hyperparameter variation curves. **(A)** Fitness. **(B)** Learning rate. **(C)** Hidden layer 1. **(D)** Hidden layer 2.

fitness function was set to the minimum MAE. The curves of fitness, the number of neurons in the two hidden layers and the learning rate obtained in the optimization process were shown in Figure 11.

As can be seen from Figure 11, the fitness value tends to be stable at the eighth iteration after two declines, and the optimal parameter after IPSO optimization is as follows: the number of neurons in hidden layer 1 is 27, the number of neurons in hidden layer 2 is 28, and the learning rate is 0.0064.

The influencing factors in Table 5 were input into the forecasting model one by one in order, and the minimum number of input features of SMAPE was taken as the optimal feature set. The relationship between the error on the validation set and the number of input features is shown in Figure 12.

In Figure 12, SMAPE values are different under different number of input features. When the number of input features is 1–12, the SMAPE value fluctuates continuously, and when the number of input features is 6, the SMAPE value is the smallest. When the number of input features is greater than 12, the SMAPE value increases rapidly, which indicates that the more input features is not the better, and too much input will make the model not selective. Therefore, the number of input features is chosen to be 6.

Finally, the optimal feature set of the forecasting model is $\{DL_1, DL_2, YN_2, HL_1, EP_3, NH_3\}$. The electric vehicle load forecast results of the city based on the IPSO-LSTM model and the optimal feature set considering the impact of the epidemic are shown in Figure 13.

As can be seen from Figure 13A, the forecast effect at the peak is poor, while the prediction effect at other points is good. In Figure 13B, when the load value is greater than 120000 kW, the point is far away from the dashed line, which also verifies the deficiency of peak prediction. When the load value is less than 120000 kW, the predicted point falls near the dashed line, which has good accuracy.

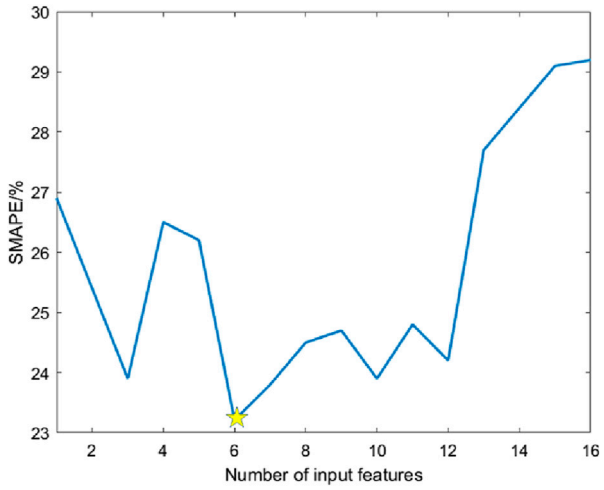

FIGURE 12
SMAPE with different number of input features.

5 Comparative analysis and discussion

In order to verify the forecast accuracy and stability of the proposed model in multiple dimensions, three experiments are compared in this section.

5.1 Comparison of forecasting models

In order to verify the forecast accuracy and stability of the proposed model, four different forecasting models, namely, BPNN, ARMA, LSTM and IPSO-LSTM, are used for comparison. Figure 14 shows the forecast results of the four forecasting models.

It can be seen from Figure 14 that the IPSO-LSTM model is better than BPNN, ARMA and LSTM. However, in general, the errors of the four models are larger when the load value is greater than 100000 kW. As a whole, the forecast effect increases with the increase of the load value, and the forecast effect further decreases when the peak value is large.

Table 6 shows the forecast performance indexes when the four forecasting models are adopted.

According to the forecast performance index results in Table 4, it can be seen that IPSO-LSTM > LSTM > ARMA > BPNN as a whole in terms of forecast effect. In terms of MAE value, IPSO-LSTM decreased by 25.02%, 18.63% and 2.41% compared with BPNN, ARMA and LSTM, respectively. In terms of RMSE and SMAPE, IPSO-LSTM is also 2%–13% lower than BPNN, ARMA and LSTM, respectively. This shows that LSTM can better learn the long-distance dependence relationship depending on its own advantages, which is suitable for application in EV charging load forecasting.

5.2 Comparison of different sets of influencing factors

To measure the influence of COVID-19 epidemic related factors on EV load forecasting, this paper divides the influencing factor set into two categories: one is all factors except epidemic factors in Table 2, which is represented by Ω_1 for convenience; One category is all the factors shown in Table 2, which is denoted by Ω_2 for convenience. Figure 15 shows the forecast results of EV charging load in the city under different influencing factor sets.

It can be seen from Figure 15 that the forecast effect is not significantly improved when the influencing factor set is Ω_1, compared with that without considering the influencing factors. However, when the influencing factor set is Ω_2, the forecast effect of the high-load area is significantly improved. Figure 10B clearly shows that in the region of 15000KW-21000 kW load value, there is a significant gap with the influencing factor set Ω_1. Compared with Figure 10A, it can be seen that the load in this range is the peak load point of non-epidemic period after the epidemic ended in March. These results show that: (1) adding epidemic factors to EV charging load forecasting can improve the forecast effect; (2) Adding epidemy-related factors can improve the forecast effect from areas with high load values, the essence of which

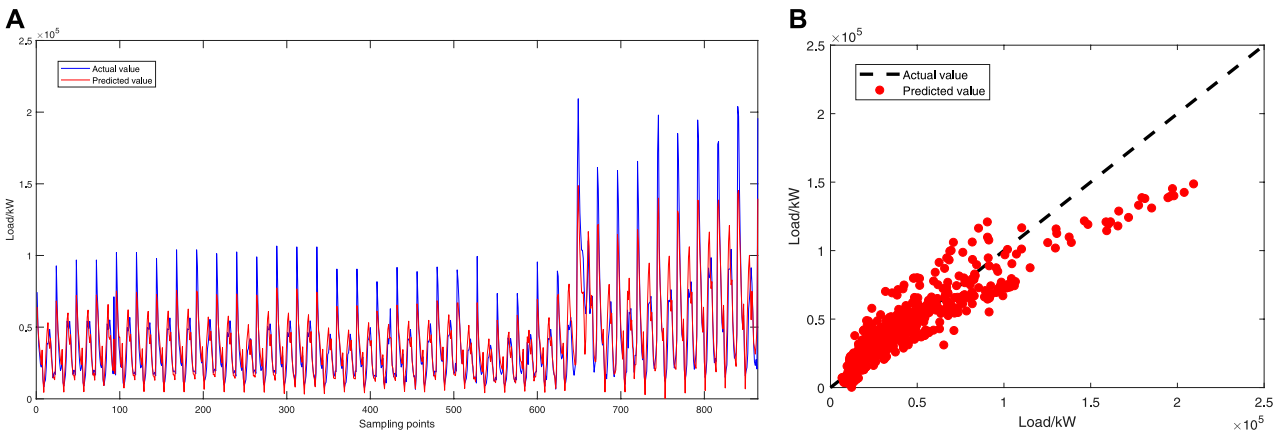

FIGURE 13
Final forecast results. **(A)** Forecast result chart, **(B)** Forecast scatter plot.

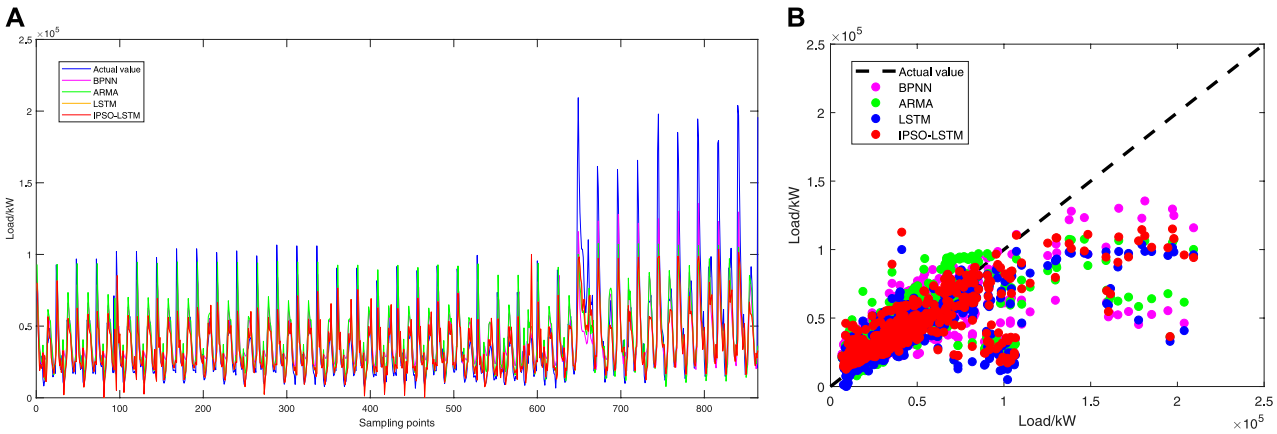

FIGURE 14
Comparison of the forecast results of the four forecasting models. **(A)** Forecast result chart, **(B)** Forecast scatter plot.

TABLE 6 Forecast performance indexes of the four forecasting models.

Forecasting model	MAE	RMSE	SMAPE
BPNN	14446.80	23083.79	36.95
ARMA	13312.23	22606.67	31.64
LSTM	11099.78	20332.21	27.80
IPSO-LSTM	10831.79	20259.53	27.10

TABLE 7 Forecast performance indexes under different sets of influencing factors.

Set of influencing factors	MAE	RMSE	SMAPE
—	10831.79	20659.53	27.10
Ω_1	10127.67	20604.54	24.20
Ω_2	8461.82	12686.39	22.61

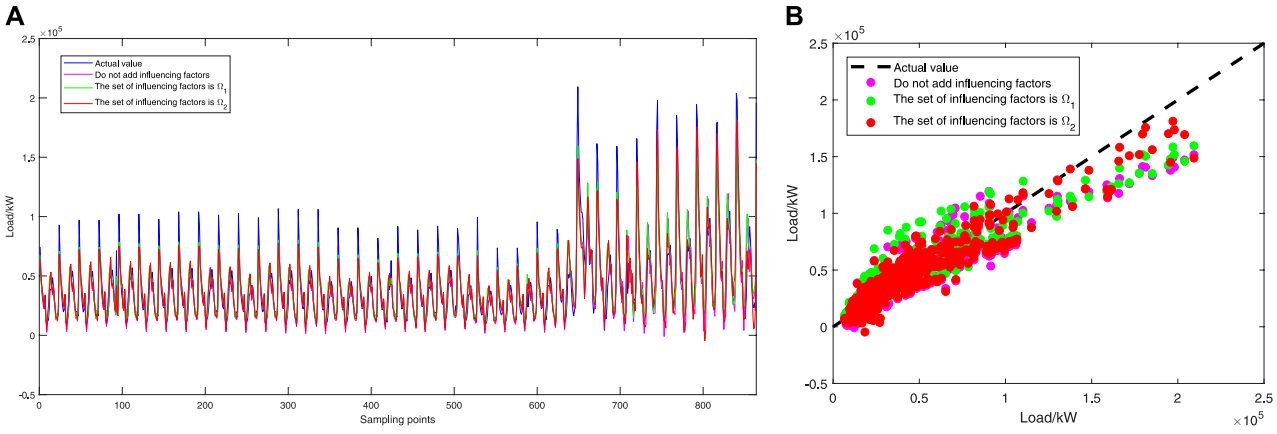

FIGURE 15
Comparison of forecast results under different influence factor sets. **(A)** Forecast result chart, **(B)** Forecast scatter plot.

is to identify the sudden change point of load by quantifying the influencing factors of epidemic.

Table 7 shows the forecast performance indexes under different sets of influencing factors.

As can be seen from Table 5, when the influencing factor set is Ω_1, MAE, RMSE and SMAPE are reduced by 6.50%, 0.26% and 10.70%, respectively, compared with when the influencing factors are not considered. When the influencing factor set is Ω_2, MAE, RMSE and SMAPE are reduced by 16.45%, 38.43% and 6.57%, respectively, compared with that when the influencing factor set is Ω_1. These results show that: (1) adding influencing factors to EV charging load forecasting can improve the forecast effect; (2) The improvement of the forecast effect by adding traditional influencing factors may be universal, that is, it is reflected in the low-load value area without mutation. That is, the top two-thirds of Figure 15A, and the lower load in the bottom third, but it is difficult to capture the turning point from

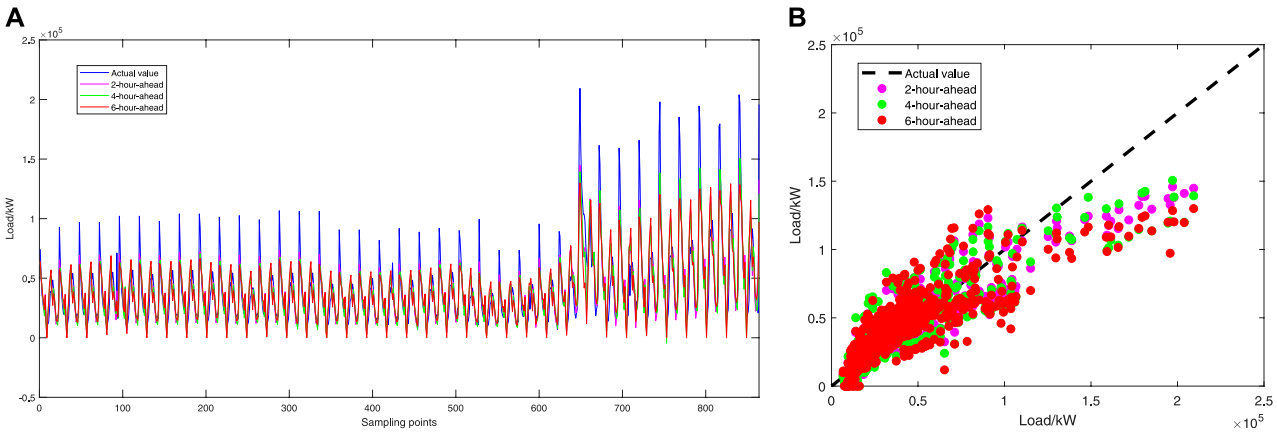

FIGURE 16
The forecast results of the model proposed in this paper in different forecast periods (2 h, 4 h, 6 h). **(A)** Forecast result chart, **(B)** Forecast scatter plot.

TABLE 8 Evaluation index values of the forecast model proposed in this paper in different forecast periods.

Forecast period (h)	MAE	RMSE	SMAPE
2	87846.89	13204.91	24.39
4	10078.42	15342.53	28.85
6	11760.03	17500.07	34.26

epidemic to non-epidemic period; (3) The addition of epidemic factors significantly improved the forecast effect.

The above research shows that the model proposed in this paper has a satisfactory effect on single-step forecasting. However, in addition to focusing on the accuracy of the forecast, the forecast results of different foresight periods are of great significance for the intraday demand-side response with EV charging loads.

5.3 Comparison of different forecast periods

The model proposed in this study is taken as an example to illustrate the impact of different forecast periods on the forecast results. Figure 16 shows the forecast results for the different forecast periods (2 h, 4 h, 6 h).

As can be seen from Figure 16, with the growth of the foresight period, the deviation on the peak and valley value gradually increases. This is due to the gradual accumulation of errors as the forecast period increases, which reduces the forecast accuracy. In addition, the accuracy of the forecasting at the turning point of the epidemic also decreased, which may be because the sensitivity of the quantitative treatment of epidemic factors for longer time changes is not obvious. Table 8 lists the evaluation index values of the forecasting model for the different forecast periods.

In Table 8, the MAE, RMSE and SMAPE all increase with the growth of the foresight period, which is consistent with the results in Figure 16.

6 Conclusion

The main purpose of this study is to design an EV charging load forecasting model with high accuracy that can quickly respond to epidemic situations (or similar emergencies). In the case study, we test the performance of the proposed model using measured data during the COVID-19 in a city in China. The results show that:

(1) Aiming at the determination of hidden layer parameters and learning rate in LSTM, IPSO was used to optimize the training parameters, and the best parameters suitable for such data were determined in the validation set, which improves the prediction accuracy. The example showed that the accuracy of the LSTM network optimized by IPSO can be improved by 2% compared with that before optimization, which proves the effectiveness of the proposed model.

(2) By affecting travel, the epidemic has affected charging loads of electric vehicles. The charging load of electric vehicles in the two epidemic periods showed great changes compared with the non-epidemic period, but the changes were different. It can be considered that COVID-19 has a very important impact on the charging load of electric vehicles, and the impact results are related to the severity and spread of the epidemic. It is therefore reasonable to take epidemic factors into account in such forecasting problems in the context of the COVID-19 pandemic.

(3) In the process of data processing, the epidemic factors were personalized, and the proportion coefficient of the corresponding moment was obtained by taking the typical characteristic curves of the epidemic period and the non-epidemic period to unify the time granularity. Increasing the range of the mapping interval to improve the sensitivity of epidemic information is conducive to capturing the amount of mutations, improving the forecast effect of peak and valley values and turning points, focusing on improving the prediction ability of high-load areas in non-epidemic periods, and thus achieving the purpose of overall forecast accuracy. Compared with the forecasting model without

considering the influencing factors, MAE, RMSE and SMAPE decreased by 21.88%, 38.59% and 16.57%, respectively, and were more consistent with the current social background.

(4) The measured data of interaction changes between epidemic and non-epidemic periods in a city in China were selected to test the forecast effect of the model in epidemic and non-epidemic periods. Compared with other forecasting models, the model proposed in this paper achieves better and more stable forecast results in both epidemic and non-epidemic periods, with MAE, RMSE and SMAPE all reduced by more than 20%, it showed that the forecasting model is consistent in improving the forecast effect of data with different characteristics. In addition, real-time demand-side response is carried out based on the forecast results of multiple foresight periods, which can alleviate the problem of large load variation during the epidemic to a certain extent.

In addition, how to more reasonably unify the time granularity of the feature series and load series, and how to more effectively dimensionless the data to improve the sensitivity to the epidemic situation are the focus of the next research when the hour-level epidemic related data cannot be obtained. In future work, the electric vehicle charging load forecasting method proposed in this paper will be applied to the smart Internet of vehicles system in the city in combination with the GPS road network system and regional special event characteristics, and the real-time updated multi-time scale forecasting results will provide reference for the demand-side response under the background of epidemic prevention and control.

Data availability statement

The original contributions presented in the study are included in the article/Supplementary material, further inquiries can be directed to the corresponding author.

Author contributions

TX: Conceptualization, Formal Analysis, Resources, Writing–original draft. YZ: Data curation, Investigation, Writing–original draft. GZ: Funding acquisition, Investigation, Writing–review and editing. KZ: Methodology, Software, Writing–review and editing. HL: Project administration, Validation, Writing–review and editing. XH: Supervision, Validation, Writing–review and editing.

Funding

The author(s) declare financial support was received for the research, authorship, and/or publication of this article. The authors gratefully acknowledge the financial support provided by Natural Science Basic Research Program of Shaanxi Province (2022JQ-534).

Conflict of interest

Author YZ was employed by LTD. Ultra high voltage company.

Author HL was employed by Electric Power Research Institute of State Grid Shaanxi Electric Power Company.

The remaining authors declare that the research was conducted in the absence of any commercial or financial relationships that could be construed as a potential conflict of interest.

Publisher's note

References

Abbas, F., Feng, D. H., Habib, S., Rasool, A., and Numan, M. (2019). An improved optimal forecasting algorithm for comprehensive electric vehicle charging allocation. *ENERGY Technol.* 7 (10). doi:10.1002/ente.201900436

Atif, Y., Ding, J., and Jeusfeld, M. A. (2016). Internet of things approach to cloud-based smart car parking. *Procedia Comput. Sci.* 98, 193–198. doi:10.1016/j.procs.2016.09.031

Bayrak, A. T., Aktas, A. A., Susuz, O., Tunalı, O., et al. (2020). "Churn prediction with sequential data using long short term memory," in 2020 4th International symposium on multidisciplinary studies and innovative technologies, 1–4. doi:10.1109/ISMSIT50672.2020.9254679

Bian, H. H., Wang, Q., Xu, G. Z., and Zhao, X. (2022). Load forecasting of hybrid deep learning model considering accumulated temperature effect. *ENERGY Rep.* 8 (1), 205–215. doi:10.1016/j.egyr.2021.11.082

Chen, Y. W., and Chang, J. M. (2016). Fair demand response with electric vehicles for the cloud based energy management service. *IEEE Trans. Smart Grid* 9, 458–468. doi:10.1109/tsg.2016.2609738

Dabbaghjamanesh, M., Moeini, A., and Kavousi-Fard, A. (2021). "Reinforcement learning-based load forecasting of electric vehicle charging station using Q-learning technique," in IEEE TRANSACTIONS ON INDUSTRIAL INFORMATICS, 17 (6), 4229–4237. doi:10.1109/tii.2020.2990397

Dai, Q., Cai, T., Duan, S. X., and Zhao, F. (2014). Stochastic modeling and forecasting of load demand for electric bus battery-swap station. *Bus. Battery-Swap Stn.* 29 (4), 1909–1917. doi:10.1109/tpwrd.2014.2308990

Feng, J. W., Yang, J. Y., Li, Y. L., Wang, H. X., Ji, H. C., Yang, W. Y., et al. (2021). Load forecasting of electric vehicle charging station based on grey theory and neural network. *ENERGY Rep.* 7 (6), 487–492. doi:10.1016/j.egyr.2021.08.015

Ge, L. J., Xian, Y. M., Wang, Z. G., Gao, B., Chi, F., and Sun, K. (2021). Short-term load forecasting of regional distribution network based on generalized regression neural network optimized by grey wolf optimization algorithm. *CSEE J. POWER ENERGY Syst.* 7 (5), 1093–1101. doi:10.17775/CSEEJPES.2020.00390

Hochreiter, S., and Schmidhuber, J. (1997). Long short-term memory. *Neural comput.* 9, 1735–1780. doi:10.1162/neco.1997.9.8.1735

Iversen, E. B., Mø ller, J. K., Morales, J. M., Madsen, H., et al. (2017). Inhomogeneous Markov models for describing driving patterns. *IEEE Trans. Smart Grid* 8 (2), 581–588. doi:10.1109/TSG.2016.2520661

Iwafune, Y., Ogimoto, K., Kobayashi, Y., and Murai, K. (2020). Driving simulator for electric vehicles using the Markov chain Monte Carlo method and evaluation of the demand response effect in residential houses. *IEEE Access* 8, 47654–47663. doi:10.1109/access.2020.2978867

Leou, R. C., Su, C. L., and Lu, C. N. (2014). Stochastic analyses of electric vehicle charging impacts on distribution network. *IEEE Trans. Power Syst.* 29 (3), 1055–1063. doi:10.1109/tpwrs.2013.2291556

Li, L., Wei, J., Li, C. B., Cao, Y. J., Song, J. Y., Fang, B. L., et al. (2015). Prediction of load model based on artificial neural network. *Trans. China Electrotech. Soc.* 30 (8), 225–230. (in Chinese).

Li, P. H., and Pye, S. (2018). Assessing the benefits of demand-side flexibility in residential and transport sectors from an integrated energy systems perspective. *Appl. ENERGY* 228, 965–979. doi:10.1016/j.apenergy.2018.06.153

Lin, S., Wang, H., Qi, L. H., Feng, H. Y, Su, Y., et al. (2021). Short-term load forecasting based on conditional generative adversarial network. *Automation Electr. Power Syst.* 45 (11), 52–60. (in Chinese).

Liu, J. (2020). "Statistical analysis on the change of economic condition in China under the influence of COVID-19," in 2020 International conference on big data economy and information management, 95–100.

National Health Commission of the People's Republic of China (2022). Office of Health emergency. Available at: http://www.nhc.gov.cn (Accessed on August 10, 2022).

Peng, H. C., Long, F. H., and Ding, C. (2005). Feature selection based on mutual information: criteria of max-dependency, max-relevance, and min-redundancy. *IEEE Trans. Pattern Analysis Mach. Intell.* 27 (8), 1226–1238. doi:10.1109/tpami.2005.159

Reshef, D. N., Reshef, Y. A., Finucane, H. K., Grossman, S. R., McVean, G., Turnbaugh, P. J., et al. (2011). Detecting novel associations in large data sets. *Science* 334 (6062), 1518–1524. doi:10.1126/science.1205438

Salah, F., Ilg, J., Flath, C., Basse, H., and Dinther, C. V. (2015). Impact of electric vehicles on distribution substations: a Swiss case study. *Apply Energy* 137, 88–96. doi:10.1016/j.apenergy.2014.09.091

Shaanxi Provincial Development and Reform Commission (2022). Energy bureau electricity division. Available at: http://sndrc.shaanxi.gov.cn (Accessed on August 10, 2022).

State-owned Assets Supervision (2022). *State-owned Assets supervision and administration commission of hubei provincial people's government*. Hubei Provincial Communications Group. Available at: http://gzw.hubei.gov.cn (Accessed on August 10, 2022).

State-owned Assets Supervision and Administration Commission of the State Council (2022). *State-owned Assets supervision and administration commission of the state Council*. State Grid Co., Ltd. Available at: http://www.sasac.gov.cn (Accessed on August 10, 2022).

Sun, H., Yang, F., Gao, Z. N., Hu, S. B., Wang, Z. H., Liu, J. S., et al. (2022). Short-term load forecasting based on mutual information and Bi-directional long short-term memory network considering fluctuation in importance values of features. *Automation Electr. Power Syst.* 46 (08), 95–103. (in Chinese).

The State Council of the People's Republic of China *The state Council of the people's Republic of China*. People's Daily. Available at: http://www.gov.cn (Accessed on August 10, 2022).

Wang, H. X., Yuan, J. H., Chen, Z., Ma, Y. M., Dong, H. N., Yuan, S., et al. (2022). Review and prospect of key techniques for vehicle-station-network integrated operation in smart city. *Trans. China Electrotech. Soc.* 37(1): 112–132. (in Chinese).

Wen, L. L., Zhou, K. L., Yang, S. L., and Lu, X. (2019). Optimal load dispatch of community microgrid with deep learning based solar power and load forecasting. *Energy*, 171: 1053–1065. doi:10.1016/j.energy.2019.01.075

Xi'an Municipal People's Government (2022). Xi'an epidemic prevention and control headquarters. Available at: http://www.xa.gov.cn (Accessed on August 10, 2022).

Xie, J. J., Zhong, Y. J., Xiao, T., Wang, Z., Zhang, J., Wang, T., et al. (2022). A multi-information fusion model for short term load forecasting of an architectural complex considering spatio-temporal characteristics. *Energy and Build.*, 277. doi:10.1016/j.enbuild.2022.112566

Xie, M., Deng, J. L., Ji, X., Liu, M. B., et al. (2017). Cooling load forecasting method based on support vector machine optimized with entropy and variable accuracy roughness set. *Power Syst. Technol.* 41 (1), 210–214. (in Chinese).

Zakernezhad, H., Nazar, M. S., Shafie-khah, M., and Catalão, J. P. (2022). Optimal scheduling of an active distribution system considering distributed energy resources, demand response aggregators and electrical energy storage. *Appl. Energy* 314, 118865. doi:10.1016/j.apenergy.2022.118865

Zhang, C., Hu, H. W., Ji, J., Liu, K., Xia, X., Nazir, M. S., et al. (2023). An evolutionary stacked generalization model based on deep learning and improved grasshopper optimization algorithm for predicting the remaining useful life of PEMFC. *Appl. Energy*, 330. (PA). doi:10.1016/j.apenergy.2022.120333

Zhang, G., Liu, H. C., Zhang, J. B., Yan, Y., Zhang, L., Wu, C., et al. (2019). Wind power prediction based on variational mode decomposition multi-frequency combinations. *J. Mod. Power Syst. Clean Energy* 7 (2), 281–288. doi:10.1007/s40565-018-0471-8

Zhang, J. A., Liu, C. Y., and Ge, L. J. (2022). Short-term load forecasting model of electric vehicle charging load based on MCCNN-TCN. *ENERGIES* 7 (6).

Zhang, T., Chen, X., Yu, Z., Zhu, X., and Shi, D. (2018). A Monte Carlo simulation approach to evaluate service capacities of EV charging and battery swapping stations. *IEEE Trans. Industrial Inf.* 14 (9), 3914–3923. doi:10.1109/tii.2018.2796498

Zhang, X., Chan, K. W., Li, H. R., Wang, H., Qiu, J., and Wang, G. (2021). Deep-learning-based probabilistic forecasting of electric vehicle charging load with a novel queuing model. *IEEE Trans. Cybern.* 51 (6), 3157–3170. doi:10.1109/tcyb.2020.2975134

Zhang, Y. G., Li, R. X., and Zhang, J. H. (2021). Optimization scheme of wind energy prediction based on artificial intelligence. *Environ. Sci. Pollut. Res.* 28 (29), 39966–39981. doi:10.1007/s11356-021-13516-2

Zhong, J., He, L., Li, C., Cao, Y., Wang, J., Fang, B., et al. (2014). Coordinated control for large-scale EV charging facilities and energy storage devices participating in frequency regulation. *Appl. Energy* 123 (15), 253–262. doi:10.1016/j.apenergy.2014.02.074

Zhu, J. C., Yang, Z. L., Mourshed, M., Guo, Y., Zhou, Y., Chang, Y., et al. (2019). Electric vehicle charging load forecasting: a comparative study of deep learning approaches. *ENERGIES* 12 (24), 2692. doi:10.3390/en12142692

10.3389/fenrg.2024.1341246

Nomenclature

BPNN	Back Propagation Neural Network
ARMA	Auto-Regressive and Moving Average
CNN	Convolutional Neural Network
LSTM	Long Short-Term Memor
MIC	Maximal Information Coefficient
mRMR	Maximum Relevance Minimum Redundancy
MI	Mutual Information
Bi-LSTM	Bidirectional Long Short-Term Memory
IPSO	Improved Particle Swarm Optimization Algorithm
IPSO-LSTM	Improved Particle Swarm Optimization-Long Short Term Memory
MAE	Mean Absolute Error
RMSE	Root Mean Square Error
SMAPE	Symmetric Mean Absolute Percentage Error
TOU	Time-of-use

frontiers | Frontiers in Energy Research

TYPE Original Research
PUBLISHED 02 April 2024
DOI 10.3389/fenrg.2024.1347581

OPEN ACCESS

EDITED BY
Nawa Baral,
The Joint BioEnergy Institute, United States

REVIEWED BY
Kai Lan,
North Carolina State University, United States
Vandit Vijay,
Sardar Swaran Singh National Institute of Bio-Energy, India

*CORRESPONDENCE
C. Igathinathane,
igathinathane.cannayen@ndsu.edu

RECEIVED 01 December 2023
ACCEPTED 26 February 2024
PUBLISHED 02 April 2024

CITATION
Tumuluru JS, Igathinathane C, Archer D and McCulloch R (2024), Energy-based break-even transportation distance of biomass feedstocks.
Front. Energy Res. 12:1347581.
doi: 10.3389/fenrg.2024.1347581

Energy-based break-even transportation distance of biomass feedstocks

J. S. Tumuluru[1], C. Igathinathane[2]*, D. Archer[3] and R. McCulloch[4]

[1]Southwestern Cotton Ginning Research Laboratory, United States Department of Agriculture-Agricultural Research Service, Las Cruces, NM, United States, [2]Department of Agricultural and Biosystems Engineering, North Dakota State University, Fargo, ND, United States, [3]Northern Great Plains Research Laboratory, United States Department of Agriculture-Agricultural Research Service, Mandan, ND, United States, [4]Biofuels and Renewable Energy Division, Idaho National Laboratory, Idaho Falls, ID, United States

The distance a solid biomass feedstock could be used to transport the feedstock when used as biobased fuel is critical information for transportation analysis. However, this information is not available. The break-even transportation distance (BTD) of various fuels from biomass feedstocks and fossil sources was analyzed for truck, rail, and ship transport modes based on bulk density, moisture content, and specific energy. Fourteen different biomass feedstocks, such as crop residues (e.g., corn stover), woody biomass (e.g., wood chips), including thermally pretreated (torrefied) and densified forms (pellets), cattle feedlot compost, and three standard fossil fuels, namely, coal, lignite, and diesel, were considered for BTD analysis and comparison. The BTD values were derived by comparing the energy content of biomass feedstocks with the energy expended in transporting the fuels through selected transportation modes. For ready reference, an alternative derivation of BTD equations and example calculations were also presented. Among the biomass feedstocks, torrefied pellets had the highest BTD (4.16×10^4, 12.47×10^4, and 54.14×10^4 km), and cattle feedlot compost had the lowest BTD (1.29×10^4, 3.88×10^4, and 9.23×10^4 km), respectively, for truck, rail, and ship. Higher bulk density and higher specific energy of the biomass feedstocks increased the BTD for all modes of transport. Transport is most efficient when mass-limited. Biomass feedstock bulk densities where transportation becomes mass-limited are 223, 1,480, and 656 kg/m^3 for truck, rail, and ship, respectively. Truck transport is typically mass-limited (payload limit restriction; increased BTD), whereas rail transport is entirely volume-limited (cargo space restriction; decreased BTD), and ship transport is mostly volume-limited for biomass feedstocks and mass-limited for densified biomass feedstocks. Ship transport is the most efficient, followed by rail and truck; on average for the materials (17) studied, rail is 3.1 times and ship is 9.2 times the truck's BTD. Based on the bulk density and higher specific energy of the biomass feedstocks, regardless of the refinery location, interstate truck transport of these feedstocks is not a limiting factor in the bio-refining process., with the studied biomass feedstock BTD per truckload representing between 0.89 and 2.88 times the US perimeter.

KEYWORDS

biomass, energy, logistics, transportation, fossil fuel, by-products

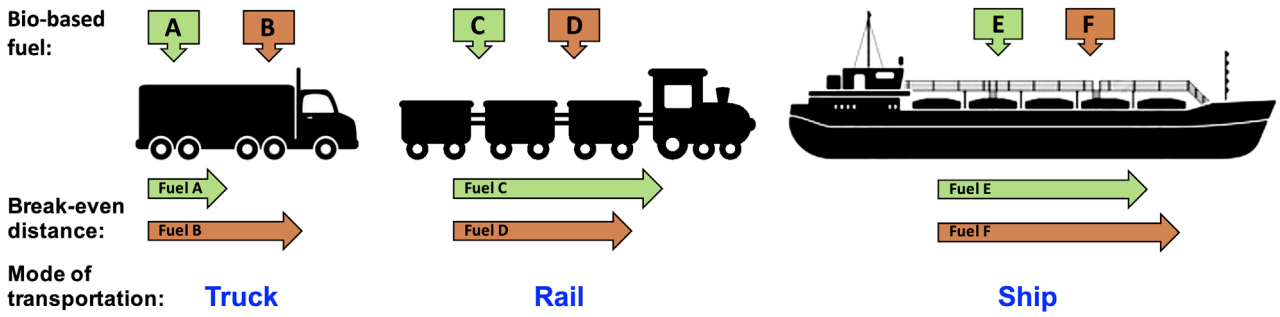

GRAPHICAL ABSTRACT
Illustration of the concept of BTDs of biomass feedstocks as bio-based fuel and the modes of transportation studied (Note: **A**–**F** are model bio-based fuels of varying energy contents. The length of the horizontal arrows symbolically represents the BTD of the selected bio-based fuels).

1 Introduction

Biomass feedstock is gaining importance due to its increased usage as a bio-based fuel in power plants and biorefineries to produce liquid and gaseous fuels. A major challenge facing the biomass industry is viable transport options for the various biomass feedstocks and products. The distance a given amount of biomass feedstock can be transported while still providing a net energy yield is crucial to the long-term implementation of biomass-related technologies. Understanding the trends associated with various biomass feedstock types is vital for biomass resource managers, transportation companies, producers, and other players in the supply chain, which has been the topic of recent investigations (Mahmudi and Flynn, 2006; Wiegmans and Konings, 2015). As ultimately energy translates to cost, energy saved leads to increased profits and subsequently promotes increased biomass feedstock usage, which in turn leads to reduced dependence on fossil fuels and a reduction of greenhouse gas emissions.

Biomass is currently the largest provider of domestic renewable energy (accounting for 47%) and supplies over 3% of total energy consumption in the United States (Perlack et al., 2011). Biomass feedstocks derived from agricultural resources, such as cereal crops and oilseeds, as well as from perennial crops as potential feedstocks for idle acres and dedicated energy crops represent an abundant feedstock resource. Given this status, the United States is well poised to make biomass a sustainable and significant part of domestic renewable energy production feedstock. Furthermore, the recent United Nations Paris Framework Convention on Climate Change called for mitigating global annual emissions of greenhouse gasses by 2020 and to hold the increase in the global average temperature to well below 2 °C from the pre-industrial levels by aggregating emission pathways (FCCC, 2015). Recently, the Intergovernmental Panel on Climate Change (IPCC) Fifth Assessment Report framed the context, knowledge base, and assessment approaches used to understand the impacts of 1.5 °C global warming above pre-industrial levels and related global greenhouse gas emission pathways (Allen et al., 2018). Among the various renewable resources available, biomass could significantly meet global energy demands and greenhouse gas mitigation goals. The vast inventory of biomass feedstocks derived from agricultural and forestry activities can be processed through established pathways to produce biofuels, bioenergy, and bioproducts, with low greenhouse gas emissions, unlike fossil fuels.

Bio-based fuels derived from various biomass feedstocks are to be transported from processing plants/refineries/fueling stations to the location of use. With fixed energy contents of different biomass feedstocks, it will be necessary to evaluate how far these feedstocks can be transported, with reference to their energy content—the proposed concept of break-even transportation distance (BTD), through various modes of transport while using the fossil fuel as transportation energy in the analysis. Given the low energy content of the biomass, one general concern/question from the user is "whether more energy is expended in transporting the biomass than the energy it contains?" Therefore, we define the BTD of biomass feedstocks (various raw biomass feedstocks and preprocessed products considered in this study) as the distance these feedstocks as bio-based fuel can travel utilizing its total available energy in a given mode of transport (e.g., truck, rail, and ship). Graphical Abstract illustrates the concept of BTD and modes of transportation considered in the study. Knowing the BTDs of different biomass feedstocks, the bio-based fuel producers or transportation logistics firms can select the suitable mode of transportation based on the available energy.

Moisture content, bulk density (kg/m^3), and energy content (specific energy, J/kg) affect the biomass feedstock quality significantly; hence, transportation logistics decisions should be made based on these quality attributes. When transporting high-moisture biomass feedstocks, the water content adds to the mass and/or volume restrictions, and the moisture also reduces the specific energy. Therefore, higher and lower heating values (HHV and LHV, respectively), which are functions of moisture contents, should be used when calculating the biomass energy potential (Bradley et al., 2014). As both bulk density and specific energy rationally have a significant impact on the BTDs, improving these properties allows transportation costs to be reduced.

Mechanical densification and thermal treatment processes, such as torrefaction, were shown to improve the bulk density and specific energies of the biomass feedstocks (Tumuluru et al., 2011;

2021; Tumuluru, 2015; Pradhan et al., 2018; Picchio et al., 2023; Tumuluru, 2023). Torrefied and densified biomass reduced the shipping costs due to increased bulk density and specific energy (Searcy et al., 2014). It was also found that the torrefied biomass costs less to transport per unit energy compared to wood chips and white pellets in ship transport. The International Energy Agency (IEA) report concludes that currently, only wood pellets are traded over a long distance in large volumes, and substantial cost reduction can be realized in the wood pellet supply chain compared to raw biomass transport (Bradley et al., 2014). For example, wood pellets, torrefied wood, and pyrolysis oil have different physical, chemical, and energy characteristics, and changes in these properties impact their transportation distances.

Every mode of transport has its own overall efficiency of transporting the payload, which is taken into account via the fuel efficiency values (e.g., truck km/L or mpg), and this reflects on the biomass feedstocks' BTDs. The standard container volume limitations and prevailing roadway mass limitations (e.g., truck transport) will impose further restrictions on the transport. Therefore, the two situations arise, namely, i) *volume-limited*: when the entire transport container volume was used, and its mass did not exceed the permissible limit; and ii) *mass-limited*: when the allowed mass limit was reached before the transport container was completely filled, are to be considered in the analysis.

The BTDs of biomass feedstocks directly influence the cost of transportation and are crucial to enable the further growth of the bioprocessing industry. The major limitations of road transportation are environmental problems, such as air pollution, congestion, and accidents, whereas inland waterway transportation is a more cost-efficient and environmentally friendly alternative (Lu and Yan, 2015). Furthermore, it was observed that usually the most critical factors in selecting the mode of freight transportation and road congestions are issues when biomass feedstock is transported, especially by trucks (Mahmudi and Flynn, 2006). Therefore, researchers suggested that rail transport can help overcome transportation costs and congestion issues (Mahmudi and Flynn, 2006; Lu and Yan, 2015).

An earlier study focused on the economics of shipping biomass feedstocks from truck to rail in a North American setting and discussed the minimum economic shipping distance for selected feedstocks (Mahmudi and Flynn, 2006). However, literature specifically relating to the concept of BTDs of various biomass feedstocks and the effect of biomass quality attributes, such as moisture content, bulk density, and energy content, on transportation logistics are not currently available, hence worth an investigation. Therefore, the overall objective of the present study was to evaluate the BTDs for various forms of biomass feedstocks based on their energy contents. Specific objectives of this research were to i) evaluate and compare the BTDs of various raw and preprocessed biomass feedstocks, such as herbaceous and woody raw biomass feedstocks, and thermally and mechanically preprocessed products with respect to the fossil fuels used in various respective standard modes of transport and ii) determine the feasibility of transporting these biomass feedstocks around the United States with a truck.

2 Materials and methods

2.1 Materials considered

For this work, 17 bio-based fuels comprising 14 potential biomass feedstocks (raw, densified, and torrefied and densified) along with three traditional fossil fuels for comparison (Table 1) were considered. It should be noted that these biomass feedstocks cannot be directly used in modern transportation vehicles, but the study is concerned about the energy content of these biomass feedstocks for the BTD calculation. All these 17 bio-based fuels are solid fuels, except diesel fuel which is a drop-in liquid fuel with reference to which the BTDs of the rest (16) were calculated. Reported values for bulk densities and specific energies of biomass feedstocks often differ (e.g., baled biomass); therefore, averages of published values were used. Referenced bales were rectangular with dimensions of 0.91 × 1.22× 2.44 m.

Specific energies (energy per unit mass) for some biomass feedstocks were calculated to maintain consistency throughout similar materials and mitigate discrepancies. Corn stover pellet (6.2% wet basis (w.b.) moisture) was used as the necessary reference material in specific energy calculation for the corn stover pellet (26% w.b.) and corn stover briquettes (Table 1). Similarly, corn stover bale (10% w.b.) was used as a reference for the other three corn stover bales with varying moisture contents (20–50% w.b.). Wood chips-50% were used as the reference for wood chips-12% and torrefied wood chips. Cattle feedlot compost was taken as the soil-surfaced feed pen, code HA-FB (Sweeten et al., 2006). Mass densities of Central Appalachian coal and North Dakota lignite were taken as the average values reported for bituminous coal and lignite, respectively (Engineering ToolBox, 2018).

2.2 Bulk density and specific energy calculations based on biomass moisture

Relevant biomass feedstock properties considered in this work, such as the bulk densities and specific energies at specific moisture contents, derived from published reports are presented in Table 1. Among the various biomass feedstocks, corn stover is one of the major feedstocks currently used for bio-based fuel production. Therefore, corn stover bales with different moisture contents were considered in the present study as different harvesting methods such as single- and multi-pass and wet and dry storage systems result in corn stover with moisture content in the range of 10–50% w.b. (Shinners et al., 2007). Furthermore, corn stover bales with moisture content in the range of 10–33% (w.b.) can be processed and used for pellet production (Tumuluru, 2023). In the case of pellets, two different types of pellets were considered: i) the conventional pelleting process produces pellets with a moisture content of about 6% w.b. (Tumuluru et al., 2010), whereas ii) the high-moisture pelleting process developed by the Idaho National Laboratory produces wood pellets with higher moisture content of typically approximately 26% w.b. before low-temperature drying (Tumuluru, 2016).

For some of the biomass feedstocks at several moisture contents, the material properties were calculated from the reported values by

TABLE 1 Bulk density and specific energy data for different biomass feedstocks and fossil fuels used in the analysis.

Material	Moisture content (MC) [% w.b.]	Bulk density (BD_{bio}) [kg/m^3]	Reference	Specific energy (SE_{bio}) [MJ/kg]	Reference
Wood chips-12%	12	265	Tumuluru et al. (2015a)	18.48	[a]
Wood chips-50%	50	320	Tumuluru et al. (2012)	10.5	Tumuluru et al. (2012)
Corn stover bales-10%	10	166	Yancey (2016)	16.17	Mani et al. (2004)
Corn stover bales-20%	20	208	Yancey (2016)	14.37	[a]
Corn stover bales-30%	30	270	Yancey (2016)	12.577	[a]
Corn stover bales-50%	50	341	Yancey (2016)	8.983	[a]
Corn stover briquettes	10	489	Tumuluru et al. (2015b)	16.33	Tumuluru et al. (2015b)
Wood briquettes	10	422	Tumuluru et al. (2015b)	17.64	[a]
Corn stover pellets-6%	6.2	645	Yancey et al. (2013)	17.02	Yancey et al. (2013)
Corn stover pellets-26%	26	520	Tumuluru et al. (2015b)	13.42	[a]
Wood pellets	7	700	Tumuluru et al. (2012)	19	Tumuluru et al. (2012)
Torrefied wood chips	1.8	225	Tumuluru et al. (2015b)	20.62	[a]
Torrefied wood pellets	5	800	Tumuluru et al. (2012)	24	Tumuluru et al. (2012)
Cattle feedlot compost	4.95	750	Sweeten et al. (2006)	7.46	Sweeten et al. (2006)
Central Appalachian coal	7.2	800	Engineering ToolBox (2018)	28.17	Tumuluru et al. (2012)
North Dakota lignite	27	750	Engineering ToolBox (2018)	17.7	Tumuluru et al. (2012)
Diesel fuel[b]	0.02	832	DieselNet (2018)	43.1	DieselNet (2018)

[a]Indicates the values were calculated.
[b]Related to the reference diesel fuel (BD_f and SE_f).
All energy values presented are based on calorific values (higher heating values, HHVs).

following the two steps: i) converting properties from the reference to bone dry moisture content (Eq. 1) and ii) obtaining the desired property through conversion from the bone dry to the desired moisture content (Eq. 2).

In such calculations, a simple linear variation of the properties with moisture was assumed without considering biomass's volume swell/shrinkage due to moisture variation. The logic followed in the calculation was that the bone dry matter bulk density is considered directly proportional and the specific energy is considered inversely proportional to the dry matter component of biomass ($1 - MC_{ref}$) (Boundy et al., 2011) as expressed in the following relationship:

$$BD_{dry} = BD_{ref} \times (1 - MC_{ref}); \qquad SE_{dry} = \frac{SE_{ref}}{(1 - MC_{ref})}, \qquad (1)$$

where BD_{dry} is the bone dry bulk density (kg/m^3), BD_{ref} is the reference bulk density (kg/m^3), MC_{ref} is the reference moisture content (w.b., decimal), SE_{dry} is the bone dry specific energy (MJ/kg), and SE_{ref} is the reference specific energy (MJ/kg). Then, these material properties at the required new moisture content using Eq. 1 are calculated as

$$BD_{bio} = \frac{BD_{dry}}{(1 - MC)}; \qquad SE_{bio} = SE_{dry} \times (1 - MC), \qquad (2)$$

where BD_{bio} is the biomass feedstock bulk density at the new moisture content (kg/m^3), MC is the new moisture content (w.b., decimal), and SE_{bio} is the specific energy of the biomass feedstock at MC (MJ/kg). From Eq. 2, the effect of moisture content on biomass feedstocks can be observed as the higher moisture contents result in higher mass densities and lower specific energies.

Biomass feedstock properties (Table 1) remain unchanged for the calculations with each mode of transportation. For each biomass feedstock, the energy in the feedstock was compared to the energy of the conventional fuel required to transport the biomass feedstock. The BTD is unique for each biomass feedstock and must incorporate the volume and mass limitations, as outlined previously, for each mode of transportation. The energy content of the transported biomass feedstock is calculated as

$$E_{bio} = \min(V \times BD_{bio}, PL) \times SE_{bio}, \qquad (3)$$

where E_{bio} is the energy content of the biomass feedstock transported (MJ), V is the volume limit of the transportation mode (m^3), and PL

is the legal payload limit (kg). Eq. 3 appropriately selects the right quantity of biomass feedstock transported based on existing volume or mass limitations.

2.3 Derivation of BTDs for different transportation modes

The bulk densities and specific energies of the considered biomass feedstocks (BD_{bio} and SE_{bio}, respectively) and those of the transportation diesel fuel (BD_f and SE_f, respectively) were used to derive the energy required and BTDs of the selected modes of transport. Characteristic to the particular transport, different units were employed for the parameters (e.g., km/L for truck fuel consumption). Each mode of transport has a payload limit, and even though more mass can be transported in the available volume, this payload limit comes into effect based on the biomass feedstock transported. In this study, we have selected the truck and ship configurations that are commonly used for biomass transport. The focus of this research is to derive equations and understand BTD for various modes of transport. Although different units were employed for different parameters, the units of transport energy and BTDs were evaluated as "MJ" and "km," respectively, for consistency. An alternative way of deriving the BTD, while showing the units, involved is presented in Supplementary Section S1.

2.3.1 Truck transport

Many types, makes, and models of tractor-drawn trucks are used to transport goods. In general, the road type, areas, and weather have a great impact on fuel economics. The study conducted by Anttila et al. (2022) evaluated fuel consumption and CO_2 emissions for 13 typical log trucks under operating conditions in Finland. These authors modeled the effects of season, transportation distance, mass, vehicle and road properties, and weather conditions on fuel consumption. They found that the fuel consumption and emissions of 68,000–76,000-kg trucks were at the same level per ton-kilometer and concluded that the highest fuel consumption was measured in January and the lowest in July. In the present study, we have used trucks with specific dimensions that are very commonly used for the transportation of various goods and meet the US Department of Transportation (DOT) payload requirements (Truckers Report Jobs, 2018). While considering specific fuel consumption efficiency, the impact of road types, geographical locations, and weather on fuel consumption is not considered in this initial study.

We have, in this study, selected the truck and ship configurations that are commonly used for biomass feedstock transport. There are seven main types of trucks, namely, semi-trailers, flatbeds, step decks, dry vans, reefers, box trucks, and tankers, used for transporting different types of cargo (https://drstrucks.com/7-common-types-of-freight-trucks-what-they-haul/). Flatbeds are commonly used for transporting biomass bales, but trailers with hopper bottoms can also be used for biomass transport. In the case of densified biomass such as pellets, we expect that these hopper bottom trailers can be more efficient for transport and unloading.

In the present study, a common wedge trailer with dimensions similar to a flatbed trailer in length (1.46 m or 48 feet) with DOT payload limit was considered for analysis. For this analysis, the volume of a tractor-drawn truck was set at 101 m^3. This is consistent with the average trailer dimensions for a 14.6-m wedge trailer (Mode Transportation, 2018). In the present study, we have assumed that the truck's fuel consumption was 2.76 km/L when fully loaded with a maximum payload of 22,500 kg (Davis et al., 2014), where the gross vehicle weight is in the range of 14,969 to 36,287 kg. In general, a heavier truck encounters a greater rolling friction, but the truck is more profitable when cargo capacity is high; hence, the weight of the vehicle is critical. Franzese and Davidson (2011) investigated the relationship between the weight of the vehicle and the fuel efficiency and found that fuel efficiency decreases with an increase in the vehicle weight. For vehicle weight in the range of 9,072–22,680 kg, the fuel efficiency is approximately 4.04 km/L, whereas increasing the vehicle weight from 22,680 kg to 36,287 kg, the fuel efficiency decreases from 3.66 km/L to 3.36 km/L.

Therefore, in this study, the equipment weight of the trailer was assumed to be 13,787 kg, which makes the payload limit of 22,500 kg according to the US DOT limit of 36,287 kg combined weight for tractor-drawn trucks (Truckers Report Jobs, 2018). Using this information, the energy required for truck transport is derived as

$$E_{truck} = \frac{D \times SE_f \times BD_f}{\eta_t \times 1000}, \tag{4}$$

where E_{truck} is the energy consumed in truck transportation using conventional fuel (MJ), D is the transported distance (km), SE_f is the specific energy of the diesel fuel (MJ/kg), BD_f is the bulk density of the diesel fuel (kg/m^3), η_t is the fuel efficiency of the truck (km/L), and 1000 is the conversion factor involved in the fuel volume in L and m^3 to have the E_{truck} unit as MJ.

Equating both the biomass feedstock and diesel fuel energies (Eqs 3, 4) and solving for D derive the BTD for truck transport of biomass feedstocks, BTD_{truck} (km), as

$$BTD_{truck} = \frac{\min\left(V \times BD_{bio}, PL\right) \times SE_{bio} \times \eta_t \times 1000}{SE_f \times BD_f}. \tag{5}$$

The payload limit (22,500 kg) is critical in road transport. The mass of material that can be fitted in the truck volume can easily exceed the payload limit. So most often the mass of material transported by the truck is restricted by this limit, which also makes the truck transport a "full-capacity" operation.

2.3.2 Rail transport

For rail transport, it was assumed that each railcar can carry 104,780 kg and has a volume capacity of 70.8 m^3 (CFCL Co, 2018). The 2014 reported fuel efficiency of 186,284 kg km/L is used to calculate the diesel fuel consumption (CSX Corporation, 2018). This large value is a result of large quantities of freight moved over large distances, and rail transport is mass-limited. Rail transport can use as little as 5 gal/h and up to 200 gal/h depending on the grade they are traveling on, the weight of items being transported, wind speed and direction, and how many engines are being used to pull the load. The efficiency reported by Chessie Seaboard Consolidated (CSX) Corporation is given in units of kg km/L as the systemwide network distances and mass of material moved are available (CSX Corporation, 2018). The energy required for transporting biomass feedstocks using rail is expressed as

$$E_{rail} = \frac{D \times SE_f \times BD_f \times \min\left(V \times BD_{bio}, PL\right)}{\eta_r \times 1000}, \tag{6}$$

where E_{rail} is the energy consumed in rail transport using conventional fuel (MJ) and η_r is the fuel efficiency of the rail transport (kg km/L). As done previously, equating the biomass feedstocks and rail energies (Eqs 3, 6) and solving for the distance D derive the BTD of rail transport of biomass feedstock, BTD_{rail} (km), as

$$BTD_{rail} = \frac{SE_{bio} \times \eta_r \times 1000}{SE_f \times BD_f}. \quad (7)$$

It should be noted that the BTD equation for rail transport does not have the same form as the BTD equation for truck and ship transport. The reason for this is the difference in the fuel efficiency of rail transport and its units (η_r).

The term "$\min(V \times BD_{bio}, PL)$" in the energy equation for rail transport (Eq. 6) will subsequently cancel out when E_{rail} is substituted by equivalent energy of biomass feedstock transported by railcar E_{bio}, as shown in Eq. 3. Furthermore, η_r contains the mass component. The same treatment is not considered for truck transport in this work because i) the reported truck fuel efficiency is in the units of "km/L" and ii) the fluctuation in fuel efficiency for a semi-truck loaded with low-bulk-density material (e.g., corn stover bales at 10% w.b. with bulk density = 166 kg/m^3) vs. high-bulk-density material (e.g., torrefied wood pellets with bulk density = 800 kg/m^3) is negligible. It should be noted that railcars can carry a heavy load limit of 104,780 kg, based on the volume limitations and low bulk densities of materials, and the payload transported is always smaller than the mass-based load limit.

2.3.3 Ship transport

Ships were considered for transporting biomass feedstocks (bulk material transport) across the sea or along a coastline. The fuel efficiency and consumption of a ship depend on many stochastic variables that are impossible to state with exact precision. Such variables are wind speed, current flow, and parasitic drag, among others. Simplifying assumptions were made for this analysis that made the problem tractable; however, a more detailed future analysis can be very beneficial for a better understanding of the actual fuel usage for this mode of transportation.

In general, bulk products such as wood pellets from North America are transported to Europe using Panamax class ship (Portz, 2016). The ship has a fuel consumption (η_s) of 1,500 kg/h (36 t/d) at a vessel velocity of 27.78 km/h (15 knots) (Goulielmos, 2021). The study concluded that by increasing the speed of a Panamax ship from 11 to 15 knots (36.4% increase in speed), the fuel consumption has increased by 157% (from 14 to 36 t/d). According to the American Association of Port Authorities (AAPA, 2009), the physical dimensions of Panamax vessels are, in general, 294 m long, 32 m beam (vessel width that is critical to passing through the Panama Canal), and 12 m draft (vessel submerged depth).

According to the Soy Transportation Coalition (STC, 2023), the Panamax vessel has a deadweight of 55,000–80,000 metric tons, seven cargo holds, and each holds 300,000 bushels of soybean. However, the cargo intake of Panamax is usually restricted to 52,500 metric tons on the Panama Canal draft (Loyd's Register, 2023). The bulk density of four cultivars of soybean ranged from 691 kg/m^3 to 739 kg/m^3, with a moisture content range of 0.12–0.32 (d.b.) (Hauth et al., 2018). From these data, the mass of soybean transported in the seven cargo holds is 57,152,550 kg (300,000 bushel/hold × 27.2155 kg/bushel × 7 holds), and the range of volume available to transport the bulk material of equivalent mass, based on soybean bulk densities range (Hauth et al., 2018), is 77,338–82,710 m^3, with an average volume of 80,024 m^3. However, based simply on the physical dimensions of the vessel (AAPA, 2009), the vessel volume is 121,896 m^3, and the cargo volume available for transporting bulk material should be less. This is to accommodate the vessel's structural and functional components, members, fuel storage, and other crew amenities.

In this study, this Panamax class ship was considered for the bulk transport of selected biomass feedstock's BTD calculation with the aforementioned data.

$$E_{ship} = \frac{D \times \eta_s \times SE_f}{v}, \quad (8)$$

where E_{ship} is the energy consumed in ship transportation using conventional fuel (MJ), η_s is the fuel consumption of the ship (kg/h), and v is the velocity of ship transport (km/h). Similarly, using the component equations (Eqs 3, 8) and solving for the BTD of ship transport, BTD_{ship} (km) is evaluated as

$$BTD_{ship} = \frac{\min\left(V \times BD_{bio}, PL\right) \times SE_{bio} \times v}{\eta_s \times SE_f}. \quad (9)$$

It should be noted that ships have large volumes, but with an allowed payload limit of 67.5 × 10^6 kg, several materials could exceed this limit, and more often this payload limit will become the allowable mass transported. This also means that ships and trucks are most often operated at full payload capacities, unlike railcars.

2.4 Fuel efficiency data

The fuel efficiency and consumption values considered for each mode of transportation in the analysis along with their sources are provided in Table 2. The fuel efficiency data taken in the study incorporate the vehicle weight, air drag, and rolling friction for trucks and rails, or skin friction for ship transport. The rolling friction between asphalt and rubber was significantly higher than that for steel on steel; thus, rail transport gained efficiency by lower steady-state resistances and not stopping for long stretches. Larger rail freight capacities operate for a much longer stretch without stopping, improving fuel efficiency and making the rail transport of the cargo more efficient. These factors were considered when taking the fuel consumption of the transportation modes tested in this study.

2.5 Limiting transportation factors

The common modes of biomass feedstock transport are ship, train, truck, barge, ocean carrier, or a combination of various transportation modes. For example, when transporting biomass feedstocks over land, railroads tend to offer a lower cost per ton-mile, can handle large volumes, and can be the most environmentally responsible transportation mode. Exporting biomass feedstocks requires more than one shipping mode. Oftentimes, railroads will ship these products to ports where they are loaded onto ocean

TABLE 2 Assumptions for each mode of transportation considered in this study and transport limitations for selected feedstocks.

Transportation mode	Parameter	Value	Reference	Example material transported[a]	Potential mass transported [kg][b]	Transport limitation[c]	Bulk density limit [kg/m^3][d]
Truck	Fuel efficiency	2.76 [km/L]	Davis et al. (2014)	Corn stover bales (10% w.b.; 166 kg/m^3)	16,766	Volume-limited	223
	Payload limit	22,500 [kg][e]	Truckers Report Jobs (2018)	Wood chips (50% w.b.; 320 kg/m^3)	32,320	Mass-limited	
	Volume	101 [m^3]	Mode Transportation (2018)	Wood pellets (7% w.b.; 700 kg/m^3)	70,700	Mass-limited	
	Trailer type—wedge	6.1 [m]	Mode Transportation (2018)	Central Appalachian coal (7.2% w.b.; 800 kg/m^3)	80,800	Mass-limited	
Rail	Fuel efficiency	186,284 [kg km/L]	CSX Corporation (2018)	Corn stover bales (10% w.b.; 166 kg/m^3)	11,753	Volume-limited	1,480
	Payload limit	104,780 [kg][e]	CFCL Co. (2018)	Wood chips (50% w.b.; 320 kg/m^3)	22,656	Volume-limited	
	Volume per car	70.8 [m^3]	CFCL Co. (2018)	Wood pellets (7% w.b.; 700 kg/m^3)	49,560	Volume-limited	
				Central Appalachian coal (7.2% w.b.; 800 kg/m^3)	56,640	Volume-limited	
Ship (Panamax)	Speed	27.78 [km/h]	Goulielmos (2021)	Corn stover bales (10% w.b.; 166 kg/m^3)	13,283,951	Volume-limited	656
	Payload limit	52,500,000 [kg]	Loyd's Register (2023)	Wood chips (50% w.b.; 320 kg/m^3)	25,607,616	Volume-limited	
	Volume total holds	80,024 [m^3][e]	STC (2023)	Wood pellets (7% w.b.; 700 kg/m^3)	56,016,660	Mass-limited	
	Vessel volume	121,896 [m^3]	AAPA (2009)	Central Appalachian coal (7.2% w.b.; 800 kg/m^3)	64,019,040	Mass-limited	

[a]Refer Table 1 for details on the example materials.
[b]Potential mass transported [kg] = volume of transport [m^3] × bulk density of example material [kg/m^3].
[c]Transport limitation obtained by comparing the payload allowed[d] and potential mass transported[b]
[d]Volume of total seven holds of bulk transport Panamax calculated based on soybean transportation and soybean average bulk density [m^3].
[e]Bulk density limit [kg/m^3] was derived from the ratio of the assumed values of payload [kg] and volume [m^3] parameters.

carriers for transport overseas. For example, wood pellets from the production site are transported to shipping terminals by rail and further transported to various domestic and international markets by ships (Searcy et al., 2014). The location of the biorefinery has a great impact on the supply chain logistics. Some of the biorefineries that use agricultural residues which are low in bulk density and specific energy are close to biomass production areas to reduce transportation costs, whereas some of the biomass feedstocks such as pellets which are high in bulk density and specific energy are not close to biomass production areas, but the higher bulk density and specific energy make them economical to transport to longer distances by truck, ship, or rail.

Volume and mass legal restrictions influence the transportation logistics. When the available transport volume is completely filled with feedstock and the weight limit has been reached or exceeded, then the transportation is said to be mass-limited, and the mass transported must be reduced. Conversely, when the available transport volume is completely filled with feedstock and the mass limit has not been exceeded, then the transportation is volume-limited as there is no room for more material despite the payload limit allowing to carry more. Therefore, in general, mass-limited transport (fully utilized) has greater potential for payload transfer, as it utilizes the maximum allowed payload, than volume-limited transport (underutilized).

The type of transport limitation is predominantly influenced by the bulk density of the transported material because the volume available and the allowed payloads are typically fixed for each type of transport. Thus, any biomass feedstock bulk density smaller than these limits will make the transport volume-limited and greater than these limits will make it mass-limited. It can be seen that a transport mode can be both mass- and volume-limited based on the biomass feedstocks transported, as illustrated by truck and ship modes presented in Table 2. The derived "bulk density limit" of the material transported from the payload allowed and volume data available as 223, 1,480, and 656 kg/m^3 for truck, rail, and ship, respectively, can be used to readily identify the type of transport limitations given the bulk density of a biomass feedstock. Therefore, based on the rail bulk density limit of 1,480 kg/m^3, which is greater than any biomass feedstock's bulk density (Table 1), the rail transport will always be volume-limited (underutilized), while the truck and ship will be mass-limited for biomass feedstocks having moderate or higher densities (e.g., ≤410 kg/m^3).

3 Results and discussion

3.1 Evaluated BTDs for the three modes of transportation

From the evaluated BTDs using Eqs 5, 7, 9 (example BTD calculations are shown in Supplementary Section S2), the ship was by far the most energy-efficient, despite being mass-limited for dense biomass feedstocks, with the largest BTDs (approximately two orders of magnitude difference) among transportation modes considered (Figure 1). This might be counterintuitive due to the large size of cargo used in ship transport (Table 3). The energy efficiency of ship transport was due to the freight capacity and the extended time taken for the trip. Ship transport takes significantly longer time than truck or rail, during which biomass feedstocks may degrade, and this time effect was not considered in the analysis. The results also show that rail transport was more efficient than trucks from the BTD standpoint.

Biomass feedstock properties, such as specific energy and bulk density, affect the BTD to a varying extent (Figure 1). Among all the transportation modes, the specific energy showed the obvious trend of direct variation with the BTD. However, the increased bulk density of the biomass feedstocks only contributed positively to the BTD in the initial range for truck (approximately ≤223 kg/m^3) and ship (approximately ≤656 kg/m^3) as these transports are both mass- and volume-limited depending on the bulk density of the biomass feedstock being transported. Rail transport, however, being only volume-limited, the BTD is not affected by bulk densities (Figure 1). This can also be seen from the unit of "kg km/L" for rail transport efficiency. The figure for rail transport shows no dependence on bulk density for BTD. This goes back to the explanation given previously that the BTD for rail transport does not depend on payload mass due to the mass being included in the efficiency term. Based on Eq. 7, only specific energy will affect the BTD for rail transport.

3.2 Bulk density and specific energy impact on BTD

The surface plot of bulk density to specific energy and its impact on the BTD of the truck indicated that with an increase in the bulk density of the biomass feedstock up to 300 kg/m^3, the BTD is higher, whereas further increasing the bulk density does not affect the BTD. On the other hand, increasing the specific energy increases the BTD at different bulk densities of the biomass feedstocks. In the case of rail transport, which is volume-limited, the bulk density does not impact the BTD, but the specific energy significantly impacts the BTD. The results for ship transport indicated that both bulk densities and specific energies significantly impact the BTD of biomass feedstocks, where increased bulk densities and specific energy increased the BTD transportation of the material.

The BTD profiles and patterns of the different biomass feedstocks and fossil fuels in the three modes of transportation show that truck and rail BTD profiles were similar, but these were different from the BTD profiles for ship, as shown in Figure 2. These BTD profiles clearly show the scale (how the three transportation modes compare among themselves—showing the dominance of ship) and the pattern (how studied biomass feedstocks compare with others—similarity between truck and rail) with each transportation mode.

On average, the rail can transport approximately 3 times farther and the ship can transport approximately 10 times farther than the truck. Compared to trucks, the larger rail freight capacities and their operation for a much longer stretch without stopping contribute to their efficiency. Given that the "start-up" after each "stop" was the most energy-intensive part of any transport and building momentum also consumed energy, rail transport reduced these energy losses better than trucks. However, maintaining momentum was much less energy-intensive and only involved overcoming the steady-state resistances. These include air drag and rolling friction for trucks and rails, or skin friction for ship transport. It follows the intuition that rolling friction between asphalt and rubber was significantly higher than that for steel on steel; thus, rail transport gained efficiency by lower steady-state resistances and not stopping for long stretches.

Given the results and overall ranking of the BTD of different biomass feedstocks and their properties (Figure 2; Table 2), the efficient transportation between the start and end destinations should be a combination of modes of transportation based on feasibility (geographical and existing transportation network). It makes sense that rail transport is not ideal for only a few

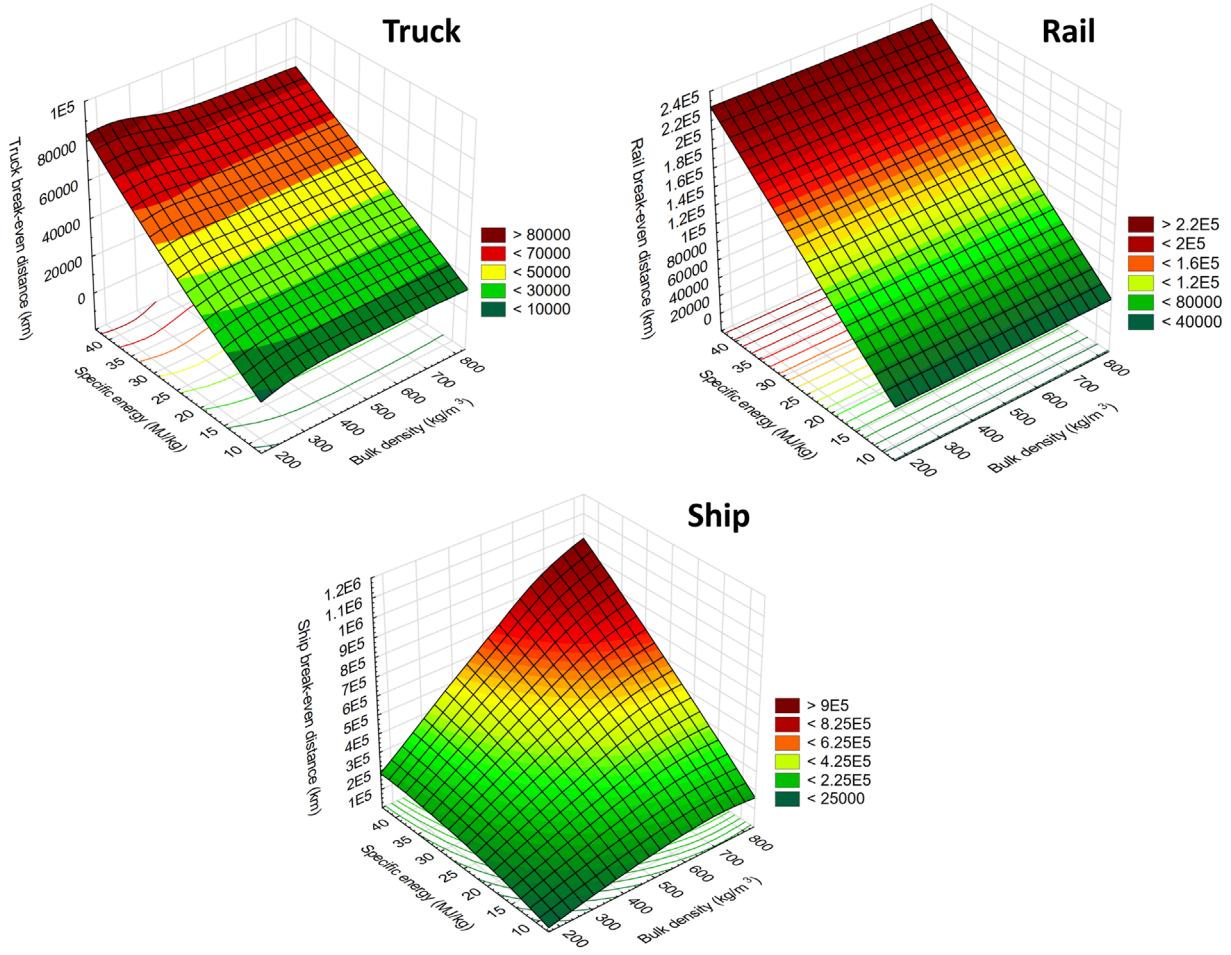

FIGURE 1
Overall trend of BTDs of biomass feedstocks and fossil fuels tested as a function of specific energy and bulk densities for all three modes of transportation. Note that the scales of *y*-axis are different.

miles of transport. It should be realized that with the ship, and sometimes with the rails, truck transport may be added to deliver the biomass feedstocks to the biorefinery. Future analysis is needed to optimize the transportation methods by integrating the three modes of transportation based on their availability and the distance the biomass feedstocks is transported involving the existing transportation network.

3.3 Moisture impact on BTD

In order to quantify the effect of changing moisture of biomass feedstocks on the BTDs (Figure 3), the case of corn stover bales between 10% and 50% w.b. moisture contents was considered (Table 1). The corn stover bales data were further analyzed to understand the impact of moisture on BTD using trucks, rail, and ships. Figure 3 shows how the BTD changes with the moisture content for the corn stover bales in the moisture content range of 10–50% w.b. The changes in the bulk density (BD_{bio}) and specific energy (SE_{bio}) in the corn stover bales were calculated based on Eqs 1, 2. These equations calculate the bulk density and specific energy based on simple linear variation with respect to moisture content but do not consider the biomass's volume swell/shrinkage due to moisture variation. It is clear from Table 1 that the bulk density of the corn stover biomass increases with an increase in the moisture content, whereas the specific energy decreases. These changes in the bulk density and specific energy with moisture (considered in the calculation) have impacted the BTD of the corn stover bales (Figure 3).

From the results, it is very clear that for the ship, which is volume-limited, the BTD increases with an increase in the moisture content of up to 30% w.b. (an increase of approximately 26%), whereas further increasing the corn stover bale moisture content to 50% w.b. decreases the BTD values (a decrease of approximately 9.8% from the moisture content of 30–50% w.b.). Regarding rail, which is volume-limited, the BTD decreases by approximately 45% with an increase in the corn stover bale moisture content from 10 to 50% w.b. For truck transportation, which is mass-limited, the increase in the corn stover bale moisture content from 10 to 40% w.b. increases the BTD values from 20,866 to 21,780 km (4.3% increase), and further increasing the corn stover bale moisture

TABLE 3 BTDs of the bio-based and fossil fuels tested for each mode of transportation at their reference capacity limits and moisture contents[a].

Material[a]	Truck [1×10^4 km]	Rail [1×10^4 km]	Ship [1×10^4 km]
Wood chips-12%	3.20	9.60	16.84
Wood chips-50%	1.82	5.45	11.55
Corn stover bales-10%	2.09	8.40	9.23
Corn stover bales-20%	2.32	7.47	10.28
Corn stover bales-30%	2.18	6.53	11.68
Corn stover bales-50%	1.56	4.67	10.53
Corn stover briquettes	2.83	8.48	27.46
Wood briquettes	3.05	9.16	25.60
Corn stover pellets-6%	2.95	8.84	37.75
Corn stover pellets-26%	2.32	6.97	24.00
Wood pellets	3.29	9.87	42.86
Torrefied wood chips	3.57	10.71	15.95
Torrefied wood pellets	4.16	12.47	54.14
Cattle feedlot compost	1.29	3.88	16.83
Central Appalachian coal	4.88	14.63	63.55
North Dakota lignite	3.07	9.19	39.93
Diesel fuel	7.46	22.39	97.23

[a]The moisture contents of these materials expressed in wet basis and are the same as presented in Table 1.

content to 50% w.b. decreases the BTD values to approximately 15,556 km [a decrease of approximately 28% compared to BTD values at 10% w.b. moisture content]. The BTD data calculated with respect to moisture should be further cross-validated with the actual bulk and specific energy of the corn stover bales at different moisture contents.

Since trucks and ships were influenced by both mass and volume limitations, with moisture content affecting these, an optimum moisture content might exist for efficient biomass feedstock transport. For these modes with corn stover, when the moisture is too low, the transport is volume-limited, and the total material transported is lower than the full payload capacity. When the moisture is too high, the transport is mass-limited for truck and ship transport, where the material transported is lower than the full volume capacity of the transportation mode. Overall, efficient transportation occurs when the mass- and volume-limited transportation modes coincide, maximizing the amount of material that is being transported.

Rail transport is impacted by moisture due to the inclusion of mass in the efficiency (units: kg km/L) as high moisture increases the overall mass and reduces the net dry matter transported and the biomass feedstock energy content. Thus, the rail transport being volume-limited, a specified volume of biomass feedstock will represent a certain mass and its corresponding BTD, based on the nature of the biomass feedstock, irrespective of the bulk density. By increasing the moisture of the biomass feedstock, the specific energy (SE_{bio}) is reduced (Table 1), which eventually reduces the fuel efficiency of rail transport (η_r). According to Eq. 7, the BTD or rail decreases linearly with decreased rail transport efficiency.

As observed with corn stover bales (Figure 3), similar results for other biomass feedstocks with moisture variation can be expected. The corn stover bale moisture content and BTD were further modeled, which can help predict the BTD values of corn stover bales in the moisture content range of 10–50% w.b. The fitted polynomial models (Table 4) have adequately described ($R^2 \geq 0.92$) the BTD with the three transportation modes as a function of moisture content. These models can be useful in calculating the BTD of the corn stover, most abundant agricultural feedstock, at commonly occurring moisture contents of this feedstock.

3.4 Limiting transportation factors

The limiting factors for each combination of moisture, biomass feedstock, and transportation method influence the logistics

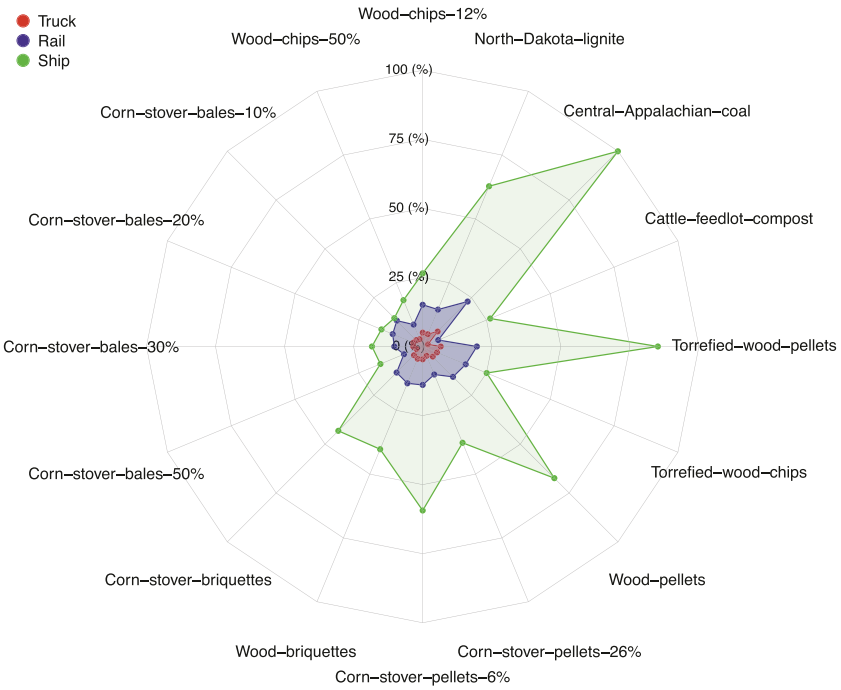

FIGURE 2
BTD (km) profiles of various biomass feedstocks and fossil fuels showing the scale and pattern among the modes of transportation. The numbers after the biomass feedstocks indicate moisture content in % w.b. In the scale, 100% corresponds to the maximum distance of 63.6×10^4 km, and 25% corresponds to 15.9×10^4 km.

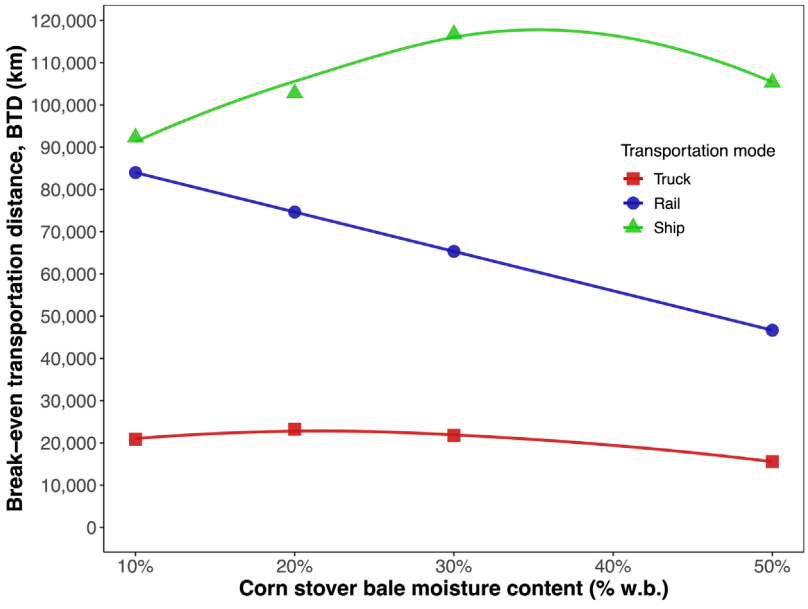

FIGURE 3
Effect of the moisture content of corn stover bales on BTD of different modes of transportation.

decision (Figure 4). For example, corn stover bales are volume-limited for moisture contents less than 20% w.b., whereas above this moisture content for truck transport, the transportation is mass-limited. Torrefied wood chips, however, are mass-limited for truck transport and volume-limited for ship and rail transport. All feedstocks considered were volume-limited for rail transport. This was because of the large payload limits on railcars. In the case of commercial wood pellets and torrefied wood pellets, both

TABLE 4 Models for BTD for corn stover bales with varying moisture contents.

Mode of transportation	Model	Model's R^2
Truck BTD (km)	$y = 13965 + 9002.7x – 2148.2x^2$	0.99
Rail BTD (km)	$y = 86344 – 482.6x – 2329.9x^2$	0.99
Ship BTD (km)	$y = 67629 + 32702x – 5487.8x^2$	0.86

Note: y is the BTD in km, and x is the moisture content in percent w.b. ranging between 10 and 50.

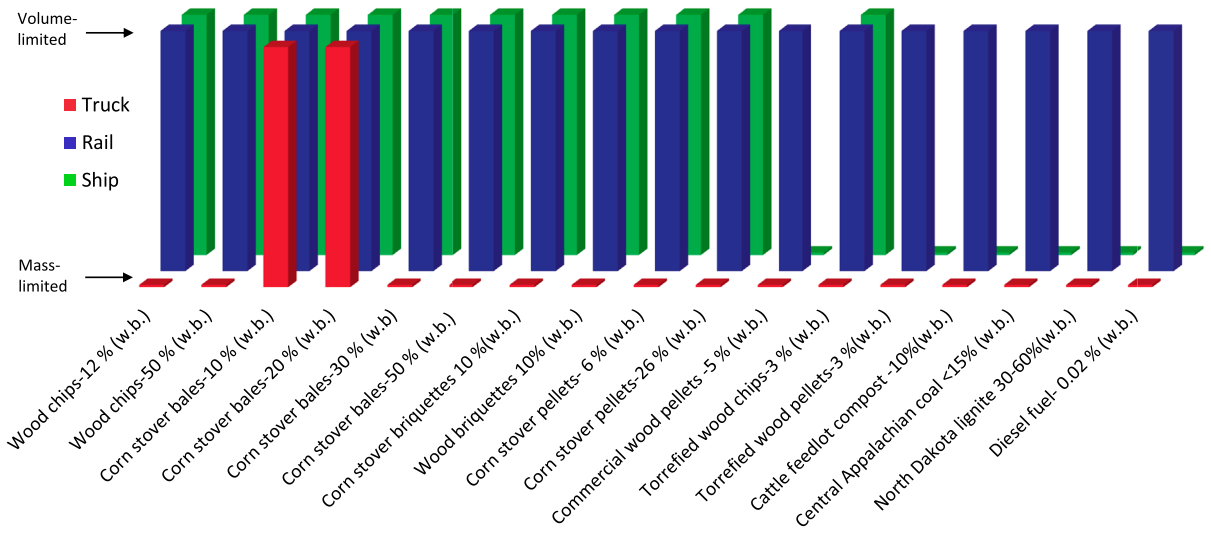

FIGURE 4
Mass-limited or volume-limited transport for the combinations of biomass feedstocks and fossil fuels and transportation modes. Lowered bars/tiles are mass-limited, and tall bars are volume-limited.

the truck and ship are mass-limited, whereas the rail is volume-limited. Fossil fuels such as different coals (Central Appalachian coal and North Dakota lignite) and diesel fuel also have similar trends like commercial and torrefied wood pellets. For instance, a railcar can carry materials with a bulk density of up to approximately 1,500 kg/m^3, and no biomass feedstocks will reach this density and thus represent the underutilization of rail transport. For volume-limited transport, any pretreatment (e.g., torrefaction) resulting in higher densities will increase the BTD, representing a logistic opportunity. The underutilized transportation space needs to be optimized for better logistics advantage.

3.5 Truck transport analysis of the biomass feedstocks in the US

Biomass feedstock is typically grown in regions with low population densities. These regions can be far from the refineries or power plants. A comparison of the BTDs of truck transport for a truck filled to its allowable limit using various biomass feedstocks within the perimeter of the US was performed. This analysis was useful for understanding the feasibility of transporting various biomass feedstocks to the stakeholder's processing facility locally within a state or transported interstate (Figure 5). For this analysis, the US perimeter was considered 14,452 km (Beaver, 2018), which is the approximate coastline of the 48 contiguous US states excluding Alaska and Hawaii. The results present the BTD pattern for 1 US ton as well as a whole truckload of bio-based fuels considered in terms of direct distance (km) and US perimeter to allow for easy unit mass (1 US ton and whole truckload) comparison. Interestingly, the BTD pattern was different for cases of the volume-limited biomass feedstocks, such as corn stover bales-10% w.b. and -20% w.b. (low bulk density materials), compared to a similar pattern (Figure 5) otherwise for mass-limited transport.

Among the biomass feedstocks considered, the torrefied pellets had the highest BTD and therefore can be transported around the US perimeter the most, namely, 2.88 times. This was mainly due to the relatively high specific energy and high bulk density of torrefied pellets. As bales, pellets, and briquettes have nearly the same specific energies, the driving factor in their comparison was the bulk density. Feedlot compost has the lowest specific energy and was mass-limited for trucks as shown previously (Figure 4). Even with these considerations, feedlot compost can be transported approximately 0.9 times around the US perimeter before reaching its

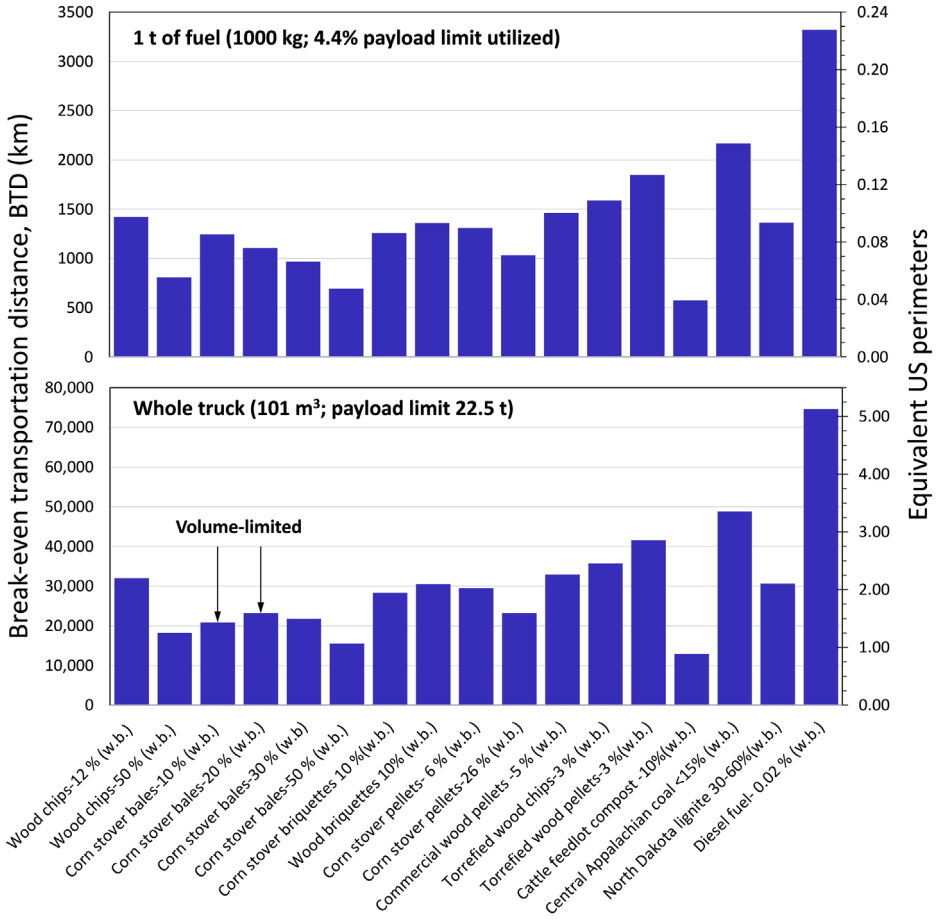

FIGURE 5
BTDs for transporting biomass feedstocks and fossil fuels with trucks, both for 1 metric ton of biomass feedstock and diesel and for whole truck transport. Changes in profile shapes are marked with an arrow due to volume-limited transportation.

BTD. This means that the feedlot compost originating in the Central US can be transported anywhere in the US and still have a net calorific value.

Overall, for the biomass feedstocks considered (14), excluding coal, the equivalent US perimeter transport distance varies from 0.9 to 2.88 times (Figure 5). This conceptual result also demonstrates that interstate biomass feedstock transport is highly practical based on the BTDs as interstate distances are significantly lower than the US perimeter. Thus, biomass-derived bio-based fuels in loose and all densified forms considered could be transported practically to all 48 contiguous US states. Furthermore, the location of biorefineries can be optimized to minimize the hauling distances, resulting in increased net energy in logistics. Regardless of the location of the biorefinery, interstate truck transport, as a single mode of transportation based on net energy in the biomass feedstock, was found not to be a limiting factor.

In the present study, the estimated BTDs presented for various biomass feedstocks and fossil fuels were based on inroad transportation logistics only. The inclusion of other energies of related biomass harvesting, preprocessing, and pretreatments like baling, densification, torrefaction, storage, handling, and biofuel conversion will make the analysis more comprehensive and reflective of the whole supply chain. The results of the present study may not provide rational upper bounds on the distances that biomass feedstocks may be economically transported; however, these data should help in making informed decisions as transportation economics are directly influenced by BTDs. In addition, the results should help identify limitations on biomass feedstock transport, leading to biomass utilization feasibility.

Based on this research, it can be concluded that each biomass feedstock has an optimum bulk density for transportation. If the biomass feedstock is dried too much (less bulk density), the transportation is volume-limited, and when the material is too wet (higher bulk density), the transportation is mass-limited. Mass-limited transportation, satisfying the payload limitation, is the most efficient mode. Therefore, the material should be processed (e.g., densification) so as to make the transportation mass-limited, whereas the volume-limited transportation represents underutilization of the allowable payload. Thoreson et al. (2014)

suggested that bulk densities of approximately 270–370 kg/m^3 are necessary to fill the truck full to its load capacity. The conventional pelleting process which produces pellets with densities of approximately 650–700 kg/m^3 may not be the right technology to transport pelleted biomass using trucks. Although it reduces the transportation cost, it may not offset the pelleting costs incurred during the conventional pelleting process (Schill, 2014).

To overcome these limitations, novel energy-efficient biomass preprocessing and pretreatment technologies should be developed to reduce the preprocessing cost and make transportation more energy-efficient. Tumuluru (2023) recently tested high-moisture pelleting at pilot and commercial scales on corn stover bales and found that the process reduces the pelleting production energy by approximately 70% compared to conventional technology followed by the industry but can help produce pellets which can meet the transportation requirements by trucks. This will coincide with the concept of minimum energy required to dry the material in preparation for transport. Furthermore, the thermal pretreatment technologies, such as torrefaction, pyrolysis, and gasification, which make bio-based fuels high in specific energy, can help improve transportation efficiencies. Future research should consider the optimum moisture and density the raw biomass material should have and incorporate factors such as material degradation and storage time requirements.

Knowledge and understanding of the transportation BTD of various biomass feedstocks help plan the layout of the biorefineries to increase sustainability and optimize the cost of transportation during their design phase. The BTD analysis provided in this paper can help the policymakers understand how the energy content in the biomass and transportation BTD calculation can be factored into the net-zero emissions in the complete supply chain analysis. The BTD of various biomass feedstocks can help plan the carbon debt that can be incurred by the transportation of biomass-based material from managed forests, cropland, and other preprocessing satellite locations.

3.6 Future research opportunities

To make better sense of the truck-based BTD results, they have to be overlaid on the existing road network, and this may constitute another practical future study. Likewise, rail transport should be evaluated on the existing railway infrastructure. Combining modes of transportation will provide a more accurate transportation profile that can then be optimized. Future studies should include the energy required for preparing the biomass materials, including processes such as harvesting, drying, chipping, grinding, densification, torrefaction, and other preprocessing and pretreatment technologies that are used to make the biomass into a ready-to-convert feedstock for bio-based fuels and biopower generation. Future studies on BTD calculations should also be focused on the material losses due to material degradation, and combining the different modes of transport can help maximize the distance transported with minimum energy. Furthermore, the impact of fuel efficiency of trucks as well as specific road conditions, weather, and truck size should be evaluated in the future. Studies related to how trucks and ships with varying sizes and efficiencies impact the BTD can be part of future studies.

In this initial study, we have designed the framework for understanding the transportation BTD of various biomass feedstocks. It is believed that the introduction of the concept and understanding of BTD, developed in this study, serves the purpose of the initial outcome. Future analysis should include how biomass preprocessing and pretreatment technologies impact the transportation BTD and sensitivity analysis of significantly influencing factors. Regarding truck transport, specific types of trucks (semi-trailers, flatbeds, step decks, dry vans, reefers, box trucks, and tankers) will be best suited to a specific type of biomass feedstock (e.g., loose crop residues, wood chips vs. densified pellets, and briquettes), and a more complete analysis of the combinations of truck and biomass feedstock types should be considered for future research. Another aspect of practical interest is the economics component; similar to BTD, a break-even cost can be derived for the different biomass feedstocks. Such a logistical economic analysis will eventually influence the decision on the biomass feedstock selection, and the mode of transport should be considered for future research. A full-scale sensitivity analysis that incorporates inter-variable dependence, such as fuel properties and fuel efficiency, needs to be performed to understand the sensitivity of the various factors influencing the BTDs of various biomass feedstocks.

4 Conclusion

The BTDs of 14 biomass feedstocks and three fossil fuels, the distance at which the energy in these bio-based fuels equals the energy in the conventional fuel used for transportation, were evaluated for various modes of transport (truck, rail, and ship). The various biomass feedstock properties (bulk density and specific energy) and transporting parameters (fuel efficiency, payload limits, volume, and velocity of transport) affected the BTD of the biomass feedstocks and fossil fuels tested. Overall, the mass-limited transportation is more efficient than the volume-limited mode. From the fuel efficiency and the cargo volume available, the biomass feedstocks' bulk density limits from which the transportation becomes efficient mass-limited are 223, 1,480, and 656 kg/m^3 for truck, rail, and ship, respectively. The torrefied wood pellets and the Central Appalachian coal in solid fossil fuels had the highest BTDs, whereas feedlot compost and corn stover bales with 50% w.b. had the least BTDs for all modes of transportation. The results indicated high bulk density and specific energy of biomass feedstocks, as well as low moisture content, increased the BTD values. Polynomial models for corn stover (most abundant agricultural feedstock) bales have adequately described ($0.86 \leq R^2 \leq 0.99$) the BTD as a function of moisture content (10–50% w.b.) for all three modes of transportation.

Ranking of the different transportation modes based on their BTDs indicated that truck was the least efficient, followed by rail, and ship was the most efficient mode of transportation. On average, the

rail gives 3.1 times and ship gives 8.4 times the BTD with respect to the least efficient truck for values were 3.1 and 9.2 for all the biomass feedstocks including the three fossil fuels. The US perimeter-based logistical results indicate that interstate transport of various biomass feedstocks was highly viable based on BTDs as the energy available in a truckload of feedstock was sufficient to go around the perimeter of the US for approximately 0.9–2.88 times for different biomass feedstocks studied. Future studies might look into the effects of overlaying the road network, road conditions, weather, varying truck or ship sizes, material degradation, preprocessing energy, impact of pretreatment technologies, optimum moisture, and sensitivity analysis on fuel efficiency as well as economic considerations in the BTD analysis.

Data availability statement

The original contributions presented in the study are included in the article/Supplementary Material; further inquiries can be directed to the corresponding author.

Author contributions

JT: conceptualization, data curation, formal analysis, funding acquisition, investigation, methodology, resources, validation, visualization, writing–original draft, and writing–review and editing. CI: conceptualization, funding acquisition, methodology, project administration, resources, supervision, writing–original draft, and writing–review and editing. DA: conceptualization, funding acquisition, methodology, resources, and writing–review and editing. RM: formal analysis, methodology, writing–original draft, and writing–review and editing.

Funding

The author(s) declare that financial support was received for the research, authorship, and/or publication of this article. This work was supported by the Department of Energy, Office of Energy Efficiency and Renewable Energy, under the Department of Energy Idaho Operations Office Contract DE-AC07-05ID14517, and the USDA National Institute of Food and Agriculture, under Hatch Project ND01493. This research was a contribution from the Long-Term Agroecosystem Research (LTAR) network, and LTAR is supported by the United States Department of Agriculture, under Fund No. FAR0036174.

Conflict of interest

The authors declare that the research was conducted in the absence of any commercial or financial relationships that could be construed as a potential conflict of interest.

Publisher's note

All claims expressed in this article are solely those of the authors and do not necessarily represent those of their affiliated organizations, or those of the publisher, the editors, and the reviewers. Any product that may be evaluated in this article, or claim that may be made by its manufacturer, is not guaranteed or endorsed by the publisher.

Author disclaimer

Mention of trade names or commercial products in this publication is solely for the purpose of providing specific information and does not imply recommendation or endorsement by the US Department of Agriculture and NDSU. USDA and NDSU are equal opportunity providers and employers. This work was prepared as an account of work sponsored by an agency of the US government. Neither the US government nor any agency thereof, nor any of their employees, nor any of their contractors, subcontractors, or their employees, makes any warranty, express or implied, or assumes any legal liability or responsibility for the accuracy, completeness, or usefulness of any information, apparatus, product, or process disclosed, or represents that its use would not infringe privately owned rights. References herein to any specific commercial product, process, or service by trade name, trademark, manufacturer, or otherwise, do not necessarily constitute or imply its endorsement, recommendation, or favoring by the US government or any agency thereof, or its contractors or subcontractors. The views and opinions of authors expressed herein do not necessarily state or reflect those of the US government or any agency thereof. Accordingly, the publisher, by accepting the article for publication, acknowledges that the US government retains a non-exclusive, paid-up, irrevocable, worldwide license to publish or reproduce the published form of this manuscript or allows others to do so for US government purposes.

Supplementary material

The Supplementary Material for this article can be found online at: https://www.frontiersin.org/articles/10.3389/fenrg.2024.1347581/full#supplementary-material

References

AAPA (2009). *American association of port Authorities. Comparison between Panamax and post-panamax container vessels*. Alexandria: Institute for Trade and Transportation Studies.

Allen, M., Dube, O., Solecki, W., Aragón-Durand, F., Cramer, W., Humphreys, S., et al. (2018). *Framing and context*. Cambridge, UK and New York, NY, USA: Cambridge University Press, 49–92. chap. Global Warming of 1.5 °C.

An IPCC Special Report on the impacts of global warming of 1.5 °C above pre-industrial levels and related global greenhouse gas emission pathways, in the context of strengthening the global response to the threat of climate change, sustainable development, and efforts to eradicate poverty. doi:10.1017/9781009157940.003

Anttila, P., Nummelin, T., Väätäinen, K., Laitila, J., Ala-Ilomäki, J., and Kilpeläinen, A. (2022). Effect of vehicle properties and driving environment on fuel consumption and CO_2 emissions of timber trucking based on data from fleet management system. *Transp. Res. Interdiscip. Perspect.* 15, 100671. doi:10.1016/j.trip.2022.100671

Beaver, J. (2018). U.S. International boarders: brief facts. Available at: https://www.ilw.com/immigrationdaily/news/2007,1115-crs.pdf.

Boundy, B., Diegel, S., Wright, L., and Davis, S. (2011). *Biomass energy data book*. 4th edn. United States: U.S. Department of Energy.

Bradley, D., Hektor, B., Wild, M., Deutmeyer, M., Schouwenberg, P. P., Hess, J. R., et al. (2014). "Low cost, long distance biomass supply chains," in *IEA bioenergy task 40*. Editors C. S. Goh, and M. Junginger

CFCL Co (2018). CFCL Co., Chicago Freight car leasing Co. Railcar types. Available at: http://www.crdx.com/Services/OpenTop.

CSX Corporation (2018). CSX Corporation. Fuel efficiency. Available at: https://www.csx.com/index.cfm/about-us/the-csx-advantage/fuel-efficiency/.

Davis, S., Diegel, S., Boundy, R., and Moore, S. (2014). *TruckEfficiency 2014 vehicle technologies market report*. Oak Ridge, TN, USA: Oak Ridge National Laboratory.

DieselNet (2018). DieselNet. Available at: https://www.dieselnet.com/standards/eu/fuel_reference.php.

Engineering ToolBox (2018). The engineering ToolBox. URL: http://www.engineeringtoolbox.com/classification-coal-d_164.html.

FCCC (2015). *United Nations framework convention on climate change, Paris, France, 30*. Available at: http://unfccc.int/resource/docs/2015/cop21/eng/l09.pdf.

Franzese, O., and Davidson, D. (2011). *Effect of weight and roadway grade on the fuel economy of class-8 freight trucks*. Tennessee, USA: Oak Ridge National Laboratory.

Goulielmos, A. M. (2021). When in shipping, do as greeks do: for a successful creation and management of a shipping company dealing with tankers and/or bulk carriers. *Mod. Econ.* 12, 1537–1562. doi:10.4236/me.2021.1210078

Hauth, M. R., Botelho, F. M., Hoscher, R. H., Botelho, S. d. C., and de Oliveira, G. H. (2018). Physical properties of different soybean cultivars during drying. *Eng. Agrícola* 38, 590–598. doi:10.1590/1809-4430-eng.agric.v38n4p590-598/2018

Loyd's Register (2023). *Loyd's Register. InfoSheet No. 30. Modern ship size definitions*. London, UK: Information Centre.

Lu, C., and Yan, X. (2015). The break-even distance of road and inland waterway freight transportation systems. *Marit. Econ. Logist.* 17, 246–263. doi:10.1057/mel.2014.14

Mahmudi, H., and Flynn, P. (2006). Rail vs truck transport of biomass. *Appl. Biochem. Biotechnol.* 129, 88–103. doi:10.1385/abab:129:1:88

Mani, S., Tabil, L., and Sokhansanj, S. (2004). Grinding performance and physical properties of wheat and barley straws, corn stover and switchgrass. *Biomass Bioenergy* 27, 339–352. doi:10.1016/j.biombioe.2004.03.007

Mode Transportation (2018). Mode transportation. Available at: http://www.jillamy.com/pdfs/Truck_Sizes_LTL.pdf.

Perlack, R., Eaton, L., Turhollow, A., Langholtz, M., Brandt, C., Downing, M., et al. (2011). *US billion-ton update: biomass supply for a bioenergy and bioproducts industry*.

Picchio, R., Di Marzio, N., Cozzolino, L., Venanzi, R., Stefanoni, W., Bianchini, L., et al. (2023). Pellet production from pruning and alternative forest biomass: a review of the most recent research findings. *Materials* 16, 4689. doi:10.3390/ma16134689

Portz, T. (2016). *Panamaxing it out*. Biomass Magazine.

Pradhan, P., Arora, A., and Mahajani, S. M. (2018). Pilot scale evaluation of fuel pellets production from garden waste biomass. *Energy Sustain. Dev.* 43, 1–14. doi:10.1016/j.esd.2017.11.005

Schill, S. R. (2014). Ethanol Producer Magazine, BBI International. Available at: https://ethanolproducer.com/articles/stover-pellets-pack-in-the-pounds-11434.

Searcy, E., Hess, J. R., Tumuluru, J., Ovard, L., Muth, D. J., Trømborg, E., et al. (2014). "Optimization of biomass transport and logistics" in *International Bioenergy Trade. Lecture Notes in Energy*. Editors M. Junginger, C. Goh, and A. Faaij (Dordrecht: Springer) 17. doi:10.1007/978-94-007-6982-3_5

Shinners, K. J., Binversie, B. N., Muck, R. E., and Weimer, P. J. (2007). Comparison of wet and dry corn stover harvest and storage. *Biomass Bioenergy* 31, 211–221. doi:10.1016/j.biombioe.2006.04.007

STC (2023). Soy Transportation Coalition. Classes of vessels and cargo capacity. Available at: https://www.soytransportation.org/Stats/Ocean_VesselClasses.pdf.

Sweeten, J., Heflin, K., Annamalai, K., Auvermann, B., McCollum, F., and Parker, D. (2006). *Combustion-fuel properties of manure or compost from paved vs unpaved cattle feedlots*. United States: American Society of Agricultural and Biological Engineers.

Thoreson, C. P., Webster, K. E., Darr, M. J., and Kapler, E. J. (2014). Investigation of process variables in the densification of corn stover briquettes. *Energies* 7, 4019–4032. doi:10.3390/en7064019

Truckers Report Jobs (2018). Truckers report. Facts about trucks — everything you want to know about eighteen wheelers. Available at: http://www.thetruckersreport.com/facts-about-trucks/.

Tumuluru, J. (2015). Comparison of chemical composition and energy property of torrefied switchgrass and corn stover. *Front. Energy Res.* 3, 46. doi:10.3389/fenrg.2015.00046

Tumuluru, J., Hess, J., Boardman, R., Wright, C., and Westover, T. (2012). Formulation, pretreatment, and densification options to improve biomass specifications for co-firing high percentages with coal. *Ind. Biotechnol.* 8, 113–132. doi:10.1089/ind.2012.0004

Tumuluru, J., Lim, C., Bi, X. T., Kuang, X., Melin, S., Yazdanpanah, F., et al. (2015a). Analysis on storage off-gas emissions from woody, herbaceous, and torrefied biomass. *Energies* 8, 1745–1759. doi:10.3390/en8031745

Tumuluru, J., Wright, C., Hess, J., and Kenney, K. (2011). A review of biomass densification systems to develop uniform feedstock commodities for bioenergy application. *Biofuels, Bioprod. Biorefin.* 5, 683–707. doi:10.1002/bbb.324

Tumuluru, J. S. (2016). Specific energy consumption and quality of wood pellets produced using high-moisture lodgepole pine grind in a flat die pellet mill. *Chem. Eng. Res. Des.* 110, 82–97. doi:10.1016/j.cherd.2016.04.007

Tumuluru, J. S. (2023). High-moisture pelleting of corn stover using pilot-and commercial-scale systems: impact of moisture content, L/D ratio and hammer mill screen size on pellet quality and energy consumption. *Biofuels, Bioprod. Biorefin.* 17, 1156–1173. doi:10.1002/bbb.2519

Tumuluru, J. S., Dansie, T., Johnson, I., and Conner, C. (2015b). *Specific energy consumption and quality of briquettes produced using woody and herbaceous biomass*. New Orleans, LA: American Society of Agricultural and Biological Engineers Annual International Meeting.

Tumuluru, J. S., Ghiasi, B., Soelberg, N. R., and Sokhansanj, S. (2021). Biomass torrefaction process, product properties, reactor types, and moving bed reactor design concepts. *Front. Energy Res.* 9, 728140. doi:10.3389/fenrg.2021.728140

Tumuluru, J. S., Sokhansanj, S., Lim, C. J., Bi, T., Lau, A., Melin, S., et al. (2010). Quality of wood pellets produced in British Columbia for export. *Appl. Eng. Agric.* 26, 1013–1020. doi:10.13031/2013.35902

Wiegmans, B., and Konings, R. (2015). Intermodal inland waterway transport: modelling conditions influencing its cost competitiveness. *Asian J. shipp. Logist.* 31, 273–294. doi:10.1016/j.ajsl.2015.06.006

Yancey, N. (2016). Bale density information. Personal communication. *Sens. Basel* 23, 1778. doi:10.3390/s23041778

Yancey, N., Tumuluru, J., and Wright, C. (2013). Drying, grinding and pelletization studies on raw and formulated biomass feedstock's for bioenergy applications. *J. Biobased Mater. Bioenergy* 7, 549–558. doi:10.1166/jbmb.2013.1390

10.3389/fenrg.2024.1347581

Nomenclature

BD_{bio}	Reference dry bulk density [kg/m^3]
BD_{dry}	Bone dry bulk density [kg/m^3]
BD_{ref}	Reference dry bulk density [kg/m^3]
BTD	Break-even transportation distance [km]
BTD_{rail}	Break-even transportation distance of rail transport [km]
BTD_{ship}	Break-even transportation distance of ship transport [km]
BTD_{truck}	Break-even transportation distance of truck transport [km]
D	Transported distance [km]
E_{bio}	Energy content of biomass feedstock [MJ]
E_{rail}	Energy consumed in rail transport [MJ]
E_{ship}	Energy consumed in ship transport [MJ]
E_{truck}	Energy consumed in truck transport [MJ]
MC	Moisture content [%, w.b.]
MC_{ref}	Reference moisture content [w.b. decimal]
PL	Legal payload limit [kg]
SE_{bio}	Specific energy of biomass feedstock [MJ/kg]
SE_{dry}	Specific energy of bone dry biomass feedstock [MJ/kg]
SE_f	Specific energy of the diesel fuel [MJ/kg]
SE_{ref}	Specific energy of reference biomass feedstock [MJ/kg]
v	Velocity of ship transport [km/h]
V	Volume limit of the transportation mode [m^3]
Greek symbols	
η_r	Fuel efficiency of rail transport [kg km/L]
η_s	Fuel efficiency of ship transport [kg/h]
η_t	Fuel efficiency of truck transport [km/L]

frontiers | Frontiers in Energy Research

TYPE Review
PUBLISHED 07 May 2024
DOI 10.3389/fenrg.2024.1332174

OPEN ACCESS

EDITED BY
Kui Jiao,
Tianjin University, China

REVIEWED BY
Rachele Lamioni,
University of Pisa, Italy
Siti Fatihah Salleh,
Petronas Research Sdn Bhd, Malaysia

*CORRESPONDENCE
Muhammad Naqvi,
✉ sayed.naqvi@aum.edu.kw
Muhammad Tajammal Munir,
✉ muhammad.munir@aum.edu.kw

RECEIVED 02 November 2023
ACCEPTED 09 April 2024
PUBLISHED 07 May 2024

CITATION
Munir MT, Naqvi M and Li B (2024), A converging path: a decade's reflection on net zero emissions and the circular economy.
Front. Energy Res. 12:1332174.
doi: 10.3389/fenrg.2024.1332174

A converging path: a decade's reflection on net zero emissions and the circular economy

Muhammad Tajammal Munir[1]*, Muhammad Naqvi[1]* and Bing Li[2]

[1]College of Engineering and Technology, American University of the Middle East, Egaila, Kuwait, [2]Water Research Center, Shenzhen International Graduate School, Tsinghua University, Shenzhen, China

In the past decade, global sustainability efforts have increasingly focused on two critical paradigms: achieving net zero emissions (NZE) and advancing the circular economy (CE). This article provides a detailed examination of the challenges and breakthroughs in harmonizing these approaches, drawing from a broad range of academic discussions, technological innovations, policy developments, and practical implementations. We identify specific obstacles, such as technological limitations, policy inertia, and economic and social barriers, that hinder progress towards NZE and CE. The paper then outlines targeted solutions, including cutting-edge technologies like carbon capture and storage, policy frameworks that incentivize sustainable practices, and examples of successful circular economy models. Through a critical analysis of both the synergies and tensions between NZE and CE, the article highlights the necessity for cross-sector collaboration, robust policy support, and ongoing innovation to overcome these challenges. Concluding with a forward-looking perspective, we emphasize strategic pathways for integrated sustainability efforts, advocating for a multi-faceted approach that combines technological advancement, policy reform, and stakeholder engagement. By offering a more nuanced understanding of the interplay between theoretical goals and practical realities, this revised abstract aims to inspire action and foster a collective move towards a sustainable global future.

KEYWORDS

net zero emissions, circular economy, sustainability, policy development, socioeconomic impact

1 Introduction

In an epoch marked by accelerating ecological degradation and growing concerns surrounding climate change, the entwined paradigms of net zero emissions (NZE) and the Circular Economy (CE) have emerged as beacon concepts for global sustainable transformation. Both of these frameworks, though distinct in their specifics, share a profound interconnectedness rooted in the need to address our anthropogenic impacts on the environment.

Net zero emissions, a term now echoing in international policy chambers and boardrooms alike, encapsulates the aspiration to strike a balance, wherein anthropogenic greenhouse gas outputs are neutralized by equivalent removals or offsets (Davis et al., 2018; Rahman and Wahid, 2021). The momentum behind this target is not solely driven by environmental urgency. As elucidated by numerous studies over the past decade, this balance embodies multifaceted implications, spanning economic, social, and geopolitical spheres (Rogelj et al., 2021). The daunting reality of sea-level rise, the increasing

volatility of climate patterns, and the subsequent socio-economic ramifications have reinforced the cruciality of this emission equilibrium (Van Soest et al., 2021; Bergero et al., 2023).

Concurrently, the circular economy offers a profound shift from the entrenched linear model that has long dominated our production and consumption habits. Eschewing the traditional "take, make, dispose" approach, the circular paradigm emphasizes a regenerative design, underpinned by reduction, reuse, and recycling. It challenges the very ethos of our consumption-driven economies, urging a transition towards systems that harmoniously coexist with ecological cycles and prioritize resource efficiency (Naqvi et al., 2017; Mies and Gold, 2021; Corvellec et al., 2022; Dzhengiz et al., 2023; Munaro and Tavares, 2023; Tunio et al., 2024).

Over the last 10 years, profound transformations have punctuated the global sustainability landscape, offering a rich tapestry of insights, challenges, and achievements. Examining this decade allows us a deeper understanding of the pivotal shifts in both perception and actions related to NZE and the CE. This examination transcends pure academic analysis; it serves as a platform to assess past milestones, discern challenges, and inform future approaches.

The primary objective of this article is to provide an exhaustive exploration of the interconnected evolution of two paramount sustainability paradigms that have dominated the last decade's discourse: NZE and the CE. By traversing through a diverse landscape of academic literature, technological breakthroughs, policy shifts, and tangible applications, we aim to elucidate the fundamental principles of these paradigms, chronicle their historical trajectory, critically assess the challenges and roadblocks they've encountered, and undertake a comparative analysis of regional adaptations and outcomes. Furthermore, we seek to unearth the intricate dance of synergies and tensions between these two paradigms, leveraging real-world case studies for in-depth insights, and gauge their broader socio-economic reverberations on the global stage.

The novelty of this article lies in its ambitious integrated approach. While many analyses have delved deep into either NZE or the CE, few have ambitiously attempted to meld the two into a singular, coherent narrative. Our article embarks on this interdisciplinary journey, marrying these seemingly distinct paradigms to reveal their overlapping trajectories, mutual reinforcements, and occasional areas of discord. Moreover, by weaving theory with practicality, our narrative also bridges the chasm between academic postulations and the gritty realities of on-the-ground implementation, presenting a fresh and pragmatic perspective on a decade's worth of sustainability endeavors.

2 Literature review and critique

The multifaceted conversation surrounding NZE and the CE over the last decade underscores the growing global emphasis on sustainability. The literature has evolved from rudimentary understandings to intricate discussions on feasibility, mechanisms, challenges, and the interconnectedness of these frameworks. The subsequent detailed exploration endeavors to provide a comprehensive overview of the academic discussions and their critiques.

2.1 Net zero emissions

A considerable part of the literature accentuates the urgency and pathways to achieving net zero. Ürge-Vorsatz et al. (2020) reviewed recent advances in key options and strategies for converting the building sector to be climate neutral. Table 1 provides a comprehensive literature review on the Net Zero Emissions (NZE) concept from 2013 to 2024. It initiates with the fundamental principles of NZE, highlighting the urgency due to increasing carbon levels and foregrounding pivotal international agreements such as the Paris Agreement. The table subsequently delves into the Paris Agreement's central role in advancing NZE, accentuating the crucial merger of global politics with environmental science. The technological routes to achieving NZE are explored, emphasizing the significance of innovations like renewable energy and carbon capture. Additionally, the economic prospects and socio-political dimensions are illuminated, indicating a potential surge in GDP growth and accentuating the necessity for aligned global policies. The table further scrutinizes the challenges and potential hindrances in the NZE trajectory, advocating for a holistic approach. Concluding, the literature review offers a forward-looking perspective, underlining the essentiality of persistent research, novel technologies, and synchronized international efforts.

2.2 Circular economy

Similarly, Table 2 provides a comprehensive literature review on the Circular Economy (CE) from 2013 to 2024. It begins by introducing CE's foundational principles, advocating for a move away from linear models. The table then delves into circular business models, highlighting their benefits and challenges.

Key technological advancements supporting CE, such as innovative recycling methods and bio-based materials, are discussed. The economic impact of CE, including a potential 1.8% rise in global GDP by 2045, and its socio-cultural implications are emphasized, underscoring the role of education. The table also examines policy frameworks, with a spotlight on the European Union's Action Plan, and outlines global cooperative initiatives. Challenges, including technological gaps and policy fragmentation, are addressed. The review concludes by projecting future trends in CE, emphasizing continuous innovation, collaboration, and adaptive policy-making.

2.3 Intersections

Table 3 explores the intersection of Net Zero Emissions (NZE) and Circular Economy (CE).

They are vital environmental approaches in the 21st century. While CE aids NZE by reducing waste, and lessening the need for energy-intensive processes, challenges arise, like potential emission increases and balancing renewables. Economically, CE benefits support NZE, but transition costs may be problematic. Policies promoting CE can accelerate NZE, though some CE practices may conflict with NZE objectives. Case studies show industries like fashion and cities using CE principles effectively reduce emissions.

TABLE 1 Literature review on net zero emissions (2013–2024).

Section	Summary	References
Introduction to the NZE Concept	Foundational concepts of NZE introduced, with a focus on rising carbon levels and upcoming international agreements like the Paris Agreement	De Jong et al. (2015); Anderson and Peters (2016); Davis et al. (2018)
The Paris Agreement and the Rise of NZE	Analysis of the Paris Agreement's emphasis on NZE, examining the convergence of international politics and environmental science during a pivotal climate moment	Anderson and Peters (2016); Anika et al. (2022); Fankhauser et al. (2022)
Technological Avenues to Achieve NZE	Overview of technological solutions, including renewables, carbon capture, and storage, with a call for swift implementation	Rogelj et al. (2015); Meys et al. (2021); Zhao et al. (2022)
Economic and Socio-Political Dimensions	Investigation into NZE indicates a potential 2.5% GDP growth by 2050, addressing economic concerns and emphasizing socio-political challenges with recommendations for global policy alignment	Geels et al. (2016); Geels (2018); Fankhauser et al. (2022)
Challenges and Potential Setbacks	A critical look at the obstacles in the NZE journey, encompassing technological, economic, and policy challenges. An integrated approach is advocated	Bridge et al. (2013); Geels (2018); Zhao et al. (2022)
Looking Forward	Future-oriented exploration projecting the next 3 decades of NZE, emphasizing innovative technologies, global collaboration, and the need for continual research and dynamic policy adjustments	Mohan and Katakojwala (2021); Hale et al. (2022); van der Spek et al. (2022)

TABLE 2 Literature review on circular economy (2013–2024).

Category	Key findings/Highlights	References
Fundamentals of CE	Introduced basic principles and strategies of CE, advocating for a shift from linear models	Stahel (2016); Shirvanimoghaddam et al. (2020); Diamantis et al. (2021)
Business Models and Implementations	Examined the benefits of circular business models using case studies and assessed corporate adoption, highlighting both challenges and positive outcomes for sustainability and profitability	Lewandowski (2016); Rizos et al. (2016); Urbinati et al. (2017)
Technological Innovations for CE	Evaluated key technological advancements like recycling technologies and bio-based materials that furthered CE.	Smol et al. (2017); Kouhizadeh et al. (2020); Ranta et al. (2021)
Economic and Socio-Cultural Impacts	Highlighted a potential 1.8% rise in global GDP by 2045 from CE models, addressing economic myths, and emphasized societal shifts and the importance of education in CE adoption	Kapsalis et al. (2019); Friant et al. (2020); Corvellec et al. (2022)
Policy Frameworks and Global Initiatives	Examined policies supporting CE, focusing on the European Union's Action Plan, and explored global initiatives highlighting international collaborations and policy alignment	Pomponi and Moncaster (2017); Domenech and Bahn-Walkowiak (2019); Padilla-Rivera et al. (2020)
Challenges and Critiques	Enumerated potential challenges in global CE adoption like technological gaps and policy fragmentation	Millar et al. (2019); Kovacic et al. (2020); Corvellec et al. (2022)
The Road Ahead	Projected future CE trends and emphasized the need for innovation, cooperation, and adaptive policymaking	Patwa et al. (2021); Ding et al. (2023); Todorović and Obradović (2023)

TABLE 3 Intersection of net zero emissions and circular economy (2013–2024).

Section	Key findings	References
Introduction	NZE and CE are major 21st-century paradigms with converging principles for climate mitigation	Arsic et al. (2023); Okorie et al. (2023)
CE's Role in NZE	CE reduces waste and energy-intensive extraction, aiding NZE.	Bonsu (2020); Mulvaney et al. (2021)
Challenges in Merging NZE & CE	CE processes can raise emissions; balancing renewables with reused tech is hard	Bonsu (2020); Meys et al. (2021); Khalifa et al. (2022)
Economic Considerations	CE offers economic benefits supporting NZE. Transition costs might pose challenges	Lee et al. (2017); Okorie et al. (2023)
Policy Synergies & Conflicts	CE-promoting policies can boost NZE, but some CE practices might conflict with NZE goals	Domenech and Bahn-Walkowiak (2019); Bonsu (2020)
Case Studies: NZE & CE	Fashion industries highlight CE's emission reduction capabilities; cities with CE principles show decreased carbon footprints	Meys et al. (2021); Govindan (2023); Okorie et al. (2023)

2.4 Critique

Upon examining the depth and breadth of this literature, certain critical gaps emerge. One such chasm is the occasional lack of context specificity in proposed solutions. While many frameworks appear effective in Western contexts, their applicability in developing or transitional economies remains underexplored. Moreover, while there's an increasing confluence of net zero and CE literature, there remains a siloed approach in many studies, highlighting the need for more interdisciplinary research that explicitly explores their intersections.

To sum up, the past decade has witnessed an expansive growth in literature centered on NZE and the CE. While it has laid a solid foundation, offering invaluable insights, there are pressing areas that need further exploration, especially as the world seeks to operationalize these ambitious yet crucial paradigms. As scholars and practitioners continue to navigate this space, future research must ensure a holistic, inclusive, and context-specific approach.

3 Methodology

Embarking on this journey to understand the intertwined realms of NZE and the CE over the past decade necessitated a rigorous methodological framework. Our data collection strategy was twofold. First, academic databases such as JSTOR, Scopus, and Google Scholar were scoured to glean peer-reviewed articles, conference proceedings, and white papers. In parallel, gray literature was incorporated into our dataset, drawing from reports of international bodies like the UN and IPCC, publications from various governments, and contributions from notable NGOs. This approach was taken to ensure we were capturing not just theoretical and empirical studies, but also real-world applications and policy directives.

With the vastness of available literature, establishing clear selection criteria became paramount. We initiated our screening process by filtering studies published between 2013 and 2023 using specific keywords related to our focal themes. This was followed by setting inclusion and exclusion benchmarks. Pertinent to our analysis were studies that directly engaged with our themes, showcased clear research methodologies, and bore relevance to either global or regional policy implications. Conversely, we sidestepped studies with tangential relevance or those without rigorous methodological outlines, making exceptions for recognized gray literature. Through this meticulous process, we curated a diverse dataset that encapsulated various geographies, sectors, and academic disciplines.

The analytical lens we adopted was tripartite. We embarked on a temporal analysis, meticulously charting the ebbs and flows in the research frequency, technological innovations, and policy shifts over the years. This allowed us to identify discernible trends and pivotal moments that shaped the decade. Next, our evaluation of successes was rooted in both quantitative metrics, such as actual reductions in emissions and adoption rates of circular practices, and qualitative insights gleaned from transformative case studies. Lastly, we delved into a gap analysis, merging content analysis with a meta-review to spotlight overlooked areas, persistent challenges, or emergent domains warranting attention.

In essence, our methodology, by synthesizing diverse sources and adopting a multifaceted analytical approach, sought to provide an encompassing, objective, and nuanced exploration of the past decade's developments in NZE and the CE.

4 Conceptual framework

As we navigate the complex web of research, practices, and policies encompassing NZE and the CE, it becomes paramount to first anchor our understanding in a robust conceptual framework. This not only offers clarity but also ensures consistency in the interpretations and implications drawn throughout this study.

4.1 Net zero emissions

At its core, the concept of net zero emissions revolves around achieving a balance between the greenhouse gases put into the atmosphere and those taken out. It does not insinuate a complete cessation of emissions but emphasizes offsetting any emissions produced through practices like carbon capture, reforestation, and the use of sustainable energy sources. The guiding principle here is equilibrium; the goal is to ensure that anthropogenic activities don't increase the net amount of greenhouse gas concentrations in the atmosphere, thus mitigating the impacts of climate change (Delafield et al., 2021; Stern and Valero, 2021; Okorie et al., 2023).

Figure 1 delineates the strategic roadmap towards achieving global net-zero carbon emissions by 2050. It charts the decline in CO_2 emissions in gigatons (Gt CO_2) over 3 decades, segmented by sectors: Buildings, Transport, Industry, Electricity and Heat, and Others (Naqvi et al., 2016; Rehan et al., 2017). Key milestones are pinpointed throughout this timeline, highlighting vital shifts such as the cessation of new coal plant approvals in 2021, the target for 60% of global car sales to be electric by 2030, and the aim for 50% of heating demand to be met by heat pumps by 2045. Cumulatively, these actions guide a global trajectory towards sustainable energy consumption and carbon neutrality by mid-century (Bouckaert et al., 2021).

4.2 Circular economy

Traditionally, our economic systems have largely followed a linear model: extract, produce, consume, and discard (Naqvi M. et al., 2017; Naqvi et al., 2021). In stark contrast, the CE champions a regenerative approach. It's grounded in three foundational principles: design out waste and pollution, keep products and materials in use, and regenerate natural systems. This model posits that economic growth can be decoupled from resource consumption. By emphasizing sustainable production, prolonging product lifespans, promoting reuse and recycling, and driving innovations that harness waste as a resource, the CE strives for a system where nothing goes to waste. Figure 2 delineates the transformative journey from a linear to a CE, spotlighting the strategic progression to boost product circularity. Initiating with "Refuse" (R0), the model advocates for the discontinuation or innovative substitution of certain products. As we ascend, strategies like "Rethink" (R1) promote more intensive product

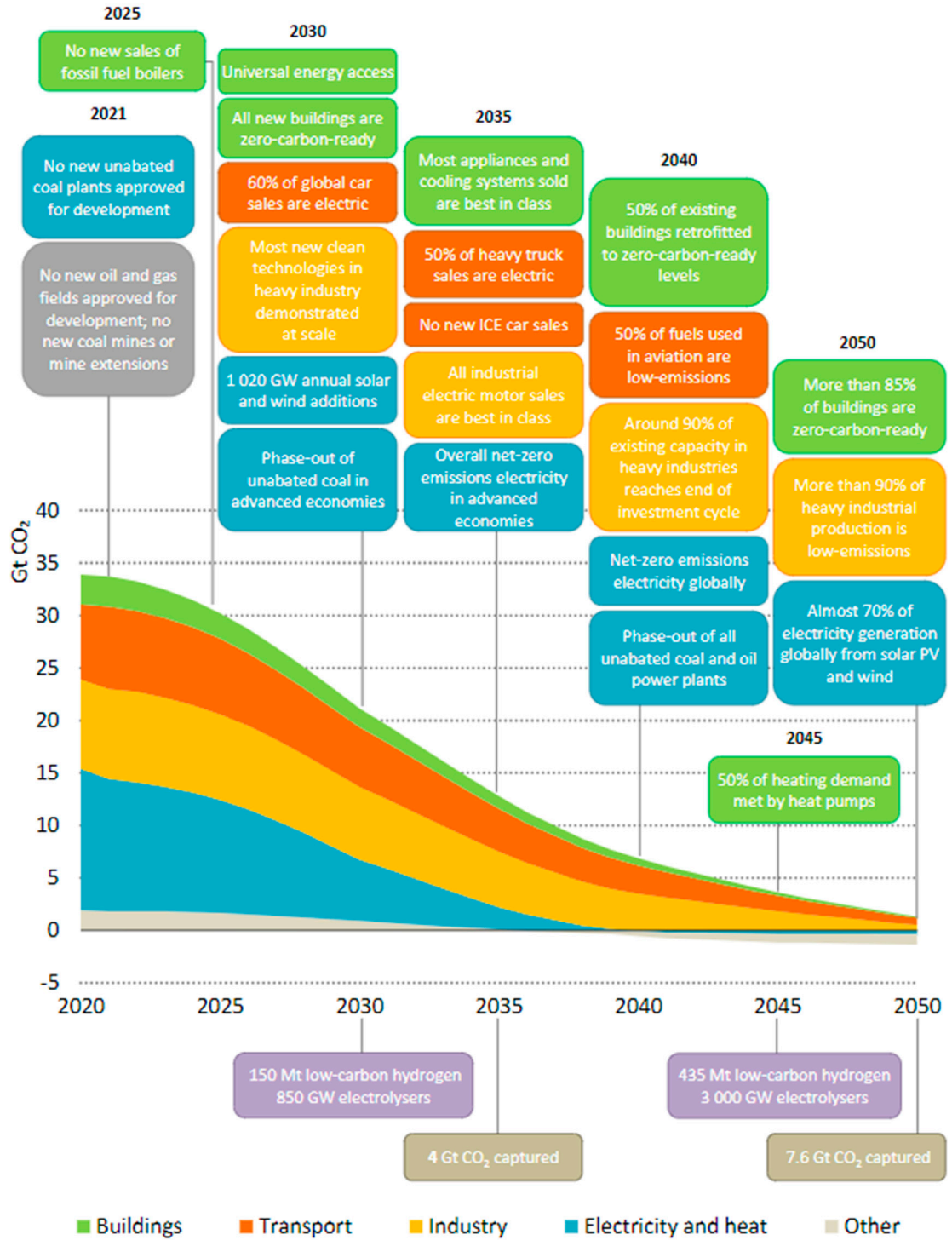

FIGURE 1
Roadmap to 2050: Key milestones and interventions for global carbon dioxide emission reduction across sectors (Bouckaert et al., 2021).

utilization, such as shared use, and "Reduce" (R2) emphasizes conservation in resource utilization. The continuum further underscores the significance of product longevity through "Reuse" (R3), "Repair" (R4), and "Refurbish" (R5). Transitioning towards repurposing, "Remanufacture" (R6) and "Repurpose" (R7) champion the ingenious reincarnation of discarded products or components. Lastly, the framework accentuates the sustainable reprocessing and energy retrieval through "Recycle" (R8) and "Recover" (R9). Collectively, the represented strategies serve as a blueprint for embedding sustainability at the core of consumption

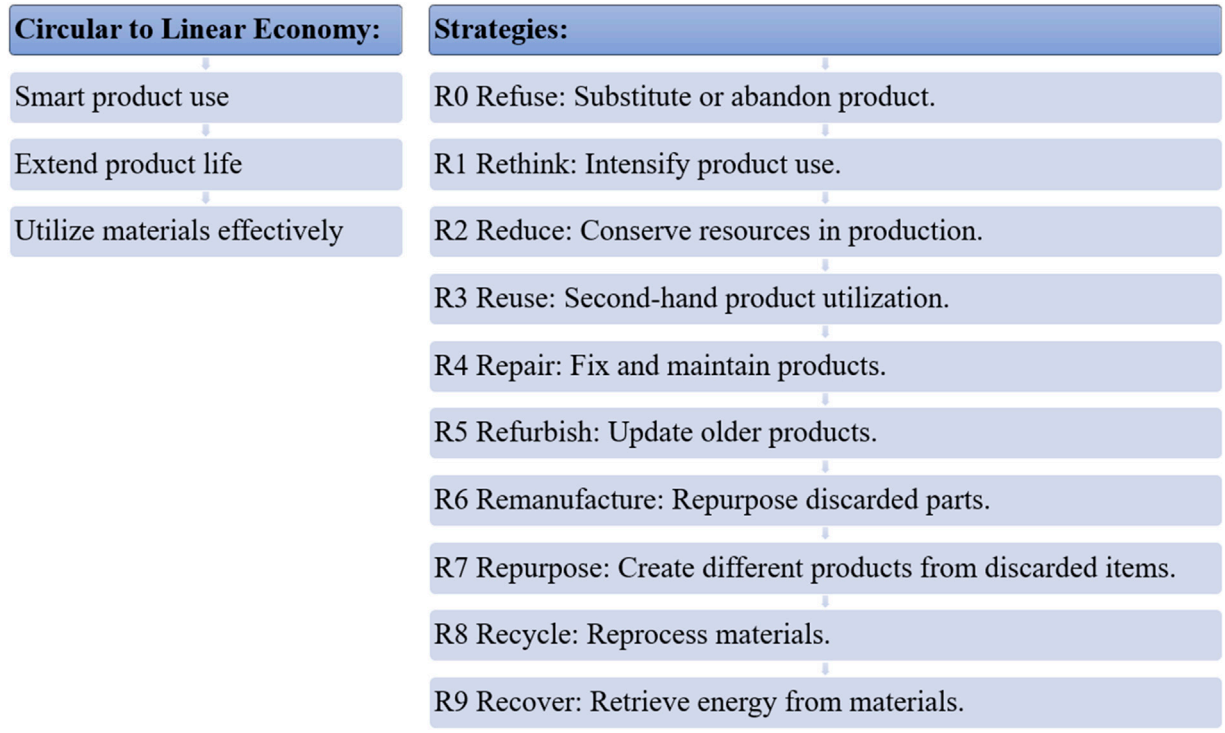

FIGURE 2
Strategies for transitioning from linear to CE: From smart product usage to material recovery (Kirchherr et al., 2017; Potting et al., 2017; Kristoffersen et al., 2020).

and production (Kirchherr et al., 2017; Potting et al., 2017; Kristoffersen et al., 2020).

4.3 Inherent connection

While on the surface, NZE and the CE might appear as distinct paradigms, a deeper exploration reveals a symbiotic relationship. The CE, with its emphasis on reducing waste, inherently reduces emissions tied to waste management, product production, and resource extraction. Meanwhile, the push for net zero directs industries towards sustainable energy sources, which further aligns with the circular philosophy of sustainable resource use. For instance, an industry adopting circular practices might prioritize recycled materials, which often have a lower carbon footprint than new materials. Similarly, in striving for net zero, industries could adopt technologies that have circular benefits, like biogas production from organic waste. This interwoven relationship suggests that the pathways to achieving NZE can be both complemented and accelerated by embracing the principles of the CE (Mohan and Katakojwala, 2021; Di Vaio et al., 2023; Mallick et al., 2023).

4.4 Progress and pathways: evaluating our journey towards 2050

In our critical assessment of the current position towards achieving the 2050 sustainability goals, we meticulously analyze the latest data on key indicators such as greenhouse gas emissions, recycling rates, and renewable energy adoption. This analysis aims to objectively evaluate our progress relative to the milestones delineated for 2025, 2030, and further, utilizing Figure 1 as a benchmark to identify both advancements and shortcomings. We also acknowledge various hurdles since the roadmap's initiation, including technological constraints, financial barriers, policy stagnation, and significant global disruptions, critically examining how these factors shape our path towards 2050. This leads to an informed evaluation of the feasibility of meeting our 2050 goals, incorporating scenarios and models that consider different levels of intervention, policy reforms, and technological developments. To navigate these challenges, we propose strategic recommendations focused on closing the identified gaps and propelling forward momentum. These include urging greater investment in green technologies, advocating for more robust policy support, fostering international collaborations for climate action, and encouraging stronger partnerships between public and private sectors. The culmination of this analysis in the manuscript's conclusion underscores the critical need for immediate and collective efforts to realign our trajectory with the ambitious targets for 2050, highlighting the urgency of adopting these strategic recommendations to ensure a sustainable future (Naqvi et al., 2013; Mont et al., 2014; Gielen et al., 2019; Moustakas et al., 2020; Moyer and Hedden, 2020; van Vuuren et al., 2022).

5 Milestones and achievements

Over the last decade, the convergence of NZE and CE principles has led to a plethora of notable milestones and achievements. This

section delves into some of the key advancements across technological, policy, and practical domains, which have not only showcased the potential of these paradigms but have also set the stage for further evolution.

5.1 Technological innovations

The nexus of net zero and circularity has been a crucible for numerous technological innovations. Carbon capture and storage (CCS) technologies, for instance, have matured significantly, offering a viable avenue for industries to mitigate their emissions (Meys et al., 2021; Sankaran, 2023). Furthermore, the rise of Industry 4.0 technologies, such as the Internet of Things (IoT) and artificial intelligence, has facilitated the tracking, management, and optimization of resources within circular supply chains, ensuring minimal waste and efficient recycling or repurposing (Fraga-Lamas et al., 2021; Bag and Pretorius, 2022).

Another breakthrough has been in the realm of renewable energy storage. The advent of advanced battery technologies and green hydrogen solutions has not only accelerated the shift towards renewable energy sources but also embedded circular principles by emphasizing the recyclability and longevity of storage mediums (Naqvi et al., 2012; Cusenza et al., 2019; Bonsu, 2020; Raza Naqvi et al., 2023).

Lastly, innovations in bio-based materials have provided sustainable alternatives to traditional plastics and other non-degradable products. These materials, often derived from agricultural waste or algae, align with both the net zero objective (by sequestering carbon) and the circular notion of leveraging waste as a resource (Leipold and Petit-Boix, 2018; Thakker and Bakshi, 2023).

A recent pilot project in the UK, involving the use of hydrogen-powered domestic condensing boilers, has showcased significant potential for reducing residential carbon emissions. This project, involved retrofitting existing gas networks to accommodate hydrogen fuel, demonstrating a scalable solution for urban and suburban households aiming for net-zero emissions (Al-Mufachi and Shah, 2022; Roy et al., 2024).

5.2 Policy developments

Policies form the backbone of systemic change, and the past decade has witnessed several landmark policy developments. Numerous countries have announced their net zero targets, bolstered by comprehensive roadmaps that factor in circular principles. For instance, the European Union's Green Deal envisions a climate-neutral continent by 2050 and has embedded circularity as a core strategy, fostering a regulatory environment that promotes sustainable production and consumption (Bonciu, 2020; Jesic et al., 2021).

Many nations have also introduced incentives for industries adopting circular practices, such as tax breaks for companies engaging in sustainable sourcing or extended producer responsibility (EPR) schemes that mandate manufacturers to manage the end-of-life phase of their products (Ghisellini et al., 2016; Ramasubramanian et al., 2023). Furthermore, the rise of cross-border coalitions and partnerships, like the Circular Economy 100 (CE100) initiative, has facilitated knowledge exchange, setting international best practices and promoting collaborative policy-making (Howard et al., 2019; Velenturf and Purnell, 2021).

A prime example of policy-driven innovation is the European Environmental Agency's "ammonia Adoption Act," a pioneering policy designed to expedite the transition of power plants to ammonia fuel in gas turbines. By offering financial incentives and regulatory support, this Act aims to reduce carbon emissions significantly, with a target of converting 30% of the EU's gas-powered plants to ammonia by 2030, thereby potentially cutting annual CO_2 emissions in the power sector by up to 20 million tons. This initiative highlights the EU's proactive approach in leveraging ammonia, a carbon-free fuel, to achieve substantial strides towards its net-zero emissions goals, setting a precedent for global energy policy (Sciences et al., 2016; Rahman and Wahid, 2021).

5.3 Case studies

The synthesis of net zero and circular principles has yielded tangible results across various sectors:

Automotive: Companies like Tesla have championed not only electric vehicles but also the circular use of materials. Their battery recycling program aims to recover critical metals and reintroduce them into the production cycle, embodying circularity while pushing for net zero transportation (Bonsu, 2021; Song and Zhou, 2023).

Fashion: Brands such as Patagonia have integrated circularity by promoting repair, reuse, and recycling of their products. Their commitment to reducing carbon footprint goes hand-in-hand with initiatives like sourcing organic materials and encouraging consumers to buy used products (Bocken et al., 2016; Dezi et al., 2022).

Urban Development: Cities like Amsterdam have embarked on a mission to become fully circular by 2050. This entails waste-to-resource initiatives, sustainable infrastructure development using recycled materials, and promoting green energy sources, all converging towards a net zero, circular urban landscape (Kurniawan et al., 2021; Mutezo and Mulopo, 2021).

By charting these milestones and achievements, it becomes evident that the marriage of NZE and CE principles has not only been conceptually enriching but has also led to tangible, impactful advancements across the global sustainability landscape.

6 Challenges and limitations

While the previous section celebrated the milestones, it's equally vital to critically engage with the challenges and setbacks that have surfaced over the decade. Integrating NZE and CE principles, despite its potential, has been a journey marred with multifaceted obstacles, ranging from technological bottlenecks to socio-political constraints.

6.1 Technological challenges

The realm of technology, although bustling with innovation, has had its share of hurdles. For instance, while Carbon Capture and

Storage (CCS) emerged as a promising avenue, its scalability and economic viability remain concerns. High operational costs and concerns about the long-term storage integrity have made widespread adoption slow. Similarly, while bioplastics hold promise, their decomposition rate, under certain conditions, is not as rapid as anticipated, posing waste management challenges.

6.2 Economic limitations

Transitioning to a CE often requires significant upfront investments. Small and medium enterprises (SMEs), in particular, find it challenging to invest in sustainable and circular innovations due to limited capital and perceived economic risks. Moreover, the global market still predominantly rewards linear economic practices, creating a competitive disadvantage for early circular adopters.

6.3 Policy and regulatory setbacks

Although many policies support circular and net zero initiatives, they sometimes exist in silos, lacking an integrated approach. Furthermore, the enforcement of these policies is inconsistent across regions. For instance, Extended Producer Responsibility (EPR) regulations vary widely, leading to discrepancies in their effectiveness. International trade policies, at times, inadvertently promote linear practices, creating barriers for circular products and services.

6.4 Socio-cultural barriers

The shift towards circularity and net zero requires a significant behavioral change. Consumerism, fueled by a culture of disposability, often clashes with the principles of the CE. The allure of "newness," whether in gadgets, fashion, or even vehicles, often supersedes the appeal of sustainable, long-lasting, or recycled products.

6.5 Supply chain complexities

As businesses aim to embed circularity into their operations, they grapple with the complexity of ensuring sustainability throughout the supply chain. Tracking the origin, lifecycle, and end-of-life of products and materials is an intricate task, often exacerbated by a lack of transparency and standardization in global supply chains.

6.6 Geopolitical challenges

Climate change, NZE, and circularity are global issues. However, geopolitical tensions can sometimes stall collaborative efforts. Differences in economic development, priorities, and capabilities mean that nations approach these paradigms at varied paces, leading to coordination challenges at international forums.

In assessing these challenges and setbacks, it's evident that the journey towards integrating NZE and CE principles is not linear. The myriad obstacles encountered underscore the need for continued innovation, robust policies, global collaboration, and a shared vision to navigate this transformative path.

7 Synergies and tensions

The interplay between NZE and the CE has undeniably forged powerful synergies, yet it has also unveiled certain tensions. This dynamic relationship, oscillating between collaboration and friction, has been instrumental in shaping the trajectory of sustainable development over the decade.

7.1 Synergies

Resource Efficiency and Emissions Reduction: CE practices emphasize the efficient use of resources, which directly translates to reduced energy consumption and consequently, lesser emissions. For example, recycling aluminum saves up to 95% of the energy required to produce it from raw materials, thus drastically reducing associated emissions.

7.2 Waste-to-energy

The principles of the CE advocate for harnessing waste as a resource. This aligns seamlessly with net zero ambitions when organic waste is transformed into bioenergy, providing renewable energy while diverting waste from landfills.

7.3 Sustainable product design

Products designed with circular principles in mind tend to have extended lifespans, are easier to repair, and are built for recycling or composting. This approach directly reduces the carbon footprint associated with frequent manufacturing of disposable products.

7.4 Case study—the ellen MacArthur foundation's jeans redesign initiative

This project brought together major fashion brands to produce jeans that last longer, can be easily recycled, and are made in ways that are better for the environment and the health of garment workers. The reduced need for constant production, owing to the durability of these jeans, complements net zero targets.

7.5 Tensions

Bio-based Materials vs. Carbon Sequestration: While bio-based materials, like those used in some bioplastics, are hailed in the CE for their potential to decompose, their production might involve the use of plants that could otherwise sequester carbon. There's a balance to

strike between using plants for materials and allowing them to act as carbon sinks.

7.6 Recycling energy intensity

Some recycling processes, though circular, are energy-intensive. For instance, certain e-waste recycling procedures, while recovering valuable materials, consume significant amounts of energy, thus posing challenges for net zero objectives.

7.7 Carbon offsetting and natural land use

Net zero often involves carbon offsetting practices like afforestation. However, if not managed with a circular mindset, these can conflict with natural land uses, potentially displacing agriculture or natural ecosystems.

7.8 Case study—palm oil biofuels

Once celebrated as a renewable alternative to fossil fuels, palm oil biofuels have come under scrutiny. While they align with the circular idea of using organic matter for energy, their production has led to deforestation, biodiversity loss, and ironically, increased greenhouse gas emissions due to the clearing of carbon-absorbing forests.

By examining these synergies and tensions, it becomes evident that while the pathways of NZE and the CE frequently converge, they sometimes also diverge. It's this intricate dance between alignment and divergence that necessitates an integrated, nuanced approach to sustainability, ensuring that in our pursuit of one objective, we don't inadvertently compromise the other.

8 Socio-economic impact

The intertwined journey towards NZE and the CE has far-reaching socio-economic implications. From the creation of new industries and the obliteration of some traditional sectors to redefining economic hierarchies globally, the transformation has been profound. A thoughtful assessment reveals both commendable strides and formidable challenges on this socio-economic frontier.

8.1 Job creation

The transition to net zero and circular models has been a catalyst for new employment opportunities. Renewable energy sectors, such as wind, solar, and bioenergy, have witnessed significant job growth. Additionally, as companies increasingly adopt circular practices, roles centered around sustainable product design, resource management, and waste-to-resource technologies have burgeoned. According to the International Renewable Energy Agency (IRENA), the renewable energy sector alone could employ up to 42 million people globally by 2050, a vast leap from around 12 million in 2020.

Skill Transition and Job Displacement: While new opportunities emerge, there's an undeniable displacement in traditional sectors, particularly fossil fuels. This transition, if not managed inclusively, poses the risk of socio-economic disparities. It necessitates reskilling programs and policy frameworks that ensure workers from declining industries find avenues in the burgeoning green sectors.

8.2 Inequality

The shift towards net zero and circularity, if not executed equitably, can exacerbate existing inequalities. On a global scale, while developed nations have the capital and technology to transition swiftly, developing nations might grapple with the costs and complexities of overhauling their systems. Within nations, there's a risk of a "green divide" where only the affluent sections of society can access and afford sustainable, circular products and services, leaving the marginalized further behind.

8.3 Economic paradigm shift

The move towards net zero and circularity is gradually redefining economic success parameters. Gross Domestic Product (GDP), traditionally a measure of success, might not encapsulate the full story anymore. New metrics that account for sustainable practices, resource efficiency, and carbon neutrality are gaining traction. Countries and companies are increasingly being evaluated based on their sustainability credentials, potentially leading to shifts in global economic power dynamics.

8.4 Local economies and decentralization

CE principles advocate for localized production and consumption cycles, reducing the dependency on global supply chains. This approach can rejuvenate local economies, fostering innovation and entrepreneurship at the grassroots level. Similarly, decentralized renewable energy systems, like microgrids, empower local communities, ensuring energy sovereignty and resilience.

8.5 Consumer behavior and costs

As companies transition to sustainable practices, there's often an associated cost—at least initially. This transition can lead to premium pricing for green products and services, influencing consumer buying behavior. Over time, however, as sustainable technologies scale and become mainstream, costs are likely to decrease.

In essence, the March towards NZE and a CE is reconfiguring the socio-economic tapestry globally. While the trajectory promises a sustainable and equitable future, it's laden with complexities that demand meticulous planning, global collaboration, and an unwavering commitment to inclusivity and equity.

9 Global and regional perspectives

The global ethos surrounding NZE and the CE is as diverse as the countries and cultures that embody it. Different regions, based

on their socio-economic contexts, historical legacies, and geopolitical considerations, have adopted varied trajectories. A comparative lens reveals both a rich tapestry of localized approaches and a foundational bedrock of global cooperation.

9.1 Europe

Regarded as a front-runner in sustainability initiatives, Europe's transition is characterized by robust policy frameworks, aggressive carbon neutrality targets, and a commitment to circularity. The European Green Deal and the Circular Economy Action Plan are testament to the region's proactive approach. The embrace of these paradigms is also seen as a strategy to bolster European economic competitiveness in the global arena (Smol et al., 2020; Friant et al., 2021; Johansson, 2021).

9.2 Asia

Asia presents a mosaic of approaches. Countries like China and Japan have made significant strides in integrating CE principles, with China's "eco-civilization" vision and Japan's "Society 5.0" strategy. However, rapid urbanization, population density, and developmental pressures pose challenges. In contrast, countries like India juggle developmental imperatives with ambitious renewable energy targets and grassroots circular innovations (Fukuyama, 2018; Hansen et al., 2018).

9.3 Africa

While Africa has a lower carbon footprint historically, its vulnerability to climate change effects is profound. The continent's approach to net zero and circularity is intertwined with developmental, energy access, and resilience objectives. Innovations like decentralized solar projects and community-based circular initiatives are gaining ground. Yet, the need for infrastructural development often competes with these sustainability goals (Filipović et al., 2022; Kalantzakos et al., 2023).

9.4 The Americas

North America, particularly the U.S., has witnessed a pendulum swing in climate policies, with the recent years indicating a renewed commitment to net zero. Advanced industries in the region are also pioneering circular innovations. Latin America, rich in biodiversity, faces the dual task of conservation and development. Countries like Chile and Costa Rica have set commendable renewable energy and conservation benchmarks (Anika et al., 2022; Da Zhu, 2022).

9.5 Oceania

Regions like Australia and New Zealand, blessed with vast renewable resources, are gravitating towards net zero targets. However, challenges like reliance on coal exports and agricultural pressures create tensions. Indigenous knowledge systems, particularly in New Zealand, are also influencing a unique flavor of circularity (Ranson and Stavins, 2016; Hall, 2021).

Global Cooperation and Knowledge Exchange: Despite diverse regional approaches, global cooperation remains the linchpin. Platforms like the United Nations Framework Convention on Climate Change (UNFCCC) and the World Circular Economy Forum facilitate knowledge exchange, technology transfer, and financial collaboration. Such global synergies are vital, ensuring that the move towards net zero and circularity is not just swift but also equitable (Joss et al., 2013; Bataille, 2020).

In conclusion, the journey towards NZE and the CE, when viewed through a global-local prism, underscores the richness of regional innovations and the indispensability of global solidarity. As the world navigates this transformative phase, it's this delicate dance between localized strategies and global cooperation that will shape the sustainability narrative for generations to come.

10 Theoretical and practical implications

The last decade's discourse surrounding NZE and the CE has been underpinned by a rich tapestry of theoretical models and practical implementations. Rooted in interdisciplinary foundations, the theoretical paradigms around these subjects aspire for a holistic transformation where economic systems operate in harmony with our planet's ecological boundaries. They propose a world that thrives on sustainable resource loops, minimizes waste, and champions inter-generational equity. But how seamlessly does this theoretical vision translate into on-the-ground realities?

In the labyrinth of real-world implementations, myriad challenges arise. Economic imperatives, for instance, often pull businesses in two directions: the pursuit of short-term profits and the longer-term sustainability vision. While CE frameworks advocate a decoupling of growth from resource exploitation, many enterprises grapple with the immediate financial implications of such a transition. Similarly, technological constraints can pose significant hurdles. Although academic models sometimes presuppose the ubiquitous presence of cutting-edge technologies, many regions, especially in the developing world, find themselves navigating a technological chasm.

Equally significant are the socio-cultural dimensions. The sustainability path isn't just carved by economic and technological considerations; it's deeply influenced by societal norms, traditions, and behavioral inclinations. A practice that gains rapid acceptance in one cultural milieu might encounter resistance in another, emphasizing the need for context-specific solutions. The policy landscape further adds to this complexity. Theoretical constructs often rest on the bedrock of strong policy and regulatory support, but the oscillating realities of political will, regulatory frameworks, and bureaucratic dynamics can either propel or hinder progress.

Yet, amid these challenges, the gap between theory and practice also spawns innovation. There have been myriad instances where constraints have catalyzed out-of-the-box solutions, adaptive strategies, and grassroots innovations. However, a critical reflection suggests caution in overly romanticizing these success

stories. Scalability remains a pertinent concern. Models that flourish in a controlled, small-scale environment might not necessarily replicate their success on a larger canvas, owing to amplified complexities.

In essence, the journey towards NZE and a CE, as viewed through the lens of the past decade, underscores the intricate dance between theoretical aspirations and practical challenges. To forge a path that's both visionary and pragmatic, a collaborative, adaptive, and context-sensitive approach is paramount. Only by bridging the chasm between what we envision in theory and what we execute in practice can we hope to steer our global systems towards a more sustainable, resilient, and equitable trajectory.

11 Future pathways

Reflecting on a decade of grappling with the intertwining paradigms of NZE and the CE reveals as much about our past as it does about the possibilities ahead. If history has shown us the challenges, it has equally illuminated pathways of promise. By understanding where we have been, we can better chart where we need to go, ensuring that the next decade is not just a continuation but an elevation.

As we stand on the cusp of this new era, several potential pathways emerge. First, the integration of digital technologies with circular principles is ripe with promise. Technologies such as Artificial Intelligence, Blockchain, and the Internet of Things could redefine how we track, manage, and optimize resource loops, creating a transparent and efficient circular system. There's a vast potential in smart grids, digital twins, and AI-driven supply chains to usher in a new age of circularity that's both effective and scalable.

Secondly, transitioning to a truly CE requires rethinking our design philosophies. The future will demand products designed not just for use, but also for reuse, refurbishment, and recycling. This concept, often termed as "Design for Circularity," will be a linchpin. Encouragingly, educational institutions are already beginning to incorporate these principles into their curricula, suggesting a new generation of designers and engineers equipped to meet these challenges.

However, while technology and design provide tools, it's the policy landscape that often paves the way. The next decade will require more robust, comprehensive, and globally harmonized policies that incentivize circular practices. Financial instruments, such as green bonds and sustainability-linked loans, can also play a pivotal role in funneling capital towards sustainable ventures.

Yet, even as we tread these pathways, areas requiring further exploration become evident. There's a pressing need to delve deeper into the socio-cultural dimensions of circularity, understanding how different communities perceive and adapt to circular principles. Behavioral economics, thus, might offer invaluable insights. Similarly, the intersection of biodiversity and circularity remains an under-explored terrain. As we harness resources, how do we ensure that we're not inadvertently compromising on the planet's biodiversity?

Furthermore, the decade ahead must focus on forging stronger global collaborations. The challenges posed by climate change and resource constraints are borderless, and our solutions must mirror that universality. Platforms for knowledge exchange, technology transfer, and capacity building, especially in regions lagging in the sustainability transition, will be paramount.

As we set our sights on the next decade, pinpointing and implementing specific, impactful strategies, projects, partnerships, and policy frameworks is essential for advancing toward our sustainability ambitions. Envisioning green technology parks that amalgamate renewable energy, sustainable water management, and waste recycling presents a blueprint for industrial evolution, while urban reforestation stands out as a key strategy for carbon sequestration and enhancing urban habitats. Crucial to this journey are strategic alliances that bridge governments, the private sector, and NGOs, enabling large-scale sustainability initiatives, such as the deployment of smart grid technologies for improved energy efficiency and renewable energy integration. Furthermore, adopting comprehensive policy frameworks, including a global carbon pricing mechanism and national mandates for sustainable materials, alongside policies that champion circular economy principles like extended producer responsibility (EPR) and zero-waste regulations, will drive businesses towards minimizing their environmental impact. This integrated approach, focusing on innovation, collaboration, and policy support, is pivotal for transforming the next decade into a period of significant progress towards our comprehensive sustainability goals.

In summary, the future pathways for NZE and the CE are as much about evolution as they are about revolution. While the last decade has laid the foundation, the next must build upon it, ensuring that the interplay between technology, policy, design, and collaboration crafts a world where sustainability is not an afterthought but the very ethos of our existence. The journey ahead is challenging but brimming with the potential of possibility.

12 Conclusion

Over the last decade, the journey towards net zero emissions (NZE) and the circular economy (CE) has revealed a rich blend of ambition, achievement, and innovation, highlighting a growing symbiosis between NZE and CE that enhances our approach to sustainability. This period has underscored the importance of adaptable, context-aware strategies that respect local nuances, and the critical role of technological advancements in fostering inclusive progress without widening social disparities. The collaborative efforts of policymakers, industry, academia, and civil society have proven essential in navigating the complexities of global sustainability efforts. Looking forward, we face a landscape filled with both challenges and opportunities, requiring us to refine our strategies, foster new partnerships, and expand our innovations. As we propose actionable steps for individuals, organizations, and policymakers, our collective endeavor towards a sustainable future is clear. Emphasizing collaboration and innovation, we aim to continue our progress towards our sustainability goals, showcasing the resilience and adaptability of humanity. The lessons learned offer guidance for future efforts, underscoring that achieving a sustainable, harmonious future is a collective journey that demands ongoing commitment and cooperation.

For effective action towards net zero emissions and a circular economy, a collective effort from all societal sectors is essential. We propose actionable steps to transform theoretical insights into meaningful outcomes. Individuals are encouraged to lower their carbon footprint via mindful decisions and recycling efforts, and organizations are called to implement circular economy strategies,

prioritizing resource efficiency and achieving carbon neutrality. Policymakers should facilitate this shift through enabling policies and fostering global cooperation. United in these endeavors, we can expedite our journey towards a sustainable future, anchored by a shared commitment to innovation and ecological responsibility, aiming to fulfill our significant sustainability goals.

Author contributions

MM: Data curation, Formal Analysis, Investigation, Methodology, Validation, Visualization, Writing–original draft. MN: Writing–original draft, Writing–review and editing, Conceptualization. BL: Supervision, Writing–review and editing, Project administration.

Funding

The author(s) declare that no financial support was received for the research, authorship, and/or publication of this article.

Acknowledgments

The authors gratefully acknowledge the support from American University of the Middle (AUM), Kuwait.

Conflict of interest

The authors declare that the research was conducted in the absence of any commercial or financial relationships that could be construed as a potential conflict of interest.

Publisher's note

References

Al-Mufachi, N. A., and Shah, N. (2022). The role of hydrogen and fuel cell technology in providing security for the UK energy system. *Energy Policy* 171, 113286. doi:10.1016/j.enpol.2022.113286

Anderson, K., and Peters, G. (2016). The trouble with negative emissions. *Science* 354 (6309), 182–183. doi:10.1126/science.aah4567

Anika, O. C., Nnabuife, S. G., Bello, A., Okoroafor, E. R., Kuang, B., and Villa, R. (2022). Prospects of low and zero-carbon renewable fuels in 1.5-degree net zero emission actualisation by 2050: a critical review. *Carbon Capture Sci. Technol.* 5, 100072. doi:10.1016/j.ccst.2022.100072

Arsic, M., O'Sullivan, C. A., Wasson, A. P., Antille, D. L., and Clarke, W. P. (2023). Beyond waste-to-energy: bioenergy can drive sustainable Australian agriculture by integrating circular economy with net zero ambitions. *Detritus* 23, 28–34. doi:10.31025/2611-4135/2023.17278

Bag, S., and Pretorius, J. H. C. (2022). Relationships between industry 4.0, sustainable manufacturing and circular economy: proposal of a research framework. *Int. J. Organ. Analysis* 30 (4), 864–898. doi:10.1108/ijoa-04-2020-2120

Bataille, C. G. (2020). Physical and policy pathways to net-zero emissions industry. *Wiley Interdiscip. Rev. Clim. Change* 11 (2), e633. doi:10.1002/wcc.633

Bergero, C., Gosnell, G., Gielen, D., Kang, S., Bazilian, M., and Davis, S. J. (2023). Pathways to net-zero emissions from aviation. *Nat. Sustain.* 6 (4), 404–414. doi:10.1038/s41893-022-01046-9

Bocken, N. M., De Pauw, I., Bakker, C., and Van Der Grinten, B. (2016). Product design and business model strategies for a circular economy. *J. industrial Prod. Eng.* 33 (5), 308–320. doi:10.1080/21681015.2016.1172124

Bonciu, F. (2020). The European Union Hydrogen Strategy as a significant step towards a circular economy. *Romanian J. Eur. Aff.* 20 (2), 36–48.

Bonsu, N. O. (2020). Towards a circular and low-carbon economy: insights from the transitioning to electric vehicles and net zero economy. *J. Clean. Prod.* 256, 120659. doi:10.1016/j.jclepro.2020.120659

Bonsu, N. O. (2021). Net-zero emission vehicles shift and equitable ownership in low-income households and communities: why responsible and circularity business models are essential. *Discov. Sustain.* 2, 14–19. doi:10.1007/s43621-021-00022-1

Bouckaert, S., Pales, A. F., McGlade, C., Remme, U., Wanner, B., Varro, L., et al. (2021). "Net zero by 2050: a roadmap for the global energy sector."doi:10.1787/c8328405-en

Bridge, G., Bouzarovski, S., Bradshaw, M., and Eyre, N. (2013). Geographies of energy transition: space, place and the low-carbon economy. *Energy policy* 53, 331–340. doi:10.1016/j.enpol.2012.10.066

Corvellec, H., Stowell, A. F., and Johansson, N. (2022). Critiques of the circular economy. *J. industrial Ecol.* 26 (2), 421–432. doi:10.1111/jiec.13187

Cusenza, M. A., Guarino, F., Longo, S., Ferraro, M., and Cellura, M. (2019). Energy and environmental benefits of circular economy strategies: the case study of reusing used batteries from electric vehicles. *J. Energy Storage* 25, 100845. doi:10.1016/j.est.2019.100845

Davis, S. J., Lewis, N. S., Shaner, M., Aggarwal, S., Arent, D., Azevedo, I. L., et al. (2018). Net-zero emissions energy systems. *Science* 360 (6396), eaas9793. doi:10.1126/science.aas9793

Da Zhu, J. (2022). Cooperative equilibrium of the China-US-EU climate game. *Energy Strategy Rev.* 39, 100797. doi:10.1016/j.esr.2021.100797

De Jong, M., Joss, S., Schraven, D., Zhan, C., and Weijnen, M. (2015). Sustainable–smart–resilient–low carbon–eco–knowledge cities; making sense of a multitude of concepts promoting sustainable urbanization. *J. Clean. Prod.* 109, 25–38. doi:10.1016/j.jclepro.2015.02.004

Delafield, G., Donnison, C., Roddis, P., Arvanitopoulos, T., Sfyridis, A., Dunnett, S., et al. (2021). Conceptual framework for balancing society and nature in net-zero energy transitions. *Environ. Sci. Policy* 125, 189–201. doi:10.1016/j.envsci.2021.08.021

Dezi, L., Hysa, X., Calabrese, M., and Mercuri, F. (2022). Open total quality management in the circular economy age: a social enterprise perspective through the case of Patagonia. *Total Qual. Manag. Bus. Excell.*, 1–15. doi:10.1080/14783363.2022.2051698

Diamantis, V., Eftaxias, A., Stamatelatou, K., Noutsopoulos, C., Vlachokostas, C., and Aivasidis, A. (2021). Bioenergy in the era of circular economy: anaerobic digestion technological solutions to produce biogas from lipid-rich wastes. *Renew. Energy* 168, 438–447. doi:10.1016/j.renene.2020.12.034

Ding, L., Wang, T., and Chan, P. (2023). Forward and reverse logistics for circular economy in construction: a systematic literature review. *J. Clean. Prod.* 388, 135981. doi:10.1016/j.jclepro.2023.135981

Di Vaio, A., Hasan, S., Palladino, R., and Hassan, R. (2023). The transition towards circular economy and waste within accounting and accountability models: a systematic literature review and conceptual framework. *Environ. Dev. Sustain.* 25 (1), 734–810. doi:10.1007/s10668-021-02078-5

Domenech, T., and Bahn-Walkowiak, B. (2019). Transition towards a resource efficient circular economy in Europe: policy lessons from the EU and the member states. *Ecol. Econ.* 155, 7–19. doi:10.1016/j.ecolecon.2017.11.001

Dzhengiz, T., Miller, E. M., Ovaska, J. P., and Patala, S. (2023). Unpacking the circular economy: a problematizing review. *Int. J. Manag. Rev.* 25, 270–296. doi:10.1111/ijmr.12329

Fankhauser, S., Smith, S. M., Allen, M., Axelsson, K., Hale, T., Hepburn, C., et al. (2022). The meaning of net zero and how to get it right. *Nat. Clim. Change* 12 (1), 15–21. doi:10.1038/s41558-021-01245-w

Filipović, S., Lior, N., and Radovanović, M. (2022). The green deal–just transition and sustainable development goals Nexus. *Renew. Sustain. Energy Rev.* 168, 112759. doi:10.1016/j.rser.2022.112759

Fraga-Lamas, P., Lopes, S. I., and Fernández-Caramés, T. M. (2021). Green IoT and edge AI as key technological enablers for a sustainable digital transition towards a smart

circular economy: an industry 5.0 use case. *Sensors* 21 (17), 5745. doi:10.3390/s21175745

Friant, M. C., Vermeulen, W. J., and Salomone, R. (2020). A typology of circular economy discourses: navigating the diverse visions of a contested paradigm. *Resour. Conservation Recyclc* 161, 104917. doi:10.1016/j.resconrec.2020.104917

Friant, M. C., Vermeulen, W. J., and Salomone, R. (2021). Analysing European Union circular economy policies: words versus actions. *Sustain. Prod. Consum.* 27, 337–353. doi:10.1016/j.spc.2020.11.001

Fukuyama, M. (2018). Society 5.0: aiming for a new human-centered society. *Jpn. Spotlight* 27 (5), 47–50.

Geels, F. W. (2018). Disruption and low-carbon system transformation: progress and new challenges in socio-technical transitions research and the Multi-Level Perspective. *Energy Res. Soc. Sci.* 37, 224–231. doi:10.1016/j.erss.2017.10.010

Geels, F. W., Berkhout, F., and Van Vuuren, D. P. (2016). Bridging analytical approaches for low-carbon transitions. *Nat. Clim. change* 6 (6), 576–583. doi:10.1038/nclimate2980

Ghisellini, P., Cialani, C., and Ulgiati, S. (2016). A review on circular economy: the expected transition to a balanced interplay of environmental and economic systems. *J. Clean. Prod.* 114, 11–32. doi:10.1016/j.jclepro.2015.09.007

Gielen, D., Boshell, F., Saygin, D., Bazilian, M. D., Wagner, N., and Gorini, R. (2019). The role of renewable energy in the global energy transformation. *Energy Strategy Rev.* 24, 38–50. doi:10.1016/j.esr.2019.01.006

Govindan, K. (2023). How digitalization transforms the traditional circular economy to a smart circular economy for achieving SDGs and net zero. *Transp. Res. Part E Logist. Transp. Rev.* 177, 103147. doi:10.1016/j.tre.2023.103147

Hale, T., Smith, S. M., Black, R., Cullen, K., Fay, B., Lang, J., et al. (2022). Assessing the rapidly-emerging landscape of net zero targets. *Clim. Policy* 22 (1), 18–29. doi:10.1080/14693062.2021.2013155

Hall, D. (2021). Expertise within democracy: the case of New Zealand's climate change commission. *Political Sci.* 73 (2), 103–122. doi:10.1080/00323187.2021.2022902

Hansen, M. H., Li, H., and Svarverud, R. (2018). Ecological civilization: interpreting the Chinese past, projecting the global future. *Glob. Environ. Change* 53, 195–203. doi:10.1016/j.gloenvcha.2018.09.014

Howard, M., Hopkinson, P., and Miemczyk, J. (2019). The regenerative supply chain: a framework for developing circular economy indicators. *Int. J. Prod. Res.* 57 (23), 7300–7318. doi:10.1080/00207543.2018.1524166

Jesic, J., Okanovic, A., and Panic, A. A. (2021). Net zero 2050 as an EU priroty: modeling a system for efficient investments in eco innovation for climate change mitigation. *Energy, Sustain. Soc.* 11 (1), 50–16. doi:10.1186/s13705-021-00326-0

Johansson, N. (2021). Does the EU's action plan for a circular economy challenge the linear economy? *Environ. Sci. Technol.* 55 (22), 15001–15003. doi:10.1021/acs.est.1c06194

Joss, S., Cowley, R., and Tomozeiu, D. (2013). Towards the 'ubiquitous eco-city': an analysis of the internationalisation of eco-city policy and practice. *Urban Res. Pract.* 6 (1), 54–74. doi:10.1080/17535069.2012.762216

Kalantzakos, S., Overland, I., and Vakulchuk, R. (2023). Decarbonisation and critical materials in the context of fraught geopolitics: europe's distinctive approach to a net zero future. *Int. Spectator* 58 (1), 3–22. doi:10.1080/03932729.2022.2157090

Kapsalis, V. C., Kyriakopoulos, G. L., and Aravossis, K. G. (2019). Investigation of ecosystem services and circular economy interactions under an inter-organizational framework. *Energies* 12 (9), 1734. doi:10.3390/en12091734

Khalifa, A. A., Ibrahim, A.-J., Amhamed, A. I., and El-Naas, M. H. (2022). Accelerating the transition to a circular economy for net-zero emissions by 2050: a systematic review. *Sustainability* 14 (18), 11656. doi:10.3390/su141811656

Kirchherr, J., Reike, D., and Hekkert, M. (2017). Conceptualizing the circular economy: an analysis of 114 definitions. *Resour. conservation Recycl.* 127, 221–232. doi:10.1016/j.resconrec.2017.09.005

Kouhizadeh, M., Zhu, Q., and Sarkis, J. (2020). Blockchain and the circular economy: potential tensions and critical reflections from practice. *Prod. Plan. Control* 31 (11-12), 950–966. doi:10.1080/09537287.2019.1695925

Kovacic, Z., Strand, R., and Völker, T. (2020). *The circular economy in Europe: critical perspectives on policies and imaginaries*. Taylor & Francis.

Kristoffersen, E., Blomsma, F., Mikalef, P., and Li, J. (2020). The smart circular economy: a digital-enabled circular strategies framework for manufacturing companies. *J. Bus. Res.* 120, 241–261. doi:10.1016/j.jbusres.2020.07.044

Kurniawan, T. A., Avtar, R., Singh, D., Xue, W., Othman, M. H. D., Hwang, G. H., et al. (2021). Reforming MSWM in Sukunan (Yogjakarta, Indonesia): a case-study of applying a zero-waste approach based on circular economy paradigm. *J. Clean. Prod.* 284, 124775. doi:10.1016/j.jclepro.2020.124775

Lee, R. P., Keller, F., and Meyer, B. (2017). A concept to support the transformation from a linear to circular carbon economy: net zero emissions, resource efficiency and conservation through a coupling of the energy, chemical and waste management sectors. *Clean. Energy* 1 (1), 102–113. doi:10.1093/ce/zkx004

Leipold, S., and Petit-Boix, A. (2018). The circular economy and the bio-based sector-Perspectives of European and German stakeholders. *J. Clean. Prod.* 201, 1125–1137. doi:10.1016/j.jclepro.2018.08.019

Lewandowski, M. (2016). Designing the business models for circular economy—towards the conceptual framework. *Sustainability* 8 (1), 43. doi:10.3390/su8010043

Mallick, P. K., Salling, K. B., Pigosso, D. C., and McAloone, T. C. (2023). Closing the loop: establishing reverse logistics for a circular economy, a systematic review. *J. Environ. Manag.* 328, 117017. doi:10.1016/j.jenvman.2022.117017

Meys, R., Kätelhön, A., Bachmann, M., Winter, B., Zibunas, C., Suh, S., et al. (2021). Achieving net-zero greenhouse gas emission plastics by a circular carbon economy. *Science* 374 (6563), 71–76. doi:10.1126/science.abg9853

Mies, A., and Gold, S. (2021). Mapping the social dimension of the circular economy. *J. Clean. Prod.* 321, 128960. doi:10.1016/j.jclepro.2021.128960

Millar, N., McLaughlin, E., and Börger, T. (2019). The circular economy: swings and roundabouts? *Ecol. Econ.* 158, 11–19. doi:10.1016/j.ecolecon.2018.12.012

Mohan, S. V., and Katakojwala, R. (2021). The circular chemistry conceptual framework: a way forward to sustainability in industry 4.0. *Curr. Opin. Green Sustain. Chem.* 28, 100434. doi:10.1016/j.cogsc.2020.100434

Mont, O., Neuvonen, A., and Lähteenoja, S. (2014). Sustainable lifestyles 2050: stakeholder visions, emerging practices and future research. *J. Clean. Prod.* 63, 24–32. doi:10.1016/j.jclepro.2013.09.007

Moustakas, K., Rehan, M., Loizidou, M., Nizami, A. S., and Naqvi, M. (2020). Energy and resource recovery through integrated sustainable waste management. *Appl. Energy* 261 (2020), 114372. doi:10.1016/j.apenergy.2019.114372

Moyer, J. D., and Hedden, S. (2020). Are we on the right path to achieve the sustainable development goals? *World Dev.* 127, 104749. doi:10.1016/j.worlddev.2019.104749

Mulvaney, D., Richards, R. M., Bazilian, M. D., Hensley, E., Clough, G., and Sridhar, S. (2021). Progress towards a circular economy in materials to decarbonize electricity and mobility. *Renew. Sustain. Energy Rev.* 137, 110604. doi:10.1016/j.rser.2020.110604

Munaro, M. R., and Tavares, S. F. (2023). A review on barriers, drivers, and stakeholders towards the circular economy: the construction sector perspective. *Clean. Responsible Consum.* 8, 100107. doi:10.1016/j.clrc.2023.100107

Mutezo, G., and Mulopo, J. (2021). A review of Africa's transition from fossil fuels to renewable energy using circular economy principles. *Renew. Sustain. Energy Rev.* 137, 110609. doi:10.1016/j.rser.2020.110609

Naqvi, M., Dahlquist, E., and Yan, J. (2017b). Complementing existing CHP plants using biomass for production of hydrogen and burning the residual gas in a CHP boiler. *Biofuels* 8 (6), 675–683. doi:10.1080/17597269.2016.1153362

Naqvi, M., Yan, J., and Dahlquist, E. (2012). Energy conversion performance of black liquor gasification to hydrogen production using direct causticization with CO2 capture. *Bioresour. Technol.* 110, 637–644. doi:10.1016/j.biortech.2012.01.070

Naqvi, M., Yan, J., and Dahlquist, E. (2013). System analysis of dry black liquor gasification based synthetic gas production comparing oxygen and air blown gasification systems. *Appl. Energy* 112, 1275–1282. doi:10.1016/j.apenergy.2012.11.065

Naqvi, M., Yan, J., Dahlquist, E., and Raza Naqvi, S. (2016). Waste biomass gasification based off-grid electricity generation: a case study in Pakistan. *Energy Procedia* 103 (2016), 406–412. doi:10.1016/j.egypro.2016.11.307

Naqvi, S. R., Naqvi, M., Taqvi, S. A. A., Iqbal, F., Inayat, A., Hussain Khoja, A., et al. (2021). Agro-industrial residue gasification feasibility in captive power plants: a South-Asian case study. *Energy* 214, 118952. doi:10.1016/j.energy.2020.118952

Naqvi, S. R., Noor, T., Hussain, A., Iqbal, N., Uemura, Y., Nishiyama, N., et al. (2017a). Catalytic pyrolysis of botryococcus braunii (microalgae) over layered and delaminated zeolites for aromatic hydrocarbon production. *Energy Procedia* 142, 381–385. doi:10.1016/j.egypro.2017.12.060

Okorie, O., Russell, J., Cherrington, R., Fisher, O., and Charnley, F. (2023). Digital transformation and the circular economy: creating a competitive advantage from the transition towards Net Zero Manufacturing. *Resour. Conservation Recycl.* 189, 106756. doi:10.1016/j.resconrec.2022.106756

Padilla-Rivera, A., Russo-Garrido, S., and Merveille, N. (2020). Addressing the social aspects of a circular economy: a systematic literature review. *Sustainability* 12 (19), 7912. doi:10.3390/su12197912

Patwa, N., Sivarajah, U., Seetharaman, A., Sarkar, S., Maiti, K., and Hingorani, K. (2021). Towards a circular economy: an emerging economies context. *J. Bus. Res.* 122, 725–735. doi:10.1016/j.jbusres.2020.05.015

Pomponi, F., and Moncaster, A. (2017). Circular economy for the built environment: a research framework. *J. Clean. Prod.* 143, 710–718. doi:10.1016/j.jclepro.2016.12.055

Potting, J., Hekkert, M. P., Worrell, E., and Hanemaaijer, A. (2017). Circular economy: measuring innovation in the product chain. *Planbur. Leefomgeving* 2544.

Rahman, M. N., and Wahid, M. A. (2021). Renewable-based zero-carbon fuels for the use of power generation: a case study in Malaysia supported by updated developments worldwide. *Energy Rep.* 7, 1986–2020. doi:10.1016/j.egyr.2021.04.005

Ramasubramanian, B., Tan, J., Chellappan, V., and Ramakrishna, S. (2023). Recent advances in extended producer responsibility initiatives for plastic waste management in Germany and UK. *Mater. Circ. Econ.* 5 (1), 6. doi:10.1007/s42824-023-00076-8

Ranson, M., and Stavins, R. N. (2016). Linkage of greenhouse gas emissions trading systems: learning from experience. *Clim. Policy* 16 (3), 284–300. doi:10.1080/14693062.2014.997658

Ranta, V., Aarikka-Stenroos, L., and Väisänen, J.-M. (2021). Digital technologies catalyzing business model innovation for circular economy—multiple case study. *Resour. Conservation Recycl.* 164, 105155. doi:10.1016/j.resconrec.2020.105155

Raza Naqvi, S., Hussain Khoja, A., Ali, I., Naqvi, M., Noor, T., Ahmad, A., et al. (2023). Recent progress in catalytic deoxygenation of biomass pyrolysis oil using microporous zeolites for green fuels production. *Fuel* 333 (Part 1), 126268. doi:10.1016/j.fuel.2022.126268

Rehan, M., Nizami, A.-S., Asam, Z.-ul-Z., Ouda, O. K. M., Gardy, J., Raza, G., et al. (2017). Waste to energy: a case study of madinah city. *Energy Procedia* 142, 688–693. doi:10.1016/j.egypro.2017.12.113

Rizos, V., Behrens, A., Van der Gaast, W., Hofman, E., Ioannou, A., Kafyeke, T., et al. (2016). Implementation of circular economy business models by small and medium-sized enterprises (SMEs): barriers and enablers. *Sustainability* 8 (11), 1212. doi:10.3390/su8111212

Rogelj, J., Geden, O., Cowie, A., and Reisinger, A. (2021). Net-zero emissions targets are vague: three ways to fix. *Nature* 591 (7850), 365–368. doi:10.1038/d41586-021-00662-3

Rogelj, J., Schaeffer, M., Meinshausen, M., Knutti, R., Alcamo, J., Riahi, K., et al. (2015). Zero emission targets as long-term global goals for climate protection. *Environ. Res. Lett.* 10 (10), 105007. doi:10.1088/1748-9326/10/10/105007

Roy, D., Samanta, S., Roy, S., Smallbone, A., and Roskilly, A. P. (2024). Techno-economic analysis of solid oxide fuel cell-based energy systems for decarbonising residential power and heat in the United Kingdom. *Green Chem.* 26, 3979–3994. doi:10.1039/d3gc02645k

Sankaran, K. (2023). Turning black to green: circular economy of industrial carbon emissions. *Energy Sustain. Dev.* 74, 463–470. doi:10.1016/j.esd.2023.05.003

Sciences, N. A. o., Engineering, D. o., Sciences, P., Affairs, G., Energy, B. O., Systems, E., et al. (2016). *The power of change: innovation for development and deployment of increasingly clean electric power technologies*. National Academies Press.

Shirvanimoghaddam, K., Motamed, B., Ramakrishna, S., and Naebe, M. (2020). Death by waste: fashion and textile circular economy case. *Sci. Total Environ.* 718, 137317. doi:10.1016/j.scitotenv.2020.137317

Smol, M., Kulczycka, J., and Avdiushchenko, A. (2017). Circular economy indicators in relation to eco-innovation in European regions. *Clean Technol. Environ. Policy* 19, 669–678. doi:10.1007/s10098-016-1323-8

Smol, M., Marcinek, P., Duda, J., and Szołdrowska, D. (2020). Importance of sustainable mineral resource management in implementing the circular economy (CE) model and the european green deal strategy. *Resources* 9 (5), 55. doi:10.3390/resources9050055

Song, A., and Zhou, Y. (2023). Advanced cycling ageing-driven circular economy with E-mobility-based energy sharing and lithium battery cascade utilisation in a district community. *J. Clean. Prod.* 415, 137797. doi:10.1016/j.jclepro.2023.137797

Stahel, W. R. (2016). The circular economy. *Nature* 531 (7595), 435–438. doi:10.1038/531435a

Stern, N., and Valero, A. (2021). Innovation, growth and the transition to net-zero emissions. *Res. Policy* 50 (9), 104293. doi:10.1016/j.respol.2021.104293

Thakker, V., and Bakshi, B. R. (2023). Ranking eco-innovations to enable a sustainable circular economy with net-zero emissions. *ACS Sustain. Chem. Eng.* 11 (4), 1363–1374. doi:10.1021/acssuschemeng.2c05732

Todorović, M., and Obradović, V. (2023). *Sustainable business change: project management toward circular economy*. Springer, 301–314.Circular economy and project management: the road ahead

Tunio, A. A., Qureshi, A. S., Khushk, I., Jatt, A. N., Chisti, Y., Naqvi, M., et al. (2024). Ionic-liquid-tolerant enzymes from an adapted Bacillus paralicheniformis for one-pot conversion of lignocellulosic substrates to ethanol. *Industrial Crops Prod.* 209, 117988. doi:10.1016/j.indcrop.2023.117988

Urbinati, A., Chiaroni, D., and Chiesa, V. (2017). Towards a new taxonomy of circular economy business models. *J. Clean. Prod.* 168, 487–498. doi:10.1016/j.jclepro.2017.09.047

Ürge-Vorsatz, D., Khosla, R., Bernhardt, R., Chan, Y. C., Vérez, D., Hu, S., et al. (2020). Advances toward a net-zero global building sector. *Annu. Rev. Environ. Resour.* 45, 227–269. doi:10.1146/annurev-environ-012420-045843

van der Spek, M., Banet, C., Bauer, C., Gabrielli, P., Goldthorpe, W., Mazzotti, M., et al. (2022). Perspective on the hydrogen economy as a pathway to reach net-zero CO 2 emissions in Europe. *Energy & Environ. Sci.* 15 (3), 1034–1077. doi:10.1039/d1ee02118d

Van Soest, H. L., den Elzen, M. G., and van Vuuren, D. P. (2021). Net-zero emission targets for major emitting countries consistent with the Paris Agreement. *Nat. Commun.* 12 (1), 2140. doi:10.1038/s41467-021-22294-x

van Vuuren, D. P., Zimm, C., Busch, S., Kriegler, E., Leininger, J., Messner, D., et al. (2022). Defining a sustainable development target space for 2030 and 2050. *One Earth* 5 (2), 142–156. doi:10.1016/j.oneear.2022.01.003

Velenturf, A. P., and Purnell, P. (2021). Principles for a sustainable circular economy. *Sustain. Prod. Consum.* 27, 1437–1457. doi:10.1016/j.spc.2021.02.018

Zhao, X., Ma, X., Chen, B., Shang, Y., and Song, M. (2022). Challenges toward carbon neutrality in China: strategies and countermeasures. *Resour. Conservation Recycl.* 176, 105959. doi:10.1016/j.resconrec.2021.105959

frontiers | Frontiers in Energy Research

TYPE Review
PUBLISHED 07 May 2024
DOI 10.3389/fenrg.2024.1373522

OPEN ACCESS

EDITED BY
Ellen B. Stechel,
Arizona State University, United States

REVIEWED BY
Venkateshkumar Prabhakaran,
Pacific Northwest National Laboratory (DOE), United States
Narayanamoorthy Bhuvanendran,
Dongguk University Seoul, Republic of Korea

*CORRESPONDENCE
Diogo M. F. Santos,
diogosantos@tecnico.ulisboa.pt

RECEIVED 19 January 2024
ACCEPTED 14 March 2024
PUBLISHED 07 May 2024

CITATION
Araújo H, Šljukić B, Gago S and Santos DMF (2024), The current state of transition metal-based electrocatalysts (oxides, alloys, POMs, and MOFs) for oxygen reduction, oxygen evolution, and hydrogen evolution reactions. *Front. Energy Res.* 12:1373522. doi: 10.3389/fenrg.2024.1373522

The current state of transition metal-based electrocatalysts (oxides, alloys, POMs, and MOFs) for oxygen reduction, oxygen evolution, and hydrogen evolution reactions

Henrique Araújo[1,2], Biljana Šljukić[1], Sandra Gago[2] and Diogo M. F. Santos[1]*

[1]Center of Physics and Engineering of Advanced Materials, Laboratory for Physics of Materials and Emerging Technologies, Chemical Engineering Department, Instituto Superior Técnico, Universidade de Lisboa, Lisbon, Portugal, [2]Associated Laboratory for Green Chemistry (LAQV) of the Network of Chemistry and Technology (REQUIMTE), Department of Chemistry, NOVA School of Science and Technology (FCT NOVA), Campus da Caparica, Caparica, Portugal

Climate change is showing its impacts now more than ever. The intense use of fossil fuels and the resulting CO_2 emissions are mainly to blame, accentuating the need to develop further the available energy conversion and storage technologies, which are regarded as effective solutions to maximize the use of intermittent renewable energy sources and reduce global CO_2 emissions. This work comprehensively overviews the most recent progress and trends in the use of transition metal-based electrocatalysts for three crucial reactions in electrochemical energy conversion and storage, namely, the oxygen evolution (OER), oxygen reduction (ORR), and hydrogen evolution (HER) reactions. By analyzing the state-of-the-art polyoxometalates (POMs) and metal-organic frameworks (MOFs), the performance of these two promising types of materials for OER, ORR, and HER is compared to that of more traditional transition metal oxides and alloy-based electrocatalysts. Both catalytic activity and stability are highly influenced by the adsorption energies of the intermediate species formed in each reaction, which are very sensitive to changes in the microstructure and chemical microenvironment. POMs and MOFs allow these aspects to be easily modified to fine-tune the catalytic performances. Therefore, their chemical tunability and versatility make it possible to tailor such properties to obtain higher electrocatalytic activities, or even to obtain derived materials with more compelling properties towards these reactions.

KEYWORDS

hydrogen evolution reaction, oxygen evolution reaction, oxygen reduction reaction, electrocatalysts, polyoxometalates, metal-organic frameworks

1 Introduction

The world is facing an environmental crisis due to the overuse of carbon-emitting energy sources, namely, fossil fuels, for transportation or energy generation to power industry and domestic households, for example. This increases global greenhouse gas emissions, namely, CO_2, consequently increasing the global temperature.

This fact comes with devastating consequences, such as more intense and extreme weather events (droughts, heat waves, flooding, and heavy rainfall), and it also brings about a rise in sea levels (IPCC, 2018). As such, it was identified that it is necessary to effectively reduce carbon dioxide emissions to a net-zero level to limit the temperature increase to 1.5 °C as ambitioned by the Paris Agreement signed by the United Nations (UN) members. Regarding the current global energy matrix, fossil fuels are a major contributor in many countries. They play a key role in supplying the energy necessary for proper economic and technological operations, accounting for over 80% of global energy consumption (Amin et al., 2022; Ritchie et al., 2022). However, the reduction in greenhouse gas emissions is mainly dependent on substituting fossil fuels (which are responsible for around 75% of these emissions) for cleaner and renewable energy sources, such as wind, solar, and hydropower energy, presenting themselves as powerful tools to combat the current climate crisis and to pave the way for a greener future.

Unfortunately, these renewable energy sources, especially wind and solar energy, which are the most abundant, have a highly intermittent character, meaning that there are periods where energy production peaks and periods where it declines (Amin et al., 2022; Chatenet et al., 2022). One solution to this intermittent character of renewable energy sources comes in the form of energy storage methods, generally via the use of batteries, which can store the surplus of electric energy during periods of low electricity demand and later release it during periods of high demand. This excess renewable energy can also be stored as green hydrogen (H_2) produced via water electrolysis, a concept known as Power-to-X. The produced green H_2 can be used for a panoply of applications, directly replacing typical grey H_2 produced from steam-methane reforming, or even act as an energy carrier for electricity generation in fuel cells during periods when energy production does not meet the total energy demand.

Thus, H_2 is seen as a promising energy carrier due to its high energy density, around 33 kWh/kg. Furthermore, the combustion of H_2 merely releases water vapor and energy, a crucial factor when considering its use as a green energy source. Specifically, green H_2 production is based on the electrochemical splitting of water powered by renewable energy sources. This process generates H_2 gas in the cathode through the hydrogen evolution reaction (HER) and oxygen (O_2) gas in the anode through the oxygen evolution reaction (OER), with no greenhouse gases emitted during the whole production process (Amin et al., 2022; Arcos and Santos, 2023). For this reason, green H_2 production and its use are widely considered a natural solution to end the energy and climate crisis, establishing the so-called hydrogen economy.

From the perspective of batteries and fuel cells, even though they have already been shown to work safely and effectively, there is an increasing need for the development of bifunctional materials that can be utilized to make them rechargeable and reversible. This becomes relevant due to the need to reduce waste generation from the production and use of disposable batteries (Arcos and Santos, 2023). The relevant chemical reactions for rechargeable batteries and regenerative fuel cells are the oxygen reduction reaction (ORR) and the OER, which happen during the discharging and charging processes, respectively. Still on the topic of bifunctionality, materials with activity towards both the HER and the OER are also highly desired for alkaline water electrolysis technologies, mainly due to stability concerns.

However, the three aforementioned electrochemical reactions exhibit sluggish reaction kinetics (particularly the OER and ORR), meaning efficient electrocatalysts are needed to accelerate production. The best-performing ones are carbon-supported platinum (Pt/C) for HER and ORR, and iridium and ruthenium oxides (IrO_2 and RuO_2) for OER. These benchmark catalysts are expensive since they are based on scarce and precious metals, which increases total production costs. Much scientific effort is devoted to finding efficient, inexpensive, and stable electrocatalysts for the cited reactions, based mostly on common transition metals such as Ni, Co, Mn, and Cu.

Many strategies have been followed to produce effective electrocatalysts. Carbon supports have been widely applied, mainly due to the enhancement in electric conductivity and surface area, directly impacting performance. Examples of commonly tested supports are multi-walled carbon nanotubes (MWCNTs), single-walled carbon nanotubes (SWCNTs), reduced graphene oxide (rGO), graphene flakes (GFs), and carbon fiber paper (CFP) (Fernandes et al., 2018a; Liu et al., 2019; Jawale et al., 2022; Marques et al., 2022; Rehman et al., 2022). On the topic of organic supports, an exciting aspect to be aware of is the capability of including heteroatoms, such as N, in the final catalyst structure; this generally means carrying out an N-doping process on the support (Sun et al., 2015; Zhu et al., 2018; Wang C. et al., 2019; Jeong et al., 2020; Peng et al., 2020). Although N is the most popular dopant, other heteroatoms, such as F, S, P, and metals, are also applied (Zhang S. et al., 2017; Abdelkader-Fernández et al., 2019; Bhuvanendran et al., 2021).

Another method used to impact electrocatalytic activity is by modifying the catalyst composition. This can be done by adding other metals, mainly via alloying. An example is the reduction of Pt content in Pt-based electrocatalysts by alloying it with Ni or Fe (Vij et al., 2017; Zhang C. et al., 2017). This modifies the catalyst's electronic structure, combining the advantages of the alloyed metals, and enhancing the overall activity. The modifications in composition may also impact the catalysts' morphology. The production of octahedral (111) alloy PtNi nanoparticles, more effective for ORR than their cubic (100) Pt counterpart, has been shown to be dependent on composition when a solid-state chemistry method is utilized (Zhang et al., 2014). Still, on the topic of morphology-dependent activity, NiFe alloys are yet another example of how morphology can impact activity; alloys of those metals with hexagonal close-packed and face-centered cubic structures present quite different OER activities. Different morphologies have different surface areas, influencing the amount and type of exposed active sites and thus affecting catalytic activity.

Traditionally, oxide and alloy-based electrocatalysts are produced and tested, but new material classes, such as metal-organic frameworks (MOFs) and polyoxometalates (POMs) have been gaining interest recently due to their inherent advantages, mainly higher surface area due to their porous structures and their ability to be tailored for each

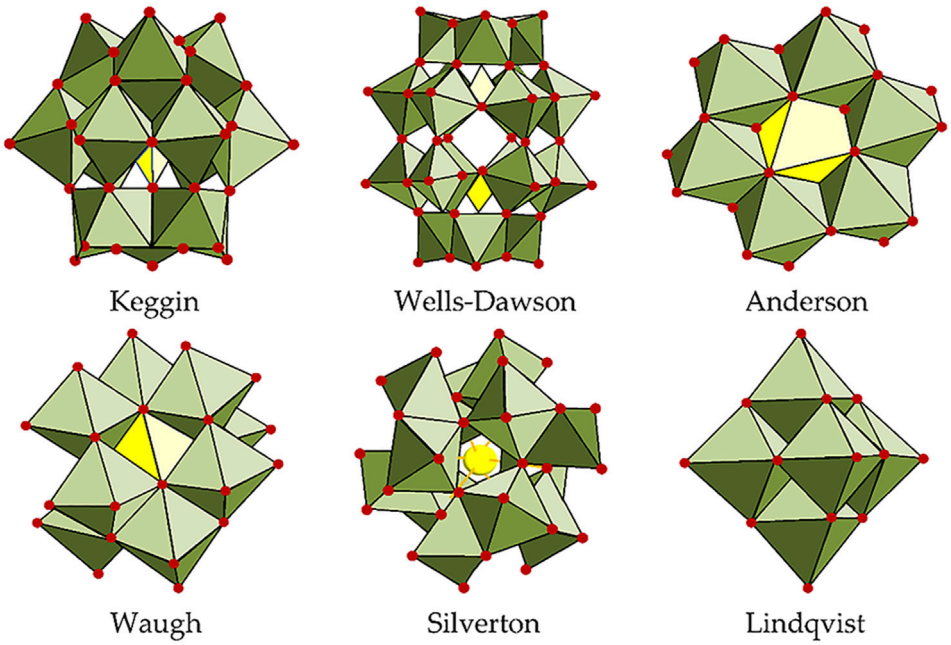

FIGURE 1
Polyoxometalates (POM) structures in polyhedral representations (Gusmão et al., 2022).

specific application due to the ease in modifying their structures (Jiang et al., 2016; Luo W. et al., 2017; Lu et al., 2017; Horn et al., 2021; Gusmão et al., 2022; Jia et al., 2022; Tseng et al., 2022). Briefly, MOFs are known to have a high abundance of metal active sites and can also act as templates to form other electrocatalysts. POMs have a high abundance of redox sites that can act as both acidic and basic sites and possess high thermal stability. Structurally, MOFs are formed by the linkage of inorganic metal ions/clusters and organic ligands, generating a 3D structure with long-range crystallinity, and POMs are metal (e.g., V, W, and Mo) oxide ion clusters linked together by oxygen atoms with a high number of redox centers.

This review summarizes the recent progress of transition metal-based POM (classic POM structures shown in Figure 1) and MOF electrocatalysts for the OER, ORR, and HER. It compares their advantages over the more traditional transition metal-based oxide and alloy electrocatalysts, which mainly reside in their higher chemical tunability and versatility, as shown in Figure 2 for MOFs. This allows, for example, tailoring properties, such as adsorption energy, to obtain higher electrocatalytic activity. For each relevant reaction, a series of electrocatalysts belonging to a different material class are analyzed, with advantages and disadvantages being highlighted regarding the class as a whole. General innovations brought by each reviewed work include the use of carbon and non-carbon materials as POM or MOF electrocatalyst supports, modifications in POMs' and MOFs' morphology stemming from varying the synthesis method and applying different precursors (leading to the production of bimetallic or even polymetallic electrocatalysts), and the introduction of dopants in the final catalyst structure, directly impacting their composition and providing different synergistic effects between the utilized elements, thus improving the catalytic activity as a whole.

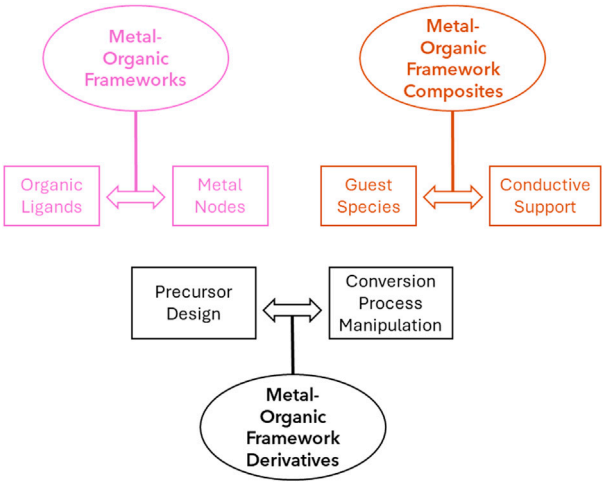

FIGURE 2
The classification and operation of MOF-based materials: pristine MOFs, MOF composite, and their derivatives.

2 Oxygen evolution reaction (OER)

The OER is an anodic reaction that can be carried out in alkaline (Equation 2.1) and acidic (Equation 2.2) media, releasing O_2 gas.

$$4OH^- \rightarrow 4e^- + O_2 + 2H_2O \quad (2.1)$$

$$2H_2O \rightarrow 4e^- + O_2 + 4H^+ \quad (2.2)$$

The equilibrium potential at standard conditions is ca. 1.23 V against the reversible hydrogen electrode (RHE). Still, to perform

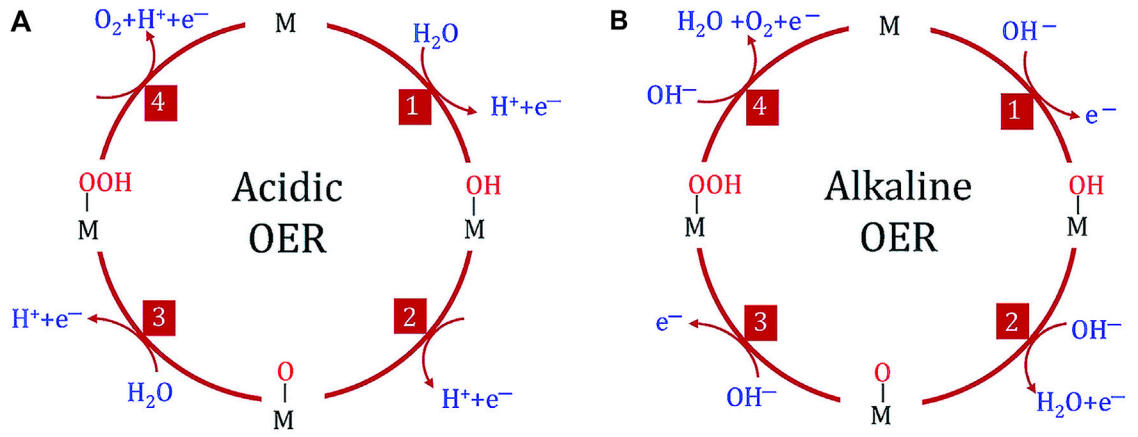

FIGURE 3
OER mechanism in both acidic **(A)** and alkaline **(B)** media (adapted from Yan et al., 2020).

this reaction at reasonable rates requires applying higher overpotentials (η) than those needed for the hydrogen evolution reaction (HER). This happens due to the sluggish kinetics of the OER caused by its inherent reaction mechanism that involves 4 proton-coupled electron transfer steps, as seen in Figure 3, resulting in higher activation energy (Xu et al., 2019; Chatenet et al., 2022; Gusmão et al., 2022). The reaction kinetics also differ depending on the pH: the OER presents more sluggish kinetics in acidic media when compared to alkaline media, which in turn causes the overpotential to achieve the same reaction rate to be higher in acidic media than in alkaline media (Tahir et al., 2017; Chatenet et al., 2022).

The need for a higher overpotential for the OER is also a bottleneck for alkaline water electrolysis, metal-air batteries (MAB), and regenerative fuel cells (RFC) since it is a main component of those technologies, and thus the high overpotentials contribute to higher energy consumption (Tahir et al., 2017; Chatenet et al., 2022). To reduce the high overpotentials associated with this reaction, electrocatalysts are applied to lower activation energies, increasing the reaction kinetics.

The most effective OER electrocatalysts to date are the noble-metal-based Ru and Ir oxides due to their remarkable activity, low overpotential, and excellent dissolution resistance in acidic conditions (Nakagawa et al., 2009; Jiang et al., 2018; Chatenet et al., 2022). This does not discard their use in alkaline conditions since they show good stability at all pH values (Katsunaros et al., 2014; Tahir et al., 2017). However, their main problem resides in their noble nature, meaning they are scarce metals with a high price, compromising their applicability on an industrial scale (Katsunaros et al., 2014; Tahir et al., 2017; Chatenet et al., 2022; Gusmão et al., 2022; Zeb et al., 2023). Because of these limitations, extensive efforts have been made to find cheaper alternatives to these noble-metal catalysts, mainly by utilizing more abundant transition metals such as Ni, Co, Cu, and Mn. These metals are more affordable, which facilitates their use in industrial conditions. Still, one should also be aware of the stability of these transition-metal-based electrocatalysts, which, in acidic conditions, is generally low (Goberna-Ferrón et al., 2015; Sun et al., 2015; Lu et al., 2019; Zand et al., 2023), hence why there are fewer studies on this type of media.

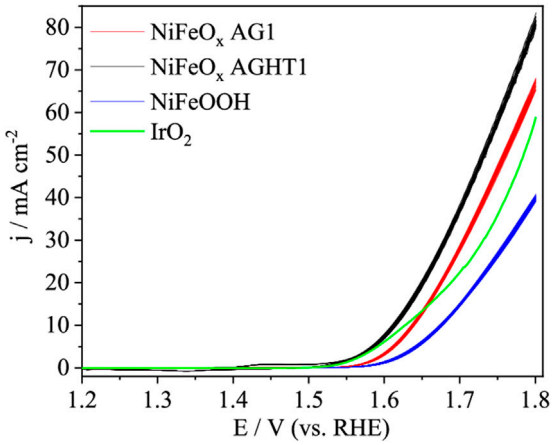

FIGURE 4
Cyclic voltammograms of NiFeO$_x$ AG1, NiFeO$_x$ AGHT1, and NiFeOOH in deaerated 1 M KOH solution at a scan rate of 50 mV/s (adapted from Moschkowitsch et al., 2022).

2.1 Transition metal oxides for OER

Metal oxides are commonly used electrocatalysts for OER due to their compositional and structural diversity, flexible tunability, low cost, abundance, and environmental friendliness (Mladenović et al., 2023a). Although pristine metal oxides are generally unsatisfactory for practical applications due to stability issues and unfavorable binding strength, mixed metal oxides are seen as a possible workaround due to the synergy of the properties of their pristine counterparts (Xu et al., 2022; Mladenović et al., 2023a; Pratama et al., 2023).

Moshkowitsch et al. studied $Ni_xFe_yO_z$ aerogels with different Ni/Fe ratios for OER activity in 1 M KOH. The best-performing material, NiFeO$_x$ AGHT1, surpassed the activity of the benchmark IrO_2 electrocatalyst (Figure 4). The Ni/Fe ratio greatly affected the catalytic performance, and the best-performing sample had 6 at% Fe, surpassing the NiO$_x$ aerogel and showing that Fe has synergistic effects in the nickel oxide

structure and that aerogels, which were initially only thought to act as supports, could also act as electrocatalysts (Moschkowitsch et al., 2022).

A phosphorus-modified hollow porous nickel-cobalt oxides nanocube with varying P content was tested for OER in 1 M KOH. The optimum P-NiO/$NiCo_2O_4$ sample was stable and presented an overpotential of 290 mV for a current density of 10 mA/cm^2 and a Tafel slope of 49.6 mV/dec, outperforming even the benchmark RuO_2 electrocatalyst. The superior performance was attributed to the effect of P-doping, which decreased the energy barrier, optimized the adsorption of intermediates, and changed the rate-determining step, and to the hollow porous hybrid structure and oxygen vacancies that increased the amount of exposed surface area (Zhang L. et al., 2022).

Similarly, Luo X.-F et al. tested, in alkaline medium (1 M KOH), MnO_x oxides grown directly on Ti foil via electrodeposition with different morphologies obtained at different reaction temperatures: cotton wool structure, nanowire arrays, and nanosheet arrays. The nanowire arrays proved to be the best-performing material in the study, presenting an OER onset potential of 1.546 V vs RHE, a Tafel slope of 106 mV/dec, and a current density of 44.7 mA/cm^2 when an overpotential of 538 mV is applied. The performance of the nanowire arrays was attributed to a larger surface area due to the direct growth of the nanostructure on the Ti foil support, which enhanced conductivity (Luo et al., 2017b). Alternatively, Zand et al. tested MnO_x and silicate-stabilized MnO_x in acidic medium (0.1 M H_2SO_4) and demonstrated that the poor stability of the Mn oxide in acidic conditions can be significantly improved by adding silicate to the structure of the Mn oxide. The results showed that the catalytic activity was less than optimal since the overpotential needed to achieve 10 mA/cm^2 was 640 mV, and the OER onset potential was 1.757 V vs RHE. On the other hand, the stability was greatly improved because the modified Mn oxide showed higher current retention and virtually no structural changes after OER (Zand et al., 2023).

Zhang et al. evaluated copper-doped cobalt oxides deposited via a reactive DC magnetron sputtering process as electrocatalysts for OER in alkaline medium (1 M KOH). The mixed oxides demonstrated relevant activity and showed that copper doping improved the electrocatalytic performance with respect to the single metal cobalt and copper oxides. The best-performing mixed oxide, $Cu_{1.97}CoO_3$, demonstrated a performance close to that of RuO_2. The increase in activity was attributed to changes in crystal structure and morphology that increased the surface-active area (Zhang et al., 2012). Later, Park et al. tested a nanosized synthetic $Cu_{0.7}Co_{2.3}O_3$ oxide prepared using a thermal decomposition method in alkaline medium (1 M KOH) for OER. The overpotential necessary to obtain a 10 mA/cm^2 current density was around 491 mV (Park et al., 2016). Xu et al. studied a cerium-doped cobalt oxide (CoO_x(Ce)) in the form of an amorphous film deposited through an electrostatic spray deposition method. It presented an OER onset potential of 1.315 V vs RHE, an overpotential of 261 mV to achieve a 20 mA/cm^2 current density, and a Tafel slope of 65.7 mV/dec for OER in 1 M KOH, exhibiting higher performance than regular CoO_x, other cerium doped OER catalysts and even commercially available RuO_2. The better performance was attributed to the increase in the electrochemical active surface area (ECSA) caused by the resulting sample's amorphous nature and the formation of cerium-related oxygen vacancies without modifying the cobalt species (Xu et al., 2019).

Roy et al. tested a self-supported copper oxide electrocatalyst grown on Ni foam substrate via an electrodeposition method, demonstrating suitable activity for OER in a 1 M KOH solution. The best-performing material, CuO/Ni@400, presented an overpotential of 364 mV and 508 mV to achieve a 10 mA/cm^2 and a 100 mV/cm^2 current density and a Tafel slope of 90 mV/dec, while also presenting stability in alkaline medium by maintaining constant current density. The superior performance of CuO/Ni@400 was attributed to its microstructure, which made an even way for electron tunneling (Roy et al., 2019). Likewise, Wang et al. tested an in situ-produced copper foam-supported copper oxide (CuO-A/CF) sample prepared via the oxidation of copper selenide (Cu_2Se) at OER conditions in 1 M KOH. The as-prepared electrocatalyst presented an overpotential of 297 mV to achieve a current density of 10 mA/cm^2 and a Tafel slope of 72.8 mV/dec, pointing to fast electron and mass transfer between the catalyst and the electrolyte. The superior performance relative to CuO produced from calcination of $Cu(OH)_2$ supported in copper foam is attributed to the nanoplate structure of CuO-A/CF, which increased the available electrochemical surface area. The catalyst stability was also stated by testing over 50 h in 1 M KOH at a constant 10 mA/cm^2 current density, maintaining a constant overpotential over this period and showing no structural changes (Wang et al., 2020).

Ye et al. tested various iron-copper oxides with different Cu/Fe ratios for OER in 1 M KOH. The oxide that demonstrated the best performance was 6CuO_2-Fe_2O_3, with an overpotential of 510 mV for 10 mA/cm^2. All the samples were stable in the reaction conditions. The performance was attributed to the coexistence of the metal oxides, but the overpotentials are still high, which shows that further improvements can be made (Ye et al., 2022). Similarly, Bai L. et al. tested amorphous ternary Fe-Co-Ni oxides, $FeNiCoO_x$, in alkaline medium (1 M KOH). The tests were made by depositing the material on a glassy carbon electrode and on a Ni foam electrode, which resulted in overpotentials of 240 and 203 mV and Tafel slopes of 45 and 75 mV/dec, respectively, showing a much better performance than the mono or binary metal oxides of those elements and showcasing good stability properties. This increase in catalytic performance was attributed to the synergistic interactions between the three employed metals in the oxide, which greatly reduced the charge transfer resistance and their homogeneous distribution in the oxide (Bai L. et al., 2019).

The OER performance parameters of the above-cited transition metal oxide-based catalysts are shown in Table 1. However, due to the generally high overpotentials presented by the metal oxides (Park et al., 2016; Xing et al., 2018; Sivakumar et al., 2019; Ye et al., 2022; Zand et al., 2023) and their generic instability in acidic medium (Zand et al., 2023), scientists have also tested another traditional catalyst class: transition metal alloys.

2.2 Transition metal alloys for OER

Alloy compounds are sought out due to their low cost and high OER/HER catalytic activity. Their high versatility by including different metals (forming binary, ternary, or multicomponent

TABLE 1 OER electrocatalysts and their key performance indicators: transition metal oxides.

Electrocatalyst	η_{10} (mV)	Tafel slope (mV/dec)	Electrolyte	Source
$NiFeO_x$ AGHT-1	380	-	1 M KOH	Moschkowitsch et al. (2022)
P-NiO/$NiCo_2O_4$	290	49.6	1 M KOH	Zhang et al. (2022b)
MnO_x nanowire arrays	538@44.7 mA/cm^2	106	1 M KOH	Luo et al. (2017b)
SiO_4/MnO_2	640	-	0.1 M H_2SO_4	Zand et al. (2023)
$Cu_{1.97}CoO_3$	-	70.15	1 M KOH	Zhang et al. (2012)
$Cu_{0.7}Co_{2.3}O_3$	491	-	1 M KOH	Park et al. (2016)
CoO_x(Ce)	261@20 mA/cm^2	65.7	1 M KOH	Xu et al. (2019)
CuO/Ni@400	364	90	1 M KOH	Roy et al. (2019)
CuO-A/CF	297	72.8	1 M KOH	Wang et al. (2020)
6CuO_2-Fe_2O_3	510	-	1 M KOH	Ye et al. (2022)
$FeNiCoO_x$/GC	240	45	1 M KOH	Bai L. et al. (2019)
$FeNiCoO_x$/NF	203	75	1 M KOH	Bai L. et al. (2019)

alloys) also allows for selectivity and activity enhancement in the final alloy. Another advantage of alloying is that Pt-based materials can be synthesized with similar or higher catalytic activity while lowering Pt content, which inevitably lowers production costs on a large-scale perspective (Mladenović et al., 2021; Mladenović et al., 2022; Mladenović et al., 2023b; Xu et al., 2023).

Lim et al. reported the synthesis of bimetallic NiFe alloy nanoparticles used as electrocatalysts for the OER in alkaline medium (1 M KOH). The produced alloy presented much better activity than its unary metal Ni and Fe counterparts, having an overpotential of 298 mV for 10 mA/cm^2 and a Tafel slope of 51.9 mV/dec, surpassing the performance of state-of-the-art RuO_2 electrocatalyst. This performance was attributed to the synergistic effects between the metals and the modification of redox properties of Ni sites and the electronic structure of Ni atoms due to the presence of the Fe atoms, as well as the partial oxidation of the alloy into metal oxyhydroxides (Lim et al., 2020). Wang C. et al. reported the synthesis of a hexagonal close-packed (hcp) crystal structure in NiFe alloys and its use as an OER catalyst in alkaline medium (1 M KOH). The samples of different Fe/Ni ratios were supported on N-doped carbon shell structures. The electrocatalytic performance of the best sample (with Fe/Ni ratio of ca. 5.4 at.%) surpassed that of regular face-centered cubic (fcc) NiFe and commercially available RuO_2, needing an overpotential of 226 mV to achieve 10 mA/cm^2 and a Tafel slope of 41 mV/dec, and showed promising stability properties. The performance was attributed to the interaction between the intrinsic crystal structure and the carbon shell, resulting in different electronic properties at its surface that favored the OER process (Wang C. et al., 2019).

From another perspective, Jeong et al. determined the effects of using graphene-encapsulated porous NiMo alloys and compared them to bare porous NiMo alloys for OER in an alkaline medium (1 M KOH). The results showed that the graphene encapsulation enhanced the catalytic performance of the alloy by lowering the overpotential necessary to achieve 10 mA/cm^2 and the Tafel slope from 396 to 351 mV and 101 to 69 mV/dec, respectively, resulting in a performance similar to RuO_2. The stability in 1 M KOH also increased when supported in nickel foam by impeding the degradation of the metals into oxides and hydroxides. The better performance was assigned to synergistic effects between N-doped graphene and NiMo alloy that impacted the adsorption of intermediates, optimizing the free adsorption energies and accelerating the OER rate-determining step (Jeong et al., 2020).

Dai et al. studied a MnFeCoNi high entropy alloy activated for OER through a cyclic voltammetry treatment in an alkaline medium (1 M KOH). The activated alloy exhibited an overpotential of 285 mV to reach a 10 mA/cm^2 current density, presented a Tafel slope of 83.7 mV/dec, and showed good stability properties, surpassing the benchmark RuO_2 catalyst. The catalytic activation of the high entropy alloy was attributed to the formation of monometallic oxides of the metals dispersed as nanosheets throughout the particle's surface, which acted as the true catalyst for OER and exposed more active sites (Dai et al., 2019).

Li et al. tested the use of 3D hierarchical flower-like materials composed of ultrathin cobalt-based bimetallic phosphide nanosheets (CoM-P-3DHFLMs, M = Mn, Cu, Ni) in a 1 M KOH solution for OER catalysis. The CoNi-P-3DHFLM, CoMn-P-3DHFLM, and CoCu-P-3DHFLM samples presented an overpotential of 292, 318, and 307 mV to reach 10 mA/cm^2 and Tafel slopes of 84, 98, and 88 mV/dec, respectively, along with good stability. The enhanced performance compared to Co-P-3DHFLM was attributed to a synergistic interaction between the metals and to the exposition of more active sites in the bimetallic samples (Li et al., 2019).

Bai X. et al. used Co-Fe-based spherical nanoparticles coated with an amorphous carbon shell, whose active species was a Co_7Fe_3 alloy, for OER in alkaline medium (1 M KOH). This material showed an overpotential of 272 mV for 10 mA/cm^2 and a Tafel slope of 40 mV/dec, surpassing most of their monometallic-based counterparts while remaining stable under the reaction conditions. The performance was attributed to the synergy between Co and Fe due to their strong electronic interaction, which lowered the activation energy for OER, favoring the reaction kinetics (Bai X. et al., 2021). Liu et al. presented the synthesis of a P-modified hollow, highly porous, and conductive CoFe alloy (Fe-Co-P) nanosphere

TABLE 2 OER electrocatalysts and their key performance indicators: transition metal alloys.

Electrocatalyst	η_{10} (mV)	Tafel slope (mV/dec)	Electrolyte	Source
NiFe NPs	298	51.9	1M KOH	Lim et al. (2020)
Hep-phase NiFe NPs	226	41	1 M KOH	Wang C. et al. (2019)
NiMo-FG	351	69	1 M KOH	Jeong et al. (2020)
MnFeCoNi	285	83.7	1 M KOH	Dai et al. (2019)
CoNi-P-3DHFLM	292	84	1 M KOH	Li et al. (2019)
CoMn-P-3DHFLM	318	98	1 M KOH	Li et al. (2019)
CoCu-P-3DHFLM	307	88	1 M KOH	Li et al. (2019)
$Fe_1Co_3O_x$@C-800	272	40	1 M KOH	Bai X. et al. (2021)
Fe-Co-P	252	33	1 M KOH	Liu et al. (2018)
$Co_{0.5}Ni_{0.5}$/rGO	288	103	1 M KOH	Zhang et al. (2020)
$Cu_{3.8}$Ni@C	233	114	1 M KOH	Kumar et al. (2020)
Cu-N-C NA/CF	314@20 mA/cm^2	115	1 M KOH	Zhu et al. (2018)
FeCoCu	265	49	1 M KOH	Jiang et al. (2021)
FeCoCuNi	269	48.9	1 M KOH	Jiang et al. (2021)

structure and tested it for OER in alkaline medium (1 M KOH). It was determined that the optimized alloy for OER had a 3:2 Fe/Co ratio and showed an overpotential of 252 mV to reach 10 mA/cm^2 and a Tafel slope of 33 mV/dec, while also presenting very good stability in the reaction conditions. The enhanced performance of the electrocatalyst was attributed to the high valent state of Fe stabilizing the low valent state of Co and the alloy formation being able to fine tune the energetics of all the intermediates involved in the water oxidation mechanism (Liu et al., 2018).

Zhang et al. reported the application of a coral-like carbon-wrapped NiCo alloy ($Co_{0.5}Ni_{0.5}$/rGO) for OER at alkaline conditions (1 M KOH). The sample showed an overpotential of 288 mV to achieve 10 mA/cm^2 and a Tafel slope of 103 mV/dec, while demonstrating stability in the tested conditions, surpassing their monometallic counterparts and the benchmark RuO_2 catalyst in the same conditions. The improved performance is attributed to the graphene sheets introducing a more homogeneous metal distribution, thus exposing more active sites, and to the synergistic interaction between Ni and Co, with Ni regulating the electronic structure of Co, favoring the OER performance (Zhang et al., 2020).

Kumar et al. described the use of bimetallic copper-nickel alloy nanorods textured nanoparticles supported on graphitic carbon ($Cu_{3.8}$Ni@C) samples for OER in alkaline conditions (1 M KOH). The best-performing sample presented an overpotential of 233 mV for 10 mA/cm^2 and a 114 mV/dec Tafel slope and good stability properties, which fared well against state-of-the-art IrO_2 (Kumar et al., 2020). Zhu et al. disclosed the use of a Cu nanoparticles-embedded N-doped carbon nanowire array on copper foam (Cu-N-C NA/CF) as an OER electrocatalyst in alkaline medium (1 M KOH). The sample presented an overpotential of 314 mV to reach 20 mA/cm^2, a Tafel slope of 115 mV/dec, and was demonstrated to be a stable catalyst in OER conditions for at least 16 h. The performance was attributed to the *in-situ* formation of CuO nanoparticles, which acted as the true OER catalyst, and to the increased electrochemical surface area, which exposed more active sites (Zhu et al., 2018). Jiang et al. tested a series of Cu-based alloys (CuM, M = Fe, Co, Ni; FeCo, FeNi, CoNi; FeCoNi) for OER in an alkaline electrolyte (1M KOH). The FeCoCu and FeCoNiCu samples presented, after optimization, an overpotential of 265 and 269 mV for 10 mA/cm^2 and Tafel slopes of 49 and 48.9 mV/dec, respectively, along with proper stability properties, outperforming the benchmark RuO_2 electrocatalyst. The enhanced performance relative to Cu was attributed to synergistic effects between the highly conductive Cu and the OER active Fe, Co, and Ni elements (Jiang et al., 2021).

Table 2 presents the performance parameters for each analyzed OER alloy-based catalyst. Metals and alloys often cannot survive in harsh acidic or basic environments mainly due to the strongly corrosive media, meaning they have to frequently be embedded or decorated in relatively stable hosts, such as carbon materials (Wu et al., 2020). This, amongst other reasons, fueled researchers to investigate more compelling and innovative materials, such as MOFs.

2.3 Transition MOFs and MOF-derived electrocatalysts for OER

MOFs are a class of porous organic-inorganic hybrid materials formed by the linkage of inorganic metal ions/clusters and organic ligands, generating a 3D structure with long-range crystallinity. Recently, MOFs have gained attention from scientists due to their inherent properties, including high surface area, low density, high porosity, and tunable structure. Additionally, they are known for their abundance of metal active sites, utility as templates to generate other materials, and the high adjustability of chemical components (Jiang et al., 2016; Lu et al., 2017; Jia et al., 2022; Tseng et al., 2022). MOFs have found numerous applications, such as in catalysis, gas storage and separation, optics, drug delivery, adsorption, and chemical sensing (Lu et al., 2017; Li et al., 2020; Jia

et al., 2022). As such, research efforts have also been dedicated to producing cost-effective and high-performance electrocatalysts based on pristine MOFs or MOF-derived materials for applications in the OER, HER, and ORR.

Ma et al. reported the *in-situ* synthesis of MOF-encapsulated bimetallic nanoparticles by etching Ni-Cu alloy nanoparticles without additional metal precursors and its performance for alkaline OER (1 M KOH). The bimetallic encapsulated MOF had better activity than its monometallic counterparts, showing a current density 1.6 and 71 times higher than for the Ni encapsulated and Cu encapsulated MOFs, respectively, at an overpotential of 624 mV and a Tafel slope of 98 mV/dec, and good stability. The higher activity was attributed to a higher number of exposed active sites and to synergistic effects between the Ni and Cu metals (Ma et al., 2019).

Tseng et al. disclosed the use of NiFe bimetallic MOFs deposited on pretreated nickel foam (NF) and processed by low-pressure plasmas with different composition atmospheres as OER electrocatalysts in alkaline electrolyte (1 M KOH). The electrocatalytically optimized sample, NiFe-MOFs/NF-AH, treated with a 95% argon +5% H_2 atmosphere, presented an overpotential of 149 mV to achieve 10 mA/cm^2 and a Tafel slope of 54 mV/dec, along with good stability (Tseng et al., 2022). MOFs are often used as precursors for low-cost highly-active electrocatalysts. One example comes from Jiang et al., who used Fe-Ni-based MOFs as self-templates to synthesize several Fe-Ni-O_x oxide architectures with different Fe/Ni ratios and tested those for OER in alkaline medium (0.1 M KOH). The obtained results indicated that the performance was closely related to the Fe/Ni ratio, and the optimized sample, $Fe_{0.5}Ni_{0.5}O_x$, needed a 584 mV overpotential to achieve 10 mA/cm^2 and had a Tafel slope of 72 mV/dec, with good stability properties and performance comparable to that of benchmark RuO_2 catalyst. The performance is attributed to the *in-situ* formation of NiOOH and to the presence of spinel $NiFe_2O_4$ species, which act as the active phases for OER (Jiang et al., 2016).

Ji et al. detailed the synthesis of a marigold flower-like MOF-aided manganese vanadium oxide and its OER performance in alkaline medium (1 M KOH). The MOF MnV oxide microflower required a 310 mV overpotential to reach 50 mA/cm^2 and had a Tafel slope of 51.4 mV/dec, comparing its performance to the benchmark RuO_2 electrocatalyst and outperforming the monometallic MOF Mn and MOF V oxide microflower counterparts while also being able to sustain OER for over 50 h at a current density of 50 mA/cm^2. The activity was attributed to a higher number and exposition of active sites (Ji et al., 2023).

Zhao et al. assembled CoNi-based ultrathin MOF nanosheets (NiCo-UMOFNs) and tested them for OER in alkaline conditions (1 M KOH). The bimetallic MOF nanosheets presented an overpotential of 250 mV to reach 10 mA/cm^2, a Tafel slope of 42 mV/dec, and good stability properties, outperforming its monometallic counterparts and the benchmark RuO_2 electrocatalyst, especially when supported in copper foam, since the overpotential to reach 10 mA/cm^2 reduces to 189 mV. The performance was attributed to the existence of unsaturated metal sites and to the coupling effect between Ni and Co metals (Zhao et al., 2016). Zhou et al. designed a series of isostructural hierarchical bimetallic CoNi MOF nanostructures (CTGU-10a2-d2) with different Co/Ni ratios and tested them towards OER in an alkaline electrolyte (0.1 M KOH). The best performing MOF, CTGU-10c2, presented an overpotential of 240 mV to achieve 10 mA/cm^2, a Tafel slope of 58 mV/dec, and was stable in the OER conditions, surpassing the performance of the benchmark RuO_2 electrocatalyst. This performance was attributed to synergistic effects between the metal atoms, the hierarchical nanobelt structure, and the presence of unsaturated metal sites (Zhou et al., 2019).

Li et al. produced a Cu-based MOF directly supported on copper foam (MOF $[Cu(OH)_2]$/CF) and tested its activity towards OER in alkaline medium (1 M KOH). The resulting material used an overpotential of 330 mV to achieve 10 mA/cm^2 and had a Tafel slope of 108 mV/dec, with activity comparable to the RuO_2 electrocatalyst, while presenting good durability. The performance is attributed to the exposition of more active sites and to the *in-situ* formation of Cu oxide species, which act as active electrocatalysts towards OER (Li et al., 2020). Cheng et al. studied a bimetallic Cu-Co-based MOF nanobox as an OER electrocatalyst in alkaline medium (1 M KOH). The material required an overpotential of 271 mV to reach 10 mA/cm^2 and presented a Tafel slope of 63.5 mV/dec, all while being stable in the OER conditions, outperforming the monometallic counterparts and the benchmark RuO_2 electrocatalyst. The improved performance was attributed to the *in situ* formation of the bimetallic oxyhydroxide, which acts as the true catalyst with intrinsically higher electrocatalytic performance, synergistically enhanced by the Cu sites, while the Co sites act as the active ones (Cheng et al., 2021).

Table 3 presents a compilation of the analyzed MOFs OER performance parameters. In general, MOFs present poor electrical conductivity, poor stability, low mass permeability, and blockage of

TABLE 3 OER electrocatalysts and their key performance indicators: transition MOFs.

Electrocatalyst	η_{10} (mV)	Tafel slope (mV/dec)	Electrolyte	Source
Ni-Cu@Cu-Ni-MOF	-	98	1 M KOH	Ma et al. (2019)
NiFe-MOFs/NF-AH	149	54	1 M KOH	Tseng et al. (2022)
$Fe_{0.5}Ni_{0.5}O_x$	584	72	1 M KOH	Jiang et al. (2016)
MOF MnVO microflower	310@50 mA/cm^2	51.4	1 M KOH	Ji et al. (2023)
NiCo-UMOFNs	250	42	1 M KOH	Zhao et al. (2016)
CTGU-10c2	240	58	0.1 M KOH	Zhou et al. (2019)
MOF$[Cu(OH)_2]$/CF	330	108	1 M KOH	Li et al. (2020)
CoCu-MOF-NBs	271	63.5	1 M KOH	Cheng et al. (2021)

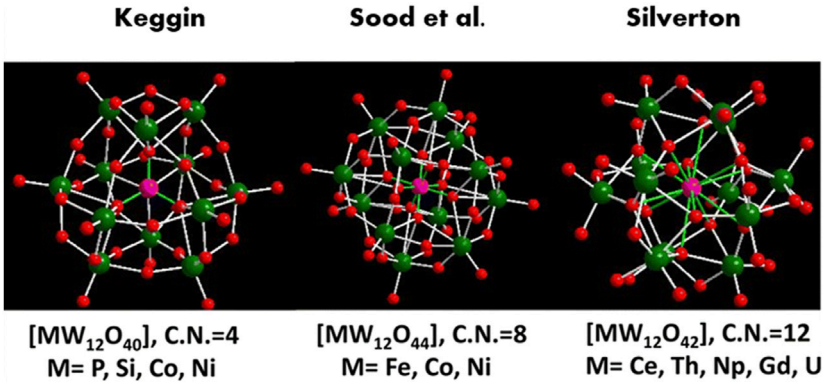

FIGURE 5
Different hetero-polyoxometalates belonging to the 1:12 series of POMs with various heteroatoms (adapted from Sood et al., 2022).

metal centers by organic ligands (Zhao et al., 2016; Lu et al., 2019; Ma et al., 2019), limiting their use in electrocatalytic applications. A way to circumvent this is the utilization of MOF-derived electrocatalysts, normally via calcination, to generate carbon materials with enhanced conductivity and stability. In spite of this, POMs have been studied as an alternative to MOF and MOF-derived electrocatalysts.

2.4 Transition metal POMs for OER

Amidst the collective effort to find alternatives to the noble metal-based electrocatalysts, POMs have appeared as a viable and highly sought-out alternative. POMs are inorganic redox-active transition metal (e.g., V, W, and Mo) oxide ion clusters linked together by oxygen atoms with a high number of redox centers, which grants them significant advantages when multi-step electron transfer reactions are involved (Horn et al., 2021; Gusmão et al., 2022). Other positive aspects of POMs include stability under oxidative OER conditions, thermal stability, rapid and highly reversible electrochemical activity, and finely tunable structures to suit the specific application needs (Luo W. et al., 2017; Horn et al., 2021; Gusmão et al., 2022).

They possess an ordered 3D framework structure that can be easily tailored to introduce redox-active transition metals (that can act as redox centers) into the framework. POMs can serve as structural agents to form nanostructures with other types of materials, such as oxides. Additionally, they can be encapsulated in various materials, such as MOFs, to derive the so-called POMOFs. These examples showcase the versatility that POMs offer (Horn et al., 2021). Still, one cannot overlook the conductivity and stability problems present in POMs, which can fortunately be circumvented by combining them with appropriate supports, such as carbon-based supports, organic supports, or by confining them in MOFs or Covalent Organic Frameworks. The incorporation of POMs in a more conductive support with adequate binding strength can prevent leaching problems and inhibit agglomerations, both increasing stability and maximizing the number of active sites present (Wang C. et al., 2023). Relative to the catalysis application, the Keggin variation structure is best suited due to its proton binding sites and electron-rich oxygen sites, which participate in acid and base-catalyzed reactions, respectively. A variation of the Keggin structure is the lacunary Keggin structure, which results from removing a M=O moiety, and M can be substituted by a transition metal such as Ni, Mn, Co, or Cu to increase the redox catalytic properties (Horn et al., 2021; Gusmão et al., 2022).

Imani et al. produced a Keggin tungsten POM containing organic-inorganic hybrid composite material directly on a carbon paste electrode and later incorporated Ni and Fe ions (Ni-Fe/oA-POM/CPE). Afterward, they tested its performance towards OER in an alkaline electrolyte (0.1 M NaOH). The resulting composite required a 330 mV overpotential to reach 10 mA/cm^2 and had a Tafel slope of 113 mV/dec. It presented good stability in alkaline OER conditions, since after 10 h at a constant overpotential of 300 mV, it lost almost no activity, with a minor decrease after 500 cycles (Imani et al., 2018).

Sood et al. constructed a rare POM cluster-based solid, $(C_5H_7N_2)_6[NiW_{12}O_{44}]$, whose structure is shown in the center section of Figure 5, and tested its performance towards OER in alkaline medium (1 M KOH). The synthesized POM was able to provide 10 mA/cm^2 at 347 mV of overpotential and showed a 130 mV/dec Tafel slope. It maintained a current density of 10 mA/cm^2 for up to 96 h, indicating good stability and outperforming state-of-the-art RuO_2 electrocatalyst. The observed performance was attributed to the *in situ* formation of WO_x (x = 1,2) and NiO, $Ni(OH)_2$, and NiOOH, which act as active phases in the electrocatalyst (Sood et al., 2022).

Al-Oweini et al. were the first ones to report the activity of a tetramanganese $[Mn^{III}_3Mn^{IV}O_4(CH_3COOH)_3(A\text{-}\alpha SiW_9O_{34})]^{6-}$ POM towards photocatalytic OER in acid conditions (a pH 5 buffer was used) (Al-Oweini et al., 2014). Goberna-Ferrón et al. researched the electrocatalytic activity of a tetramanganese $[Mn_4(H_2O)_2(PW_9O_{34})_2]^{10-}$ sandwich-type POM towards OER in neutral conditions. The tested POM showed considerable activity for OER, although it reached negligible levels after 30 min. This was owed to the formation of MnO_2, which is inactive for water oxidation, indicating degradation and instability of the POM under harsh oxidative reaction conditions. The same effect was observed when the POM was used as a heterogeneous catalyst (Goberna-Ferrón et al., 2015).

Imani et al. designed a Mn-containing POM-based composite that was later deposited onto a rotating carbon paste electrode by two

TABLE 4 OER electrocatalysts and their key performance indicators: transition metal POMs.

Electrocatalyst	η_{10} (mV)	Tafel slope (mV/dec)	Electrolyte	Source
Ni-Fe/oA-POM/CPE	330	113	0.1 M NaOH	Imani et al. (2018)
$(C_5H_7N_2)_6[NiW_{12}O_{44}]$	347	130	1 M KOH	Sood et al. (2022)
Mn/oMA-PW/RCPE	380	111	1 M KOH	Imani et al. (2021)
Mn-oMA-PW + RCPE	440	133	1 M KOH	Imani et al. (2021)
$FeCoPMo_{12}$	258	33	1 M KOH	Zhai et al. (2017)
CNCP-6	241	75.8	1 M KOH	Kang et al. (2022)
NiCo-POM/Ni	360	126	0.1 M KOH	Luo et al. (2017a)
SiW_9Co_3@ZIF-67	470	113.6	0.1 M KOH	Abdelkader-Fernández et al. (2020)
SiW_9Co_3@ZIF-8	-	69.4	0.1 M KOH	Abdelkader-Fernández et al. (2020)
$[Cu_3(SbW_9O_{33})_2(H_2O)_3]^{12-}$	-	113	80 mM Tris–HCl solution	Yu et al. (2018)

immobilization methods: direct formation and physical mixing. The resulting electrodes were tested for OER in basic medium (1 M KOH), attaining a 380 and 440 mV overpotential to reach 10 mA/cm^2 and a Tafel slope of 111 and 133 mV/dec, respectively. In terms of stability and durability, they were able to perform for over 10 h while retaining 93.6% and 93.3% of current density, showing a small increase in overpotential (18 and 20 mV, respectively) after 600 cycles to keep 10 mA/cm^2 (Imani et al., 2021).

Zhai et al. disclosed the synthesis of $FeCoPMo_{12}$ POM through a room-temperature coprecipitation method, resulting in a porous and amorphous compound tested for OER in alkaline electrolyte (1 M KOH). The POM presented an overpotential of 258 mV to reach 10 mA/cm ^{2}, a Tafel slope of 33 mV/dec, and stability for over 10 h of OER with a current loss of 8.3%, surpassing $FePMo_{12}$, $CoPMo_{12}$ and hydroxide counterparts, and benchmark RuO_2 electrocatalyst. The performance was attributed to the synergistic effects of Fe incorporation, which activates the active sites (Zhai et al., 2017).

Kang et al. reported the synthesis and use of dodecahedral Co, N, and C co-doped POMs with a frame-like yolk-shell nanostructure as OER electrocatalysts in an alkaline solution (1 M KOH). After optimization, the best-performing sample required an overpotential of 241 mV to achieve 10 mA/cm^2, while also having a Tafel slope of 75.8 mV/dec and long-term electrochemical stability (over 24 h with only a slight change in the output current density), outperforming the benchmark IrO_2 electrocatalyst. The performance is credited to uniform N, C, and Co doping and a higher exposition of active sites (Kang et al., 2022).

Luo W. et al. described the deposition of Dexter-Silverton POM microcrystals, $Co_{6.8}Ni_{1.2}W_{12}O_{42}(OH)_4(H_2O)_8$, in a nickel foam substrate and its use as an OER electrocatalyst in alkaline medium (0.1 M KOH). The resulting composite needed a 360 mV overpotential to reach a 10 mA/cm^2 current density and showed a Tafel slope of 126 mV/dec, while also retaining 85% of its current density in a 10 h test at a 440 mV overpotential test with no degradation of its crystal structure and morphology (Luo W. et al., 2017).

Abdelkader-Fernández et al. reported the synthesis of two POM@MOFs hybrids, SiW_9Co_3@ZIF-8 and SiW_9Co_3@ZIF-67, and tested their activities towards OER in 0.1 M KOH electrolyte. It is demonstrated that the SiW_9Co_3@ZIF-67 hybrid has a more effective electron transfer process due to the presence of Co^{2+} nodes in the ZIF-67 skeleton, resulting from a synergistic interaction between the Co-based-POM encapsulated in the Co-based-MOF. This effect increases performance greatly: the resulting SiW_9Co_3@ZIF-67 presented a performance that well exceeded benchmark RuO_2 and IrO_2 electrocatalysts even though these benchmark materials exhibit higher "intrinsic" non-area dependent performances towards the OER in the roughness-corrected polarization curves (Abdelkader-Fernández et al., 2020).

Yu et al. studied the activity of the sandwich-type $[Cu_3(SbW_9O_{33})_2(H_2O)_3]^{12-}$ POM towards OER in neutral conditions and as a homogeneous catalyst. The tested POM presented good overall stability properties and a Tafel slope of 113 mV/dec, and it was demonstrated that the POM acted as the real catalyst in the OER conditions (Yu et al., 2018).

Table 4 summarizes the discussed POM-based electrocatalysts and their main OER performance parameters.

3 Oxygen reduction reaction (ORR)

The ORR converts molecular oxygen to water via electron acceptance, which can occur through a 4e$^-$ direct formation path or through a two-step 2e$^-$ pathway that produces a peroxide as an intermediate. Similar to the OER, there are slight differences in the reaction intermediates when the reaction proceeds in alkaline media *versus* when it proceeds in acidic media, as shown below in equations 2.3 through 2.8 for:

Alkaline conditions

4e$^-$ pathway:

$$O_2 + 2H_2O + 4e^- \rightleftharpoons 4OH^- \quad (2.3)$$

2e$^-$ pathway:

$$O_2 + H_2O + 2e^- \rightleftharpoons HO_2^- + OH^- \quad (2.4)$$

$$HO_2^- + H_2O + 2e^- \rightleftharpoons 3OH^- \quad (2.5)$$

Acidic conditions
4e⁻ pathway:

$$O_2 + 4H^+ + 4e^- \rightleftharpoons 2H_2O \quad (2.6)$$

2e⁻ pathway:

$$O_2 + 2H^+ + 2e^- \rightleftharpoons H_2O_2 \quad (2.7)$$

$$H_2O_2 + 2H^+ + 2e^- \rightleftharpoons 2H_2O \quad (2.8)$$

The main applications of ORR are in fuel cells and metal-air batteries, occurring during discharge at the cathode. Like OER, it presents sluggish kinetics and thus requires high overpotentials (Horn et al., 2021), emphasizing the need for highly active electrocatalysts. Furthermore, from an ideal perspective, the electrocatalyst would be bifunctional, i.e., it would also show good activity towards OER, as the reaction occurs during the charging process in these applications.

Generally, the 4e⁻ pathway is preferred because it has higher reaction kinetics and efficiency (Lu et al., 2019). Additionally, peroxide formation is avoided, which is particularly critical because it is a strong oxidant that can lower the electrode performance over time and damage the structure of fuel cells via degradation of the polymer electrolyte membrane (Lee and Popov, 2007). However, the 2e⁻ pathway can be preferred if the objective is peroxide production, since the electrochemical process may be more cost-effective than conventional technologies (Zheng et al., 2021).

The best metal electrocatalyst for ORR is Pt, as it shows high activity and selectivity towards the 4e⁻ pathway. However, Pt is scarce (more than gold and silver) (Zhang C. et al., 2017), and thus an expensive noble metal, while also having durability issues, especially when Pt-based materials are concerned (Zhang C. et al., 2017; Lu et al., 2019). This encourages researchers to seek out more cost-effective, highly active, and durable electrocatalysts based on cheaper and earth-abundant early transition metals (Ni, Co, Cu, Mn, etc.) to make these applications economically viable at an industrial scale.

3.1 Transition metal oxides for ORR

Cui et al. prepared porous $NiO/NiCo_2O_4$ nanotubes and tested their activity for the ORR in alkaline conditions (0.1 M KOH). The prepared composite performs similarly to state-of-the-art Pt/C electrocatalysts, having close onset potentials but with the oxides having a higher limiting current density. Additionally, the tested electrocatalyst showed higher stability than Pt/C (87% of current retention after 40,000 s vs 70% for Pt/C) and exhibited resistance to methanol crossover. The obtained Tafel slope was 61.8 mV/dec, and the reaction mechanism followed the 4e⁻ direct reduction path. The activity was attributed to the unique porous tubular structure with homogeneous oxide distribution along the surface (Cui et al., 2014).

Sidhureddy et al. disclosed the synthesis of $Ni_xCo_{3-x}O_4$ mesoporous spinel nano-oxides with different morphologies based on the Ni/Co ratio and tested their activities towards the ORR in alkaline electrolyte (0.1 M KOH). The best-performing sample, NCO-1 (1:2.06 Ni/Co ratio), presented an onset potential of 0.9 V vs RHE and was three times more active than its mono-metal oxide counterparts, while also exhibiting great tolerance to methanol crossover (higher than benchmark Pt/C electrocatalyst), good general stability (94% current retention after 300 min) and a selective 4e⁻ reduction pathway. The performance was attributed to the abundance of octahedral site cations and defective oxygen sites in the structure (Sidhureddy et al., 2019).

Liu and Qin tested graphene-supported β-MnO_2 nanoparticles (MnO_x/graphene) for the ORR using an alkaline electrolyte (6 M KOH). The composite showed a Tafel slope of 91 mV/dec and an average number of exchanged electrons of 2.5, meaning that the composite was more selective towards the 2e⁻ peroxide forming path. The activity was attributed to the synergistic interactions between MnO_2 and graphene sheets (Liu and Qin, 2015).

Swetha et al. designed manganese oxide samples with different morphologies (nanowires, nanoflowers, and nanoparticles) and tested them towards the ORR in alkaline medium (0.1 M KOH). The best-performing Mn oxide morphology was the nanowire structure, which showed an onset potential of 0.83 V vs RHE and a 1.75 mA/cm^2 current density. This increased activity was attributed to the higher surface area contained by the nanowire structure, which increases active site exposition (Swetha et al., 2018).

Draskovic and Wu tested a series of cuprous delafossite oxides ($CuBO_2$; B = Sc, Y, La) supported on carbon black towards the ORR in an alkaline electrolyte (0.1 M KOH). The results demonstrated superior activity in the presence of carbon support. The oxides exhibited similar onset potentials and diffusion limiting currents, with a number of exchanged electrons in the range of 2.1–2.2 for $CuScO_2$ and $CuYO_2$ and in the range of 2.3–2.9 for $CuLaO_2$, indicating that the first two oxides prefer the 2e⁻ peroxide pathway while $CuLaO_2$ tends for the 4e⁻ pathway. In addition, the samples had Tafel slopes of −59, −55, and −56 mV/dec for $CuScO_2$, $CuYO_2$, and $CuLaO_2$ (Draskovic and Wu, 2017).

Saianand et al. reported the use of dispersed Cu/CuO nanospecies on mesoporous fullerenes (Cu-MFC_{60}) samples for the ORR in alkaline conditions (0.1 M KOH). The optimized electrocatalyst, Cu(15%)-MFC_{60}, presented an onset potential of 0.86 V vs RHE, a half-wave potential of 0.76 V vs RHE a diffusion limiting current density of −5.18 mA/cm^2, Tafel slope of 82 mV/dec, high selectivity towards the 4e⁻ transfer path, and improved stability, a performance comparable to that of benchmark commercial Pt/C electrocatalyst. The activity of the composite was attributed to the well-defined mesoporous features, abundant active sites, moderate surface area, and synergistic interactions between the metal and the support matrix (Saianand et al., 2020).

Table 5 compares the ORR performance parameters for the discussed oxide-based electrocatalysts.

3.2 Transition metal alloys for ORR

Sun et al. disclosed the synthesis and use of a 3D low-cost Co_3Fe_7 nanoparticles/nitrogen, manganese-codoped porous carbon (Co_3Fe_7/N, Mn-PC) as an ORR electrocatalyst in an alkaline electrolyte (0.1 M KOH). The composite material exhibited an onset and half-wave potential of 0.98 and 0.87 V and a Tafel slope of 86.9 mV/dec, outperforming the mono and bimetallic counterparts and the benchmark Pt/C electrocatalyst. Additionally, the average number of exchanged electrons was

TABLE 5 ORR electrocatalysts and their key performance indicators: transition metal oxides.

Electrocatalyst	Onset potential (V vs RHE)	Tafel slope (mV/dec)	Number of exchanged e^-	Electrolyte	Source
$NiO/NiCo_2O_4$ nanotubes	0.92	61.8	3.9	0.1 M KOH	Cui et al. (2014)
NCO-1	0.90	-	3.96	0.1 M KOH	Sidhureddy et al. (2019)
MnO_x/graphene	-	91	2.5	6 M KOH	Liu and Qin (2015)
MnO_x nanowires	0.83	-	-	0.1 M KOH	Swetha et al. (2018)
$CuScO_2$	-	59	2.1–2.2	0.1 M KOH	Draskovic and Wu (2017)
$CuYO_2$	-	55	2.1–2.2	0.1 M KOH	Draskovic and Wu (2017)
$CuLaO_2$	-	56	2.3–2.9	0.1 M KOH	Draskovic and Wu (2017)
Cu(15%)-MFC_{60}	0.86	82	3.99	0.1 M KOH	Saianand et al. (2020)

TABLE 6 ORR electrocatalysts and their key performance indicators: transition metal alloys.

Electrocatalyst	Onset potential (V vs RHE)	Half-wave potential (V vs RHE)	Tafel slope (mV/dec)	Number of exchanged e^-	Electrolyte	Source
Co_3Fe_7/N, Mn/PC	0.98	0.87	86.9	4.01	0.1 M KOH	Sun et al. (2021)
$Co_{0.5}Mo_{0.5}N_y$/NCNCs	0.81	-	-	3.65–3.85	0.5 M H_2SO_4	Sun et al. (2015)
NiCoSn	0.80	0.72	-	3.9	1 M KOH	Sajeev et al. (2023)
50 nm CuPd tetrapod	-	0.90	54	4	0.1 M KOH	Zhang L. et al. (2018)

4.01, and impressive methanol crossover resistance and stability were exhibited (i.e., current almost unchanged after adding 1 M CH_3OH and negative shift of 9 mV to the onset potential after 2,000 CV scans). The performance was attributed to a higher number of active sites and nitrogen ligands chelated with Fe and Co, increasing the charge transfer kinetics, and to the synergistic effects of Mn and N doping, which adjusted the electronic structure, thus favoring catalysis (Sun et al., 2021).

Sun et al. studied Mo-Co alloyed nitrides supported on nitrogen-doped carbon nanocages ($Co_xMo_{1-x}N_y$/NCNCs) as an electrocatalyst for ORR in acidic medium (0.5 M H_2SO_4). The best-performing electrocatalyst, $Co_{0.5}Mo_{0.5}N_y$/NCNCs, combined the advantages of high activity of Co nitride and good stability of Mo nitride in acidic conditions, which translated into an onset potential of 0.81 V vs RHE, good selectivity to the $4e^-$ reduction pathway, high stability (>80% current retention after 100 h and immunity to methanol crossover. The activity was attributed to the cobalt active reaction sites, smaller particle size that inhibited agglomeration, thus exposing more sites, and the synergistic effects between the metals (Sun et al., 2015).

Sajeev et al. synthesized a trimetallic NiCoSn alloy and tested its electrocatalytic properties towards the methanol oxidation reaction and the ORR in alkaline medium (1 M KOH). Regarding the ORR, the trimetallic sample presented an onset and half-wave potential of 0.80 and 0.72 V vs RHE, respectively. Additionally, it had good selectivity for the 4-electron reduction pathway and exhibited good stability under ORR conditions and during methanol crossover. The verified performance was attributed to a higher abundance of metal redox active sites, larger surface area, and enhanced electron transport (Sajeev et al., 2023).

Zhang L. et al. disclosed the use of 50 nm Cu/Pd tetrapod as an ORR electrocatalyst in alkaline medium (0.1 M KOH). The material exhibited a half-wave potential of 0.90 V vs RHE and a 54 mV/dec Tafel slope, performing closely to state-of-the-art Pt/C electrocatalyst. The reduction was verified to follow the $4e^-$ direct reduction mechanism, and accelerated durability tests showed excellent retention of both current and morphology after 10,000 cycles at ORR conditions. This performance was attributed to the synergistic effects of the alloy and sharp-tip effects, which enabled negative charge accumulation on Pd atoms at the tetrapod tips (Zhang L. et al., 2018).

Table 6 contains the performance indicators for the analyzed ORR alloy-based electrocatalysts. Transition metals tend to leach out of alloy catalysts under fuel cell operating conditions, causing a reduction of the catalytic activity for ORR (Lee and Popov, 2007). As such, other types of materials are also being investigated for this reaction, including MOFs and POMs.

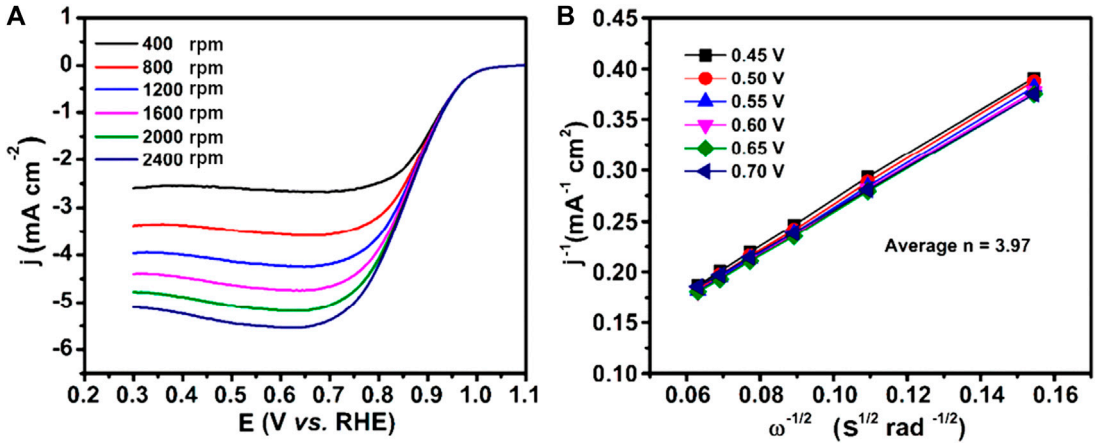

FIGURE 6
(A) Steady-state voltammograms of the ORR profiles at Cu@Cu_2O core-shell nanocatalyst in O_2-saturated 0.1 M KOH solution at different rotation rates and scan rate of 20 mV/s and **(B)** the corresponding Koutecky–Levich (K–L) plots (adapted from Kim et al., 2018).

3.3 Transition MOFs and MOF-derived electrocatalysts for ORR

Qin et al. designed a series of nanocomposites derived from bimetallic iron/nickel MOFs and nitrogen-doped graphene denoted as Fe/Ni-MOFs/NG, which was tested in alkaline electrolyte for the ORR (0.1 M KOH). The best performance was shown by Fe/Ni-MOF/NG-20, which had an onset potential of 1.09 V, exchanged an average of 3.93 electrons, a Tafel slope of 58.2 mV/dec, methanol crossover resistance, and good stability features at ORR conditions. The performance was attributed mainly to the unique structure, which has Fe/Ni-MOF acting as catalyst and NG acting as cocatalyst, and high exposed surface area due to the hierarchical porous structure (Qin et al., 2019).

Rehman et al. synthesized Ni-N carbon nanotubes (Ni-N-CNTs) derived from ZIF-8 MOF crystals and tested their activities for ORR at alkaline conditions (0.1 M KOH). The electrocatalyst presented an onset and half-wave potential of 0.87 and 0.75 V vs RHE, a Tafel slope of 84 mV/dec, a transferred number of electrons around 3.9, and good stability properties. It also presented a −5.51 mA/cm^2 limiting-current density, outperforming state-of-the-art Pt/C electrocatalyst, which showed a limiting-current density of −5.2 mA/cm^2 (Rehman et al., 2022).

Tong et al. reported the synthesis of a series of cobalt nanoparticles/N-doped carbon catalysts derived from ZIF/CNT nanonecklaces and tested their use for the ORR in alkaline electrolyte (0.1 M KOH). The best-performing sample had an onset potential of 0.92 V vs RHE, exchanged 4 electrons during the reaction, and showed good stability after 1,000 cycles at ORR conditions. The verified performance was attributed to the synergistic effect of cobalt content and the well-dispersed one-dimensional structure (Tong et al., 2020).

Feng et al. developed a N-doped porous graphitized carbon-supported cobalt disulfide derived from ZIF-67 MOF and tested its activity towards ORR in alkaline conditions (0.1 M KOH). The sample showed an onset and a half-wave potential of 0.86 and 0.79 V vs RHE, a Tafel slope of 56 mV/dec, and a number of transferred electrons in the 3.62–3.72 range, exhibiting similar performance to the benchmark Pt/C ORR electrocatalyst, while showing better stability properties in methanol crossover conditions and after prolonged exposure to ORR conditions (1,000 cycles). The performance was attributed to N-doping, enhanced conductivity given by the porous graphitized carbon support, and the presence of active N-Co sites (Feng et al., 2019).

Mani et al. produced a Cu-based MOF $[(Cu_4Cl)_3(H_{0.5}BTT)_8(H_2O)_{12}]\cdot 3MeOH\cdot 9DMF$ with tetrazole ligand (H_3BTT = 5,5'-(1,4-phenylene) bis(1H-tetrazole)) and tested its performance in alkaline medium (0.05 M KOH). The MOF showed an onset and half-wave potential of 0.94 and 0.78 V vs RHE, a number of transferred electrons of approximately 4, exceptional methanol crossover (no changes after addition of 1 M MeOH), and good cycling stability (84% of current retained after 12 h), with no changes to the porous morphology detected after ORR. The high activity was attributed to the formation of nascent copper(I) moiety from copper (II), which is also surrounded by nitrogen-rich tetrazole moiety, thus increasing ORR activity (Mani et al., 2019).

Kim et al. reported the use of a Cu(II)-MOF-derived Cu@CuO_2 core-shell nanocatalyst obtained via reduction with borohydride as an electrocatalyst for the ORR in alkaline medium (0.1 M KOH). The material presented an onset and half-wave potential of 0.93 and 0.86 V vs RHE, and an average of 3.97 electrons exchanged, as shown in Figure 6, thus demonstrating good selectivity towards the preferred ORR pathway. The activity was attributed to the synergistic morphological effects of the core-shell structure, high dispersion of CuO_2, and strong adsorption of O_2 on the catalyst surface (Kim et al., 2018).

Table 7 compiles the key ORR performance parameters for the MOF and MOF-derived electrocatalysts shown in this section.

3.4 Transition metal POMs for ORR

Zhang S. et al. designed a series of carbonaceous supported (thermalized triazine-based frameworks (TTF), fluorine-doped TTF (TTF-F), reduced graphene oxide or carbon Vulcan XC-72)

TABLE 7 ORR electrocatalysts and their key performance indicators: transition MOFs and MOF-derived electrocatalysts.

Electrocatalyst	Onset potential (V vs RHE)	Half-wave potential (V vs RHE)	Tafel slope (mV/dec)	Number of exchanged e^-	Electrolyte	Source
Fe/Ni-MOF/NG-20	1.09	-	58.2	3.925	0.1 M KOH	Qin et al. (2019)
Ni-N-CNTs	0.87	0.75	84	3.9	0.1 M KOH	Rehman et al. (2022)
ZIF/CNT-800-AL (Zn/Co = 2/8)	0.92	-	-	4	0.1 M KOH	Tong et al. (2020)
CoS_2@NC	0.86	0.79	56	3.62–3.72	0.1 M KOH	Feng et al. (2019)
$[(Cu_4Cl)_3(H_{0.5}BTT)_8\ (H_2O)_{12}]\cdot$ 3MeOH·9DMF	0.94	0.78	-	4	0.05 M KOH	Mani et al. (2019)
Cu@CuO_2 core-shell	0.93	0.86	-	3.97	0.1 M KOH	Kim et al. (2018)

precious-metal free POMs (based on Ni, Co, and Cu) and tested their activities for ORR in alkaline medium (0.1 M KOH). The best-performing composite, Cu_6Ni_7/TTF-F, presented an onset potential of 0.91 V vs RHE and had an electron transfer number in the 3.92–3.94 range, while also presenting excellent stability (negligible changes after 6,000 cycles). They also tested the influence of the POM-core in the electrocatalyst, concluding that the Ni and Cu-based POMs (either individually or having both metals in the POM) induce higher activity when compared to the Co-POMs (Zhang S. et al., 2017).

Zheng et al. produced a new Ni-POM compound, NiP_4Mo_6, and later vulcanized it, testing both materials' electrocatalytic activity towards the ORR in alkaline conditions (0.1 M KOH). The materials presented different selectivities for the ORR, with NiP_4Mo_6 being selective to the $4e^-$ path and its vulcanized counterpart being selective to the $2e^-$ path. The vulcanized material also presented higher half-wave potential and lower Tafel slope: 0.77 and 0.73 V vs RHE, and 98.1 and 106.2 mV/dec, respectively, for vulcanized and unvulcanized samples. Both materials also presented excellent stability with virtually no change after 8,000 cycles. The change in the ORR mechanism was attributed to the vulcanization process, which substituted O^{2-} atoms with S^{2-} atoms, affecting the adsorption energies, thus weakening it in such a way that H_2O_2 production would be favored (Zheng et al., 2021).

Sanji et al. reported the use of a POM-modified Pd_8Ni_2/rGO (Pd_8Ni_2/rGO-POM) as an ORR electrocatalyst in alkaline conditions (0.1 M KOH). It presented an onset potential of ~0.83 V vs RHE, a Tafel slope of 59.8 mV/dec, and an average of 3.9 electrons exchanged during the ORR. Furthermore, the composite exhibited excellent methanol crossover tolerance and better current retention properties after 10 h at ORR conditions, outperforming the Pt/C state-of-the-art electrocatalyst. Lastly, the performance was attributed to the Pd-Ni alloy interaction (their interactions modify their electronic structures, contributing to enhanced ORR performance), the rGO support (improves conductivity and mass transfer), and the synergistic effects between them and the POM (Sanji et al., 2021).

Ammam et al. performed cyclic voltammetry tests on the Mn-substituted dissymmetrical Dawson-sandwich type and the Keggin sandwich banana-shaped POMs, $[Mn^{II}_4(H_2O)_2(H_4AsW_{15}O_{56})_2]^{18-}$ and $[((Mn^{II}OH_2)Mn^{II}_2PW_9O_{34})_2(PW_6O_{26})]^{17-}$ ($Mn_4As_2W_{30}$ and $Mn_6P_3W_{24}$). Subsequently, they evaluated their activity towards the ORR at pH 5 and pH 3, respectively. The results indicated that both catalysts demonstrated activity towards the ORR, but a deposited layer of Mn oxides (mainly MnO_2) acted as the true catalyst. This was further corroborated by performing additional CV cycles, revealing an increase in the thickness of the oxide layer and a corresponding enhancement in ORR activity (Ammam et al., 2011).

Fernandes et al. disclosed the use of the Co-based sandwich $(TBA)_7H_3[Co_4(H_2O)_2(PW_9O_{34})_2]$ POM, TBA-$Co_4(PW_9)_2$, supported on different carbon-based materials such as single-walled carbon nanotubes (SWCNT), graphene flakes (GF), nitrogen-doped carbon nanotubes (N-CNT), and nitrogen-doped few-layer graphene (N-FLG), as ORR electrocatalysts in alkaline medium (0.1 M KOH). The electrocatalysts had onset potentials ranging from 0.77 to 0.9 V vs RHE, Tafel slopes ranging from 68 to 96 mV/dec, and electron exchange numbers ranging from 2.7 to 4. POM@N-CNT is shown to have an activity that surpasses the state-of-the-art Pt/C electrocatalyst. Additionally, the electrocatalysts presented a cyclic stability similar to that of commercial Pt/C and much higher methanol stability. Lastly, all composite materials performed better than their isolated supports, with $Co_4(PW9)_2$@N-CNT catalytic activity outperforming Pt/C (Fernandes et al., 2018a).

Song et al. confined a cobalt-centered POM, $[CoPW_{12}]^{6-}$, in the void space of the ZIF-8 MOF and later prepared a Co-POM@MOF-derived N-doped porous carbon composite via pyrolysis treatment to test its performance towards ORR in alkaline electrolyte (0.1 M KOH). The material presented a half-wave potential of 0.84 V vs RHE, a Tafel slope of 63 mV/dec, an electron transfer number of 4.1, and good stability properties (retains activity after 1,000 cycles) (Song et al., 2022).

Rousseau et al. synthesized a noble metal-free Co/Zn POM complex supported on Vulcan carbon XC-72 (Co_7Zn/C) and tested its activity towards the ORR in alkaline medium (0.1 M KOH). The material had an electron exchange number between 3.6 and 4, signifying its selectivity towards the 4e-reduction path. It presented activity comparable to commercial Pt/C, showing higher stability after 11 h at ORR conditions and much higher

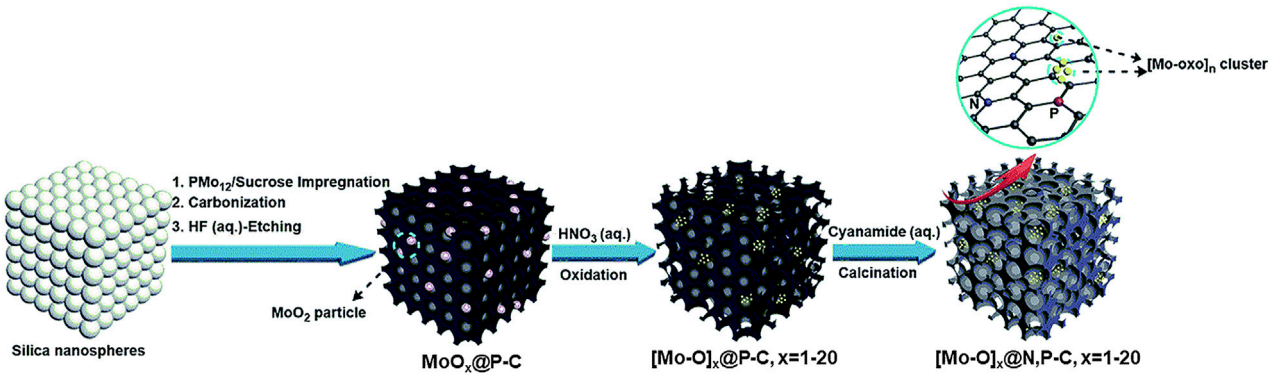

FIGURE 7
Fabrication route of composites with high ORR activity. The composites were based on Keggin-type polyoxomolybdate $H_3PMo_{12}O_{40}$ (PMo_{12}) as a precursor to deposit $[Mo\text{-}oxo]_n$ (n = 1–20) cluster on mesoporous carbon (adapted from Liu et al., 2020).

methanol crossover tolerance. The material also showed good activity in neutral medium, compared to commercial Pt/C, but with higher stability (Rousseau et al., 2015).

Liu et al. disclosed a top-down approach to deposit POM-like metal oxo clusters by using the solution-stable Keggin-type polyoxomolybdate $H_3PMo_{12}O_{40}$ (PMo_{12}) as a precursor to deposit $[Mo\text{-}oxo]_n$ (n = 1–20) cluster on mesoporous carbon, synthesizing three different composites, whose synthesis processes are presented schematically in Figure 7. Their electrocatalytic activity for the ORR in alkaline electrolyte (0.1 M KOH) was tested. The composites had an onset potential in the range of 0.75–0.93 V vs RHE, Tafel slopes in the range of 44.2–109 mV/dec, and the first two composites favored the $2e^-$ reaction path, while the third composite favored the $4e^-$ reaction pathway. Additionally, the third composite demonstrated an activation behavior during chronoamperometric tests to determine its stability, showing an increase in current after 20 h and no further changes after a total period of 50 h, and demonstrated high methanol crossover tolerance, outperforming the commercial Pt/C electrocatalyst both in activity and stability. The activity was attributed to good dispersion of the $[Mo\text{-}oxo]_n$ clusters, high surface area, and N-doping of the carbon substrate (Liu et al., 2019).

Zhao et al. combined a lacunary Keggin POM cluster, $[PW_{11}O_{39}]^{7-}$, with 3D ordered microporous graphitic carbon nitride (3DOM g-C_3N_4) to generate an electrocatalyst with favorable selectivity for the 2 electrons ORR pathway, testing it electrochemically on neutral medium and via light-driven reaction. The synthesized composite showed activity for the light-driven production of H_2O_2, with a production rate of 2.4 μmol/h, and electrochemical tests demonstrated that it had an electron transfer number around 2.3, indicating its selectivity towards the intended ORR mechanism (Zhao et al., 2017).

Table 8 summarizes the ORR performance parameters for the discussed POM-based electrocatalysts.

4 Hydrogen evolution reaction (HER)

The HER is the cathodic reaction occurring in water electrolysis. The HER kinetics differ according to pH: at acidic conditions, it has higher kinetics, while in alkaline and neutral conditions, it has slower kinetics (around 2 to 3 orders of magnitude slower), constituting a disadvantage for alkaline water electrolysis technologies. The reason lies in the inherent HER mechanism, which differs from acid to alkaline/neutral conditions (Chatenet et al., 2022; Pratama et al., 2023), as shown in Figure 8.

Interestingly, the choice of alkaline electrolytes relative to acidic ones for water electrolysis comes down to the high cost of noble metal electrode materials and equipment limitations, since acid conditions cause equipment corrosion, lowering its lifetime (Zeb et al., 2023). Additionally, the reaction products, akin to OER and ORR, change slightly depending on the pH, as can be seen in equations 2.9 and 2.10 for acidic and neutral/alkaline medium, respectively:

$$2H^+ + 2e^- \rightarrow H_2 \quad (2.9)$$

$$2H_2O + 2e^- \rightarrow H_2 + 2OH^- \quad (2.10)$$

Furthermore, the inherent HER mechanism only involves two electron transfers, meaning it has fewer thermodynamic demands (resulting in a lower activation barrier) (Horn et al., 2021; Chatenet et al., 2022). Thus, lower overpotentials are generally needed to reach reasonable reaction rates compared to the OER.

Regarding the state-of-the-art electrocatalysts, the one with the highest performance is, akin to ORR, commercial Pt/C, which shows the ideal adsorption energies (not too high and not too low), and thus presents high performance for the HER (Chatenet et al., 2022; Zeb et al., 2023). However, given the noble nature of Pt, it is an expensive and scarce material, and this limits the potential for large-scale applications due to cost-related reasons, meaning that much interest and investment has been applied in the discovery of stable, low-cost, and high-performance alternative electrocatalysts, generally based on early transition metals such as Ni, Mn, Co, and Cu.

4.1 Transition metal oxides for HER

Mukherjee et al. designed a reduced graphene oxide embedded nickel ferrite oxide (rGO-$NiFe_2O_4$) and tested its electrocatalytic activity for the HER in acidic medium (0.5 M H_2SO_4). The observed

TABLE 8 ORR electrocatalysts and their key performance indicators: transition metal POMs.

Electrocatalyst	Onset potential (V vs RHE)	Tafel slope (mV/dec)	Number of exchanged e^-	Electrolyte	Source
Cu_6Ni_7/TTF-F	0.91	-	3.92–3.94	0.1 M KOH	Zhang S. et al. (2017)
NiP_4Mo_6	-	98.1	3.86–3.88	0.1 M KOH	Zheng et al. (2021)
S-NiP_4Mo_6	-	106	2.02–2.08	0.1 M KOH	Zheng et al. (2021)
Pd_8Ni_2/rGO-POM	0.83	59.8	3.9	0.1 M KOH	Sanji et al. (2021)
$Co_4(PW_9)_2$@N-CNT	0.90	92	4	0.1 M KOH	Fernandes et al. (2018a)
$Co_4(PW_9)_2$@SWCNT	0.77	68	3.9	0.1 M KOH	Fernandes et al. (2018a)
$Co_4(PW_9)_2$@GF	0.89	71	2.7	0.1 M KOH	Fernandes et al. (2018a)
$Co_4(PW_9)_2$@N-FLG	0.89	63	3.6	0.1 M KOH	Fernandes et al. (2018a)
Co-W-NC	-	63	4.1	0.1 M KOH	Song et al. (2022)
Co-Zn/C	-	-	3.6–4	0.1 M KOH	Rousseau et al. (2015)
MoO_x@P-C	0.75	109	2	0.1 M KOH	Liu et al. (2020)
$[Mo\text{-}O]_x$@P-C, X = 1–20	0.88	68.1	2	0.1 M KOH	Liu et al. (2020)
$[Mo\text{-}O]_x$@N,P-C, X = 1–20	0.93	44.2	3.8–3.9	0.1 M KOH	Liu et al. (2020)
3DOM g-C_3N_4	-	-	2.3	0.1 M PBS[a]	Zhao et al. (2017)

a) PBS, phosphate buffer solution.

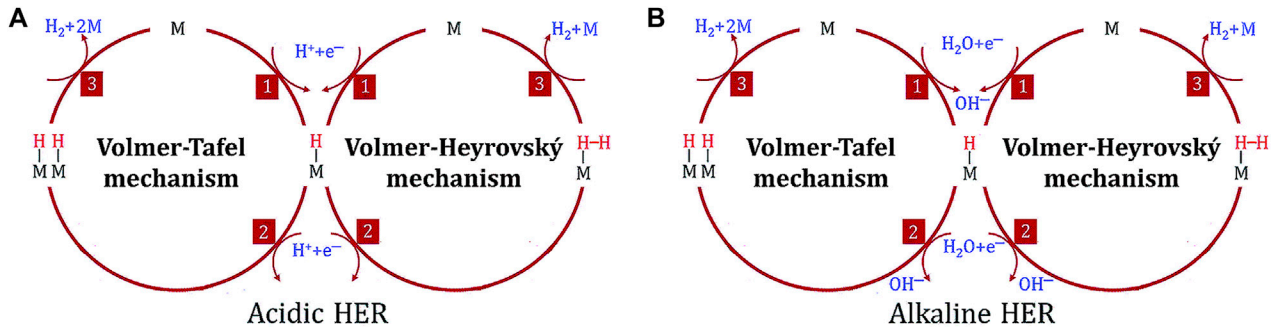

FIGURE 8
HER mechanisms in acidic **(A)** and alkaline **(B)** media (Gusmão et al., 2022).

onset overpotential and the necessary overpotential to achieve current densities of 10, 30, and 100 mA/cm^2 were 5, 42, 87, and 158 mV, respectively. Additionally, the obtained Tafel slope was 58 mV/dec. The electrocatalyst also presented great stability, with virtually no change in the cathodic current after 5,000 cycles and a stable current after 12 h of operation at HER conditions. The activity was attributed to the strong chemical-electronic coupling between rGO and $NiFe_2O_4$, the formation of non-agglomerated small nanoparticles, and the creation of oxygen vacancies in the electrocatalyst structure (Mukherjee et al., 2018), Chu et al. prepared and tested a hybrid Ni/NiO@C/GR-t-w (derived from the carbonization of Ni-MOF-74 and graphene oxide composites at different temperatures (t) and with different graphene oxide contents (w)) for the HER reaction in acid electrolyte (0.5 M H_2SO_4). The best-performing sample, Ni/NiO@C/GR-900-8, presented an onset potential of −34.7 mV vs RHE and an overpotential of 108 mV to reach 10 mA/cm^2, a Tafel slope of 44 mV/dec, and good stability properties, with no observed relevant change after 24 h of operation at 10 mA/cm^2 and after 1,000 HER cycles. The performance was attributed to the synergistic interactions at the Ni/NiO interface and the high surface area due to graphene incorporation (Chu et al., 2018).

Zeng et al. synthesized a series of NiMnO oxides with differing structures by adjusting the crystallization process via the addition of polyethylene glycol (PEG) in varying quantities and tester their properties towards the HER in alkaline medium (1 M KOH). The

best-performing oxide was NMO-PEG-3g, which presented an onset potential of −36.3 mV vs RHE and an overpotential of 140 and 256 mV to reach 10 and 100 mA/cm^2, respectively. Additionally, it presented a Tafel slope of 94 mV/dec, great stability properties with stable current after 24 h of HER, and activation with increased activity after 2,000 cycles. The enhanced performance was attributed to the petal-like scales in the structure, which increased surface area and thus exposed more active sites (Zeng et al., 2020).

Huang et al. produced a nanosized spinel Co-Mn oxide strongly coupled with ultrathin $Ti_3C_2T_x$ Mxene nanosheets ($MnCo_2O_4$/$Ti_3C_2T_x$) with different oxide loadings and tested its electrocatalytic potential toward the HER in acidic medium (0.5 M H_2SO_4). The best-performing sample had 50% oxide content, presented an onset overpotential of 51 mV, an overpotential to reach 10 mA/cm^2 of 177 mV, and a Tafel slope of 79 mV/dec, along with good stability and cyclic properties (nearly unchanged current after 16 h of operation and after 2,000 cycles). The activity was attributed to high electric conductivity and electronic structure optimization due to the incorporation of Mxene nanosheets, thus enhancing the intrinsic catalytic activity and higher surface area with more exposed active sites (Huang et al., 2022).

Wu Y. et al. reported the synthesis of octahedral cobalt oxide particles via a hydrothermal method and tested its capacities towards catalyzing the HER in basic medium (1 M KOH). The material presented an overpotential of 112 mV to achieve 20 mA/cm^2, and a Tafel slope of 94 mV/dec. It also had good cyclic and stability properties, with little observed difference after 2,000 cycles and after 20 h of operation. The activity was attributed to a higher surface area, which exposes more active sites (Wu Y. et al., 2020).

Flores-Lasluisa et al. studied the Cu-doping of Co spinel oxides supported on high porosity activated carbon and their activity for the HER electrocatalysis in alkaline medium (0.1 M KOH). The obtained results indicate that the best-performing sample, AC-CuCo20, presented a Tafel slope of 300 mV/dec and −14.6 mA/cm^2 for 400 mV of overpotential. The higher activity was attributed to better particle agglomeration control and higher electrical conductivity caused by the supporting activated carbon, substitution by Cu atoms at the octahedral position, and a higher number of oxygen vacancies and Co^{3+} sites, creating synergistic effects that enhanced catalytic activity (Flores-Lasluisa et al., 2019).

Muralikrishna et al. disclosed the production of graphene oxide and Cu hybrid (GO-Cu^{2+}) by controlling pH and Cu^{2+} concentrations during synthesis. They tested their ability to electrocatalyze the HER in an acidic medium (0.1M H_2SO_4). The results indicated that the optimal synthesis was done at neutral pH and with a concentration of 30 mM of Cu^{2+}. The hybrids had Tafel slopes around 120 mV/dec, along with moderate cyclic properties, with a brief reduction in current after 100 cycles (Muralikrishna et al., 2015).

Katubi et al. evaluated the performance of a hybrid nanocomposite comprising mixed metal oxides (Cu and W) and reduced graphene oxide (WO_3/CuO/rGO nanohybrid) towards HER in alkaline medium (1 M KOH). The composite presented an overpotential of 400 mV to achieve 200 mA/cm^2 and a Tafel slope of 44 mV/dec, along with good stability properties showing only a slight reduction in current after 12 h of operation, outperforming the unsupported and mono-metallic oxide counterparts. The verified activity was attributed to the high conductivity of rGO, higher number of exposed catalytic sites, and the synergistic interactions between the WO_3 and CuO nanoparticles (Katubi et al., 2023).

Table 9 condenses the performance indicators for the discussed oxide-based HER electrocatalysts.

4.2 Transition metal alloys for HER

Zhang et al. designed porous nickel-supported nanostructured Ni-Co electrodes with different morphologies that depended on the electrodeposition current and tested their activities towards the HER in alkaline electrolyte (1 M KOH). The results demonstrated that the best-performing morphology were the Ni-Co nanocones, which presented an onset potential of −14 mV vs RHE, an overpotential of 86.7 mV to achieve 10 mA/cm^2, and a Tafel slope of 69.8 mV/dec. Additionally, catalyst morphology was unchanged, and the overpotential to reach 10 mA/cm^2 only increased slightly after 10 h of operation at HER conditions. Finally, the activity was attributed to the synergism between the catalytic properties of Ni and Co, and the hierarchical morphology and sharp edges structure (Zhang et al., 2019).

Cao et al. fabricated radially aligned NiMo alloy microtubes on nickel foam (NiMo MT/NF) and verified its performance towards the HER in basic conditions (1 M KOH). The electrocatalyst

TABLE 9 HER electrocatalysts and their key performance indicators: transition metal oxides.

Electrocatalyst	η_{10} (mV)	Tafel slope (mV/dec)	Electrolyte	Source
rGO-$NiFe_2O_4$	42	58	0.5 M H_2SO_4	Mukherjee et al. (2018)
Ni/NiO@C/GR-900–8	108	44	0.5 M H_2SO_4	Chu et al. (2018)
NMO-PEG-3g	140	94	1 M KOH	Zeng et al. (2020)
$MnCo_2O_4/Ti_3C_2T_x$	177	79	0.5 M H_2SO_4	Huang et al. (2022)
Octahedral CoO_x particles	112@20 mA/cm^2	94	1 M KOH	Wu Y. et al. (2020)
AC-CuCO20	-	300	0.1 M KOH	Flores-Lasluisa et al. (2019)
GO-Cu^{2+}	-	120	0.1 M H_2SO_4	Muralikrishna et al. (2015)
WO_3/CuO/rGO nanohybrid	400@200 mA/cm^2	44	1 M KOH	Katubi et al. (2023)

presented an overpotential of 119 mV to reach 10 mA/cm^2 and a Tafel slope of 119 mV/dec. Additionally, the material shows good cyclic and stability properties, since a negligible current density is lost after 1,000 cycles, and it can retain its activity for at least 10 h. The verified performance is attributed to a higher number of active sites and facilitated electron transport because of the unique tubular structure and low boundary resistance (Cao et al., 2019).

Liu et al. synthesized Ni-Mn-P electrocatalysts via electrochemical deposition method and tested their abilities towards HER catalysis in a basic electrolyte (1 M KOH). The results demonstrated that the best sample presented an overpotential of 113 mV to achieve 10 mA/cm^2 and a 74 mV/dec Tafel slope. Additionally, good stability properties were verified since the structural integrity was maintained after 20 h of HER operation (at 10 mA/cm^2 and 60 mA/cm^2), and only a slight current drop was observed. The activity was attributed to Mn doping, which promoted the formation of a coral structure, and the synergistic effects between Ni, Mn, and P (Liu et al., 2021).

Ge et al. used Mn metal as a dopant to enhance the HER activity of urchin-like CoP electrocatalysts at alkaline and acidic media (1 M KOH and 0.5 M H_2SO_4). The results demonstrated that the best performance in both media was attained by the sample with 15 wt% Mn. Accordingly, the overpotentials needed to reach 10 mA/cm^2 were 100 and 65 mV, and Tafel slopes were 53 and 32 mV/dec, respectively, in alkaline and acid conditions, thus performing closely to benchmark Pt/C electrocatalyst and outperforming pristine CoP. Additionally, after 20 h of operation, the electrocatalyst showed a very small increase in overpotential (2.4 mV and 1.1 mV for alkaline and acid media, respectively) at 10 mA/cm^2 and no morphological changes, thus demonstrating good stability properties. The observed activity was attributed to a reduction in the hydrogen adsorption energy with the Mn doping, which enhanced the HER rate (Ge et al., 2018).

Wang H. et al. proposed preparing a nitrogen-doped porous carbon-supported cobalt material with a high graphitization degree and different dispersant content as a HER electrocatalyst in alkaline medium (1 M KOH). The best-performing sample, Co@NPC-F4, exhibited an overpotential of 259 mV to achieve 10 mA/cm^2 and a Tafel slope of 99 mV/dec. It also showed good stability properties, retaining 83% of current after 6 h of operation. The performance was attributed to the high surface area of the NPC and the optimization of the porous bundle structure during synthesis (Wang H. et al., 2019).

Guan et al. prepared Co-Ni alloys supported on N-doped carbon nanofibers via *in-situ* growth and tested their activity towards the HER in basic medium (1 M KOH). The material presented an 86 mV overpotential to reach 10 mA/cm^2 and a Tafel slope of 152.3 mV/dec, alongside good cyclic and stability properties, with almost no change in activity after 1,000 cycles and 25 h of operation, respectively, performing closely to the state-of-the-art Pt/C electrocatalyst. The enhanced activity is related to more useable active sites due to the N-doped carbon nanofibers' 3D structure, the NiCo alloy's synergistic effects, and the presence of smaller and more uniform alloy nanoparticles (Guan et al., 2021).

Butt et al. deposited a layer of metallic Cu on thermally synthesized CuO nanowires via a dielectric barrier discharge method and tested its performance towards the HER in 0.1 M K_2SO_4 electrolyte. The best-performing sample, Cu500 (indicating that the CuO synthesis temperature was 500°C), presented an overpotential of 210 mV to achieve 10 mA/cm^2, a Tafel slope of 178 mV/dec, and an exchange current density of 0.6 mA/cm^2, along with good stability properties after almost 4 h of operation. The performance was attributed to the presence of the metallic Cu nanowires alongside the CuO nanowires (Butt et al., 2021).

Shen et al. produced a series of Ni-Cu alloy nanoparticles encapsulated into graphitic shells with different shell thicknesses and tested their performances toward HER electrocatalysis in different pH values (0, 7, and 14). The catalysts showed, in general, better performance on acidic media, and the best-performing sample (NiCo@C-1) presented an overpotential of 48 mV to achieve 10 mA/cm^2 and a Tafel slope of 63.2 mV/dec under these conditions. Furthermore, accelerated durability tests demonstrated good cyclic properties, with virtually negligible differences after 2,000 HER cycles, and chronoamperometric tests showed good stability properties, with a current retention of around 63% and no structural changes. The performance was much better than the pristine NiCu alloy and closely resembled that of the benchmark Pt/C electrocatalyst. This was attributed to the interactions between the alloy and the carbon shell, which affected the electronic structure and adjusted the hydrogen adsorption energy to enhance activity (Shen et al., 2017).

Table 10 summarizes the performance indicators for the considered Alloy-based HER electrocatalysts.

TABLE 10 HER electrocatalysts and their key performance indicators: transition metal alloys.

Electrocatalyst	η_{10} (mV)	Tafel slope (mV/dec)	Electrolyte	Source
Ni-Co nanocones	86.7	69.8	1 M KOH	Zhang et al. (2019)
NiMo MT/NF	119	119	1 M KOH	Cao et al. (2019)
Ni-Mn-P	113	74	1 M KOH	Liu et al. (2021)
15Mn-CoP	100	53	1 M KOH	Ge et al. (2018)
15Mn-CoP	65	32	0.1 M H_2SO_4	Ge et al. (2018)
Co@NPC-F4	259	99	1 M KOH	Wang H. et al. (2019)
Co-Ni/NCNFs	86	152.3	1 M KOH	Guan et al. (2021)
Cu500	210	178	0.1 M K_2SO_4	Butt et al. (2021)
NiCO@C-1	48	63.2	acidic electrolyte	Shen et al. (2017)

4.3 Transition MOFs for HER

Dao et al. developed graphene-doped Ni-MOFs via the solvothermal method with different graphene contents and tested their HER electrocatalytic properties in alkaline electrolyte (1 M KOH). The best-performing sample, MOF(Ni)-GR(4%), needed an overpotential of 268 mV to reach 10 mA/cm^2 and had a Tafel slope of 108 mV/dec. Furthermore, chronopotentiometric tests indicated that the MOF catalyst had better stability than the benchmark Pt/C electrocatalyst, and the activity was attributed to a higher surface area, which contributed to exposing more active sites and to the better electronic conductivity of graphene, which facilitated charge transfer and thus enhanced HER catalysis (Dao et al., 2022).

Wu et al. designed Ni (II) based MOFs, $[Ni(bib)_2(SO_4)]_n$; bib = 1,4-bis(1-imidazoly)benzene via hydrothermal method and calcination at different temperatures. These MOFs were tested for HER electrocatalysis in acid medium (0.5 M H_2SO_4). The best-performing sample, Ni-MOF-800, presented an overpotential of 356 mV to achieve 10 mA/cm^2 and a Tafel slope of 127.3 mV/dec. The catalyst stability was also tested, and it was verified that after 2,000 cycles, the HER activity was almost unchanged, and the morphology was completely intact. The performance was attributed to the enhanced conductive properties, which increased charge transfer kinetics and thus incremented HER rate (Wu et al., 2022).

Duan et al. prepared peony petal-like CoMnP nanoparticles supported on nickel foam via solvothermal growth route on CoMn-MOF-71 nanosheets and tested its HER electrocatalytic properties in acid and basic media (0.5 M H_2SO_4 and 1 M NaOH). The sample presented overpotentials of 66.6 and 53.9 mV to reach 10 mA/cm^2 and Tafel slopes of 38.8 and 63 mV/dec for acid and alkaline medium, respectively, which had close performance to Pt/C benchmark electrocatalyst. Additionally, in acid conditions, the current retention after 12 h only shows a small decrease, and the performance after 1,000 cycles slightly increased, while no morphological changes were observed after 1,500 cycles. The same results were observed for alkaline conditions. The enhanced performance was attributed to higher specific surface area, exposing more active sites and facilitating electrolyte diffusion, and to synergistic effects between Mn and Co that can modulate the electronic structure to optimize the adsorption energies and enhance the HER process (Duan et al., 2022).

Liu et al. described a phosphorization process to create carbon fiber paper-supported CoP species in a Co-MOF, thus originating a CoP/Co-MOF/CF hybrid, and tested its catalytic activity toward the HER in acidic (0.5 M H_2SO_4), neutral (pH 7 PBS buffer solution) and alkaline (1 M KOH) media. The overpotential needed to achieve a 10 mA/cm^2 was 27, 34, and 49 mV, and the Tafel slope was 43, 56, and 63 mV/dec, for acidic, basic, and neutral conditions, respectively, performing closely to the benchmark Pt/C electrocatalyst. Additionally, the material demonstrated good cyclic and stability properties in acid, neutral, and alkaline conditions, with negligible differences in performance after 2,000 cycles. It showed a slight morphology degradation in alkaline medium but remained intact in the other testing conditions. The performance was attributed to the electronic interactions of CoP and Co-MOF, which modulated H_2O and H adsorption energies to more optimal values, thus enhancing HER, and to the MOF porous network, which exposes more active sites and facilitates gas release (Liu et al., 2019).

Pan et al. reported a method to develop a Co,N-doped graphitic carbon electrocatalyst (Co-MOF-800) based on a flower-like MOF ($\{[Co(BIPA)(5\text{-}OH\text{-}bdc)](DMF)\}_n$; BIPA = bis(4-(1H-imidazole-1-yl) phenyl)amine and 5-OH-bdc = deprotonated 5-hydroxyisophthalic acid) and tested its HER electrocatalysis properties in acidic medium (0.5 M H_2SO_4). An onset potential of ca. −120 mV vs RHE, an overpotential of 193 mV to achieve 10 mA/cm^2, and a Tafel slope of 77.1 mV/dec were determined for those conditions, along with appreciable current retention after 20 h of operation and only a slight loss in performance after the elapsed time. The activity was attributed to synergistic interactions between Co and N, which optimized adsorption energies and modified the electronic structure of carbon, enhancing the HER rate (Pan et al., 2019).

Nivetha et al. synthesized a Meso-Cu-BTC MOF and tested its performance towards HER electrocatalysis in an alkaline electrolyte (1 M NaOH). The catalyst demonstrated an onset overpotential of 25 mV, an exchange current density of 6 mA/cm^2, and a Tafel slope of 33.4 mV/dec, but still underperformed the benchmark Pt/C electrocatalyst. After 1,000 cycles, there was no observable change in performance, confirming the good stability properties of the material. The observed activity was attributed to the highly porous network of the octahedral MOF, which enhanced electronic and ionic transfer, thus increasing the HER rate (Nivetha et al., 2020).

Zhang et al. disclosed the synthesis of three different porous MOFs based on different transition metals, Ni, Co, and Cu, and on H_3BTC (benzene-1,3,5-tricarboxylic acid), originating rhombic octahedral Cu-BTC, rod-shaped Co-BTC, and spherical Ni-BTC materials, which were tested towards HER electrocatalysis on acidic medium (0.5 M H_2SO_4). The materials presented an overpotential to reach 10 mA/cm^2 of 53, 123, and 270 mV and Tafel slopes of 62, 100, and 155 mV/dec for Ni-BTC, Co-BTC, and Cu-BTC, respectively, with Ni-BTC performing similarly to Pt/C state-of-the-art electrocatalyst. The MOFs demonstrated different stability properties, with Ni-BTC demonstrating no current retention drops and Co-BTC and Cu-BTC showing 60% and 72% current retention, although no structural or morphological changes were detected after the tests. The performance was attributed to structural features such as large surface area, porous and adjustable structure, and transition metal center regulation (Zhang et al., 2020).

Table 11 compiles the relevant HER performance parameters for the discussed MOF electrocatalysts.

4.4 Transition metal POMs for HER

Sun et al. prepared an electrocatalyst of Ni and Mo_2C nanoparticles painted with N-doped carbon layers (Ni/Mo_2C@NC) based on giant POM clusters of $((NH_4)_{42}[Mo_{132}O_{372}(CH_3COO)_{30}(H_2O)_{72}].{}_{10}CH_3COONH_4.300H_2O)$ (Mo_{132}) and tested its activity towards HER electrocatalysis in basic and acid media (1 M KOH and 0.5 M H_2SO_4). The material had an overpotential of 107 and 125 mV at 10 mA/cm^2 and a Tafel slope of 88 and 117 mV/dec, outperforming its monometallic counterparts and performing similarly to Pt/C benchmark electrocatalyst. The durability and stability properties were similar in acidic and alkaline conditions, with only a slight current drop after 48 h of operation and no structural or morphological changes after HER stability tests. The

TABLE 11 HER electrocatalysts and their key performance indicators: transition MOFs.

Electrocatalyst	η_{10} (mV)	Tafel slope (mV/dec)	Electrolyte	Source
MOF(Ni)-GR(4%)	268	108	1 M KOH	Dao et al. (2022)
Ni-MOF-800	356	127.3	0.5 M H_2SO_4	Wu et al. (2022)
CoMnP/NF	66.6	38.8	0.5 M H_2SO_4	Duan et al. (2022)
CoMnP/NF	53.9	63	1 M NaOH	Duan et al. (2022)
CoP/Co-MOF/CF	27	43	0.5 M H_2SO_4	Liu et al. (2019)
CoP/Co-MOF/CF	34	56	pH 7 PBS[a] buffer	Liu et al. (2019)
CoP/Co-MOF/CF	49	63	1 M KOH	Liu et al. (2019)
Co-MOF-800	193	77.1	0.5 M H_2SO_4	Pan et al. (2019)
Meso-Cu-BTC MOF	-	33.41	1 M NaOH	Nivetha et al. (2020)
rhombic octahedral Cu-BTC	53	62	0.5 M H_2SO_4	Zhang et al. (2020)
rod-shaped Co-BTC	123	100	0.5 M H_2SO_4	Zhang et al. (2020)
spherical Ni-BTC	270	155	0.5 M H_2SO_4	Zhang et al. (2020)

a) PBS, phosphate buffer solution.

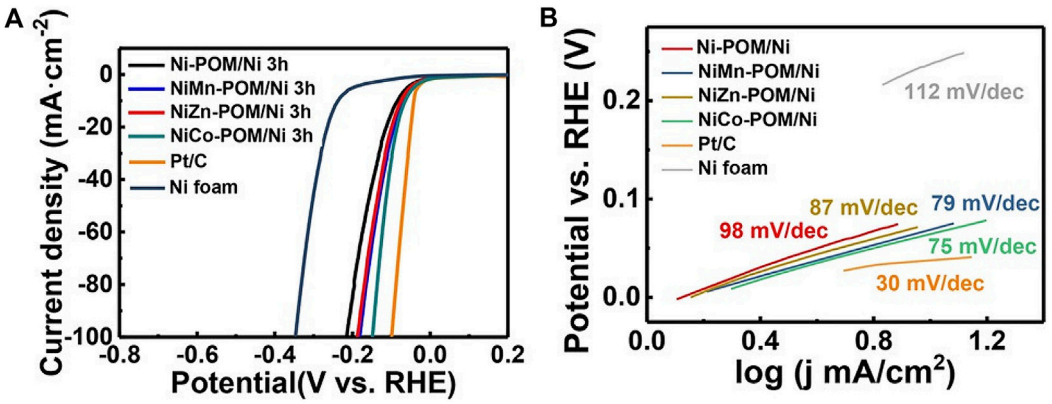

FIGURE 9
(A) Polarization curves of NiM-POM/Ni electrode, commercial Pt/C, and Ni foam in 1.0 m KOH at a scan rate of 5 mV/s. **(B)** Tafel plots of NiM-POM/Ni electrodes, Ni foam, and Pt/C (adapted from Jia et al., 2019).

performance was attributed to the improved electronic structure with nickel doping and the higher exposition of active sites due to the mesoporous structure (Sun et al., 2023).

Jia et al. reported the production of nickel foam-supported Dexter-Silverton-type bimetallic POMs NiM-POMs (M = Co, Zn, Mn) using Keggin POM clusters as building blocks and tested their catalytic activities towards HER in basic conditions (1 M KOH). The POMs HER polarization curves are presented in Figure 9. These materials exhibited overpotentials at 10 mA/cm^2 of 64, 68, 74, and 83 mV, and Tafel slopes of 75, 79, 87, and 98 mV/dec, respectively for NiCo-POM/Ni, NiMn-POM/Ni, NiZn-POM/Ni, and Ni-POM/Ni. The performance was correlated to the microcrystal size, with the range between 2–4 μm associated with the highest activity. The stability of NiCo-POM/Ni was also demonstrated, as no reasonable differences in performance or morphology were observed after 2,000 cycles. The good performance was attributed to the intrinsic reactivity of POM microcrystals with abundant active sites (Jia et al., 2019).

Zhang Z. et al. have designed Ni-modified PW_{12} clusters with 3D nanoflower structure grown on Ni foam (NF) and tested its electrocatalytic potential towards HER in alkaline medium (1 M KOH). The study demonstrated that the overpotential needed to reach 10 mA/cm^2 was 75 mV and that the Tafel slope was 86 mV/dec, slightly underperforming the benchmark Pt/C electrocatalyst. Additionally, there was practically no activity loss after 2,000 cycles, being kept for at least 30 h with no morphological or structural changes. The activity was attributed to the synergistic effect between Ni and W, the electric conductivity of the NF support, and the enhanced number of exposed active sites due to the unique micro-nanostructure (Zhang et al., 2022).

Zhang Z. et al. synthesized a two-fold interpenetrating POMOF compound, $[(Ni_3(bpp)_3{\cdot}(H_2O)_{11}(PW_9{}^{VI}W_3{}^{V}O_{40})]{\cdot}2H_2O$ (bpp = 3, 5′-bis(pyrid-4-yl)pyridine), and tested it for HER in basic electrolyte (1 M KOH). The produced electrocatalyst presented an overpotential of 74.6 mV to achieve 10 mA/cm^2 and a Tafel slope

of 111 mV/dec, slightly underperforming the benchmark Pt/C electrocatalyst, but demonstrating great stability properties due to no apparent decline in activity after 2,000 cycles and stable activity for more than 48 h. The activity was attributed to the synergistic effects between the enclosed POM and MOF complex and the highly exposed surface area (Zhang et al., 2023a).

Jawale et al. immobilized Ni-containing Dawson and sandwich-type POMs on the surface of carbon nanotubes and later tested their electrocatalytic properties towards HER in acid conditions (0.5 M H_2SO_4). It was verified that the Tafel slopes were in the 121–125 mV/dec range, but the catalysts still underperformed the Pt/C benchmark electrocatalyst. The enhanced performance was attributed to the number of Ni centers in the structure (a higher number of centers implied higher performance) and to the structure of the POM itself (the sandwich structure was able to contain a higher number of Ni centers) (Jawale et al., 2022).

Ahmad et al. immobilized a Mn sandwich POM, $Na_{10}[Mn_4(H_2O)_2(VW_9O_{34})_2].26H_2O$, on the surface of $CoSe_2$ nanobelts ($CoSe_2$-NB) and tested its catalytic activity towards HER in acidic medium (0.5 M H_2SO_4). The composite attained a 187 mV overpotential at 10 mA/cm^2 and a Tafel slope of 55 mV/dec, with no difference in performance or morphology after 2,000 cycles and no noticeable current drop after 24 h of operation. The performance was attributed to the 3D structural framework, high conductivity and surface area of the support, and the synergistic effects in the microenvironment induced by decorating sandwich-type POMs on the surface of CoS_2-NBs (Ahmad et al., 2020).

Xu et al. designed a cobalt and tungsten-based bimetallic electrocatalyst based on a bimetallic POM, $[Co_9(OH)_3(H_2O)_6(HPO_4)_2(PW_9O_{34})_3]^{16-}$ via a one-step calcination process, Co/WC@NC, and tested its properties toward HER electrocatalysis in acid and basic solutions (0.5 M H_2SO_4 and 1 M KOH). The results demonstrated that Co/WC@NC presented an overpotential of 129 and 142 mV to reach 10 mA/cm^2 and a Tafel slope of 93 and 91 mV/dec for acid and basic conditions, respectively, outperforming the catalyst's monometallic counterparts. Furthermore, the activity shows only a small decline after 2,000 cycles, with no significant decrease after 24 h of continuous operation in both solutions, and no morphological or structural changes. The activity was attributed to the synergistic interactions between the two metals, which regulate the electronic structure of the catalyst and enhance conductivity and activity, as well as the protective effect of the carbon layers, which prevents metal corrosion, and N-doping, contributing to a faster charge transfer (Xu et al., 2021).

Chen C. et al. disclosed the use of a POMOF-derived bi-transition metal carbide (Mo_xCo_xC) confined in uniform carbon polyhedrons synthesized via calcination after the formation of a POMOF-based on PMo_{12} Keggin POM and ZIF-67 MOF as an HER electrocatalyst in basic conditions (1 M KOH). Regarding the cathodic water splitting reaction, the material, PMo/ZIF-67-6-6N, needed an overpotential of 83 mV to deliver 10 mA/cm^2 and had a Tafel slope of 50 mV/dec. Additionally, there was a negligible change in activity after 1,000 cycles, and the performance remained stable for 22 h. The activity was attributed to the small particle size of the formed carbides, which exposed more active sites, to the N-doped carbon coating that stabilized the carbides, the synergistic effects between the metals and the support structure, and the porous structure itself (Chen C. et al., 2018).

Wang et al. reported the synthesis of 2D CoMo-POMOF nanopillar arrays on a conductive Ni foam substrate and its electrocatalytic activity in acid medium (0.5 M H_2SO_4). The results demonstrated that it needed an overpotential of 137 mV to attain 10 mA/cm^2 and that it had a Tafel slope of 59 mV/dec, slightly underperforming the state-of-the-art Pt/C electrocatalyst. Additionally, good stability was verified, since the performance was practically unchanged and the morphological and structural characteristics were well maintained after 2,000 cycles. The activity was attributed to the self-supported open construction of nanopillar arrays, optimized Gibbs free energy of hydrogen adsorption, and the 2D nanosheets of CoMo-POMOF (Wang et al., 2022).

Shen et al. studied the HER performance of a new XC-72 carbon black supported Lindqvist POM-based inorganic-organic compound with a porous intercalation structure, $[Cu_2(bimb)_2(ox)](W_6O_{19})\cdot 4H_2O$ [bimb = 1,3-bis(1-imidazoly) benzene, ox = oxalic acid] in acid conditions (0.5 M H_2SO_4). The material needed an overpotential of 146 mV to reach 10 mA/cm^2 and had a Tafel slope of 69 mV/dec, performing closely to benchmark Pt/C HER electrocatalyst. The performance was attributed to the higher electronic conductivity of the carbon black support, hexatungstate fragments originating from the Lindqvist structure that act as active sites, and the porous intercalation structure present in the material (Shen et al., 2019).

Zang et al. disclosed the synthesis of Anderson-type POM-modified Cu nanomaterials on TiO_2 nanotube array and tested their potential as HER electrocatalysts in acid medium (0.5 M H_2SO_4). The best composite material, $NiMo_6O_{24}$@Cu/TNA, presented a 215 mV overpotential to attain 10 mA/cm^2 and presented a Tafel slope of 89.2 mV. Furthermore, there was a negligible shift in performance after 500 cycles, and no apparent current decrease after 3 h of operation. The activity was attributed to the synergy between the utilized POMs and Cu to produce a dendrite morphology that exposed more active surface area and modified the local electrochemical environment of the active sites, enhancing the HER (Zang et al., 2019).

Fernandes et al. prepared a series of nanocomposites based on three different POMs supported on reduced oxidized graphene flakes, P_2W_{18}@rGF_ox, P_5W_{30}@rGF_ox, and P_8W_{48}@rGF_ox, and tested their HER electrocatalytic properties in acid medium (0.5 M H_2SO_4). The materials showed an overpotential for 10 mA/cm^2 of 35, 33, and 44 mV, and a Tafel slope of 37, 33, and 41, for P_2W_{18}@rGF_ox, P_5W_{30}@rGF_ox, and P_8W_{48}@rGF_ox, respectively, with performances that closely resembled that of benchmark Pt/C electrocatalyst. However, stability tests were only made for P_5W_{30}@rGF_ox and showed no significant changes after 1,000 cycles. The activity was attributed to the well-known POM property of undergoing reversible multi-electron reduction/oxidation without structural changes and the high electronic conductivity and porous network of the support, enhancing charge transfer rate and catalyst loading capabilities (Fernandes et al., 2018b).

Table 12 contains the HER key performance indicators for the analyzed POM-based electrocatalysts.

5 Bifunctional materials for OER/ORR

Wu et al. produced mesoporous NiO and $NiCo_2O_4$ using a hydrothermal template-free synthesis and tested them as

TABLE 12 HER electrocatalysts and their key performance indicators: transition metal POMs.

Electrocatalyst	η_{10} (mV)	Tafel slope (mV/dec)	Electrolyte	Source
Ni/Mo_2C@NC	107	88	1 M KOH	Sun et al. (2023)
Ni/Mo_2C@NC	125	117	0.5 M H_2SO_4	Sun et al. (2023)
NiCo-POM/Ni	64	75	1 M KOH	Jia et al. (2019)
NiMn-POM/Ni	68	79	1 M KOH	Jia et al. (2019)
NiZn-POM/Ni	74	87	1 M KOH	Jia et al. (2019)
Ni-POM/Ni	83	98	1 M KOH	Jia et al. (2019)
Ni-WO/NF	75	86	1 M KOH	Zhang et al. (2022a)
$Ni_3W_9^{VI}W_3^{V}$	74.6	111	1 M KOH	Zhang Z. et al. (2023a)
$Mn_4V/CoSe_2$	187	55	0.5 M H_2SO_4	Ahmad et al. (2020)
Co/WC@NC	129	93	0.5 M H_2SO_4	Xu et al. (2021)
Co/WC@NC	142	91	1 M KOH	Xu et al. (2021)
CoMo-POMOF nanopillar arrays	137	59	0.5 M H_2SO_4	Wang et al. (2022)
PMo/ZIF-67–6-6N	83	50	1 M KOH	Chen et al. (2018)
Cu_2W_6	146	69	0.5 M H_2SO_4	Shen et al. (2019)
$NiMo_6O_{24}$@Cu/TNA	215	89.2	0.5 M H_2SO_4	Zang et al. (2019)
P_2W_{18}@rGF_ox	35	37	0.5 M H_2SO_4	Fernandes et al. (2018b)
P_5W_{30}@rGF_ox	33	33	0.5 M H_2SO_4	Fernandes et al. (2018b)
P_8W_{48}@rGF_ox	44	41	0.5 M H_2SO_4	Fernandes et al. (2018b)

bifunctional catalysts for the OER/ORR reactions pair in alkaline medium (0.1 M KOH). Concerning the OER, $NiCo_2O_4$ showed a lower Tafel slope, indicating better kinetics towards this reaction. $NiCo_2O_4$ also showed a better performance towards the ORR, which is confirmed by a higher onset potential and higher number of exchanged electrons, demonstrating higher selectivity towards the $4e^-$ reduction pathway. This is further corroborated by the lower observed local yield of H_2O_2, 20% for NiO, against 5% for $NiCo_2O_4$. Additionally, $NiCo_2O_4$ showed good stability properties, with only ~50 mV potential loss during 50 h of operation. The exhibited performance was attributed to the higher number of surface hydroxyl adsorbates that can promote the $4e^-$ ORR path in $NiCo_2O_4$, as well as the synergistic effects of having a bimetallic Co and Ni oxide composition (Wu et al., 2023).

In a more innovative fashion, Sivakumar et al. tested three ternary Ni-Co-Mn oxides as bifunctional catalysts for OER/ORR in alkaline medium (0.1 M KOH), $NiCoMnO_4$, $Ni_{1.5}Co_{0.75}Mn_{0.75}O_4$ and $Ni_2Co_{0.5}Mn_{0.5}O_4$. They all presented good stability, and the best-performing material, $Ni_{1.5}Co_{0.75}Mn_{0.75}O_4$, showed similar behavior to IrO_2 for OER. Although its ORR activity was still far behind Pt/C, its bifunctional activity was higher than both IrO_2 and Pt/C (Sivakumar et al., 2019).

Xing et al. tested OER/ORR bifunctionality of two nanoparticulate manganese vanadium oxide deposited on a nitrogen-doped reduced graphene oxide in alkaline medium (0.1 M KOH). The samples differed in the total time they were subjected to a thermal treatment. The OER study showed that the composites had good stability under the reaction conditions and good electrocatalytic performance, as they could achieve a 10 mA/cm^2 current density at overpotentials of 440 and 420 mV. However, the materials had a Tafel slope of 286 and 271 mV/dec, indicating that there is still much room for improvement in terms of OER performance. For the ORR, both electrocatalysts demonstrated a $4e^-$ pathway and stability over at least a 4-h period, as well as superior activity when compared to the benchmark Pt/C electrocatalyst (Xing et al., 2018).

Belkessam et al. synthesized spinel structure Ni and Co mixed metal transition oxides by using a facile sol-gel method with different metal salt precursors, namely, their chlorides (Cl-NiCoO), sulfates (S-NiCoO), and nitrates (N-NiCoO), and tested their activity for OER and ORR in alkaline conditions (0.1M KOH). Regarding the OER, the best-performing electrocatalyst was S-NiCoO. This was linked to the presence of Ni^{3+} as the main oxidation state for Ni and to the presence of sulfide, which increased the number of active sites and the coordination of Ni/Co. Relative to the ORR, the results showed Cl-NiCoO had the highest activity, albeit its selectivity to the $2e^-$ pathway. These different activities were attributed to the different morphologies obtained for each sample and to the presence of the precursor anion, which could act as a doping element (Belkessam et al., 2020).

Wang et al. designed iron, nickel, and nitrogen-doped carbon nanofibers (Fe/Ni-N-CNFs) via an electrospinning technique and tested their activities for the OER/ORR pair in alkaline conditions (0.1 M KOH). The best-performing composite, with a 1:1 Fe to Ni ratio, performed better than the mono-metallic composites and compared itself to the benchmark Pt/C electrocatalyst,

exchanging an average of 3.97 electrons during the reduction process. This electrocatalyst also demonstrated the best OER performance, with the lowest Tafel slope and higher currents for the tested OER polarization region, and it was determined to have the best bifunctional characteristics towards those reactions. The electrocatalyst also demonstrated stability after 2,000 CV cycles, and its performance was attributed to the metal alloying synergistic interactions, N doping, structural defects, and the 3D porous cross-linked microstructure (Wang et al., 2017).

Abdelkader-Fernández et al. reported the synthesis of noble-metal-free dual N,S-doped MOF-74-derived nanostructured carbon-based materials, outlining the effects of the type of doping and the metal composition in the MOF-74 template in the OER and ORR performances in 0.1 M KOH. They found that, individually, N,S-dual-doping (mainly in the Co-based MOF-74) and the use of two metals (Ni and Co) in the MOF-74 template structure were able to enhance the OER activities, making them comparable to state-of-the-art IrO_2 and other similar reported materials. However, they demonstrated an adverse effect when used simultaneously. This was explained by the fact that the bimetallic dual-doped sample involves $Co_xNi_{1-x}S$ sulfide instead of CoS, present in the purely dual-doped sample and more active for OER, and that it does not show "active" core/shell nanostructures, unlike the purely bimetallic sample. For the ORR, the dual-doping strategy increased the exhibited performances, albeit in a more limited manner, while the metal composition showed no significant effect on performance (Abdelkader-Fernández et al., 2019).

Yusinova et al. performed the pyrolysis of a mixed metal Mn/Co MOF (TAL-42) to produce an electrocatalyst active towards ORR and OER in alkaline medium (0.1 M KOH). The best-performing composite material towards ORR, TAL-42-900, presented an activity comparable to Pt/C, and superior stability properties. TAL-42-900 also exhibited the lowest overpotentials and Tafel slopes for the OER, performing better than the RuO_2 benchmark electrocatalyst and being classified as the best bifunctional material amongst the tested electrocatalysts. The activity was attributed to the mesoporous structure, large surface area, and the presence of M-N_x species (M = Mn,Co) (Yusibova et al., 2023).

Wahab et al. reported the use of Mn-MOF@rGO nanocomposite as a bifunctional catalyst for both ORR and OER in alkaline conditions (0.1 M KOH and 1 M KOH, respectively). Regarding the ORR, the best-performing sample, MnBDC@75%rGO, compared itself to the benchmark Pt/C electrocatalyst and presented good methanol crossover resistance. Relatively to the OER, the electrocatalyst demonstrated better activity than Pt/C, with a 610 mV overpotential to achieve 10 mA/cm^2 and a Tafel slope of 83 mV/dec The good performance was attributed to the synergistic effects between the mesoporous 3D framework and the transition metal-organic composition (Wahab et al., 2020).

Zhang M.-C. et al. synthesized a bimetallic CuCo MOF to work as a bifunctional electrocatalyst for OER/ORR in alkaline (0.1 M KOH) and neutral media. Regarding the alkaline OER, the material needed a 400 mV overpotential to achieve 10 mA/cm^2 and had a Tafel slope of 122.3 mV/dec with good current retention properties. Regarding the neutral OER, the overpotential needed to reach 10 mA/cm^2 was 550 mV, and the obtained Tafel slope was 276.1 mV/dec, also with good retention properties. In both cases, the bimetallic MOF had better performance than the monometallic Cu MOF. The ORR performance followed the same trend: the bimetallic MOF performed better than the monometallic Cu MOF, and the performance of both materials was higher in alkaline conditions, with the bimetallic MOF being ultimately considered the best bifunctional material. The higher activity was attributed to a higher exposition of active sites and the synergistic effect of the bimetallic active sites, which increased charge transfer efficiency at the catalyst electrode/electrolyte interface (Zhang et al., 2023c).

Lu et al. reported the synthesis of metallic Co nanoparticles embedded in N-doped porous carbon layers (Co@NPC-T, T = 800, 900, or 1,000°C), using macroscale Co-MOF crystals as a precursor, and its use as a bifunctional electrocatalyst for ORR and OER in alkaline medium (0.1 M KOH). For the OER, the best-performing material, Co@NPC-900, needed 380 mV of overpotential to achieve 10 mA/cm^2 and presented good stability properties. Regarding the ORR, the activity was comparable to that of benchmark Pt/C with higher stability properties, and it was determined that Co@NPC-900 and Co@NPC-1,000 have similar bifunctional characteristics that are superior to those of Co@NPC-800. The verified performance was attributed to the improved electron transfer due to the graphitic carbon structure and to the synergistic effects between the metal and the graphitic carbon structure (Lu et al., 2017).

Marques et al. assembled sandwich-type Dawson family POMs anchored in N-doped multi-walled carbon nanotubes (MWCNT_N6) and tested their electrocatalytic properties towards OER and ORR in alkaline medium (0.1 M KOH). Regarding the OER, the three POMS@MWCNT_N6 (Ni_4, Fe_4, and Ni_2Fe_2) composites presented overpotentials of 580, 460, and 360 mV to achieve 10 mA/cm^2 and Tafel slopes of 102, 54, and 45 mV/dec for Fe_4@MWCNT_N6, Ni_4@MWCNT_N6, and Ni_2Fe_2@MWCNT_N6, respectively. Furthermore, tests at 500 mV of overpotential for 12 h showed that Fe_4 and Ni_4 retained 80% and 87% of their current and Fe_2Ni_2 retained 64%, indicating that the bimetallic Fe-Ni composite had the worst stability properties, even though it was the best-performing material. Relative to the ORR, the results indicate that an onset potential of ~0.8 V vs RHE was obtained for all materials, and Tafel slopes of 35.4, 34.7, and 37.9 mV/dec were obtained for Fe_4, Ni_4, and Fe_2Ni_2, respectively. Lastly, the number of transferred electrons is around 3, thus suggesting a mixed regime between the 4 and 2 electrons pathway, and good stability for the Fe_4 and Ni_2Fe_2 (84% and 80% of current retention after 12 h) was observed at ORR conditions (Marques et al., 2022).

Limani et al. prepared a series of Co-POMs anchored on doped carbon materials (MWCNT_N8_Co4, GF_N8_Co4, GF_ND8_Co4, and GF_NS8_Co4) and tested their performance for ORR and OER at alkaline conditions (0.1 M KOH). The ORR results demonstrated that the best-performing material (MWCNT_N8_Co4) had a performance comparable to that of benchmark Pt/C and good stability properties, along with high methanol crossover tolerance, indicating its durability. Relative to the OER results, the catalysts demonstrated activities that very closely resembled those of benchmark IrO_2 and RuO_2 electrocatalysts, with the best-performing material, GF_N8_Co4, outperforming IrO_2 and showing relatively good stability after almost 10 h of operation. No metric was calculated to determine the best bifunctional

TABLE 13 MOF and POM(-derived) bifunctional OER/ORR electrocatalysts.

Electrocatalyst	OER η_{10} (mV)	OER Tafel slope (mV/dec)	ORR Tafel slope (mV/dec)	ΔE^b (V)	Electrolyte	Source
$NiCo_2O_4$	340	50	-	-	0.1 M KOH	Wu et al. (2023)
NiO	380	56	-	-	0.1 M KOH	Wu et al. (2023)
$Ni_{1.5}Co_{0.75}Mn_{0.75}O_4$	570	68	-	0.79	0.1 M KOH	Sivakumar et al. (2019)
MnVOx@N-rGO–440	440	286	66.6	-	0.1 M KOH	Xing et al. (2018)
$MnVO_x$@N-rGO–900	420	271	130.9	0.85	0.1 M KOH	Xing et al. (2018)
N-NiCoO	-	-	-	-	0.1 M KOH	Belkessam et al. (2020)
S-NiCoO	340	-	-	-	0.1 M KOH	Belkessam et al. (2020)
Cl-NiCoO	-	-	-	-	0.1 M KOH	Belkessam et al. (2020)
Fe/Ni-N-CNFs	372	106.1	61.2	0.80	0.1 M KOH	Wang et al. (2017)
TAL-42–900	410	71	45	0.80	0.1 M KOH	Yusibova et al. (2023)
MnBDC@75%rGO	610	83	93.5	-	1 M KOH	Wahab et al. (2020)
CuCo-HITP	400	122.3	96.4	0.94	0.1 M KOH	Zhang M.-C. et al., 2023
CuCo-HITP	550	276.1	319.3	1.41	0.1 M PBS[a]	Zhang M.-C. et al., 2023
Co@NPC-900	380	-	-	0.85	0.1 M KOH	Lu et al. (2017)
Ni_4@MWCNT_N6	580@0.1 mA/cm^2	102	34.7	-	0.1 M KOH	Marques et al. (2022)
Fe_4@MWCNT_N6	460@0.1 mA/cm^2	54	35.4	-	0.1 M KOH	Marques et al. (2022)
Ni_2Fe_2@MWCNT_N6	360@0.1 mA/cm^2	45	37.9	-	0.1 M KOH	Marques et al. (2022)
MWCNT_N8_Co4	400	55	41	-	0.1 M KOH	Limani et al. (2022)
GF_N8_Co4	340	67	50	-	0.1 M KOH	Limani et al. (2022)
GF_ND8_Co4	490	68	90	-	0.1 M KOH	Limani et al. (2022)
GF_NS8_Co4	460	62	40	-	0.1 M KOH	Limani et al. (2022)

a) PBS, phosphate buffer solution.
b) ΔE, means the difference between the ORR, half-wave potential and the OER, potential to attain 10 mA/cm^2. Lower values indicate a better material in terms of bifunctionality. The ORR, potential to achieve 3 mA/cm^2 may be used instead of the half-wave potential.

electrocatalyst, but all the tested materials presented bifunctionality towards those two reactions (Limani et al., 2022).

Table 13 groups the aforementioned bifunctional OER/ORR electrocatalysts and their performance parameters.

6 Bifunctional materials for OER/HER

Zhou et al. described the use of trimetallic MOF-74 (Mn_xFe_yNi-MOF-74) films grown on nickel foam as bifunctional electrocatalysts for OER and HER in alkaline medium (1 M KOH). The OER activity of the optimized film, $Mn_{0.52}Fe_{0.71}Ni$-MOF-74, surpassed its bimetallic counterparts, $Mn_{2.67}Ni$-MOF-74 and $Fe_{1.88}Ni$-MOF-74, as well as the state-of-the-art IrO_2 electrocatalyst. HER activity of the same optimized film was superior to its bimetallic counterparts and comparable to the benchmark Pt/C electrocatalyst, and the film showed good stability in both OER and HER polarization conditions. The enhanced performance was attributed to Mn doping, which exposed more active sites, regulated charge transfer, and formed oxyhydroxides, acting as active phases in the electrocatalyst. Finally, a 2-electrode water electrolyzer (1 M KOH) with the optimized film as both cathode and anode was built to test the material's overall water splitting capabilities, with 10 mA/cm^2 being achieved at a 1.48 V and overall stability for over 100 h at 200 mA/cm^2 being observed (Zhou et al., 2020).

Chen et al. reported the synthesis of a carbon-coated Co-doped selenide nanomaterial derived from nickel-cobalt bimetallic MOF, NiCoSe/C, and tested it as an overall water splitting electrocatalyst in alkaline medium (1 M KOH). The OER tests demonstrated a superior performance, with a low overpotential of 249 mV at 10 mA/cm^2, and good stability properties, outperforming the benchmark RuO_2 electrocatalyst. HER results, albeit not superior to benchmark Pt/C, were still significantly lower than other NiCo-based materials, with the material presenting excellent stability properties. Finally, a two-electrode cell was constructed to verify the overall water-splitting activity, with NiCoSe/C acting as both cathode and anode. The resulting cell was able to deliver 10 mA/cm^2 at 1.68 V and showed stability both for over 20 h of operation and after 1,000 operation cycles. The performance was attributed to the synergy between Ni and Co, which modulated the material's electronic structure, and to the highly porous and high specific surface area structure inherited from the parent MOF (Chen Z. et al., 2019).

Zhao et al. prepared Mo-CoS_2 nanoparticles embedded in a hierarchically porous carbon hollow sphere, Mo-CoS_2/NC (H),

derived from ZIF-67 MOF, phosphomolybdic acid POM and polystyrene sphere. The resulting composite was tested as an overall water-splitting electrocatalyst in 1 M KOH. The OER results demonstrated that the produced nanoparticles outperformed the benchmark RuO_2 electrocatalyst and exhibited good stability properties. Regarding HER, the material presented activity comparable to that of state-of-the-art Pt/C, alongside good stability. Regarding the overall water splitting activity, an electrolyzer where Mo-CoS_2/NC (H) acted as both cathode and anode was constructed, and it delivered 10 mA/cm^2 at 1.59 V vs RHE, which is comparable to other state-of-the-art water splitting catalysts. The enhanced activity was attributed to strengthened chemical adsorption of H and O, higher electrical conductivity due to Mo incorporation, and the micro/meso/macro porous structure, which offers a large specific surface area and a high number of active sites (Zhao et al., 2023).

Zhao et al. disclosed the use of a Ni-Fe bimetallic MOF-derived electrocatalyst, Fe-Ni@NC-CNTs, as an overall water-splitting electrocatalyst in alkaline solution (1 M KOH). The OER results indicated a good overall activity, with a 274 mV overpotential at 10 mA/cm^2 and a 45.5 mV/dec Tafel slope. Relative to the HER, the tested material exhibited a performance comparable to that of benchmark Pt/C, and also demonstrated good stability properties at HER and OER polarization conditions. The performance of Fe-Ni@NC-CNTs as an overall water-splitting electrocatalyst was tested in an electrolyzer where it acts both as the cathode and as the anode, attaining a 145 mA/cm^2 current density at 1.98 V vs RHE, which is comparable to the performance of an electrolyzer containing Pt/C as the cathode and Ir/C as the anode. The observed performance was attributed to the high conductivity and hierarchical pore structure, which resulted in both high activity and fast mass transport (Zhao et al., 2018).

Gao et al. deposited a mixed Cu, Co, and W metal oxide nanostructure onto a copper foam electrode by using $[SiW_{11}O_{39}]^{8-}$ POM as a structure directing agent and tested its performance towards OER and HER in alkaline conditions (0.1 M KOH). Regarding the OER, the obtained electrocatalyst needed an overpotential of 313 mV to reach a current density of 10 mA/cm^2. The HER results show that a 103 mV overpotential was needed to achieve 10 mA/cm^2, and the material presented stability for over 10 h in both HER and OER polarization conditions. The material was also tested as an overall water-splitting bifunctional material in a 2-electrode water electrolyzer (0.1 M KOH electrolyte), with sustained gas evolution being observed at 1.8 V vs RHE (Gao et al., 2019).

Zhang Z. et al. derived $CoMoO_4$ hollow tubes (HT) from the annealing of a PMo_{12}@Co-BTC POMOF hybrid and tested its ability to act as an overall water-splitting electrocatalyst in 1 M KOH. The OER activity proved superior to benchmark RuO_2, and the material exhibited excellent stability properties. The HER activity was comparable to state-of-the-art Pt/C but did not surpass it, and $CoMoO_4$ HTs also demonstrated excellent stability properties. Finally, a two-electrode cell with the CoMoO4 HTs acting as both cathode and anode was constructed to test the overall water-splitting capabilities and was compared to a similar cell constructed with Pt/C as the cathode and RuO_2 as the anode. The results indicated that a current density of 10 mA/cm^2 was attained at 1.57 V vs RHE for the first cell and 1.50 V vs RHE for the second cell, demonstrating that the material presented impressive overall water-splitting capabilities. The superior performance was attributed to the presence of a hollow and rough surface, which increased specific surface area, the mesoporous structure, which increased mass-transfer and charge-transfer rates due to more access points, and the inherent conductivity of Co-based materials (Zhang Z. et al., 2023b).

Gautam et al. designed a POM-anchored zinc cobalt sulfide nanowires on 3D Ni foam substrate (POM@ZnCoS/NF, POM = PW_{12}) to be used as an overall water splitting electrocatalyst in alkaline electrolyte (1 M KOH). The material presented better OER activity than benchmark RuO_2, and also had good stability properties, maintaining activity for over 20 h without structural changes. It also presented impressive HER activity, surpassing even benchmark Pt/C, and good stability, being able to consistently demonstrate activity for over 20 h without structural changes. A 2-electrode water splitting cell using POM@ZnCoS/NF as both cathode and anode was tested: it delivered 10 mA/cm^2 at 1.55 V vs RHE, outperforming a similar cell that used Pt/C as cathode and RuO_2 as anode (1.64 V vs RHE at 10 mA/cm^2). The observed performance was attributed mainly to the mesoporous hierarchical heterostructure, which improved the conductivity and increased both the number of available active sites and the electrochemical surface area (Gautam et al., 2021). The discussed bifunctional materials for OER/HER are summarized in Table 14, along with the relevant performance indicators.

TABLE 14 MOF and POM(-derived) bifunctional OER/HER electrocatalysts.

Electrocatalyst	OER η_{10} (mV)	OER Tafel slope (mV/dec)	HER η_{10} (mV)	HER Tafel slope (mV/dec)	Electrolyte	Source
$Mn_{0.52}Fe_{0.71}$Ni-MOF-74	267@ 100 mA/cm^2	36.7	190@ 100 mA/cm^2	103.8	1 M KOH	Zhou et al. (2020)
NiCoSe/C	249	54	143	104.8	1 M KOH	Chen Z. et al. (2019)
Mo-CoS_2/NC (H)	296	65	158	150	1 M KOH	Zhao et al. (2023)
Fe-Ni@NC-CNTs	274	45.5	202	113.7	1 M KOH	Zhao et al. (2018)
$CuCoWO_x$	313	162	103	335	0.1 M KOH	Gao et al. (2019)
$CoMoO_4$ HTs	210	80.3	75	89.1	1 M KOH	Zhang et al. (2023b)
POM@ZnCoS NWs	200@20 mA/cm^2	67.7	170	53.5	1 M KOH	Gautam et al. (2021)

The future perspective of transition metal-based catalysts as a whole is one of optimism. There are dozens of studies highlighting the advantages of combining those abundant metals to replace current state-of-the-art noble metals in electrochemical energy conversion and storage, be it in the form of the more traditional oxide and alloy catalysts or in the form of the more modern POM and MOF catalysts (and their derivatives). Additionally, the versatility of transition metal catalysts is not limited to those four material classes, as other transition metal-based materials are also reviewed herein, including carbides, phosphides, and nitrides, which can also be derived from POMs and MOFs. Finally, the high tunability and structural versatility of POMs and MOFs means that there are multiple combinations to be applied in electrocatalyst materials, each with its own catalytic prowess, and some of them are yet to be studied. As such, this review's main scope was to analyze some of those combinations for those two classes and compare them to the traditional electrocatalyst classes to bring a comprehensive understanding of the real catalytic capabilities of POMs and MOFs.

7 Conclusion

The electrochemical reactions involved in the main energy conversion and storage systems, OER, ORR, and HER, are sluggish, and their electrocatalysts are expensive since they are based on scarce noble metals. As alternatives to these benchmark electrocatalysts, transition metal-based POM and MOF-derived electrocatalysts are being studied. Their main advantage resides in the tailorability these structures present, meaning that one can easily modify it in the desired manner, normally through simple adaptations in the synthetic process. This means that when one of those materials is faced with performance or stability issues, they can be easily adapted, for example, by adding moieties that can enhance these aspects, thus generating a better-performing material. Additional strategies include inducing the formation of a core-shell nanostructure, where the active material in the core is protected by the external shell, enhancing stability, and anchoring POMs or MOFs on conductive supports, which can both enhance the activity and stability of the utilized materials. Their performance is comparable to that of the more traditional transition metal-based oxide and alloy electrocatalysts, meaning they show a promising future in the electrocatalysis application.

Author contributions

HA: Investigation, Validation, Writing–original draft. BS: Conceptualization, Funding acquisition, Project administration, Writing–review and editing. SG: Conceptualization, Resources, Supervision, Writing–review and editing. DS: Conceptualization, Project administration, Resources, Supervision, Writing–review and editing.

Funding

The author(s) declare that no financial support was received for the research, authorship, and/or publication of this article. The authors would like to thank Fundação para a Ciência e a Tecnologia (FCT, Portugal) for funding EXPL/EQU-EQU/0517/2021 project, contract IST-ID/156/2018 (BŠ), and a contract in the scope of programmatic funding UIDP/04540/2020 (D.M.F. Santos), and projects LA/P/0008/2020 DOI 10.54499/LA/P/0008/2020, UIDP/50006/2020 DOI 10.54499/UIDP/50006/2020 and UIDB/50006/2020 DOI 10.54499/UIDB/50006/2020), through national funds.

Conflict of interest

The authors declare that the research was conducted in the absence of any commercial or financial relationships that could be construed as a potential conflict of interest.

Publisher's note

References

Abdelkader-Fernández, V. K., Fernandes, D. M., Balula, S. S., Cunha-Silva, L., and Freire, C. (2020). Oxygen evolution reaction electrocatalytic improvement in POM@ZIF nanocomposites: a bidirectional synergistic effect. *ACS Appl. Energy Mat.* 3, 2925–2934. doi:10.1021/acsaem.0c00009

Abdelkader-Fernández, V. K., Fernandes, D. M., Balula, S. S., Cunha-Silva, L., Pérez-Mendonza, M. J., López-Garzon, F. J., et al. (2019). Noble-metal-free MOF-74-derived nanocarbons: insights on metal composition and doping effects on the electrocatalytic activity toward oxygen reactions. *ACS Appl. Energy Mat.* 2, 1854–1867. doi:10.1021/acsaem.8b02010

Ahmad, W., Gao, Q., Zhang, X.-L., Tan, W., Zhang, L., Gao, M.-R., et al. (2020). Sandwich-type polyoxometalate mediates cobalt diselenide for hydrogen evolution in acidic electrolyte. *Chem. Nano. Mat.* 6, 1164–1168. doi:10.1002/cnma.202,000106

Al-Oweini, R., Sartorel, A., Bassil, B. S., Mirco, N., Berardi, S., Scandola, F., et al. (2014). Photocatalytic water oxidation by a mixed-valent $Mn^{III}_3Mn^{IV}O_3$ manganese oxo core that mimics the natural oxygen-evolving center. *Angew. Chem. Int. Ed. Engl.* 53, 11182–11185. doi:10.1002/anie.201404664

Amin, M., Shah, H. H., Fareed, A. G., Khan, W. U., Chung, E., Zia, A., et al. (2022). Hydrogen production through renewable and non-renewable energy processes and their impact on climate change. *Int. J. Hydrogen Energy* 47, 33112–33134. doi:10.1016/j.ijhydene.2022.07.172

Ammam, M., Keita, B., Nadjo, L., Mbomekalle, I.-M., Ritorto, M. D., Anderson, T. M., et al. (2011). Cyclic voltammetry study of the Mn-substituted polyoxoanions $[MnII4(H2O)2(H4AsW15O56)2]18^-$ and $[((Mn^{II}OH_2)Mn^{II}_2PW_9O_{34})_2(PW_6O_{26})]^{17-}$: electrodeposition of manganese oxides electrocatalysts for dioxygen reduction. *Electroanalysis* 23, 1427–1434. doi:10.1002/elan.201,000735

Arcos, J. M. M., and Santos, D. M. F. (2023). The hydrogen color spectrum: techno-economic analysis of the available technologies for hydrogen production. *Gases* 3, 25–46. doi:10.3390/gases301,0002

Bai, L., Wen, X., and Guan, J. (2019). Amorphous Fe Co Ni oxide for oxygen evolution reaction. *Mater. Today Energy* 12, 311–317. doi:10.1016/j.mtener.2019.02.004

Bai, X., Wang, Q., and Guan, J. (2021). "Bimetallic Iron–Cobalt nanoparticles coated with amorphous carbon for oxygen evolution. *ACS Appl. Nano Mat.* 4, 12663–12671. doi:10.1021/acsanm.1c03208

Belkessam, C., Bencherif, S., Mechouet, M., Idiri, N., and Ghilane, J. (2020). The effect of heteroatom doping on nickel cobalt oxide electrocatalysts for oxygen evolution and reduction reactions. *ChemPlusChem* 85, 1710–1718. doi:10.1002/cplu.202,000436

Bhuvanendran, N., Ravichandran, S., Kandasamy, S., Zhang, W., Xu, Q., Khotseng, L., et al. (2021). Spindle-shaped CeO_2/biochar carbon with oxygen vacancy as an effective and highly durable electrocatalyst for oxygen reduction reaction. *Int. J. Hydrogen Energy* 46, 2128–2142. doi:10.1016/j.ijhydene.2020.10.115

Butt, F. A., Anwar, M., and Unal, U. (2021). Synthesis of metallic copper nanowires using dielectric barrier discharge plasma and their application in hydrogen evolution reaction. *Int. J. Hydrogen Energy* 46, 18866–18877. doi:10.1016/j.ijhydene.2021.03.020

Cao, J., Li, H., Pu, J., Zeng, S., Liu, L., Zhang, L., et al. (2019). Hierarchical NiMo alloy microtubes on nickel foam as an efficient electrocatalyst for hydrogen evolution reaction. *Int. J. Hydrogen Energy* 44, 24712–24718. doi:10.1016/j.ijhydene.2019.07.229

Chatenet, M., Pollet, B. G., Dekel, D. R., Dionigi, F., Deseure, J., Millet, P., et al. (2022). Water electrolysis: from textbook knowledge to the latest scientific strategies and industrial developments. *Chem. Soc. Rev.* 51, 4583–4762. doi:10.1039/D0CS01079K

Chen, C., Wu, A., Yan, H., Xiao, Y., Tian, C., and Fu, H. (2018). Trapping $[PMo_{12}O_{40}]^{3+}$ clusters into pre-synthesized ZIF-67 toward Mo_xCo_xC particles confined in uniform carbon polyhedrons for efficient overall water splitting. *Chem. Sci.* 9, 4746–4755. doi:10.1039/C8SC01454J

Chen, Z., Xu, B., Yang, X., Zhang, H., and Li, C. (2019). Bimetallic metal-organic framework derived electrocatalyst for efficient overall water splitting. *Int. J. Hydrogen Energy* 44, 5983–5989. doi:10.1016/j.ijhydene.2019.01.082

Cheng, W., Wu, Z.-P., Luan, D., Zang, S.-Q., and Lou, X. W. (2021). Synergetic cobalt-copper-based bimetal–organic framework nanoboxes toward efficient electrochemical oxygen evolution. *Angew. Chem. Int. Ed.* 60, 26397–26402. doi:10.1002/anie.202112775

Chu, M., Wang, L., Li, X., Hou, M., Li, N., Dong, Y., et al. (2018). Carbon coated nickel - nickel oxide composites as a highly efficient catalyst for hydrogen evolution reaction in acid medium. *Electrochim. Acta* 264, 284–291. doi:10.1016/j.electacta.2018.01.140

Cui, Z., Wang, S., Zhang, Y., and Cao, M. (2014). Engineering hybrid between nickel oxide and nickel cobaltate to achieve exceptionally high activity for oxygen reduction reaction. *J. Power Sources* 272, 808–815. doi:10.1016/j.jpowsour.2014.08.097

Dai, W., Lu, T., and Pan, Y. (2019). Novel and promising electrocatalyst for oxygen evolution reaction based on MnFeCoNi high entropy alloy. *J. Power Sources* 430, 104–111. doi:10.1016/j.jpowsour.2019.05.030

Dao, X., Nie, M., Sun, H., Dong, W., Xue, Z., Li, Q., et al. (2022). Electrochemical performance of metal-organic framework MOF(Ni) doped graphene. *Int. J. Hydrogen Energy* 47 (2022), 16741–16749. doi:10.1016/j.ijhydene.2022.03.176

Draskovic, T. I., and Wu, Y. (2017). Electrocatalytic properties of cuprous delafossite oxides for the alkaline oxygen reduction reaction. *ChemCatChem* 9, 3837–3842. doi:10.1002/cctc.201700712

Duan, D., Feng, J., Guo, D., Gao, J., Liu, S., Wang, Y., et al. (2022). MOF-derived cobalt manganese phosphide as highly efficient electrocatalysts for hydrogen evolution reaction. *Int. J. Hydrogen Energy* 47, 12927–12936. doi:10.1016/j.ijhydene.2022.02.037

Feng, C., Li, Z., Wang, J., Yan, T., Dong, H., Feng, J., et al. (2019). Synthesis of metal-organic framework-derived cobalt disulfide with high-performance oxygen reduction reaction catalytic properties. *J. Electroanal. Chem.* 840, 27–34. doi:10.1016/j.jelechem.2019.03.056

Fernandes, D. M., Araújo, M. P., Haider, A., Mougharbel, A. S., Fernandes, A. J. S., Kortz, U., et al. (2018b). Polyoxometalate-graphene electrocatalysts for the hydrogen evolution reaction. *Chemelectrochem* 5, 273–283. doi:10.1002/celc.201701210

Fernandes, D. M., Novais, H. C., Bacsa, R., Serp, P., Bachiller-Baeza, B., Rodríguez-Ramos, I., et al. (2018a). Polyoxotungstate@Carbon nanocomposites as oxygen reduction reaction (ORR) electrocatalysts. *Langmuir* 34, 6376–6387. doi:10.1021/acs.langmuir.8b00299

Flores-Lasluisa, J. X., Quilez-Bermejo, J., Ramirez-Pérez, A. C., Huerta, F., Cazorla-Amorós, D., and Morallón, E. (2019). Copper-doped cobalt spinel electrocatalysts supported on activated carbon for hydrogen evolution reaction. *Materials* 12, 1302. doi:10.3390/ma12081302

Gao, D., Liu, R., Biskupek, J., Kaiser, U., Song, Y.-F., Streb, C., et al. (2019). Modular design of noble metal-free mixed metal oxide electrocatalysts for complete water splitting. *Angew. Chem. Int. Ed.* 58, 4644–4648. doi:10.1002/anie.201900428

Gautam, J., Liu, Y., Gu, J., Ma, Z., Zha, J., Dahal, B., et al. (2021). Fabrication of polyoxometalate anchored zinc cobalt sulfide nanowires as a remarkable bifunctional electrocatalyst for overall water splitting. *Adv. Funct. Mat.* 31. doi:10.1002/adfm.202106147

Ge, Y., Chen, J., Chu, H., Dong, P., Craig, S. R., Ajayan, P. M., et al. (2018). Urchin-like CoP with controlled manganese doping toward efficient hydrogen evolution reaction in both acid and alkaline solution. *ACS Sustain. Chem. Eng.* 6, 15162–15169. doi:10.1021/acssuschemeng.8b03638

Goberna-Ferrón, S., Soriano-López, J., and Galán-Mascarós, J. R. (2015). Activity and stability of the tetramanganese polyanion $[Mn_4(H_2O)_2(PW_9O_{34})_2]^{10-}$ during electrocatalytic water oxidation. *Inorganics* 3, 332–340. doi:10.3390/inorganics3030332

Guan, J., Liu, Y., Fang, Y., Du, X., Fu, Y., Wang, L., et al. (2021). Co-Ni alloy nanoparticles supported by carbon nanofibers for hydrogen evolution reaction. *J. Alloys Compd.* 868, 159172. doi:10.1016/j.jallcom.2021.159172

Gusmão, F. M. B., Mladenović, D., Radinović, K., Santos, D. M. F., and Šljukić, B. (2022). Polyoxometalates as electrocatalysts for electrochemical energy conversion and storage. *Energies* 15, 9021. doi:10.3390/en15239021

Horn, M. R., Singh, A., Alomari, S., Goberna-Ferrón, S., Benages-Vilau, R., Chodankar, N., et al. (2021). Polyoxometalates (POMs): from electroactive clusters to energy materials. *Energy Environ. Sci.* 14, 1652–1700. doi:10.1039/D0EE03407J

Huang, H., Shen, B., Yan, M., He, H., Yang, L., Jiang, Q., et al. (2022). Coupled spinel manganese– cobalt oxide and MXene electrocatalysts towards efficient hydrogen evolution reaction. *Fuel* 328, 125234. doi:10.1016/j.fuel.2022.125234

Imani, A. H., Ojani, R., and Raoof, J. B. (2018). *In situ* synthesis of a novel organic-inorganic composite as a non-noble metal electrocatalyst for the oxygen evolution reaction. *Int. J. Hydrogen Energy* 43, 8267–8277. doi:10.1016/j.ijhydene.2018.03.032

Imani, A. H., Ojani, R., and Raoof, J. B. (2021). Novel polyoxometalate-based composite as efficient electrocatalyst for alkaline water oxidation reaction. *J. Iran. Chem. Soc.* 18, 2079–2089. doi:10.1007/s13738-021-02169-0

Intergovernmental Panel for Climate Change (IPCC) (2018). "Summary for policymakers," in *: global Warming of 1.5°C. An IPCC Special Report on the impacts of global warming of 1.5°C above pre-industrial levels and related global greenhouse gas emission pathways in the context of strengthening the global response to the threat of climate change, sustainable development and efforts to eradicate poverty*, 3–24. doi:10.1017/9781009157940.001

Jawale, D. V., Fossard, F., Miserque, F., Geertsen, V., Teillout, A.-L., de Oliveira, P., et al. (2022). Carbon nanotube-polyoxometalate nanohybrids as efficient electrocatalysts for the hydrogen evolution reaction. *Carbon* 188, 523–532. doi:10.1016/j.carbon.2021.11.046

Jeong, S., Hu, K., Ohto, T., Nagata, Y., Masuda, H., Fujita, J., et al. (2020). Effect of graphene encapsulation of NiMo alloys on oxygen evolution reaction. *ACS Catal.* 10, 792–799. doi:10.1021/acscatal.9b04134

Ji, S.-M., Muthurasu, A., and Kim, H. Y. (2023). Marigold flower-shaped metal–organic framework supported manganese vanadium oxide electrocatalyst for efficient oxygen evolution reactions in an alkaline medium. *Chem. Eur. J.* 29, e202300137. doi:10.1002/chem.202300137

Jia, X., Streb, C., and Song, Y.-F. (2019). Devisable POM/Ni foam composite: precisely control synthesis toward enhanced hydrogen evolution reaction at high pH. *Chem. Eur. J.* 25, 15548–15554. doi:10.1002/chem.201903059

Jia, Y., Xue, Z., Li, Y., and Li, G. (2022). Recent progress of metal organic frameworks-based electrocatalysts for hydrogen evolution, oxygen evolution, and oxygen reduction reaction. *Energy Environ. Mat.* 5, 1084–1102. doi:10.1002/eem2.12290

Jiang, B., Wang, T., Cheng, Y., Liao, F., Wu, K., and Shao, M. (2018). Ir/g-C3N4/Nitrogen-Doped graphene nanocomposites as bifunctional electrocatalysts for overall water splitting in acidic electrolytes. *ACS Appl. Mat. Interfaces* 10, 39161–39167. doi:10.1021/acsami.8b11970

Jiang, J., Zhang, C., and Ai, L. (2016). Hierarchical iron nickel oxide architectures derived from metal-organic frameworks as efficient electrocatalysts for oxygen evolution reaction. *Electrochim. Acta* 208, 17–24. doi:10.1016/j.electacta.2016.05.008

Jiang, S., Duan, C., Li, X., Wand, D., Wang, Z., Sun, H., et al. (2021). Alloying strategy for constructing multi-component nano-catalysts towards efficient and durable oxygen evolution in alkaline electrolyte. *Electrochim. Acta* 391, 138933. doi:10.1016/j.electacta.2021.138933

Kang, Q., Lai, D., Su, M., Xiong, B., Tang, W., Lu, Q., et al. (2022). Tailored dodecahedral polyoxometalates nanoframes with *in situ* encapsulated Co, N, C for oxygen evolution reaction. *Chem. Eng. J.* 430, 133116. doi:10.1016/j.cej.2021.133116

Katsunaros, I., Cherevko, S., Zeradjanin, A. R., and Mayrhofer, K. J. J. (2014). Oxygen electrochemistry as a cornerstone for sustainable energy conversion. *Angew. Chem. Int. Ed.* 53, 102–121. doi:10.1002/anie.201306588

Katubi, K. M., Warsi, A.-Z., Aziz, F., Khattak, Z., Warsi, M. F., Al-buriahi, M. S., et al. (2023). Tungsten oxide-copper oxide supported on reduced graphene oxide as a proficient electrocatalyst with enhanced hydrogen evolution efficiency in an alkaline media. *Curr. Appl. Phys.* 51, 80–90. doi:10.1016/j.cap.2023.05.002

Kim, A., Muthuhamy, N., Yoon, C., Joo, S. H., and Park, K. H. (2018). MOF-derived Cu@Cu2O nanocatalyst for oxygen reduction reaction and cycloaddition reaction. *Nanomaterials*, 8. doi:10.3390/nano8030138

Kumar, M., Jeong, D. I., and Yoon, D. H. (2020). Copper nickel alloy nanorods textured nanoparticles for oxygen evolution reaction. *Electrochim. Acta* 333, 135545. doi:10.1016/j.electacta.2019.135545

Lee, J.-W., and Popov, B. N. (2007). Ruthenium-based electrocatalysts for oxygen reduction reaction—a review. *J. Solid State Electrochem.* 11, 1355–1364. doi:10.1007/s10008-007-0307-3

Li, G., Zhang, X., Zhang, H., Liao, C., and Jiang, G. (2019). Bottom-up MOF-intermediated synthesis of 3D hierarchical flowerlike cobalt-based homobimetallic ficiente composed of ultrathin nanosheets for highly efficient oxygen evolution reaction. *Appl. Catal. B-Environ.* 15, 147–154. doi:10.1016/j.apcatb.2019.03.007

Li, H., Liu, Y., He, F., Yang, H., Li, Z., Zhou, Q., et al. (2020). *In situ* grown Cu-Based metal-organic framework on copper foam as high-performance electrocatalysts for oxygen evolution reaction. *Int. J. Hydrogen Energy* 45, 21540–21546. doi:10.1016/j.ijhydene.2020.05.234

Lim, D., Oh, E., Lim, C., Shim, S. E., and Baeck, S.-H. (2020). Bimetallic NiFe alloys as highly efficient electrocatalysts for the oxygen evolution reaction. *Catal. Today* 352, 27–33. doi:10.1016/j.cattod.2019.09.046

Limani, N., Marques, I. S., Jarrais, B., Fernandes, A. J. S., Freire, C., and Fernandes, D. M. (2022). Cobalt phosphotungstate-based composites as bifunctional electrocatalysts for oxygen reactions. *Catalysts* 12, 357. doi:10.3390/catal12040357

Liu, K., Zhang, C., Sun, Y., Zhang, G., Shen, X., Zou, F., et al. (2018). High-performance transition metal phosphide alloy catalyst for oxygen evolution reaction. *ACS Nano* 12, 158–167. doi:10.1021/acsnano.7b04646

Liu, R., Cao, K., Clark, A. H., Lu, P., Anjass, M., Biskupek, J., et al. (2020). Top-down synthesis of polyoxometalate-like subnanometer molybdenum-oxo clusters as high-performance electrocatalysts. *Chem. Sci.* 11, 1043–1051. doi:10.1039/C9SC05469C

Liu, S.-W., and Qin, X. (2015). Manganese oxides/graphene composite as cathode catalyst for the oxygen reduction reaction in alkaline solution. *Fullerenes, Nanotub. Carbon Nanostructures* 23, 824–830. doi:10.1080/1536383X.2015.1009533

Liu, T., Li, P., Yao, N., Cheng, G., Chen, S., Luo, W., et al. (2019). CoP-doped MOF-based electrocatalyst for pH-universal hydrogen evolution reaction. *Angew. Chem. Int. Ed.* 58, 4679–4684. doi:10.1002/anie.201901409

Liu, X., Niu, J., Rajendran, S., Lei, Y., Qin, J., and Zhang, X. (2021). Electrodeposition of the manganese-doped nickelphosphorus catalyst with enhanced hydrogen evolution reaction activity and durability. *Int. J. Hydrogen Energy* 47, 41994–42000. doi:10.1016/j.ijhydene.2021.10.105

Lu, H.-S., Zhang, H., Liu, R., Zhang, X., Zhao, H., and Wang, G. (2017). Macroscale cobalt-MOFs derived metallic Co nanoparticles embedded in N-doped porous carbon layers as efficient oxygen electrocatalysts. *Appl. Surf. Sci.* 392, 402–409. doi:10.1016/j.apsusc.2016.09.045

Lu, X. F., Xia, B. Y., Zang, S.-Q., and Lou, X. W. (2019). Metal–organic frameworks based electrocatalysts for the oxygen reduction reaction. *Angew. Chem. Int. Ed.* 59, 4634–4650. doi:10.1002/anie.201910309

Luo, W., Hu, J., Diao, H., Schwarz, B., Streb, C., and Song, Y.-F. (2017a). Robust polyoxometalate/nickel foam composite electrodes for sustained electrochemical oxygen evolution at high pH. *Angew. Chem. Int. Ed.* 56, 4941–4944. doi:10.1002/anie.201612232

Luo, X.-F., Wang, J., Liang, Z.-S., Chen, S.-Z., Liu, Z.-L., Xu, C.-W., et al. (2017b). Manganese oxide with different morphology as efficient electrocatalyst for oxygen evolution reaction. *Int. J. Hydrogen Energy* 42, 7151–7157. doi:10.1016/j.ijhydene.2016.04.162

Ma, X., Qi, K., Wei, S., Zhang, L., and Cui, X. (2019). *In situ* encapsulated nickel-copper nanoparticles in metal-organic frameworks for oxygen evolution reaction. *J. Alloys Compd.* 770, 236–242. doi:10.1016/j.jallcom.2018.08.096

Mani, P., Devadas, S., Gurusamy, T., Karthik, P. E., Ratheesh, B. P., Ramanujam, K., et al. (2019). Sodalite-type Cu-based three-dimensional metal–organic framework for efficient oxygen reduction reaction. *Chem. Asian J.* 14, 4814–4818. doi:10.1002/asia.201901242

Marques, I. S., Jarrais, B., Mbomekallé, I.-M., Teillout, A. – L., de Oliveira, P., Freire, C., et al. (2022). Synergetic effects of mixed-metal Polyoxometalates@Carbon-based composites as electrocatalysts for the oxygen reduction and the oxygen evolution reactions. *Catalysts* 12, 440. doi:10.3390/catal12040440

Mladenović, D., Daş, E., Santos, D. M. F., Yurtcan, A. B., Miljanić, Š., and Šljukić, B. (2022). Boosting oxygen electrode kinetics by addition of cost-effective transition metals (Ni, Fe, Cu) to platinum on graphene nanoplatelets. *J. Alloys Compd.* 905, 164156. doi:10.1016/j.jallcom.2022.164156

Mladenović, D., Daş, E., Santos, D. M. F., Yurtcan, A. B., and Šljukić, B. (2023b). Highly efficient oxygen electrode obtained by sequential deposition of transition metal-platinum alloys on graphene nanoplatelets. *Materials* 16, 3388. doi:10.3390/ma16093388

Mladenović, D., Mladenović, A., Santos, D. M. F., Yurtcan, A. B., Miljanić, Š., Mentus, S., et al. (2023a). Transition metal oxides for bifunctional ORR/OER electrocatalysis in unitized regenerative fuel cells. *J. Electroanal. Chem.* 946, 117709. doi:10.1016/j.jelechem.2023.117709

Mladenović, D., Santos, D. M. F., Bozkurt, G., Soylu, G. S. P., Yurtcan, A. B., Miljanić, Š., et al. (2021). Tailoring metal-oxide-supported PtNi as bifunctional catalysts of superior activity and stability for unitised regenerative fuel cell applications. *Electrochem. Commun.* 124, 106963. doi:10.1016/j.elecom.2021.106963

Moschkowitsch, W., Zion, N., Honig, H. C., Levy, N., Cullen, D. A., and Elbaz, L. (2022). Mixed-metal Nickel–Iron oxide aerogels for oxygen evolution reaction. *ACS Catal.* 12, 12162–12169. doi:10.1021/acscatal.2c03351

Mukherjee, A., Chakrabarty, S., Su, W.-N., and Basu, S. (2018). Nanostructured nickel ferrite embedded in reduced graphene oxide for electrocatalytic hydrogen evolution reaction. *Mat. Today Energy* 8, 118–124. doi:10.1016/j.mtener.2018.03.004

Muralikrishna, S., Ravishankar, T. N., Ramakrishnappa, T., Nagaraju, D. H., and Pai, R. K. (2015). Non-noble metal graphene oxide-copper (II) ions hybrid electrodes for electrocatalytic hydrogen evolution reaction. *Environ. Prog. Sustain. Energy* 35, 565–573. doi:10.1002/ep.12238

Nakagawa, T., Bjorge, N. S., and Murray, R. W. (2009). Electrogenerated IrO_x nanoparticles as dissolved redox catalysts for water oxidation. *J. Am. Chem. Soc.* 131, 15578–15579. doi:10.1021/ja9063298

Nivetha, R., Sajeev, A., Paul, A. M., Gothandapani, K., Gnanasekar, S., Bhardwaj, P., et al. (2020). Cu based Metal Organic Framework (Cu-MOF) for electrocatalytic hydrogen evolution reaction. *Mat. Res. Express* 7, 114001. doi:10.1088/2053-1591/abb056

Pan, Z., Pan, N., Chen, L., He, J., and Zhang, M. (2019). Flower-like MOF-derived Co-N-doped carbon composite with remarkable activity and durability for electrochemical hydrogen evolution reaction. *Int. J. Hydrogen Energy* 44, 30075–30083. doi:10.1016/j.ijhydene.2019.09.117

Park, Y. S., Park, C. S., Kim, C. H., Kim, Y. D., Park, S., and Lee, J. H. (2016). Characteristics of the oxygen evolution reaction on synthetic copper – cobalt – oxide electrodes for water electrolysis. *J. Korean Phys. Soc.* 69, 1187–1190. doi:10.3938/jkps.69.1187

Peng, K., Bhuvanendran, N., Ravichandran, S., Xu, Z., Zhang, W., Ma, Q., et al. (2020). Sewage sludge-derived Fe- and N-containing porous carbon as efficient support for Pt catalyst with superior activity towards methanol electrooxidation. *Int. J. Hydrogen Energy.* 45, 9795–9802. doi:10.1016/j.ijhydene.2020.01.140

Pratama, D. S. A., Haryanto, A., and Lee, C. W. (2023). Heterostructured mixed metal oxide electrocatalyst for the hydrogen evolution reaction. *Front. Chem.* 11, 1141361. doi:10.3389/fchem.2023.1141361

Qin, X., Huang, Y., Wang, K., Xu, T., Wang, Y., Wang, M., et al. (2019). Highly efficient oxygen reduction reaction catalyst derived from Fe/Ni mixed-Metal–Organic frameworks for application of fuel cell cathode. *Ind. Eng. Chem. Res.* 58, 10224–10237. doi:10.1021/acs.iecr.9b01412

Rehman, I. u., Zhang, J., Chen, J., and Wang, R. (2022). *In situ* derived Ni-N-CNTs from ZIF-8 crystals as efficient electrocatalysts for oxygen reduction reaction. *Inorg. Chem. Commun.* 144, 109922. doi:10.1016/j.inoche.2022.109922

Ritchie, H., Roser, M., and Rosado, P. (2022). Energy published online at OurWorldInData.org. Available at: https://ourworldindata.org/energy.

Rousseau, G., Zhang, S., Oms, O., Dolbecq, A., Marrot, J., Liu, R., et al. (2015). Sequential synthesis of 3 d–3d, 3 d–4d, and 3 d–5d hybrid polyoxometalates and application to the electrocatalytic oxygen reduction reactions. *Chemistry* 21, 12153–12160. doi:10.1002/chem.201501609

Roy, A., Jadhav, H. S., Cho, M., and Seo, J. G. (2019). Electrochemical deposition of self-supported bifunctional copper oxide electrocatalyst for methanol oxidation and oxygen evolution reaction. *J. Ind. Eng. Chem.* 76, 515–523. doi:10.1016/j.jiec.2019.04.019

Saianand, G., Gopalan, A.-L., Lee, J.-C., Sathish, Cl, Gopalakrishnan, K., Unni, G. E., et al. (2020). Mixed copper/copper-oxide anchored mesoporous fullerene nanohybrids as superior electrocatalysts toward oxygen reduction reaction. *Small* 16, e1903937. doi:10.1002/smll.201903937

Sajeev, A., Sathyaseelan, A., Bejigo, K. S., and Kim, S. J. (2023). Trimetallic non-noble NiCoSn alloy as an efficient electrocatalyst towards methanol oxidation and oxygen reduction reactions. *J. Colloid Interface Sci.* 637, 363–371. doi:10.1016/j.jcis.2023.01.064

Sanji, F. D., Balakrishnan, P., Su, H., Khotseng, L., and Xu, Q. (2021). Fabrication of polyoxometalate-modified palladium–nickel/reduced graphene oxide alloy catalysts for enhanced oxygen reduction reaction activity. *RSC Adv.* 11, 39118–39129. doi:10.1039/D1RA06936E

Shen, Q., Zhang, C., Wang, M., Pang, H., Ma, H., Wang, X., et al. (2019). A novel Lindqvist intercalation compound: synthesis, crystal structure and hydrogen evolution reaction performance. *Inorg. Chem. Commun.* 99, 64–69. doi:10.1016/j.inoche.2018.11.013

Shen, Y., Zhou, Y., Wang, D., Wu, X., Li, J., and Xi, J. (2017). Nickel–copper alloy encapsulated in graphitic carbon shells as electrocatalysts for hydrogen evolution reaction. *Adv. Energy Mat.* 8. doi:10.1002/aenm.201701759

Sidhureddy, B., Prins, S., Wen, J., Thiruppathi, A. R., Govindhan, M., and Chen, A. (2019). Synthesis and electrochemical study of mesoporous nickel-cobalt oxides for efficient oxygen reduction. *ACS Appl. Mat. Interfaces* 11, 18295–18304. doi:10.1021/acsami.8b22351

Sivakumar, P., Subramanian, P., Maiyalagan, T., Gedanken, A., and Schecter, A. (2019). Ternary nickel cobalt manganese spinel oxide nanoparticles as heterogeneous electrocatalysts for oxygen evolution and oxygen reduction reaction. *Mater. Chem. Phys.* 229, 190–196. doi:10.1016/j.matchemphys.2019.03.017

Song, Y., Peng, Y., Yao, S., Zhang, P., Wang, Y., Gu, J., et al. (2022). Co-POM@MOF-derivatives with trace cobalt content for highly efficient oxygen reduction. *Chin. Chem. Lett.* 33, 1047–1050. doi:10.1016/j.cclet.2021.08.045

Sood, P., Joshi, A., and Singh, M. (2022). A rare polyoxometalate cluster $[NiW_{12}O_{44}]^{14-}$ based solid as a pre-catalyst for efficient and long-term oxygen evolution. *Nanoscale Adv.* 4, 5015–5020. doi:10.1039/D2NA00646D

Sun, B., Wang, S., Li, X., Zhang, W., Li, J., Pan, Q., et al. (2023). Giant polyoxomolybdate clusters -derived bimetallic Ni/Mo2C catalyst for electrochemical

hydrogen evolution. *Int. J. Hydrogen Energy* 48, 9353–9361. doi:10.1016/j.ijhydene.2022.12.101

Sun, R.-M., Yao, Y.-Q., Wang, A.-J., Fang, K.-M., Zhang, L., and Feng, J.-J. (2021). One-step pyrolysis synthesis of nitrogen, manganese-codoped porous carbon encapsulated cobalt-iron nanoparticles with superior catalytic activity for oxygen reduction reaction. *J. Colloid Interface Sci.* 592, 405–415. doi:10.1016/j.jcis.2021.02.071

Sun, T., Wu, Q., Che, R., Bu, Y., Jiang, Y., Li, Y., et al. (2015). Alloyed Co–Mo nitride as high-performance electrocatalyst for oxygen reduction in acidic medium. *ACS Catal.* 5, 1857–1862. doi:10.1021/cs502029h

Swetha, J. V., Parse, H., Kakade, B., and Geetha, A. (2018). Morphology dependent facile synthesis of manganese oxide nanostructures for oxygen reduction reaction. *Solid State Ion.* 328, 1–7. doi:10.1016/j.ssi.2018.11.002

Tahir, M., Pan, L., Idrees, F., Zhang, X., Wang, L., Zou, J.-J., et al. (2017). Electrocatalytic oxygen evolution reaction for energy conversion and storage: a comprehensive review. *Nano Energy* 37, 136–157. doi:10.1016/j.nanoen.2017.05.022

Tong, Y., Liang, Y., Hu, Y., Shamsaei, E., Wei, J., Hao, Y., et al. (2020). Synthesis of ZIF/CNT nanonecklaces and their derived cobalt nanoparticles/N-doped carbon catalysts for oxygen reduction reaction. *J. Alloys Compd.* 816, 152684. doi:10.1016/j.jallcom.2019.152684

Tseng, C.-Y., Cheng, I.-C., and Chen, J.-Z. (2022). Low-pressure-plasma-processed NiFe-MOFs/nickel foam as an efficient electrocatalyst for oxygen evolution reaction. *Int. J. Hydrogen Energy* 47, 35990–35998. doi:10.1016/j.ijhydene.2022.08.179

Vij, V., Sultan, S., Harzandi, A. M., Meena, A., Tiwari, J. N., Lee, W.-G., et al. (2017). Nickel-based electrocatalysts for energy-related applications: oxygen reduction, oxygen Evolution, and hydrogen evolution reactions. *ACS Catal.* 7, 7196–7225. doi:10.1021/acscatal.7b01800

Wahab, A., Iqbal, N., Noor, T., Ashraf, S., Raza, M. A., Ahmad, A., et al. (2020). Thermally reduced mesoporous manganese MOF @reduced graphene oxide nanocomposite as bifunctional electrocatalyst for oxygen reduction and evolution. *RSC Adv.* 10, 27728–27742. doi:10.1039/D0RA04193A

Wang, C., Song, Y., Cong, W., Yan, Y., Wang, M., and Zhou, J. (2023). From surface loading to precise confinement of polyoxometalates for electrochemical energy storage. *Chin. Chem. Lett.* 34, 108194. doi:10.1016/j.cclet.2023.108194

Wang, C., Yang, H., Zhang, Y., and Wang, Q. (2019). NiFe alloy nanoparticles with hcp crystal structure stimulate superior oxygen evolution reaction electrocatalytic activity. *Angew. Chem. Int. Ed.* 58, 6099–6103. doi:10.1002/anie.201902446

Wang, H., Ma, N., Cao, Y., Yu, H., Zuo, J., Fan, W., et al. (2019). Cobalt and cobalt oxide supported on nitrogen-doped porous carbon as electrode materials for hydrogen evolution reaction. *Int. J. Hydrogen Energy* 44, 3649–3657. doi:10.1016/j.ijhydene.2018.12.107

Wang, L., Wang, A., Xue, Z.-Z., Hu, J.-X., Han, S.-D., and Wang, G.-M. (2022). Ultrathin two-dimensional polyoxometalate-based Metal–Organic framework nanosheets for efficient electrocatalytic hydrogen evolution. *Inorg. Chem.* 61, 18311–18317. doi:10.1021/acs.inorgchem.2c03431

Wang, X., Hou, X., Lee, H., Lu, L., Wu, X., Sun, L., et al. (2020). Copper selenide–derived copper oxide nanoplates as a durable and efficient electrocatalyst for oxygen evolution reaction. *Energy Technol.* 8. doi:10.1002/ente.202,000142

Wang, Z., Li, M., Fan, L., Han, J., and Xiong, Y. (2017). Fe/Ni-N-CNFs electrochemical catalyst for oxygen reduction reaction/oxygen evolution reaction in alkaline media. *Appl. Surf. Sci.* 401, 89–99. doi:10.1016/j.apsusc.2016.12.242

Wu, L.-Z., Zhou, X.-Y., Zeng, P.-C., Huang, J.-Y., Zhang, M.-D., and Qin, L. (2022). Hydrothermal synthesis of Ni(II) or Co(II)-based MOF for electrocatalytic hydrogen evolution. *Polyhedron* 225, 116035. doi:10.1016/j.poly.2022.116035

Wu, Y., Sun, R., and Cen, J. (2020). Facile synthesis of cobalt oxide as an efficient electrocatalyst for hydrogen evolution reaction. *Front. Chem.* 8, 386. doi:10.3389/fchem.2020.00386

Wu, Z., Vagin, M., Boyd, R., Ding, P., Pshyk, O., Greczynski, G., et al. (2023). Selectivity control of oxygen reduction reaction over mesoporous transition metal oxide catalysts for electrified purification technologies. *ACS Appl. Mat. Interfaces* 15, 26093–26103. doi:10.1021/acsami.3c01196

Wu, Z.-P., Lu, X. F., Zang, S.-Q., and Lou, X. W. (2020). Non-noble-metal-based electrocatalysts toward the oxygen evolution reaction. *Adv. Funct. Mat.* 30. doi:10.1002/adfm.201910274

Xing, X., Liu, R., Cao, K., Kaiser, U., Zhang, G., and Streb, C. (2018). Manganese vanadium Oxide–N-doped reduced graphene oxide composites as oxygen reduction and oxygen evolution electrocatalysts. *ACS Appl. Mat. Interfaces* 10, 44511–44517. doi:10.1021/acsami.8b16578

Xu, C., Li, J., Sun, D., Li, X., Wang, X., and Su, Z. (2021). Co/WC@NC electrocatalysts derived from polyoxometalates (POM) for efficient hydrogen evolution. *Nanotechnology* 32. doi:10.1088/1361-6528/ac084d

Xu, H., Li, F., Li, Z., Liu, Q., Li, B., Xu, L., et al. (2022). Research progress of metal oxide as cathode materials for hydrogen evolution. *Int. J. Electrochem. Sci.* 17, 221249. doi:10.20964/2022.12.49

Xu, S., Lv, C., He, T., Huang, Z., and Zhang, C. (2019). Amorphous film of cerium doped cobalt oxide as a highly efficient electrocatalyst for oxygen evolution reaction. *J. Mat. Chem. A* 7, 7526–7532. doi:10.1039/C9TA00061E

Xu, Y., Zhang, X., Liu, Y., Wang, R., Yang, Y., and Chen, J. (2023). A critical review of research progress for metal alloy materials in hydrogen evolution and oxygen evolution reaction. *Environ. Sci. Pollut. Res.* 30, 11302–11320. doi:10.1007/s11356-022-24728-5

Yan, Z., Liu, H., Hao, Z., Yu, M., Chen, X., and Chen, J. (2020). Electrodeposition of (hydro)oxides for an oxygen evolution electrode. *Chem. Sci.* 11, 10614–10625. doi:10.1039/D0SC01532F

Ye, C., Wang, Z., and Shen, Y. (2022). Preparation of iron-copper oxalates and oxides for the oxygen evolution reaction. *J. Electrochem. Soc.* 169, 064503. doi:10.1149/1945-7111/ac7259

Yu, L., Lin, J., Zheng, M., Chen, M., and Ding, Y. (2018). Homogeneous electrocatalytic water oxidation at neutral pH by a robust trinuclear copper(II)-substituted polyoxometalate. *Chem. Commun.* 54, 354–357. doi:10.1039/C7CC08301G

Yusibova, G., Assafrei, J.-M., Ping, K., Aruväli, J., Paiste, P., Käärik, M., et al. (2023). Bimetallic metal-organic-framework-derived porous cobalt manganese oxide bifunctional oxygen electrocatalyst. *J. Electroanal. Chem.* 930, 117161. doi:10.1016/j.jelechem.2023.117161

Zand, Z., Mohammadi, M. R., Sologubenko, A. S., Handschin, S., Bagheri, R., Chernev, P., et al. (2023). Oxygen evolution reaction by silicate-stabilized manganese oxide. *ACS Appl. Energy Mat.* 6, 1702–1713. doi:10.1021/acsaem.2c03587

Zang, D., Huang, Y., Li, Q., Tang, Y., and Wei, Y. (2019). Cu dendrites induced by the Anderson-type polyoxometalate NiMo6O24 as a promising electrocatalyst for enhanced hydrogen evolution. *Appl. Catal. B-Environ* 249, 163–171. doi:10.1016/j.apcatb.2019.02.039

Zeb, Z., Huang, Y., Chen, L., Zhou, W., Liao, M., Jiang, Y., et al. (2023). Comprehensive overview of polyoxometalates for electrocatalytic hydrogen evolution reaction. *Coord. Chem. Rev.* 482, 215058. doi:10.1016/j.ccr.2023.215058

Zeng, J., Chen, L., Li, L., Yang, W., Zou, H., and Chen, S. (2020). Effect of PEG on performance of NiMnO catalyst for hydrogen evolution reaction. *Front. Chem.* 8, 281. doi:10.3389/fchem.2020.00281

Zhai, H., Gao, T., Qi, T., Zhang, Y., Zeng, G., and Xiao, D. (2017). Iron–cobalt phosphomolybdate with high electrocatalytic activity for oxygen evolution reaction. *Chem. Asian J.* 12, 2694–2702. doi:10.1002/asia.201700905

Zhang, C., Hwang, S. Y., Trout, A., and Peng, Z. (2014). Solid-state chemistry-enabled scalable production of octahedral Pt-Ni alloy electrocatalyst for oxygen reduction reaction. *J. Am. Chem. Soc.* 136, 7805–7808. doi:10.1021/ja501293x

Zhang, C., Shen, X., Pan, Y., and Peng, Z. (2017). A review of Pt-based electrocatalysts for oxygen reduction reaction. *Front. Energy* 11, 268–285. doi:10.1007/s11708-017-0466-6

Zhang, L., Chen, S., Dai, Y., Shen, Z., Wei, M., Huang, R., et al. (2018). Copper–Palladium tetrapods with sharp tips as a superior catalyst for the oxygen reduction reaction. *ChemCatChem* 10, 925–930. doi:10.1002/cctc.201701578

Zhang, L., Pang, D., Cao, X., Ma, Y., Kou, Y., Liu, Z., et al. (2022a). Phosphorus modified hollow, porous Nickel-Cobalt oxides nanocubes with heterostructure for oxygen evolution reaction in alkaline. *J. Alloys Compd.* 925, 166338. doi:10.1016/j.jallcom.2022.166338

Zhang, M., Hu, D., Xu, Z., Liu, B., Boubeche, M., Chen, Z., et al. (2021). Facile synthesis of Ni-Co-Cu-metal organic frameworks electrocatalyst boosting for hydrogen evolution reaction. *J. Mat. Sci. Technol.* 72, 172–179. doi:10.1016/j.jmst.2020.09.028

Zhang, M.-c., Liu, M.-y., Yang, M.-x., Liu, X.-x., Shen, S.-y., Wu, J.-s., et al. (2023c). Copper-cobalt bimetallic conductive metal–organic frameworks as bifunctional oxygen electrocatalyst in alkaline and neutral media. *J. Solid State Chem.* 325, 124133. doi:10.1016/j.jssc.2023.124133

Zhang, Q., Wei, Z. D., Liu, C., Liu, X., Qi, X. Q., Chen, S. G., et al. (2012). Copper-doped cobalt oxide electrodes for oxygen evolution reaction prepared by magnetron sputtering. *Int. J. Hydrogen Energy* 37, 822–830. doi:10.1016/j.ijhydene.2011.04.051

Zhang, S., Oms, O., Hao, L., Liu, R., Wang, M., Zhang, Y., et al. (2017). High oxygen reduction reaction performances of cathode materials combining polyoxometalates, coordination complexes, and carboneous supports. *ACS Appl. Mat. Interfaces* 9, 38486–38498. doi:10.1021/acsami.7b10989

Zhang, X., Ding, K., Weng, B., Liu, S., Jin, W., Ji, X., et al. (2020). Coral-like carbon-wrapped NiCo alloys derived by emulsion aggregation strategy for efficient oxygen evolution reaction. *J. Colloid Interface Sci.* 573, 96–104. doi:10.1016/j.jcis.2020.03.124

Zhang, X., Li, Y., Guo, Y., Hu, A., Li, M., Hang, T., et al. (2019). 3D hierarchical nanostructured Ni–Co alloy electrodes on porous nickel for hydrogen evolution reaction. *Int. J. Hydrogen Energy* 44, 29946–29955. doi:10.1016/j.ijhydene.2019.09.193

Zhang, Z., Enze, F., Shuangqi, Z., Zhaojun, W., Wenzhi, Z., Ming, Z., et al. (2023a). A new two-fold interpenetrating metal-organic framework based on polyoxometalate: synthesis, structure, efficient hydrogen evolution and dye degradation. *J. Solid State Chem.* 323, 124066. doi:10.1016/j.jssc.2023.124066

Zhang, Z., Ran, J., Fan, E., Zhou, S., Chai, D.-F., Zhang, W., et al. (2023b). Mesoporous $CoMoO_4$ hollow tubes derived from POMOFs as efficient electrocatalyst for overall water splitting. *J. Alloys Compd.* 968, 172169. doi:10.1016/j.jallcom.2023.172169

Zhang, Z., Ran, J., Wu, Z., and Zhao, B. (2022). Hierarchical Ni modifed PW_{12} clusters *in situ* integrated on Ni foam for efcient alkaline hydrogen evolution. *J. Clust. Sci.* 34, 1475–1482. doi:10.1007/s10876-022-02318-2

Zhao, L., Gong, C., Chen, X., He, X., Chen, H., Du, X., et al. (2023). ZIF-67 derived Mo-CoS_2 nanoparticles embedded in hierarchically porous carbon hollow sphere for efficient overall water splitting" in. *Appl. Surf. Sci.* 623, 16184. doi:10.1016/j.apsusc.2023.157030

Zhao, S., Wang, Y., Dong, J., He, C.-T., Yin, H., An, P., et al. (2016). Ultrathin metal-organic framework nanosheets for electrocatalytic oxygen evolution. *Nat. Energy* 1, 16184–16210. doi:10.1038/nenergy.2016.184

Zhao, S., Zhao, X., Zhang, H., Li, J., and Zhu, Y. (2017). Covalent combination of polyoxometalate and graphitic carbon nitride for light-driven hydrogen peroxide production. *Nano Energy* 35, 405–414. doi:10.1016/j.nanoen.2017.04.017

Zhao, X., Pachfule, P., Li, S., Simke, J. R. J., Schimdt, J., and Arne, T. (2018). Bifunctional electrocatalysts for overall water splitting from an iron/nickel-based bimetallic metal-organic framework/dicyandiamide composite. *Angew. Chem. Int. Ed.* 57, 9059–9064. doi:10.1002/ange.201803136

Zheng, Y., Xu, X., Chen, J., and Wang, Q. (2021). Surface O_2-regulation on POM electrocatalyst to achieve accurate $2e^-/4e^-$ ORR control for H_2O_2 production and Zn-air battery assemble. *Appl. Catal. B-Environ.* 285, 119788. doi:10.1016/j.apcatb.2020.119788

Zhou, W., Huang, D.-D., Wu, Y.-P., Zhao, J., Wu, T., Zhang, J., et al. (2019). Stable hierarchical bimetal–organic nanostructures as high performance electrocatalysts for the oxygen evolution reaction. *Angew. Chem. Int. Ed.* 58, 4227–4231. doi:10.1002/anie.201813634

Zhou, W., Xue, Z., Liu, Q., Li, Y., Hu, J., and Li, G. (2020). Trimetallic MOF-74 films grown on Ni foam as bifunctional electrocatalysts for overall water splitting. *ChemSusChem* 13, 5647–5653. doi:10.1002/cssc.202001230

Zhu, X., Shi, X., Asiri, A. M., Luo, Y., and Sun, X. (2018). Efficient oxygen evolution electrocatalyzed by a Cu nanoparticle-embedded N-doped carbon nanowire array. *Inorg. Chem. Front.* 5, 1188–1192. doi:10.1039/C8QI00119G

frontiers | Frontiers in Energy Research

TYPE Original Research
PUBLISHED 01 July 2024
DOI 10.3389/fenrg.2024.1372916

OPEN ACCESS

EDITED BY
Haiping Yang,
Huazhong University of Science and Technology, China

REVIEWED BY
Zhaoxian Xu,
Nanjing University of Science and Technology, China
Caoxing Huang,
Nanjing Forestry University, China

*CORRESPONDENCE
Shishir P. S. Chundawat,
shishir.chundawat@rutgers.edu

‡These authors have contributed equally to this work

RECEIVED 18 January 2024
ACCEPTED 04 June 2024
PUBLISHED 01 July 2024

CITATION
Nemmaru B, Douglass J, Yarbrough JM, DeChellis A, Shankar S, Thokkadam A, Wang A and Chundawat SPS (2024), Supercharged cellulases show superior thermal stability and enhanced activity towards pretreated biomass and cellulose.
Front. Energy Res. 12:1372916.
doi: 10.3389/fenrg.2024.1372916

Supercharged cellulases show superior thermal stability and enhanced activity towards pretreated biomass and cellulose

Bhargava Nemmaru[1‡], Jenna Douglass[1‡], John M. Yarbrough[2], Antonio DeChellis[1], Srivatsan Shankar[1], Alina Thokkadam[1], Allan Wang[1] and Shishir P. S. Chundawat[1*]

[1]Department of Chemical and Biochemical Engineering, Rutgers the State University of New Jersey, Piscataway, NJ, United States, [2]National Renewable Energy Lab, Biosciences Center, Golden, CO, United States

Non-productive binding of cellulolytic enzymes to various plant cell wall components, such as lignin and cellulose, necessitates high enzyme loadings to achieve efficient conversion of pretreated lignocellulosic biomass to fermentable sugars. Protein supercharging was previously employed as one of the strategies to reduce non-productive binding to biomass. However, various questions remain unanswered regarding the hydrolysis kinetics of supercharged enzymes towards pretreated biomass substrates and the role played by enzyme interactions with individual cell wall polymers such as cellulose and xylan. In this study, CBM2a (from *Thermobifida fusca*) fused with endocellulase Cel5A (from *T. fusca*) was used as the model wild-type enzyme and CBM2a was supercharged using Rosetta, to obtain eight variants with net charges spanning −14 to +6. These enzymes were recombinantly expressed in *E. coli*, purified from cell lysates, and their hydrolytic activities were tested against pretreated biomass substrates (AFEX and EA treated corn stover). Although the wild-type enzyme showed greater activity compared to both negatively and positively supercharged enzymes towards pretreated biomass, thermal denaturation assays identified two negatively supercharged constructs that perform better than the wild-type enzyme (~3 to 4-fold difference in activity) upon thermal deactivation at higher temperatures. To better understand the causal factor of reduced supercharged enzyme activity towards AFEX corn stover, we performed hydrolysis assays on cellulose-I/xylan/pNPC, lignin inhibition assays, and thermal stability assays. Altogether, these assays showed that the negatively supercharged mutants were highly impacted by reduced activity towards xylan whereas the positively supercharged mutants showed dramatically reduced activity towards cellulose and xylan. It was identified that a combination of impaired cellulose binding and lower thermal stability was the cause of reduced hydrolytic activity of positively supercharged enzyme sub-group. Overall, this study demonstrated a systematic approach to investigate the behavior of supercharged enzymes and identified supercharged enzyme constructs that show superior activity at elevated temperatures. Future work will address the impact of parameters such as pH, salt concentration, and assay temperature on the hydrolytic activity and thermal stability of supercharged enzymes.

KEYWORDS

cellulase, carbohydrate-binding module, computational protein design, thermal stability, enzyme supercharging, lignin inhibition, non-productive binding, cellulosic biomass hydrolysis

Introduction

The future circular economy is based on conversion of wastes from a variety of streams to useful products that are currently produced from fossil fuels (Tuck et al., 2012; Ubando et al., 2020). Bioethanol is one such product that can be produced from lignocellulosic biomass such as agricultural residues (e.g., corn stover, wheat/rice straws, sugarcane bagasse) and forest residues (e.g., wood chips) (Chundawat et al., 2011a). The versatility of available biomass sources and the variety of bioproducts that can be generated, lends itself to development of customized conversion strategies tailor-made for various feedstocks in an integrated biorefinery (Kokossis et al., 2014; Maity, 2015). One conversion strategy that has received significant attention is the enzymatic conversion of cellulose and hemicellulose to C6/C5 based mixed sugar streams (Chundawat et al., 2011a), while employing tailored valorization strategies for extracted lignin based on the pretreatment strategy (Ragauskas et al., 2014; Wang et al., 2019). These sugars can be converted to a variety of platform chemicals such as ethanol, organic acids, or polymer-precursors in an integrated biorefinery (Takkellapati et al., 2018).

Various techno-economic analyses have been performed to assess the feasibility of producing bioethanol in a cost-effective and sustainable manner from biomass (Humbird et al., 2011; Scown et al., 2021). These studies have highlighted the role of high enzyme costs prohibiting commercialization of biofuels (Klein-Marcuschamer et al., 2012). Hence, there is a need to develop enzyme engineering strategies to improve the overall conversion of lignocellulosic biomass to reducing sugars, while reducing biomass recalcitrance via thermochemical pretreatment (McCann and Carpita, 2015; Holwerda et al., 2019). Non-productive binding of enzymes to lignin and cellulose along with limited enzyme accessibility to the substrate are considered the key factors that limit enzyme activity towards pretreated biomass substrates (Studer et al., 2011; Zeng et al., 2014; Strobel et al., 2015; Nemmaru et al., 2021). As a result, pretreatment efforts have focused on extraction of lignin for valorization while also improving overall enzyme accessibility to the residual polysaccharides (Narron et al., 2016; Galbe and Wallberg, 2019).

However, most modes of pretreatment technologies (e.g., dilute acid, extractive ammonia, alkaline, deacetylation and mechanical refining or DMR) only extract lignin partially, leaving behind residual lignin that can still deactivate or inhibit enzymes (Chundawat et al., 2011b; Chen et al., 2016). Lignin has been shown to deactivate cellulases through various mechanisms, the most significant of which involves protein conformational changes upon adsorption to lignin driven via hydrophobic interactions (Salas et al., 2013; Guo et al., 2014; Sammond et al., 2014). Broadly speaking, the three strategies that have been employed to reduce cellulase non-productive binding to lignin include: (i) addition of sacrificial proteins such as BSA (Yang and Wyman, 2006) or soy protein (Luo et al., 2019), (ii) inclusion of negatively charged groups such as acetyl groups on the surface of enzymes via chemical conjugation (Nordwald et al., 2014), and (iii) enzyme surface supercharging via computational re-design (Haarmeyer et al., 2017; Whitehead et al., 2017). Although the first two strategies have been shown to reduce lignin inhibition, they require an additional reagent (BSA or soy protein) or treatment procedure (acetylation), which increases the operating or capital cost of the bioconversion process. On the other hand, enzyme supercharging is an inexpensive method of genetically engineering enzymes to alter their surface electrostatic properties (Lawrence et al., 2007; Der et al., 2013).

Protein supercharging has been used to accomplish a variety of useful applications including but not limited to macromolecule or drug delivery into mammalian cells (Thompson et al., 2012), DNA detection and methylation analysis (Lei et al., 2014), complex coacervation with polyelectrolytes (Obermeyer et al., 2016), self-assembly into organized structures (Simon et al., 2019) such as protein nanocages (Sasaki et al., 2017) and Matryoshka-type structures (Beck et al., 2015) and encapsulation of cargo proteins into such higher-order structures (Azuma et al., 2016). Previously, we have utilized a supercharging strategy based on Rosetta (Das and Baker, 2008; Alford et al., 2017) and FoldIt standalone interface (Kleffner et al., 2017) for engineering green fluorescent protein (GFP) (Haarmeyer et al., 2017) and CelE (from *Ruminiclostridium thermocellum*) (Whitehead et al., 2017). We found that net negative charge was correlated weakly with reduced lignin binding capacity for GFP supercharged mutants, whereas the charge density was not found to have a clear impact on lignin binding capacity (Haarmeyer et al., 2017). In our follow-up study (Whitehead et al., 2017), a cellulase catalytic domain CelE was fused with CBM3a and both domains were individually negatively supercharged. Negatively supercharged CBM3a designs showed relatively improved hydrolysis yields on model amorphous cellulose in the presence of lignin, compared to the wild-type enzyme. However, all tested designs showed reduced absolute activity than wild-type controls on amorphous cellulose substrates (and with no data reported on pretreated lignocellulosic biomass) which was hypothesized to be due to reduced binding to cellulose induced by electrostatic repulsions.

Although these studies show proof-of-concept for the potential beneficial impact of cellulase negative supercharging on biomass hydrolysis, there remain multiple unanswered mechanistic questions to fully leverage the potential of enzyme supercharging for lignocellulosic biomass hydrolysis. Broadly speaking, there are three unanswered questions: (i) how does supercharging impact enzyme kinetics on pretreated biomass substrates? (ii) how can biomass hydrolysis performance of mutant enzymes be rationalized by understanding the activity and binding on individual polymers (cellulose, xylan, and lignin)? (iii) how does supercharging impact thermal stability and cellulase function at elevated temperatures? Here, we sought to address these questions in greater detail, using a model endocellulase enzyme Cel5A from *T. fusca (Thermobifida fusca)*, which has been well-characterized in our lab previously (Liu et al., 2020). *T. fusca* is a thermophilic microbe that secretes cellulase enzymes belonging primarily to glycosyl hydrolase (GH) families 5, 6, 9, and 48, with most cellulase CDs tethered to a type-A CBM2a (Wilson, 2004). Testing the protein supercharging strategy on a model Cel5A enzyme and its CBM2a from this cellulolytic enzyme system will also allow for extension of these design principles to other enzymes, potentially leading to a supercharged cellulase mixture with superior performance.

More specifically, we computationally designed a library of eight CBM2a designs spanning a net charge range of −14 to +6. These

CBM2a designs were fused with the Cel5A catalytic domain and green fluorescent protein (GFP) separately, to study the hydrolysis activity and binding behavior of the constructs on a variety of substrates, respectively. Firstly, we characterized the hydrolysis yields of CBM2a-Cel5A fusion constructs at various reaction times (2–24 h) on ammonia fiber expansion (AFEX) and extractive ammonia (EA) pretreated corn stover substrates. To further rationalize the activity of supercharged enzymes towards pretreated biomass substrates, we assayed enzyme activity towards cellulosic substrates and xylan. Moreover, we performed binding assays to study the binding of GFP-CBM2a fusion constructs to cellulose using previously established QCM-D assay procedures (Haarmeyer et al., 2017; Nemmaru et al., 2021). We followed it up with thermal shift assays to measure melting temperatures of supercharged enzymes and tested enzyme activity upon thermal deactivation at elevated temperatures. Overall, this study presents a rational approach to understand the mechanistic underpinnings of supercharged enzyme action on pretreated biomass substrates by deconvoluting the impact of cellulose and xylan hydrolysis and thermal stability.

Experimental section

Reagents

AFEX and EA pretreated corn stover were prepared and provided in kind by Dr. Rebecca Ong's lab (Michigan Technological University, Houghton) and Bruce Dale's lab (Michigan State University, East Lansing), according to previously established protocols (Da Costa Sousa et al., 2016; Sousa et al., 2019; Chundawat et al., 2020). Avicel (PH 101, Sigma-Aldrich, St Louis) was used to prepare cellulose-III allomorph with the following pretreatment conditions (90°C, 6:1 anhydrous liquid ammonia to cellulose loading, and 30 min of total residence time) and phosphoric acid swollen cellulose (PASC) as described previously (Chundawat et al., 2011c). Sarvada Chipkar from the Ong lab kindly prepared and provided cellulose-III used in this study. Lignin extracted from corn stover was prepared using the organosolv extraction process (Bozell et al., 2011) and kindly provided by Stuart Black of the National Renewable Energy Laboratory (NREL). All other chemicals and analytical reagents were procured either from Fisher Scientific or Sigma Aldrich, or as noted in the relevant experimental section.

Mutant energy scoring using rosetta

Creation of computational designs carrying a certain net charge necessitated computing the change in energy scores upon mutation of a native amino acid residue to either a positively charged (K, R) or a negatively charged residue (D, E). These mutations were scored using Rosetta. The wild-type protein PDB file is obtained either via homology modeling using Rosetta CM[49] or via the protein data bank (Burley et al., 2021). PyMOL (Schrodinger) was used to generate the desired mutation in amino acid sequence of a given protein and exported as a PDB file that represents the mutated protein. Customized scripts were developed in Rosetta to perform fast relax (Khatib et al., 2011) of any input PDB file. PDB files of both the wild-type and mutated proteins were relaxed separately using ten fast relax operations at a time. Each round of energy minimization enabled by ten fast relax operations was repeated until the Rosetta energy score of protein equilibrated and did not vary by more than 0.1 Rosetta Energy Units (REU) between one round of energy minimization (comprising of 10 fast relaxes) to another. The mutation energy score for a given mutation was calculated by measuring the difference between Rosetta energy scores of the wild-type protein and the mutant after energy minimization.

Plasmid generation, protein expression and purification

Thermobifida fusca native Cel5A (Watson et al., 2002; Jung et al., 2003) (UniprotKB–Q01786) gene was cloned into pET28a(+) (Novagen) and was kindly provided by Nathan Kruer-Zerhusen (from late Prof. David Wilson's lab at Cornell University). An N-terminal 8X His tag was inserted and the native signal peptide removed from the original gene construct. The gene was then cloned into our in-house expression vector pEC to optimize protein expression yields as described previously (Blommel et al., 2009; Lim et al., 2014). The plasmid maps for pEC-CBM2a-Cel5A and pEC-GFP-CBM2a are provided in Supplementary Figures S1, S2 respectively. The full nucleotide sequences with color coding for each gene segment are reported in the Supplementary Material titled SI_Appendix_Sequences.docx. CBM2a mutant designs were ordered from Integrated DNA Technologies, Inc (IDT) as custom-synthesized gBlocks. These CBM2a design gBlocks were then swapped with wild-type CBM2a to generate mutant CBM2a-Cel5A fusion constructs using standard sequence and ligation independent cloning (SLIC) protocols. A similar approach was used to insert CBM2a designs into previously reported pEC-GFP-CBM vector (Lim et al., 2014). Molecular cloning for *T. fusca* β-glucosidase (UniprotKB–Q9LAV5) gene These colonies were then inoculated in LB medium and grown overnight to prepare 20% glycerol stocks for long-term storage at −80°C. These glycerol stocks were then used to inoculate 25 mL of LB media with 50 µg/mL kanamycin and incubated at 37°C, 200 rpm for 16 h. These overnight cultures were then transferred to 500 mL auto-induction medium (TB + G) (Studier, 2005) and incubated at 37°C, 200 rpm for 6 h to allow optical density to reach the exponential regime. Protein expression was then induced by reducing the temperature to 25°C for 24 h at 200 rpm. Cell pellets were then harvested using Beckman Coulter centrifuge and JA-14 rotor by spinning the liquid cultures in 250 mL plastic bottles at 30,100 g for 10 min at 4°C. All the cell culturing experiments were performed using an Eppendorf Innova™ incubator shaker. Cell pellets were lysed using 15 mL cell lysis buffer (20 mM phosphate buffer, 500 mM NaCl, 20% (v/v) glycerol, pH 7.4), 0.5 mM Benzamidine (Calbiochem 199,001), 200 µL protease inhibitor cocktail (1 µM E-64 (Sigma Aldrich E3132), 15 µL lysozyme (Sigma Aldrich, USA) and 1 mM EDTA (Fisher Scientific BP1201)) for every 3 g wet cell pellet. The cell lysis mixture was sonicated using Misonix™ sonicator 3,000 for 5 min of total

process time at 4.5 output level and specified pulse settings to avoid sample overheating (pulse-on time: 10 s and pulse-off time: 30 s). An Eppendorf centrifuge (5810R) with F-34-6-28 rotor was then used to separate the cell lysis extract from insoluble cellular debris at 15,500 g, 4°C for 45 min. Immobilized metal affinity chromatography (IMAC) using His-Trap FF Ni^{+2}-NTA column (GE Healthcare) attached to BioRad™ NGC system, was then performed to purify the his-tagged proteins of interest from the background of cell lysate proteins. Briefly, there were three steps involved during IMAC purification: 1. equilibration of column in buffer A (100 mM MOPS, 500 mM NaCl, 10 mM imidazole, pH 7.4) at 5 mL/min for five column volumes, 2. Soluble cell lysate loading at 2 mL/min, and 3. His-tagged protein elution using buffer B (100 mM MOPS, 500 mM NaCl, 500 mM imidazole, pH 7.4). The purity of eluted proteins was validated using SDS-PAGE before buffer exchange into 10 mM sodium acetate (pH 5.5) buffer for long-term storage after flash freezing at −80 °C and/or follow-on activity characterization.

Pretreated lignocellulosic biomass hydrolysis assays

AFEX and EA corn stover (milled to 0.5 mm) were suspended in deionized water to obtain slurries of 25 g/L total solids concentration. All biomass hydrolysis assays were performed in 0.2-mL round-bottomed microplates (PlateOne™), with at least four replicates for each reaction condition. Reactions quenched at different time points (2, 6 and 24 h) were performed in different microplates. Each reaction was composed of 80 µL biomass slurry (25 g/L), 20 µL sodium acetate buffer (0.5 M), 50 µL cellulase enzyme (at appropriate concentration), 25 µL β-glucosidase (at appropriate concentration), and 25 µL of deionized water to make up the total reaction volume to 200 µL. For reaction blanks, the enzyme solutions were replaced with deionized water while biomass slurry and buffer volumes remained the same. The cellulase enzyme loading was maintained at 120 nmol per Gram biomass substrate and the β-glucosidase enzyme loading was maintained at 12 nmol per Gram biomass substrate (leading to 10% of cellulase enzyme concentration). Since supercharged constructs have varying molecular weights, a molar basis was used for all hydrolysis assays to keep concentrations between enzymes normalized. A conversion of enzyme loading for each concentration to a mass basis can be viewed in the Supplementary Appendix SA1. Upon addition of all the requisite reaction components, the microplates were covered with a plate mat, sealed with packaging tape, and incubated at 60°C for the specified time duration (2, six or 24 h) with end-over-end mixing at 5 rpm in a VWR hybridization oven. Upon reaction completion, the microplates were centrifuged at 3,900 rpm for 10 min at 4°C to separate the soluble supernatant (comprised of soluble reducing sugars) from insoluble biomass substrate. The supernatants were then recovered and dinitrosalicylic acid (DNS) assays were performed as previously described to estimate total soluble reducing sugars (Liu et al., 2020). This data was fitted to a two-parameter kinetic model that was previously deployed to study reaction kinetics of *T. fusca* cellulases on biomass substrates (Kostylev and Wilson, 2013). Origin software was used to perform the curve fitting analysis and obtain the pseudo-kinetic time-dependent parameters 'A' and 'b' which represent the net activity of bound enzyme and the time-dependent ability of enzyme to overcome recalcitrance, respectively. An increase in b might indicate the ability of enzyme to sample new substrate sites as reaction progresses, thereby reducing substrate recalcitrance.

Cellulose hydrolysis assays and lignin inhibition assays

The cellulose hydrolysis assays were performed in a similar manner as biomass hydrolysis assays, except for the reaction composition. Avicel PH101 derived cellulose-I and cellulose-III were suspended in deionized water to form slurries of 100 g/L total solids concentration. A 0.2-mL round-bottomed microplate (PlateOne™) was used for each discrete reaction timepoint (2, 6 and 24 h) and each reaction was performed with at least four replicates. Each reaction was composed of 40 µL cellulose slurry (100 g/L), 20 µL sodium acetate buffer (0.5 M, pH 5.5), 50 µL cellulase enzyme (at appropriate concentration), 25 µL β-glucosidase (at appropriate concentration) and 65 µL of deionized water to make up the total reaction volume to 200 µL. The cellulase enzyme loading was maintained at 120 nmol per Gram biomass substrate and the β-glucosidase enzyme loading was maintained at 12 nmol per Gram biomass substrate (leading to 10% of cellulase enzyme concentration). Upon reaction completion, supernatants were removed, and DNS assays were performed as described in the previous section on biomass hydrolysis assays. The reaction mixture for lignin inhibition assays was composed of 20 µL cellulose slurry (100 g/L), 40 µL lignin slurry (20 g/L), 20 µL sodium acetate buffer (0.5 M, pH 5.5), 50 µL cellulase enzyme (at appropriate concentration), 25 µL β-glucosidase (at appropriate concentration) and 65 µL of deionized water to make up the total reaction volume to 200 µL. The enzyme loadings and all the follow-on steps were conducted in a similar manner to cellulose hydrolysis assays. 24 h was used as the preferred reaction time for lignin inhibition assays, owing to the prevalence of lignin and cellulose non-productive binding at longer reaction times.

Xylan hydrolysis assays

The xylan hydrolysis assays were performed in a similar manner as biomass hydrolysis assays, with a slight change to the reaction composition. Beechwood xylan suspended in deionized water to form slurries of 100 g/L total solids concentration. Equipment, procedures and reaction timepoint remained the same. Each reaction was composed of 20 µL xylan slurry (100 g/L), 20 µL sodium acetate buffer (0.5 M, pH 5.5), 50 µL cellulase enzyme (at appropriate concentration), 25 µL β-glucosidase (at appropriate concentration) and 85 µL of deionized water to make up the total reaction volume to 200 µL. The cellulase enzyme loading was maintained at 120 nmol per Gram xylan substrate and the β-glucosidase enzyme loading was maintained at 12 nmol per Gram biomass substrate (leading to 10% of cellulase enzyme concentration). All the follow-on steps were conducted in a similar manner to biomass hydrolysis assays.

pNPC kinetic hydrolysis assays

The pNPC hydrolysis assays were adapted from previously established protocols laid out in Whitehead et al. (2017). The assay was conducted in a 0.2-mL flat-bottomed clear microplate (PlateOne™) and the enzyme activity was tested at pH 5.5 and pH 7.5. Each reaction was composed of 100 µL pNPC slurry (2 mM), 7.5 µL 1 M sodium acetate buffer pH 5.5 or 7.5 µL 1 M MOPS (pH 7.5), 42.5 µL cellulase enzyme (at an appropriate concentration to constitute five ug of enzyme per g pNPC). The reaction was performed for a duration of up to 700 min and the progress of hydrolysis reaction was tracked via pNP absorbance through a UV-vis spectrophotometer.

Quartz crystal microbalance with dissipation (QCM-D) based binding assays

Preparation of cellulose and lignin films for characterization of GFP-CBM binding, was performed as described elsewhere (Brunecky et al., 2020; Nemmaru et al., 2021). Quartz sensors functionalized with nanocrystalline cellulose or lignin were mounted on the sensor holder of QSense E4 instrument and equilibrated with buffer (50 mM sodium acetate, pH 5.5 with 100 mM NaCl) for 10 min at a flow rate of 100 µL/min using a peristaltic pump. The films were left to swell in buffer overnight and the films were considered stable if the third harmonic reached a stable baseline after overnight incubation. GFP-CBM2a protein stocks were then diluted to a concentration of 2.5 µM using 50 mM sodium acetate (pH 5.5) and flown over the sensors at a flow rate of 100 µL/min for 10–15 min until the system reached saturation, as observed by the third harmonic. The system was then allowed to equilibrate for at least 30 min and protein unbinding was then tracked by flowing buffer (50 mM sodium acetate, pH 5.5 with 100 mM NaCl) over the sensors at a flow rate of 100 µL/min for at least 30 min. Data analysis for QCM-D traces was performed as described previously (Nemmaru et al., 2021). However, for lignin, binding was observed to be mostly irreversible (Gao et al., 2014) and hence, only the maximum number of binding sites and percent irreversible protein bound, calculated based on the maximum number of binding sites and the amount of protein bound towards the end of unbinding regime.

Pretreated biomass/cellulose hydrolysis assays with thermally treated enzymes

This assay was performed in a similar way to the pretreated lignocellulosic biomass hydrolysis assays and the cellulose hydrolysis assays described above. However, the enzyme dilution used in those assay procedures was exposed to 70°C in an Eppendorf thermocycler for 30 min followed by 10°C for 10 min directly before being added into the microplate for reaction. The reaction was incubated for 60°C for 24 h only. The initial assay used all the enzyme designs with a denaturation temperature of 70°C. From this the thermally stable enzyme designs, D1, D2 and the WT were exposed to temperatures of 73°C, 76°C, and 79°C for 30 min prior to incubation at 60°C for 24 h.

Cellulase thermal shift assay

The protocol for thermal shift assays was similar to that reported previously (Whitehead et al., 2017). Briefly, 5 µL 200X SYPRO reagent, 5 µL 0.5 M sodium acetate buffer (pH 5.5), enzyme dilution to make up an effective concentration of 5 µM and deionized water to make up the total volume to 50 µL were added to MicroAmp™ EnduraPlate™ 96-well clear microplate (Applied Biosystems™). QuantStudio3 (Applied Biosystems™) was then used to measure the fluorescence using the channel allocated to FAM dye (excitation: 470 nm, emission: 520 nm) under a temperature ramp from 25°C to 99°C at a rate of 0.04°C per second. The melting curves obtained were then analyzed using an open-source tool called SimpleDSFViewer (Sun et al., 2020).

Results and discussion

Selection of a wild-type construct from CBM family two for supercharging

CBM family two comprises a large collection of mostly bacterial CBMs, with ~11,000 entries and 10 solved structures. *T. fusca*, an industrially relevant cellulolytic microbe, secretes multi-modular cellulase enzymes comprised of CBMs from family 2. Cel5A (endocellulase from GH5) was chosen as the model cellulase and tested for expression and activity, both with its native CBM2a and CBM2a from exocellulase Cel6B. The objective was to fuse each CBM to the Cel5A catalytic domain and identify the fusion enzyme that shows greater thermal stability as a target for supercharging. These two fusion cellulases are labeled as CBM2a (native) Cel5A and CBM2a (Cel6B) Cel5A from hereon. Supplementary Figure S3 shows the hydrolytic activity of both enzyme constructs towards AFEX corn stover and cellulose-I. Surprisingly, CBM2a (Cel6B) Cel5A showed 1.8 to 2.5-fold improvement in activity towards both substrates compared to CBM2a (native) Cel5A, across all timepoints considered. This experiment was followed up with a measurement of enzyme activity upon thermal treatment at 70°C, as reported in Supplementary Figure S4. CBM2a (Cel6B) Cel5A loses ~60% of activity towards both substrates (AFEX corn stover and cellulose-I) whereas CBM2a (native) Cel5A loses up to ~90% activity. The fusion of the cellulose binding module CBM2a from Cel6B with the catalytic domain from Cel5A showed the greatest hydrolytic activity and thermal resistance. As a result, we chose CBM2a (Cel6B) Cel5A as the wild-type construct to be engineered in this study. CBM2a (Cel6B) Cel5A will be referred to as wild-type CBM2a Cel5A or WT for the remainder of this paper.

Design of supercharged CBM2a library

A homology model was constructed for the target CBM2a (Cel6B) wild-type protein using Rosetta CM tool (Song et al., 2013) based on templates from CBM family 2a with at least 50% sequence identity.

Surface residues were then identified using an appropriate residue selector in Rosetta. Previous studies have shown that 10% of the total amino acid sequence length of globular proteins can be mutated using the supercharging strategy, while still allowing the proteins to fold properly (Lawrence et al., 2007). Given that CBM2a is 100 amino acids long and has a net charge of −4, we sought to generate designs that spanned a net charge range of −14 to +6 using 10 mutations of polar uncharged amino acid residues. Overall, 31 polar uncharged amino acid residues were identified on the protein surface and these residues were scored individually for mutations to lysine (K), arginine (R), aspartic acid (D) and glutamic acid (E).

The mutation energy scores were then averaged for any given position and surface polar uncharged residues were sorted based on these average mutation energy scores. From the original pool of 31 polar uncharged residues, three categories of residues were considered immutable due to their potential implications for protein folding or interaction with cellulose as follows: 1. residues within 10 Å distance from evolutionarily conserved planar aromatic residues (Georgelis et al., 2012) essential for CBM function, 2. residues on the CBM binding face (Nimlos et al., 2012), and 3. residues with a positive average mutation energy score (predicting structural instability upon mutation). Upon exclusion of these three categories of residues, 11 mutable polar uncharged residues were identified and sorted into two spatially distinct clusters and sorted based on their mutation energy scores from highest to lowest. The individual and average mutation energy scores of mutable residues are reported in Supplementary Table S1. Eight designs were then generated to have net charges of −14 (D1), −12 (D2), −10 (D3), −8 (D4), −6 (D5), −2 (D6), +2 (D7) and +6 (D8) as shown in Figure 1. Negatively supercharged space was sampled more granularly because negative supercharging has been shown to reduce lignin inhibition in our previous work (Whitehead et al., 2017). The mutations used to generate each design, are reported in Supplementary Table S2 whereas the full amino acid sequence for wild-type CBM2a with these mutable residues highlighted in red font, are reported in a separate file titled 'SI_Appendix_Sequences.docx'.

Hydrolytic activities of supercharged CBM2a-Cel5A constructs towards pretreated biomass

All CBM2a-Cel5a designs were cloned, expressed, and purified as described in the experimental procedures section. The hydrolytic activity of the supercharged and wild type cellulases were tested against pretreated biomass, namely, AFEX corn stover. The hydrolysis yields are reported in the form of glucose equivalent reducing sugars released at three time points (2 h, 6 h and 24 h) resulting in reaction progress curves shown in Figure 2. Based on the raw hydrolysis data reported in Figure 2A, the negatively supercharged and positively supercharged mutants were separated into two groups and their average hydrolysis yields were reported in Figure 2B.

From Figure 2A, it is evident that the wild-type enzyme (WT) has the highest activity compared to any supercharged mutant. The wild-type showed ~1.2 to 1.8-fold greater activity compared to negatively supercharged mutants and ~1.5 to 24.1-fold greater activity compared to positively charged mutants. D6 was an outlier amongst the positively supercharged group, showing higher activity compared to D7 and D8 across all timepoints considered. Similar trends were observed with EA corn stover, another model pretreated biomass substrate, for which the hydrolysis yields are reported in a similar format in Supplementary Figure S5. To further compare the hydrolysis yields of mutants on AFEX and EA corn stover, T-tests were performed between each mutant pair within the negatively supercharged (D1-D5) and positively supercharged (D6-D8) groups, as reported in Supplementary Table S3. On AFEX corn stover, mutants within D1–D5 group were found to not show statistically significant differences at 2 h although certain mutant pairs showed $p < 0.05$ at 6 h and 24 h. Within D6–D8, D6 showed statistically significant differences from D7 and D8 at most timepoints. To understand the behavior of each group compared to the wild-type, the activities of negatively supercharged mutants (D1–D5) and positively supercharged mutants (D6–D8) were averaged separately and reported in Figure 2B. Positively supercharged mutants ranked the least as a group, at every time point considered, followed by negatively supercharged mutants with the wild type consistently ranking higher than both.

The reaction kinetic data on AFEX and EA corn stover for each individual mutant was then fit to a two-parameter model as described previously (shown in Supplementary Table S4). Parameter 'A' represents the net activity of the bound enzyme whereas parameter 'b' represents the enzyme's ability to reduce biomass recalcitrance over time. On AFEX corn stover, the wild-type showed ~0.8 to 1.5-fold improvement in parameter 'A' over the negatively supercharged enzymes and ~2 to 6-fold improvement over positively supercharged enzymes. D1 was the only mutant to show an improvement in 'A' over wild-type indicating that the net activity of bound enzyme for this mutant may have been greater than the wild-type but the mutant perhaps lacks the ability to access new binding sites that can reduce recalcitrance of the enzyme. Similar trends were observed for EA corn stover, with D1 being the only mutant to show improvement in A.

Since electrostatic interactions between supercharged mutants and biomass may be influenced by the presence of salt, a hydrolysis assay was run at the 2-h timepoint in the presence of 100 mM NaCl (see Supplementary Figure S6). The presence of salt showed little to no impact for most mutants, except in the case of D7 on AFEX corn stover for which the presence of salt improved activity by more than 2-folds.

Overall, the wild type showed improved activity compared to all the supercharged mutants. The trends observed for the different cellulases towards pretreated biomass could arise from a combination of various factors: (i) cellulolytic activity, (ii) xylanolytic activity, (iii) lignin interactions, or (iv) thermal stability. We designed specific assays to understand each of these contributions to pretreated biomass hydrolysis as discussed below.

Hydrolytic activities of supercharged CBM2a-Cel5A constructs towards cellulosic substrates

Hydrolysis yields for cellulose-I were measured in terms of reducing sugar release at three time points (2 h, 6 h and 24 h) using 120 nmol enzyme per Gram substrate loading, resulting in

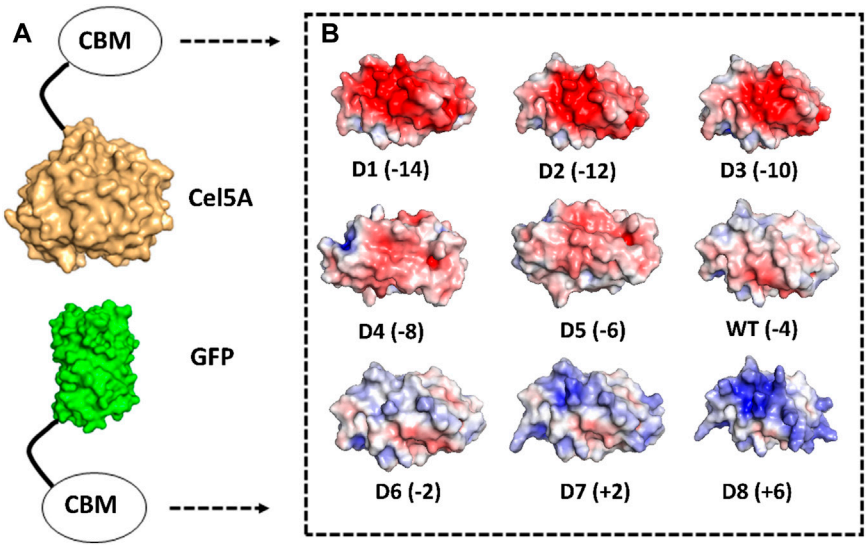

FIGURE 1
Computational design of supercharged CBM2a mutants and generation of fusion protein constructs. Rosetta was used to identify amino acids on the surface of CBM2a wild-type protein which are amenable to positively charged (K, R) or negatively charged (D, E) amino acid mutations to achieve a target net charge spanning the −14 to +6 range. **(A)** CBM2a designs were fused with Cel5A and GFP separately. **(B)** Electrostatic potential maps of the 8 CBM2a designs and their wild-type (represented as WT) are generated using APBS Electrostatics Tool in PyMOL. The name of each construct (D1–D8 and WT) is followed by the net charge of each design in parenthesis.

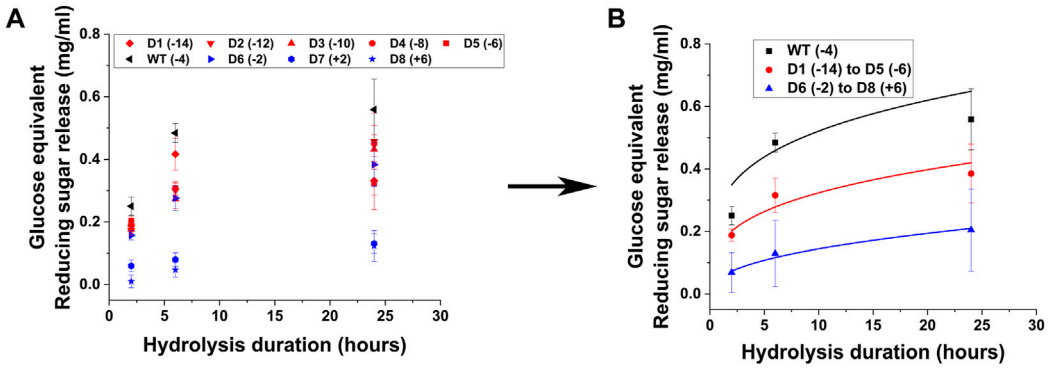

FIGURE 2
Hydrolytic activity of supercharged cellulases towards AFEX Corn Stover. 80 µL of 25 g/L AFEX Corn Stover was hydrolyzed using an enzyme loading of 120 nmol CBM2a Cel5A fusion enzyme per Gram biomass substrate with 12 nmol β-glucosidase enzyme (10% of cellulase loading) per Gram biomass substrate for reaction times of 2, 6, and 24 hrs. The solubilized reducing sugar concentrations in the supernatant after hydrolysis were determined by the DNS assay **(A)** Glucose equivalent reducing sugar release (mg/mL) as a function of time (2, 6, and 24 h) for the hydrolysis of AFEX Corn Stover by D1–D8 CBM2a Cel5A and WT CBM2a Cel5A. Error bars represent standard deviation from the mean, based on at least four replicates. **(B)** Based on the data reported in **(A)**, CBM2a Cel5A fusion constructs with negatively supercharged CBMs (D1–D5) were grouped together and average hydrolysis yields were obtained for the group, with the error bars representing standard deviation from the mean. Similarly, CBM2a-Cel5A fusion constructs with positively supercharged CBMs (D6–D8) were grouped together and average hydrolysis yields were obtained. Trend curves have been added to represent the kinetic profiles of the hydrolysis reaction. Wild-type CBM2a-Cel5A is referred to as WT throughout this figure.

reaction progress curves shown in Figure 3A for Avicel Cellulose-I and Supplementary Figure S7A for Avicel Cellulose-III. Cellulose-I and Cellulose-III were chosen as the target substrates because these are the predominant cellulose allomorphs that comprise AFEX corn stover and EA corn stover respectively. The wild-type showed activity that was ~0.8 to 1.2-folds compared to negatively supercharged mutants (D1–D5) and ~0.9 to 4.5-folds that of positively supercharged mutants (D6–D8). Unlike the trends observed towards pretreated biomass in the previous section, negatively supercharged mutants (D1–D5) show either increased or comparable activities to the wild type. On cellulose-III, most negatively supercharged mutants performed better than the wildtype, as observed in Supplementary Figure S7A. T-tests revealed that there were no statistically significant differences between each mutant pair in the negatively supercharged group (D1–D5) or within the negatively supercharged group (D6–D8), with a few exceptions (see Supplementary Table S5). To understand the behavior of each group compared to the wild-type, the activities of negatively supercharged mutants (D1–D5) and positively supercharged mutants (D6–D8) were averaged separately and

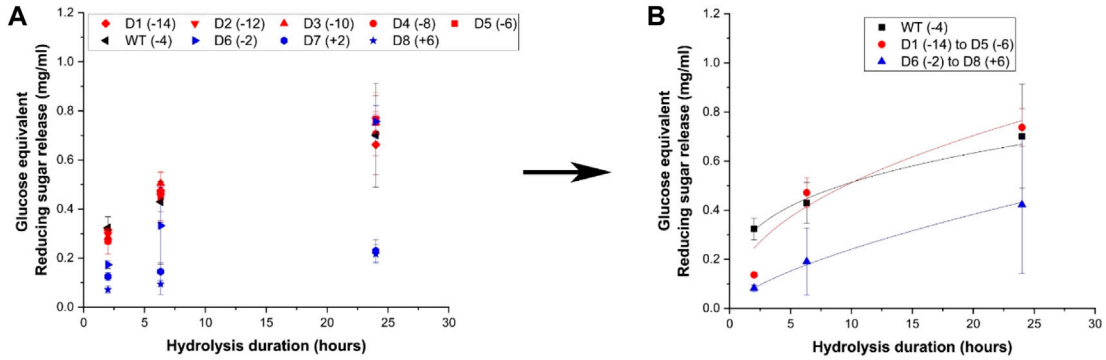

FIGURE 3
Hydrolytic activity of supercharged cellulases towards Avicel cellulose-I. 40 µL of 100 g/L Avicel cellulose-I substrate was hydrolyzed using an enzyme loading of 120 nmol CBM2a Cel5A fusion enzyme per Gram cellulose substrate supplemented with 12 nmol of β-glucosidase enzyme (10% of cellulase loading) per Gram cellulose substrate for reaction times of 2, 6, and 24 hrs. The solubilized reducing sugar concentrations in the supernatant after hydrolysis were determined by the DNS assay **(A)** Glucose equivalent reducing sugar release (mg/mL) as a function of time (2, 6, and 24 h) for the hydrolysis of Cellulose-I by D1–D8 CBM2a Cel5A and WT CBM2a Cel5A. Error bars represent standard deviation from the mean, based on at least four replicates. **(B)** Based on the data reported in **(A)**, CBM2a Cel5A fusion constructs with negatively supercharged CBMs (D1–D5) were grouped together and average hydrolysis yields were obtained for the group, with the error bars representing standard deviation from the mean. Similarly, CBM2a-Cel5A fusion constructs with positively supercharged CBMs (D6–D8) were grouped together and average hydrolysis yields were obtained. Trend curves have been added to represent the kinetic profiles of the hydrolysis reaction. Wild-type CBM2a-Cel5A is referred to as WT throughout this figure.

reported in Figure 3B and Supplementary Figure S7B for Cellulose-I and Cellulose-III respectively. The two-parameter kinetic model fits, achieved as described for biomass, are reported for cellulose-I and cellulose-III in Supplementary Table S6.

Overall, positively supercharged mutants (D6–D8) consistently ranked below wild type and negatively supercharged mutants (D1–D5) across both substrates. On the other hand, negatively supercharged mutants showed comparable performance to wild type in the case of cellulose-I and outperformed the wild type in the case of Cellulose-III. Combining these results along with trends observed towards pretreated biomass substrates in the previous section, it is evident that the reduced activity of negatively supercharged mutants towards AFEX and EA corn stover may be resulting from one of the other factors such as xylanolytic activity, interactions with lignin or thermal stability. Similar results were obtained in previous works where a decrease in hydrolytic activity towards PASC was observed for negatively supercharged mutants (Whitehead et al., 2017). However, the lower activity of positively supercharged mutants towards cellulose may be one of the causal factors behind their overall lowered activity towards pretreated biomass.

Hydrolytic activities of supercharged CBM2a-Cel5A constructs towards xylan and pNPC

Certain cellulases like Cel5A are multifunctional and exhibit activity on xylan, thus the mutants were screened for their activity towards beechwood xylan and the raw data is reported in Figure 4A These results show that the negatively supercharged mutants show reduced activity compared to the wild-type, with the difference becoming more prominent at longer hydrolysis durations such as 24 h. Upon averaging the activities of all supercharged mutants of the same type (negative (D1–D5) vs. positive (D6–D8)) as shown in Figure 4B, it is evident that the negatively supercharged mutants collectively show greater than 1.5-fold reduction in activity. The positively supercharged mutants also show a reduction in activity compared to the wild-type but their activity is very similar to that of negatively supercharged mutants. This is unlike the case of insoluble substrates such as AFEX corn stover or cellulose-I where the positively supercharged mutants showed demonstrably reduced activity compared to the wildtype and negatively charged subgroup. Surprisingly, the mutant D8 showed improved activity compared to the wild-type, despite showing drastically activity amongst the cohort, towards AFEX corn stover and cellulose-I. This trend could likely be due to the reduced significance of CBM function for soluble substrates such as Xylan. Summarizing the results of activity towards biomass, cellulose and xylan, it can be inferred that the reduced activity of negatively supercharged mutants (D1–D5) towards biomass arises predominantly from reduced activity towards Xylan. Positively supercharged mutants D7 and D8 show consistently reduced activity towards all substrates tested although they show activity similar to that of the.

To validate these trends towards another model soluble substrate, we tested hydrolytic activity towards pNPC (see Supplementary Figure S8). This assay was originally designed to test activity at pH 7.5 (as reported by Whitehead et al. (2017)); however, we adapted the assay to pH 5.5 to keep the pH consistent across all substrates tested in this study. The raw data reported in Supplementary Figure S8A was analyzed further to obtain averages for each individual group (D1–D5 and D6–D8), which is reported in Supplementary Figure S8B. At pH 5.5, all mutants show a negligible reduction in activity towards pNPC (Supplementary Figure S8B) whereas at pH 7.5, negatively supercharged mutants on average showed improved activity compared to the wild-type (Supplementary Figure S8D). Mutant D8 was amongst the top performers in the pNPC assay at pH 7.5, performing distinctly better than the other positively supercharged enzymes. Overall, the activity towards pNPC shows that in the case of positively supercharged mutants (D7 and D8 specifically), the structural integrity of cellulase enzyme may not have been affected in an adverse manner and that the reduced activities observed towards pretreated corn stover or cellulosic substrates may be a result of

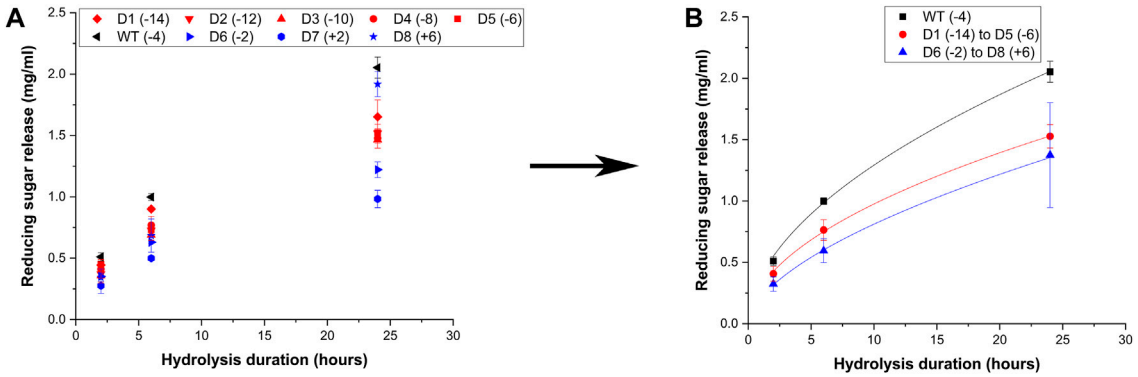

FIGURE 4
Hydrolytic activity of supercharged cellulases towards Beechwood xylan. 20 µL of 100 g/L Beechwood xylan substrate was hydrolyzed using an enzyme loading of 120 nmol CBM2a Cel5A fusion enzyme per Gram xylan substrate supplemented with 12 nmol of β-xylosidase enzyme (10% of cellulase loading) per Gram xylan substrate for reaction times of 2, 6, and 24 hrs. The solubilized reducing sugar concentrations in the supernatant after hydrolysis were determined by the DNS assay **(A)** Reducing sugar release (mg/mL) as a function of time (2 h, 6 h and 24 h) for the hydrolysis of Beechwood xylan by D1–D8 CBM2a Cel5A and WT CBM2a Cel5A. Error bars represent standard deviation from the mean, based on at least four replicates. **(B)** Based on the data reported in **(A)**, CBM2a Cel5A fusion constructs with negatively supercharged CBMs (D1–D5) were grouped together and average hydrolysis yields were obtained for the group, with the error bars representing standard deviation from the mean. Similarly, CBM2a-Cel5A fusion constructs with positively supercharged CBMs (D6–D8) were grouped together and average hydrolysis yields were obtained. Trend curves have been added to represent the kinetic profiles of the hydrolysis reaction. Wild-type CBM2a-Cel5A is referred to as WT throughout this figure.

reduced binding interactions of CBMs to cellulose/lignin or an impact to thermal stability caused due to supercharging.

Binding of mutants to cellulose and lignin

To fully understand the role of CBM binding interactions on the activities of supercharged mutants towards cellulose and thereby pretreated biomass, we performed QCM-D assays (see Supplementary Figure S9 for raw data in the form of sensorgrams) which capture the total number of binding sites and the desorption rate constant (k_{off}). As reported in Table 1, all mutants except for D5 and D6 showed comparable or a reduced number of binding sites (up to 1.5-fold as observed for D1) with respect to the wild-type. D6 shows the highest binding of all mutants, showing up to 1.5-fold improvement, which could partially explain the higher activity seen for this mutant towards cellulose-I (see Figure 3) compared to other positively supercharged mutants D7 and D8. On the other hand, all mutants except for D5 and D8 show an improvement in (k_{off}), with D2 showing the most improvement (~1.3-fold). The most dramatic reduction was observed for D8, which has ~ 9-fold reduction in k_{off}. These results could explain the large decrease in activity observed for D8 CBM2a-Cel5A toward cellulose-I and thereby AFEX corn stover.

Lignin is a key polymer in pretreated biomass, which has the potential to restrict access to cellulose binding sites and thereby reduce overall biomass hydrolysis yields. QCM-D assays were performed to understand the binding of supercharged CBM2a mutants to lignin (see Supplementary Figure S10 for raw data). As reported in Supplementary Table S7, all mutants show an improvement in the percentage of protein recovered, indicating that supercharging may have resulted in increased reversibility of interactions between lignin and the CBM. Interestingly, D6 shows the highest percentage of protein recovered amongst all mutants, in stark contrast to D7 and D8, which could partially explain the reason for D6 outperforming its positively supercharged peers (D7 and D8) towards pretreated biomass and cellulose. Lignin inhibition assays were then performed to understand the inhibitory potential of lignin towards hydrolysis of cellulose-I and cellulose-III (see Supplementary Figure S11 for hydrolysis results and Supplementary Table S8 for T-tests comparing mutant activities in lignin inhibition assays). Results from lignin inhibition assays were not too instructive due to the high level of error observed in this assay although the overall trends of negatively supercharged mutants outperforming positively supercharged mutants (with the exception of D6) still remained the same.

Overall, the binding assays to cellulose and lignin shed some light on the behavior of D6 as an outliar from the rest of the positively supercharged sub-group, due to increased binding to cellulose-I and reduced irreversible binding to lignin. In addition, D8 shows a dramatic reduction (~9-fold) in desorption rate constant towards cellulose-I, indicating that the mutant may struggle with accessing binding sites on cellulose during hydrolysis. However, these results do not explain the reduced activity of D7 toward cellulose-I and AFEX corn stover. It is to be noted that these binding assays are performed at 25 °C as opposed to the hydrolysis assays which are performed at 60 °C. Hence, to understand the potential role of thermal stress on enzyme activity, we subjected these constructs to thermal exposure at elevated temperatures (70 °C), followed by testing of hydrolytic activities at 60 °C.

Hydrolysis of pretreated biomass/cellulose by CBM2a-Cel5A mutants upon thermal treatment

Exposure of the enzymes to 70°C prior to hydrolysis of AFEX corn stover or cellulose-I revealed differences in thermal stability of the cellulase variants (see Figure 5 for AFEX Corn Stover and Cellulose-I and Supplementary Figure S12 for EA Corn Stover

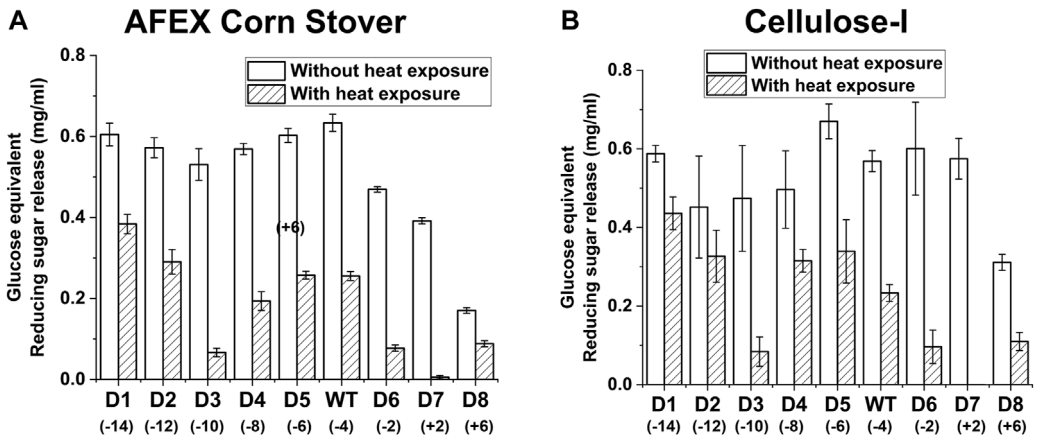

FIGURE 5
Impact of enzyme thermal denaturation at 70°C on reducing sugar yields from AFEX corn stover **(A)** and Avicel cellulose-I **(B)** Cellulase enzyme (0.0048 nmol/μL concentration) was thermally denatured at 70°C for 30 min using an Eppendorf thermocycler. 50 μL of denatured cellulase enzyme was added to either 80 μL of 25 g/L AFEX Corn Stover **(A)** or 40 μL of Cellulose-I **(B)** to establish an effective enzyme loading of 120 nmol enzyme per Gram AFEX Corn Stover or Cellulose-I substrate. 12 nmol of β-glucosidase enzyme (10% of cellulase loading) per Gram substrate was added to the reaction mixture and incubated at 60°C for 24 h. A control reaction was performed with enzyme that was incubated on an ice bath (0°C) for 30 min. The results of enzyme activity upon thermal denaturation at 70°C are labelled as 'With heat exposure' and those without thermal denaturation are labelled as 'Without heat exposure'. At least three replicates were run for each condition and the error bars represent standard deviation from the mean. Reducing sugar yields from hydrolysis of AFEX Corn Stover are reported in **(A)** and those from Avicel cellulose-I are reported in **(B)**.

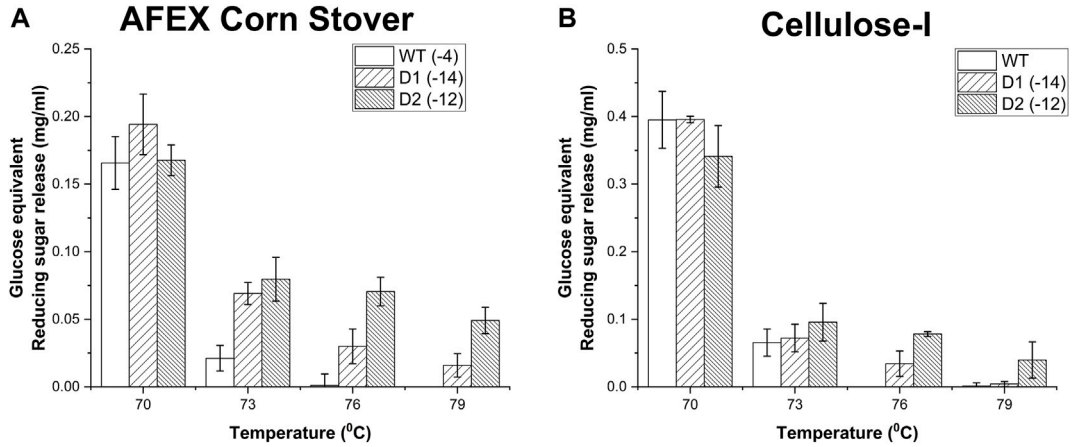

FIGURE 6
Impact of thermal denaturation at varying temperatures (70°C, 73°C, 76°C and 79°C) on reducing sugar yields from AFEX Corn Stover **(A)** and Avicel cellulose-I **(B)**. Cellulase enzyme (0.0048 nmol/μL concentration) was thermally denatured for 30 min at one of the following temperatures (70°C, 73°C, 76°C, 79°C) using an Eppendorf thermocycler. 50 μL of denatured cellulase enzyme was added to either 80 μL of 25 g/L AFEX Corn Stover **(A)** or 40 μL of Cellulose-I **(B)** to establish an effective enzyme loading of 120 nmol enzyme per Gram AFEX Corn Stover or Cellulose-I substrate. 12 nmol of β-glucosidase enzyme (10% of cellulase loading) per Gram substrate was added to the reaction mixture and incubated at 60°C for 24 h. A control reaction was performed with enzyme that was incubated on an ice bath (0°C) for 30 min. At least three replicates were run for each condition and the error bars represent standard deviation from the mean. Reducing sugar yields from hydrolysis of AFEX Corn Stover are reported in **(A)** and those from Avicel cellulose-I are reported in **(B)** under each of the denaturation temperatures (70°C, 73°C, 76°C and 79°C).

and Cellulose-III). To quantify this trend, we calculated the percent reduction in activity caused due to thermal treatment which is reported in Supplementary Table S9. While all enzymes showed decreased reducing sugar release, D3, D6 and D7 showed the most reduction in activity (~80–99%) towards all substrates tested. On the other hand, D1 and D2 showed better activity upon thermal treatment compared to the wildtype and show the least percent reduction in activity compared to all other mutants.

To build on this trend further, D1, D2 and WT were analyzed further by exposing them to a wider range of temperatures (70°C, 73°C, 76°C and 79 °C) as shown in Figure 6. D1 and D2 outshine the wild type especially at higher temperatures such as 76°C and 79°C towards AFEX corn stover (see Figure 6A) where the wildtype shows practically no activity. For instance, after thermal treatment at 73°C, D1 and D2 showed ~ 3-fold and ~ 4-fold improvement in activity compared to WT respectively. This difference is even starker at 76°C

although the wild-type activity is closer to the detection limit thereby making activity improvements harder to quantify. However, on cellulose-I (see Figure 6B), D1 and D2 showed a steep decrease in activity when the thermal exposure temperature was reduced from 70°C to 73°C, which continues to decline at higher temperatures. This may likely be caused by the fact that the reducing sugar release from biomass may be arising from xylan at higher temperatures, which is easily accessible compared to cellulose which requires CBM binding for the catalytic domain to be engaged.

The thermal stability was also measured using a thermal shift assay with SYPRO reagent, and the melting temperatures are reported in Supplementary Table S10 (the raw thermal shift assay data is reported in Supplementary Figure S13). There was not an appreciable difference seen in the melting temperatures. This assay measures the melting temperature of the enzyme as a whole and hence these results may be more biased towards the melting temperature of the catalytic domain as opposed to that of the CBM.

Overall, functional hydrolysis assays after thermal treatment of enzymes indicated that supercharging strategy gave rise to thermally stable mutants (D1 and D2) that find direct applications in industry in high-temperature biomass conversion processes. The structural basis of what renders certain supercharged mutants superior to others, still needs to be understood at greater detail which will be the subject of future studies.

Conclusion

Carbohydrate-binding modules (CBMs) play a crucial role in targeting appended glycoside hydrolase enzymes to plant cell wall polymers such as cellulose and hemicellulose (McLean et al., 2002; Herve et al., 2010; Fox et al., 2013; Reyes-Ortiz et al., 2013). However, recent studies have shown that CBMs can also play a role in non-productive binding of appended cellulase catalytic domains to cellulose surface (Karuna and Jeoh, 2017; Nill and Jeoh, 2020; Nemmaru et al., 2021). In addition, CBMs can bind non-productively to lignin via hydrophobic interactions, leading to deactivation of the enzymes on biomass surface (Haarmeyer et al., 2017). To address these bottlenecks, a previous study from our lab has used selective supercharging of cellulase enzymes to reduce lignin inhibition although the mechanistic details were yet to be elucidated (Whitehead et al., 2017). In this study, we expanded the supercharging approach to address mechanistic questions surrounding the impact of CBM supercharging on the hydrolysis of real-world pretreated biomass substrates.

This study is the first comprehensive study to test the impact of enzyme supercharging on activity towards various pretreated biomass substrates and systematically deconvolute the interactions of supercharged enzymes with cellulose, xylan and lignin. Although negatively and positively supercharged enzymes showed reduced activity compared to the wild-type, it was identified that some of these mutants show up to 4-fold improved activity upon exposure to higher temperatures. The reduced activity for negatively supercharged mutants was found to be predominantly driven by reduced activity towards xylan, whereas positively supercharged mutants showed reduced activity towards both cellulose and xylan. Future studies should focus on understanding the structural basis of hydrolytic activity and binding of supercharged mutants to lignocellulosic substrates. Recent work has shown that supercharging CBMs may improve catalytic activity on cellulosic biomass due to improved binding, but this outcome may be dependent on supercharging design strategy and the choice of enzymes (DeChellis et al., 2024). Moreover, the role of solution pH and salt concentration also need to be studied in greater detail due to their outsized impact on the net charge of the protein and alteration of electrostatic potential of supercharged proteins.

Data availability statement

The original contributions presented in the study are included in the article/Supplementary Material, further inquiries can be directed to the corresponding author.

Author contributions

BN: Conceptualization, Formal Analysis, Investigation, Methodology, Validation, Visualization, Writing–original draft, Writing–review and editing. JD: Investigation, Validation, Visualization, Writing–review and editing. JY: Investigation, Methodology, Resources, Writing–review and editing. AD: Investigation, Validation, Writing–review and editing. SS: Investigation, Validation, Writing–review and editing. AT: Investigation, Validation, Writing–review and editing. AW: Investigation, Validation, Writing–review and editing. SC: Conceptualization, Funding acquisition, Project administration, Supervision, Writing–review and editing.

Funding

The author(s) declare that financial support was received for the research, authorship, and/or publication of this article. The authors acknowledge support from the NSF CBET (Award 1604421 and Career Award 1846797), ORAU Ralph E. Powe Award, Rutgers Global Grant, Rutgers Division of Continuing Studies, Rutgers School of Engineering, and the Great Lakes Bioenergy Research Center (DOE BER Office of Science DE-FC02-07ER64494).

Acknowledgments

The authors thank Nathan Kruer-Zerhusen (from late Prof. David Wilson's lab) for kindly providing the *Thermobifida fusca* strain and original Cel5A plasmid DNA. Special thanks to Sarvada Chipkar and Dr. Rebecca Ong at Michigan Technological University, for conducting ammonia pretreatment to provide us with cellulose-III and AFEX corn stover. SPSC would also like to thank Dr. Leonardo Da Sousa (Dale lab at Michigan State University) for conducting ammonia pretreatment to generate cellulose III and EA corn stover that was used here in this study as well. BN would like to thank Patrick Doran (Boston University)

for his help initially with setting up protocols for computational protein design using Rosetta. JY acknowledges support from the Department of Energy, Office of Energy Efficiency and Renewable Energy (EERE) under agreement no. 28598.

Conflict of interest

The authors declare that the research was conducted in the absence of any commercial or financial relationships that could be construed as a potential conflict of interest.

The author(s) declared that they were an editorial board member of Frontiers, at the time of submission. This had no impact on the peer review process and the final decision.

Publisher's note

Supplementary material

The Supplementary Material for this article can be found online at: https://www.frontiersin.org/articles/10.3389/fenrg.2024.1372916/full#supplementary-material

References

Alford, R. F., Leaver-Fay, A., Jeliazkov, J. R., O'Meara, M. J., DiMaio, F. P., Park, H., et al. (2017). The Rosetta all-atom energy function for macromolecular modeling and design. *J. Chem. Theory Comput.* 13, 3031–3048. doi:10.1021/acs.jctc.7b00125

Azuma, Y., Zschoche, R., Tinzl, M., and Hilvert, D. (2016). Quantitative packaging of active enzymes into a protein cage. *Angew. Chem.–Int. Ed.* 55, 1531–1534. doi:10.1002/anie.201508414

Beck, T., Tetter, S., Künzle, M., and Hilvert, D. (2015). Construction of matryoshka-type structures from supercharged protein nanocages. *Angew. Chem.* 127, 951–954. doi:10.1002/ange.201408677

Blommel, P. G., Martin, P. A., Seder, K. D., Wrobel, R. L., and Fox, B. G. (2009). "Flexi vector cloning," in *High throughput protein expression and purification: methods and protocols*. Editor S. A. Doyle (Humana Press), 55–73. doi:10.1007/978-1-59745-196-3_4

Bozell, J. J., Black, S. K., Myers, M., Cahill, D., Miller, W. P., and Park, S. (2011). Solvent fractionation of renewable woody feedstocks: organosolv generation of biorefinery process streams for the production of biobased chemicals. *Biomass Bioenergy* 35, 4197–4208. doi:10.1016/j.biombioe.2011.07.006

Brunecky, R., Subramanian, V., Yarbrough, J. M., Donohoe, B. S., Vinzant, T. B., Vanderwall, T. A., et al. (2020). Synthetic fungal multifunctional cellulases for enhanced biomass conversion. *Green Chem.* 22, 478–489. doi:10.1039/c9gc03062j

Burley, S. K., Bhikadiya, C., Bi, C., Bittrich, S., Chen, L., Crichlow, G. V., et al. (2021). RCSB Protein Data Bank: powerful new tools for exploring 3D structures of biological macromolecules for basic and applied research and education in fundamental biology, biomedicine, biotechnology, bioengineering and energy sciences. *Nucleic Acids Res.* 49, D437–D451. doi:10.1093/nar/gkaa1038

Chen, X., Kuhn, E., Jennings, E. W., Nelson, R., Tao, L., Zhang, M., et al. (2016). DMR (deacetylation and mechanical refining) processing of corn stover achieves high monomeric sugar concentrations (230 g L^{-1}) during enzymatic hydrolysis and high ethanol concentrations (>10% v/v) during fermentation without hydrolysate purification or concentration. *Energy Environ. Sci.* 9, 1237–1245. doi:10.1039/c5ee03718b

Chundawat, S. P. S., Beckham, G. T., Himmel, M. E., and Dale, B. E. (2011a). Deconstruction of lignocellulosic biomass to fuels and chemicals. *Annu. Rev. Chem. Biomol. Eng.* 2, 121–145. doi:10.1146/annurev-chembioeng-061010-114205

Chundawat, S. P. S., Bellesia, G., Uppugundla, N., da Costa Sousa, L., Gao, D., Cheh, A. M., et al. (2011c). Restructuring the crystalline cellulose hydrogen bond network enhances its depolymerization rate. *J. Am. Chem. Soc.* 133, 11163–11174. doi:10.1021/ja2011115

Chundawat, S. P. S., Donohoe, B. S., da Costa Sousa, L., Elder, T., Agarwal, U. P., Lu, F., et al. (2011b). Multi-scale visualization and characterization of lignocellulosic plant cell wall deconstruction during thermochemical pretreatment † ‡. *Energy & Environ. Sci.* 4, 973. doi:10.1039/c0ee00574f

Chundawat, S. P. S., Sousa, L. d. C., Roy, S., Yang, Z., Gupta, S., Pal, R., et al. (2020). Ammonia-salt solvent promotes cellulosic biomass deconstruction under ambient pretreatment conditions to enable rapid soluble sugar production at ultra-low enzyme loadings. *Green Chem.* 22, 204–218. doi:10.1039/c9gc03524a

Da Costa Sousa, L., Jin, M., Chundawat, S. P. S., Bokade, V., Tang, X., Azarpira, A., et al. (2016). Next-generation ammonia pretreatment enhances cellulosic biofuel production. *Energy Environ. Sci.* 9, 1215–1223. doi:10.1039/c5ee03051j

Das, R., and Baker, D. (2008). Macromolecular modeling with Rosetta. *Annu. Rev. Biochem.* 77, 363–382. doi:10.1146/annurev.biochem.77.062906.171838

DeChellis, A., Nemmaru, B., Sammond, D., Douglass, J., Patil, N., Reste, O., et al. (2024). Supercharging carbohydrate binding module alone enhances endocellulase thermostability, binding, and activity on cellulosic biomass. *ACS Sustain. Chem. Eng.* 12, 3500–3516. doi:10.1021/acssuschemeng.3c06266

Der, B. S., Kluwe, C., Miklos, A. E., Jacak, R., Lyskov, S., Gray, J. J., et al. (2013). Alternative computational protocols for supercharging protein surfaces for reversible unfolding and retention of stability. *PLoS One* 8, e64363. doi:10.1371/journal.pone.0064363

Fox, J. M., Jess, P., Jambusaria, R. B., Moo, G. M., Liphardt, J., Clark, D. S., et al. (2013). A single-molecule analysis reveals morphological targets for cellulase synergy. *Nat. Chem. Biol.* 9, 356–361. doi:10.1038/nchembio.1227

Galbe, M., and Wallberg, O. (2019). Pretreatment for biorefineries: a review of common methods for efficient utilisation of lignocellulosic materials. *Biotechnol. Biofuels* 12, 294. doi:10.1186/s13068-019-1634-1

Gao, D., Haarmeyer, C., Balan, V., Whitehead, T. A., Dale, B. E., and Chundawat, S. P. (2014). Lignin triggers irreversible cellulase loss during pretreated lignocellulosic biomass saccharification. *Biotechnol. Biofuels* 7, 175. doi:10.1186/s13068-014-0175-x

Georgelis, N., Yennawar, N. H., and Cosgrove, D. J. (2012). Structural basis for entropy-driven cellulose binding by a type-A cellulose-binding module (CBM) and bacterial expansin. *Proc. Natl. Acad. Sci. U. S. A.* 109, 14830–14835. doi:10.1073/pnas.1213200109

Guo, F., Shi, W., Sun, W., Li, X., Wang, F., Zhao, J., et al. (2014). Differences in the adsorption of enzymes onto lignins from diverse types of lignocellulosic biomass and the underlying mechanism. *Biotechnol. Biofuels* 7, 38–10. doi:10.1186/1754-6834-7-38

Haarmeyer, C. N., Smith, M. D., Chundawat, S. P. S., Sammond, D., and Whitehead, T. A. (2017). Insights into cellulase-lignin non-specific binding revealed by computational redesign of the surface of green fluorescent protein. *Biotechnol. Bioeng.* 114, 740–750. doi:10.1002/bit.26201

Herve, C., Rogowski, A., Blake, A. W., Marcus, S. E., Gilbert, H. J., and Knox, J. P. (2010). Carbohydrate-binding modules promote the enzymatic deconstruction of intact plant cell walls by targeting and proximity effects. *Proc. Natl. Acad. Sci.* 107, 15293–15298. doi:10.1073/pnas.1005732107

Holwerda, E. K., Worthen, R. S., Kothari, N., Lasky, R. C., Davison, B. H., Fu, C., et al. (2019). Multiple levers for overcoming the recalcitrance of lignocellulosic biomass. *Biotechnol. Biofuels* 12, 15–12. doi:10.1186/s13068-019-1353-7

Humbird, D., et al. (2011). "Process design and economics for biochemical conversion of lignocellulosic biomass to ethanol: dilute-acid pretreatment and enzymatic hydrolysis of corn stover," in *NREL/TP-5100-47764* (Golden, CO, USA: National Renewable Energy Laboratory).

Jung, H., Wilson, D. B., and Walker, L. P. (2003). Binding and reversibility of Thermobifida fusca Cel5A, Cel6B, and Cel48A and their respective catalytic domains to bacterial microcrystalline cellulose. *Biotechnol. Bioeng.* 84, 151–159. doi:10.1002/bit.10743

Karuna, N., and Jeoh, T. (2017). The productive cellulase binding capacity of cellulosic substrates. *Biotechnol. Bioeng.* 114, 533–542. doi:10.1002/bit.26193

Khatib, F., Cooper, S., Tyka, M. D., Xu, K., Makedon, I., Popović, Z., et al. (2011). Algorithm discovery by protein folding game players. *Proc. Natl. Acad. Sci. U. S. A.* 108, 18949–18953. doi:10.1073/pnas.1115898108

Kleffner, R., Flatten, J., Leaver-Fay, A., Baker, D., Siegel, J. B., Khatib, F., et al. (2017). Foldit Standalone: a video game-derived protein structure manipulation interface using Rosetta. *Bioinformatics* 33, 2765–2767. doi:10.1093/bioinformatics/btx283

Klein-Marcuschamer, D., Oleskowicz-Popiel, P., Simmons, B. A., and Blanch, H. W. (2012). The challenge of enzyme cost in the production of lignocellulosic biofuels. *Biotechnol. Bioeng.* 109, 1083–1087. doi:10.1002/bit.24370

Kokossis, A. C., Tsakalova, M., and Pyrgakis, K. (2014). Design of integrated biorefineries. *Comput. Chem. Eng.* 81, 40–56. doi:10.1016/j.compchemeng.2015.05.021

Kostylev, M., and Wilson, D. (2013). Two-parameter kinetic model based on a time-dependent activity coefficient accurately describes enzymatic cellulose digestion. *Biochemistry* 52, 5656–5664. doi:10.1021/bi400358v

Lawrence, M. S., Phillips, K. J., and Liu, D. R. (2007). Supercharging proteins can impart unusual resilience. *J. Am. Chem. Soc.* 129, 10110–10112. doi:10.1021/ja071641y

Lei, C., Huang, Y., Nie, Z., Hu, J., Li, L., Lu, G., et al. (2014). A supercharged fluorescent protein as a versatile probe for homogeneous DNA detection and methylation analysis. *Angew. Chem.–Int. Ed.* 53, 8358–8362. doi:10.1002/anie.201403615

Lim, S., Chundawat, S. P. S., and Fox, B. G. (2014). Expression, purification and characterization of a functional carbohydrate-binding module from streptomyces sp. SirexAA-E. *Protein Expr. Purif.* 98, 1–9. doi:10.1016/j.pep.2014.02.013

Liu, Y., Nemmaru, B., and Chundawat, S. P. S. (2020). Thermobifida fusca cellulases exhibit increased endo – exo synergistic activity, but lower exocellulase activity, on cellulose-III. *ACS Sustain. Chem. Eng.* 8, 5028–5039. doi:10.1021/acssuschemeng.9b06792

Luo, X., Liu, J., Zheng, P., Li, M., Zhou, Y., Huang, L., et al. (2019). Promoting enzymatic hydrolysis of lignocellulosic biomass by inexpensive soy protein. *Biotechnol. Biofuels* 12, 51–13. doi:10.1186/s13068-019-1387-x

Maity, S. K. (2015). Opportunities, recent trends and challenges of integrated biorefinery: Part i. *Renew. Sustain. Energy Rev.* 43, 1427–1445. doi:10.1016/j.rser.2014.11.092

McCann, M. C., and Carpita, N. C. (2015). Biomass recalcitrance: a multi-scale, multi-factor, and conversion-specific property: fig. 1. *J. Exp. Bot.* 66, 4109–4118. doi:10.1093/jxb/erv267

McLean, B. W., Boraston, A. B., Brouwer, D., Sanaie, N., Fyfe, C. A., Warren, R. A. J., et al. (2002). Carbohydrate-binding modules recognize fine substructures of cellulose. *J. Biol. Chem.* 277, 50245–50254. doi:10.1074/jbc.m204433200

Narron, R. H., Kim, H., Chang, H. M., Jameel, H., and Park, S. (2016). Biomass pretreatments capable of enabling lignin valorization in a biorefinery process. *Curr. Opin. Biotechnol.* 38, 39–46. doi:10.1016/j.copbio.2015.12.018

Nemmaru, B., Ramirez, N., Farino, C. J., Yarbrough, J. M., Kravchenko, N., and Chundawat, S. P. S. (2021). Reduced type-A carbohydrate-binding module interactions to cellulose I leads to improved endocellulase activity. *Biotechnol. Bioeng.* 118, 1141–1151. doi:10.1002/bit.27637

Nill, J., and Jeoh, T. (2020). The role of evolving interfacial substrate properties on heterogeneous cellulose hydrolysis kinetics. *ACS Sustain. Chem. Eng.* 8, 6722–6733. doi:10.1021/acssuschemeng.0c00779

Nimlos, M. R., Beckham, G. T., Matthews, J. F., Bu, L., Himmel, M. E., and Crowley, M. F. (2012). Binding preferences, surface attachment, diffusivity, and orientation of a family 1 carbohydrate-binding module on cellulose. *J. Biol. Chem.* 287, 20603–20612. doi:10.1074/jbc.M112.358184

Nordwald, E. M., Brunecky, R., Himmel, M. E., Beckham, G. T., and Kaar, J. L. (2014). Charge engineering of cellulases improves ionic liquid tolerance and reduces lignin inhibition. *Biotechnol. Bioeng.* 111, 1541–1549. doi:10.1002/bit.25216

Obermeyer, A. C., Mills, C. E., Dong, X. H., Flores, R. J., and Olsen, B. D. (2016). Complex coacervation of supercharged proteins with polyelectrolytes. *Soft Matter* 12, 3570–3581. doi:10.1039/c6sm00002a

Ragauskas, A. J., Beckham, G. T., Biddy, M. J., Chandra, R., Chen, F., Davis, M. F., et al. (2014). Lignin valorization: improving lignin processing in the biorefinery. *Science* 344, 1246843. doi:10.1126/science.1246843

Reyes-Ortiz, V., Heins, R. A., Cheng, G., Kim, E. Y., Vernon, B. C., Elandt, R. B., et al. (2013). Addition of a carbohydrate-binding module enhances cellulase penetration into cellulose substrates. *Biotechnol. Biofuels* 6, 93. doi:10.1186/1754-6834-6-93

Salas, C., Rojas, O. J., Lucia, L. a., Hubbe, M. A., and Genzer, J. (2013). On the surface interactions of proteins with lignin. *ACS Appl. Mater. Interfaces* 5, 199–206. doi:10.1021/am3024788

Sammond, D. W., Yarbrough, J. M., Mansfield, E., Bomble, Y. J., Hobdey, S. E., Decker, S. R., et al. (2014). Predicting enzyme adsorption to lignin films by calculating enzyme surface hydrophobicity. *J. Biol. Chem.* 289, 20960–20969. doi:10.1074/jbc.m114.573642

Sasaki, E., Böhringer, D., van de Waterbeemd, M., Leibundgut, M., Zschoche, R., Heck, A. J. R., et al. (2017). Structure and assembly of scalable porous protein cages. *Nat. Commun.* 8, 14663–14710. doi:10.1038/ncomms14663

Scown, C. D., Baral, N. R., Yang, M., Vora, N., and Huntington, T. (2021). Technoeconomic analysis for biofuels and bioproducts. *Curr. Opin. Biotechnol.* 67, 58–64. doi:10.1016/j.copbio.2021.01.002

Simon, A. J., Zhou, Y., Ramasubramani, V., Glaser, J., Pothukuchy, A., Gollihar, J., et al. (2019). Supercharging enables organized assembly of synthetic biomolecules. *Nat. Chem.* 11, 204–212. doi:10.1038/s41557-018-0196-3

Song, Y., DiMaio, F., Wang, R. R., Kim, D., Miles, C., Brunette, T., et al. (2013). High-resolution comparative modeling with RosettaCM. *Structure* 21, 1735–1742. doi:10.1016/j.str.2013.08.005

Sousa, L. da C., Humpula, J., Balan, V., Dale, B. E., and Chundawat, S. P. S. (2019). Impact of ammonia pretreatment conditions on the cellulose III allomorph ultrastructure and its enzymatic digestibility. *ACS Sustain. Chem. Eng.* 7, 14411–14424. doi:10.1021/acssuschemeng.9b00606

Strobel, K. L., Pfeiffer, K. A., Blanch, H. W., and Clark, D. S. (2015). Structural insights into the affinity of Cel7A carbohydratebinding module for lignin. *J. Biol. Chem.* 290, 22818–22826. doi:10.1074/jbc.m115.673467

Studer, M. H., DeMartini, J. D., Davis, M. F., Sykes, R. W., Davison, B., Keller, M., et al. (2011). Lignin content in natural populus variants affects sugar release. *Proc. Natl. Acad. Sci. U. S. A.* 108, 6300–6305. doi:10.1073/pnas.1009252108

Studier, F. W. (2005). Protein production by auto-induction in high-density shaking cultures. *Protein Expr. Purif.* 41, 207–234. doi:10.1016/j.pep.2005.01.016

Sun, C., Li, Y., Yates, E. A., and Fernig, D. G. (2020). SimpleDSFviewer: a tool to analyze and view differential scanning fluorimetry data for characterizing protein thermal stability and interactions. *Protein Sci.* 29, 19–27. doi:10.1002/pro.3703

Takkellapati, S., Li, T., and Gonzalez, M. A. (2018). An overview of biorefinery-derived platform chemicals from a cellulose and hemicellulose biorefinery. *Clean. Technol. Environ. Policy* 20, 1615–1630. doi:10.1007/s10098-018-1568-5

Thompson, D. B., Cronican, J. J., and Liu, D. R. (2012). Engineering and identifying supercharged proteins for macromolecule delivery into mammalian cells. *Methods Enzymol.* 1067, 293–319. doi:10.1016/b978-0-12-396962-0.00012-4

Tuck, C. O., Perez, E., Horvath, I. T., Sheldon, R. A., and Poliakoff, M. (2012). Valorization of biomass: deriving more value from waste. *Science* 338, 604. doi:10.1126/science.1218930

Ubando, A. T., Felix, C. B., and Chen, W. H. (2020). Biorefineries in circular bioeconomy: a comprehensive review. *Bioresour. Technol.* 299, 122585. doi:10.1016/j.biortech.2019.122585

Wang, H., Pu, Y., Ragauskas, A., and Yang, B. (2019). From lignin to valuable products–strategies, challenges, and prospects. *Bioresour. Technol.* 271, 449–461. doi:10.1016/j.biortech.2018.09.072

Watson, D. L., Wilson, D. B., and Walker, L. P. (2002). Synergism in binary mixtures of Thermobifida fusca cellulases Cel6b, Cel9a, and Cel5a on BMCC and Avicel. *Appl. Biochem. Biotechnol.–Part A Enzym. Eng. Biotechnol.* 101, 097–112. doi:10.1385/abab:101:2:097

Whitehead, T. A., Bandi, C. K., Berger, M., Park, J., and Chundawat, S. P. S. (2017). Negatively supercharging cellulases render them lignin-resistant. *ACS Sustain. Chem. Eng.* 5, 6247–6252. doi:10.1021/acssuschemeng.7b01202

Wilson, D. B. (2004). Studies of Thermobifida fusca plant cell wall degrading enzymes. *Chem. Rec.* 4, 72–82. doi:10.1002/tcr.20002

Yang, B., and Wyman, C. E. (2006). BSA treatment to enhance enzymatic hydrolysis of cellulose in lignin containing substrates. *Biotechnol. Bioeng.* 94, 611–617. doi:10.1002/bit.20750

Zeng, Y., Zhao, S., Yang, S., and Ding, S. Y. (2014). Lignin plays a negative role in the biochemical process for producing lignocellulosic biofuels. *Curr. Opin. Biotechnol.* 27, 38–45. doi:10.1016/j.copbio.2013.09.008

frontiers | Frontiers in Energy Research

TYPE Hypothesis and Theory
PUBLISHED 22 August 2024
DOI 10.3389/fenrg.2024.1392634

OPEN ACCESS

EDITED BY
Shripad T. Revankar,
Purdue University, United States

REVIEWED BY
Rudrodip Majumdar,
National Institute of Advanced Studies, India
Erik Grönlund,
Mid Sweden University, Sweden

*CORRESPONDENCE
Daniel Elliott Campbell,
emergyacctfin@gmail.com

RECEIVED 27 February 2024
ACCEPTED 21 June 2024
PUBLISHED 22 August 2024

CITATION
Campbell DE and Lu H (2024) Emergy and the rules of emergy accounting applied to calculate transformities for some of the primary, secondary, and tertiary exergy flows of the Geobiosphere.
Front. Energy Res. 12:1392634.
doi: 10.3389/fenrg.2024.1392634

Emergy and the rules of emergy accounting applied to calculate transformities for some of the primary, secondary, and tertiary exergy flows of the Geobiosphere

Daniel Elliott Campbell[1]* and Hongfang Lu[2]

[1]International Society for the Advancement of Emergy Research, Edgewater, MD, United States, [2]Guangdong Provincial Key Laboratory of Applied Botany, South China Botanical Garden, Chinese Academy of Sciences, Guangzhou, China

Emergy is a concept that is important for understanding problems in accounting for the health and integrity of ecological and social systems. Success in the evolutionary competition among systems depends on maximizing the emergy captured by a system that is then fed back to bring in more exergy. For this reason, "emergy" in the form of maximum empower (i.e., maximum emergy flow measured in solar emjoules or sej/unit time) provides a unified, thermodynamically controlled decision criterion by which the behavior of all systems is constrained. The fact that maximum empower and not maximum profit is nature's decision criterion makes it critical that more people become familiar with emergy evaluations and how to use the results of these analyses in decision-making. A new approach to emergy evaluation is proposed that focuses on developing more accurate assessments of the spatial and temporal emergy accounting required for the creation of products and services. These emergy evaluations include the accumulated past action of exergy in creating key system components such as vegetation biomass and the accumulated knowledge of workers in the economy, which will result in emergy assessments that better reflect the capacity of the products and services to do work in their systems. An analysis of the Geobiosphere is presented as a "white box" model of the secondary and tertiary flows of wind and water in the global system. The key factors identified are the separation of wind into two components: a factor controlling vertical diffusion with transformity of ≈715 sej J^{-1} and a second transformity governing surface friction of ≈1,215 sej J^{-1}. Also, water systems are fully defined with transformities of 302,900 sej J^{-1} to 1,440,000 sej J^{-1} for geostrophic flows. Past emergy analyses show that managers should develop policies that will maximize the empower flowing through their systems. The problem of maximizing the empower captured occurs within the context of a set of forcing functions impinging on a system from the next larger system, and since these forcing functions are always changing, maximum power should not be thought of as a fixed endpoint but rather as a constant state of seeking this goal.

KEYWORDS

environmental accounting, emergy analysis, Geobiosphere wind and water flows, new accounting rules, accurate assessment

1 Introduction

The importance of emergy as an accounting quantity and its physical basis in the laws of equilibrium and nonequilibrium thermodynamics that govern all phenomena are considered in this article and by Odum (1996). The overview perspective on emergy accounting presented here is to be used with the existing emergy accounting rules (Brown and Herendeen, 1996; Odum, 1996) and the further modification of those rules proposed in this article. The modifications of the emergy methodology proposed here build on the strong foundation of four articles establishing the solar equivalent exergy (SEE) baseline for the Geobiosphere, measured as solar equivalent joules, seJ (Brown et al., 2016; Brown and Ulgiati, 2016; Campbell, 2016; De Vilbiss et al., 2016) and on the earlier work of Campbell and Lu (2009) on the recursive structure of the formal education system of the United States (Campbell et al., 2014a), on examining educational attainment and its role in determining value in the US economy (Campbell et al., 2011), and on the method for attaining closure on the emergy balance sheet and emergy income statement of systems, e.g., a state or a nation (Campbell, 2013). Further consideration of the nature of emergy leads to proposed modifications of the methodology and disagreements faced in calculating solar transformities for secondary and tertiary emergy inflows to the Earth, and from further thought on determining the SEEs of the primary SEE inflows to the Geobiosphere (Campbell, 2016) that has also led to proposed changes. The major focus of this article is to present detailed new calculations for the emergy of the secondary and tertiary exergy flows of the Earth's air and water systems, which is the logical next step in emergy accounting after establishing a strong scientific determination of the planetary SEE baseline for emergy calculations. Exergy from the three primary sources of exergy to the Earth: sun, S, earth's deep heat, E, and solar and lunar tidal attractions, G, enter the Earth's Geobiosphere (Figure 1). These exergies are then transformed into additional flows that are derived from the original flows as secondary or tertiary inputs to the Geobiosphere, depending on the number of transformations that the original exergy flows experience as they move away from their sources, i.e., one transformation yields a secondary flow and two transformations a tertiary flow. For example, secondary flows of exergy to the Geobiosphere include wind, rain on land, rain on the sea, and tidal dissipation in coastal areas, etc. and tertiary flows are found in waves, wind driven currents, runoff, evapotranspiration, infiltration, etc.

1.1 Emergy and its importance

Emergy is a scientifically powerful yet an often poorly understood concept that has great importance in understanding many important problems in accounting for the health and integrity of ecological systems (Campbell, 2000; Berrios et al., 2018), and in the analysis and understanding of causality in all kinds of systems (Odum, 1971; Odum, 1996). Emergy is important because success in

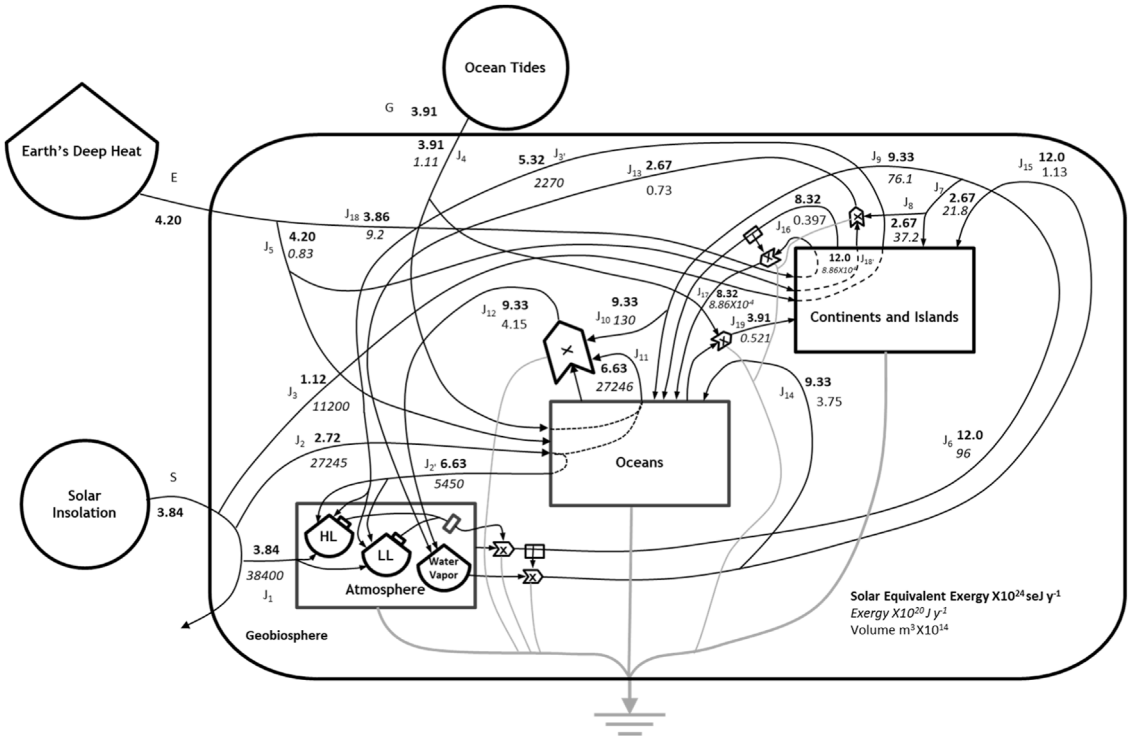

FIGURE 1
An Energy Systems Language "white box" model of the Geobiosphere tracing the SEE, input from each of the three primary sources (circles) and showing how they interact to support the exergy flows of the system (solid lines with arrowheads). The interconnections among the SEE sources and the system components, i.e., atmosphere, oceans, and continents, show the SEE sources required for the secondary emergy flows of the Geobiosphere (i.e., the labeled pathways) as defined in Table 1. SEEs are given in bold, exergy flows in italics, and water volumes in plain text.

the evolutionary competition among systems and designs depends on maximizing the emergy flow captured by a system and then being fed back to bring in more available energy (Odum, 1996; Campbell, 2001). For this reason, "emergy" in the form of maximum empower (i.e., maximum emergy flow measured in solar emjoules or sej/unit time) provides a unified, comprehensive, thermodynamically controlled decision criterion by which the behavior of all systems is ultimately constrained. The fact that maximum empower and not maximum profit is nature's decision criterion makes it critical that more people become familiar with emergy evaluations and how to use the results of these analyses in decision-making. Thus, managers responsible for the success of their systems should have as a primary goal the development and implementation of policies that will maximize the empower (emergy/unit time) flowing through their systems, and thereby maximize their system's functional integrity or health, i.e., the system's competitiveness in the competition among all systems to capture the available energy of resources from the Geobiosphere (Odum, 1996; Campbell, 2000). The relative empower generated provides managers a general criterion to use in choosing among alternative systems. The problem of maximizing the empower captured always occurs within the context of a set of forcing functions impinging on a system from the next larger system, and since these forcing functions are always changing at faster or slower rates, the maximum power should not be thought of as a fixed endpoint to be attained but rather as a constant state of seeking this goal, thus maximum empower is a moving target (Campbell, 2001). This property of maximum empower makes it essential to consider the temporal boundaries of the system under evaluation. Quantifying the flows of available energy (i.e., exergy) in a network over time provides data on system condition to support decision-making by managers responsible for the wellbeing of their respective ecological and socioeconomic systems. Some examples of the use of the Energy Systems Theory in the management of ecological and social systems are found in Odum et al. (1998) in the "Environment and Society in Florida" and in Campbell et al. (2005a) that provide examples of the application of Energy Systems Theory in the management of a US state. Kangas (2004) gives examples of the use of the Energy Systems Theory and other key articles in the development of a new discipline of ecological engineering. Campbell et al., 2014a provide a discussion of the use of the Energy Systems Theory in the analysis of energy use in the United States from 1900 to 2011 with a particular emphasis on understanding the "Great Recession of 2008".

1.1.1 Emergy and empower

Emergy is of universal importance because the transformation of energy potentials underlies and is responsible for all actions that have been observed in the universe. Emergy has been operationally defined (Odum, 1996) as the available energy (i.e., the exergy)[1] of one kind that has been used-up, both directly and indirectly, in the process of producing a product (i.e., a quantity of mass, energy, and information) or a service (i.e., the provision of a flow of mass, electricity, human labor, horsepower, and information). Emergy is a quantitative property of the evolution of system networks over time that can be derived directly from the requirements of the first[2] and second[3] laws of thermodynamics and the proposed fourth[4] law or the maximum empower principle and its corollaries, e.g., the proposed fifth law or the principle of energy hierarchy[5] (Odum, 1996). As mentioned above, emergy derives its explanatory and predictive power from the fact that maximizing empower (emergy flow) in a process, system, or network has been hypothesized to be nature's decision criterion (Lotka, 1922a; Lotka, 1922b; Odum, 1996; Campbell, 2000; 2001). Thus, in the competition among systems (mineral, human, animal, ecological, or socioeconomic), success at all hierarchical levels of an organization depends on maximizing empower at the level within the universal hierarchy of natural phenomena at which the system exists and this condition radiates or propagates to all other levels in the hierarchy.

The suite of emergy inputs, or the emergy signature of forcing functions driving system behavior, is derived from the system operating at the next higher level of the organization, and these inputs are constantly changing, whether at a faster or slower rate. As a result, a system at the level in the hierarchy receiving these inputs will be constrained to adjust its structure and function to outcompete its competitors (i.e., other system designs) in capturing the available energy in the signature. This must be true if a system is to prevail in competition or fails to persist as part of the mix of systems that survive. In general, persistence is only possible under the constraint to maximize empower because of the variability present in systems at all hierarchical levels. This variability opens the way for redundancy to be built into systems, for which additional choices provide the flexibility to maximize empower at other times and places; therefore, entities that can only persist under one set of forcing functions may prevail under a future forcing regime. Nature through its laws does not respect species, *per se*, only the functionality of a species is respected, which is demonstrated by its ability to maximize empower within the context of the system's current emergy signature (Campbell et al., 2009).

Based on the arguments given above, it is easy to see the importance of knowing the expected change in emergy flow (empower) through a system before choosing among possible alternatives or changes to be made to the system. More exactly,

1 Available energy or exergy is energy with the potential to do work against a background state and is degraded in this process. It has measurable units of joules, kilocalories, etc.; however, the energy potential is relative to conditions in the designated reference environment.

2 The energy conservation principle, i.e., energy is neither created nor destroyed in its circulation and transformations within a system.

3 Some available energy must be degraded to an unusable form, whenever energy is stored or transformed in a system, resulting in an increase in entropy of the whole system.

4 Under the evolutionary competition among systems, those with self-organizing processes (e.g., systems with autocatalytic or positive feedback) and network designs (e.g., hierarchy) that maximize empower will prevail (Odum, 1996).

5 Energy flows of the universe are organized into hierarchical structures as the result of energy transformations taking place under the second law. The position of storage or flow within the hierarchy is measured by its transformity (Odum, 1996).

maximizing empower is nature's decision criterion, and we ignore such natural laws at our own peril. While a manager who understands the importance of the arguments given above to the future of a system will surely want to know the changes in the emergy flow that may result from a management action that has been authorized, making the decision to evaluate these changes will lead to a set of further considerations.

1.1.2 Emergy is an accounting quantity

First, unlike many easily measurable holistic indicators of a system's condition, such as the body temperature of a human being the summary measure of health, emergy cannot be measured directly. Emergy is not an observable state variable; therefore, there is no place in the universe where an instrument can be placed to make a direct measurement of the emergy of a stored quantity or flow. Emergy and changes in emergy flow can only be measured using an accounting process, for example, the available energy that is used in the production process of a product or service can be tracked and then summed over the time and path used to form the output (Tennenbaum, 1988). By contrast, the output or product of these exergy transformations is observable and can be directly measured in energy, mass, or information units. Also, the available energy or exergy of a quantity is not a state variable because its value is defined relative to a background energy level or its environmental context, which can change, and therefore it must be specified by measuring the quantity, e.g., the geopotential energy of water is measured by the elevation of water on the landscape relative to the sea level, the specified ground state. Once the background reference has been chosen, the available energy of an entity can be quantified in a uniform manner, i.e., measured relative to the background. Thus, the major emphasis in emergy quantification has always been laid on the rules that are used to perform the accounting, because maximum emergy flow is a predictive universal quantity that can only be measured through an accounting process (Brown and Herendeen, 1996; Odum, 1996). These accounting rules can be expressed in somewhat different terms depending on the method used to quantify the emergy of storages and flows for example, Le Corre and Truffet (2012) and Le Corre and Truffet (2015) formulated the rules somewhat differently, but in a consistent manner with past rules, to allow making emergy calculations in a network using the graph theory. This focus on the accounting rules has, at times, led to some confusion and sometimes a tendency toward blind obeisance due to the failure of investigators to keep in mind the deeper meaning of emergy, i.e., what it is.

1.1.3 The deeper meaning of emergy

The deeper meaning of emergy arises from its identity as a thermodynamically controlled variable that quantifies nature's decision criteria within the context of evolutionary competition. Specifically, hypothesizing to maximize the empower captured by a process or system to determine its success in the competition among alternative system designs that are competing for the use of available resources, given that all processes are operating at maximum power efficiencies. An exergy flow from a given system or component to an exploiting process can allow the capture of more energy in available resources, because it provides a higher quality feedback (i.e., entities with higher emergy per unit of available energy, seJ J^{-1}) than an equivalent quantity of feedback from other components with which it is in competition. The underlying assumption for such comparisons to be valid is that all the processes are operating at their maximum power states. Under this condition, more effective feedback can do more work per unit of available energy dissipated. This is a fundamental prerequisite in determining the existence of an increase in the emergy of a component or process in a system, i.e., exergy with higher quality per unit quantity must have an increased ability to do useful work[6] in its system, with all other factors being equal. This condition serves as a fundamental constraint on the calculation of emergy and on its accounting rules, i.e., the quality, or the ability to do work, of the quantity of available energy must increase, if the emergy delivered per unit exergy of the component or process increases, given that all processes are operating at their maximum power points. This profound connection between maximizing emergy flow and success in the evolutionary competition for resources and the role of high-quality available energy feedback in this maximization is explored in this article as the basis for promulgating an emphasis on the deeper meaning of emergy as a guiding context for performing emergy calculations and for applying the existing rules of emergy algebra to carry out these calculations (Tennenbaum, 1988; Brown and Herendeen, 1996; Odum, 1996) more effectively. In this article, the existing emergy accounting rules are modified to incorporate some important aspects of the emergy accounting methods mentioned in Odum (1996) and later considered further by Brown (2005) and Brown and Brandt-Williams (2011), but these possible innovations, though pointed out, are not fully applied in most emergy accounting studies. In this article, we expand the rules of emergy accounting using a *meta framework* that includes the broader temporal and spatial emergy flows required to account for the development of system structures essential to bring about the emergy flows of concern in an evaluation. This approach often results in including temporal boundaries that are required for the creation of certain items that are broader and those usually included in a typical emergy analysis. The effects of this approach can be most clearly seen in the role of the emergy required for the creation of biomass accumulations in determining present emergy flows that are required for different plant processes, such as growth and reproduction. Other examples of the meta framework are seen in the inclusion of the emergy required for the education and training of workers in the evaluation of human labor use in economic systems. The foremost macroscopic modification of the accounting rules proposed here is that the first consideration in all emergy analyses should be the recognition that there *must be* a fundamental connection between the ability of an entity to do work in its system and its emergy intensity or transformity and *vice versa*. In this regard, the emergy accounting rules should lay their primary emphasis on *an exact accounting*, neither overcounting nor undercounting, of the emergy required for creating an entity and understanding the actions that will result from its use.

6 "Useful work" can capture additional exergy from external resources for use in building or operating system structures that, in turn, facilitates the further use of available resources within the system.

1.2 Objectives of this study and preliminary information

The reader should note that critical material and ideas for understanding this study are given in Supplementary Material A and B, which should not be neglected in obtaining an understanding of the origins of the material presented in this article. First, the effects of the radiation of the emergy methodology on the accounting process are considered (Supplementary Section A1.0—*Radiation of the Emergy Methodology*). Next, the development of the emergy methodology during the period from 2002 to 2016 (from H.T. Odum's death to the publication of the four key baseline articles) is considered in Supplementary Section A1.1—*Environmental Accounting: Past Problems and Current Advances*. In the context of this study, the SEE basis for the Earth system was reexamined to ensure greater methodological consistency in Supplementary Section A1.2—*A reexamination of the solar equivalences of the Earth's primary exergy inflows* is presented. This reexamination of the baseline yielded data that further supported our estimate of 12.0E24 seJ y^{-1} as the value for the SEE baseline for Earth in Supplementary Section A1.3 giving *further support for 12.0E+24 seJ* y^{-1} *as the value of the SEE Geobiosphere baseline*. Finally, differences between the determinations of the baseline carried out by Brown and Ulgiati (2016) and Campbell (2016) are examined and a commentary on the significance of the differences is given in Supplementary Section A1.4—*Differences between the Geobiosphere models used by* Brown and Ulgiati (2016) and Campbell (2016).

The immediate objectives of this study are (1) to reexamine the emergy evaluation of the flows of air and water within their thermodynamic context in the global Geobiosphere and to develop a *meta framework* with expanded spatial and temporal boundaries within which the rules used to calculate emergy flows for a given system can be applied more accurately, i.e., more exactly, in determining all the exergy required for a particular flow or storage; (2) to propose self-consistent solar equivalence ratios for tidal exergy dissipated in oceans and by Earth's deep heat flow based on refined baseline calculations (Supplementary Section A1.2); (3) the data given in Campbell (2016) are reexamined to reaffirm the value calculated for the SEE baseline of the Geobiosphere (Supplementary Section A1.3), and we present a "white box" Energy Systems Language (ESL) model for calculating the exergy in the most important secondary and tertiary wind and water emergy flows of the Geobiosphere; and (4) to carry out the new calculations of the transformities of the major secondary and tertiary emergy flows using the "white box" framework for applying the calculation rules proposed under (1) mentioned above. A refinement of the flows of materials on Earth, such as rocks and minerals, is not considered in this article but can be found in a new United States Environmental Protection Agency (USEPA) publication mentioned below.

2 Advances in modeling the Geobiosphere

In this section, we consider the primary theoretical advances presented in this article that are related to the determination of the secondary emergy flows of the Geobiosphere. The first innovation is to examine the Geobiosphere and develop calculation methods for the major secondary exergy flows within an explicit "white box" model of the major planetary processes. The "white box" modeling approach has been used in emergy analyses in earlier studies when details of an interacting system were of interest (Odum, 1983; Odum, 1994). For example, see **Figure 25-9**, simulation of a coastal county with an oyster fishery from Boynton (1975). In this article, a white box model will be applied in modeling and calculating the secondary (Figure 1) and tertiary exergy flows of the Geobiosphere (Section 4). The second advance is to examine the premise that methodological self-consistency in determining spatial and temporal boundaries is the primary characteristic required to ensure a valid emergy evaluation. If followed, this approach will guarantee that future emergy analyses will be transparent, self-consistent, and reproducible.

2.1 A "white box" model of the Geobiosphere

The theoretical model used by Odum (1996) to calculate transformities for the secondary and tertiary emergy flows of the Geobiosphere is shown in **Figure 3.2** of Odum (1996). In this model, all emergy inputs, solar insolation, Earth's deep heat, and tides are connected to all system components: air, ocean, and crust, which are, in turn, all connected to one another. Odum's premise for the calculation of the transformities of flows in the global web of processes follows from this model, i.e., in the global network, everything is assumed to be connected to everything else, thus the total inflow of solar equivalent exergy (formerly emergy inflow) to the Geobiosphere is required for all pathways in the model. This is a "black box" model, and the details of the interactions among sources and components in the model were not specified or evaluated by Odum (1996). Campbell (2000) and Campbell (2016) recognized that while this model might be valid in the long run, it may not be valid on the scale of annual processes that occur over periods of approximately 1 year, which is the scale upon which many transformities are calculated and most emergy evaluations are carried out. The ESL model of the Geobiosphere given in Figure 1 shows the major connections within the global network and how the primary inputs: S, solar exergy; E, exergy of Earth's deep heat; and G, exergy of ocean tides interact to produce the secondary planetary emergy flows. Table 1 includes first-order estimates of the transformities of these global flows in the notes, which can be calculated from the flows given in Figure 1; see Supplementary Section 2.3.

2.2 Evidence for relationships shown in the "white box" model of the Geobiosphere

The ESL model in Figure 1 shows the primary SEE inflows supporting the major secondary exergy flows of the Geobiosphere on the time scale of 1 year. The model pathways are defined in Table 1 and here below. Although some secondary flows require the entire Geobiosphere baseline, as hypothesized by Odum (1996), others may not. By diagraming and defining the connections within a simplified web of the primary and secondary planetary processes, the connectivity of the network can be explicitly defined compared

TABLE 1 The solar equivalent exergy (SEE) base for the major primary and secondary exergy flows of the Geobiosphere (Figure 1), where S is the exergy of solar radiation, E, is the exergy of earth's deep heat, and G, the exergy of the gravitational attraction of the Moon and sun causing the ocean tides. Oceans constitute 70.95% of Earth's surface area and the land 29.05%. The SEE base for the global flows is explained in the text.

Note	Flow	Definition	SEE base	SEE base, seJ y^{-1}	Exergy[a], J y^{-1}, $unit^{-1}$
1	J_1	Solar radiation absorbed heating the atmosphere	S	3.84E + 24	3.84E + 24
2	J_2	Solar radiation absorbed by the oceans: heating	S_O	2.72E + 24	2.72E + 24
3	$J_{2'}$	The oceans transferring heat to the atmosphere	S_O, G	6.63E + 24	5.45E + 23
4	J_3	Solar radiation absorbed on land: heating, etc.	S_L	1.12E + 24	1.12E + 24
5	$J_{3'}$	Land heating the atmosphere	S_L, E	5.32E + 24	2.23E + 23
6	J_4	Tidal energy absorbed: mixing and currents	G	3.91E + 24	1.11E + 20
7	J_5	Molten rock injected to the surface as hot spots	E	4.20E + 24	8.30E + 19
8	J_6	Wind generated by latitudinal heat gradients	SEG	12.0E + 24	9.60E + 21
9	J_7	Wind energy absorbed on land, frictional	T. 4[b]	2.67E + 24	2.18E + 21
10	J_8	Wind energy driving land evaporation, v. diffusion	T. 4[b]	2.67E + 24	3.72E + 21
11	J_9	Wind energy absorbed by the oceans, frictional	T. 4[b]	9.33E + 24	7.61E + 21
12	J_{10}	Wind energy driving sea evaporation, v. diffusion	T. 4[b]	9.33E + 24	1.30E + 22
13	J_{11}	Ocean influences on evaporation: heating, mixing	S_O, G	6.63E + 24	2.72E + 24
14	J_{12}	Evaporation from the sea to the atmosphere, m^3	T. 4[b]	9.33E + 24	4.15E + 14
15	J_{13}	Evapotranspiration from land to atmosphere, m^3	T. 4[b]	2.67E + 24	7.31E + 13
16	J_{14}	Precipitation falling on the sea, m^3	T. 4[b]	9.33E + 24	3.75E + 14
17	J_{15}	Precipitation falling on land, m^3	SEG	12.0E + 24	1.13E + 14
18	J_{16}	Runoff from the land to the sea, m^3	T. 5[c]	8.32E + 24	3.97E + 13
19	J_{17}	Sediments carried from land to the sea	T. 5[c]	8.32E + 24	8.86E + 16[d]
20	J_{18}	Deep heat contributions to isostasy and uplift	E	3.86E + 24	9.20E + 20[d]
21	$J_{18'}$	Isostasy and uplift of the continents	SEG	12.0E + 24	8.86E + 16[d]
22	J_{19}	Tidal energy dissipated in coastal and shelf waters	G	3.91E + 24	5.21E + 19

Definition of the row notes 1–22 can be found in Supplementary Table A3.

[a]Unless otherwise defined in column 3.

[b]Table 4 notes a and b and Figure 1. The emergy of wind energy doing work over the sea and land is treated as a split, when the specific process, e.g., evaporation, occurring in each place is largely dependent on the work done in that regime and not on work in the other regimes, i.e., land vs sea. The emergy base for precipitation over the sea, J_{14}, can also be seen as SEG; see note 16 in Supplementary Material A.

[c]Table 5, note 15 in Supplementary Material A. The emergy required to deliver runoff to the sea is the emergy of the chemical exergy of runoff minus the emergy of the chemical exergy lost to surface water evaporation and deep groundwater infiltration, plus the emergy of the geopotential exergy used up in delivering the chemical exergy of runoff to sea level.

[d]Campbell (2016). Sediment lost is from the Pleistocene or before the modern age, when erosion is affected by agriculture and other human activities. Deep heat flow does not include hot spots. Uplift is assumed to balance erosion from the continents.

to the "black box" model used by Odum (1996). In Figure 1, flows J_1, J_2, and J_3 are the primary inflows of solar radiation that are absorbed by the atmosphere, oceans, and earth, respectively. If the atmosphere, oceans, and earth are all passive receptors, nothing other than solar energy (S) is required to cause this heating. The flows, J_2 and J_3, represent heating of the atmosphere over oceans and land, respectively. In this case, both the solar radiation to cause the initial heating and the presence of the oceans and earth to reradiate heat and warm the atmosphere are required for these processes; thus, these flows require the fractions of solar exergy, S, falling on land or water and the emergy input from E or G, respectively. The role of G in heat transfer from the surface of oceans may not be immediately apparent. However, tidal energy influences the heating and cooling of oceans through mixing cooler bottom waters to the surface, lowering the temperature there and decreasing heat transfer to the atmosphere. While tidal mixing often affects surface temperatures in coastal and shelf areas (Tokinaga and Xie, 2009), it may also be important in mixing deeper ocean waters[7], thereby lowering the surface temperature and reducing heat transfer to the atmosphere. Also, tidal exergy, J_4, directly affects oceans where it is dissipated in mixing and through tidal currents, mostly in the shelf

7 Brierley and Fedorov (2011) model tidal effects on ocean circulation and show that "an increase in such mixing could cause changes in the ocean thermal structure, such as a ~1°C warming of the ocean surface in the eastern equatorial Pacific and a similar cooling in the west. The mechanism of these changes involves mixing the relatively cold waters of the Equatorial Undercurrent with warmer surface waters."

and coastal areas, and also in deep oceans, especially near sea mounts (Egbert and Ray, 2000).

An additional, direct input of exergy from the mantle to crust that was not considered by Campbell (2016) and Brown et al. (2016a) is the molten rock or magma, J_5, emerging as "hot spots" interspersed over the oceans and continents. The formation of hot spots is assumed to be due to plumes of magma arising from somewhere in the mantle and being driven by the same gradient of the Earth's deep heat that drives uplift and isostasy (Morgan, 1971). Although there has been much debate over the depth in the mantle at which these flows originate (Kerr, 2013a), the physical evidence indicates that their origin within the mantle is below 660 km or the boundary between the upper and lower mantle (Smith et al., 2009) and possibility as deep as the core–mantle boundary (Kerr, 2013b). In the mantle plume hypothesis, hot spots arise from the dynamics of the mantle alone, thus the SEE basis for hot spots is E alone.

2.3 Generation of secondary flows in the Geobiosphere

Solar heating is differentially distributed over Earth, as shown in Figure 1, where the heat gradient between the higher level (HL) and lower level (LL) latitudes is shown. The first major class of secondary planetary energy flows, i.e., the winds are generated by the pressure differences between the atmosphere at high and low latitudes, causing global atmospheric circulation or winds, J_6. The winds are a secondary energy flow generated on a planetary basis; thus, all primary solar exergy inflows contribute to their formation, and the SEE base for the winds is S, E, G, or 12.0E+24 seJ y^{-1}. Wind energy flows intersect with the planetary hydrological cycle through mediating evaporation from the land, J_8, and from the sea, J_{10}. Wind energy affects evaporation from the water surface by transporting water vapor away from the surface, thereby maintaining the water vapor gradient and to a lesser degree by disturbing the water surface, with winds increasing the surface area and further enhancing evaporation. Evaporative processes require the entire baseline of the Geobiosphere, since they are mediated by the actions of the wind. The calculations of emergy driving vertical diffusion and frictional work over land and sea and their exergies were determined using the data from Boville and Bretherton (2003), who provided a means to separate the work done by the wind in driving vertical diffusion from that done in frictional work on the surface. As already mentioned, wind is also absorbed over the land and water surfaces, J_7 and J_9, respectively, where it supports tertiary exergy flows doing work on land, e.g., erosion, and on water, i.e., generating waves and currents. Influences of waterbodies on evaporation from oceans, J_{11}, include solar heating of the water surface modified by tidal mixing, which provides a vast amount of heat to drive the hydrological cycle, but it double counts the wind emergy supporting evaporation from the sea. The global hydrological cycle is shown by the next five flows, which are given as volumes of water in 1E+14 m^3. The cycle begins with flow, J_{12}, evaporation from the sea to atmosphere, followed by flows, J_{13}, J_{14}, J_{15}, and J_{16}, which are, respectively, evapotranspiration from the land to atmosphere, precipitation falling on the sea, precipitation falling on land, and runoff from the land to sea. The next three coefficients refer to the earth cycle of uplift and subsidence, with J_{17} showing the exergy of sediments carried to the sea (Campbell, 2016), J_{18} giving the contribution of deep heat to drive isostasy and uplift continents, and $J_{18'}$ giving the exergy required to support isostasy and uplift the land mass of continents, which, over a long time, is assumed to balance the exergy of erosion, e.g., over millions of years (Campbell, 2016). Finally, flow J_{19} gives the tidal exergy dissipated in coastal and shelf waters.

Only the known major pathways supplying substantive amounts of SEE to a global process over a period of approximately 1 year are included in Figure 1. In each emergy evaluation, the investigators are responsible for determining the forcing functions and components that are relevant for answering their research questions. Thus, not all pathways may be included initially in an analysis, and missing pathways that are essential or important on the scale chosen for an emergy evaluation may have to be evaluated to complete a particular study as they are revealed. For example, when planetary systems or processes are evaluated over longer time scales (e.g., >10,000 years) other factors that are relevant at those scales must be included in the analysis (Campbell, 2016).

3 Methods

Consider the definition of emergy in Odum (1996) as a starting point for deliberations on the emergy methods presented in this article: "EMERGY is the available energy of one kind of [energy] previously used up directly and indirectly to make a service or product. Its unit is the emjoule (Odum, 1986; Odum, 1988; Scienceman, 1987)." In this article, the deeper thermodynamic meaning of emergy and emergy methods as they are connected to the proposed 4th law of nonequilibrium thermodynamics defined as the maximum 4th empower principle[8] (Odum, 1996) and the modifications to these methods that are required to accurately determine the transformities of the secondary and tertiary exergy flows of the Earth's Geobiosphere are presented.

3.1 Energy systems language diagrams

The primary tool developed by Odum (1971), Odum (1983) and Odum (1994) to understand and model systems of all kinds is the ESL. Odum (1996) extended the ESL and the models derived from it to characterize and simulate the variations of emergy in all kinds of systems. The ESL is a diagrammatic language in which all symbols and relationships have mathematical definitions. It is a universal language that uses an open set of symbols to add a thermodynamic (energetic) and kinetic context to the representation of systems and their interactions. Odum (2007) extended the ideas set forward in

8 Several energy principles have been defined as the fourth law of thermodynamics. Without entering this debate, we have used Odum (1996) as the basis for assigning the maximum empower principle (MEmP) this role. Essentially, the MEmP is the thermodynamic principle determining success in the evolutionary competition that exists for capturing and using exergy or available energy in a system.

the seminal book *Environment, Power, and Society* (Odum, 1971) to include the insights from the Energy Systems Theory and emergy analysis that developed during the intervening 30 years. In this article, the ESL is used to construct models of the secondary and tertiary available energy (exergy) flows of the Geobiosphere and their concomitant emergy flows. The ESL and its use have been extensively documented and illustrated in Odum (1983, 1994) and many additional publications, thus further description and explanation will not be repeated in this article.

3.2 What is emergy?

Although emergy has been defined above using the definitions in Odum (1996), it is sometimes easiest to understand a complex quantity like emergy by stating what it is not. Emergy, *per se*, is not a quantitatively observable or directly measurable quantity, i.e., there is no place in the universe where one can measure emergy with an instrument or sensor. Nevertheless, it is qualitatively observable in the range of properties that exists in all things. For example, the element carbon appears in many forms of increasing "quality," i.e., emergy density and transformity or specific emergy (emergy intensity)—e.g., peat, lignite, subbituminous coal, bituminous coal, anthracite or amorphous carbon, graphite, and diamond describe a series of materials of increasing quality or transformity for the element carbon, all of which are not necessarily directly connected. As the potential to do work or the special properties of an entity increase along a chain of exergy transformations, the emergy of that entity must also increase. In some cases, increased emergy and the concomitant ability to do work is manifested by the special properties that an item, often a mass, has when compared with other variations of the same material. For example, diamond is a form of concentrated carbon like coal, but it is not generated from coal, rather it is formed from carbon under conditions of extreme heat and pressure deep in the earth, and as a result, it is resistant to chemical reactions and has the highest thermal conductivity of any natural material, which makes it useful as a cutting tool. Although diamond is not derived from coal, because of its properties, one would expect it to have a much higher transformity or specific emergy than that of coal, and in fact it does, 4.9E+04 seJ J^{-1} or 1.42E+09 seJ g^{-1} for coal (Odum, 1996; Campbell and Ohrt, 2009) versus 3.4 E+10 seJ g^{-1} for diamonds found stored ubiquitously in deep earth (~180 km below the surface) as determined by estimates of changes in global seismic wave velocities (Garber et al., 2018) and a rough estimate of 6.07E+19 seJ g^{-1} for the diamonds extracted from earth (Haggerty, 1999; Janse, 2007) during roughly the last 5,000 years, or since recorded human settlement.

3.2.1 Determination of emergy

The emergy required for any item at a point in time can be quantified, if the production process for that product or service is known. This quantification is performed by integrating the available energy transformed directly and indirectly in the process that was responsible for the development of that item with its special properties. Because the transformation of available energy occurs within the milieu of evolutionary competition among processes, when a product emerges from this competition as the "winner," that product will be of higher "quality," i.e., be of higher transformity, in that the item will have special properties; e.g., it will be rarer, or it will have a greater capacity to do work (i.e., a higher empower density) than it did before the available energy was transformed and subjected to the competition among production processes in making the item. The emergy required for any item can be quantified by summing up the transformations of the available energy used up, directly and indirectly, in the production process after converting all the different kinds of available energy input to units of the same kind, e.g., to solar joules (Odum, 1996). In this case, the solar emjoule (sej) is the unit of emergy, where the prefix "em-" denotes the past use of exergy in the production process.

3.2.2 Transformity is a universal measure of quality

Solar emergy is usually taken as the base for determining transformities or the emergy required per unit of exergy flow (sej J^{-1}). Using transformities, the relative quality of all things can be measured and compared on a universal scale by summing up the solar emjoules required to produce any storage or flow within a system and then dividing by the joules of exergy in the product. This ratio, the emergy per unit of exergy (sej J^{-1}) is called transformity, which is a universal measure of quality[9] (Odum, 1996).

The EST indicates that all production processes are constrained by the operation of the maximum empower principle (Odum, 1996; Campbell, 2001) so that to remain competitive in the long run, the emergy flows generated by the feedback from the process to its system must be, at least, as great as the emergy required for the generation of the process or product in the first place. This condition is enforced by the unavoidable evolutionary competition among entities and processes, which ensures that the entities or processes that fail to generate greater empower flow in their networks will be outcompeted by their rivals that do. **Figure 7.8** in Odum (1994) demonstrates this condition with mathematical models of competition among the systems where feedback is mediated by linear, autocatalytic, and hierarchical processes.

3.2.3 The meaning of an increase or decrease in emergy

While emergy is not a directly measurable quantity, it is always associated with quantities that are measurable, e.g., the enthalpy of a biomass, such as a mass of fish eggs, and if that physical quantity is removed or destroyed, the emergy associated with it is also removed or destroyed (Odum, 1996). A common misunderstanding about emergy is the failure to recognize that the emergy per unit or the transformity of a quantity must be a direct measure of the quality of that product or its service, e.g., it must be a measure of the work that a storage, flow, or process can do in its system, and the rules for calculating this work must meet this constraint. For example, the emergy of a female fish will increase with an increase in length;

9 Even though, in theory, transformity is a universal measure of quality, emergy accounting can only yield a comparative measure of quality. Thus, two storages or processes may have the same emergy or transformity, yet very different physical properties. The equivalence of their emergy inputs tells us that the system must invest an equivalent quantity of emergy in resources to have each storage or process as a functional part of the system, although the same resources are not necessarily invested.

however, even at the maximum length, its emergy will continue to increase, if its fecundity increases with age. Once the length and fecundity (i.e., the special useful property of the female fish) reaches the maximum, the emergy of the fish and, by extension, her transformity will no longer increase, regardless of the available energy transformed to maintain the fully developed female fish and its eggs. This understanding of emergy as an accounting quantity that tracks the relationship between the quality or transformity of a product and the exergy transformed to attain that product is seen in the rules for simulating emergy given in Odum (1996). His accounting rules used in simulation do not allow the emergy of a fully formed product to increase indefinitely, even though exergy still may be used to maintain the form of the product against entropic degradation. This is true because the transformity of an item must be an exact measure of the work that an entity can do in its system.

3.2.4 Determining the emergy base for a system by concentrating resources in space and time

It is clear from the ESL models in Odum (1996) that the emergy inflowing to a local system from other areas or other times is to be counted in the emergy base for that local system, i.e., this additional emergy flow is counted along with the share of the Geobiosphere emergy received by the local system's area (**Figure 3.7** in Odum, 1996). The total emergy inflow to the system in the present is responsible for the order and organization being produced there, i.e., the order created within its defined spatial and temporal boundaries. A river flowing across the boundary of a territorial system is an example of emergy supplied to the system through the spatial concentration of renewable resources from outside the system's boundaries. Imported minerals, fuels, goods, services, and people are all valuable resources that bring emergy into a system from other areas and times to augment the emergy that can be used to produce order and organization in the system under evaluation at the present time. Fossil fuels are a clear example of resources formed at an earlier time that are being used in the present to support the system structure and function, and thus all agree that they are to be counted in the emergy supporting a system under evaluation. With the publications of Campbell and Lu (2009, 2014a) and Campbell et al. (2011), the necessary time delay for the formation of human knowledge and experience prior to the possibility of its application in operating a system was the basis for proposing that educational attainment of the population be considered as part of the emergy supporting the system, e.g., in the United States. In the present study, the temporal separation between resource formation and its application to support system operations is allowed on even shorter time scales than was previously considered, when determining the emergy basis for transpiration of various vegetation types.

The time scale for an evaluation of network energy and material flows in most emergy evaluations is >1 year. In this regard, resources generated on the scale of 1 year or less can be double counted, if the inputs are coproducts. However, if resources require longer times for their generation, the temporal separation might be great enough that these resources created in the past should be counted in the emergy supporting the exergy flows of the system in the present. For example, this new rule was applied to calculate the transformity of transpiration in several types of ecosystems of the world. Specifically, the time that it takes to generate biomass with its spatial structure was quantified as part of the emergy base for evapotranspiration in systems, i.e., those systems that take several years or longer to generate the biomass required to support the evapotranspiration that is realized in the present year. For example, if the contribution of biomass structure to annual crop growth falls within the 1-year time boundary of the evaluation, it would not augment the emergy basis for evapotranspiration. However, a tropical rainforest with structural biomass that takes 30 years or longer to be formed would have the emergy base for this structure quantified and prorated over the replacement time of the forest to determine the support required from the forest biomass for rainforest evapotranspiration within the temporal boundary of a single year.

3.2.5 The emergy associated with different exergies in water

In addition to better quantify the concentration of emergy from different spaces and times in determining the emergy basis for a system, the study of hydrological systems over a long period of time (Odum, 1996; Odum et al., 1998; Campbell, 2003) has made it clear that a refinement is required in accounting for the emergy associated with the various forms of exergy in water. Odum (1986) originally defined emergy in terms of its association with the available energy of a storage or flow. Initially, the conceptualization of available energy in emergy evaluations focused on a single type of energy, such as the energy of combustion in biomass, even though biomass also has another form of available energy associated with it, i.e., the available chemical potential energy in the bonds of its constituent compounds that can be used in chemical reactions. While this form of available energy in biomass might be relevant in certain chemical processes, it is, in general, irrelevant in the use of biomass as food in a trophic web. Exergy is a concept like the available energy that was applied by Szargut et al. (1988) for use in evaluating chemical and industrial processes, and in this approach, care is taken to quantify all the forms of available energy (i.e., exergy) that exist in a quantity. Both available energy and exergy indicate the energy potential available to do work against a ground or background state, which must be defined. Odum (1971, 1983, p.105) originally used the term *potential energy* to refer to the aspect of energy that is used up in performing work, which he associated with the thermodynamic term "availability". Afterward the term *available energy* was used to refer to this concept in the literature, but in Odum (1996), emergy was defined based on *exergy* instead of on available energy. However, this change in definition has only been partially integrated into the emergy methodology.

As mentioned above, in all cases, emergy must be associated with an underlying quantity of exergy; therefore, it is logical to assume that each source of exergy in an entity has an available energy (potential to do work) associated with it. This must be true because emergy must track the capacity to produce order and organization in a system, and this capacity can only be and always is derived from the transformation of an energy potential, i.e., a quantity of available energy that has the potential to do work. Furthermore, the two different forms of exergy in water do different kinds of work in the system, and the work done is not always mutually exclusive. The existence of two forms of exergy in a single quantity does not satisfy the definition of a coproduct, which is

defined as two different quantities with non-substitutable functions and uses that are products of the same production function. In this case, two different capacities to do work, i.e., exergies, reside in the same quantity of water. A different accounting scheme is required for this situation. A logical solution is to assign to each quantity, i.e., the geopotential or chemical potential energy, the emergy required to give a quantity of water that exergy. This accounting scheme leads to the potential for the two different types of exergies in water to interact over the landscape with the geopotential energy, in general, serving as the means of concentrating the chemical potential emergy at places within a watershed. The complex interactions of these two different types of exergies and their associated emergy on the landscape was considered by Romitelli (1997). The most important result of this accounting concept is that both the chemical potential energy delivered to a location and the geopotential energy of water used in transporting and concentrating water flows at that location contribute to the transformity of water entering the sea or arriving at various locations in the watershed.

These proposed changes in the rules for calculating the emergy supporting a system are required because according to the fundamental accounting rule emphasized above, emergy must be a measure of the capacity to produce order and organization within the defined spatial and temporal boundaries of a given system. Since each type of exergy in water is a separate and independent source for creating order and organization, both must be considered when they are mutually reinforcing such as in the case of landscape water flows. The emergy inputs to a system must be fully documented in accounting to accurately reflect the capacity for organizing the system inherent in the inputs. Thus, both the emergy of resources concentrated in a system from different space and time domains and the emergy associated with different exergies found within a single material must be fully accounted for in determining the emergy base of a system. Strict balances are maintained in first-law diagrams of the underlying energy measures upon which emergy is based on, but emergy itself is not a conservative quantity nor could it be or still track the transformations of available energy required for current exergy storages and flows. Instead, emergy is an accounting quantity that tracks the concentration and transformation of energy potentials that have the capacity to produce order and organization when used in a system. Therefore, emergy always follows the underlying energy potentials as they are formed or removed by destruction, use, or transfer out of the system. The underlying energy quantities always satisfy the conservation principle and are observable and measurable, whereas emergy is defined by exact accounting rules, but it is neither directly observable nor measurable as explained above.

3.3 The emergy accounting rules applied within the context of the deeper meaning of emergy

The present rules of emergy accounting are primarily designed to make accurate determinations of the emergy of any product or service by avoiding double counting. They are important because, as pointed out above, the quantification of emergy is fundamentally an accounting problem, and thus its value and the accuracy and comparability of results depend upon the consistent application of the rules and assumptions used in its determination. The rules of emergy algebra (Scienceman, 1987; Brown and Herendeen, 1996; Odum, 1996) as given in Li et al. (2010) are as follows:

(1) For a system at steady state, all the emergy inflows to a production process are assigned to the outputs.
(2) When an output pathway splits into two or more pathways of the same type, the emergy input is assigned to each "leg" of the split on the basis of its fraction of total available energy or material flow on the pathway; therefore, the transformity or specific emergy of each branch of the split is the same.
(3) For a process with more than one unique output, i.e., coproducts, each output pathway from the process carries the total emergy input to the process, i.e., the entire emergy required for a process is also required for each of its functionally different products.
(4) No emergy input to a system can be counted twice. Thus, if an input or feedback flow to a component is derived from itself, i.e., it carries emergy already counted in the emergy required for the component, then the input or feedback flow is not added to the emergy required for that component, i.e., input emergy is not double-counted. A corollary to the prohibition against double counting (i.e., counted twice) is that coproducts of the same production process when reunited cannot be added to obtain an emergy input greater than the original emergy input. Thus, when adding emergy inflows or outflows that are coproducts, only the largest one should be considered.

The primary purpose of the emergy accounting rules is to allow the accurate determination of the emergy of a product or service within a network of available energy transformations. The meta framework proposed in this article states that regardless of the exact form of the rules for the calculation of emergy, the general context within which the rules are carried out is the same, i.e., exergy use always increases the quality of the product of or service provided to the system given that the product is being made in its process of formation; however, these actions will occur with greater or lesser efficiency, which results in higher or lower transformity products as a result. For processes making equivalent products, a lower transformity for an equivalent product indicates a higher efficiency process, and it is the one that will ultimately maximize empower in the network (Tilley, 2015). Therefore, attaining maximum empower in a network is an endeavor of the whole system that is also hierarchical in its nature, so while less-efficient processes are ultimately less competitive, they are also secondary contributors to the competitiveness of the whole network. The main result of applying a deeper understanding of emergy is to balance the prohibition to avoid double counting with an equal weight on avoiding undercounting, the reason being that we want to obtain more accurate assessments of the emergy required for an item, which should be closely related to its action and effectiveness upon use in the network. Often the missing piece in this chain of causality is the verification of the improvements made in system structure or function that result from the use of exergy in

the system. The goals of developing and demonstrating a more accurate accounting method will require more research to document the relationships between increasing transformity and the resulting greater performance observed for all kinds of quantities and processes within their networks. In general, in scientific studies, too little attention has been given to documenting the changed relationships that result from the use of exergy in a system. This concern to avoid undercounting manifests itself in two ways: one is through the separate accounting for the actions of different exergies in creating the same product or service, when both are used together. The second is through performing a more exact accounting of the emergy contributions made from temporal and spatial regimes that are separated from the annual and local scales of the production of products and services in the evaluated system by times longer than the period of evaluation or territories beyond the local system boundaries.

4 Results

The primary results of this emergy accounting study are presented in the form of a set of evaluated models with pathways identified and quantified in a series of tables with explanatory notes, where calculations of the transformities of the secondary and tertiary exergy flows of the Geobiosphere derived from wind and water can be found along with the necessary assumptions and supporting references. The article also presents a new approach to quantifying exergy inputs, the meta framework, which more exactly documents past exergy inputs required for quantifying some system storages and flows. The ultimate result of this study will be to allow emergy accountants to produce more accurate assessments of the wind and water emergy inputs to many systems and document other inputs that are dependent on stored emergy more accurately, e.g., products of some stored biomass and educational expertise. Once the solar equivalent exergy for the primary emergy inflows has been established (Brown et al., 2016), the emergy of the secondary exergy storages and flows can be calculated within the system boundaries of the Geobiosphere. In Section 2.1, a "white box" model of the Geobiosphere was presented as an ESL diagram, which shows the major secondary exergy flows of the system and their interactions with explicit formulations as documented in Sections 2.1 and 2.2. Since the model is documented extensively in Table 1, these descriptions will not be repeated in the text, except as specifically called for as a context for discussion. A similar approach using ESL diagrams documented with detailed notes and calculations is used to present the evaluation of transformities of the major tertiary exergy flows of the Geobiosphere, as presented in this section.

4.1 Secondary flows: wind

The white box model of the Earth's Geobiosphere as presented in Figure 1 outlines the major interactions of the primary exergy inflows to the Geobiosphere, showing how exergy is transformed and secondary emergy flows are developed. The emergy basis for these flows is given in Table 1. The largest secondary exergy flow of the Geobiosphere is the wind, and for this reason, we will consider ways to determine its transformity first.

4.1.1 Transformity of wind energy determined from a general circulation model of the atmosphere

Wind energy dissipation in the atmosphere below the 100 mb surface [i.e., the elevation of the planetary boundary layer (PBL)] was determined from the general atmospheric circulation model of Wiin-Nielsen and Chen (1993); see Supplementary Figures A1, A2, Table A4. Their estimates ranged from 0.95 W m^{-2} (Northern Hemisphere summer) under conditions shown in Supplementary Figure A1 to 2.95 W m^{-2} (Northern Hemisphere winter) under conditions shown in Supplementary Figure A2. Supplementary Table A4 shows the transformities of the wind in the PBL and Geobiosphere boundary layer (GBL), i.e., the layer below the 900 mb (≈1,000 m) surface for maximum and minimum estimates of summer and winter winds taken from the general circulation model of Wiin-Nielsen and Chen (1993) and for maximum and minimum estimates of the amount of kinetic energy in the GBL that are given by Ellsaesser (1969).

4.1.2 Determination of the transformity of the wind from observations of average wind velocity

The transformity of the wind was determined from the global average wind velocity measurements taken at 10 m over the continents and oceans from 1998 to 2002, as compiled by Archer and Jacobson (2005). They reported global average velocities at 10 m, V_{10}, of 6.64 m s^{-1} over the oceans and 3.28 m s^{-1} over land. These average velocities, V_{10}, were substituted into **Eq. 2** given in Supplementary Material A after first converting them to the geostrophic velocity, V_g, or the wind velocity predicted at the top of the boundary layer, GBL ≈ 1,000 m. A range of plausible values was substituted into **Eq. 2** for determining the factor relating V_{10} to V_g and for the geostrophic drag coefficients over land and water to estimate the transformity of the global wind (Table 2).

Table 2 shows the results of 11 different determinations of the transformity of the global wind calculated from seven different studies that were based on different assumptions about the factors relating V_{10} to V_g. We used these studies to determine the best values for the geostrophic drag coefficients to use over land and water. Column notes a–h in the table explain the origin and derivation of the numbers in the columns representing each calculation method used by the different authors and the assumptions supporting their calculations (see Supplementary Table A5). The estimates are divided into two sets as noted in the table, one representing the minimum transformity found at the maximum power generated by the wind using the assumptions of the method and the other representing the average value for the method. The row notes, Numbers 1–7, explain the variables and parameters, which are defined in Column 2. Row 8 reports the average transformity of global wind energy found by each calculation method for average and maximum power conditions. Rows 9–15 present statistical analyses of the determinations, such as the mean, standard deviation, and range, the geometric mean velocity, and the geometric mean of the model (i.e., the formulae for wind energy given in Notes 5–7). The maximum power estimate of the transformity of the wind from the global atmospheric circulation model of 1,047 seJ J^{-1} was combined with the four maximum power estimates of the wind transformity from the empirical determinations (Table 2) to give an estimate of 1,245 seJ J^{-1} for the transformity of wind energy dissipated in the

TABLE 2 Estimation of the transformity of the wind from models and empirical data. Constants used in the calculation: ρ, density of air, 1.225 kg m^{-3} at 1 atm pressure, and 15°C; A_{ocean}, ocean surface area, 3.62E+14 m^2; A_{land}, land surface area such as freshwater lakes, 1.48E+14 m^2; average ocean wind velocity, OV_{10}, 6.6 m s^{-1}; and average land wind velocity, LV_{10}, 3.28 m s^{-1} (Archer and Jacobsen, 2005), both measured at 10 m; number of seconds in a year, T = 3.16E+07 s y^{-1}. Geobiosphere solar equivalent exergy baseline, GEB, is 12.0E+24 seJ y^{-1}. See explanatory notes appended below.

Note	Variable or parameter	Units	Campbell and Erban (2017) considers atmospheric stability	Odum's average values, e.g., Campbell et al. (2005b)[b]	Campbell and Erban (2017) with global momentum balance	DeVilbiss and Brown (2015) corrected	Garratt (1977), his Table 4	Garratt (1977) his Table 4 considering mountain area	Kara et al. (2007), corrected for mountains, and atmospheric stability
1	K_{GW} geostrophic drag coefficient, ocean	dimless	5.9E-04	1E-03	4.1 E-04	1.26 E-03	1.25 E-03	1.25 E-03	1.25 E-03
2	K_{GL} geostrophic drag coefficient, land	dimless	1.79E-03	2 E-03	1.64 E-03	1.64 E-03	1.80 E-03	1.94 E-03	2.20 E-03
3	V_{ocean} geostrophic wind vel. max. pwr.[h]	m s^{-1}	9.49	11.1	9.49	9.73	9.96	9.96	9.49
	V_{ocean} geostrophic wind vel., ocean, avg. v.	m s^{-1}	9.49	9.49	9.49				9.49
4	V_{land} geostrophic wind vel max. pwr.[h]	m s^{-1}	10.91	5.47	10.9	7.97	7.29	7.29	10.9
	V_{land} geostrophic wind vel., land avg. v.	m s^{-1}	6.98	6.98	6.98				6.98
5	E_{ocean} = ½ ρ*K_{GW}*V_{ocean}^3*A_{ocean}*T, m. pwr.[h]	J y^{-1}	3.05E+21	9.48 E+21	2.45 E+21	8.12 E+21	8.64 E+21	8.64 E+21	7.47 E+21
	E_{ocean} = ½ ρ*K_{GW}*V_{ocean}^3*A_{ocean}*T, avg. v.	J y^{-1}	3.05E+21	5.97 E+21	2.45 E+21				7.47 E+21
6	E_{land} = ½ ρ*K_{GL}*V_{land}^3*A_{land}*T, max. pwr.[h]	J y^{-1}	6.54 E+21	9.35 E+20	6.13 E+21	2.38 E+21	1.99 E+21	2.44 E+21	8.23 E+21
	E_{land} = ½ ρ*K_{GL}*V_{land}^3*A_{land}*T, avg. v.	J y^{-1}	1.70 E+21	1.94 E+20	1.59 E+21				2.14 E+21
7	Total exergy = E_{ocean} + E_{land}, max. pwr.[h]	J y^{-1}	9.59 E+21	10.4 E+21	8.58 E+21	10.5 E+21	10.6 E+21	11.1 E+21	1.57 E+22
	Total exergy = E_{ocean} + E_{land}, avg. v.	J y^{-1}	4.75 E+21	7.92 E+21	4.04 E+21				9.54 E+21
8	Wind transformity, max pwr.[h]	seJ J^{-1}	1,250	1,150	1,400	1,140	1,130	1,080	760
		seJ J^{-1}	2,530	1,520	2,970				1,250

(Continued on following page)

10.3389/fenrg.2024.1392634

TABLE 2 (*Continued*) Estimation of the transformity of the wind from models and empirical data. Constants used in the calculation: ρ, density of air, 1.225 kg m^{-3} at 1 atm pressure, and 15°C; A_{ocean}, ocean surface area, 3.62E+14 m^2; A_{land}, land surface area such as freshwater lakes, 1.48E+14 m^2; average ocean wind velocity, OV_{10}, 6.6 m s^{-1}; and average land wind velocity, LV_{10}, 3.28 m s^{-1} (Archer and Jacobsen, 2005), both measured at 10 m; number of seconds in a year, T = 3.16E+07 s y^{-1}. Geobiosphere solar equivalent exergy baseline, GEB, is 12.0E+24 seJ y^{-1}. See explanatory notes appended below.

Note	Variable or parameter	Units	Campbell and Erban (2017) considers atmospheric stability	Odum's average values, e.g., Campbell et al. (2005b)[b]	Campbell and Erban (2017) with global momentum balance	DeVilbiss and Brown (2015) corrected	Garratt (1977), his Table 4	Garratt (1977) his Table 4 considering mountain area	Kara et al. (2007), corrected for mountains, and atmospheric stability
	Wind transformity, average v.								
			Max. power[h]	Average v.	Combined values				
9	Mean transformity from mean exergy	seJ J^{-1}	1,098	1,436	1,288				
10	Mean transformity, μ, of n determinations	seJ J^{-1}	1,130, n = 7	1,660, n = 7	1,470 (n = 11)				
11	Std dev.	seJ J^{-1}	± 180	± 712	± 637				
12	Range	seJ J^{-1}	950–1,310	948–2,372	834–2,108				
13	Geometric mean transformity, μ_{geo}	seJ J^{-1}	1,310	1,520	1,480				
14	Geometric mean of model, $\mu_{geo\ of\ model}$	seJ J^{-1}	1,640	2,150	1930				
15	Atmospheric circulation model, μ_{acm}	seJ J^{-1}	1,047	1,241	1,144				
16	Average of five means	seJ J^{-1}	1,245	1,601	1,462				

See Supplementary Table A5 for the definition of column head notes and for the definitions of row notes (1–16).

10.3389/fenrg.2024.1392634

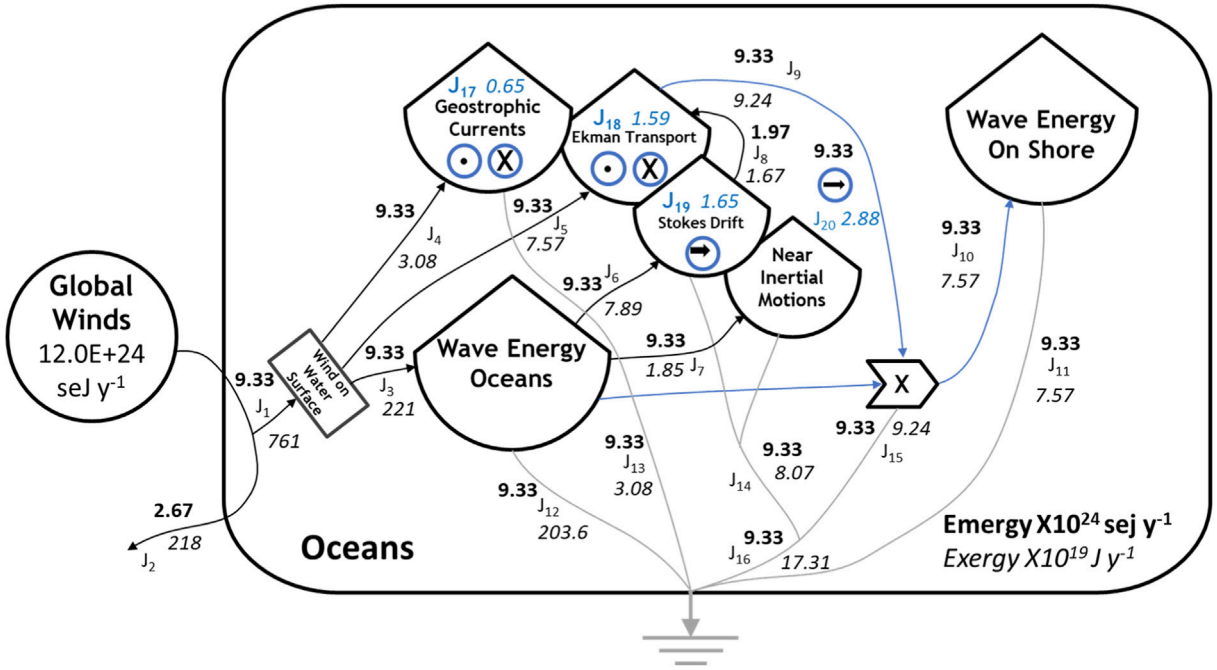

FIGURE 2
An Energy Systems Language "white box" model of the world oceans tracing the SEE input from the global winds (circle) and showing the way that wind work on the ocean surface that generates tertiary emergy flows in the oceans. The major storages and flows of exergy generated by the wind energy dissipated in the oceans are shown in the model, but only the exergy flows are evaluated in this study (Table 3). Water flows are shown in blue with the arrows directed into the page (X) or out of the page (●), showing the effects of the Coriolis force in the Southern and Northern hemispheres, respectively. Stokes drift (➡) moves water in the direction of the wind. Emergy flows (seJ y^{-1}) are given in bold, and exergy flows (J y^{-1}) are in italics.

GBL at maximum power. Using NCAR's CAM2 model, Boville and Bretherton (2003) have provided another analysis of the transformity of the wind that allows us to distinguish the wind energy dissipated in frictional effects on the surface (1,226 seJ J^{-1}) from the wind energy dissipated in diffusion (715 seJ J^{-1}).

4.1.3 The tertiary exergy inputs to the oceans derived from the wind

The major tertiary emergy flows derived from the wind are shown in Figure 2 and include waves on the ocean surface, waves transmitted to the shore, geostrophic wind-driven currents (i.e., currents at the scale of the ocean basins), Ekman layer transport (local surface currents affected by the Coriolis force), Stoke's transport (local currents moving in the direction of the wind), and near-inertial motions. In Figure 2, the wind blowing on the ocean surface, J_1, generates waves, J_3, and drives geostrophic currents, J_4, as well as Ekman transport, J_5. Some of the wind energy passing over the oceans, J_2, continues to be dissipated over the land. Wave energy drives Stokes drift, J_6, and generates near-inertial motions, J_7. Water movements driven by Stokes drift interact with Ekman transport, J_8, to augment the wind energy basis for total surface water flow and because of the Coriolis force alters its direction away from a 90° displacement from the wind direction as expected for surface currents. In other words, the current direction is commonly displaced less than 90° from the wind direction. Surface currents in the Ekman layer interact with the wind-driven wave field, J_9, to help move wave energy shoreward, J_{10}. Some fraction of the wave energy is dissipated in the surf zone, J_{11}; here, we assume it is 100%, when the entire continental shelf is considered. Wave energy is also dissipated in the oceans as white caps in breaking, along with other processes, J_{12}. The energy dissipated in friction by the wind energy driving water movements—i.e., geostrophic currents, J_{13}, Ekman transport, and Stokes drift, J_{14}, wave energy transmitted to the shore, J_{15}, and near-inertial motions, which appear in the total, J_{16}—is assumed to balance the exergy inflows to these storages over a year's time. The exergy flows of some ocean currents are evaluated in Figure 2 and are shown in blue italics. Geostrophic currents, J_{17}, and Ekman transport, J_{18}, are affected by the Coriolis force with the direction of the flow shown by arrows directed into or out of the page, indicating the flow in the Southern and Northern Hemispheres, respectively. Stokes drift, J_{18}, is wave-driven transport that moves in the direction of the wind part of which J_{19} augments Ekman transport. The combined surface water flow (Ekman transport augmented by Stokes drift) is shown as, J_{20}, and this combined water flow helps transmit wave energy to the shore.

4.2 Secondary flows: water and the hydrological cycle

The white box model of Earth's Geobiosphere (Figure 1) outlines the major interactions of the primary exergy inflows to the Geobiosphere, showing how the secondary emergy flows related to water within the hydrological cycle are developed. The secondary exergy flows related to the hydrological cycle are the second category of major biophysical flows generated by the primary SEE inputs to

TABLE 3 The emergy basis for the tertiary exergy flows in the world oceans are generated by wind (a secondary flow) and are used for the empirical determination of the drag coefficient over the oceans (Kara et al., 2007). They result in the oceans absorbing a larger fraction of the total wind energy. Definitions of the pathways shown in Figure 2 are given in this table along with the annual flows of the exergy of the wind in the world oceans driving waves and surface currents of various kinds and showing the SEE basis for these flows. Also, the exergy and transformities of some surface currents and motions are shown. All flows are coproducts, and coproducts are recombined in several flows.

Note	Flow	Definition	SEE base seJ y^{-1}	Exergy J y^{-1}	Transformity sej J^{-1}
a	J_1	Wind energy absorbed over the oceans	9.33E + 24	7.61E + 21	1,226
b	J_2	Wind energy that is not absorbed over the oceans	2.67E + 24	2.18E + 21	1,226
c	J_3	Wind energy absorbed in creating ocean waves	9.33E + 24	2.21E + 21	4,220
d	J_4	Wind energy driving geostrophic currents	9.33E + 24	3.08E + 19	302,900
e	J_5	Wind energy driving surface ageostrophic (Ekman) currents	9.33E + 24	7.57E + 19	123,000
f	J_6	Wave energy driving Stokes drift and dissipation	9.33E + 24	7.89E + 19	118,300
g	J_7	Wave energy generating near-inertial wave motion	9.33E + 24	1.85E + 19	505,000
h	J_8	Stokes drift augmenting Ekman transport (a split)	1.97E + 24	1.67E + 19	118,300
i	J_9	Wind energy driving Ekman transport including Stokes drift	9.33E + 24	9.24E + 19	101,000
j	J_{10}	Wave energy transmitted to the shoreline	9.33E + 24	1.17E + 20	79,800
k	J_{11}	Wave energy dissipated on the shoreline	9.33E + 24	1.17E + 20	79,800
l	J_{12}	Wave energy dissipated in the oceans	9.33E + 24	2.00E + 21	4,700
m	J_{13}	Wind energy dissipated in driving geostrophic currents	9.33E + 24	3.08E + 19	302,900
n	J_{14}	Wind energy dissipated in near inertial and Stokes motions	9.33E + 24	8.07E + 19	115,600
o	J_{15}	Wind energy dissipated by Ekman transport plus Stokes drift	9.33E + 24	9.24E + 19	101,000
p	J_{16}	Total ageostrophic energy dissipated in the surface layer	9.33E + 24	1.73E + 20	53,900
		Wind-driven ocean currents			
Q	J_{17}	Wind-driven geostrophic currents	9.33E + 24	6.46E + 18	1,444,000
R	J_{18}	Wind-driven Ekman transport	9.33E + 24	1.59E + 19	588,000
S	J_{19}	Wave-driven Stokes drift	9.33E + 24	1.65E + 19	564,000
T	J_{20}	Wind-driven surface flow (Ekman transport and Stokes drift)	9.33E + 24	2.88E + 19	324,000

See Supplementary Table A6 for the explanatory notes for Table 3.

the Geobiosphere. The determination of the transformities of the secondary flows of the hydrological cycle is considered in this section. Some of the transformities calculated as in the notes to Table 1, such as the quotient of the SEE and exergy flows on the pathways, may be somewhat different from the values obtained from the tertiary analysis of global wind and water flows described in Figure 2 and Table 3, and in Figure 3 and Table 4 (see the footnotes to Table 1).

The water flows of the hydrological cycle were determined using the three methods described in Supplementary Section A3.0—*Methods for calculating the secondary available energy inputs to the Geobiosphere*: Supplementary Section A3.1—*Equations governing the wind*, Supplementary Section A3.2—*Methods for determining the exergy of water flows in the hydrological cycle*, and the method for evaluating the transformity of the tides, which is described in the Supplementary Section A3.3—*Methods for determining the transformity of tides.* Supplementary Section A3.4 describes *Calculating transformities for the secondary and tertiary exergy flows of the Geobiosphere.* In Supplementary Section A4.0—*Uncertainty in the calculations,* we consider three kinds of uncertainties that are relevant to the calculations of the secondary and tertiary available emergy flows of the Geobiosphere. Supplementary Section A4.1 considers *Uncertainty in the determination of the fraction of wind energy dissipated over the oceans.*

4.2.1 Quantification of the global hydrological cycle

Supplementary Table B1 gives 10 global hydrological budgets reported in studies carried out from 1974 to 2015, nine of which were reported in Marcinek (2007). A 10th study by Rodell et al. (2015) was added, and the mean, standard deviation, coefficient of variation, and the maximum and minimum of these estimations are reported in the table. The global flows of water in the hydrological cycle used in this study are from Adler et al. (2003), assuming a hydrological balance over the annual cycle. The statistical parameters from this study were compared to similar values obtained by analyzing the 10 global budgets mentioned above (see the last row in Supplementary Table B1). The estimates of Dai and Trenberth (2002) were chosen to complete the hydrological

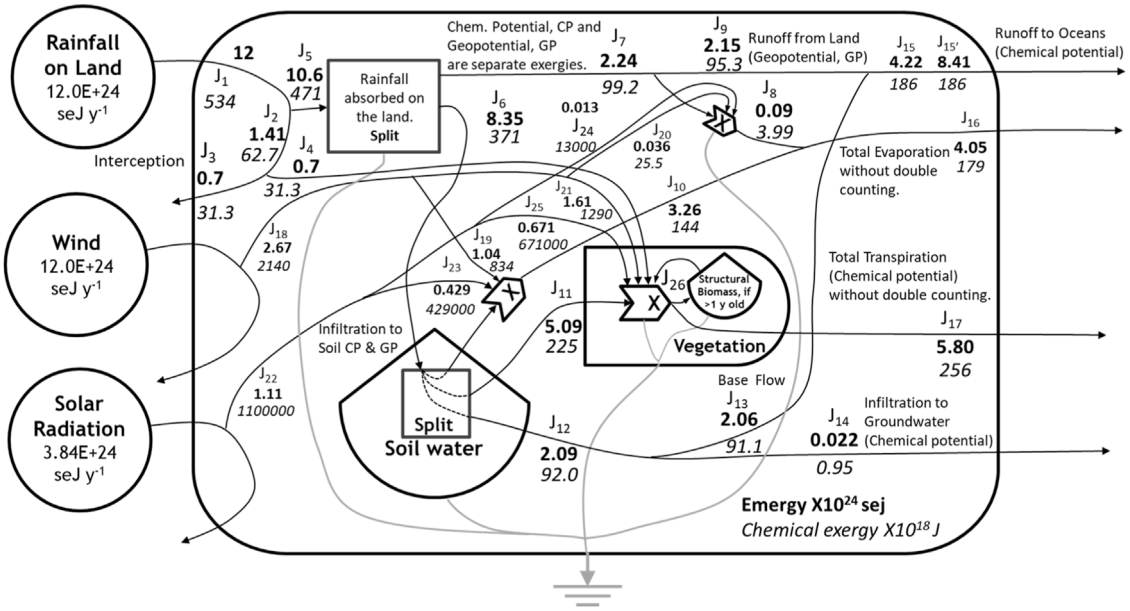

FIGURE 3
An Energy Systems Language "white box" model of the terrestrial hydrological cycle tracing the SEE input from precipitation falling on land, the wind dissipated over land, and solar radiation incident on the land (circles) and showing the emergy and chemical exergy of tertiary water flows generated in the terrestrial hydrosphere. Table 4 gives the definitions of the pathways, storages, and the annual flows of emergy, volume, mass, and chemical and geopotential exergy in each pathway, as well as, the transformities of the flows of chemical and geopotential exergy and their specific emergy. See Supplementary Table A7 for the explanatory notes for Figure 3.

cycle by supplying a value for global runoff from the land to oceans. After accounting for infiltration into the deep groundwater, this number is 39.7 1,000 km^3 y^{-1}. Assuming closure of the hydrological budget, these choices lead to estimates in 1,000 km^3 y^{-1} of 113, 73.1, 39.9, 414.9, and 375 for precipitation on land, evaporation on land, runoff to the sea, evaporation over the sea, and precipitation over the sea, respectively.

4.2.2 The tertiary available energy flows of the terrestrial hydrological cycle

The tertiary emergy flows of the terrestrial hydrological cycle derived from precipitation on land are shown in the model given in Figure 3, and the data sources, values, assumptions, and methods of calculation for these flows are given in Table 4. The exergies of the tertiary emergy flows derived from the rain were determined based on studies in the literature, and the descriptions of these calculations and the sources for the values used are given in Table 4, following the network of relationships described in Figure 3.

The ESL diagram of the tertiary flows of the hydrological cycle (Figure 3) is briefly described as follows: the diagram shows that rainfall, J_1, from Figure 1 can be intercepted, J_2, before being absorbed by the land surface, after which it can evaporate from the surface of the vegetation, J_3, or it can be absorbed and can contribute to supporting the productive processes of the plants, J_4. The precipitation not intercepted, J_5, reaches the ground surface and can be absorbed there. Precipitation absorbed by the land surface is handled as a split between water that infiltrates into the soil, J_6, and that which runs off at or close to the surface, J_7. Runoff includes the surface water flows, which are subject to evaporative losses, J_8, and contribute to stream flows, J_9, e.g., rivers. The fate of water that infiltrates into the soil, J_6, is shown by another split that occurs within the soil. This split includes water that is evaporated from the soil, J_{10}, water that is absorbed by vegetation, J_{11}, and water that infiltrates deeper into the ground, J_{12}. Water that infiltrates below the soil can return to the streams and rivers as base flow, J_{13}, or can infiltrate into the deep groundwater, J_{14}. The chemical potential energy delivered to the sea is J_{15}, if only the concentration of chemical potential energy in the hydrological network is considered in determining the emergy of river water delivered to the sea (Table 4). However, if the geopotential energy used up in bringing the river water to sea level is also considered, the value is given by $J_{15'}$. Total evaporation from the system, J_{16}, includes intercepted water and surface water evaporated along with evaporation from the soil surface. Total transpiration, J_{17}, includes the portion of intercepted water contributing to plant growth and plant transpiration. Flows J_{18} to J_{25} quantify the inputs from the sun and wind used to support evaporation and transpiration. These flows are not counted in the emergy base for the water flows because they are not larger than the inputs from the hydrological cycle, and if included, they would double count the emergy inflows supporting the water cycle (see Table 4).

4.2.2.1 Estimating interception in the ecoregions of the world

Interception is one of the tertiary water flows listed in Figure 3 and Table 4. Interception is the rainfall captured by the vegetation, e.g., tree canopy, stems, and forest floor, before it can seep into the soil; it has not been commonly evaluated in past emergy assessments of the hydrological cycle. Supplementary Table B2 gives an estimate of the average value for interception in the global hydrological cycle

TABLE 4 Definitions of the pathways and storages in Figure 3; the annual flows of emergy, volume, mass, and chemical and geopotential exergy are given on each pathway, as well as, the transformities of the flows of chemical and geopotential exergy and specific emergy. The emergy and flows of solar and wind exergy supporting the water flows of the hydrological cycle are also given.

Note	Flow	Definition	Emergy, E + 24 seJ	Volume, E + 03 km^3	Mass, E + 18 g	Exergy, chemical, E + 18 J	Exergy, geopotential, E + 18 J	Transformity, chemical potential, sej J^{-1}	Transformity geopotential, sej J^{-1}	Specific emergy, sej g^{-1}
	Global water flow									
1	J_1	Precipitation on land	12.00	113	113	534	887	22,490	13,530	106,195
2	J_2	Interception	1.41	13.3	13.3	62.7		22,490		106,195
3	J_3	Interception evaporated	0.704	6.63	6.63	31.3		22,490		106,195
4	J_4	Interception used by vegetation	0.704	6.63	6.63	31.3		22,490		106,195
5	J_5	Precipitation reaching the land	10.59	99.7	99.7	471	783	22,490	13,530	106,195
6	J_6	Water infiltrating into the soil	8.35	78.7	78.7	371	606	22,490	13,790	106,195
7	J_7	Water running off the land	2.24	21.1	21.1	99.2	166	22,560	13,530	106,195
8	J_8	Evaporation from surface water	0.090	0.849	0.849	3.99		22,590		106,195
9	J_9	Stream flow	2.15	20.3	20.3	95.3	159	22,560	13,530	106,195
10	J_{10}	Water evaporated from the soil	3.26	30.7	30.7	144		22,680		106,195
11	J_{11}	Soil water transpired by plants	5.09	48.0	48.0	225		22,680		106,195
12	J_{12}	Water infiltrating below soil	2.09	19.7	19.7	92.0	148	22,680	14,060	106,195
13	J_{13}	Base flow returning to streams	2.07	19.4	19.4	91.1	135	22,680	15,250	106,195
14	J_{14}	Infiltration to deep groundwater	0.022	0.0204	0.0204	0.95	1.30	22,800	16,650	106,195
15	J_{15}	Chem. exergy delivered to the sea	4.22	39.7	39.7	186		22,620		106,195

(Continued on following page)

10.3389/fenrg.2024.1392634

TABLE 4 (*Continued*) Definitions of the pathways and storages in Figure 3; the annual flows of emergy, volume, mass, and chemical and geopotential exergy are given on each pathway, as well as, the transformities of the flows of chemical and geopotential exergy and specific emergy. The emergy and flows of solar and wind exergy supporting the water flows of the hydrological cycle are also given.

Note	Flow	Definition	Emergy, E + 24 seJ	Volume, E + 03 km^3	Mass, E + 18 g	Exergy, chemical, E + 18 J	Exergy, geopotential, E + 18 J	Transformity, chemical potential, sej J^{-1}	Transformity geopotential, sej J^{-1}	Specific emergy, sej g^{-1}
15′	$J_{15'}$	J_{15} with necessary geopotential	8.41	39.7	39.7	186	293	45,120	14,380	211,840
16	J_{16}	Total evaporation from land	4.05	38.1	38.1	179		22,640		106,195
17	J_{17}	Transpiration and interception	5.80	54.6	54.6	256		22,660		106,195
Verification that solar and wind exergy supporting global water flows are secondary coproduct emergy inflows										
			Emergy, E + 24 seJ		Exergy, E + 18 J					
18	J_{18}	Wind exergy absorbed on land	2.67		2,140					
19	J_{19}	Wind evaporating soil water	1.04		834					
20	J_{20}	Wind evaporating surface water	0.036		25.5					
21	J_{21}	Wind facilitating transpiration	1.61		1,290					
22	J_{22}	Solar exergy absorbed on land	1.11		1,100,000					
23	J_{23}	Sun evaporating soil water	0.429		429,000					
24	J_{24}	Sun evaporating river water	0.013		13,000					
25	J_{25}	Sun supporting transpiration	0.671		671,000					
26	J_{26}	Feedback from biomass to GPP	variable		variable					

See Supplementary Table A7 for data and references explaining the origin of the numbers in Notes 1–26. Table 4 accompanies Figure 3.

10.3389/fenrg.2024.1392634

TABLE 5 Determination of the emergy base for long-term structural biomass and transpiration of vegetation found in the ecoregions of the world as defined by Schlesinger and Jasechko (2014). Data on transpiration as a percent of evapotranspiration and the percent of terrestrial precipitation falling on each ecoregion were used to determine the emergy required for transpiration of vegetation in the ecoregions.

Note	Flow	Ecoregion	Emergy inflow in precipitation, E + 24 seJ y^{-1}	Emergy of transpiration, E + 24 sej y^{-1}	Fraction of GPP building long-term structure	Emergy building long-term structure, E + 24 sej y^{-1}	Biomass turnover time (n –1) yrs.	Emergy of long-term structure, E + 24 sej	Total emergy for eco-regional transpiration, E + 24 sej
26	J_{26a}	Tropical rainforest	4.2	1.55	0.325	0.505	15.2	7.672	9.225
27	J_{26b}	Tropical grassland	1.68	0.835	0.400	0.334	10.6	3.540	4.375
28	J_{26c}	Temperate deciduous forests	1.2	0.485	0.375	0.182	16.1	2.929	3.414
29	J_{26d}	Boreal forest	0.96	0.425	0.400	0.170	16.6	2.822	3.247
30	J_{26e}	Temperate grassland	0.6	0.293	0.400	0.117	3.7	0.433	0.726
31	J_{26f}	Desert	0.48	0.273	0.388	0.106	6.4	0.678	0.951
32	J_{26g}	Temperate coniferous forest	0.48	0.128	0.400	0.051	16.1	0.827	0.956
33	J_{26h}	Steppe	0.24	0.093	0.400	0.037	5.75	0.215	0.308
34	J_{26i}	Mediterranean shrubland	0.12	0.0476	0.388	0.018	9.3	0.171	0.219
35	J_{26j}	Barren land	2.04	0.0	0.0	0.0	0.0	0.0	0.0
		Total	12.0	4.13		1.52		19.29	23.42

Notes:

Data on the 9 ecoregions listed in notes 26–34 and the definition of these regions are found in Schlesinger and Jasechko (2014). The remainder of the Earth's surface, which includes surface water, is assumed to be barren land (note 35). The flows J_{26a} to J_{26i} refer to pathway J_{26} in Figure 3, which represents the feedback from structural biomass that supports annual primary production of the vegetation in an ecoregion. The methods for obtaining the numbers in columns 4 through 10 are as follows.

The emergy inflow to each ecoregion (column 4) is determined by multiplying the percent of terrestrial precipitation falling on an ecoregion (from **Table 1**, column 5 in Schlesinger and Jasechko, 2014) by the emergy base for terrestrial precipitation 12.0E+24 seJ y^{-1}. The volume of water evapo-transpired in each ecoregion is determined using the United Nations Food and Agriculture Organization (FAO) data for the percent of terrestrial ET accounted for by each ecoregion (numbers in parentheses in column 7 of **Table 1** in Schlesinger and Jasechko, 2014) multiplied by total global evapotranspiration. Total global ET is found by subtracting runoff from total precipitation (113 – 39.7 = 73.3 10^3 km^3 y^{-1}, Supplementary Table B1). This gives an estimate of the volume of ET for each ecoregion. Using data from Schlesinger and Jasechko (2014) on the percent of terrestrial precipitation falling in each ecoregion and the total terrestrial precipitation given above, the volume of rain falling in each ecoregion was determined.

Next, using the volume of ET and the volume of rainfall for each ecoregion, we calculated ET as a fraction of the total precipitation. This number was multiplied by the emergy base for the ecoregion (column 4) determined above to find the emergy base for ET in the ecoregion. This number was multiplied by transpiration as a fraction of ET (column 2 in Schlesinger and Jasechko, 2014) to find the emergy base for ecoregional transpiration (column 5).

The annual emergy of transpiration building long-term biomass (column 7) was found by multiplying the emergy base for transpiration by the fraction of GPP allocated to build long-term biomass (woody structure plus fine roots), column 6 in this table. Data in column 6 are estimated from the unperturbed case in **Figure S4** of the supplement to Bloom et al. (2016), where values for tropical broadleaf forests, W, temperate forests, T, grasslands, D, and boreal forests, B, are reported. In this table, similar ecoregions are assumed to have ratios like those reported in Bloom et al. (2016) or to be averages of two of the reported systems, e.g., Mediterranean shrubland and desert are assumed to be approximated by the average of grasslands and deciduous forests.

The turnover time of biomass, n, in the ecoregions (column 8) comes from **Table S11**, column 3, in the supplement to Erb et al. (2016). The biomes in this table are defined in Olsen et al. (2001) and are approximately equivalent to the ecoregions defined by Schlesinger and Jasechko (2014), except that we averaged Olsen's montane grassland and tundra category with his grassland category to estimate the turnover time of Schlesinger and Jasechko's steppe category. Estimated potential turnover times minus 1 year (n – 1) are reported to account for the fact that current annual transpiration has not yet contributed to the existing stock of long-term biomass.

The emergy required for building long-term structure of the vegetation in each ecoregion (column 9) is found by multiplying the turnover times of the vegetation minus 1 year (n – 1) by the annual emergy used for building the long-term structure of the vegetation in each ecoregion. The emergy of this year's transpiration plus the emergy required for building long-term structure gives the total emergy required for the transpiration of the vegetation of each ecoregion in each year (numbers in column 10).

10.3389/fenrg.2024.1392634

TABLE 6 Determination of the transformity and specific emergy of transpiration of the vegetation found in the ecoregions of the world as defined by Schlesinger and Jasechko (2014). Transformities and specific emergy evaluations include the effects of accumulated biomass and are rounded to the nearest 100 seJ.

Note	Flow	Ecoregion	Emergy base transpiration, E + 24 seJ	Water transpired, $m^3\ y^{-1}$	Chemical exergy of transpiration, $J\ y^{-1}$	Transformity transpiration, $sej\ J^{-1}$	Specific emergy of transpiration, $sej\ g^{-1}$
36	J_{26a}	Tropical rainforest	9.225	1.20E + 13	5.61E + 19	167,500	769,800
37	J_{26b}	Tropical grassland	4.375	6.44E + 12	3.02E + 19	147,700	679,100
38	J_{26c}	Temperate deciduous forests	3.414	3.74E + 12	1.75E + 19	198,400	912,000
39	J_{26d}	Boreal forest	3.247	3.28E + 12	1.53E + 19	215,400	990,100
40	J_{26e}	Temperate grassland	0.726	2.26E + 12	1.06E + 19	69,900	321,400
41	J_{26f}	Desert	0.951	2.11E + 12	9.87E + 18	98,100	451,000
42	J_{26g}	Temperate coniferous forest	0.956	9.91E + 11	4.64E + 18	209,800	964,200
43	J_{26h}	Steppe	0.308	7.21E + 11	3.37E + 18	93,000	427,700
44	J_{26i}	Mediterranean shrubland	0.219	3.67E + 11	1.72E + 18	129,800	596,600
45	J_{26j}	Barren land	0.0	0.0	0.0	0.0	0.0
		Total average value	23.42	3.19E + 13	1.47E + 20	159,700	734,300

Notes 36–45: the same definitions given for notes 26–35 of Table 5 applies to notes 36–45 of Table 6.

The numbers in column 4 of Table 6 are transferred from column 10 in Table 5 and give the emergy required for annual transpiration in each ecoregion.

The water transpired in each ecoregion is calculated as a fraction of total ET, which can be calculated based on Figure 3 as the water infiltrating into the soil, J_6, minus the water infiltrating below the soil, J_{12} (or 78.7–19.7 = 59E + 03 km^3) and from ecoregional ET as a fraction of terrestrial ET (61.1E + 03 km^3) using the numbers in parentheses in column 7 of **Table 1** in Schlesinger and Jasechko (2014) giving an average estimate of 60×10^3 km^3. This value is multiplied by the fraction of total ET occurring in each ecoregion (i.e., the numbers in parentheses in column 7, **Table 1** in Schlesinger and Jasechko, 2014) times the ratio of transpiration to total ET in each ecoregion (column 2 in Schlesinger and Jasechko, 2014) to find the volume of water transpired in each ecoregion (values in column 5).

The chemical exergy of water transpired ($J\ y^{-1}$) is calculated by multiplying the volume of water transpired by its density (1.0 $g\ cc^{-1}$) times the chemical exergy per gram for soil water (4.684 $J\ g^{-1}$), i.e., for water of 305 ppm solute concentration (Note 3, Table 7).

The transformity of transpiration in each ecoregion (column 7) is found by dividing the emergy base for transpiration (column 4) by the chemical exergy of the water transpired (column 6). In a similar manner, the specific emergy of the water transpired in each ecoregion (column 8) is the emergy base for eco-regional transpiration (column 4) divided by the mass of the water transpired (the values in column 5 multiplied by 1.0E6 $g\ m^{-3}$).

using values from the ecoregions of the world as defined by Schlesinger and Jasechko (2014).

4.2.2.2 Estimating the contributions of structural biomass to transpiration

In Figure 3, flow J_{26} represents the feedback from stored plant biomass to facilitate plant production processes such as transpiration. These flows are evaluated in Table 5 and 6 where the emergy base for long-term structural biomass and the transpiration of vegetation found in the ecoregions of the world (Schlesinger and Jasechko, 2014) is determined (Table 5). Table 6 shows the emergy base for transpiration from Table 5 and estimates the water transpired by the ecoregion. These values are reported and are used to calculate the transformity and specific emergy of transpiration of the major vegetation types by the ecoregion.

Some important transformities derived from this work and rounded to the closest 10 seJ J^{-1} are precipitation and the related surface water flows: chemical potential energy of 22,490 seJ J^{-1} and geopotential energy of 13,530 seJ J^{-1}. The specific emergy of precipitation is 106,200 seJ g^{-1}. The transformity of water evaporated from the soil surface or transpired by plants is 22,680 seJ J^{-1}, and the transformity of total evapotranspiration which includes that from the surfaces of the soil, plants, and fresh water is 22,640 seJ J^{-1}, while the transformity of all water used to support plant growth such as transpiration and intercepted water absorbed by plants is 22,660 seJ J^{-1}. The number for evapotranspiration (22,680 seJ J^{-1}) is a base number applicable to processes with structure built on the scale of 1 year, such as annual crop growth. For ecosystems with vegetation that require at least several years to develop, the structure required to facilitate transpiration, the transformities of plant processes such as transpiration and gross primary production (GPP) are higher (Tables 5, 6), e.g., the transformity of tropical rainforest transpiration is estimated to be 167,500 seJ J^{-1}, which is more than 7 times higher than that of annual crops). A complete description of the calculations required to determine all the transformities and specific emergy evaluations of the tertiary exergy flows of the hydrological cycle is given in Tables 4–6 and in the explanatory notes associated with these tables.

TABLE 7 Transformities and specific emergy evaluations of the annual flows of water passing through the major storages of the hydrosphere and the stored natural capital in the Geobiosphere. The emergy required for all flows is 12.0E + 24 seJ y^{-1}, as all flows and storages listed are ultimately dependent on terrestrial precipitation. Most numbers are from Babkin et al. (2003) and given in Shiklomanov and Rodda (2003) except as noted.

Note	Major water storages	Volume, 1,000 km^3	Turnover time, y	TDS, ppm	Exergy, J g^{-1}	Mass flux, g y^{-1}	Chemical exergy flux, J y^{-1}	Specific emergy, sej g^{-1}	Transformity, sej J^{-1}	Natural capital stored, sej
1	World ocean	1,338,000	2,500	35,000	0.0000	5.35E + 20	0.00E + 00	2.24E + 04	0.00E + 00	3.00E + 28
2	Groundwater (salt and fresh)	25,400	1,400			1.81E + 19		6.61E + 05		
3	Predominantly fresh ground water	11,530	1,400	305	4.6826	8.24E + 18	3.86E + 19	1.46E + 06	3.11E + 05	1.68E + 28
4	Soil moisture	16.5	1	305	4.6826	1.65E + 19	7.73E + 19	7.27E + 05	1.55E + 05	1.20E + 25
5	Glaciers, permanent snow	24,604	9,686	7.10	4.7221	2.48E + 18	1.17E + 19	4.83E + 06	1.02E + 06	1.19E + 29
6	–Antarctica	21,600	9,700	7.12	4.7221	2.23E + 18	1.05E + 19	5.39E + 06	1.14E + 06	
7	–Greenland	2,340	9,700	7.12	4.7221	2.41E + 17	1.14E + 18	4.97E + 07	1.05E + 07	
8	–Arctic Islands	83.5	9,700	7.12	4.7221	8.61E + 15	4.07E + 16	1.39E + 09	2.95E + 08	
9	–Mountainous regions	40.6	1,600	7.19	4.7221	2.54E + 16	1.20E + 17	4.73E + 08	1.00E + 08	1.92E + 28
10	Ground ice: permafrost	300	10,000	950	4.5971	3.00E + 16	1.38E + 17	4.00E + 08	8.70E + 07	1.20E + 29
11	Lakes	176.4	17	13,000	2.9884	1.04E + 19	3.10E + 19	1.16E + 06	3.87E + 05	
	–Fresh	91		207	4.6956	5.35E + 18	2.51E + 19	2.24E + 06	4.78E + 05	2.04E + 26
	–Salt	85.4		13,000	2.9884	5.02E + 18	1.50E + 19			
12	Swamp and bogs	11.47	5	51	4.7163	2.29E + 18	1.08E + 19	5.23E + 06	1.11E + 06	6.00E + 25
13	River/stream	2.12	0.104	120	4.7072	2.03E + 19	9.57E + 19	5.91E + 05	1.25E + 05	1.25E + 24
14	Biological	1.12	0.0027	9,000	3.5246	4.09E + 20	1.44E + 21	2.93E + 04	8.30E + 03	3.28E + 22
15	Atmosphere	12.9	0.022	10	4.7218	5.89E + 20	2.78E + 21	2.04E + 04	4.30E + 03	2.63E + 23
Total water storage		1,388,511								
Total fresh water storage		36,555								

See Supplementary Table A8 for the explanatory notes accompanying Table 7.

10.3389/fenrg.2024.1392634

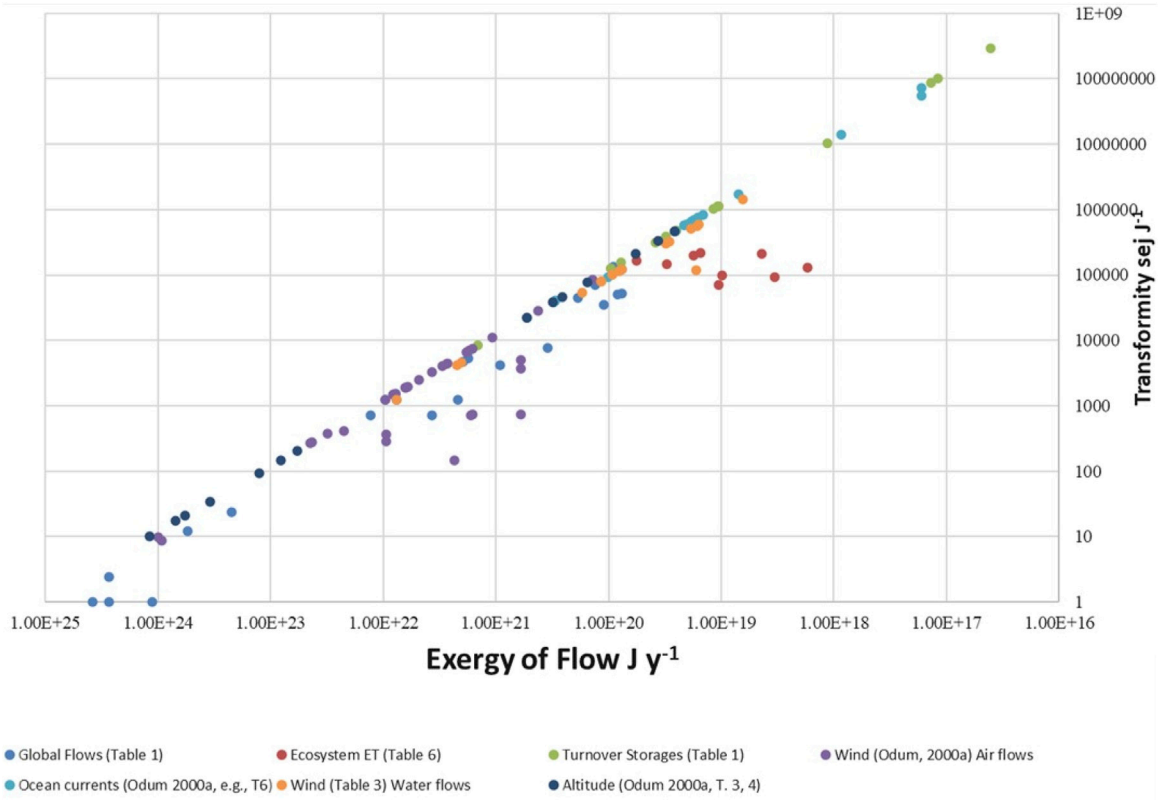

FIGURE 4
Plot of all transformities (sej J^{-1}) of the secondary and tertiary exergy flows (J y^{-1}) of the Geobiosphere that were evaluated in this study. The transformities of the flows are plotted by functional analysis groups as defined below. The functional groups refer to tables in this article and in Odum (2000a) and are as follows: global flows, Table 1; ecosystem ET, Table 6; turnover of storages, Table 7; wind flows (Odum, 2000a), his Table 2 and Supplementary Table B4; ocean currents, Odum (2000a), Table 3 and Supplementary Table B4 in this study; wind-driven flows, Table 3 in this study; and "Altitude" in Odum (2000a), **Tables 3 and 4**. The data plotted in this figure are summarized in Supplementary Table B6.

4.3 The emergy of water flows in the hydrological cycle estimated from global storage and turnover time

Table 7 gives values for the major storages of water in Earth's hydrological cycle as identified by Babkin et al. (2003). Four estimates of the volume of the major water storages on Earth are reported in Supplementary Table B3 for comparison to Babkin et al. (2003). The sources for the water volumes, turnover times, solute concentrations, and density of the various storages of water in the hydrosphere are given in Table 7, and the exergy, mass flux, and exergy flux are calculated from these data. The specific emergy evaluations and transformities of the water fluxes are also determined from the data and shown in the table as are the estimates of the value of the natural capital of the various water storages. The key values that result from this analysis are the transformities of predominantly fresh groundwater, 311,000 sej J^{-1}, fresh water in lakes, 478,000 sej J^{-1}, water in swamps and bogs, 1,100,000 sej J^{-1}, and permafrost, 87,000,000 sej J^{-1}. Among the natural capital storages of water in the Geobiosphere, permafrost has the highest value, 1.20E+29 sej, followed closely by permanent ice cover, such as that found in the Arctic and Antarctic, 1.16E+29 sej. The next largest natural capital water storage in the Geobiosphere is predominantly fresh groundwater, 1.68E+28 sej.

4.4 Comparison of new calculations of the secondary and tertiary emergy flows of wind and water with earlier values in Odum

The primary existing source of calculations for secondary and tertiary emergy flows of the Geobiosphere is Folio #2 of the Handbook of Emergy Evaluations (Odum, 2000a). In this small pamphlet, **Tables 2 and 6**, respectively, report emergy analyses of the energetics of atmospheric circulation and ocean circulation, both of which are considered in this study. Supplementary Table B4 gives the solar emergy base, the exergy flows, and the transformities associated with each of the flows in Odum (2000a) that were reexamined in this article along with some recalculations of existing flows and new calculations of missing flows that were performed as additional examples to check the existing estimates. **Tables 3 and 4** in Odum (2000a) present an analysis of the exergy and transformities of latent heat and continental rainfall as a function of height (these data are reported in the "Altitude" class in Figure 4 and in Supplementary Table B4). These functions are combined, checked, and where necessary recalculated in Supplementary Table B5. Odum (2000a) also considered the emergy of Earth processes, but a reexamination of these and other analyses in Odum (2000a) is left for a later time. The table notes document the data sources and assumptions used in making

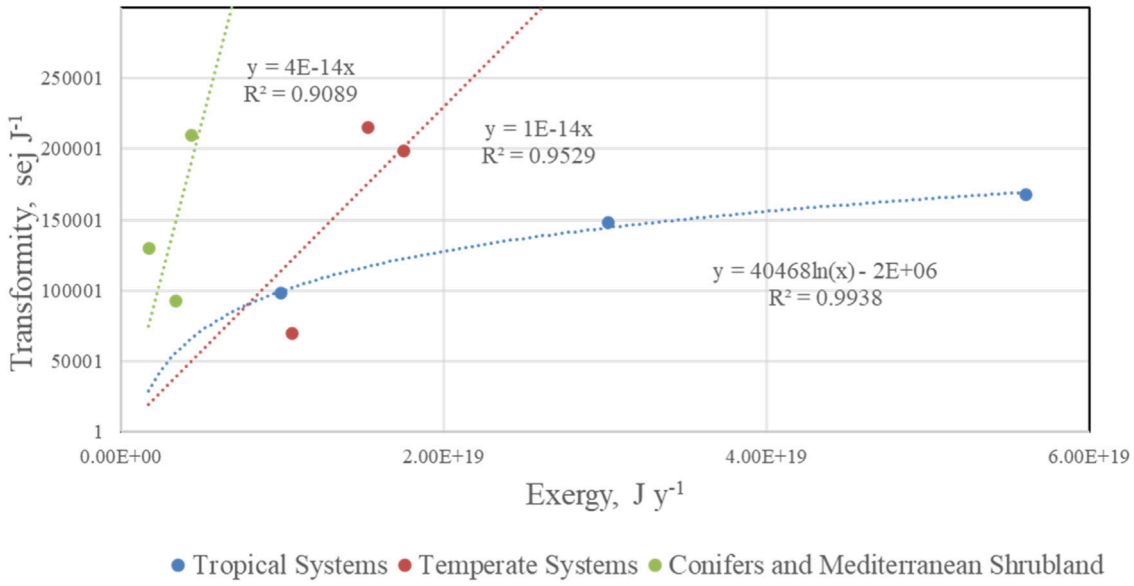

FIGURE 5
A plot of the transformity of transpiration in the ecoregions of the world (Supplementary Table B7) as a function of exergy flow. The vegetation falls into three functional groups defined by different relationships of transformity with exergy flow. The transformities of tropical systems have a logarithmic relationship of transpiration with exergy flow, whereas the transformities of transpiration in temperate systems and in the constructed category "Conifers and Mediterranean Shrublands" exhibit more linear relationships with exergy flow.

the calculations. Unlike in the folios, mathematical errors in the original calculations are noted and corrected in the table. Recalculated values are marked with a (') and new values that represent alternate estimates using different data or those that consider flows that are not formerly determined are indicated by an (*). In both cases, an additional superscript is added for each new calculation.

4.5 Transformity as a function of exergy flows in the Geobiosphere

Data on the secondary and tertiary exergy flows of the Geobiosphere and the resulting transformities associated with these flows are compared and summarized using a master plot of transformities of all the phenomenon examined in this study vs exergy flow (Figure 4). The data for this figure are reported in Supplementary Table B6. The well-defined diagonal in this figure is created by Geobiosphere processes that require the entire baseline for their formation. Off-diagonal flows are based on regional processes, have temporal components affecting their formation, or have other formation conditions, requiring less than the full Geobiosphere baseline to produce the flows, e.g., molten rock ejected to Earth's surface (J_5 in Table 1).

4.6 The relationship of the transformity of ET with exergy flow for ecoregional functional groups

The group of red dots in Figure 4 give an analysis of ecosystem evapotranspiration, ET, examined by ecological functional groups. These systems form a group for which exergy flow and transformity appear to have a different relationship from the general pattern observed for global processes. These relationships are examined in detail in Supplementary Table B7 and Figure 5 below, where the ecoregions of the world are divided into three functional groups: tropical systems, temperate systems, and a constructed category, i.e., conifers and Mediterranean shrublands. Each of the three groups includes a grassland ecoregion (Supplementary Table B7) with steppe included in the constructed category. Figure 5 shows that the transformity of ET in tropical ecoregions has a strong logarithmic relationship (R^2 = 0.9938) with exergy flow, whereas both temperate ecoregions and the constructed category have strong linear relationships with exergy flow. The relationships between exergy flow and the variables account for the departure or conformance of the relationship between transformity and the exergy of ecoregional transpiration with the diagonal. The relationship between the transformity of tropical rainforest ET and its exergy flow is closest to the relationship of transformity to global exergy flows in global processes.

5 Discussion

The emergy basis for systems is better defined by expanding the time frame of its quantification to include the work done by the system in the past that is required for the creation of components that are actively used in the present evaluation, e.g., vegetation biomass created over many years in the past is used in creating plant processes in the present. The operation of the maximum empower principle is observable in the hierarchy of quality observed in all phenomena, but its defining quantity, emergy intensity, is not directly measurable, as it depends on the history of past use of available energy. For this reason, the rules of emergy accounting in space and time become very important and must be continually

tested and refined to increase the accuracy of emergy quantifications. This article focuses on the further development and testing of the rules by which the emergy of storages and flows within a system can be determined with greater fidelity to the underlying thermodynamic processes and the time required for their development. In this regard, we consider the importance of self-consistency in the use of the emergy methodology as the primary characteristic of a cogent emergy evaluation, and therefore ways to ensure that an emergy evaluation will be self-consistent and become of paramount importance. Building on the firm foundation of the four articles to determine a new planetary baseline for emergy analyses, we have taken the next step in verifying and revising the transformities and other emergy evaluations per unit value of the secondary and tertiary exergy flows of the Geobiosphere that will be required to perform self-consistent and cogent emergy evaluations of all of Earth's phenomena. Specifically, in this article, we have documented the emergy flows of the secondary and tertiary exergy flows of wind and water as they are derived from the network of exergy flows in the Geobiosphere. These revised data provide the input required to perform more accurate emergy evaluations.

5.1 Application of the primary rule of emergy accounting

The primary rule of emergy accounting superseding all other rules is that when an increase in the emergy of a component or process in a system is determined by the chosen accounting method, i.e., the quality or emergy per unit of the evaluated quantity increases, then this quantity must have an increased ability to do useful work in its system. Also, the converse of the rule must be true. This rule places the emphasis on obtaining an accurate accounting of all past use of exergy required for the product or service being evaluated, neither over nor under counting exergy in the evaluations. In pursuit of greater accuracy in accounting, the separation distance between the use of the required emergy in space and time is reduced, but it cannot be equal to or smaller than the evaluation limit for an annual evaluation. In the limit, the evaluation can consider as potential inputs all entities that are separated by more than the period of the evaluation, usually 1 year in most emergy analyses. Brown and Brandt-Williams (2011) called for consideration of both space and time domains in evaluating the emergy inputs to all systems. This rule accomplishes this, although other alternatives might be put forward. Several examples of the application of this rule are given above, but perhaps the most significant for overall emergy evaluations is the requirement to consider the emergy of educational attainment in the evaluation of systems such as human work. The integral of the emergy required to accomplish the past years of schooling (Campbell and Lu, 2014b) is required in the evaluation of national systems to allow the accurate determination of the emergy basis for national economies and to determine the emergy balance in the equity of trade.

5.2 The evolution of the emergy methodology

The International Society for the Advancement of Emergy Research, also known as the Emergy Society, was formed in July 2007. Soon after this organization was established, which included a Standards Committee, the society recognized the tension that would inevitably develop between establishing a standard method of analysis and the intellectual creativity required by a young methodology that continues to be under development. Campbell et al. (2005a) identified this and several additional problems that the emergy methodology was facing at that time, and chief among them was the problem of disagreement on the value of the planetary baseline to be used in emergy accounting. Now, the baseline questions have been resolved for the time being with the publication of the four strong articles mentioned in the *Introduction* section that converge on the value of 12.0E+24 seJ y^{-1}. Furthermore, the additional data and analysis in Supplementary Material A of this article further strengthen the evidence supporting this number.

A solution of the conflict between intellectual creativity and standardization of the emergy methods can be resolved through insights in this article because the fundamental characteristic of the measurement of emergy depends on the fact that it is an accounting quantity, and therefore, its quantification depends on the suite of accounting rules chosen to govern the evaluations. As a result, the most important characteristic in determining the emergy of an item is the self-consistency of the accounting method. Furthermore, the validity of the quantification of emergy can be judged by how accurately the emergy of the item represents the observed properties and actions of the item in the system of which it is a part. The integrity of any proposed rules can be judged by their conformance to scientific laws and the principles of the Energy Systems Theory (Odum, 1983, 1994). To further ensure the self-consistency of the methodology, an open access database of transformities and other emergy evaluations per unit factors could be set up, using a blockchain accounting model (Tapscott and Tapscott, 2016). The entries would include the emergy per unit factors (also called "Unit Emergy Values" or "Emergy Characterization Factors") and the ESL model required to produce each item, such as the references for all sources and antecedents. The use of the database would be free after registration, but all users would be required to add their new calculations, ESL diagrams, and documentation to the website once these are complete. The Emergy Society offers a dataset last worked on by Tilley et al. (2012) that can be accessed from http://www.emergysociety.com/emergy-society-database/ and might be suitable to build upon.

Most recently, the USEPA has just completed a new database (De Vilbiss et al., 2024) of Emergy Characterization Factors (ECFs), *i.e.*, emergy per unit values or transformities, which if expressed in energy units, can serve as a basis for creating consistent emergy analyses and evaluation models (https://www.epa.gov/water-research/uev-library). This database not only covers most of the air and water flows given in this article but also provides data on Earth processes and other systems important for completing emergy analyses. This new publicly accessible database of ECFs, if adopted internationally, will greatly improve the consistency and reliability of emergy evaluations around the world. Science is not fixed and improvements to knowledge are constant, so we still require a system like the blockchain accounting model of database construction proposed above to help emergy evaluation develop at a maximum rate.

5.3 Use of "white box" models of the Geobiosphere, global wind–driven circulation, and hydrological cycle

As mentioned above, Odum (1996) used a black box model to determine the transformities of the global secondary and tertiary exergy flows. An innovation in this article is that we used "white" box models to evaluate the exergy flows of the Geobiosphere (Figure 1), the wind-driven circulation system (Figure 2), and the hydrological cycle of Earth (Figure 3). The primary difference between these two accounting models is that in the former (Odum, 1996), the network is assumed to be completely interconnected, and thus, the entire SEE base for system flows is necessary to support every flow in the network, whereas in the later, the requirements for any flow or process must be traced through the network from the points of use to the points of origin (this study). Some flows in the "white" box system require all the SEE inputs to support them, but other flows do not. The advantage of "white" box models is that they provide a chance to use all the knowledge that we have about a system to obtain a more accurate determination of the system's exergy flows and the relative transformities of these flows. A disadvantage is that if we increase the information required to evaluate the system, the chance to introduce errors into the calculations increases. Despite the use of different models for the emergy evaluation of secondary and tertiary exergy flows of wind and water, the transformities determined in this article correspond well (Supplementary Table B4) to the transformities determined for some similar flows in Odum (2000a). "White" box models are easier to check for errors because more specific information on the mechanisms of interaction is provided, therefore they are subjected to more verification and subsequent correction, if shown to be wrong.

5.4 Examples of the proposed methods for determining the chemical potential energy of water

Under the method proposed in this article, determining the transformity or specific emergy of an exergy flow in the system requires an estimate of all the types of exergies present in that flow that must be used up in the process of creating it, along with an estimate of the emergy required for the existence of the types of interacting exergies. This new method of accounting for interactions when more than one type of exergy is required for the same flow is applied to determine transformities for water flows in the hydrological cycle. The proposed changes make the determination of the emergy of water more consistent with our knowledge of the two exergies required for a given chemical potential exergy flow to be used at a particular location on the landscape. In this study, accounting for the emergy of water in the hydrological cycle is performed under the assumption that both the chemical potential of the water flow and the geopotential of the same water flow that is used up in the process of delivering the chemical potential in the water to its point of use are required to accurately capture the emergy required for the water flow to be used at a location. For example, the chemical potential energy of fresh water delivered to sea carries both the emergy of its chemical potential and that of the geopotential used up in the process of delivering the water parcel to sea level. Similarly, the emergy of runoff augments the emergy of water pooling in places such as floodplain forests and augments transpiration there, above that supported by local rainfall alone. In both cases, the test of accuracy of the altered accounting scheme is in the observations that the organizing power of exergy flows is greater than expected from the use of the base transformity for chemical potential energy alone. Floodplain forests are complex systems that may be governed by the subsidy–stress gradient as proposed by Odum et al. (1979). The emergy of the chemical potential of water, concentrated there, depends on both local rainfall and on the water transported to that location from higher in the watershed. To determine whether or not the concentration of the emergy of chemical exergy in floodplain forests results in a greater order and organization than is found in an upland forest requires the study of the whole system in all its aspects (biological, chemical, physical, and geological) and may not be indicated by the comparison of a single parameter such as forest productivity, which because of the role of water as a stressor, a subsidy, or both may not tell the whole story (Odum et al., 1979; Megonigal et al., 1997). In the case of the water debouched into the sea at river mouths, the importance of river discharge to maintain the thermohaline circulation of the oceans has been recently demonstrated through model simulations (Huang and Mehta, 2010).

The proposed *meta* framework of emergy evaluation put forward in this article requires that the assessed value of the emergy of a product or service must be a true reflection of the ability of that entity to do work in its system and *vice versa*. In other words, if the ability of an entity to do work increases, then its emergy must also increase. If this second condition does not hold, then the method of calculating emergy of an entity must be modified to better reflect the change in its ability to do work in the system. An example of this principle begins with the observation that different types and qualities of plant production are observed in the various ecological regions of the world, and these various forms of plant structure require various time periods to develop to their mature state. Thus, there is a temporal separation between the past use of exergy to create structural biomass and its use in the present to produce the exergy flows associated with various kinds of plant production. This fact leads to the realization that the historical emergy flows that create the structural biomass of plants over periods longer than 1 year (Table 6) should be accounted for as an input in determining the transformity of the present emergy flows of different vegetation types, e.g., transpiration, gross primary production, etc.

5.5 Significance of the proposed changes in determining the emergy required for items

Implementation of the proposed changes in the methods for determining the emergy of items may make a difference in many transformities and may or may not make large differences in the overall results, depending on the specific processes evaluated (i.e., historically, emergy analyses have been extremely robust in the face of errors and omissions). Odum (2000b) examined the ecological–economic process of salmon pen culture in the Pacific Northwest section of the United States and found that the buyer of

pen-raised salmon received twice the emdollar value compared to the dollars paid for the fish. The most significant fundamental principle of emergy analysis is the recognition that the most important characteristic of a valid emergy evaluation is self-consistency in the methods and models used to perform the calculations. Odum (2000b) showed that once the salmon are processed and used by consumers, seven emdollars from the outside economy are attracted for each emdollar of local environmental product. In this study and in Campbell (2016), a functional approach to emergy evaluations has been proposed and used. This approach is like the original work on emergy evaluations, which is tied to quantify a series of functional processes creating order and organization in a system within defined spatial and temporal boundaries (Tennenbaum, 1988; Odum, 1996). The thread of self-consistency in these analyses is the tracking and summing of all the directly and indirectly required emergy inflows (i.e., exergy × transformity) necessary to make a new exergy flow.

In this article, we have urged that additional attention be placed on quantifying the extended spatial and temporal boundaries required to account for all necessary inflows producing activities in the present system. From this perspective, determining the emergy of an item is performed by tracing the path of all its inputs and ensuring the independence of each one. Emergy evaluations that are most likely to experience changes in their evaluations are vegetation assessments that include plants with large older biomass accumulations and human systems where the education of people is considered in the evaluation of exchanges. This article focuses on advancing the emergy accounting methodology, clarifying it, and ensuring that more accurate assessments can be made, especially regarding the emergy flows of wind and water.

5.6 Comparison with other methods of determining emergy

In general, determining the emergy of an item requires the identification of secondary and tertiary emergy flows that are responsible for organizing the exergy flow or storage of interest within the system. Thus, the exergy flows that are directly and indirectly used up in producing the exergy of another item or process are determined and then multiplied by their transformities and summed to determine the emergy necessary for creating an exergy flow or storage. Approaches such as the use of primary SEE inflows on a proportionate basis over the surface of Earth, an idea called the "tripartite" by Brown and Brandt-Williams (2011), and using them to assign emergy values would not make sense in the accounting scheme proposed here, although this idea could be used in other accounting schemes. The reason that this method is not consistent with a process-based approach to quantify is that it does not follow identified and verified lines of interaction from the emergy sources to the products made.

Emergy evaluation covers all the sciences, and it was left in a certain state of development by Odum (1996) and Odum and Odum (2000). One point of contention has been the way that Odum characterized the equations for describing changes in emergy over time (i.e., dynamic emergy). Odum's conceptualization of emergy and of the problem of describing it dynamically was that it is not a state variable and therefore requires a different set of equations centered on the emergy accounting rules to describe its temporal changes accurately. In Odum's (1996, pp. 9–13) view, three phases are required to accurately describe the change in emergy over time. In the first phase, while emergy is being stored, i.e., the emergy of the product is increasing, but the formation process is not yet complete, the emergy of the product increases and this includes the emergy lost to the heat sink in the formation process, as this emergy use is also required for building the product. In the second phase, the product is built and there is no change in its emergy (Odum, 1996, **Figures 1–7**), and thus the rate of change of the emergy stored is 0. In the third stage of emergy simulation, the product is made but suffers a net loss, either from removal of the product to another system or from the depreciation of the stored product's mass, i.e., the loss of its ability to do work. In both cases, the stored emergy of the product declines. Odum and Odum (2000, p. 157) make it clear that both changes in the emergy stored or a change in its nature, i.e., its ability to do work, can be responsible for a change in the stored emergy of the product. All emergy calculations are based on a correspondence with a real quantity of exergy represented in the ESL model. The dynamic rules governing the transformations of the emergy in a storage are always subject to these real processes. Emergy has no existence when it is separated from the real quantities (e.g., enthalpy) that it is associated with.

In another case, Odum and Odum (2000) propose a solution for dealing with the question of when a product is fully formed. This is a key question for simulations of the development of a product. In the case of an industrial process, it is apparent when the product is available, e.g., the time when a chair or table built from wood is completed. There is no question about the existence of the product, even though it may be characterized in terms of the quality of its construction, durability, etc. However, the completion of a product within an ecosystem may be somewhat more difficult to determine. Odum and Odum (2000) proposed a solution to this problem by assuming that such products are generated within a spectrum of natural variability that will set statistical boundaries on the quantity of emergy generated in the final product. Despite this modeled solution, there are many quantities in nature where the emergy of a product can be easily determined. For example, the transformity of a female fish will continue to increase, if her capacity to produce eggs increases. This capacity may increase up to the maximum size of the fish. Again, the key to any emergy assessment goes back to the system that is responsible for producing the item of concern. Given the system or item of concern, variables can always be found that capture the development of quality within that item. Theoretical constructs can be chosen when better real variables are not available.

Although models can be created and simulated using Odum's rules (Campbell et al., 1998), in most cases, these rules do not make simulation easy. In a series of articles, Tilley (2014, 2015) proposed a set of alterations to the Odum equations that make them easier to simulate. In my view, it is valid and reasonable to use different methods to try to get a better understanding of dynamic emergy accounting. Tilley has developed a productive method that has been used by others (Lee, 2014) to investigate important problems such as the role of resource pulses in power acquisition by ecosystems. Tilley's articles yield interesting insights into the method and possible nature of emergy when viewed dynamically; however,

the redefinition of terms in his modeling scheme removes the main constraint on Odum's definition of emergy, i.e., emergy is not a state variable and requires different rules and a different set of equations for its simulation to be accurately represented. However, despite these rule changes, Tilley's simulations and analyses give what appear to be reasonable and interesting results.

In conclusion, neither Brown and Brandt-Williams (2011) approach to emergy evaluation using manipulations of the tripartite (solar equivalent exergy baseline) nor Tilley's redefinition of the rules governing dynamic emergy flows are entirely consistent with the understanding of path-based emergy evaluations put forward in this article. However, these approaches are from the same tree of knowledge as are the proposals for evaluating emergy presented here, and are therefore not incompatible with one another.

5.7 Expansion of emergy analysis of the wind

Wind is a complex quantity that is often the second most important environmental emergy input to a system found on the surface of the Earth. Under certain conditions, it can be the largest emergy inflow, and in other cases, it is responsible for the largest negative environmental impact on system wellbeing, e.g., the effects of wind causing erosion affecting agriculture (Asgharipour, et al., 2020). The properties of the wind are determined by pressure and temperature gradients in the atmosphere, which in turn determine the stability of the fluid and govern its mixing properties. Wind is often considered only superficially in emergy analyses, nevertheless, it can be the most important variable in determining certain environmental impacts, such as land erosion and the vertical mixing and distribution of pollutants. Supplementary Section A5.7.1 considers the effects of atmospheric stability on the transfer of wind energy to Earth's surface, and Supplementary Section A5.7.2 gives an estimate of the transformity of the energy dissipated in the GBL by wind.

5.8 The choice of the best transformity for wind for a given study

There is uncertainty in all our calculations, especially in the values reported for wind and the calculations made using these values (Table 2; Supplementary Table A3). Nevertheless, all the studies converge on numbers that are self-consistent and give a reasonable approximation even though they may be superseded by more accurate or authoritative values in the future. One understanding that emerges from this examination of the wind and its transformity is that the transformity of wind energy differs depending on the aspect of wind energy that is of interest in a particular study. For this reason, it is important to understand the purpose of wind transformity values that have been calculated in the past and the appropriate value to use for any research project in the future. For example, Boville and Bretherton (2003) showed that wind energy doing frictional work on Earth's surface (Table 3, notes a and b) has a different and higher transformity (1,226 seJ J^{-1}) than the wind work dissipated in driving atmospheric vertical diffusion (715 seJ J^{-1}). The aggregate work in the boundary layer is a combination of these two values, but consideration of wind exergy may lose this practical context of its application in synthesis.

5.9 The importance of scientific accuracy

Both wind and sun are important and necessary inputs to the hydrological processes of evaporation and transpiration; however, these inputs would double count the evaluation of transformities based on global water flows if included in the calculation of the transformities without first checking to see if they are the largest inputs of emergy to the processes. In Table 4, a comparison of the emergy of flows J_{19}, J_{20}, and J_{21} for wind and J_{23}, J_{24}, and J_{25} for sun with flows J_9, J_{10}, and J_{11} based on the hydrological cycle shows that the sun and wind are secondary sources of emergy supporting the processes of evaporation and transpiration from the soil and vegetation. The feedback from structural biomass to current plant production (e.g., GPP and transpiration) is a necessary input required to account for the variations in the different qualities of plant production, e.g., grasslands vs forests.

5.10 Data choices and uncertainty

The estimates of global precipitation given in Adler et al. (2003) were thought to be the most accurate because they used a combination of low-orbit microwave satellite data and geosynchronous-orbit satellite infrared data adjusted with surface rain gauge observations to make their estimates of global precipitation over land and water as part of version 2 of the Global Precipitation Climatology Project. The estimates of Dai and Trenberth (2002) of runoff from the land to oceans were chosen to complete the hydrological model because they estimated global river flow at the points of discharge to the sea and used several methods to check their estimate. Further discussion of uncertainty in the model can be found in Supplementary Sections A.3.0 and A. 3.1.

Values from Trenberth et al. (2007) in Supplementary Table A2 were not chosen, but they illustrate plausible variations from the generally accepted values. For example, they report a slightly smaller total volume of the world oceans due to an ostensibly more accurate account obtained by using the National Geophysical Data Center's terrain database with 5-min ocean depth data and land elevations. Other departures from Babkin et al. (2003) seen in Supplementary Table A2 were not used, e.g., the volume of permafrost reported by Trenberth et al. (2007) is markedly lower than that reported by the other three global budgets.

6 Conclusion

The work done by exergy transformed over time and concentrated within the spatial and temporal boundaries of the global system is responsible for the order and organization observed in wind and water systems found within those boundaries. One of the main products of this study is to provide updated values for the wind and water flows of the Geobiosphere, so that they can be used to create more accurate and consistent emergy evaluations. The numbers presented here are self-consistent and have been calculated using common accounting

rules and perspectives given in the article, such as the inclusion of resources necessary to quantify emergy storages accumulated from the past use of resources yet necessary to support present flows. An overall plot of the transformities of the wind and water flows evaluated in this study is given as a global comparison plot (Figure 4). Wind and water flows are defined here with functional definitions, requiring specific biophysical processes and the underling exergy transformations with the emergy of the products that they deliver explaining the order and organization observed within the global system. Furthermore, in this study, we propose the use of a meta framework for the determination of transformities. This framework extends the spatial and temporal boundaries for systems that include components that require additional development times to produce important energy flows in the system under analysis. Many ecosystems include components, such as plant biomass and the accumulated knowledge of workers and many others in social systems. The consideration of this larger window to capture the essential exergy inputs to key system components may result in major changes to the results of some emergy analyses. We have presented a functional approach to the accounting problem of determining the emergy required for any product or process using a meta framework or filter for recognizing important inflows that provides an updated analysis of the inputs from the wind and water flows of the global system. Emergy evaluations are accounting problems and the accounting rules and body of values required to determine accurate transformities of emergy flows are key pieces of information to allow emergy accounts to be accurately constructed. These flows are self-consistent and are clarified, extended, and further evaluated in this article. Also, they are consistent with a new USEPA database that provides the potential to create better emergy evaluations throughout the world. From this perspective, the order and organization observed in a system in the present depends solely on the biophysical processes operating within these spatial and temporal boundaries or concentrated there from other spatial and temporal realms and on the useful work (emergy) that they deliver to the organizing processes within a system.

Data availability statement

The original contributions presented in the study are included in the article/Supplementary Materials, further inquiries can be directed to the corresponding author.

Author contributions

DC: Writing–review and editing, writing–original draft, visualization, validation, supervision, software, resources, project administration, methodology, investigation, funding acquisition, formal analysis, data curation, and conceptualization. HL: Writing–review and editing.

Funding

The authors declare that financial support was received for the research, authorship, and/or publication of this article. Partially funded by the United States Environmental Protection Agency, Narragansett, RI, USA, and the Project of the National Natural Science Foundation of China (31770487).

Acknowledgments

This work was begun while DC was an employee of the USEPA, but the major portion of the work was completed during the 3 years after DC retired in 2019. Most of this time was during the assault of COVID-19 on the world system. Initially, DC was a reviewer and later a participant in the recent USEPA database publication on emergy characterization factors https://www.epa.gov/water-research/uev-library, which is now completed after about 9 years in development. Part of this time was spent in resolving and correcting errors and the remainder in the careful US government review process for major publications. Samuel Arden was an author in later versions of the USEPA Emergy Characterization Factors report, and he provided the reference to the article by Boville and Bretherton (2003) used to better understand atmospheric systems described in this report. Xin (Cissy) Ma, Mark T. Brown, Christopher De Vilbiss, and Wesley Ingwersen were also contributors to this work through their work on the USEPA report.

Conflict of interest

The authors declare that the research was conducted in the absence of any commercial or financial relationships that could be construed as a potential conflict of interest.

Publisher's note

Supplementary material

The Supplementary Material for this article can be found online at: https://www.frontiersin.org/articles/10.3389/fenrg.2024.1392634/full#supplementary-material

References

Adler, R. F., Huffman, G. J., Chang, A., Ferraro, R., Xie, P. P., Janwiak, J., et al. (2003). The version-2 global precipitation climatology project (GPCP) monthly precipitation analysis (1979-present). *J. Hydrometeorol.* 4, 1147–1167. doi:10.1175/1525-7541(2003)004<1147:tvgpcp>2.0.co;2

Archer, C. L., and Jacobson, M. Z. (2005). Evaluation of global wind power. *J. Geophys. Res.* 110, D12110. doi:10.1029/2004jd005462

Asgharipour, M. R., Amiri, Z., and Campbell, D. E. (2020). Evaluation of the sustainability of four greenhouse vegetable production ecosystems based on an analysis of emergy and social characteristics. *Ecol. Model.* 424 (2020), 109021. doi:10.1016/j.ecolmodel.2020.109021

Babkin, V. J., Vuglinsky, V. S., and Klige, R. K. (2003). "The Earth and its physical features," in *World Water Resources at the Beginning of the Twenty-First Century*. Editors I. A. Shiklomanov Rodda, et al. (Cambridge, United Kingdom: Cambridge University Press), 1–18.

Berrios, F., Campbell, D. E., and Ortiz, M. (2018). Emergy-based indicators for evaluating ecosystem health: a case study of three benthic ecosystem networks influenced by coastal upwelling in northern Chile (SE Pacific coast). *Ecol. Indic.* 95, 379–393. doi:10.1016/j.ecolind.2018.07.055

Bloom, A. A., Exbrayat, J.-F., van der Velde, I. R., Feng, L., and Williams, M. (2016). The decadal state of the terrestrial carbon cycle: global retrievals of terrestrial carbon allocation, pools, and residence times. *PNAS* 113 (5), 1285–1290.

Boville, B. A., and Bretherton, C. S. (2003). Heating and kinetic energy dissipation in the NCAR community atmosphere model. *J. Clim.* 16, 3877–3887. doi:10.1175/1520-0442(2003)016<3877:hakedi>2.0.co;2

Boynton, W. (1975). *Energy basis of a coastal region: franklin county and apalachicola bay, Florida*. Gainesville: University of Florida. Ph.D. dissertation. Environmental Engineering Sciences.

Brierley, C. M., and Fedorov, A. V. (2011). Tidal mixing around Indonesia and the Maritime continent: implications for paleoclimate simulations. *Geophys. Res. Lett.* 38, L24703. doi:10.1029/2011GL050027

Brown, M. T. (2005). "Areal empower density, unit emergy values, and emformation, pp. 1-15," in *Emergy synthesis 3. Proceedings of the third biennial emergy analysis conference. Center for environmental policy*. Editors M. T. Brown, E. Bardi, D. E. Campbell, V. Comar, S.-L. Huang, T. Rydberg, et al. (Gainesville: University of Florida).

Brown, M. T., and Brandt-Williams, S. L. (2011). ""Quantus" emergy, pp. 1-8," in *Emergy synthesis 6. Proceedings of the sixth biennial emergy analysis conference. Center for environmental policy*. Editors M. T. Brown, S. Sweeney, D. E. Campbell, S.-L. Huang, E. Ortega, T. Rydberg, et al. (Gainesville: University of Florida).

Brown, M. T., Campbell, D. E., De Vilbiss, C., and Ulgiati, S. (2016). The geobiosphere emergy baseline: a synthesis. *Ecol. Model.* 339, 92–95. doi:10.1016/j.ecolmodel.2016.03.018

Brown, M. T., and Herendeen, R. A. (1996). Embodied energy analysis and emergy analysis: a comparative view. *Ecol. Econ.* 19, 219–235. doi:10.1016/s0921-8009(96)00046-8

Brown, M. T., and Ulgiati, S. (2016). Assessing the global environmental sources driving the geobiosphere: a revised emergy baseline. *Ecol. Model.* 339, 126–132. doi:10.1016/j.ecolmodel.2016.03.017

Campbell, D. E. (2000). Using energy systems theory to define, measure, and interpret ecological integrity and ecosystem health. *Ecosyst. Health* 6 (3), 181–204. doi:10.1046/j.1526-0992.2000.006003181.x

Campbell, D. E. (2001). Proposal for including what is valuable to ecosystems in environmental assessments. *Environ. Sci. Technol.* 35 (14), 2867–2873. doi:10.1021/es001818n

Campbell, D. E. (2003). "A note on the uncertainty in estimates of transformities based on global water budgets," in *Emergy synthesis 2. Proceedings of the second biennial emergy analysis conference. Center for environmental policy*. Editors M. T. Brown, H. T. Odum, D. Tilley, and S. Ulgiati (Gainesville: University of Florida), 349–353.

Campbell, D. E. (2013). Keeping the books for the environment and society: the unification of emergy and financial accounting methods. *J. Environ. Account. Manag.* 1, 25–41. doi:10.5890/jeam.2012.01.003

Campbell, D. E. (2016). Emergy baseline for the Earth: a historical review of the science and a new calculation. *Ecol. Model.* 339, 96–125. doi:10.1016/j.ecolmodel.2015.12.010

Campbell, D. E., Brandt-Williams, S. L., and Cai, T. T. (2005b). "Current technical problems in emergy analysis," in *Emergy synthesis 3. Proceedings of the third biennial emergy analysis conference. Center for environmental policy*. Editors M. T. Brown, E. Bardi, D. E. Campbell, V. Comar, S.-L. Huang, T. Rydberg, et al. (Gainesville: University of Florida), 143–157.

Campbell, D. E., Brandt-Williams, S. L., and Meisch, M. E. A. (2005a). *Environmental accounting using emergy: evaluation of the state of West Virginia*. Washington, DC: USEPA Project Report. EPA/600/R-05/006.

Campbell, and Erban, (2017). Carbon dioxide utilization using chlorella microalgae. *Emergy Synthesis*. Available at: www.emergysociety.com

Campbell, D. E., Galloway, W. B., and Pesch, G. G. (1998). "Appreciative Inquiry: a mechanism for maximizing empower in social systems," in *Proceedings of the 42nd annual meeting of the international society for systems sciences*. Editors J. K. Allen, and J. Wilby (Atlanta GA). ISBN 0-9664183-0-1.

Campbell, D. E., Lu, H., and Walker, H. A. (2014a). Relationships among the energy, emergy, and money flows of the United States from 1900 to 2011. *Front. Energy Res. Hypothesis Theory Article* 2. doi:10.3389/fenrg.2014.00041

Campbell, D. E., and Lu, H. F. (2009). "The emergy basis for formal education in the United States," in *Emergy synthesis 5. Proceedings of the fifth biennial emergy analysis conference. Center for environmental policy*. Editors M. T. Brown, S. Sweeney, D. E. Campbell, S.-L. Huang, E. Ortega, T. Rydberg, et al. (Gainesville: University of Florida), 467–484.

Campbell, D. E., and Lu, H. F. (2014b). Emergy evaluation of formal education in the United States: 1870 to 2011. *Systems* 2 (3), 328–365. doi:10.3390/systems2030328

Campbell, D. E., Lu, H. F., Knox, G. A., and Odum, H. T. (2009). Maximizing empower on a human-dominated planet: the role of exotic *Spartina*. 2009. *Ecol. Eng.* 35, 463–486. doi:10.1016/j.ecoleng.2008.07.022

Campbell, D. E., Lu, H. F., and Kolb, K. (2011). "Emergy evaluation of educational attainment of in the United States," in *Emergy synthesis 6. Proceedings of the sixth biennial emergy analysis conference. Center for environmental policy*. Editors M. T. Brown, S. Sweeney, D. E. Campbell, S.-L. Huang, E. Ortega, T. Rydberg, et al. (Gainesville: University of Florida), 483–500.

Campbell, D. E., and Ohrt, A. (2009). *Environmental accounting using emergy: evaluation of Minnesota*. Washington, DC: USEPA Project Report, 138. EPA 600/R-09/002.

Dai, A., and Trenberth, K. E. (2002). Estimates of freshwater discharge from continents: latitudinal and seasonal variations. *J. Hydrometeorol.* 3, 660–687. doi:10.1175/1525-7541(2002)003<0660:eofdfc>2.0.co;2

De Vilbiss, C., Arden, S., Brown, M. T., Campbell, D. E., Cissy, M., Ingwersen, W., et al. (2024). *The unit emergy value (UEV) library and characterization factor library for characterizing environmental support in life cycle assessment*. EPA/600/R-23/202.

De Vilbiss, C., and Brown, M. T. (2015) "The emergy characterization factor library for characterizing environmental support in life cycle assessment. Final technical report to the USEPA," in *Center for environmental policy, school of sustainable infrastructure and environment, college of engineering*. Gainesville, FL: University of Florida.

De Vilbiss, C., Brown, M. T., Seigel, E., and Arden, S. (2016). Computing the geobiosphere emergy baseline: a novel approach. *Ecol. Model.* 339, 133–139. doi:10.1016/j.ecolmodel.2016.05.002

Economics (2004). *The analysis of a major interface*. Geneva: R. Leimgruber, 257–276.

Egbert, G. D., and Ray, R. D. (2000). Significant dissipation of tidal energy in the deep ocean inferred from satellite altimeter data. *Nature* 405, 775–778. doi:10.1038/35015531

Ellsaesser, H. W. (1969). A climatology of epsilon (atmospheric dissipation). *Mon. Weather Rev.* 97 (6), 415–423. doi:10.1175/1520-0493(1969)097<0415:acoed>2.3.co;2

Erb, K.-H., Fetzel, T., Plutzar, c., Kastner, T., Lauk, C., Mayer, A., et al. (2016). Biomass turnover time in terrestrial ecosystems halved by land use. *Nat. Geosci.* 9, 674–678. Supplementary information. doi:10.1038/NGEO2782

Garber, J. M., Maurya, S., Hernandez, J.-A., Duncan, M. S., Zeng, L., Zhang, H. L., et al. (2018). Multidisciplinary constraints on the abundance of diamond and eclogite in the cratonic lithosphere. *Geochem. Geophys. Geosystems* 19, 2062–2086. doi:10.1029/2018GC007534

Garratt, J. R. (1977). Review of drag coefficients over oceans and continents. *Mon. Weather Rev.* 105, 915–929. doi:10.1175/1520-0493(1977)105<0915:rodcoo>2.0.co;2

Haggerty, S. E. (1999). A diamond trilogy: superplumes, supercontinents, and supernovae. *Science* 285, 851–860. doi:10.1126/science.285.5429.851

Huang, B. Y., and Mehta, V. M. (2010). Influences of freshwater from major rivers on global ocean circulation and temperatures in the MIT ocean general circulation model. *Adv. Atmos. Sci.* 27 (3), 455–468. doi:10.1007/s00376-009-9022-6

Janse, A. J. A. (2007). Global rough diamond production since 1870. *GEMS GEMOLOGY* 43 (2), 98–119. © 2007 Gemological Institute of America. doi:10.5741/gems.43.2.98

Kangas, P. C. (2004). *Ecological engineering, principles and practice*. Boca Raton, FL: Lewis Publishers, A CRC Press Company.

Kara, A. B., Wallcraft, A. J., Metzger, E. J., Hurlburt, H. E., and Fairall, C. W. (2007). Wind stress drag coefficient over the global ocean*. *J. Clim.* 20, 5856–5864. doi:10.1175/2007jcli1825.1

Kerr, R. A. (2013a). The deep Earth machine is coming together. *Science* 340, 22–24. doi:10.1126/science.340.6128.22

Kerr, R. A. (2013b). Geophysical exploration linking deep earth and backyard geology. *Science* 340, 1283–1285. doi:10.1126/science.340.6138.1283

Le Corre, O., and Truffet, L. (2012). Exact computation of emergy based on a mathematical reinterpretation of the rules of emergy algebra. *Ecol. Model.* 230, 101–113. doi:10.1016/j.ecolmodel.2011.12.018

Le Corre, O., and Truffet, L. (2015). Emergy paths computation from interconnected energy system diagram. *Ecol. Model.* 313, 181–200. doi:10.1016/j.ecolmodel.2015.06.030

Lee, S. (2014). Resource pulses can increase power acquisition of an ecosystem. *Ecol. Model.* 271, 21–31. doi:10.1016/j.ecolmodel.2012.11.028

Li, L. J., Lu, H. F., Campbell, D. E., and Ren, H. (2010). Emergy algebra: improving matrix methods for calculating transformities. *Ecol. Model.* 221, 411–422. doi:10.1016/j.ecolmodel.2009.10.015

Lotka, A. J. (1922a). Contribution to the energetics of evolution. *Proc. Natl. Acad. Sci.* 8, 147–151. doi:10.1073/pnas.8.6.147

Lotka, A. J. (1922b). Natural selection as a physical principle. *Proc. Natl. Acad. Sci.* 8, 151–154. doi:10.1073/pnas.8.6.151

Marcinek, J. (2007). "Hydrological cycle and water balance – a global survey," in *Enough water for all? Wissenschaftliche Auswertungen*. Editors J. L. Lozan, H. Grassl, P. Hupfer, L. Menzel, and C.-D. Schönwiese (Hamburg), 33–37. Available at: www.klima-warnsignale.uni-hamburg.de.

Megonigal, J. P., Conner, W. H., Kroeger, S., and Sharitz, R. R. (1997). Aboveground production in southeastern floodplain forests: a test of the subsidy-stress hypothesis. *Ecology* 78 (2), 370–384. doi:10.1890/0012-9658(1997)078[0370:apisff]2.0.co;2

Morgan, W. J. (1971). Convection plumes in the lower mantle. *Nature* 230 (42), 42–43. doi:10.1038/230042a0

Odum, E. P., Finn, J. T., and Franz, E. H. (1979). Perturbation theory and the subsidy-stress gradient. *Bioscience* 29 (6), 349–352. doi:10.2307/1307690

Odum, H. T. (1971). *Environment, power, and society*. New York, NY: John Wiley &Sons.

Odum, H. T. (1983). *Ecological and general systems: an introduction to systems ecology*. Revised edition. Niwot, CO: Univ. Colorado Press, 644.

Odum, H. T. (1904). *Ecological and general systems: an introduction to systems ecology*. 2nd edn. Niwot, CO: Univ. Colorado Press, 644.

Odum, H. T. (1986). "Enmergy* in ecosystems," in *Ecosystem theory and application. For environmental monographs and symposia*. Editor N. Polunin (John Wiley and Sons, Ltd), 337–369.

Odum, H. T. (1988). Self-organization, transformity, and information. *New Ser.* 242 (4882), 1132–1139. doi:10.1126/science.242.4882.1132

Odum, H. T. (1996). *Environmental accounting: emergy and environmental decision making*. New York, NY: John Wiley and Sons, 370p.

Odum, H. T. (2000a). *Handbook of emergy evaluation. Folio #2. Emergy of global processes. Center for environmental policy, environmental engineering sciences*. Gainesville, FL: University of Florida, 30p.

Odum, H. T. (2000b) "Emergy evaluation of salmon pen culture," in *IIFET 2000 proceedings*. Available at: https://ir.library.oregonstate.edu/downloads/4t64gp065.

Odum, H. T. (2007). *Environment, power, and society for the twenty-first century*. New York, NY: Columbia University Press.

Odum, H. T., and Odum, E. C. (2000). *Modeling for all scales: an introduction to system simulation*. Cambridge, MA, USA: Academic Press.

Odum, H. T., Odum, E. C., and Brown, M. T. (1998a). *Environment and society in Florida*. Boca Raton, FL: Lewis Publishers. Lucie Press.

Odum, H. T., Romitelli, S., and Tighe, R. (1998b). "Evaluation overview of the cache river and black swamp in Arkansas. Final report on contract #DACW39-94-K-0300," in *Energy systems perspectives for cumulative impacts assessment between waterways experiment station, U.S. Dept. Of the army, vicksburg, Mississippi and the university of Florida, center for environmental policy, environmental engineering sciences* (Gainesville, FL: University of Florida), 128.

Olson, D. M., Dinerstein, E., Wikramanayake, E. D., Burgess, N. D., Powell, G. V. N., Underwood, E. C., et al. (2001). Terrestrial ecoregions of the world: a new map of life on Earth. *Bioscience* 51 (11), 933–938. doi:10.1641/0006-3568(2001)051[0933:teotwa]2.0.co;2

Rodell, M., Beaudoing, H. K., L'ecuyer, T. S., Olson, W. S., Famiglietti, J. S., Houser, P. R., et al. (2015). The observed state of the water cycle in the early twenty-first century. *J. Clim.* 28, 8289–8318. doi:10.1175/jcli-d-14-00555.1

Romitelli, M. S. (1997). *Emergy analysis of watersheds*. Gainesville, FL: University of Florida. PhD. Dissertation.

Schlesinger, W. H., and Jasechko, S. (2014). Transpiration in the global water cycle. *Agric. For. Meteorology* 189-190, 115–117. doi:10.1016/j.agrformet.2014.01.011

Scienceman, D. M. (1987). Energy and emergy. *Environmental Economics*. Editors G. Pillet, and T. Murota 257–276 (Geneva: Roland Leimgruber).

Smith, R. B., Jordan, M., Steinberger, B., Puskas, C. M., Farrell, J., Waite, G. P., et al. (2009). Geodynamics of the Yellowstone hotspot and mantle plume: seismic and GPS imaging, kinematics, and mantle flow. *J. Volcanol. Geotherm. Res.* 188, 26–56. doi:10.1016/j.jvolgeores.2009.08.020

Szargut, J., Morris, D. R., and Steward, F. R. (1988). *Exergy analysis of thermal, chemical, and metallurgical processes*. New York, NY: Hemisphere.

Tapscott, D., and Tapscott, A. (2016). *Blockchain revolution*. LLC., New York, New York: Penguin Random House.

Tennenbaum, S. E. (1988) "Network energy expenditures for subsystem production,". Gainesville, FL: University of FL, 131. (CFW-88-08).

Tilley, D. (2014). Exploration of Odum's dynamic emergy accounting rules for suggested refinements. *Ecol. Model.* 279, 36–44. doi:10.1016/j.ecolmodel.2014.01.031

Tilley, D. (2015). Transformity dynamics related to maximum power for improved emergy yield estimations. *Ecol. Model.* 315, 96–107. doi:10.1016/j.ecolmodel.2014.10.035

Tilley, D. R., Agostinho, F., Campbell, E., Ingwersen, W., Lomas, P., Winfrey, B., et al. (2012). The ISAER transformity database. *Int. Soc. Adv. Emergy Res.* Available at: http://www.pnas.org/lookup/suppl/10.1073/pnas.1515160113/-/DCSupplemental.

Tokinaga, H., and Xie, S.-P. (2009). Ocean tidal cooling effect on summer sea fog over the Okhotsk Sea. *J. Geophys. Res.* 114, D14102. doi:10.1029/2008JD011477

Wiin-Nielsen, A., and Chen, T. (1993). *Fundamentals of atmospheric energetics*. NY: Oxford Press, 376.

Frontiers in
Energy Research

Advances and innovation in sustainable, reliable and affordable energy

Explores sustainable and environmental developments in energy. It focuses on technological advances supporting Sustainable Development Goal 7: access to affordable, reliable, sustainable and modern energy for all.

Discover the latest Research Topics

See more →

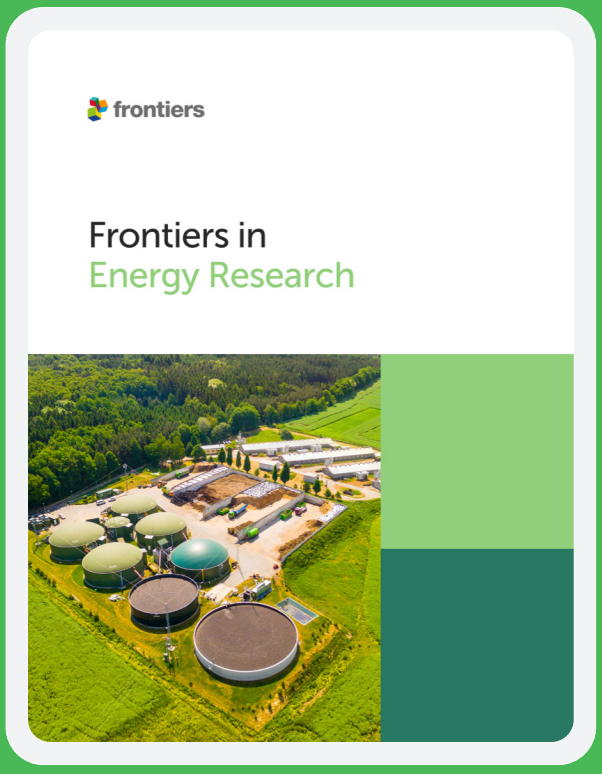

Frontiers

Avenue du Tribunal-Fédéral 34
1005 Lausanne, Switzerland
frontiersin.org

Contact us

+41 (0)21 510 17 00
frontiersin.org/about/contact